Angular analysis of $\Lambda b \to \Lambda(1520)\ \mu^+\ \mu$ decays with the LHCb detector

Felicia Volle

université PARIS-SACLAY

Angular analysis of $\Lambda_b^0 \to \Lambda(1520)\mu^+\mu^-$ decays with the LHCb detector

Analyse angulaire des désintégrations $\Lambda_b^0 \to \Lambda(1520)\mu^+\mu^-$ avec le détecteur LHCb

Thèse de doctorat de l'université Paris-Saclay

École doctorale n° 576, Particules, Hadrons, Énergie et Noyau: Instrumentation, Imagerie, Cosmos et Simulation (PHENIICS)
Spécialité de doctorat: Physique des particules
Graduate School : Physique. Référent : Faculté des sciences d'Orsay

Thèse préparée dans l'unité de recherche **IJCLab** (Université Paris-Saclay, CNRS), sous la direction de **Yasmine Sara AMHIS**, Chargée de recherche

Thèse soutenue à Paris-Saclay, le 15 Septembre 2023, par

Felicia Carolin VOLLE

Composition du jury

Membres du jury avec voix délibérative

Achille STOCCHI Professeur, Université Paris-Saclay	Président
Lesya SHCHUTSKA Professeure assistante (HDR), École polytechnique fédérale de Lausanne	Rapporteure & Examinatrice
Gianluca INGUGLIA Docteur (HDR), Österreichische Akademie der Wissenschaften	Rapporteur & Examinateur
Luca SILVESTRINI Professeur, INFN Rome	Examinateur
Tim GERSHON Professeur, University of Warwick	Examinateur

THESE DE DOCTORAT

NNT : 2023UPASP094

université PARIS-SACLAY

ÉCOLE DOCTORALE
Particules, hadrons, énergie et noyau : instrumentation, imagerie, cosmos et simulation (PHENIICS)

Titre: Analyse angulaire des désintégrations $\Lambda_b^0 \to \Lambda(1520)\mu^+\mu^-$ avec le détecteur LHCb

Mots clés: Physique de la saveur, LHCb, physique du B, analyse angulaire, baryons, désintégrations rares, Run 3

Résumé:

Les transitions $b \to s\ell^+\ell^-$ forment un laboratoire très intéressant pour rechercher la Nouvelle Physique (NP) de manière indirecte. En effet, des contributions de NP pourraient entrainer des déviations importantes par rapport aux prédictions du Modèle Standard (MS). Des mesures existantes d'observables angulaires et de rapports d'embranchement dans les désintégrations de $b \to s\mu^+\mu^-$ montrent des écarts consistants par rapport au MS.

Dans cette thèse, une analyse angulaire des désintégrations de $\Lambda_b^0 \to \Lambda(1520)\mu^+\mu^-$ est effectuée pour la première fois en utilisant les ensembles de données du Run 1 et 2 enregistrés par l'expérience LHCb. Les observables angulaires $A^{\ell}_{FB,3/2}$ et S_{1cc} sont mesurées dans cinq régions de la masse invariante au carré des dimuons q^2.

Le modèle d'ajustement angulaire a été développé pour la première fois incluant la résonance $\Lambda(1520)$, les contributions de résonances Λ^* avec un spin-1/2 et les effets d'interférence non-négligeables entre les trois résonances Λ^*. Les mesures de $A^{\ell}_{FB,3/2}$ dans les modes de contrôle J/ψ et $\psi(2S)$ sont compatibles avec zéro à moins d'un écart type, comme attendu. Les observables angulaires de la région non-résonante dans q^2 sont maintenues cachées dans cette thèse.

Par ailleurs, les désintégrations $B^+ \to K^+J/\psi(\to e^+e^-)$ et $B^+ \to K^+\psi(2S)(\to e^+e^-)$ ont été étudiées avec les données du Run 3 collectées en 2022. Le but de cette étude est d'avoir un aperçu des données issues du détecteur "upgradé" et une évaluation de l'efficacité des électrons dans le Run 3. Les nombres de particules $\psi(2S) \to e^+e^-$ issues des désintégrations secondaires et de $B^+ \to K^+\psi(2S)(\to e^+e^-)$ ont été déterminés sur les données Run 3 et comparés au mode contenant un J/ψ. De plus, les distributions des variables pertinentes dans la désintégration $B^+ \to K^+J/\psi(\to e^+e^-)$ sont comparées entre des échantillons de simulation et les données soustraites du bruit de fond.

université PARIS-SACLAY

ÉCOLE DOCTORALE
Particules, hadrons, énergie et noyau : instrumentation, imagerie, cosmos et simulation (PHENIICS)

Title: Angular analysis of $\Lambda_b^0 \to \Lambda(1520)\mu^+\mu^-$ decays with the LHCb detector

Keywords: Flavour Physics, LHCb, B physics, Angular analysis, Baryons, Rare Decays, Run 3

Abstract:

New Physics (NP) searches via $b \to s\ell^+\ell^-$ transitions are powerful methods since NP contributions could cause sizeable deviations from the Standard Model (SM) predictions. Previous measurements of angular observables and branching fractions in $b \to s\mu^+\mu^-$ decays show consistent deviations with respect to the SM.

In this thesis, an angular analysis of $\Lambda_b^0 \to \Lambda(1520)\mu^+\mu^-$ decays is performed for the first time using the full Run 1 and 2 datasets collected by the LHCb experiment. The angular observables $A_{FB,3/2}^{\ell}$ and S_{1cc} are attempted to be measured in five bins of the dimuon invariant mass squared q^2. This is the first attempt to write a complete angular model, including the $\Lambda(1520)$ resonance, the spin-1/2 Λ^* resonance contributions and the non-negligible interference effects between the three Λ^* resonances. The measurements of $A_{FB,3/2}^{\ell}$ in the J/ψ and $\psi(2S)$ control modes are compatible with zero within one standard deviation, as expected. The angular observables in the non-resonant q^2 region are kept blind in the thesis.

Furthermore, the $B^+ \to K^+J/\psi(\to e^+e^-)$ and $B^+ \to K^+\psi(2S)(\to e^+e^-)$ decays have been studied with Run 3 data recorded in 2022. The aim of this study is to have a first look at the data taken with the upgraded detector and to understand the electron efficiencies in Run 3. The yields of secondary $\psi(2S) \to e^+e^-$ and $B^+ \to K^+\psi(2S)(\to e^+e^-)$ have been determined for the first time with Run 3 data and compared to the J/ψ yields. In addition, a comparison of relevant distribution in the simulation samples and the background-subtracted data has been performed using $B^+ \to K^+J/\psi(\to e^+e^-)$ decays.

Contents

Synthèse en français

Le Modèle Standard (MS) de la physique des particules est une théorie très puissante puisqu'elle permet de prédire précisément un grand nombre de phénomènes en physique des particules, comme par exemple la valeur du moment magnétique anormal du muon avec une précision de 10^{-11} [1, 2]. En revanche, il y a des phénomènes qui ne sont pas explicables par le MS. Des exemples sont la matière noire qui n'est pas incluse, l'asymétrie détectée entre la matière et l'antimatière dans notre univers ou les oscillations des neutrinos. Ces lacunes sont compensées par des extensions du MS, que l'on appelle la Nouvelle Physique (NP).

Les transitions de $b \to s\ell^+\ell^-$ sont un laboratoire unique pour la recherche de la NP, puisqu'elles sont sensibles à des particules de NP qui ont des masses jusqu'à l'échelle du TeV/c^2 [3]. Pour exprimer la NP d'une façon indépendante de modèles spécifiques et pour pouvoir comparer les modèles facilement avec les résultats expérimentaux, il existe la théorie effective des champs dans laquelle le hamiltonien des transitions $b \to s\ell^+\ell^-$ s'exprime comme

$$\mathcal{H}_{\text{eff}}(b \to s\ell^+\ell^-) = -\frac{4G_F}{\sqrt{2}} V_{tb}V_{ts}^* \sum_i (\mathcal{C}_i\mathcal{O}_i + \mathcal{C}_i'\mathcal{O}_i') + h.c.\,. \tag{1}$$

Les coefficients de Wilson $\mathcal{C}_i$ contiennent la partie de haute énergie de l'interaction. En supposant que la NP est présente à haute énergie, ce sont ceux-là qui recevraient des contributions de NP. Traditionnellement, ces déviations sont écrites en fonction de $\mathcal{C}_i^{\text{NP}} = \mathcal{C}_i - \mathcal{C}_i^{\text{MS}}$. La partie hadronique est incluse dans les opérateurs $\mathcal{O}_i$. Dans le rapport d'embranchement, ils sont exprimés dans des facteurs de forme. Plusieurs méthodes existent pour les calculer.

Cette thèse est dédiée à l'analyse angulaire d'une désintégration de $b \to s\ell^+\ell^-$, à savoir $\Lambda_b^0 \to pK^-\mu^+\mu^-$. Les diagrammes dominants de cette désintégration sont illustrés dans la Fig. 1. La motivation de cette analyse est de vérifier les déviations des observ-

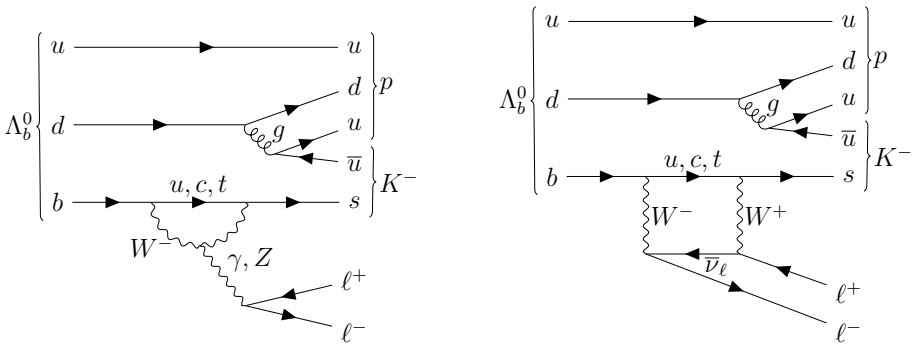

Figure 1 – Deux des diagrams dominates de la désintégration $\Lambda_b^0 \to pK^-\ell^+\ell^-$.

ables angulaires mesurées dans des désintégrations rares des mésons b par une nouvelle désintégration du hadron b Λ_b^0. Les désintégrations à l'arbre via une résonance J/ψ ou $\psi(2S)$ sont les modes de contrôle de cette analyse grâce à leurs efficacités supérieures. Une analyse complète en amplitude a pu être réalisée dans la désintégration à l'arbre, $\Lambda_b^0 \to pK^- J/\psi(\to \mu^+\mu^-)$ [4]. Dans cette analyse, le spectre de masse invariante pK^- a été mesuré et est celui de la Fig. 2. Le spectre de masse indique la présence de la résonance abondante et étroite $\Lambda(1520)$. A cause du manque d'événements dans le mode rare, le focus de l'analyse est mis sur la résonance $\Lambda(1520)$, puisqu'elle peut être séparée le plus facilement des autres en gardant la majorité des événements.

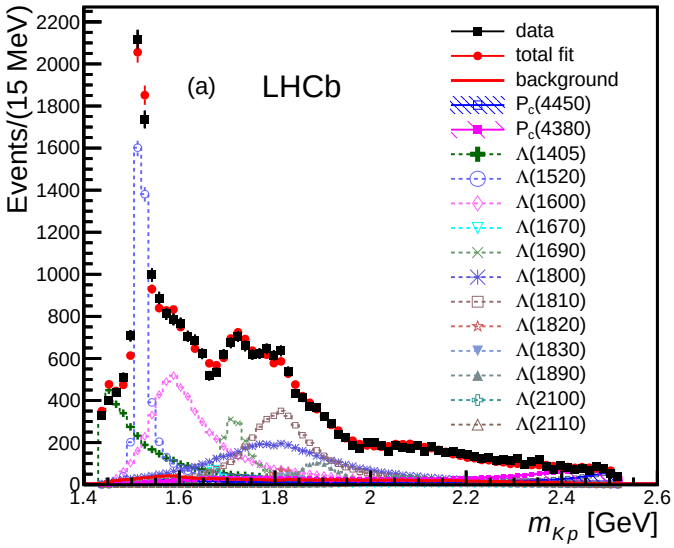

Figure 2 – Résonances Λ^* et pentaquark mesurés dans le spectre de masse invariante pK^- par l'analyse en amplitudes de la désintégration $\Lambda_b^0 \to pK^- J/\psi(\to \mu^+\mu^-)$ [4].

En plus, des prédictions du rapport d'embranchement différentiel et des observables angulaires existent pour cette résonance [5] et sont formulées comme

$$\begin{aligned}
&\frac{8\pi}{3}\frac{d^4\Gamma}{dq^2 d\cos\theta_\ell d\cos\theta_p d\phi} \\
&\quad = \cos^2\theta_p\left(L_{1c}\cos\theta_\ell + L_{1cc}\cos^2\theta_\ell + L_{1ss}\sin^2\theta_\ell\right) \\
&\qquad + \sin^2\theta_p\left(L_{2c}\cos\theta_\ell + L_{2cc}\cos^2\theta_\ell + L_{2ss}\sin^2\theta_\ell\right) \\
&\qquad + \sin^2\theta_p\left(L_{3ss}\sin^2\theta_\ell\cos^2\phi + L_{4ss}\sin^2\theta_\ell\sin\phi\cos\phi\right) \\
&\qquad + \sin\theta_p\cos\theta_p\cos\phi(L_{5s}\sin\theta_\ell + L_{5sc}\sin\theta_\ell\cos\theta_\ell) \\
&\qquad + \sin\theta_p\cos\theta_p\sin\phi(L_{6s}\sin\theta_\ell + L_{6sc}\sin\theta_\ell\cos\theta_\ell).
\end{aligned} \tag{2}$$

Les angles de désintégrations apparaissant dans Éq. 2 sont définis dans la base d'hélicité, comme montré dans la Fig. 3.

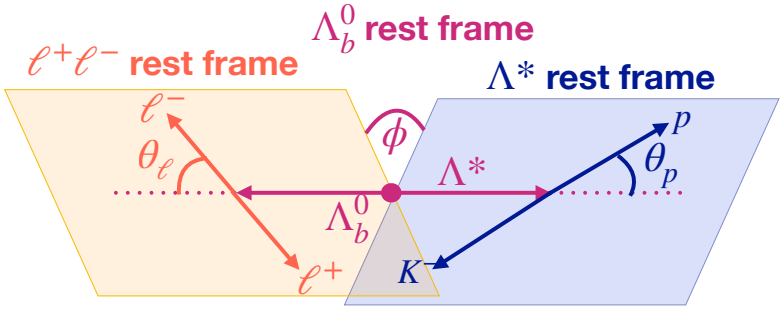

Figure 3 – Définition des angles de désintégration du $\Lambda_b^0 \to pK^-\mu^+\mu^-$.

Les observables angulaires sont construites à l'aide des coefficients angulaires des désintégrations du Λ_b^0, L_i, et du $\overline{\Lambda}_b^0$, $\bar{L}_i$. La somme des deux coefficients est appelée symtrie de CP, définie comme

$$S_i = \frac{L_i + \bar{L}_i}{d(\Gamma + \bar{\Gamma})/dq^2}, \tag{3}$$

Particulièrement sensible aux contributions de NP, l'asymétrie leptonique avant-arrière peut être exprimée comme

$$A_{FB}^{\ell} = \frac{3}{2}\frac{L_{1c} + 2L_{2c}}{L_{1cc} + 2L_{1ss} + 2L_{2cc} + 4L_{2ss} + 2L_{3ss}}. \tag{4}$$

La moyenne de A_{FB}^{ℓ} et $\bar{A}_{FB}^{\ell}$ va être mesurée. Des prédictions pour les observables angulaires sont obtenues en se basant sur différentes prédictions des facteurs de forme. Les facteurs de forme du modèle des quarks non-relativiste (NRQM) sont prédits en

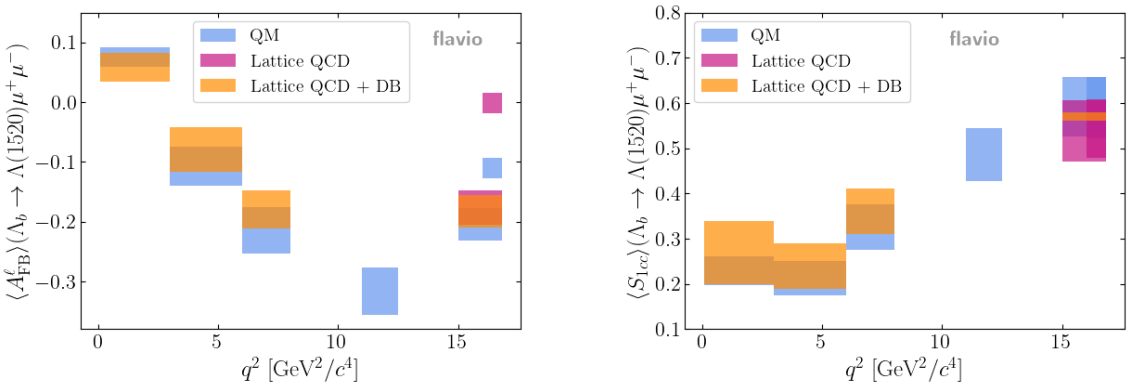

Figure 4 – Prédictions des observables angulaires A_{FB}^{ℓ} et S_{1cc} avec différents facteurs de forme [6–8], en fonction de q^2.

Ref. [6]. Des prédictions de la QCD sur réseau existent (Lattice QCD) [7] dans la région de $q^2 \in [16, 16.8]\,\text{GeV}^2/c^4$, qui ont été extrapolées dans la région $q^2 \in [15, 16.8]\,\text{GeV}^2/c^4$. La prédiction de la QCD sur réseau conjointe aux limites dispersives permet de prédire les observables dans le q^2 bas [8]. Les observables angulaires dans les différentes régions en q^2 sont présentées dans la Fig. 4. Malgré les différents modèles, les prédictions sont cohérentes entre elles dans les régions de q^2 visées à être mesurées.

Dans cette thèse, toutes les données enregistrées par l'expérience LHCb entre 2011 et 2018 à une énergie dans centre de masse de 7, 8 et 13 TeV sont analysées. Cela correspond à une luminosité intégrée de $9.1\,\text{fb}^{-1}$. Les observables angulaires A_{FB}^{ℓ} et S_{1cc} sont prévues d'être analysées dans cinq régions de q^2, notamment [0.1, 3], [3, 6], [6, 8], [11, 12.5] et [1.1, 6] GeV^2/c^4.

La désintégration du signal a été sélectionnée et les contributions du bruit de fond ont été étudiées dans le mode rare et les modes de contrôle. Le bruit de fond originaires des combinaisons aléatoires a été supprimé par un classificateur multivarié. Les bruits de fond restants ont soit été enlevés par un véto, soit sont modélisés dans l'ajustement de la masse invariante de $pK^-\mu^+\mu^-$. L'ajustement est montré dans la figure 5 pour le mode de contrôle J/ψ et une région rare en q^2. Le signal est modélisé par une fonction Hypatia 2 [9], dont la forme est fixée par rapport à l'ajustement aux simulations LHCb. Le même modèle est pris pour décrire le Ξ_b. Le bruit de fond des combinaisons aléatoires est décrit par une exponentielle. La forme des contributions du bruit de fond $B_s^0 \to K^+K^-J/\psi$ et $B^0 \to K^{*0}J/\psi$ est extraite des simulations et leurs contributions relatives fixées à la valeur déterminée par les données.

L'ajustement de la masse $pK^-\mu^+\mu^-$ permet l'extraction de poids avec lesquels il est possible de soustraire de façon statistique la contribution du bruit de fond. Ces poids

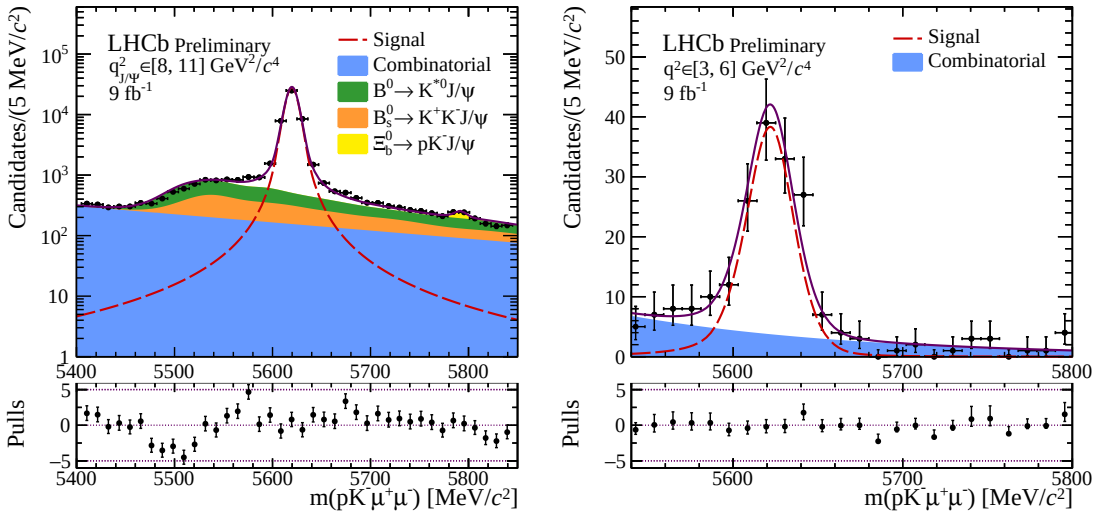

Figure 5 – Ajustement de la masse invariant $pK^-\mu^+\mu^-$ dans les données de l'expérience LHCb pour le mode de contrôle J/ψ (gauche) et un mode rare (droite).

sont appliqués par la suite.

La sélection a une forte influence sur la forme des angles. La variation introduite par cette "acceptance angulaire" doit être corrigée dans les données. Puisque les données sont limitées dans le mode rare, l'ajustement angulaire présenté dans l'équation 2, est simplifié dans la limite des quarks lourds. La fonction de distribution de probabilité correspond au premier terme dans la somme dans Éq. 5. Les observables angulaires S_{1cc} et A^ℓ_{FB} vont être mesurées. Pour la distinguer du paramètre de nuisance $A^\ell_{FB,1/2}$, l'observable A^ℓ_{FB} va être nommée $A^\ell_{FB,3/2}$ par la suite. Il a été vérifié que l'ajustement d'un échantillon généré avec le modèle complet en utilisant les facteurs de forme du NRQM avec le modèle réduit n'introduit pas de changement des valeurs d'observables angulaires.

La figure 2 indique la présence des résonances $\Lambda(1405)$ et $\Lambda(1600)$ dans la fenêtre de masse invariante pK^- autour de la résonance $\Lambda(1520)$. Ces deux résonances ont un spin 1/2 et la distribution angulaire a été adaptée de Réf. [10] pour la désintégration forte des résonances Λ^*. La fonction de distribution de probabilité est écrite dans la partie en vert de l'équation 5, et n'a pas de dépendance en $\cos\theta_p$. Puisque elles sont mesurées ensemble dans une fenêtre de masse réduite, les observables K_{1cc} et $A^\ell_{FB,1/2}$ sont des paramètres de nuisance.

Les valeurs des termes d'interférences entre les trois résonances Λ^* ne peuvent pas être prédits par la théorie. C'est pour cela que des simulations Monte Carlo dédiées à étudier des scénarios d'interférences différents ont été générées par des collègues de LHCb. Il a été trouvé que l'impact des interférences est de causer un changement de forme de $\cos\theta_p$. Cela est pris en compte par des termes d'interférence, notés par $i_{1,2}$, qui sont multipliés à

la distribution des résonances Λ^* de spin 1/2.

A cause de la ressemblance des deux termes dans la somme, une nouvelle dimension est utilisée pour séparer les contributions de $\Lambda(1520)$ et celles de Λ^* avec un spin 1/2. Cette dimension est la masse invariante pK^- avec laquelle la fraction des résonances $\Lambda(1520)$, qui s'appelle $f_{3/2}$, peut être déterminée. La résonance $\Lambda(1520)$ est décrite par la fonction de Breit-Wigner relativiste. Les résonances de spin 1/2 sont modélisées par un polynôme d'ordre un.

En combinant tous ces termes, la fonction de distribution de probabilité a été développée et écrite comme

$$
\begin{aligned}
&\mathrm{PDF}_{\mathrm{ang}}^{\mathrm{Int}1/2} \\
&= f_{3/2}\left(\left(1-\frac{1}{2}S_{1cc}\right)\left(1-\cos^2\theta_\ell\right)+S_{1cc}\cos^2\theta_\ell+\frac{4}{3}A^\ell_{FB,3/2}\cos\theta_\ell\right) \\
&\times\left(\frac{1}{4}+\frac{3}{4}\cos^2\theta_p\right) \\
&+(1-f_{3/2})\left(\frac{1}{2}\left(1-K_{1cc}\right)\left(1-\cos^2\theta_\ell\right)+K_{1cc}\cos^2\theta_\ell+\frac{2}{3}A^\ell_{FB,1/2}\cos\theta_\ell\right) \\
&\times\left(\frac{3-i_2}{3}+i_1\cos\theta_p+i_2\cos^2\theta_p\right). \qquad (5)
\end{aligned}
$$

En testant ce modèle avec ces simulations de Monte Carlo, l'ajustement donne des valeurs de $A^\ell_{FB,3/2}$ et S_{1cc} compatibles avec les valeurs générées, comme visible dans la fig. 6.

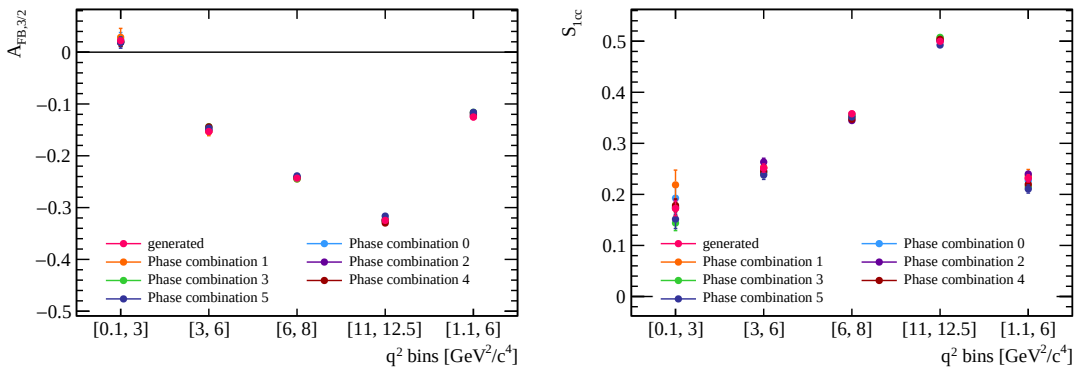

Figure 6 – Stabilité des résultats de l'ajustement aux échantillons de Monte Carlo dédiés à l'étude de l'impact de différentes interférences sur les observables angulaires.

Ces échantillons sont très grands, donc la taille ne correspond pas à l'attente. Il est donc nécessaire de tester le modèle avec le mode de contrôle sur les données. Pour cela les poids pour enlever le bruit de fond et corriger l'acceptance angulaire sont appliqués. Les projections de l'ajustement de la masse invariante pK^- et des angles sont montrées dans Fig. 7. La valeur de l'asymétrie $A^\ell_{FB,3/2}$ résultant est 0.008 ± 0.008, ce qui est compatible

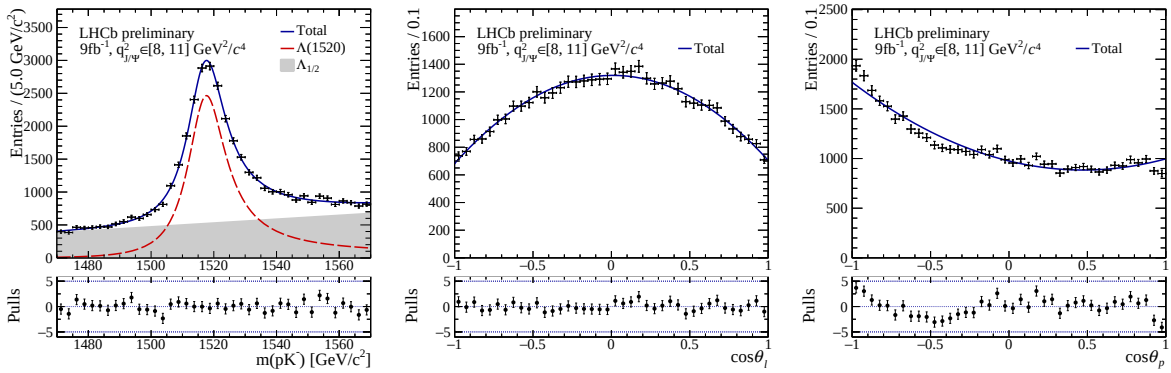

Figure 7 – Projections de l'ajustement à la masse invariante pK^- et des angles $\cos\theta_\ell$ et $\cos\theta_p$ dans le mode de contrôle J/ψ.

avec zéro, comme attendu dans les désintégrations à l'arbre.

Dû à la petite taille des données dans le mode rare, le fit angulaire a des problèmes de convergence dans ces régions. C'est la raison pour laquelle la stratégie du bruit de fond des combinaisons aléatoires a changé. Au lieu d'enlever le bruit de fond par des poids, le bruit de fond est modélisé. Un polynôme d'ordre un modélise la masse pK^- et les angles sont décrits par le produit de deux polynômes d'ordre deux. L'ajustement dans une région du mode rare est montré dans la Fig. 4.40. Les valeurs des observables

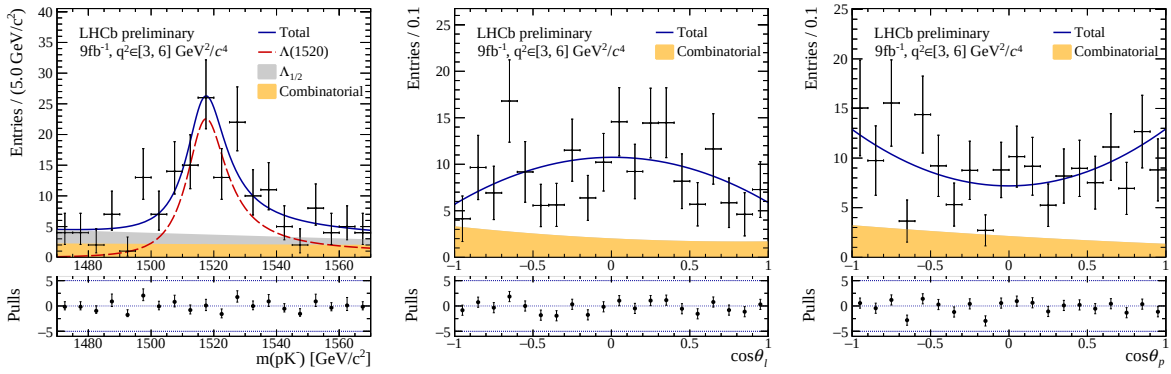

Figure 8 – Projection de l'ajustement à la masse invariante pK^- et des angles dans une des régions dans le mode rare.

angulaires sont cachées. Un biais a été constaté qui doit être corrigé dans le futur. En plus, les incertitudes systématiques doivent être traitées.

En parallèle, des nouvelles données ont été prises en 2022 par le détecteur amélioré de l'expérience LHCb. Les données du dernier weekend de la prise des données sont analysées. La motivation de cette analyse est de valider la nouvelle stratégie de déclenchement en regardant l'efficacité des électrons. Pour la première fois les désintégration de $\psi(2S) \rightarrow$

e^+e^- originaires d'un vertex secondaire sont découvertes dans les nouvelles données. Elles peuvent être vues dans la Fig. 9.

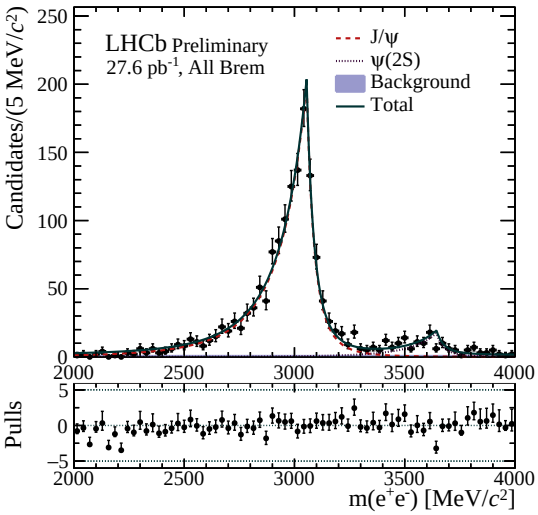

Figure 9 – Ajustement à la masse invariante de e^+e^- dans les nouvelles données de LHCb.

Pour la première fois, les désintégrations de $B^+ \to K^+\psi(2S)(\to e^+e^-)$ sont observées dans les données. L'ajustement de la masse invariante $K^+e^+e^-$ calculé avec une contrainte de $\psi(2S)$ est montré dans la Fig. 10.

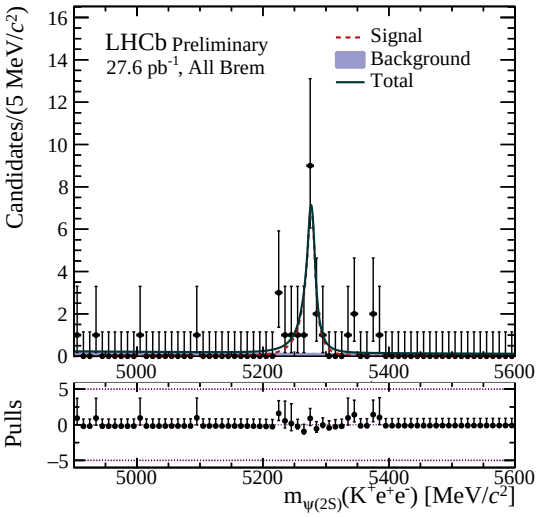

Figure 10 – Ajustement à la masse invariante de $K^+e^+e^-$ dans les nouvelles données.

Le rapport des désintégrations $B^+ \to K^+\psi(2S)(\to e^+e^-)$ sur $B^+ \to K^+J/\psi(\to e^+e^-)$ est calculé et inférieur aux résultats précédents. En raison de la petite taille de cet échantillon, les rapports doivent être recalculés avec un échantillon plus grande.

Avec l'aide de l'ajustement des désintégrations $B^+ \to K^+ J/\psi(\to e^+e^-)$, des poids sont extraits pour supprimer de façon statistique les bruits de fonds. Cela permet une comparaison des distributions de différentes variables dans les données et les échantillons de simulation. En conclusion, les variables topologiques et cinématiques sont en accord entre les deux échantillons. Par contre, les variables d'identification des électrons par rapport aux pions, nommées $\mathrm{DLL}_{e\pi}$ montrent de grands désaccords. En plus, une amélioration de l'alignement temporel et spatial du détecteur est nécessaire pour exploiter tout le potentiel du détecteur amélioré. Cette analyse est importante pour surveiller la qualité des données et améliorer les simulations du nouveau détecteur LHCb.

Glossary

The meaning of common acronyms and abbreviations is explained in the table below.

A_{FB}^{ℓ}	Leptonic forward-backward asymmetry of the Λ_b^0 decay to a $\Lambda(1520)$ resonance and a lepton pair.
$A_{\mathrm{FB},1/2}^{\ell}$	Leptonic forward-backward asymmetry of the Λ_b^0 decay to a spin-1/2 Λ^* resonance and a lepton pair.
BDT	A machine learning technique trained to distinguish between signal and background, called Boosted Decision Tree. The technique attributes usually a value in the interval $[-1, 1]$ or $[0, 1]$ to an event, which is translated into background- and signal-like classification.
$\chi^2_{\text{decay-length}}$	χ^2 of the decay length of the corresponding particle track.
χ^2_{DTF}/ndof	Goodness of the PV quality, which is evaluated by the DecayTreeFitter algorithm.
χ^2_{FD}	χ^2 of the distance between the vertex of origin and the decay vertex, indicating the significance of the flight distance of a particle candidate.
χ^2_{IP}	χ^2 of the impact parameter between the reconstructed track and the PV of the candidate.
DIRA	Angle between the direction between the line from the PV to the SV and the sum of the final-state particle four-momenta.
χ^2_{vertex}	χ^2 of the vertex quality, associated to the decay vertex of the corresponding particle.
DOCA	Distance of closest approach between two tracks.
η	Pseudo-rapidity is a measure of positions in the detector relative to the beam axis. At high energies ($m \ll p$), it equals the rapidity y.
hasMuon	Boolean variable indicating if the track has hits in the muon station.

hasRich	Boolean variable requiring RICH signatures, which are associated to the track.
IP	Impact parameter, indicating the smallest distance between a track and a PV.
isMuon	Boolean variable to check if muon sub-detector hits match the reconstructed track of the muon candidate.
K_{1cc}	Angular observable of the Λ_b^0 decaying into a a spin-1/2 Λ^* resonance and a lepton pair.
LHC	The Large Hadron Collider is colliding protons and is situated close to Geneva.
Λ^0	Ground-state Λ resonance, which decays weakly.
Λ^*	Excited Λ resonances, which can decay via the strong interaction to pK^-.
$\Lambda_{1/2}$	Λ^* resonance with spin $J = 1/2$.
MVA	Multivariate analysis tool, often but not necessarily machine-learning based.
MC	Monte-Carlo simulation sample.
NP	New Physics, referring to phenomena un-explained by the Standard Model of particle physics.
nTracks	Number of reconstructed tracks in an event.
nSPDHits	Number of hits in the Scintillating Pad Detector (SPD) detected in a pp-collision.
P	Positive (+) and negative (-) parity of a particle.
PDF	(Angular) Probability Distribution Function.
$\text{PDF}_{3/2}$	Angular PDF of the $\Lambda_b^0 \to \Lambda(1520)(\to pK^-)\mu^+\mu^-$ decay.
$\text{PDF}_{1/2}$	Angular PDF of the $\Lambda_b^0 \to \Lambda_{1/2}(\to pK^-)\mu^+\mu^-$ decay.
phase-space	Model for the generation of MC simulation samples based on a probability distribution, which is flat in the decay angles defined in the helicity basis.
ProbNNX	Machine-learning technique trained to identify different particles by attributing a probability to the hypothesis of a particle to be X ($\text{X} \in \{p, K, \pi, \mu, ...\}$).
$\text{Prob}_{\text{ghost-track}}$	Probability to be a ghost track.
p_T	Component of the particle momentum transversal to the beam axis.
PV	Primary vertex, located at the pp-collision point.
J	Spin of a particle.
S_{1cc}	Angular observable of the Λ_b^0 decaying into a $\Lambda(1520)$ resonance and a lepton pair.
SM	Standard Model of Particle physics.
SV	Secondary vertex of the particle decay. In the studied decay it is the Λ_b^0 decay vertex.
q^2	Dilepton invariant mass squared. The angular observables are measured in bins of this quantity.
τ	Lifetime of an unstable particle.

Chapter 1

Theoretical and experimental overview

1.1 The Standard Model of particle physics

The idea of having elementary constituents, composing all types of matter in our universe, was already debated in ancient Greece. Democritus, a Greek philosopher born around 460 BC, is the founder of the atomist theory, postulating that matter is composed of indivisible, eternal and perfectly solid constituents [11].

Even though atoms are nowadays known not to be the indivisible components of Nature, elementary constituents exist. Those elementary particles and three of the four fundamental forces are described in the Standard Model (SM) of particle physics, which was derived about 2400 years after Democritus' birth [1].

Although the theory of classical mechanics fits the observations of macroscopic objects at velocities much smaller than the speed of light c, it cannot predict the behaviour of elementary particles. The uncertainty principle of quantum mechanics is necessary to describe those quantum objects. Since massless particles travel at the speed of light, neither classical nor quantum mechanics can explain their relativistic behaviour. The solution is Einstein's theory of special relativity. Combining quantum mechanics with special relativity yields a quantum field theory (QFT), adapted to describe particles of microscopic size moving at velocities close to or equal to the speed of light. QFTs are, therefore, well suited to model the SM.

The scientific community celebrates the SM as "one of the most successful theories in physics" [13]. The euphoria is caused by the precise prediction of phenomena, which were later validated by experiments at colliders.

1. This paragraph is following the argumentation of Ref. [12].

Nevertheless, some questions cannot be solved by the SM. Examples are the matter-antimatter asymmetry in our universe, the missing Dark Matter particle, the neutrino oscillations and the non-inclusion of gravity. Therefore, studying the SM provides information about the microscopic world of elementary particles and enriches knowledge at the cosmological and astrophysical scales.

In flavour physics, precision measurements of the SM properties are performed since New Physics (NP) could contribute and give rise to deviations. Higher energy ranges can be scanned for NP than it is producible at collider experiments. Promising candidates are $b \to s\ell^+\ell^-$ transitions since they occur on loop level, and their branching fractions are, thus, suppressed in the SM. Even small NP contributions could cause sizable deviations. This is the reason why those electroweak penguin decays are judged to be good candidates to search for NP.

By measuring electroweak penguin decays, the LHCb experiment reported discrepancies with respect to the SM predictions. Since most up-to-date measurements are performed with $B^{0,\pm}$ mesons, studies of b-baryons are important to cross-check theoretical as experimental results. Thanks to their spin, b-baryons offer access to complementary information. This thesis focuses on attempting to perform for the first time an angular analysis in $\Lambda_b^0 \to \Lambda(1520)\mu^+\mu^-$ decays using Run 1 and 2 data collected by the LHCb experiment.

The theoretical and experimental status is presented in the first chapter to introduce the context of this work. Its first section is composed of an overview of the SM, including the presentation of the elementary particle table, its mathematical description [2], the properties of flavour physics and its shortcomings. In the second section, the theoretical formalism to describe electroweak penguin decays and experimental results are presented. In the third section, the focus is set on $\Lambda_b^0 \to pK^-\ell^+\ell^-$ decays. The measurement is motivated, and the experimental status of art is explained. Theoretical predictions related to the signal decay are presented afterwards. This section will become essential for the construction of the angular fit model.

1.1.1 Elementary particles and interactions

The Standard Model (SM) of particle physics describes the elementary particles of which our universe is composed and three of the four fundamental forces. Gravity is not included since it is many orders of magnitudes weaker than the weak, electromagnetic and strong force. However, the gravitational force holds large objects in our universe together, thanks to its attractivity even at enormous distances [14]. The great success of the SM

2. This subsection is based on Ref. [12, 14, 15].

is the prediction of the Z, $W^{\pm}$ and H^0 boson. Their discovery at collider experiments is seen as validation of the SM [16–19]. Nowadays, all the SM particles are discovered.

Figure 1.1 shows a table of all the SM particles. According to their spin, the SM particles can be classified into fermions and bosons. Spin is one of the fundamental properties defining the particle type. An integer spin number defines bosons and a half-integer number to fermions. While all the baryonic matter is made of fermions, the force carriers and the Higgs are bosons.

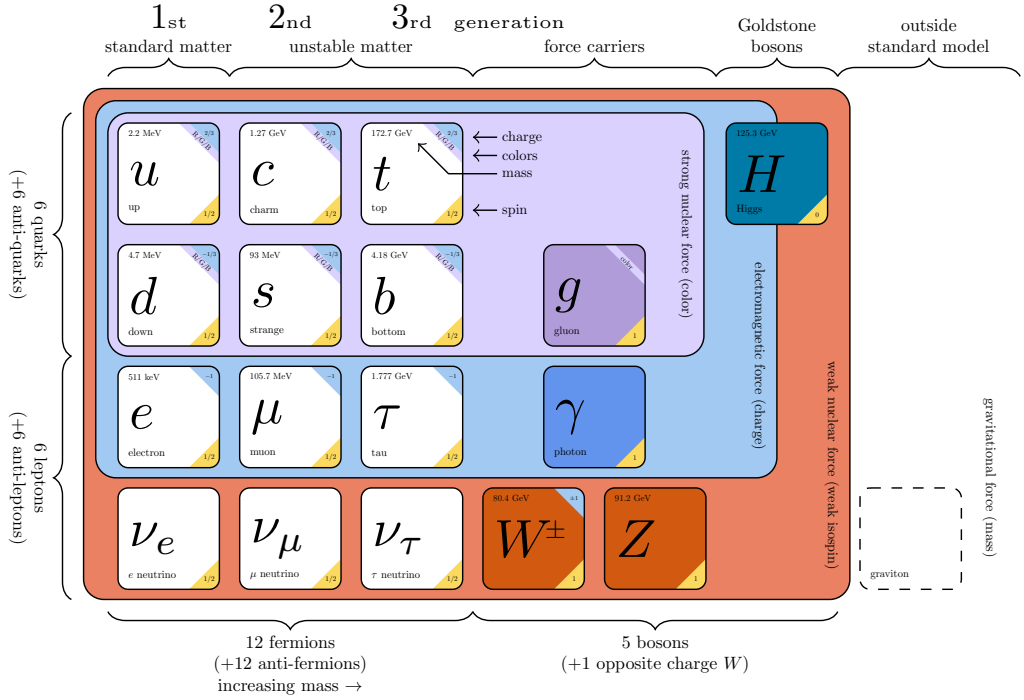

Figure 1.1 – All the Standard Model's elementary particles and force carriers are shown. The table is adapted from Ref. [20]. The particle masses are taken from Ref. [21] and written in natural units.

Fermions

Fermions are the elementary constituents of our universe, and consequently all the atoms we know. Atoms consist of electrons e^- and a nucleus. The nucleus is made of protons p and neutrons n, which are themselves composed of up u and down d quarks. The proton composition is uud, and the neutron is made of udd valence quarks. The electron, the up and the down quark are part of the first lepton family. In literature, it is also spoken of as the first lepton generation. In total, there are three generations. Fermions from the second and third generation are mainly produced in accelerators, but

not exclusively. Atmospheric showers are natural sources of fermions from higher generations, produced by interactions of cosmic rays and the nuclei in the high atmosphere [3]. The ordering of the fermions follows the principle: "The higher the generation, the higher are the masses of its constituents".

Each fermion f has an antiparticle $\overline{f}$ with inverted quantum numbers [4], while the mass and the spin stay the same. The transformation of the quantum numbers from a particle to its antiparticle is performed by the charge conjugation operator C. Since the neutrinos have only been observed to be left-handed and their antiparticles to be right-handed [5], charge conjugation is not a good symmetry of the SM. The parity operator P is needed to project the momentum of a particle to its negative counterpart. The combined application of CP correctly converts left-handed neutrinos into their right-handed antiparticles. For simplicity, the corresponding antiparticle of each presented fermion is implied in the following.

Fermions are distinguished into two groups, the quarks and the leptons. Let us start with the quarks. An important feature is that each quark carries a colour charge. The colour charge is defined as red, green and blue in analogy to the colours of light. The corresponding anti-quarks carry anti-colours. Depending on the electromagnetic charge of the quarks, they are classified as up or down-type quarks. The up-type quarks are namely the up u, charm c and truth t quark with an electromagnetic charge $Q = \frac{2}{3}e$. Down d, strange s and beauty b are the flavours of the down-type quarks. Their charge equals $Q = -\frac{1}{3}e$. Counting all the quarks with their different colour charges and antiparticles, the SM contains 36 different quark types.

Due to the colour confinement, quarks never appear alone in Nature. They hadronise. The top quark is so heavy that it decays before forming a bound state. A meson is composed of a quark q and an anti-quark $\overline{q}$. Baryons consist of either three quarks or three anti-quarks. Furthermore, exotic states as pentaquarks ($q\overline{q}qqq$) and tetraquarks ($q\overline{q}q\overline{q}$) have already been observed [22]. In each interaction, the number of baryons, defined as

$$\mathcal{B} = \frac{1}{3}\left(N_q - N_{\bar{q}}\right), \tag{1.1}$$

is conserved. This property is called baryon number conservation.

3. In atmospheric showers mainly kaons, D mesons and muons are produced.
4. An anti-quark possesses, for example, an anti-colour and carries inversed flavour numbers.
5. Left-handed helicity is defined as the projection of the spin $\vec{s}$ of a particle on the direction of its momentum $\vec{p}$. Mathematically expressed, left-handed particles have a positive helicity $h = \frac{\vec{s}\cdot\vec{p}}{|\vec{p}|} > 0$.

Leptons constitute the second group of fermions. Each generation comprises an electromagnetically charged lepton, namely the electron e^-, the muon μ^- and the tau lepton τ^-, and a corresponding neutral and massless neutrino, denoted by ν_e, ν_μ and ν_τ. The number of leptons minus the number of anti-leptons within each family is conserved in all interactions. The so-called lepton numbers are marked as L_e, L_μ, L_τ.

For the analysis, it is important to understand the properties of leptons and quarks, to get a feeling of the interaction.

Forces and their mediators

Following the particle-wave duality of quantum mechanics, each force in the SM has an associated force carrier. The strong force is mediated by a massless gluon g, carrying a colour and an anti-colour. Combining the three colours and anti-colours naively, nine combinations exist. Since a gluon cannot occupy a colour singlet state, only eight gluons are part of the SM. The strong force acts on particles carrying colour charges, which are the quarks and the gluons. The strong force holds atomic nuclei together, while the electromagnetic interaction bounds the electrons on the nucleus.

Electromagnetic interactions are mediated by photons γ. Only electromagnetically charged particles can interact with the γ. These are quarks, charged leptons and the $W^\pm$ boson. In all interactions, the electromagnetic charge Q is conserved.

The third force is the weak force, which interacts with all leptons and quarks. It is the sole force interacting with neutrinos in the SM. The gauge bosons of the weak force are the massive $W^\pm$ and the Z boson. Interactions with the $W^\pm$ boson are unique because they do not conserve the quark flavours. Interactions with the $W^\pm$ boson, the Z boson and the photon are present in the signal decay and, therefore, crucial for this thesis.

As described previously, the combined *CP* operation transforms a particle into its antiparticle. While the electromagnetic and strong interactions conserve the *CP* symmetry, the weak interaction does not. The violation of *CP* symmetry is due to the Cabibbo–Kobayashi–Maskawa (CKM) matrix, described in detail in section 1.1.2. Nevertheless, it is a small effect and cannot explain the enormous matter dominance in our universe. Since the SM is built to be symmetric under *CPT* transformations, *CP* violation implies violation of the time inversion operator T.

A special place in the SM occupies the recently discovered Higgs boson H^0. It provides masses to the particles with which it interacts. These are, namely, the charged leptons, the quarks, the weak bosons and itself. Even if the Higgs boson is not studied in this analysis; it is important to understand its need to introduce particle masses.

The Standard Model Lagrangian density

After the phenomenological introduction of fermions and bosons, the mathematical formulation of the SM is presented in this section. The SM of particle physics is expressed as a Quantum Field Theory (QFT), which is invariant under the local gauge transformation of the

$$\mathrm{SU}(3)_C \otimes \mathrm{SU}(2)_L \otimes \mathrm{U}(1)_Y \tag{1.2}$$

group. The strong interaction is described by a $\mathrm{SU}(3)_C$ symmetry generated by the colour charge C. The corresponding QFT is called Quantum Chromodynamics (QCD). The electroweak unification is based on the $\mathrm{SU}(2)_L \otimes \mathrm{U}(1)_Y$ symmetry. The corresponding quantum numbers are the weak isospin I and the weak hypercharge Y, which is related to the third component of the weak isospin I_3 and the electromagnetic charge Q by the Gell-Mann-Nishijima formula

$$Q = I_3 + \frac{Y}{2}. \tag{1.3}$$

The subscript L reminds the different treatment of left- and right-handed fermions in weak interactions.

The electroweak (EWK) symmetry is spontaneously broken to the $\mathrm{U}(1)_Q$ symmetry of electromagnetic interactions, which occurs at low energies and is formulated as Quantum Electrodynamics (QED). The symmetry breaking gives rise to the Higgs boson and fermion masses, expressed by the Yukawa terms.

The SM Lagrangian density $\mathcal{L}_{SM}$, in the following abbreviated by Lagrangian, describes the dynamics and interactions of the SM particles. It can be decomposed into the terms

$$\mathcal{L}_{\mathrm{SM}} = \mathcal{L}_{\mathrm{QCD}} + \mathcal{L}_{\mathrm{EWK}} + \mathcal{L}_{\mathrm{H}} + \mathcal{L}_{\mathrm{Yukawa}}. \tag{1.4}$$

Each term of the SM Lagrangian will be explained in the next subsections.

Quantum Chromodynamics

To simplify the QCD Lagrangian, the quark fields are introduced with their corresponding colours as the three-component vectors

$$\psi = \begin{pmatrix} \psi_r \\ \psi_g \\ \psi_b \end{pmatrix}, \qquad \bar{\psi} = \begin{pmatrix} \bar{\psi}_r & \bar{\psi}_g & \bar{\psi}_b \end{pmatrix}. \tag{1.5}$$

Their components $\psi_{r,g,b}$ are Dirac spinors, composed of left- and right-handed fields. The SU(3) generators T^a are defined as a function of the Gell-Mann matrices λ^a with $a \in \{1, 2, ..., 8\}$ and multiplied by a factor 1/2. The local SU(3) gauge transformation can be written as

$$\psi \to e^{ig_s\alpha^a(x)T_a}\psi \tag{1.6}$$

and is interpreted as a rotation in the colour space. $\alpha^a(x)$ are the real functions of the space-time coordinate x. To keep local gauge invariance, the tensor field

$$G^a_{\mu\nu} = \partial_\mu G^a_\nu - \partial^a_\nu G^a_\mu - g_s f^{abc} G_{\mu,b} G_{\nu,c} \tag{1.7}$$

is introduced with the help of the commutator relation f^{abc}. The eight gluon fields are appearing as G^a_μ. The Lagrangian of the strong interaction is expressed as

$$\mathcal{L}_{\mathrm{QCD}} = \bar{\psi}(i\gamma^\mu\delta_\mu - m)\psi + g_s(\bar{\psi}\gamma^\mu T_a\psi)G^a_\mu - \frac{1}{4}G^a_{\mu\nu}G^{\mu\nu}_a. \tag{1.8}$$

The γ^μ matrices are defined in the Dirac-Pauli representation as functions of the unity matrix and the Pauli matrices σ^k. The first term in $\mathcal{L}_{\mathrm{QCD}}$ is interpreted as the kinetic term of the quarks, while the second stands for the colour-changing interaction of two quarks with a gluon. The coupling strength of the strong interaction is written as g_s. The third term corresponds to the kinetic term of the gluon plus the self-coupling of three and four gluons to each other.

The strong coupling constant $\alpha_s = \frac{g_s}{4\pi}$ is modified by virtual quark and gluon loop contributions. Corrections to the quark propagator cancel with the vertex correction [6], while contributions to the gluon propagator persist. Those contributions are included in the strong running coupling, $\alpha_s(\mu^2)$, and cause a dependence of α_s on the momentum

6. The values of each correction depend on the chosen gauge.

transfer squared, μ^2. The full expression of the strong running coupling is written as

$$\alpha_{\mathrm{s}}(\mu^2) = \frac{12\pi}{11n_c - 2n_f} \frac{1}{\ln \frac{\mu}{\Lambda_{QCD}}} \quad (\mu^2 \gg \Lambda^2_{\mathrm{QCD}}). \tag{1.9}$$

Logarithmic terms in radiative corrections are resumed through the Renormalisation Group. The introduced fundamental scale is parametrised by the QCD scale parameter Λ_{QCD} [23]. The Λ_{QCD} parameter depends itself on the renormalisation scheme and the number of active flavours n_f [23]. In Eq. 1.9, the number of colours (3 in the SM) is marked with n_c. The running coupling gets weaker with increasing momentum transfer. This effect is called asymptotic freedom. Decreasing the energy leads to a diverging running coupling and causes the confinement of quarks.

For low-energetic processes, the coupling constant attains a value of the order $\mathcal{O}(1)$ and QCD expansions in powers of α_s are non-reliable anymore. One speaks about non-perturbative QCD. While the b-quark production is governed by an energy scale of the order $m_b \approx 4\,\mathrm{GeV}/c^2 \gg \Lambda_{\mathrm{QCD}}$ and, thus, part of the perturbative regime, the hadron propagation is non-perturbative and difficult to predict. How the hadronic part of the interaction can, nevertheless, be predicted as form factors, will be presented in section 1.2.2.

Electroweak interaction

For the electroweak interaction, the handedness of the fermions matter. Left-handed fermions are separated from their right-handed counterparts by the chiral projection operators

$$P_{L(R)} = \frac{1 \mp \gamma_5}{2}. \tag{1.10}$$

While for massive fermions, the helicity depends on the reference frame, chirality is frame independent. To describe the electroweak interaction, all the left-handed fermions are arranged in six weak isospin doublets

$$\Psi_L \in \left\{ \begin{pmatrix} \nu_e \\ e^- \end{pmatrix}_L, \quad \begin{pmatrix} \nu_\mu \\ \mu^- \end{pmatrix}_L, \quad \begin{pmatrix} \nu_\tau \\ \tau^- \end{pmatrix}_L, \quad \begin{pmatrix} u \\ d' \end{pmatrix}_L, \quad \begin{pmatrix} c \\ s' \end{pmatrix}_L, \quad \begin{pmatrix} t \\ b' \end{pmatrix}_L \right\}. \tag{1.11}$$

In the upper element, the third component of the weak isospin I_3 equals $+1/2$ and I_3 takes a value of $-1/2$ in the lower element. The primed quarks are the weak interaction eigenstates and will be presented below. Right-handed fermions are written as spinor

singlets

$$\Psi_R \in \{e_R^-, \quad \mu_R^-, \quad \tau_R^-, \quad u_R, \quad d_R, \quad c_R, \quad s_R, \quad t_R, \quad b_R\}, \tag{1.12}$$

where $I = I_3 = 0$. According to Eq. 1.3, the weak hypercharge of right-handed neutrinos vanishes. This is the reason why they do not interact via the weak interaction. The primed quarks in Eq. 1.11 are rotations of the initial quark flavours by the CKM matrix via

$$\begin{pmatrix} d' \\ s' \\ b' \end{pmatrix} = V_{\mathrm{CKM}} \begin{pmatrix} d \\ s \\ b \end{pmatrix}. \tag{1.13}$$

The primed quarks are the weak interaction eigenstates, and the unprimed ones are the mass or flavour eigenstates. The $\mathrm{SU}(2)_L \otimes \mathrm{U}(1)_Y$ gauge symmetry corresponds to the local phase transformations [7]

$$\Psi_L \to e^{ig\alpha_k(x)\tau^k + ig'\frac{Y}{2}\beta(x)}\Psi_L, \tag{1.14}$$

$$\Psi_R \to e^{ig'Y\beta(x)}\Psi_R. \tag{1.15}$$

The isospin singlet Ψ_R is unaffected by the local $\mathrm{SU}(2)_L$ gauge transformation. The matrices τ^k with $k \in \{1, 2, 3\}$ are equivalent to the Pauli matrices σ^k multiplied by a factor 1/2. $\beta(x)$ and $\alpha_k(x)$ are real functions of the space-time coordinate x.

The gauge symmetry $\mathrm{U}(1)_Y$ is related to the gauge field B_μ. The gauge fields W_μ^k appear due to the $\mathrm{SU}(2)_L$ symmetry. The covariant derivatives

$$D_{\mu,L} = \partial_\mu - ig'\frac{Y}{2}B_\mu - ig\tau^k W_\mu^k, \tag{1.16}$$

$$D_{\mu,R} = \partial_\mu - ig'\frac{Y}{2}B_\mu \tag{1.17}$$

include the four boson fields. g and g' are the coupling strengths corresponding to the $\mathrm{SU}(2)_L$ and $\mathrm{U}(1)_Y$ gauge symmetries. The boson fields can be rewritten as

$$W_\mu^\pm = \frac{1}{2}(W_\mu^1 \mp W_\mu^2), \tag{1.18}$$

$$Z_\mu = \cos\theta_{\mathrm{W}} W_\mu^3 - \sin\theta_{\mathrm{W}} B_\mu, \tag{1.19}$$

$$A_\mu = \sin\theta_{\mathrm{W}} W_\mu^3 + \cos\theta_{\mathrm{W}} B_\mu. \tag{1.20}$$

7. In the literature, instead of writing the coupling constants explicitly, they are sometimes included in the real functions $\alpha_k(x)$ and $\beta(x)$.

The mass eigenstates of the bosons can be read from this representation. A_μ is the photon field, Z_μ represents the Z-boson field and $W_\mu^\pm$ the $W^\pm$ bosons. θ_W is called the weak mixing angle. The generators of the symmetry group are written out in Eq. 1.21 and 1.22. ϵ^{ijk} is the Levi-Civita tensor and has the indices $i, j, k \in \{1, 2, 3\}$. By defining the tensor fields

$$B_{\mu\nu} = \partial_\nu B_\mu - \partial_\mu B_\nu, \tag{1.21}$$

$$W^k_{\mu\nu} = \partial_\nu W^k_\mu - \partial_\mu W^k_\nu + g\epsilon^{ijk} W^i_\mu W^j_\nu, \tag{1.22}$$

the full electroweak Lagrangian yields the expression

$$\mathcal{L}_\mathrm{EWK} = i\bar{\Psi}_L \gamma^\mu D_{\mu,L} \Psi_L + i\bar{\Psi}_R \gamma^\mu D_{\mu,R} \Psi_R - \frac{1}{4} B_{\mu\nu} B^{\mu\nu} - \frac{1}{4} W^k_{\mu\nu} W^{\mu\nu,k}. \tag{1.23}$$

The first two terms correspond to the propagation of fermions and their interactions with the gauge bosons $W^\pm$, γ and Z. The $W^\pm$ bosons interact solely with left-handed chiral fermions and right-handed chiral anti-fermions, whereas the photon couples to both fermion chiralities equally. Since the Z boson is composed of a combination of the W^3_μ and the B_μ field, its coupling differs depending on the fermion chiralities. Using the weak mixing angle θ_W, the two coupling constants g and g' can be expressed as the electromagnetic charge $e = g \sin\theta_\mathrm{W} = g' \cos\theta_\mathrm{W}$.

The two last terms in the electroweak Lagrangian describe the propagation and the interactions of the three gauge bosons. A $W^\pm$ bosons pair can either interact in three- or four-boson interactions. Hence, the $W^\pm$ boson pair can interact with a γ or a Z boson, or it undergoes an interaction with two photons, two Z bosons, a photon and a Z boson or another $W^\pm$ boson pair. The three-boson interaction is present in one of the dominant Feynman diagrams for the $b \to s\ell^+\ell^-$ transition, which is shown in Fig. 1.2.

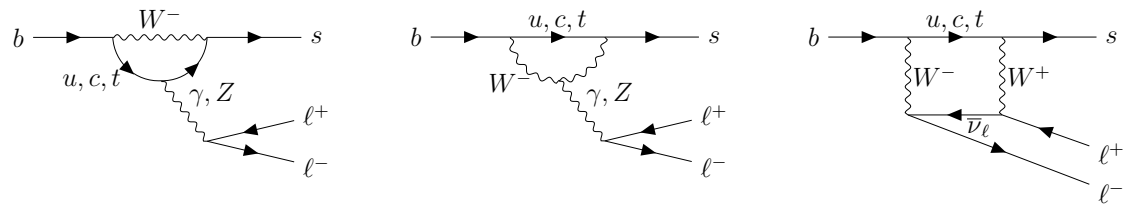

Figure 1.2 – The three dominant Feynman diagrams of the $b \to s\ell^+\ell^-$ transition in the Standard Model.

Brout-Englert-Higgs mechanism

Up to now, the gauge bosons and the fermions in the SM Lagrangian are massless. Mass terms are included by breaking the $\mathrm{SU}(2)_L \otimes \mathrm{U}(1)_Y$ symmetry spontaneously to become the $\mathrm{U}(1)_Q$ symmetry. For this purpose, a complex scalar Higgs field is introduced as the weak isospin doublet

$$\phi = \begin{pmatrix} \phi^+ \\ \phi^0 \end{pmatrix} = \frac{1}{\sqrt{2}} \begin{pmatrix} \phi_1 + i\phi_2 \\ \phi_3 + i\phi_4 \end{pmatrix}. \tag{1.24}$$

The Higgs boson has a weak hypercharge $Y = 1$. The Lagrangian of the Higgs boson is introduced as

$$\mathcal{L}_H = (D^\mu \phi)^\dagger (D_\mu \phi) - V(\phi). \tag{1.25}$$

D_μ is the same covariant derivative as introduced in Eq. 1.16 and 1.17. $V(\phi)$ is the Higgs potential, which is defined as

$$V(\phi) := \mu^2 \phi^2 + \lambda \phi^4. \tag{1.26}$$

The parameters μ^2 and λ are both real. λ has to be bigger than zero to get a finite minimum of the Higgs potential, while μ^2 can be positive or negative. However, only in the case of $\mu^2 < 0$, $V(\phi)$ has an infinite set of absolute minima. The minima can be expressed as

$$\phi_{min} = \frac{1}{\sqrt{2}} \begin{pmatrix} 0 \\ \upsilon e^{i\theta} \end{pmatrix}. \tag{1.27}$$

The phase θ defines the rotation of $|\phi_{min}|$ in the complex plane. Because the Higgs boson "chooses" a particular minimum of the Higgs potential, the rotational symmetry of the Higgs Lagrangian is broken. By convention, the phase θ is set to zero. The potential minimum ϕ_{min} is expanded around the vacuum state by exploiting gauge invariance [8] and reads

$$\phi = \frac{1}{\sqrt{2}} \begin{pmatrix} 0 \\ \upsilon + h(x) \end{pmatrix}. \tag{1.28}$$

By inserting Eq. 1.28 in 1.25, terms depending on υ arise. Those are the mass terms. While the photon stays massless, the $W^\pm$ and Z boson receive masses of $m_W = \frac{1}{2} g \upsilon$

8. Gauge invariance is exploited in order to choose the unitary gauge, which removes the three would-be Gauge bosons.

and $m_Z = \frac{v}{2}\sqrt{g^2 + g'^2}$. The weak mixing angle relates the two masses via $\cos\theta_W = \frac{m_W}{m_Z}$. In addition, the Higgs boson emerges from the Higgs scalar field $h(x)$ with a mass of $m_H = \sqrt{2\lambda}v$. Interactions of one or two Higgs bosons with two vector bosons ($W^\pm$ or Z) arise. Self-interactions of three or four Higgs bosons are part of the SM as well.

Yukawa interactions

After the electroweak symmetry breaking, the $W^\pm$, Z and the Higgs boson acquire masses, whereas the fermions remain massless. Yukawa interactions generate masses for fermions. To better understand the interactions, the left-handed fermions in the isospin doublets, displayed in Eq. 1.11, are separated into the lepton doublets Ψ_L^ℓ and quark doublets Ψ_L^q. The right-handed fermions in the isospin singlets, shown in Eq. 1.12, are likewise divided into leptonic singlets Ψ_R^ℓ, up-type Ψ_R^u and down-type quark singlets Ψ_R^d. Since it is again the Higgs, which generates masses for fermions, the Higgs isospin doublet, written down in Eq. 1.28, is needed. Another Higgs doublet with the conjugated weak hypercharge, $Y = -1$ is constructed as

$$\phi_c = -i\sigma^2\phi^* = \begin{pmatrix} -\phi^{0*} \\ \phi^- \end{pmatrix} = \frac{1}{\sqrt{2}} \begin{pmatrix} v + h(x) \\ 0 \end{pmatrix}. \tag{1.29}$$

Both of them are part of the Lagrangian defining the Yukawa interactions

$$\mathcal{L}_{\text{Yukawa}} = y_{ij}^\ell \left(\bar{\Psi}_L^{\ell i}\phi\Psi_R^{\ell j}\right) + y_{ij}^d \left(\bar{\Psi}_L^{qi}\phi\Psi_R^{dj}\right) + y_{ij}^u \left(\bar{\Psi}_L^{qi}\phi_c\Psi_R^{uj}\right) + h.c.\,. \tag{1.30}$$

The indices i and j run above the three generations. The hermitian conjugate is marked with $h.c.$ [9]. The first term generates the masses of the charged leptons. The second and third terms represent the masses of the down- and up-type quarks. It is important to note that the Yukawa interaction does not generate neutrino masses. The matrix y_{ij} contains the coupling strengths of the Higgs boson to the fermions. The Yukawa couplings are proportional to the fermion masses and inversely proportional to the vacuum expectation value v, which yields 246 GeV. With the help of bi-unitary transformations, the Yukawa matrix can be diagonalized [24]. Its diagonal matrix elements are related to the fermion masses via $y_{ii}^f = \frac{\sqrt{2}m_f}{v}$.

1.1.2 Flavours and vector bosons

The study of the properties of quarks and leptons is grouped under the term "flavour physics". Especially interesting for this thesis are their interactions with a $W^\pm$ boson,

9. The hermitian conjugate of a matrix M is marked as $M^\dagger = (M^*)^\top = (M^\top)^*$, meaning complex conjugation and transposing the matrix. An important property is $(M^\dagger)^\dagger = M$.

which are called charged current, and the neutral current interactions, which are mediated by a Z boson.

The γ and Z boson couplings to fermions are independent of the particle masses and generations. They depend exclusively on Q and I_3, which are the same between particles from the same type (ν_ℓ, ℓ, u, d). While the charged current interactions with quarks are more complicated, the couplings of the $W^\pm$ bosons to the leptons are flavour universal, too. This behaviour is called Lepton Universality (LU) and has been tested experimentally [25–27].

The complication of the charged current couplings is that they couple to the quark weak eigenstates, while the quarks themselves propagate in mass eigenstates. The CKM matrix describes the transformation between the two eigenstates, as described by Eq. 1.13. By convention, the down-type quarks are rotated from their mass eigenstates to the weak eigenstates, while the up-type quarks stay the same. Hence, the CKM matrix modifies the coupling strength of the quarks to the $W^\pm$ boson.

In the standard parametrisation, the CKM matrix is parametrised by three angles and one complex phase, which is the origin of *CP* violation in weak decays. Another parametrisation is the Wolfenstein parameterisation [28, 29], where the CKM matrix is expanded in terms of λ up to order four. The expansion yields the CKM matrix

$$\begin{aligned} V_{\text{CKM}} &= \begin{pmatrix} V_{ud} & V_{us} & V_{ub} \\ V_{cd} & V_{cs} & V_{cb} \\ V_{td} & V_{ts} & V_{tb} \end{pmatrix} \\ &= \begin{pmatrix} 1-\frac{\lambda^2}{2} & \lambda & A\lambda^3(\rho - i\eta) \\ -\lambda & 1-\frac{\lambda^2}{2} & A\lambda^2 \\ A\lambda^3(1-\rho-i\eta) & -A\lambda^2 & 1 \end{pmatrix} + \mathcal{O}(\lambda^4). \end{aligned} \tag{1.31}$$

The CKM matrix has a hierarchical structure in the SM. Coupling strengths between quarks of the same generation are close to one, while matrix elements describing transitions between generations are small. The flavour transitions between the first two generations are proportional to λ, between the last two to λ^2 and the one between the first and third generation to λ^3. Decays suppressed by CKM matrix elements are called Cabibbo-suppressed (CS).

The weak charged current is the only interaction in the SM, allowing quark flavour transitions. As visible in Eq. 1.31, those flavour changes are always between an up- and a down-type quark. Therefore, transitions between down-type quarks as $b \to s$ are forbidden at tree-level.

The values of the CKM matrix elements are not predicted by the SM. The measured

values of the CKM parameters are taken from Ref. [21] and equal

$$\begin{aligned} \lambda &= 0.22500 \pm 0.00067, & A &= 0.826^{+0.018}_{-0.015}, \\ \bar{\rho} &= 0.159 \pm 0.010, & \bar{\eta} &= 0.348 \pm 0.010. \end{aligned} \tag{1.32}$$

The unitarity condition of the CKM matrix implies $\sum_i V_{ij} V_{ik}^* = \delta_{jk}$ and $\sum_j V_{ij} V_{kj}^* = \delta_{ik}$. The six vanishing relations can be drawn as triangles in the complex plane. The area of the triangles always yields half of the Jarlskog invariant J [30], a measure of *CP* violation. J is determined to be $(3.08^{+0.15}_{-0.13}) \times 10^{-5}$. This small *CP* violating effect due to the CKM matrix is quoted as insufficient to explain the baryon asymmetry observed in our universe [31].

1.1.3 Shortcomings of the Standard Model

Although the SM is able to predict some phenomena extremely precisely, for example, the anomalous magnetic moment of the muon to the order 10^{-10} [32], some issues remain. Those issues can be separated into experimental problems and conceptual shortcomings. Some of them are listed in the following.

* During the Big Bang, equal amounts of matter and antimatter were created. Nowadays, predominantly matter composes the universe. Consequently, a process preferring the creation of matter is needed to establish this *matter-antimatter asymmetry*. *CP* violation introduced by the CKM matrix is not sufficient to explain the size of the observed asymmetry [31].
* Astrophysical and cosmological observables, such as fluctuations in the Cosmic-Microwave Background, the rotation curves of spiral galaxies and gravitational lensing, suggest the matter-energy content of our universe to be composed only of about 5% by baryonic matter [33]. 26% are attributed to *Dark Matter* (DM), which is barely interacting and as a result difficult to detect. The majority of 69% of the energy content is provided by the *Dark Energy* (DE), which accelerates the universe's expansion. Even though DM and DE are part of the most common cosmological model, ΛCDM, the SM of particle physics does neither provide a DM candidate nor describe DE.
* The Homestake Chlorine Experiment detected, as one of the first experiments, fewer electronic neutrinos emitted by the sun than expected by the stellar theory [34]. Moreover, the ratio of muonic to electronic neutrinos originating from the atmosphere was measured to be inferior to the expectation [35]. The missing neutrinos are explained by neutrino flavour oscillations of $\nu_e \leftrightarrow \nu_\tau$ [36] and $\nu_\mu \leftrightarrow \nu_\tau$ [37]. These *neutrino flavour oscillations* are not part of the SM.
* The SM does not include *gravity*, which is expressed in the most general way as

General Relativity (GR) by Albert Einstein. The recent discovery of gravitational waves, released by a binary black hole merger, confirms the prediction of Einstein's theory [38]. This discovery enforces the need for a Grand Unified Theory, which combines the SM and GR and is validated by experiments.

* Conceptual problems of the SM are the open questions: Why does the SM include precisely three generations of leptons and quarks? Why are the fermion masses and the CKM elements arranged in such a hierarchical order? Why interactions between leptons and quarks at the same time are not part of the SM? Why are 19 parameters, including the fermion masses, the coupling strengths and the CKM parameters, not predicted by the SM? Why is the mass range of the particles so dispersed? Why is the electric charge quantized?

All of these shortcomings of the SM suggest the existence of NP. In modern particle physics, two distinct approaches are, in principle, applied to search for signs of NP. The first approach involves the production of NP particles on-shell and measuring their properties. These direct searches are typically performed in collider experiments with high centre-of-mass energies. An example of this approach is the famous discovery of the Higgs-boson by the ATLAS and CMS experiment at the Large Hadron Collider (LHC) [18,19]. However, this approach is limited to NP particle masses equal to or below the centre-of-mass energy of the collision $\sqrt{s}$.

The second approach, which is commonly used in flavour physics, is known as the *indirect searches*. The idea behind this second approach is to measure the amplitudes of well-known SM processes. Virtual NP particles could contribute and cause deviations in the observables. Due to the virtual nature of quantum loops, NP particles with masses in the TeV range can be implied by those measurements. [10]

Thanks to the indirect searches, several important discoveries have been made. One example is the prediction of the existence of a third quark family through the CP violation measurement in kaon decays even before the discovery of the charm quark [39,41]. Another example is the observation of B^0- $\overline{B}^0$ mixing [42]. Through the virtual presence of the t quark in the mixing diagram, a larger t quark mass than expected could be derived [43,44].

1.2 Rare *b*-hadron decays

Searching for NP in $b \to s\ell^+\ell^-$ transitions [11] is promising because those transitions are forbidden in the SM at tree-level and occur, thus, via penguin and box diagrams. Additional to the loop suppression, these transitions are Cabibbo-suppressed by the $|V_{qs}^* V_{qb}|$

10. Measurements of CP violation in kaon mixing can even access NP scales up to 4.7×10^5 TeV. [**?**,40]
11. Particle conjugation is implied throughout this thesis, when not stated otherwise.

CKM matrix elements, where q stands for an up-type quark. The contribution of the virtual t quark dominates in the box diagram and the electroweak penguin diagram via virtual Z-bosons, while the electroweak penguin diagram via a virtual photon can have large contributions of the c quark [45]. Due to these suppressions, the branching fractions of those decays are of the order $\mathcal{O}(10^{-6})$ or below. This is the reason why they are called *rare decays*. The three leading-order Feynman diagrams are shown in figure 1.2.

In several NP models, supplementary interactions of a beauty quark to a strange quark and a dilepton pair are allowed. Those transitions would contribute to the branching ratios and angular observables. Exemplary NP Feynman diagrams are shown in figure 1.3. The left two diagrams are tree-level interactions with a Z' boson and a leptoquark [46,47]. On the right side a box diagram with a charged Higgs-bosons pair is shown, as predicted for example in the two Higgs doublet model (2HDM) [48], and in supersymmetric (SUSY) models [49].

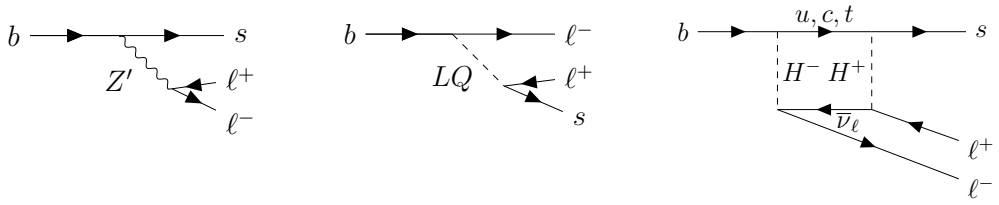

Figure 1.3 – Three Feynman diagrams of $b \to s\ell^+\ell^-$ transitions with possible NP particles are sketched, namely interactions of a Z' boson (left), a scalar leptoquark with charge $q = 2/3$ (center) and two oppositely charged Higgs bosons (right).

Due to the low branching ratio of $b \to s\ell^+\ell^-$ decays, even small NP contributions could cause large deviations. In addition, those rare decays are accessible with the data collected by collider experiments. Therefore, rare decays are especially suited for NP searches and their study is essential in order to shape the landscape of possible NP scenarios.

1.2.1 Effective Hamiltonian

Theoretical predictions of observables in rare decays are challenging to compute, because of the presence of three largely separated energy scales. The first one is defined by the flavour-changing transition via the weak gauge boson to be at $m_W \sim 80\,\text{GeV}$. The second energy scale is the b-quark mass, which is set by the b-hadron decay. It is situated at around 4 GeV. The energy scale of strong interactions within the hadrons is the Λ_{QCD} scale. Those largely separated energy scales make the computation of the rare decay amplitudes difficult and non-reliable due to the involvement of large logarithms [50].

Effective Field Theories (EFT) allow a model-independent treatment to calculate those amplitudes. Within their validity range, EFTs are more powerful and straightforward than the full theory. An EFT is a QFT, which is only valid in a smaller energy range. The main idea is to separate long- and short-distance physics with respect to a factorisation scale μ, where the process takes place. The high-energy part is integrated out in the Wilson Coefficients (WCs) $\mathcal{C}_i^{(\prime)}$ [50]. In the presence of NP at high energies, the WCs would be shifted. The low-energy part is described by the operators $\mathcal{O}_i^{(\prime)}$, which contain the hadronic part of the interaction. Separating the two scales is referred to as the factorisation of the high- and low-energy effects. The effective theory below the electroweak scale is called the Weak Effective Theory (WET).

For the tree-level process of a $W^{\pm}$ boson exchange in the s-channel, the WC of the four-point interaction is the Fermi-coupling G_F multiplied by the CKM matrix elements. Gluon exchanges between the in- and out-coming quarks introduce corrections, which are described in WET by the operators $\mathcal{O}_1^q$ and $\mathcal{O}_2^q$ with $q \in \{u, c\}$. Those are called current-current operators, and expressed as

$$\mathcal{O}_1^q = (\bar{s}\gamma_\mu T^a P_L q)(\bar{q}\gamma^\mu T^a P_L b), \tag{1.33}$$

$$\mathcal{O}_2^q = (\bar{s}\gamma_\mu P_L q)(\bar{q}\gamma^\mu P_L b). \tag{1.34}$$

Semileptonic electroweak penguin decays are described by the operators $\mathcal{O}_9$ and $\mathcal{O}_{10}$. The operator for the radiative electroweak penguin decays is denoted by $\mathcal{O}_7$. According to Ref. [5], those operators are defined as

$$\mathcal{O}_7 = \frac{e}{16\pi^2} m_b (\bar{s}\sigma_{\mu\nu} P_R b) F^{\mu\nu}, \tag{1.35}$$

$$\mathcal{O}_9 = \frac{e^2}{16\pi^2} (\bar{s}\gamma_\mu P_L b)(\bar{\ell}\gamma^\mu \ell), \tag{1.36}$$

$$\mathcal{O}_{10} = \frac{e^2}{16\pi^2} (\bar{s}\gamma_\mu P_L b)(\bar{\ell}\gamma^\mu \gamma_5 \ell). \tag{1.37}$$

The tensor $\sigma_{\mu\nu}$ can be expressed as the commutator of the gamma matrices $\sigma_{\mu\nu} = \frac{i}{2}[\gamma_\mu, \gamma_\nu]$. $F^{\mu\nu}$ is the electromagnetic field strength tensor

$$F_{\mu\nu} = \partial_\nu A_\mu - \partial_\mu A_\nu. \tag{1.38}$$

All of the above-mentioned operators are depicted in figure 1.4. Using those combined operators, the effective SM Hamiltonian for $b \to s\ell^+\ell^-$ transitions [5, 51–53] is written

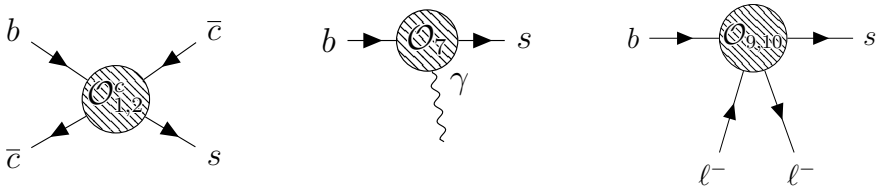

Figure 1.4 – Sketch of the hadronic current-current operators $\mathcal{O}^c_{1,2}$, the semileptonic electroweak penguin operators $\mathcal{O}_{9,10}$ and the radiative dipole operator $\mathcal{O}_7$.

as [12]

$$\mathcal{H}_{\text{eff}}(b \to s\ell^+\ell^-) = -\frac{4G_F}{\sqrt{2}} V_{tb}V_{ts}^* \sum_{i=1}^{10} \mathcal{C}_i \mathcal{O}_i + h.c.\,. \tag{1.39}$$

The decay amplitude of a given process is calculated by

$$\begin{aligned} \mathcal{A}(B \to f) &= \langle f|\mathcal{H}_{\text{eff}}|B\rangle \\ &= -\frac{4G_F}{\sqrt{2}} V_{tb}V_{ts}^* \sum_{i=1}^{10} \mathcal{C}_i(\mu)\langle f|\mathcal{O}_i(\mu)|B\rangle + h.c.\,. \end{aligned} \tag{1.40}$$

The WCs of an EFT are well-known since they can be matched to the full SM Lagrangian at m_W and run down to the factorisation scale. However, the calculation of the hadronic operators is demanding.

1.2.2 Hadronic contributions

The leptonic term in the decay amplitude, $\bar{\ell}\gamma^\mu(\gamma_5)\ell$, which are part of the operators $\mathcal{O}_{9,10}$ can be calculated in perturbation theory. The hadronic part of a given decay amplitude is difficult to calculate because of the non-perturbative nature of QCD at low energies.

For the matrix elements of currents, the hadronic contribution can be written as a sum of independent Lorentz structures multiplied by form factors. These form factors need to be predicted and depend on kinematic variables, especially the squared di-lepton invariant mass q^2. Different methods are employed to calculate the form factors. The most precise one is the Lattice QCD prediction. It does not depend on perturbative expansions but calculates QCD on the lattice. The shape of the form factors in terms of q^2 are then extrapolated from those points. This method is limited by the computational power and

12. In this effective Hamiltonian, corrections proportional to $V_{ub}V_{us}^*$ are neglected, since $|V_{ub}V_{us}^*/V_{tb}V_{ts}^*| < 0.2$ [52].

is usually only available in the high-q^2 region. Other methods can be applied in specific q^2 regions. Those are for example the heavy quark expansion, quark models or QCD and light-cone sum rules. Form factors can be extracted from experimental data, too.

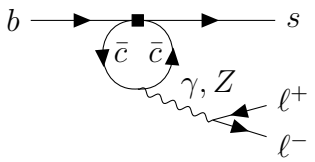

Figure 1.5 – Charm loops occuring at the $b \to s$ vertex are from a theoretical point of view problematic for c quark energies below the b mass.

At the $b \to s$ vertex, $c\bar{c}$ loops can occur, as depicted in figure 1.5. For charm quarks with energies above the b mass, the effect is local. The hadronic $\mathcal{O}^c_{1,2}$ can, therefore, be factorized and expressed in perturbation theory by form factors times a coefficient. [13] In the case of charm quark energies below the b mass, the effect is non-local. What happens is that the charm quarks form hadrons already after travelling finite distances. These hadronic non-local effects cannot be computed from the first principles and are subject of debates in the theory community.

The problem with the charm loops is that they can mimic NP contributions, as they can be interpreted as shifts of the WCs $\mathcal{C}_7$ and $\mathcal{C}_9$. In Ref. [54], a new parametrisation and uncertainty estimation of non-local form factors was developed for the $B \to K^{(*)}\mu^+\mu^-$ and $B^0_s \to \phi\mu^+\mu^-$ decays. Similar to an extrapolation of local form factors between the Lattice QCD predictions, available at high q^2, and the light-cone sum rule predictions, calculated at low q^2, the non-local form factors are evaluated in two kinematic regimes. The local operator product expansion (OPE) is used at $|q^2| \gtrsim m_b^2$ and theory points at $q^2 < 0$ are calculated via the light-cone OPE [55]. The non-local contributions can be constrained by fitting experimental BF results at the charmonium resonances and the branch cut, due to the $D^{(*)}_{(s)}$-meson production. The theoretical uncertainties are constrained by dispersive bounds, received from the $e^+e^- \to \bar{b}s$ cross-section.

The key point is that NP at energy scales of $\Lambda_{NP} \gg m_W$ can be described by an EFT. Either NP can modify already existing WCs or add new operators. Indirect searches of NP measure these WCs. An example of existing operators are the chirality flipped [14]

13. However, for the actual value of the b mass, power corrections to factorization, i.e. non-perturbative, long-distance contributions, might be significant.

14. The chirality flip is expressed mathematically by switching the chiral projection operator $P_L \leftrightarrow P_R$.

operators or the (pseudo-)scalar operators

$$\mathcal{O}_S^{(\prime)} = (\bar{s}P_{R(L)}b)(\bar{\ell}\ell), \tag{1.41}$$

$$\mathcal{O}_P^{(\prime)} = (\bar{s}P_{R(L)}b)(\bar{\ell}\gamma_5\ell). \tag{1.42}$$

The chirality flipped operators are suppressed in the SM by a factor $\frac{m_s}{m_b}$. The above-mentioned (pseudo-)scalar operators and the $\mathcal{O}_{10}$ are important for the $B^0_{(s)} \to \mu^+\mu^-$ decay. The dominant contribution is found numerically to be the $\mathcal{O}_{10}$ operator. The branching fraction of this decay is very small due to the additional helicity suppression. In the case of NP, it could be particularly sensitive to NP contributions [56]. In the SM, the chromomagnetic operator $\mathcal{O}_8$ and four-quark operators $\mathcal{O}^{(\prime)}_{1-6}$ exist, too. However, $b \to s\ell^+\ell^-$ transitions are less sensitive to NP contributions to the operators $\mathcal{O}^{(\prime)}_{1-6}$ [15].

1.2.3 Experimental measurements

As said before, $b \to s\ell^+\ell^-$ transitions are a good probe of the SM since NP could contribute to the loop-mediated SM process, which would change the measurement of the observables. Several observables exist to test the SM, but they possess different theoretical "cleanness". Branching fraction (BF) measurements are, for example, the less clean observables because the hadronic form factors have large uncertainties. It is possible to construct observables, which are less affected by the hadronic contributions [16]. Those can be accessed in angular analyses. The cleanest observables are Lepton Flavour Universality tests. Those are measured as a ratio of the muonic and electronic decay. The hadronic contributions are the same for both decays and cancel entirely in the SM. The remaining effect is due to Final State Radiation and is a source of a deviation of at most 1% [58]. Differences in lepton masses contribute only at the order of 0.1%. The experimental measurements of the various observables in different decay modes are listed in this subsection. In this thesis, the theoretical predictions used in the experimental publications are referred to as "SM predictions" without judging their completeness and correctness.

Differential branching fraction measurements

A differential branching fraction measurement denotes the measurement of a BF as a function of another observable. The BF of rare decays is usually measured with re-

15. NP contributions could leak into the semileptonic operators through renormalization group evolution [57].

16. The cleanness of the angular observables would be decreased in the case power corrections to factorization are a dominant source of hadronic uncertainties.

spect to the dilepton invariant mass q^2. A sketch of the differential BF, expected in $\Lambda_b^0 \to \Lambda(1520)\mu^+\mu^-$ decays, is shown in figure 1.6. Depending on the q^2 region, the differ-

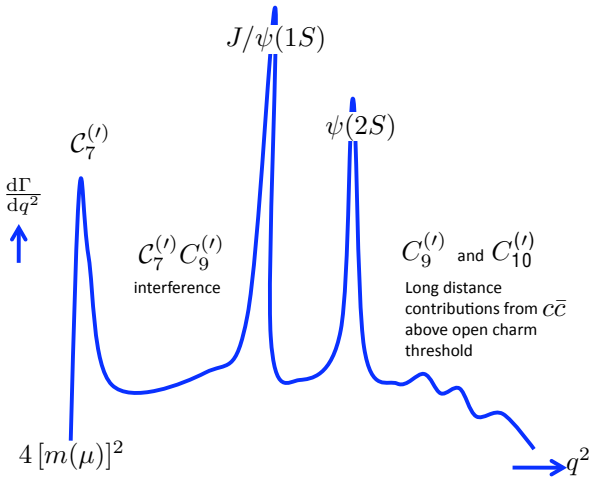

Figure 1.6 – Sketch of the expected spectrum of the differential branching ratio of the $\Lambda_b^0 \to \Lambda^{(*)}\mu^+\mu^-$ decay as a function of the squared dilepton invariant mass. The left peak represents the photon pole. The peaks of the charmonium resonance states J/ψ and $\psi(2S)$ are visible, too. Taken from Ref. [59].

ential branching fraction measurement accesses different WCs. At the photon pole, $\mathcal{C}_7^{(\prime)}$ contributions are measured. Thanks to the abundance of the $b \to c\bar{c}s$ transitions in comparison to the $b \to s\ell^+\ell^-$ decays, the decay modes $\Lambda_b^0 \to pK^-J/\psi$ and $\Lambda_b^0 \to pK^-\psi(2S)$ serve as the control modes of the analysis. The corresponding leading-order diagram is shown in Fig. 1.7.

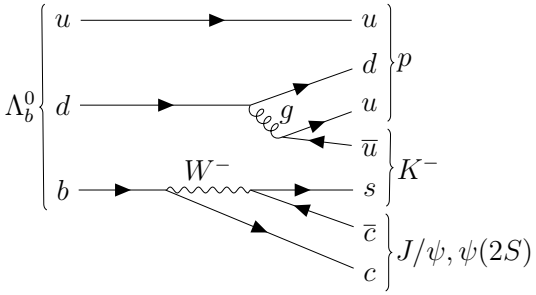

Figure 1.7 – Leading order diagram of the $\Lambda_b^0 \to pK^-J/\psi$ and $\Lambda_b^0 \to pK^-\psi(2S)$ decay.

The differential BF measurements are usually normalised by the J/ψ mode [60]. The

expression of the $\Lambda_b^0 \to \Lambda(1520)\mu^+\mu^-$ differential BF is exemplarily written as

$$\int_{q^2{}_{\min}}^{q^2{}_{\max}} \frac{d\mathcal{B}(\Lambda_b^0 \to \Lambda(1520)\mu^+\mu^-)}{dq^2} dq^2 \tag{1.43}$$
$$= \frac{1}{(q^2{}_{\max} - q^2{}_{\min})} \frac{\mathcal{B}(\Lambda_b^0 \to pK^- J/\psi)\mathcal{B}(J/\psi \to \mu^+\mu^-)}{\mathcal{B}(\Lambda(1520) \to pK^-)} \frac{N_{\Lambda(1520)\mu^+\mu^-}}{N_{pK^- J/\psi}} \frac{\varepsilon_{pK^- J/\psi}}{\varepsilon_{\Lambda(1520)\mu^+\mu^-}}.$$

The yields $N_{pK^- J/\psi}$ and $N_{\Lambda(1520)\mu^+\mu^-}$ are measured by a fit to the data points. The efficiencies $\varepsilon_{\Lambda(1520)\mu^+\mu^-}$ and $\varepsilon_{pK^- J/\psi}$ are calculated with the help of the simulation sample. Ref. [21] provides the branching fractions of $\mathcal{B}(J/\psi \to \mu^+\mu^-) = (5.961 \pm 0.033)\%$ and $\mathcal{B}(\Lambda(1520) \to pK^-) = (22.5 \pm 0.5)\%$ by considering the isospin symmetry.

The LHCb collaboration measured the differential BFs of the $B^+ \to K^{(*)+}\mu^+\mu^-$, $B^0 \to K^{(*)0}\mu^+\mu^-$, $B^\pm \to \pi^\pm\mu^+\mu^-$ and $\Lambda_b^0 \to \Lambda^0\mu^+\mu^-$ decays using the Run 1 dataset [61–65]. Λ^0 denotes the ground-state Λ resonance. The differential BF of $B_s^0 \to \phi\mu^+\mu^-$ decays is determined with the full Run 1 and 2 dataset [66]. Some of those measurements are shown in figure 1.8. The measurement of the $B^0 \to K^{*0}\mu^+\mu^-$ decay includes SM predictions from Lattice QCD (Lattice) and Light-Cone Sum Rules (LCSR). The theoretical predictions of the $\Lambda_b^0 \to \Lambda^0\mu^+\mu^-$ differential BF are Lattice QCD predictions [68]. The LHCb collaboration published several differential BF measurements of $b \to s\mu^+\mu^-$ decays, where the resulting values are situated below the SM prediction. Ref. [66] claims a deviation of $3.6\,\sigma$ in the 1.1-6.0 GeV^2/c^4 q^2 bin between the measured BF of $B_s^0 \to \phi\mu^+\mu^-$ decays and the predicted one.

The Belle, BaBar and CMS collaboration measured BFs of the $B \to K^{(*)}\mu^+\mu^-$ decay, too [67,69–72]. Measurement of $B \to K^{(*)}\mu^+\mu^-$, $B_s^0 \to \phi\mu^+\mu^-$ and $\Lambda_b^0 \to \Lambda^0\mu^+\mu^-$ decays were performed by the CDF collaboration [73]. All of those results are consistent with the SM prediction but have larger uncertainties than the LHCb measurements. Some are represented in Fig. 1.8 for illustration.

Thanks to the leptonic final state, the $B_{(s)}^0 \to \mu^+\mu^-$ BF measurement is theoretically clean. The hadronic part of the decay is encoded in the decay constants f_B and f_{B_s}, which are precisely known from Lattice QCD [74]. Due to the additional helicity suppression of this $b \to s\ell^+\ell^-$ decay, the BFs of those decays are predicted to be in the SM [75, 76] of about

$$\mathcal{B}(B_s^0 \to \mu^+\mu^-) = (3.66 \pm 0.14) \times 10^{-9}, \tag{1.44}$$
$$\mathcal{B}(B^0 \to \mu^+\mu^-) = (1.03 \pm 0.05) \times 10^{-10}. \tag{1.45}$$

The pure leptonic final state is experimentally very clean, too. This decay is interesting since it constrains many NP scenarios, for example, SUSY models [77].

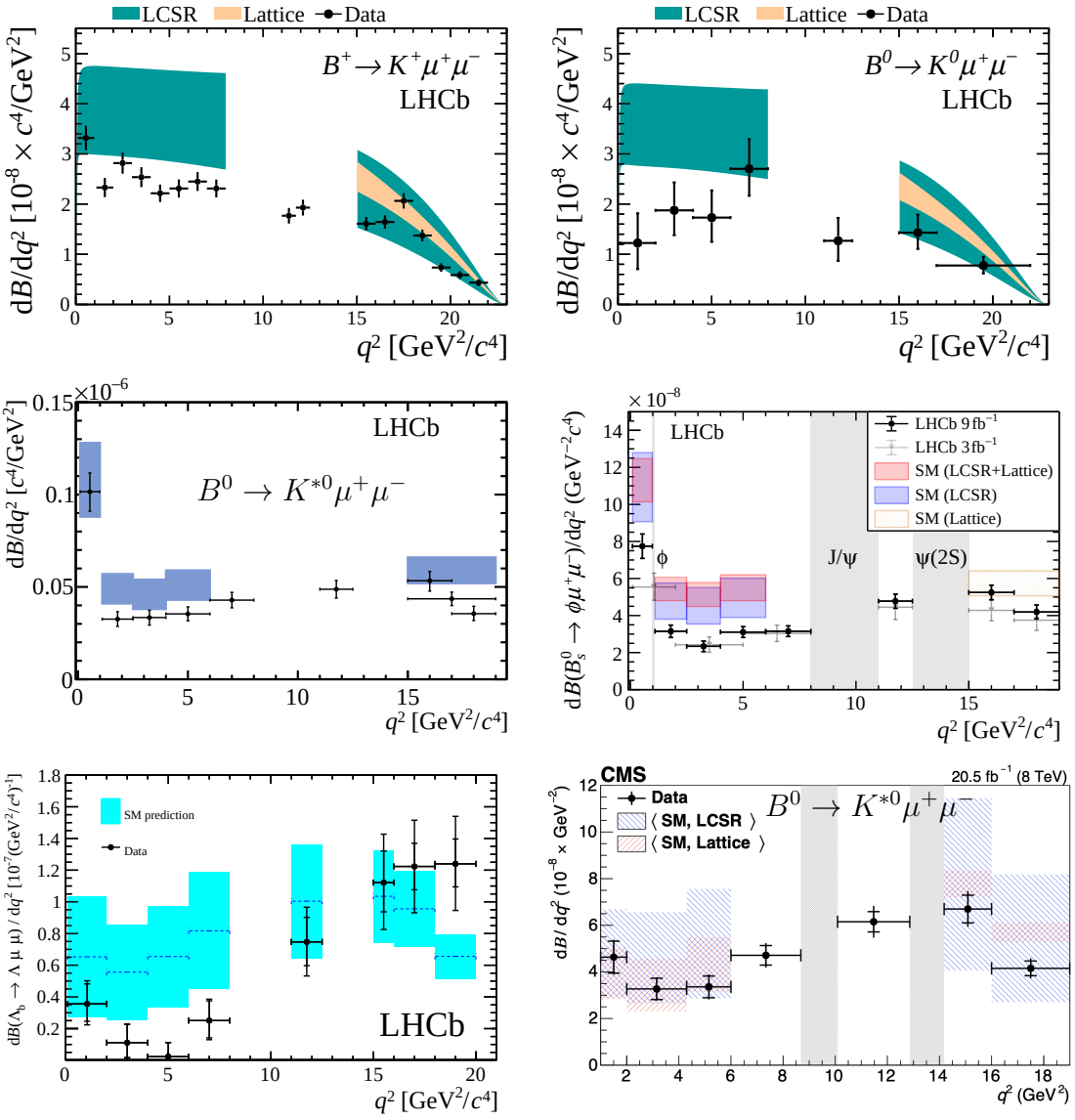

Figure 1.8 – The LHCb measurements of the differential BFs of the $B^+ \to K^+\mu^+\mu^-$ (top left), $B^0 \to K^0_S\mu^+\mu^-$ (top right), $B^0 \to K^{*0}\mu^+\mu^-$ (center left), $B^0_s \to \phi\mu^+\mu^-$ (center right) and $\Lambda^0_b \to \Lambda^0\mu^+\mu^-$ decays (bottom left) are drawn [61, 62, 65, 66]. As a comparison, the differential BF of the $B^0 \to K^{*0}\mu^+\mu^-$ decay, measured by the CMS collaboration, is presented (bottom right) [67].

Angular analyses and how they work

The principle of angular analyses is to measure the differential decay width as a function of the decay angles. The decay angles $\vec{\Omega}$ are usually defined in the helicity frame, which is shown exemplarily for the $\Lambda_b^0 \to \Lambda(1520)\mu^+\mu^-$ decay in figure 1.9.

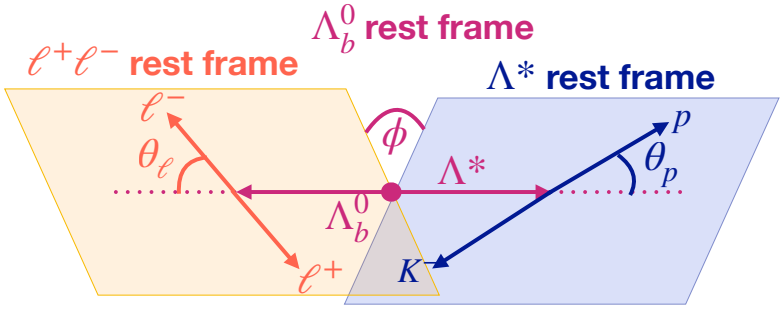

Figure 1.9 – The definition of the $\Lambda_b^0 \to pK^-\mu^+\mu^-$ decay angles is sketched in the helicity frame.

The differential decay width is defined as

$$\frac{d^4\Gamma}{dq^2 d\vec{\Omega}} = k \sum_i L_i(q^2, \mathcal{C}, \text{ff}) \times f_i(\vec{\Omega}). \tag{1.46}$$

k represents a factor guaranteeing the normalisation. The polynomials f_i depend on the decay topology. The angular coefficients L_i encode the physics since they depend on the WCs. However, form factor predictions are needed to compute the angular coefficients, if assuming factorization.

The angular coefficients describing the Λ_b^0 and $\overline{\Lambda}_b^0$ decay are represented as L_i and $\bar{L}_i$. Using them, the *CP*-symmetric and asymmetric angular observables

$$S_i = \frac{L_i + \bar{L}_i}{d(\Gamma + \bar{\Gamma})/dq^2}, \tag{1.47}$$

$$A_i = \frac{L_i - \bar{L}_i}{d(\Gamma + \bar{\Gamma})/dq^2}. \tag{1.48}$$

are constructed. Theoretically optimised observables are built by combining several angular observables in order to minimise the effect of hadronic uncertainties. Examples of such optimised observables are the leptonic forward-backwards asymmetry A_{FB}^ℓ and P_5'. Their definitions depend on the studied process. In Ref. [78, 79], P_5' is defined as

$$P_5' = \frac{S_5}{2\sqrt{F_L(1-F_L)}}. \tag{1.49}$$

F_L represents the fraction of longitudinal polarised $K^{(*)}$ hadrons.

The LHCb collaboration measured the angular observable P_5' in $B^0 \to K^{*0}\mu^+\mu^-$ and $B^+ \to K^{*+}(\to K^0_S\pi^+)\mu^+\mu^-$ decays, which are performed with the Run 1 and 2016 dataset and the full Run 1 and 2 dataset [78, 79]. Local tensions with respect to the SM are detected in the P_5' observable of about 2.9σ and 3.0σ in the $6.0 < q^2 < 8.0\,\mathrm{GeV}^2/c^4$ bin. The hadronic longitudinal polarisation of $B^0_s \to \phi(\to K^+K^-)\mu^+\mu^-$ decays is determined using the Run 1 and 2016-18 dataset [80]. The distributions of the angular observables are shown in Fig. 1.10. The angular observables measured in Ref. [78,79] reach independently a deviation of 3.3σ and 3.1σ in the real part of the WC $\mathcal{C}_9$. All of them show the same pattern of a negative shift in the effective coupling strength.

Angular observables of electroweak penguin decays are analyzed by the Belle, CMS and ATLAS experiment, too [81–83]. Compared to the LHCb results, those measurements have larger uncertainties. The Belle collaboration performed a lepton-flavour-dependent angular analysis in the $B \to K\ell^+\ell^-$ decays. The strongest local tension between the measured P_5' value and the SM prediction is determined to be in the $q^2 \in [4, 8]\,\mathrm{GeV}^2/c^4$ bin. The muon mode shows local tensions of about 2.6σ, while a deviation of 1.3σ is measured in the electron mode. The overall combined value deviates by 2.5σ from the SM prediction [82]. The ATLAS collaboration reported in the $q^2 \in [4, 6]\,\mathrm{GeV}^2/c^4$ bin a local tension of 2.7σ in the $B^0 \to K^{*0}\mu^+\mu^-$ decay using both angular observables, P_5' and P_4'. In turn, the CMS collaboration does not measure tensions of the measured value of the P_5' observable in $B^0 \to K^{*0}\mu^+\mu^-$ decays and the SM prediction.

The $\mathcal{C}_7^{(\prime)}$ photon pole can be accessed by measuring the angular observables in the very low q^2 bin ($q^2 \to 0$). The most precise measurements of the virtual photon polarisation up-to-date were performed by the LHCb experiment using $B^0 \to K^{*0}e^+e^-$ decays with the full Run 1 and 2 datasets in the $q^2 \in [0.00008, 0.257]\,\mathrm{GeV}^2/c^4$ bin [84] and was found to be compatible with the SM prediction. A ratio of right- over left-handed photon polarisation amplitudes was performed in $B^0_s \to \phi\gamma$ decays with the 2011 - 2016 dataset collected by the LHCb detector [85]. Angular analyses to access the virtual photon polarisation with measurements on the photon pole are performed for example in $\Lambda_b^0 \to \Lambda^0\gamma$ decays using the Run 2 dataset [86] and $B^\pm \to K^\pm\pi^\mp\pi^\pm\gamma$ decays using the Run 2 and Run 1 dataset only [87]. The photon polarisation can also be accessed by measurements of CP-induced asymmetries, which have been measured for example by BaBar, Belle and LHCb [88–90]. All of these measurements constrain the C_7' enhancement, which is predicted in some NP models.

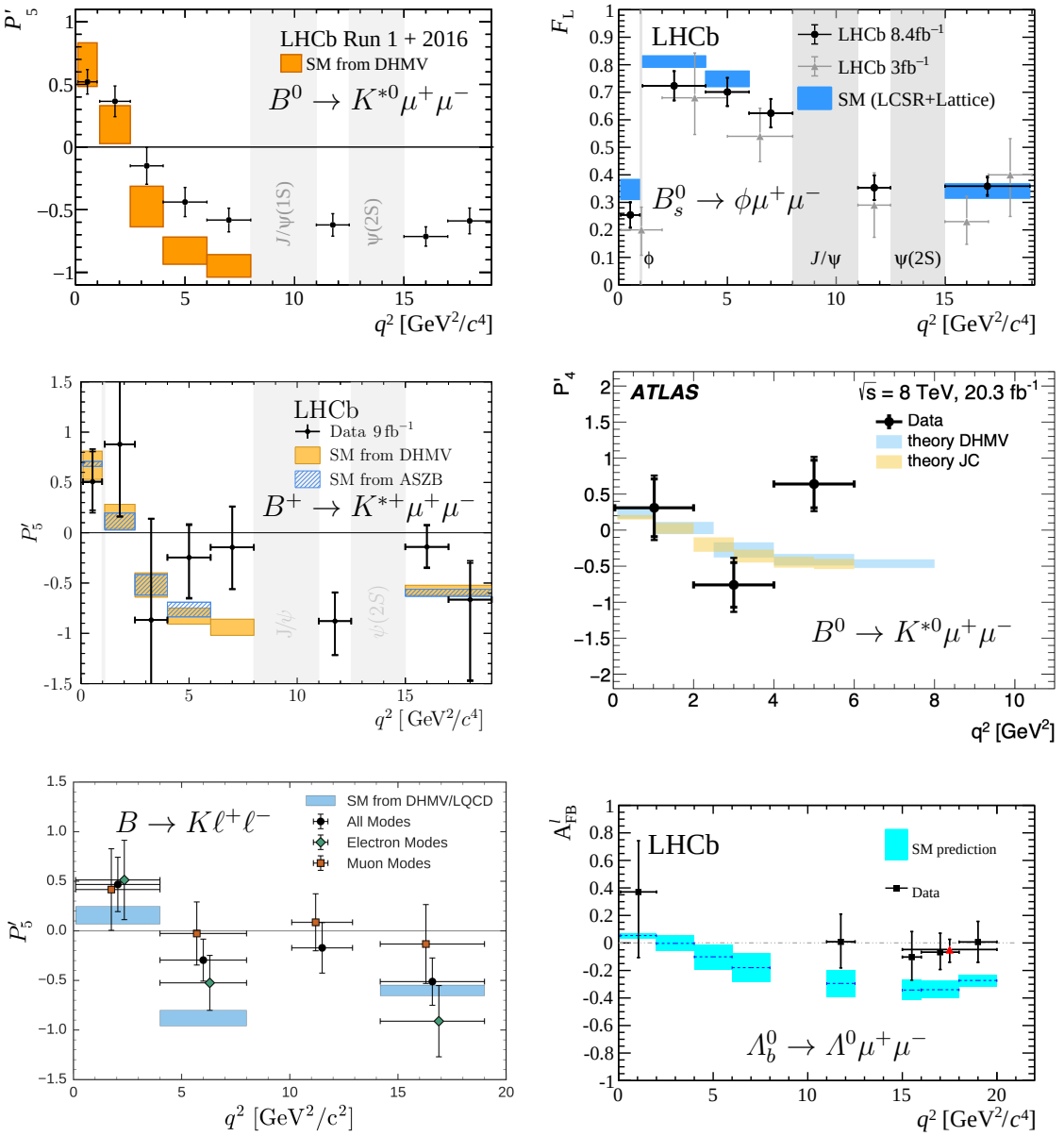

Figure 1.10 – LHCb measurements of the angular observables in $B^0 \to K^{*0}\mu^+\mu^-$ (top left), $B_s^0 \to \phi\mu^+\mu^-$ (top right), $B^+ \to K^{*+}\mu^+\mu^-$ (center left) and $\Lambda_b^0 \to \Lambda^0\mu^+\mu^-$ decays (bottom right) [65, 78–80]. The ATLAS collaboration performed an angular analysis with $B^0 \to K^{*0}\mu^+\mu^-$ decays (center right) [81]. An angular analysis of the Belle collaboration using several $B \to K\mu^+\mu^-$ decay modes is presented (bottom left) [82].

Lepton Flavour Universality tests

In the B meson sector, a test of Lepton Flavour Universality (LFU) can be constructed to be the ratio of the $b \to s\mu^+\mu^-$ over the $b \to se^+e^-$ transition of the same hadronic transition. Because of the cancellation of hadronic uncertainties in the SM ratio, LFU tests are the theoretically cleanest observables in the SM. Furthermore, the ratio is experimentally advantageous since a large number of systematic uncertainties cancel. The LFU ratios of a b-hadron H_b decaying into a strange hadron H_s and two leptons can be written in bins of $q^2 \in [q^2_{\text{min}}, q^2_{\text{max}}]$ as

$$R_{H_s} = \frac{\int_{q^2_{\text{min}}}^{q^2_{\text{max}}} \frac{d\mathcal{B}(H_b \to H_s \mu^+\mu^-)}{dq^2} dq^2}{\int_{q^2_{\text{min}}}^{q^2_{\text{max}}} \frac{d\mathcal{B}(H_b \to H_s e^+e^-)}{dq^2} dq^2}. \tag{1.50}$$

Due to the lepton universal coupling of the weak bosons, the SM prediction of the R-ratios are close to unity with theoretical uncertainties at per cent level [91,92]. At very low q^2 values, close to the muon mass threshold $q^2 = 4m^2_\mu \approx 0.045$ GeV$^2/c^4$, the kinematic region of the muon is reduced, and the LFU ratio gets slightly smaller than one [92]. This effect is negligible by considering the q^2 region above 0.1 GeV$^2/c^4$.

The LHCb collaboration tested the LFU ratios of the $B^0 \to K^0_S \ell^+\ell^-$, $B^+ \to K^{*+}(\to K^0_S\pi^+)\ell^+\ell^-$ decays with the full Run 1 and 2 dataset. Those have been found to be smaller than unity and are drawn in Fig. 1.11 [93]. However, the first decay includes the critical q^2 region below 0.1 GeV$^2/c^4$. The recent simultaneous fit of R_{K^+} and $R_{K^{*0}}$ has been published with the full Run 1 and 2 dataset [58,94]. The measurements in the two q^2 bins agree with unity within one standard deviation and supersede the previous individual determinations of R_{K^+} and $R_{K^{*0}}$ [97,98]. The LHCb experiment published the LFU ratio of the $\Lambda^0_b \to pK^-\ell^+\ell^-$ decay, measured with Run 1 and 2016 data, which was found to be compatible with the SM within one standard deviation [95]. BaBar and Belle performed LFU tests in $B \to K^{(*)}\ell^+\ell^-$ decays and are compatible with the SM, as well [69–71,96].

Even though the LFU ratios are mostly compatible with the SM, a tendency to lower R values is visible. Therefore, it is important to check their behaviour with a higher data sample size.

1.2.4 Global EFT fits

The behaviour of angular observables, LFU tests and BFs can be interpreted by global fits, with which the consistency of the results, in terms of WCs for example, is checked. The global fit of the $b \to s\ell^+\ell^-$ BFs and angular observables is shown in figure 1.12.

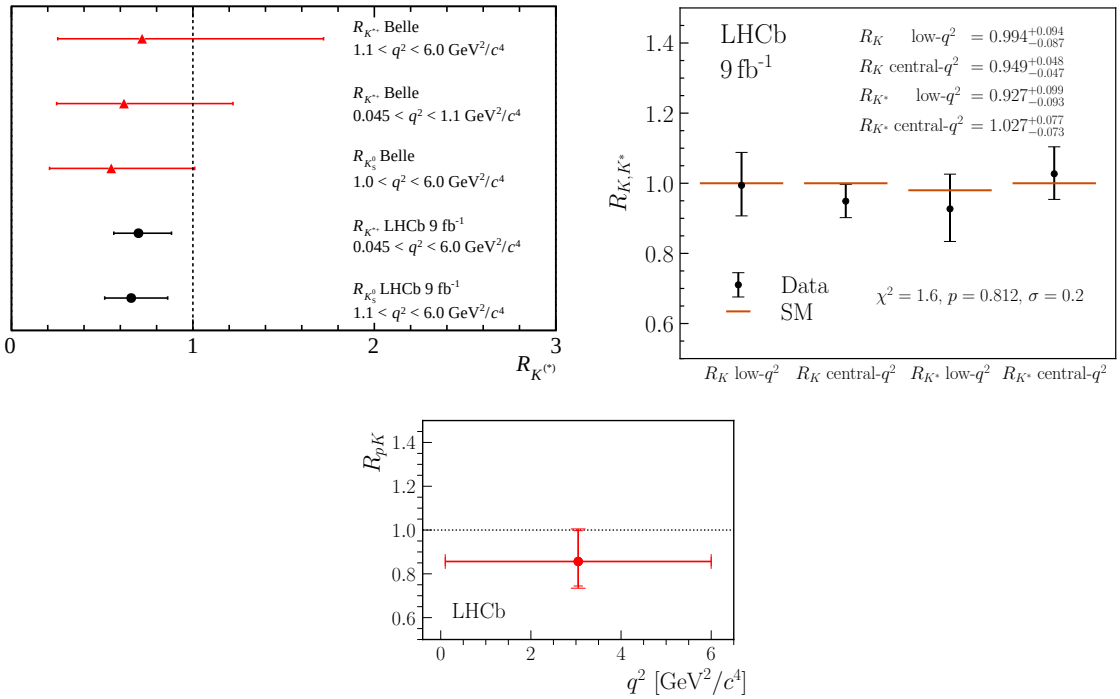

Figure 1.11 – The LFU ratios of the $B^0 \to K^0_S \ell^+\ell^-$, $B^+ \to K^{*+}(\to K^0_S\pi^+)\ell^+\ell^-$ (top left), the $B^+ \to K^+\ell^+\ell^-$ and $B^0 \to K^{*0}\ell^+\ell^-$ (top right) and the $\Lambda^0_b \to pK^-\ell^+\ell^-$ decays (bottom) are presented [58, 93–95]. The Belle measurements of $R_{K^{*+}}$ and R_{K^+} are also drawn [70, 96].

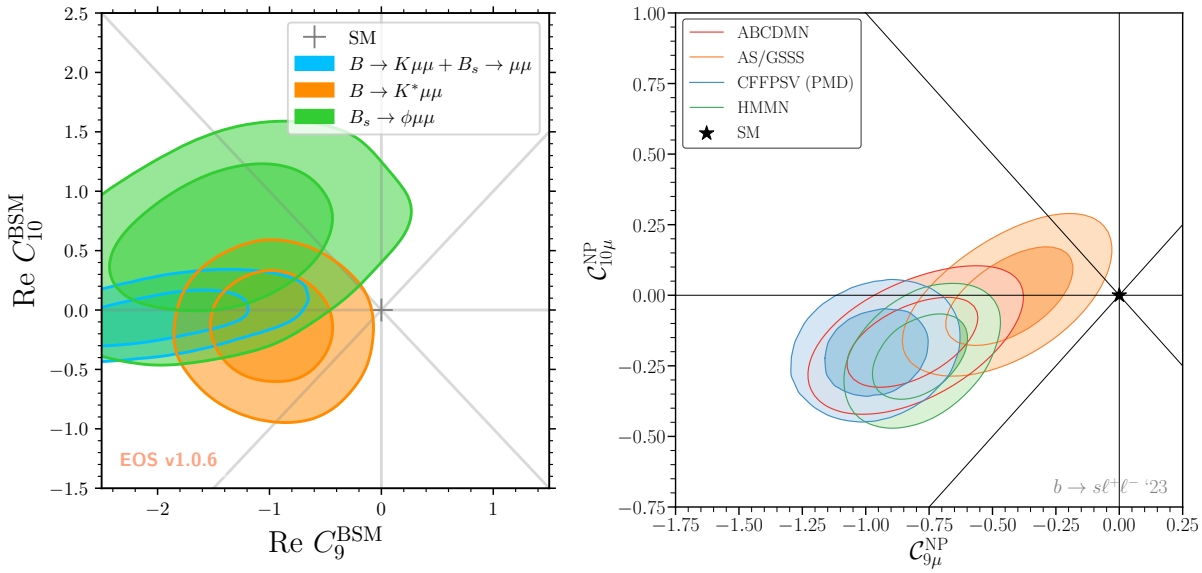

Figure 1.12 – The combination of angular observables and differential branching fractions of $b \to s\ell^+\ell^-$ decays are drawn on the left (from Ref. [99]), using the Lattice QCD form factor for $B \to K\ell^+\ell^-$ decays [100] and the CMS measurement of $B_s^0 \to \mu^+\mu^-$. Baryonic decays are not yet part of this combination. The Wilson coefficients $\mathcal{C}_i^{\rm NP}$ and $\mathcal{C}_i^{\rm BSM}$ describe both the New Physics contribution. On the right, four Global fits (from Ref. [101]) based on different form factor predictions, different $b \to s\ell^+\ell^-$ observables, different assumptions about the non-local matrix elements and different statistical frameworks are presented [102–104] (and update of Ref. [105]). All four theory groups treat the hadronic uncertainties model dependently.

Drawn are the Wilson coefficients describing NP, which are defined as

$$\mathcal{C}_i^{\mathrm{NP}} = \mathcal{C}_i - \mathcal{C}_i^{\mathrm{SM}}. \tag{1.51}$$

The notation of $\mathcal{C}_i^{\mathrm{NP}}$ and $\mathcal{C}_i^{\mathrm{BSM}}$ is equivalent.

Ref. [99] studied the deviations of the BF measurements from the different experiments. The authors believe in having a better handle on the charm loops by using a new parametrisation of the non-local form factors. Using their parametrisation, a tension of $5.7\,\sigma$ is observed with the combined BF measurements of the $B \to K\mu^+\mu^-$ and $B_s^0 \to \mu^+\mu^-$ decay mode with respect to the SM. Those measurements are combined to constrain simultaneously $\mathcal{C}_9$ and $\mathcal{C}_{10}$. Combining the BF measurements and angular analyses of the different experiments, a tension of the $B \to K^*\mu^+\mu^-$ and $B_s^0 \to \phi\mu^+\mu^-$ of $2.7\,\sigma$ and $2.6\,\sigma$ respectively is established. The best fit to the measurements is achieved by a shift in the WCs with respect to the SM WCs of

$$(\mathrm{Re}\ \mathcal{C}_9^{\mathrm{NP}}, \mathrm{Re}\ \mathcal{C}_{10}^{\mathrm{NP}}) \simeq (-1.0, +0.4). \tag{1.52}$$

Four independent Global fits, with separate statistical frameworks, are performed in Ref. [102–104]. The selection of the experimental results of the angular analyses, BF and LFU measurements differ between the theory groups. In addition, the theoretical form factors and the assumptions about non-local matrix elements differ. Using model-dependent treatment of the hadronic uncertainties, a consistent deviation in the WCs $\mathcal{C}_{9\mu}$ and $\mathcal{C}_{10,\mu}$ is observed in Fig. 1.12. In Ref. [104], the impact of a data-driven treatment of the hadronic uncertainties is studied. If strong, q^2 independent contributions are neglected in the model-dependent approach, the hadronic parameter could mimic NP effects in the $\mathcal{C}_9$ WC. On the contrary, the data-driven approach could absorb potential NP effects.

The real part of the WC ratio $\mathcal{C}_7'/\mathcal{C}_7$ is evaluated by a global fit in $\mathcal{C}_7$ and $\mathcal{C}_7'$. The combination of the measurements from BaBar, Belle and LHCb in different decay channels is consistent with the SM prediction, as presented in figure 1.12.

1.3 $\Lambda_b^0 \to pK^-\ell^+\ell^-$ decays

As seen in the previous section, the B anomalies in BFs and angular observables suggest a deviation of the WCs from the SM values. For validating or refuting the measured deviations, it is important to perform measurements in different $b \to s\ell^+\ell^-$ decay channels. In this work, the lightest b-baryon, the Λ_b^0, is studied. It decays via an electroweak penguin loop or box diagram to an excited Λ baryon, denoted as Λ^*, and a muon pair, as depicted in the dominant diagrams in Fig. 1.13. The Λ^* baryon decays via the strong

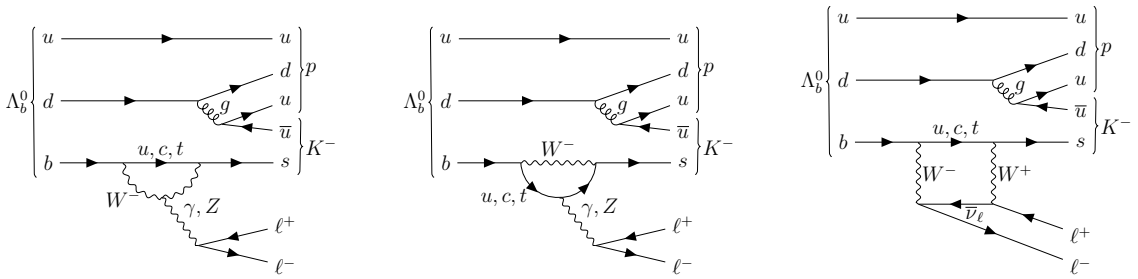

Figure 1.13 – Dominant diagrams of the $\Lambda_b^0 \to \Lambda(\to pK^-)\ell^+\ell^-$ decay.

interaction to a proton and a kaon. The ground-state Λ resonance, denoted as Λ^0, is forbidden to decay to the pK^- final state due to energy conservation.

1.3.1 Motivation

Up-to-date most of the measurements of $b \to s\ell^+\ell^-$ transitions are performed in b-meson decays. b-baryons carry spin, contrary to the B^0 and B^+ mesons, and give, thus, access to complementary information. Additionally, b-baryons possess a different hadronic environment than b-mesons. All in all, it is urgent to exploit the potential of b-baryon decay channels. This is the reason why for the first time an angular analysis of $\Lambda_b^0 \to pK^-\ell^+\ell^-$ decays is attempted. Another reason is the availability of theoretical predictions for the differential decay width and the form factors for specific Λ^* resonances. Therefore, a measurement of the angular observables could be compared to those predictions.

1.3.2 Experimental state of the art

An LFU test has already been performed in $\Lambda_b^0 \to pK^-\ell^+\ell^-$ decays using data collected by the LHCb experiment during Run 1 and 2016 [95]. The q^2 bin in-between 0.1 and 6.0 GeV$^2/c^4$ has been analyzed. R_{pK} has been found to be compatible with the SM, as shown in fig 1.11. The m_{pK^-} spectrum of the muon mode was measured to be as shown in Fig. 1.14 [106]. The muon mode was chosen, because of the larger yields compared to the electron mode. A peak around the $\Lambda(1520)$ resonance mass is distinguishable. The yields have been extrapolated in Ref. [107] to be within $0.1 < q^2 < 3.0$ GeV$^2/c^4$ of about 50 events using the total Run 1 and 2 datasets. Therefore, a limited data sample size is available. A detailed amplitude analysis over the full pK^- mass spectrum would be extremely difficult to realise with the current precision.

In 2015, LHCb published an angular analysis of $\Lambda_b^0 \to pK^-J/\psi(\to \mu^+\mu^-)$ decays. This measurement uses the full Run 1 data sample, it amounts to an integrated luminosity of

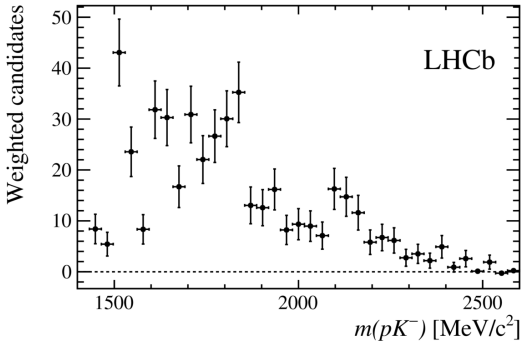

Figure 1.14 – The $\Lambda(1520)$ resonance is visible "by eye" in the background subtracted pK^- mass spectrum measured by the LFU analysis in $\Lambda_b^0 \to pK^-\mu^+\mu^-$ decays [106].

$3\,\text{fb}^{-1}$ collected in pp collisions at 7 and 8 TeV center-of-mass energies. Given the high yields of the $\Lambda_b^0 \to pK^- J/\psi(\to \mu^+\mu^-)$ decay mode, it is used as the control mode of the studied decay [4]. The angular fit of the pK^- mass spectrum is shown in Fig. 1.15. A lot of resonances with different quantum numbers are present. With the expected yields in the rare mode, fitting the full pK^- mass spectrum would be very challenging. Therefore, the focus is set on the narrow $\Lambda(1520)$ resonance, which dominates the m_{pK^-} spectrum. The $\Lambda(1405)$ and $\Lambda(1600)$ resonances are underlying the $\Lambda(1520)$ peak. A small contribution from the $\Lambda(1800)$ is present, too. All three of them are spin-1/2 resonances, as listed in table 1.1.

A priori, there is no evidence that the spectrum looks the same in the rare mode as in the J/ψ resonant mode. However, the m_{pK^-} shape in Fig. 1.14 and 1.15 show a similar structure "by eye". Unfortunately, no better comparison can be provided, since no full angular analysis has been performed up-to-date due to the small sample size.

In the amplitude analysis of $\Lambda_b^0 \to pK^- J/\psi(\to \mu^+\mu^-)$ decays, a pentaquark state was discovered [4]. This pentaquark state is visible in Fig. 1.16. It is expected to be reduced by the tight cut on m_{pK} around the $\Lambda(1520)$ resonance.

The LHCb collaboration measured the polarisation of the Λ_b^0 baryon with the data collected during Run 1 and 2015-16 in $\Lambda_b^0 \to \Lambda^0 J/\psi$ decays, produced in pp collisions [108]. The Λ_b^0 production polarisation was found to be consistent with zero. In this thesis, the polarisation will always be taken as null.

A BF and angular analysis of $\Lambda_b^0 \to \Lambda^0\mu^+\mu^-$ decays have been published with the Run 1 and Run 1 plus 2015-16 dataset collected by the LHCb experiment [65, 109]. The ground-state Λ resonance is noted by Λ^0 to distinguish it from the excited Λ^* resonances in the pK^- mass spectrum. Since the Λ^0 resonance decays via the weak interaction to $p\pi^-$, it is long-lived, and its decay vertex is usually situated outside of the VELO detector.

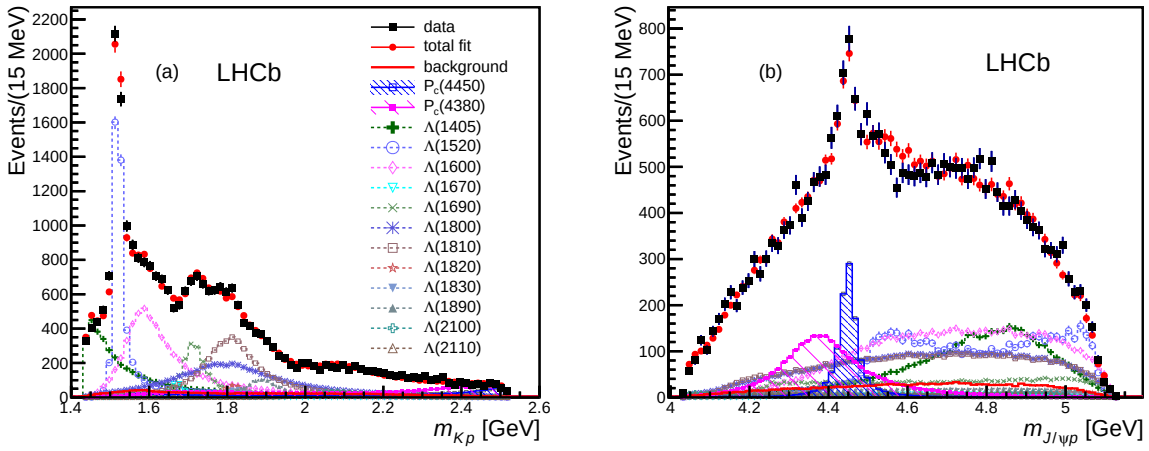

Figure 1.15 – The fit projection of the pK^- and pJ/ψ invariant mass spectrum from the amplitude analysis in $\Lambda_b^0 \to pK^- J/\psi(\to \mu^+\mu^-)$ decays is presented and the different Λ^* resonances and the pentaquarks marked. Taken from Ref. [4].

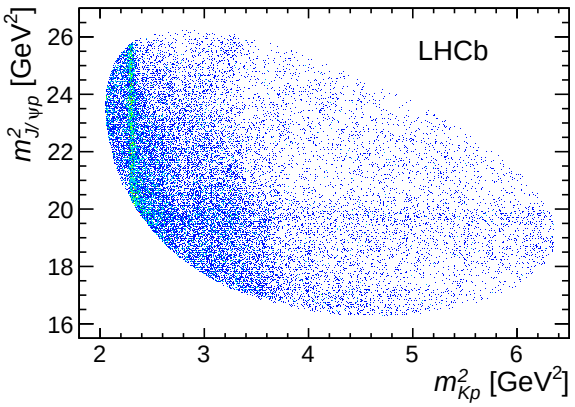

Figure 1.16 – The pentaquark state appears as a horizontal band, while the $\Lambda(1520)$ is represented as a vertical band. Taken from Ref. [4].

Resonance	J^P	Overall status	$N\bar{K}$
$\Lambda(1380)$	$1/2^-$	**	✓
$\Lambda(1405)$	$1/2^-$	****	✓
$\Lambda(1520)$	$3/2^-$	****	✓
$\Lambda(1600)$	$1/2^+$	****	✓
$\Lambda(1670)$	$1/2^-$	****	✓
$\Lambda(1690)$	$3/2^-$	****	✓
$\Lambda(1710)$	$1/2^+$	*	✓
$\Lambda(1800)$	$1/2^-$	***	✓
$\Lambda(1810)$	$1/2^+$	***	✓
$\Lambda(1820)$	$5/2^+$	****	✓
$\Lambda(1830)$	$5/2^-$	****	✓
$\Lambda(1890)$	$3/2^+$	****	✓
$\Lambda(2000)$	$1/2^-$	*	✓
$\Lambda(2050)$	$3/2^-$	*	✓
$\Lambda(2070)$	$3/2^+$	*	✓
$\Lambda(2080)$	$5/2^-$	*	✓
$\Lambda(2085)$	$7/2^+$	**	✓
$\Lambda(2100)$	$7/2^-$	****	✓
$\Lambda(2110)$	$5/2^+$	***	✓
$\Lambda(2325)$	$3/2^-$	*	✓
$\Lambda(2350)$	$9/2^+$	***	✓
$\Lambda(2585)$	?	*	✓

Table 1.1 – Spin, parity and the overall status of the Λ^* resonances are listed. The status goes from poorly known (*) to established resonances (****). The last column indicates if the decay to $N\bar{K} \in \{pK^-, nK^0\}$ have already been detected. Taken from Ref. [21].

In addition to the different decay topologies, the theoretical predictions of the BF and angular distribution differ due to the different masses and quantum numbers.

In parallel to the angular analysis, treated in this thesis, a branching fraction measurement of $\Lambda_b^0 \to \Lambda(1520)\mu^+\mu^-$ decays was prepared [60] with the full LHCb dataset from Run 1 and 2. A common strategy was adopted, in order to align the q^2 definitions, the selection and the corrections. The reason is the desired comparability of the differential BF measurement and the angular observables.

q^2 interval $[\,\mathrm{GeV}^2/c^4]$	$N_{\Lambda(1520)\mu^+\mu^-}$	$\frac{d\mathcal{B}(\Lambda_b^0\to\Lambda(1520)\mu^+\mu^-)}{dq^2}$ $[10^{-8}\,\mathrm{GeV}^{-2}c^4]$
$0.1 - 3.0$	96 ± 18	$1.89 \pm 0.35 \pm 0.19 \pm 0.36$
$3.0 - 6.0$	138 ± 18	$2.42 \pm 0.32 \pm 0.17 \pm 0.45$
$6.0 - 8.0$	65 ± 14	$1.58 \pm 0.36 \pm 0.16 \pm 0.30$
$11.0 - 12.5$	59 ± 14	$2.07 \pm 0.47 \pm 0.26 \pm 0.39$
$15.0 - 17.0$	12 ± 5	$0.57 \pm 0.24 \pm 0.13 \pm 0.11$
$1.1 - 6.0$	175 ± 21	$1.95 \pm 0.23 \pm 0.16 \pm 0.37$

Table 1.2 – The measured differential branching fractions and yields of $\Lambda_b^0 \to \Lambda(1520)\mu^+\mu^-$ decays are listed per q^2 bin (from Ref. [60]). The uncertainties are split into the statistical (first), systematic uncertainty (second) and the uncertainties due to the knowledge of the $\Lambda_b^0 \to pK^-J/\psi$ and $J/\psi \to \mu^+\mu^-$ branching fractions (third uncertainty).

The differential BF values and the measured yields are collected in Tab. 1.2. The presence of only 12 ± 5 $\Lambda_b^0 \to \Lambda(1520)\mu^+\mu^-$ decays in the high q^2 bin is challenging for performing an angular analysis. A comparison of the measured differential BFs and the SM predictions are presented in Fig. 1.17. The SM predictions differ from each other, such that no conclusion about the agreement with the measured values can be drawn. In the high-q^2 bin, the predictions are less model-dependent and consistency with the measured differential BF values is found.

As it will be shown in the next section, the current SM predictions of the angular observables are more coherent with each other.

1.3.3 Differential decay width of $\Lambda_b^0 \to \Lambda(1520)\ell^+\ell^-$ decays

To perform an angular analysis in $\Lambda_b^0 \to \Lambda(1520)\mu^+\mu^-$ decays, the decay angles need to be defined first. The decay angles are defined in the helicity basis, following the definition in Ref. [65, 109, 111]. A sketch of the angle definition is shown in Fig. 1.9 and their calculation is described in appendix I.

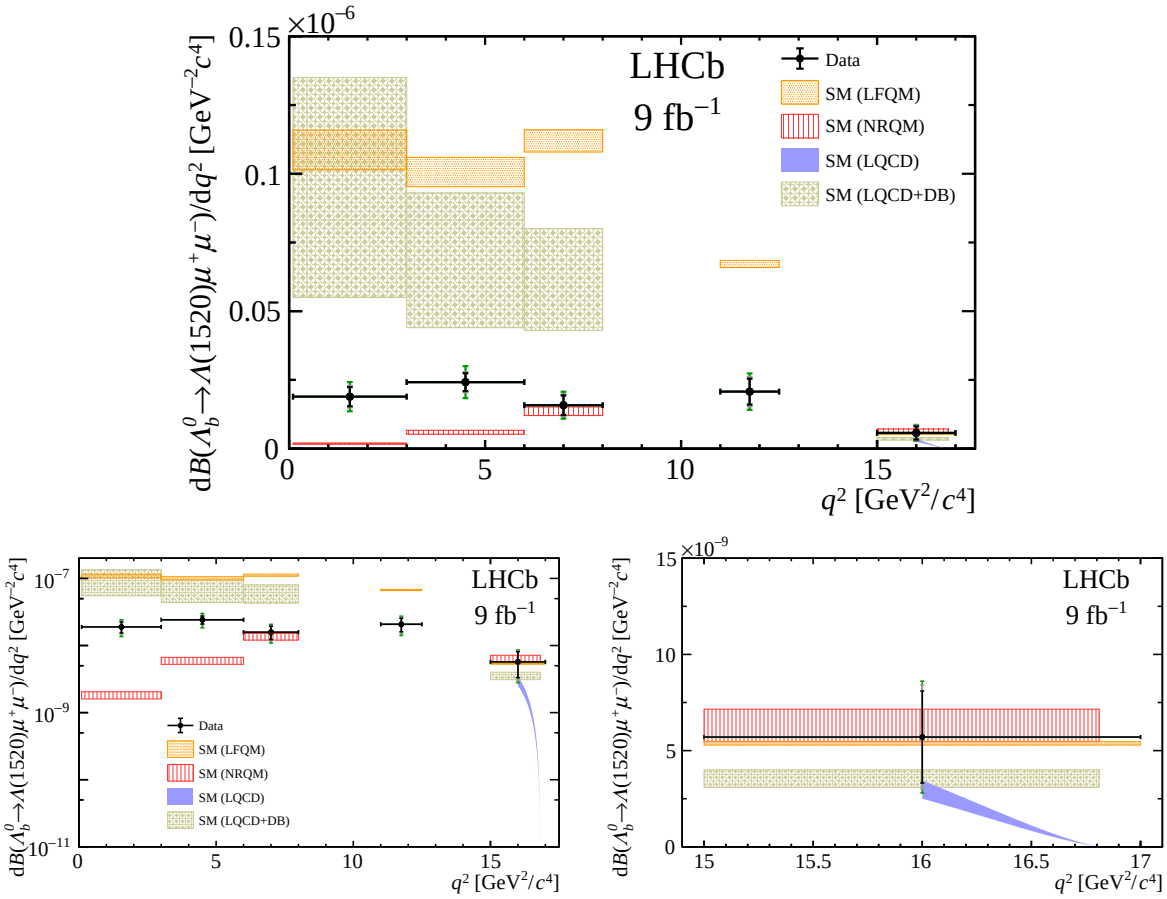

Figure 1.17 – The differential branching fraction of the $\Lambda_b^0 \to \Lambda(1520)\mu^+\mu^-$ decays in bins of q^2 [60], drawn in the full range in the linear (top) and logarithmic scale (bottom left) and a zoom into the high-q^2 bin (bottom right). The error bars represent the statistical (black), systematic (gray) and the $\mathcal{B}(\Lambda_b^0 \to pK^-J/\psi)$ uncertainties (green). The boxes indicate the SM predictions using different form factors. Form factors from the non-relativistic Quark Model (NRQM) [6] are presented in red, the light-front Quark Model (LFQM) form factors [110] are used in the orange prediction, and the green boxes indicate the prediction using the joint Lattice QCD and dispersive bound form factor prediction [8]. Because of the availability of the Lattice QCD prediction [7] only in a limited range, it is represented as a continuous blue band.

As it will be discussed in subsection 1.3.2, the pK^- mass spectrum is composed of a multitude of Λ^* resonances with different spin and parity properties. The differential decay width and the angular observables depend on the spin of the Λ^* resonances.

The studied $\Lambda(1520)$ resonance is a $J^P = 3/2^-$ state. The full differential decay width of the Λ_b^0 baryon decaying to a Λ^* resonance with spin $J = \frac{3}{2}$ has been calculated in Ref. [5] by neglecting the lepton masses. It can be expressed by the decay angles $(\theta_\ell, \theta_p, \phi)$ and the di-lepton invariant mass q^2 as

$$\begin{aligned}
&\frac{8\pi}{3}\frac{d^4\Gamma}{dq^2 d\cos\theta_\ell d\cos\theta_p d\phi} \\
&\quad = \cos^2\theta_p \left(L_{1c}\cos\theta_\ell + L_{1cc}\cos^2\theta_\ell + L_{1ss}\sin^2\theta_\ell\right) \\
&\qquad + \sin^2\theta_p \left(L_{2c}\cos\theta_\ell + L_{2cc}\cos^2\theta_\ell + L_{2ss}\sin^2\theta_\ell\right) \\
&\qquad + \sin^2\theta_p \left(L_{3ss}\sin^2\theta_\ell\cos^2\phi + L_{4ss}\sin^2\theta_\ell\sin\phi\cos\phi\right) \\
&\qquad + \sin\theta_p\cos\theta_p\cos\phi(L_{5s}\sin\theta_\ell + L_{5sc}\sin\theta_\ell\cos\theta_\ell) \\
&\qquad + \sin\theta_p\cos\theta_p\sin\phi(L_{6s}\sin\theta_\ell + L_{6sc}\sin\theta_\ell\cos\theta_\ell).
\end{aligned} \tag{1.53}$$

The differential decay width including the lepton masses has been calculated in Ref. [112] and agrees with the above-presented expression in the limit $m_\ell \to 0$.

For a Λ^* resonance with the same spin, but opposite parity, equation 1.53 stays the same. However, the vector and axial-vector helicity amplitudes are swapped, which results in different hadronic transversity amplitudes A_j, B_j. Those hadronic transversity amplitudes are absorbed in the angular coefficients L_i and defined in Ref. [5].

The CP-symmetries and asymmetries are defined as shown in Eq. 1.47 and 1.48. The differential decay width

$$\frac{d\Gamma}{dq^2} = \frac{1}{3}(L_{1cc} + 2L_{1ss} + 2L_{2cc} + 4L_{2ss} + 2L_{3ss}) \tag{1.54}$$

is used as normalisation of the angular observables. The fraction of longitudinal polarised Λ^* baryons is defined as

$$F_L = 1 - 2\frac{L_{1cc} + 2L_{2cc}}{L_{1cc} + 2L_{1ss} + 2L_{2cc} + 4L_{2ss} + 2L_{3ss}}. \tag{1.55}$$

An optimised angular observable represents the leptonic forward-backwards asymmetry

$$A_{FB}^\ell = \frac{3}{2}\frac{L_{1c} + 2L_{2c}}{L_{1cc} + 2L_{1ss} + 2L_{2cc} + 4L_{2ss} + 2L_{3ss}}, \tag{1.56}$$

which is especially sensitive to NP.

Ref. [107] presents a simplification of the angular distribution using the heavy quark

limit $m_b \to \infty$, which is expressed as

$$\frac{8\pi}{3}\frac{d^4(\Gamma+\bar{\Gamma})}{dq^2 d\cos\theta_\ell d\cos\theta_p d\phi} \simeq \frac{1}{4}\left(1+3\cos^2\theta_p\right)(L_{1c}\cos\theta_\ell + L_{1cc}\cos^2\theta_\ell + L_{1ss}\sin\theta_\ell^2). \quad (1.57)$$

Several form factor predictions are available to predict the hadronic contributions [17]. These are hidden inside the angular coefficients L_i. Some form factors are predicted by a non-relativistic Quark Model (QM) and numerically extracted from the full quark model wave function [6].

The first principles form factor prediction comes from Lattice QCD because the QCD is calculated on the lattice [7, 113]. An important cross-check of the Lattice QCD results is the form factor prediction of the Heavy Quark Expansion [114]. In the expansion terms of next-to-leading-order $\mathcal{O}(\alpha_s)$ corrections and next-to-leading-power $\mathcal{O}(1/m_b)$ corrections has been included. Unknown parameters are fixed through a fit to the Lattice QCD form factors. This calculation could detect a wrong sign in the tensor and pseudo-tensor form factors in the Lattice QCD publication and provides, thus, an important crosscheck.

Unfortunately, the Lattice QCD form factor prediction is only available in a high q^2 region, which is defined in the interval of $[16.0, 16.8]$ GeV$^2/c^4$. With the available data sample size, this window is too tight for an angular analysis. Using the Lattice QCD predictions with SCET, endpoint [115] and dispersive bound relations, the form factor predictions of Ref. [8] are achieved. The advantage of those is the availability of predictions in the low-q^2 region. Nevertheless, it would be great to have Light-Cone Sum Rule (LCSR) predictions in the low-q^2 region in the future.

The open source package FLAVIO is useful to calculate combinations of several observables and global fits. I implemented the differential decay width, expressed in Eq. 1.53, in FLAVIO. QM and Lattice QCD form factor predictions from Ref. [6, 113] are available. For the QM form factor predictions, uncertainties of 10% are applied on the form factors $f_{0,\perp,t}$ and 30% on f_g, following the proposition in Ref. [5]. The angular observables $A_{\rm FB}^\ell$, $F_{\rm L}$ and the *CP*-symmetric and asymmetric observables can be accessed. The distributions of the differential BF, A_{FB}^ℓ and S_{1cc} are shown in Fig. 1.18. The SM and an NP model are drawn. The NP model is defined by $C_9^{NP} = -1.11$, which was supported by the data in the past. A separation between the SM and NP distributions with the QM form factor prediction is visible. While the Lattice QCD prediction of the BF and the S_{1cc} observable agrees with the SM QM prediction within two Standard deviations, the predictions of the A_{FB}^ℓ observable deviate by about three Standard deviations.

17. However, there is no theoretical basis for the factorization in the Λ_b^0 decay, so that form factors are not guaranteed to give a good description of the hadronic dynamics.

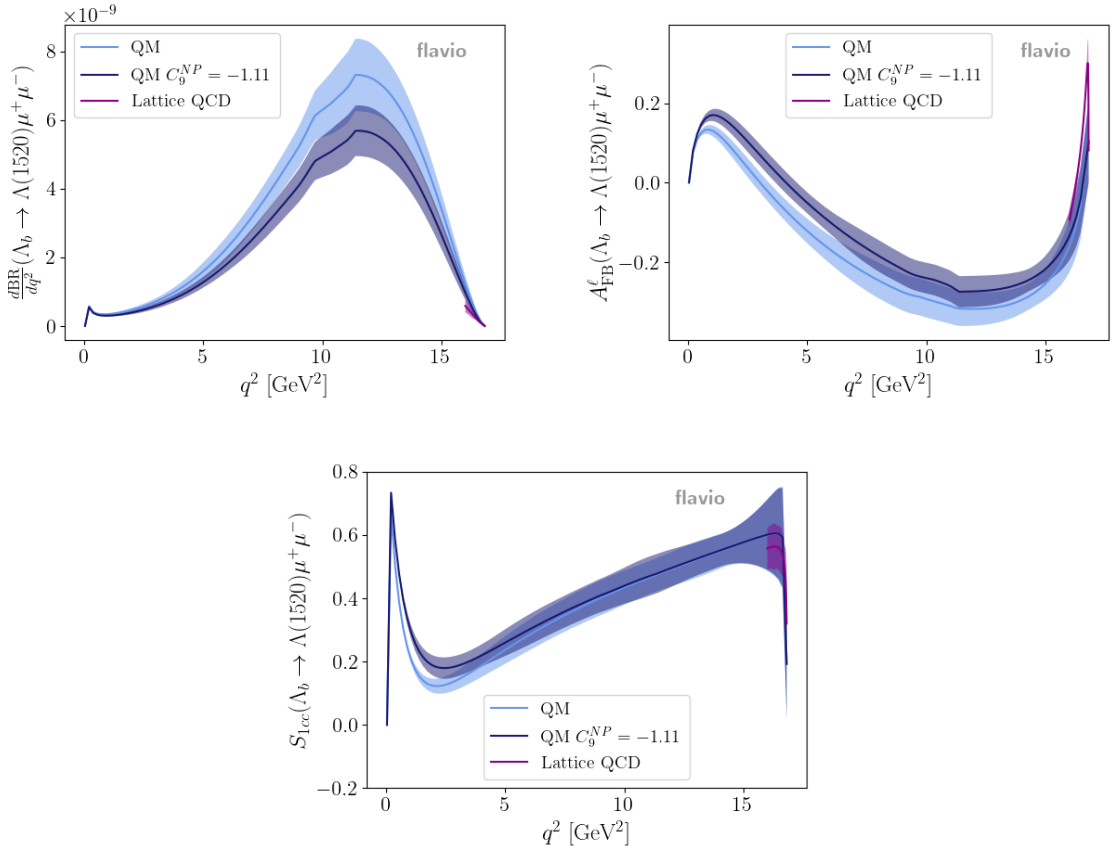

Figure 1.18 – Differential BF, A_{FB}^{ℓ} and S_{1cc} predictions in the full q^2 region, using the non-relativistic Quark Model form factors [6] for the SM case and an NP case with $C_9^{NP} = -1.11$, are compared with the distributions based on the Lattice QCD form factor predictions [7, 113], which are drawn only in the q^2 range of their validity.

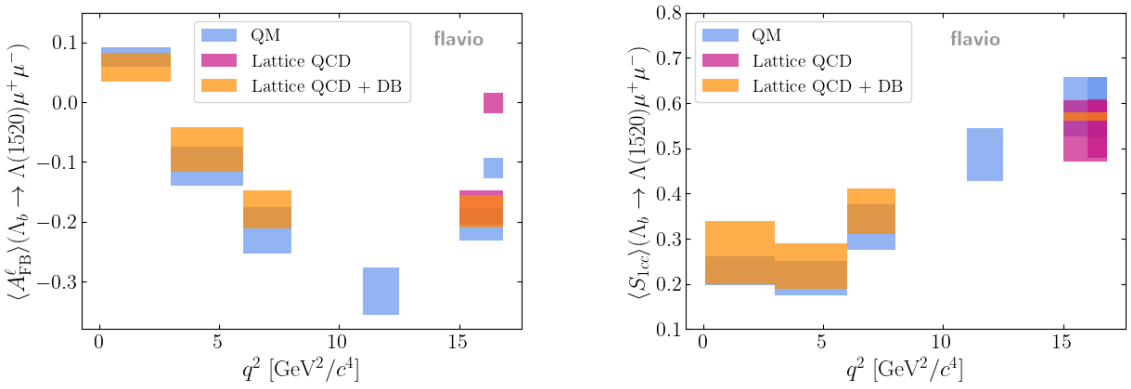

Figure 1.19 – The angular observables A_{FB}^{ℓ} and S_{1cc} are drawn in bins of q^2, using the form factor predictions from Lattice QCD, the joint Lattice and dispersive bound, plus the Quark Model (QM) prediction. The q^2 bin between 16 and 16.8 GeV$^2/c^4$ is added, because of the validity of the Lattice QCD form factors in this range only. For comparison, the Lattice QCD form factor predictions have been extrapolated to the $q^2 \in [15, 16.8]$ GeV$^2/c^4$ bin.

The angular observables are aimed to be measured in bins of q^2. The measurement is foreseen in the q^2 bins $[0.1, 3.0], [3.0, 6.0], [6.0, 8.0], [11.0, 12.5], [15.0, 17.0]$ GeV$^2/c^4$. The SM predictions of the QM and the joint Lattice QCD and dispersive bound prediction are depicted for these bins in Fig. 1.19. They are compatible with each other within one Standard deviation.

The Lattice QCD prediction is only available for the $q^2 \in [16, 16.8]$ GeV$^2/c^4$ bin. Therefore, the Lattice QCD and QM predictions in this bin has been added. In this bin, the two predictions are calculated to differ by about 3 Standard deviations. An extrapolation of the Lattice QCD prediction to the full high q^2 bin has been drawn, too. This one is compatible with the QM and joint Lattice QCD and dispersive bound prediction within one Standard deviation. Therefore, the theoretical predictions are compatible with each other within one Standard deviation in all of the q^2 bins, which are aimed to be measured. This underlines the better consistency of the angular observable predictions than the BF predictions.

To conclude, deviations between the measurements and SM predictions are observed in the BFs and angular observables of $b \to s\mu^+\mu^-$ decays. In this thesis, an angular analysis is attempted to be measured in a new decay channel, namely the $\Lambda_b^0 \to \Lambda(1520)\mu^+\mu^-$ decays. In this chapter, the signal process was presented, including all the particles and interactions involved. The theoretical predictions of the angular observables and the differential BF are shown. Theoretically difficult to predict are the non-perturbative QCD contributions, which are encoded in the form factors. In spite of the difficulty, several

form factor predictions exist for the signal decay. Using different form factor predictions, the angular observables seem to be consistent. Nevertheless, additional theoretical input, as for example LCSR for factor predictions, would be helpful for the future. Previous measurements indicated the presence of spin-1/2 Λ^* resonances below the $\Lambda(1520)$ peak, which needs to be considered later as well.

Chapter 2

The LHCb experiment

The technical design report of the Large Hadron Collider beauty (LHCb) experiment, situated at the Large Hadron Collider (LHC), was already published in 2003 [116]. The initial aim of LHCb was focused on CKM and CP violation measurements but also on the study of rare decays of b- and c-hadrons. This motivation leads to a detector design as a forward spectrometer, covering the regions where b-hadrons are predominantly produced while keeping the construction cost small. Moreover, the electronics can be placed outside of the detector, which protects them from radiation damage and limits the multiple scattering of particles inside the detector.

The first section is dedicated to the LHC machine and the proton acceleration. Since b-hadrons are studied in this thesis, it is necessary to understand the b-hadron production in the hadronic environment of the LHC, which is explained in Sec. 2.2. The LHCb experiment is situated at the LHC ring, recording pp collisions. The data recorded from 2011 on is still being analysed. The main analysis of this thesis is the angular analysis of $\Lambda_b^0 \to \Lambda(1520)\mu^+\mu^-$ decays, which is performed with the full LHCb dataset of Run 1 and 2. The LHCb detector during this period is described in Sec. 2.3.

In view of the data-taking in Run 3 with five times higher instantaneous luminosity, the LHCb detector is undergoing a significant upgrade. In order to help with the commissioning of the upgraded detector, 2022 data is studied in Ch. 5 of this thesis. This analysis is using $B^+ \to K^+ J/\psi(\to e^+e^-)$ and $B^+ \to K^+\psi(2S)(\to e^+e^-)$ decays. For this purpose, the Upgrade LHCb detector is discussed in Sec. 2.4.

2.1 The Large Hadron Collider

The Large Hadron Collider (LHC) is a circular hadron accelerator and collider, providing the highest centre-of-mass energy in the world. The LHC is part of the CERN facility, located at the French-Swiss border, close to Geneva. The CERN accelerator complex is sketched in Fig. 2.1.

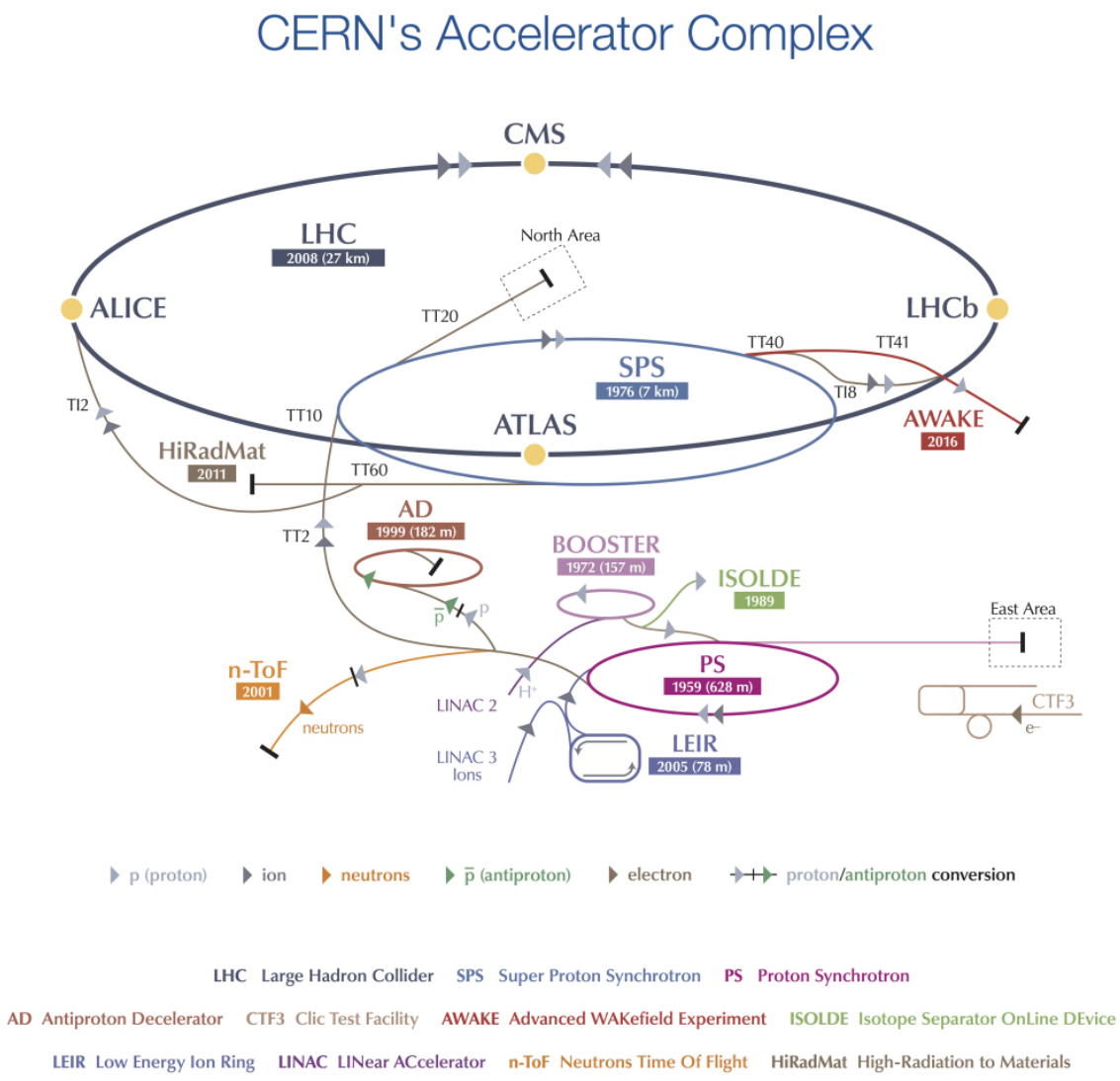

Figure 2.1 – The CERN accelerator complex during Run 2 is depicted. Taken from Ref. [117].

The initial design of the LHC aims to deliver proton-proton collisions at a centre-of-mass energy of $\sqrt{s} = 14\,\text{TeV}$. However, the highest centre-of-mass energy reached to date was 13.6 TeV during Run 3. The LHC has a circumference of 26.7 km and is situated underground.

The LHC provides proton-proton collisions, which are studied in this thesis. However, heavy ions, such as lead, can also be collided at the LHC. The protons are extracted from hydrogen atoms by stripping down the valence electron via an electric field. The protons are accelerated starting from the *Linear Accelerator (LINAC) 2*. After the LINAC 2, the protons have an energy of 450 MeV and are injected into the *Proton Synchrotron Booster* (PSB). The PSB is a circular accelerator, which brings the proton energy up to 1.4 GeV. The next circular accelerator is the *Proton Synchrotron* (PS), where the protons reach an energy of 25 GeV and are already separated into bunches of approximately 1.5×10^{11} protons each. These bunches are spaced by at least 25 ns. The next acceleration happens in the *Super Proton Synchrotron* (SPS), where the proton energy increases to 450 GeV. Reaching this energy, the proton bunches are injected into the LHC. At maximum 2808 bunches can be injected into the LHC per beam.

As a side note, the acceleration scheme for heavy ions differs from the above-described one. The acceleration process of heavy ions starts in the LINAC 3. Afterwards, they are injected into the PS and continue the acceleration in the same way as the protons.

In Run 3, the acceleration process is revisited. LINAC 2, responsible for the initial acceleration of protons, is replaced by LINAC 4. The new machine accelerates singly negatively charged hydrogen ions H^- up to 160 GeV in LINAC 4 before stripping off their electrons. Protons are then injected into the PSB. The advantage of the LINAC 4 working principle is the ability to pack the protons more densely, which will be essential for the high-luminosity LHC in Run 4.

The LHC ring is sketched in Fig. 2.2. The proton bunch injection into the LHC ring happens at the interaction points 2 and 8. The two "trains" of proton bunches then circulate clockwise and anticlockwise in a vacuum of 10×10^{-10} to 10×10^{-11} mbar. The purpose of the vacuum is to avoid beam-gas interactions as much as possible.

The LHC ring can be separated into eight octants, which are each composed of a curved "arc" and a straight "insertion" section. The proton beams are bent in the arcs by 1232 superconducting dipole magnets, producing a magnetic field strength of 8.33 T. The dipole magnets need to be cooled down to 1.9 K by superfluid helium in order to enable their superconductivity. Quadropole magnets are employed to focus the proton beams vertically and horizontally. Higher-order magnets are used to correct for an unwanted beam spread caused by perturbations of the beam dynamics.

In the insertion regions of the LHC, either particle physics experiments or beam instrumentation devices are placed. Interaction point 4 is equipped with eight superconducting radio-frequency (RF) cavities for each beam, accelerating the proton beams from 450 GeV

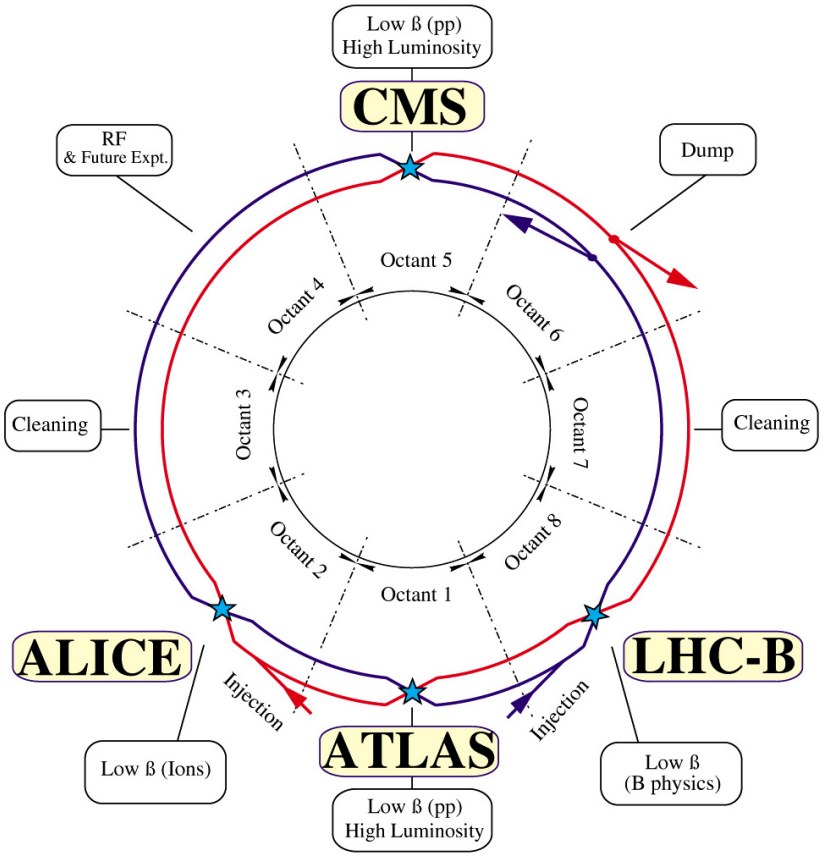

Figure 2.2 – The layout of the LHC during Run 2 is sketched. The two beams are depicted in red and blue. The comment "low-β" refers to a small transversal size of the beam. Taken from Ref. [118].

to their final beam energy and compensating for the energy loss induced by synchrotron radiation. In addition, the RF cavities focus the beam in the longitudinal direction. Outlier protons are removed at the interaction points 3 and 7 by collimators. A block of stainless-steel-jacketed concrete is built up at interaction point 6, into which the beams are dumped at the end of each LHC fill or in case of operational problems.

At the locations of the particle detectors, the proton beams cross each other, and the proton bunches collide. The following four particle detectors are installed at the LHC:

- The **ALICE experiment** [119], situated at the interaction point 2, is specialised in QCD physics and studies of the Quark-Gluon plasma in heavy-ion collisions.
- The interaction points 1 and 5 are occupied by the **ATLAS** [120] **and CMS detector** [121], covering nearly the full solid angle. Both of them are general-purpose detectors aiming to study a wide range of physics. They are particularly suited for high-p_{T} physics, direct searches for NP, Higgs-boson physics and determining the top-quark properties. Furthermore, both experiments have a flavour physics program. However, the absence of a detector identifying charged hadrons, the tight trigger thresholds, the high track multiplicity and the large pp interaction rate per bunch crossing are the primary constraints of the flavour physics programme of these two experiments.
- The **LHCb forward spectrometer** [122], described in Sec. 2.3, is placed at interaction point 8. Although the LHCb detector was constructed mainly for precision measurements in flavour physics, LHCb is outperforming itself and showing an excellent performance also in other physics fields, such as *e.g.* electroweak and QCD physics.

By circulating in the LHC ring, the beams deplete with time because of the pp-collisions and the collimation. As a result, the luminosity of frontal collisions is exponentially reduced during the LHC "fill". During Run 1 and 2, the ATLAS and CMS experiments exploited the maximal instantaneous luminosity. At the LHCb experiment, the "luminosity levelling" enables a stable instantaneous luminosity of $\mathcal{L}_{\mathrm{inst}} = 4 \times 10^{32}\,\mathrm{cm}^{-2}\mathrm{s}^{-1}$ during most of the fill. The luminosity is levelled by adapting the overlap of the two beams, which controls the average number of visible pp-interactions per bunch crossing $\langle\mu\rangle$. During the Run 1 and 2, the $\langle\mu\rangle$ was set to about 1 [123]. A sketch of the working principle of the luminosity levelling is depicted in Fig. 2.3. In addition, the instantaneous luminosities for the different experiments during Run 1 are presented.

The advantages of levelling the instantaneous luminosity are the stable data-taking conditions, a reduction of the radiation damage of the detector, and a more straightfor-

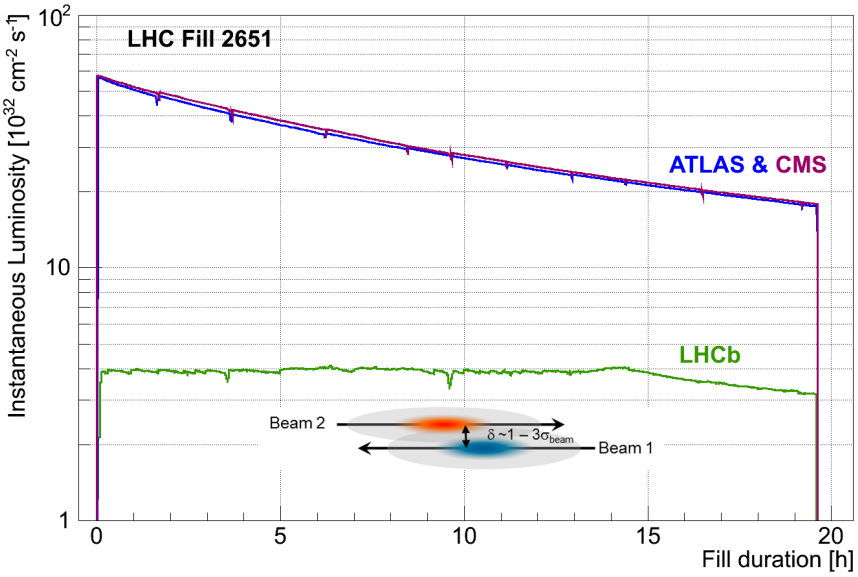

Figure 2.3 – The decrease of the instantaneous luminosity for ATLAS and CMS and the luminosity levelling of LHCb is shown for a long LHC fill in Run 1. Taken from Ref. [124].

ward particle reconstruction. For Run 3 and 4, the LHCb experiment will be operated at an instantaneous luminosity of factor 5 higher than in Run 2, which will be discussed in Sec. 2.4.

2.2 Production of *b*-hadrons at the LHC

The LHCb detector is built as a forward spectrometer rather than a hermetic detector such as ATLAS and CMS. This choice is motivated by the b-hadron production at the LHC, which will be explained further in this section.

Protons comprise the (uud) valence quarks, integrated into a sea of gluons and quark-antiquark pairs, so-called sea quarks. The constituents of those compound objects are called partons. The hadronic environment of pp collisions provokes less clean conditions than those available in electron-positron collisions. In the high-energetic pp collisions at the LHC, parton interactions are the most probable. b quarks are primarily produced by gluon fusion $gg \to b\bar{b}$ and quark-antiquark annihilation $q\bar{q} \to b\bar{b}$. The distinct momenta of the interacting partons, combined with the great difference between the LHC centre-of-mass energy and the b-quark mass, results in a boost towards the forward or backward direction, defined as the tangential to the beam axis at the collision point.

As a side note, the boost of b and c quarks is an important feature since it causes a larger displacement of b and c hadron decay vertices in the LHCb detector. Particles or resonances produced directly in the pp interaction vertex are called "prompt", while displaced (secondary) particles or resonances originate from decays of c or b hadrons. This property will be important in Ch. 5.5.1.

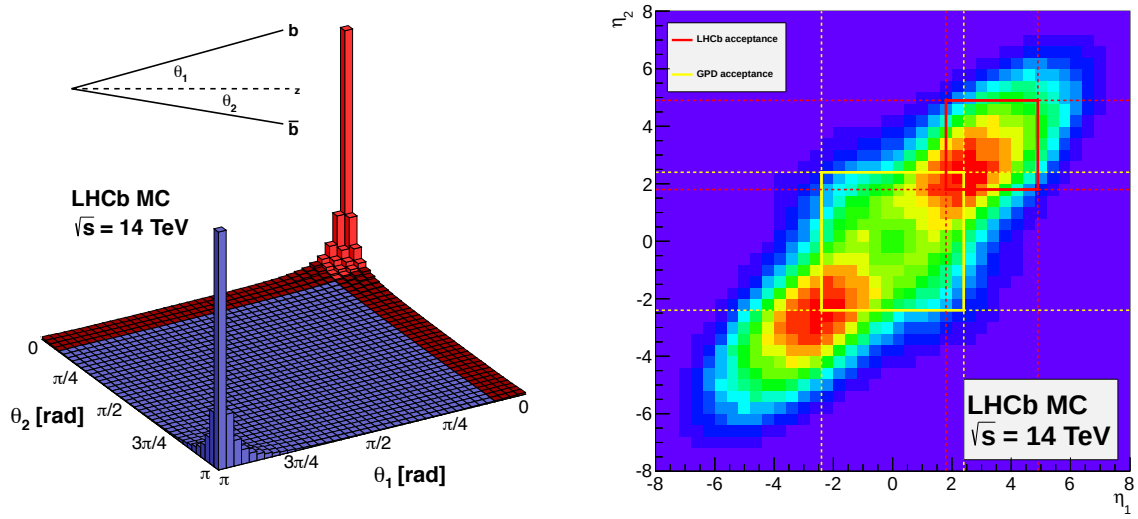

(a) (b)

Figure 2.4 – (a) The geometrical acceptance of simulated $b\bar{b}$ quark pairs from gluon-gluon fusion and quark-anti-quark annihilation at $\sqrt{s} = 14$ TeV is shown. All $b\bar{b}$ quark pairs in red are inside the LHCb acceptance. (b) The geometrical acceptance of the LHCb detector is compared to that of a general-purpose detector. Both plots are taken from Ref. [125].

The forward design of the LHCb detector allows containing 27% of the produced b or $\bar{b}$ quarks and 24% of the $b\bar{b}$ quark pairs despite the reduced solid angle [125] [1]. The geometrical acceptance of the LHCb detector is depicted in Fig. 2.4. The polar angle of the b or $\bar{b}$ direction to the beam axis is indicated by θ, while η represents their pseudorapidity defined as

$$\eta = -\ln \tan \frac{\theta}{2}. \tag{2.1}$$

A pseudorapidity range of $2 < \eta < 5$ is covered by the LHCb detector. The LHCb detector acceptance has only a small overlap with the general-purpose detector, giving access to an uncommon phase space.

1. In comparison, 49% of b or $\bar{b}$ quarks and 41% of $b\bar{b}$ quark pairs are produced in the acceptance of a general-purpose detector, covering nearly the full solid angle [125].

As described in Ch. 1.1, the b and $\bar{b}$ quarks hadronise immediately into hadrons. The hadronisation fractions f_u, f_d, f_s and f_c express the probability of a $\bar{b}$ (b) to hadronise into a $B^{\pm}$, $\overline{(}B^0\overline{)}$, $\overline{(}B_s^0\overline{)}$ and $B_c^{\pm}$ mesons. The fractions decrease with the additional quark mass and scale roughly as 4:4:1:0.01. The production fraction of the B_s^0 meson, averaged over its kinematics, is measured in pp collisions at 13 TeV within the LHCb acceptance [126] to be

$$\frac{f_s}{f_u + f_d} = 0.122 \pm 0.006. \tag{2.2}$$

The most abundantly produced b baryon is the Λ_b^0 baryon, which decay is studied in this thesis. The Λ_b^0 hadronisation fraction was found in Ref. [126, 127] to depend on the Λ_b^0 transverse momentum. Its average hadronisation fraction at 13 TeV was published by the LHCb collaboration [126] to be

$$\frac{f_{\Lambda_b^0}}{f_u + f_d} = 0.259 \pm 0.018. \tag{2.3}$$

Those production fractions will be needed to estimate the background yield in Ch. 3.3.6. It is important to note that the hadronic environment at the LHC and the high centre-of-mass energy enable the LHCb experiment to study Λ_b^0 baryons, which have not been produced at B factories yet.

2.3 The LHCb detector during Run 1 and 2

As mentioned previously, the LHCb experiment is placed at the interaction point 8 of the LHC ring. A sketch of the detector with its subsystems is presented in Fig. 2.5. The coordinate system within the LHCb detector has its origin placed at the interaction point. The z-axis is set parallel to the direction of the clockwise circulating beam. In order to be right-handed, the x-direction points towards the inside of the LHC ring, while the y-axis is oriented upwards. To facilitate their installation, most of the subdetectors are separated into two halves depending on their x position. The A-side is situated at $x > 0$, and the C-side is installed at $x < 0$.

The LHCb detector design was optimised for studying b- and c-hadron decays. *Unstable particles* decay inside the Vertex Locator (VELO). *Long-lived particles* such as K_S^0, Λ^0 and Ξ^- may decay outside of the VELO detector [106]. In the LHCb jargon, particles, which do typically not decay within the LHCb detector, are called *stable particles*. Those stable particles are namely the charged pions π^+, charged kaons K^+, protons p, electrons e^-, muons μ^-, photons γ and deuterons d [106].

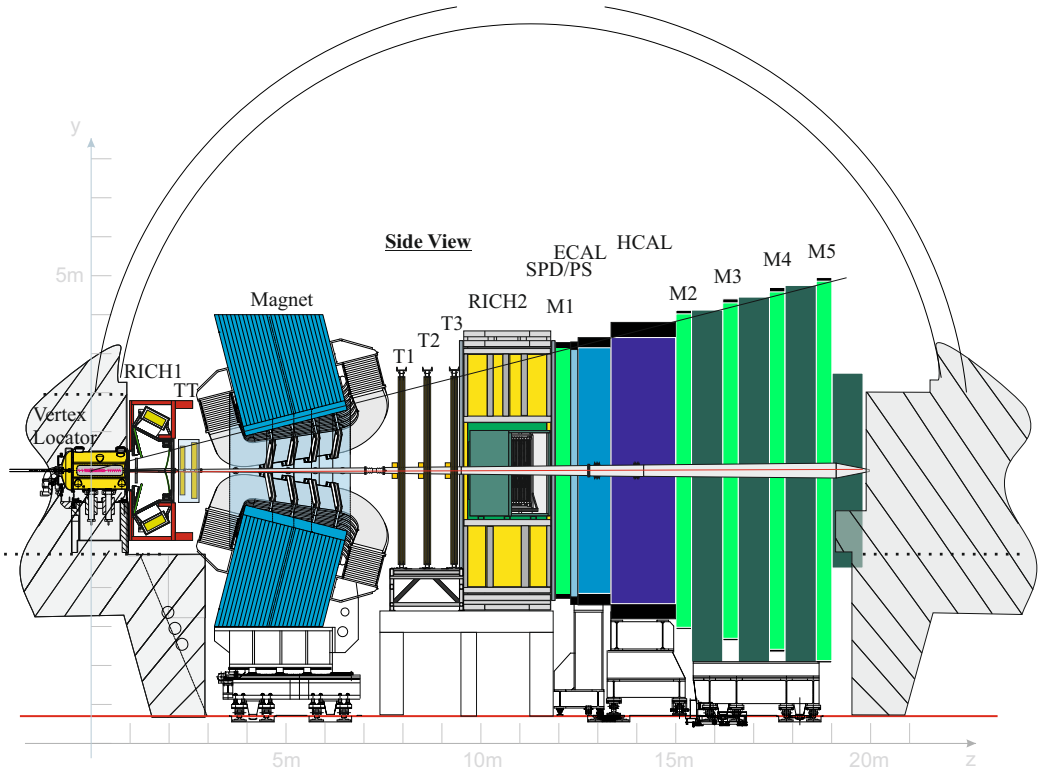

Figure 2.5 – Sketch of the LHCb detector during Run 1 and 2. Taken from Ref. [128]

To perform precision measurements, an accurate determination of the interaction vertices and the particle tracks is crucial. Operation of the vertex and tracking detectors in LHCb is explained in Sec. 2.3.1. Flavour physics measurements require reliable particle identification (PID), which is handled by a system of several PID detectors. Their functioning is described in Sec. 2.3.2. Another essential element is the trigger that allows filtering for interesting events in a wide bandwidth of physics areas. The employed trigger system is treated in Sec. 2.3.3.

2.3.1 Tracking detectors

Tracking detectors are essential in measuring b- and c-hadron decays since they provide the position of the primary and secondary vertices. The distance between those can be parametrised as flight distance or decay time. This property enables triggering on such decays and helps to suppress backgrounds. Moreover, charged particle tracks provide a momentum measurement by the curvature of the particle tracks in a magnetic field. In LHCb, the magnetic field is provided by a dipole magnet, which is treated in Sec. 2.3.1.

The working principle of tracking detectors is based on the fact that charged particles

interact with the detector material. The energy deposed in the sensitive layers of the subdetectors is referred to as "hit". Tracking algorithms are optimised to identify patterns of hits originating from the same particle and reconstruct them as tracks.

The closest tracking detector to the pp interaction region is the VELO. It provides the vertex information of unstable particles. Long-lived particles may decay outside of the VELO. To measure precisely the momenta of stable charged particles, as well as to reconstruct the decays of long-lived particles, hits from other tracking detectors are needed. The Tracker Turicensis (TT) is situated in front of the magnet. Three tracking stations, T1 – 3, are placed right after the magnet. Each of the subsystems will be discussed in detail in this section. At first, the dipole magnet is treated since its magnetic field affects the whole detector. Then, the functioning of the tracking detectors is explained from the detector closest to the interaction point to the farthest.

The Dipole Magnet

As stated before, the dipole magnet is an indispensable ingredient in retrieving a momentum estimate of charged particles. The Lorentz force bends charged particle trajectories. The magnetic field is applied in y direction, causing a bending in the horizontal plane. The direction of the curvature indicates the sign of the particle charge.

In general, the stronger the applied magnetic field, the better the momentum resolution of the charged particles. An outstanding momentum resolution implies an improved mass resolution for particles with negligible natural widths. This also helps with the reduction of background contributions. Another factor is considered for the choice of the best magnetic field strength. Only a small field should be applied on the Ring Imaging Cherenkov (RICH) detector 1 to provide good functioning [129]. A dipole magnet with an integrated field strength of $B_y = 4\,\mathrm{Tm}$ is retained, resulting in a momentum resolution of $\Delta p/p = 0.3\%$ if p is within 5 – 200 GeV/c [129].

A sketch of the LHCb magnet is provided in Fig. 2.6. The nomenclature of the different charged particle tracks is indicated. The tracks used in this analysis are the long tracks, which start in the VELO detector and cross the whole tracking system. Downstream tracks are produced outside of the VELO detector. They traverse the TT to the T1 - 3 stations.

The interesting feature of dipole magnets is the ability to switch the polarisation. LHCb is operated with *MagUp* and *MagDown* polarisations, allowing the reduction of potential sources of coordinate-dependent systematic biases, which is particularly important for *CP* violation measurements.

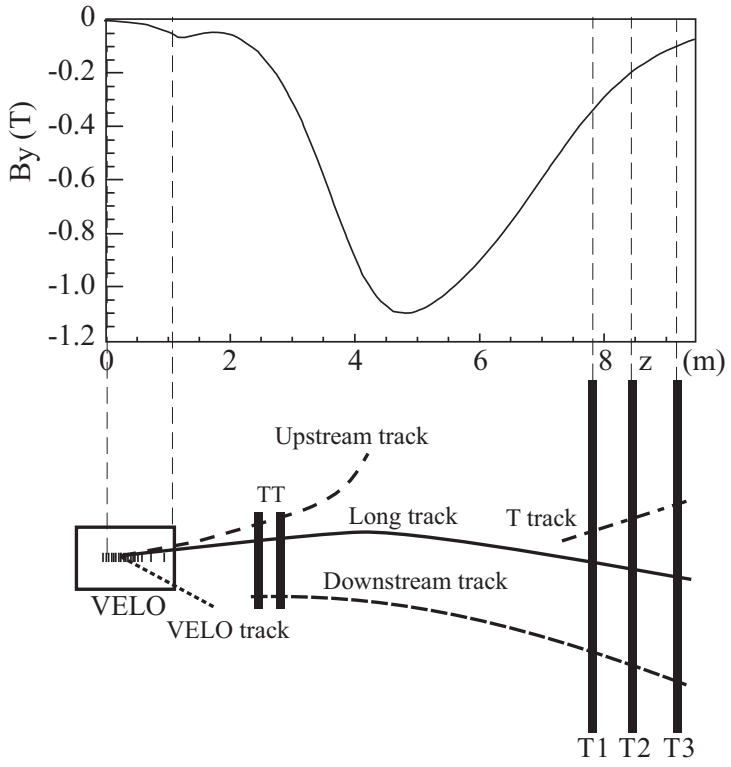

Figure 2.6 – The strength of the magnetic field component B_y inside the detector and the curvature of the different track types. Taken from Ref. [124].

Vertex Locator

The VELO detector is a silicon-strip detector [130]. It comprises two halves, the A- and C-side. 21 modules of each type are arranged in z-direction, such that charged particles, which are produced at $z = 0$ and directed within $1.6 < \eta < 4.9$, cross at least six modules. Two supplementary "veto" stations are installed, permitting to remove events with high multiplicity. The VELO setup is shown in Fig. 2.7.

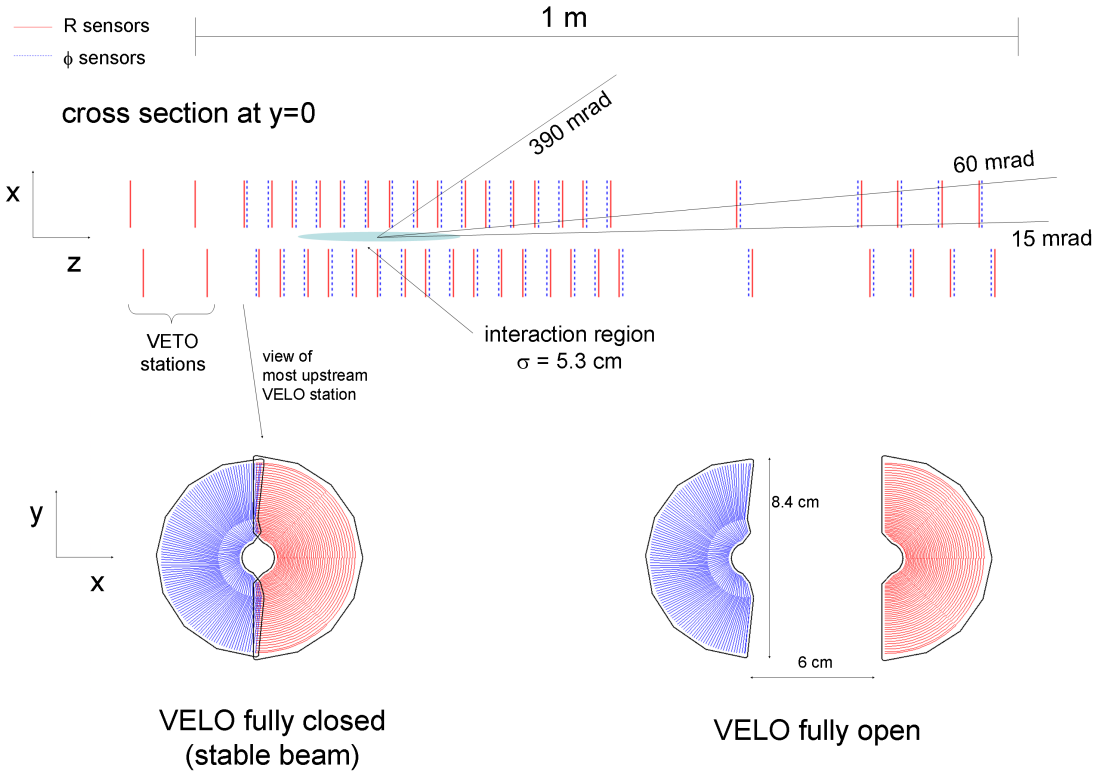

Figure 2.7 – Sketch of the relative locations of the VELO modules, plus the two veto stations, along the beam axis and their opened and closed position in the x-y plane. Taken from Ref. [131].

During the beam injection in the LHC and the proton acceleration, the two VELO halves are separated by 6 cm. The VELO is called to be in an "open" position, which protects it from radiation damage by outlier hadrons in the beam. Cooling the VELO modules to -5°C is another measure to reduce the radiation-induced damage. Only when stable beams are reached the VELO is "closed". The inner distance between the sensitive layer of the sensor and the beam is 8.2 mm only. The two overlapping sensors are illustrated in Fig. 2.8.

Each module is shaped as a semicircle and comprises a R-sensor and ϕ sensor. The radial distance measurement is provided by the R-sensor, for which the strips are arranged in a circular direction. The ϕ sensor determines the azimuthal angle via radially aligned

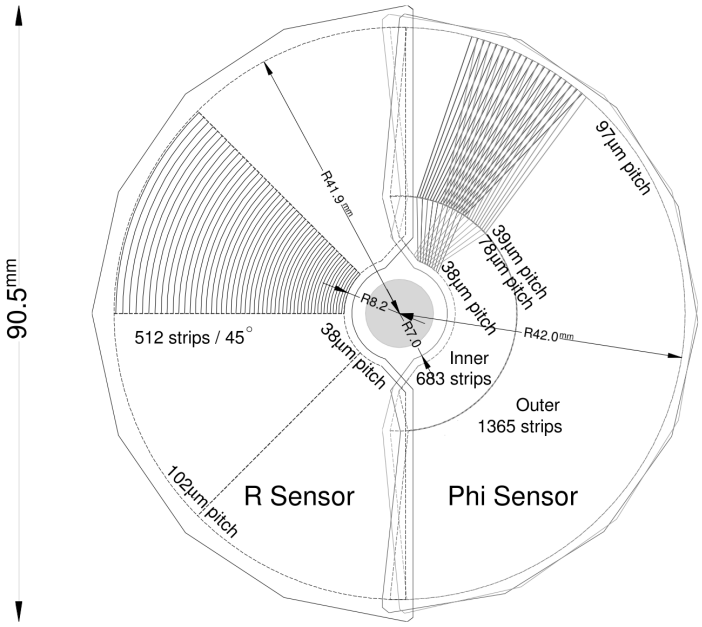

Figure 2.8 – An illustration of the VELO modules, separated in the R- and ϕ-sensor. Taken from Ref. [122].

strips. The sensors are read out in several segments in order to reduce occupancy. The ϕ sensor is divided into two sectors, and the R sensor into four. The small strip sizes and the large number of strips and modules enable the high precision needed to determine the vertex and track position. The resolution of one hit is evaluated in Ref. [124] to be within 5 and 25 µm.

The VELO is placed in a secondary vacuum, separated from the beam vacuum, in order to shield the detector from noise caused by radio-frequency (RF) interferences from the beam. The secondary vacuum is separated by a so-called RF foil. The RF foil is 0.5 mm thin since its thickness impacts the vertex resolution. The reason is the multiple scattering, which particles undergo by traversing material and deviates them from the initial track directory. Therefore, it is beneficial to reduce the amount of detector material crossed by studied particles. The material budget in the VELO detector corresponds to only about 1/6 of the radiation length, granting the superb momentum resolution in LHCb.

Tracker Turicensis

The Tracker Turicensis (TT) is a large-area silicon-strip detector. It is composed of two rectangular modules with two layers each, as depicted in Fig. 2.9. On each of the layers, the strips are arranged in the vertical direction, enabling a better momentum

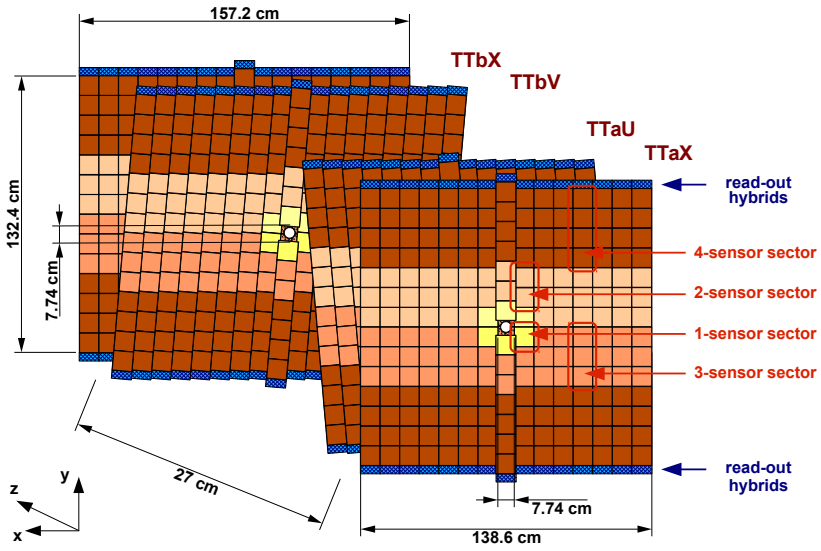

Figure 2.9 – Assembling of the four rectangular layers of the TT stations. The four colours represent different modules of several sensors, which are read out together. Taken from Ref. [128].

resolution in the bending plane. The occupancy is reduced by dividing each layer into different readout sectors. The two middle layers are rotated by $\pm 5°$ with respect to the first and last layers. The tilting improves the x and y momentum measurement and the reduction of fake tracks, which are wrongly reconstructed tracks by combining random or unrelated hits. The resolution of a single hit was determined in 2012 to be about 61 µm [132]. Another goal of the TT subdetector is its use in the Run 2 tracking. The additional hits in the TT stations accelerate the track reconstruction algorithm [133].

Downstream tracking stations

The purpose of the downstream tracking stations [134] is the position measurement after the magnet, which is necessary to determine the bending of the charged particle track. As discussed before, the momentum is calculated from the bending.

Three downstream tracker stations are installed, which are called T1 – 3. A sketch of the construction is shown in Fig. 2.10. The two different colours indicate the two detection techniques used. In violet, the silicon-strip tracker elements are drawn. Because of its position close to the beam pipe, this detector part is named *inner tracker* (IT). The silicon-strip trackers cover the region characterised by high track multiplicity. Four boxes are positioned in a circle around the beam pipe, while the longer side is located in the x direction. Each T station consists of four layers of vertically placed silicon strips arranged in the same way as in the TT. The hit resolution of the x coordinate equals 54 µm in

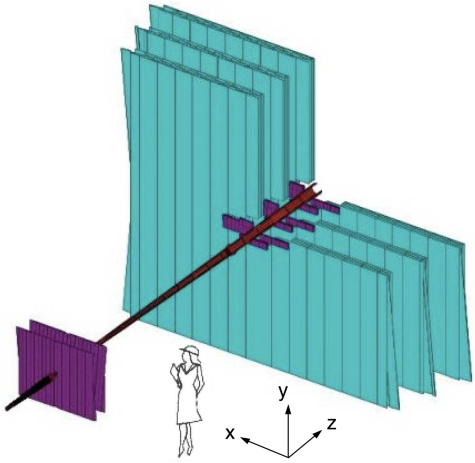

Figure 2.10 – The small trackers represent the TT, while the large rectangles are the T1-3 tracking stations. While the silicon trackers are coloured violet, the straw tubes are marked in turquoise. Taken from Ref. [122].

2012 [132].

The turquoise colour illustrates the *outer tracker* (OT), covering the regions with lower track multiplicity. The OT is based on the technology of straw drift tubes, having a diameter of 4.9 mm. The length of those tubes varies between 2.5 and 4 m. As the strips, the tubes are oriented upwards. Their composition resembles that of the TT stations since the OT stations consist of four layers each. The inner layers are again tilted by $\pm 5°$. Charged particles passing through the OT ionise the gas. The time-of-flight of the ionisation electrons in the tube, measured by its front-end electronics, and the physical boundaries of each straw tube indicate the x and y positions. The x-position of a hit in the OT is resolved with an uncertainty of 200 µm [135]. In Run 2, the resolution could be improved to 170 µm thanks to the *real-time alignment* [134].

2.3.2 Particle identification

As shown in the previous section, the trajectories of charged particles are reconstructed as tracks. However, the identity of those particles is not known from the tracking system, nor is there information about neutral particles. The particle identification (PID) denotes the assignment of a hypothesis on the nature of the track or a neutral particle. In flavour physics experiments, the PID is crucial since it permits to distinguish between different exclusive decay modes of a certain unstable particle.

In typical particle physics experiments, such as LHCb, several subdetectors are employed, relying on different physics phenomena to identify particles. The PID information is retrieved by combining the information from those subsystems, as sketched in

Fig. 2.11. The first employed detector type is the tracking detector, determining the

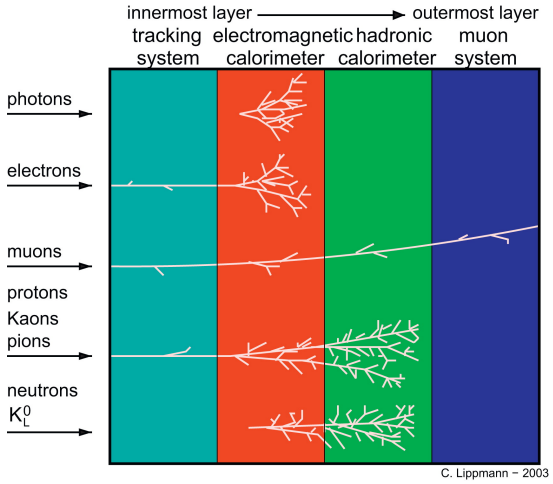

Figure 2.11 – The detection and identification principle of typical particle detectors from the inner to the outer subdetectors. Taken from Ref. [136].

track (and charge) of charged particles. Afterwards, the electromagnetic calorimeter system is installed, where photons, electrons and positrons are usually stopped. Since these particles transmit nearly all of their energy, the electromagnetic calorimeter provides an energy measurement of those particles. Although hadrons deposit a part of their energy in the electromagnetic calorimeter, they tend to penetrate into the hadronic calorimeter, which is made of more dense material. Muons, being minimally-ionising particles at the LHC energies, are not stopped by the calorimeter system, but pass to the muon stations. Muons have, therefore, rather clean signatures and are unambiguously identified.

Through the simplified detector setup in Fig. 2.11, there is no reliable way to distinguish between different hadrons. For this reason, two Ring Imaging Cherenkov (RICH) detectors have been installed in LHCb. Several subdetector outputs are combined in order to optimise PID variables. In the following, the subdetectors serving to determine the particle identity are explained, starting from the ones closest to the interaction point to the outer ones.

Ring Imaging Cherenkov detectors

The working principle of Ring Imaging Cherenkov detectors (RICH) relies on Cherenkov radiation. The Cherenkov light is produced by particles, travelling at a speed v higher than the phase velocity of light in this medium c_n with refraction index n. Cherenkov light is emitted in a cone with angle θ around the particle trajectory. The Cherenkov

angle θ is related to the particle speed v via the equation

$$\cos\theta = \frac{c}{nv}. \tag{2.4}$$

In LHCb, θ is measured by two different RICH detectors RICH 1 and 2, placed forward and downstream of the magnet. The layout of the two detectors in Run 2 is sketched in Fig. 2.12. In Run 1, RICH 1 possessed additional volumes filled with aerogel, which was eliminated at the end of Run 1 due to its performance decrease in high-multiplicity events [137]. RICH 1 is filled with CF_4 gas, having a refraction index of 1.0014, and

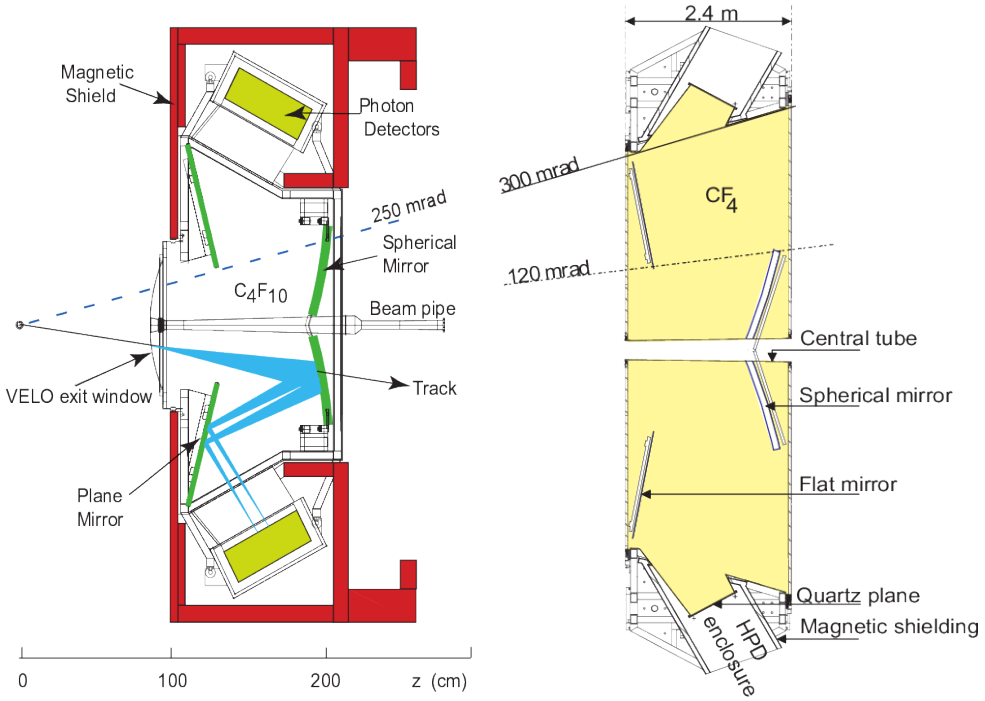

(a) RICH 1 (b) RICH 2

Figure 2.12 – Design of the RICH 1 (left) and RICH 2 (right) detectors during Run 2. Taken from Ref. [137].

is well suited for measuring Cherenkov angles of particles with momenta between 2 and 60 GeV/c. CF_4 gas with $n = 1.0005$ is inserted in the second RICH detector, RICH 2. RICH 2 is employed for Cherenkov cone measurements of particles with high momenta $p \gtrsim 15\,\text{GeV}/c$. It covers only the high-η region of $-3 < \eta < 5$, which is the typical flight direction of particles with a large forward boost. The interplay of the two detectors permits the PID determination in a broad momentum range.

The emitted Cherenkov light is deflected by spherical and flat mirrors, directing them to a matrix of Hybrid Photon Detectors (HPDs). The size of the HPDs is $2.5 \times 2.5\,\text{mm}^2$. To protect the HPDs from the magnetic field and from radiation damage, the HPDs are

situated outside of the LHCb detector acceptance, secured by a metal shield. Dedicated algorithms reconstruct the Cherenkov ring and retrieve θ.

The angle θ alone does not permit a conclusion about the particle type. Only in combination with the momentum estimate p from the tracking detectors the mass of the particle identity can be obtained. The performance of the RICH 1 detector to discriminate between particles is plotted in Fig. 2.13.

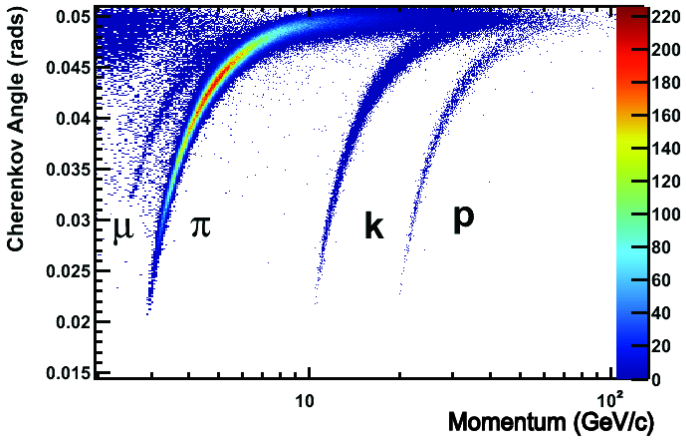

Figure 2.13 – Reconstructed Cherenkov angle θ in the RICH 1 detector as a function of the particle momentum p. Taken from Ref. [138].

The hadronic and electromagnetic calorimeter

While the tracking detectors are intended to contribute as little as possible to the material budget, calorimeters are designed to stop particles. Therefore, a large material budget is necessary. The interactions of high-energy electrons, photons and hadrons with the dense calorimeter material produce showers of secondary particles. Those cascades propagate further until the nearly entire kinetic energy of the particle is transmitted. Charged particles, including those produced in the showers, cause an excitation of the scintillator atoms. In the deexcitation of those atoms, scintillation light is created, which is collected by photomultipliers. The total energy is obtained by integrating over the energy of all the shower particles.

The LHCb experiment possesses a calorimeter system located upstream of the tracking stations and the RICH 2. Four different detectors are assembled, relying all on scintillating material. The first one is the Scintillating Pad Detector (SPD), followed by the PreShower detector (PS), the electromagnetic calorimeter (ECAL) and the hadronic calorimeter (HCAL). An illustration of this assembly is presented in Fig. 2.14. The SPD and PS are both scintillation pad detectors. They are separated by a lead plate, which is

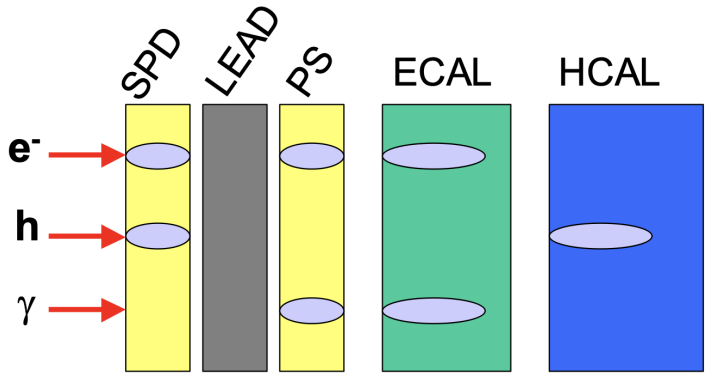

Figure 2.14 – The composition of the calorimeter system during Run 1 and 2 is sketched, and the expected energy deposit of different particle types is indicated. Taken from Ref. [139].

2.5 radiation lengths thick, but only ≈ 0.06 hadronic interaction lengths. As a result, photons and electrons are likely to start showering in the PS, while hadrons are not. Hits in the SPD detector indicate the presence of a charged particle [140], which discriminates between photons and electrons. The ECAL, placed behind the PS, is built with alternating scintillator and lead absorber plates, which is known under the "shaslik" design. With a length of 25 radiation lengths, the ECAL design permits to contain the whole electromagnetic showers. Hadrons start showering in the ECAL and continue in the HCAL, which has a thickness of about 5.6 hadronic interaction lengths. The HCAL is made of iron and scintillation tiles. ECAL and HCAL are both segmented in regions with different granularity as a function of the distance from the beam pipe. The ECAL possesses three of them, while the HCAL is separated into two.

The ECAL and HCAL are important not only for assigning a particle identity but also for providing a position measurement. Furthermore, the calorimeters are essential ingredients for the hardware trigger since it searches for clusters with high transverse energy, E_{T}. In Ref. [141,142], the ECAL energy resolution, measured in GeV, is given by

$$\frac{\sigma_E}{E} = \frac{10\%}{\sqrt{E}} + 1\%. \tag{2.5}$$

The energy measurement is especially important for photons due to the absence of tracks. The exactness of the electron's energy measurement is discussed later. The energy resolution provided by the HCAL is worse than the precision on the obtained momentum estimate p from the tracking stations [141,142].

The electron reconstruction in LHCb is especially challenging since electrons emit plenty of bremsstrahlung photons by interacting with the detector material [143]. Bremsstrahlung

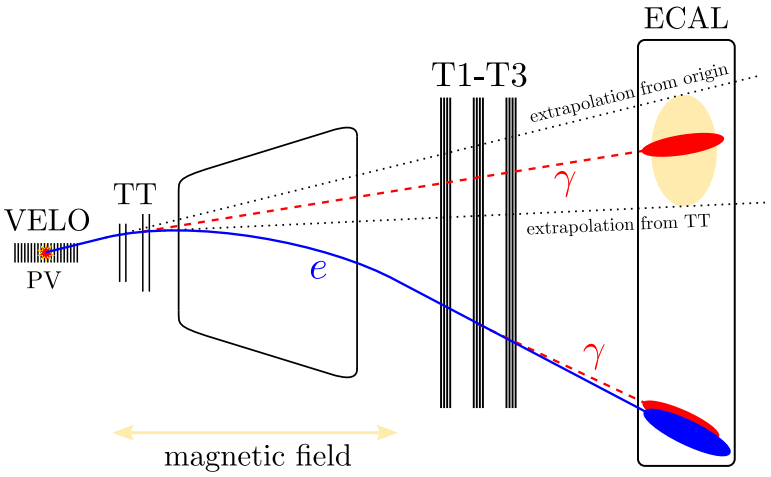

Figure 2.15 – Bremsstrahlung emission in LHCb before and after the magnet. Taken from Ref. [144].

emission before the magnet region has the problem that the magnetic field bends the electron track while the photon direction is not influenced. Therefore, the photon ends up in a different cell of the electromagnetic calorimeter compared to the electron cluster. Due to the photon emission, the electron momentum is estimated to be lower than its true value. However, the electron energy over momentum ratio, E/p, used for electron identification is unaffected [106]. An algorithm is employed to recuperate the energy of the emitted photons, as depicted in Fig. 2.15. Via the slope of the $e^{\pm}$ track, the four-momentum of the photon is reconstructed and added to the electron [143]. However, occasionally, random photons may be attached to the electrons, leading to over-estimation of their momenta [143]. Furthermore, the energy resolution of the calorimeter is worse compared to the resolution of the tracking system. Therefore, even in the case of correct recovery of bremsstrahlung photons, the resolution on the electron momentum is worse compared to the resolution on momenta of other charged particles in LHCb. Emissions after the magnet region do not affect the energy measurement since the photon energy deposit happens in the same cell of the electromagnetic calorimeter. In addition, the momentum estimation is performed before the emission and is unaffected.

The muon stations

The LHCb detector comprises five muon stations, M1 – 5 [145]. M1 is placed forward of the calorimeter system, permitting a fast and accurate estimate of the muon traverse momentum, which is essential for the hardware trigger, as described in Sec. 2.3.3. M2 – 5 are situated downstream of the calorimeter. Thanks to their finer granularity, the M2 and M3 muon stations achieve the best position resolution. As a result, these two stations

played a crucial role in the muon p_{T} estimation for the hardware trigger [146], while the main goal of the outer M4 and M5 stations was the muon identification since only muons with $p_{\mathrm{T}} > 6\,\mathrm{GeV}/c$ pass through them.

Since the inner part of the first muon station is exposed to higher multiplicities and radiation damage, a Gas Electron Multiplier technique is used [147]. The rest of M1 and the four other muon stations are equipped with multi-wire proportional chambers. Both detector types are classified as proportional ionisation chambers. The working principle is based on gas ionisation by traversing charged particles. The electrons, freed by the ionisation process, are amplified and collected at the anode. The two chambers are filled with the same gas components, while the individual proportions change between the M1 station and M2 – 5. In between stations M2 – 5, iron plates are installed to limit the crossing of all five stations to muons with $p \geq 6\,\mathrm{GeV}/c$ in order to reduce the misidentification rates further.

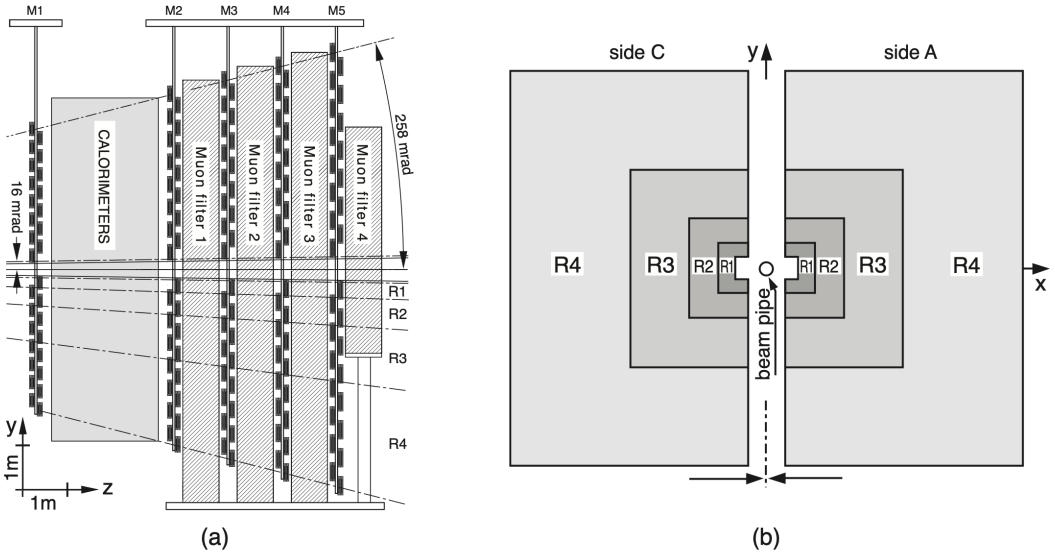

Figure 2.16 – Muon station layout in the yz (a) and xy plane (b). Taken from Ref. [145].

The layout of the muon stations is depicted in Fig. 2.16. On the right plot, the rectangular areas R1 – 4 indicate different granularity regions. In general, the granularity of the detector increases the closer the position to the beam pipe. However, a better resolution of the x coordinate is chosen for a better momentum estimate. In the precisest stations M2 – 3, the best hit position resolution in the x-direction equals 4 mm and 10 mm in the y-direction [145].

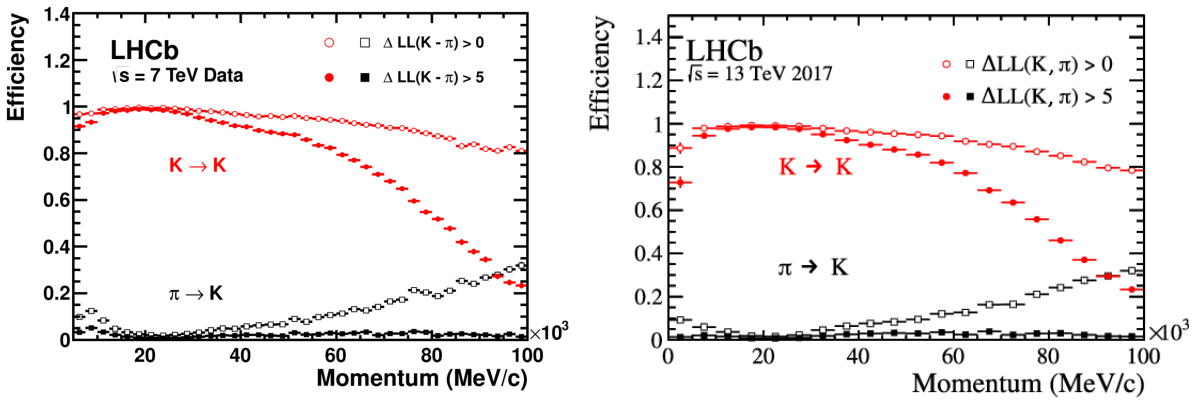

Figure 2.17 – Kaon identification performance during Run 1 (left) and Run 2 (right) [138, 148].

Particle identification variables

Combining the PID information of the RICH detectors, the calorimeters and the muon stations, a log-likelihood is calculated, which indicates the probability of a track to be a specific particle x. In analysis, the difference of the log-likelihoods of the particle to be particle x and a pion is usually employed, which is named $\mathrm{DLL}_{x\pi}$ in this thesis. The kaon and proton identification performances are shown for the proton and kaon in Fig. 2.17 and Fig. 2.18 [2].

It can be seen that at low and high momentum, the PID is less reliable, which is especially visible for the proton identification in the top plot of Fig. 2.18 and Fig. 2.17. The reason for the small PID efficiency at low particle momentum is that below the $p = 9.3\,\mathrm{GeV}/c$ threshold, neither protons nor kaons create a Cherenkov ring (see Fig. 2.13). As a consequence, no reliable kaon-proton separation is possible. In the $\Lambda_b^0 \to pK^-\mu^+\mu^-$ angular analysis, the proton is required to exceed this momentum threshold.

Another PID variable is available, which is called ProbNN, in the rest of this thesis. It is based on a neural network [149]. As input for the neural network training served the information of all LHCb subdetectors, including also the tracking detectors. As an output of this neural network, each charged ID hypothesis can receive a score from 0 to 1. In Ref. [58, 94], the ProbNN variable has been seen to be more powerful in suppressing misidentification background contributions. In the presented analysis, requirement on the DLL and the ProbNN variables are applied (see Ch. 3).

2. The variable ΔLL(K-π) in the figures is called $\mathrm{DLL}_{K\pi}$ in this thesis. The same holds for the variables DLL_{pK} and $\mathrm{DLL}_{p\pi}$ variables.

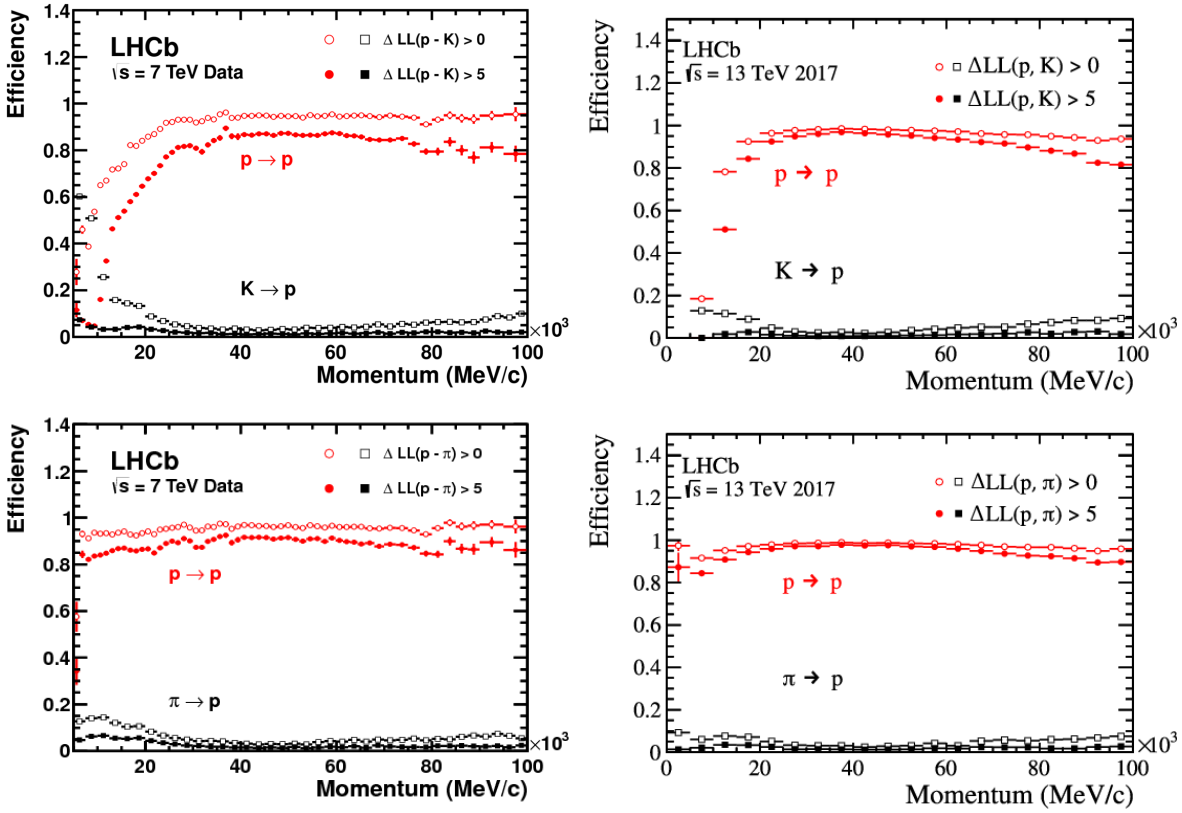

Figure 2.18 – Proton identification performance during Run 1 (left) and Run 2 (right), compared with the rate of kaon (top) and pion (bottom) misidentification as protons [138, 148].

2.3.3 Trigger

The proton bunch spacing of 25 ns results in a bunch crossing rate of 40 MHz at the LHC. Due to the LHC bunch filling scheme, not all bunches collide at the LHCb position, and the rate is reduced to 30 MHz. On one hand, the detector cannot be read out at such rates, and, on the other hand, saving all of the bunch crossings, called "events" in the jargon, is expensive. As a consequence, the data has to be filtered. Triggers are employed to select interesting events and reduce the data rate to $\mathcal{O}(10)$ kHz [150]. The LHCb trigger system is optimised to select typical signatures of b and c-hadron decays.

The Run 2 trigger architecture in LHCb has been sketched in Fig. 2.19. The first stage is the hardware trigger L0. Selected events pass the software selections by the High-Level-Triggers (HLT) 1 and 2. The different trigger steps are discussed in the following.

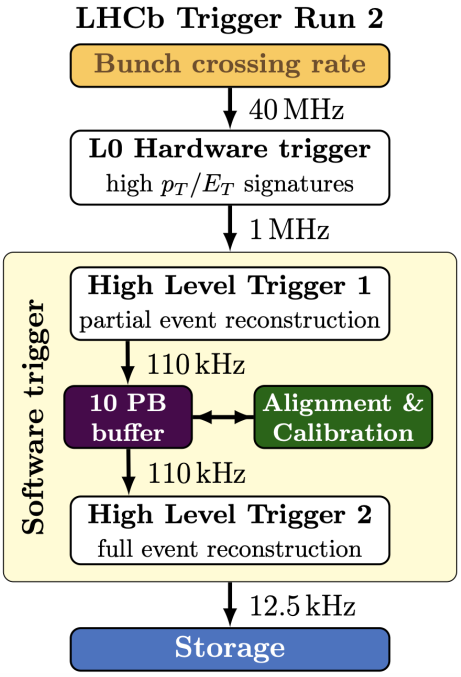

Figure 2.19 – Illustration of the trigger and offline analysis architecture during Run 2. Taken from Ref. [133].

Hardware trigger

The first stage of the LHCb trigger system in Run 1 and 2 is the hardware trigger L0. Its aim is to reduce the rate to about 1 MHz within a decision time of maximal 4 µs [151] by retaining events with highly energetic candidates. The reason for this is that the decay products from b hadron decay are likely to be highly energetic due to the large

b hadron mass. As a significant fraction of b hadrons decays into final states containing muons, providing a clean signature, the L0 trigger searches for tracks in the muon stations with high p_{T}, or dimuon candidates with a high product of muon p_{T}. Furthermore, the triggers on hadrons, electrons and photons are fired if clusters with high E_{T} are present in the calorimeter. If the E_{T} or p_{T} threshold is succeeded, the event is passed to the HLT 1 trigger. The L0 trigger vetoes events with high multiplicity, which would exceed the HLT 1 trigger decision time [152], by requiring the number of hits in the SPD to be inferior to 600 in Run 1 and 450 in Run 2 for most of the triggers. This rejection is motivated by the fact that the number of b meson decays selected in the offline analysis decreases with an increasing number of SPD hits [152]. At high multiplicity, the PID and tracking performances worsen, making background rejection less reliable.

Software-based high-level trigger

After passing the L0 trigger, selected events are handed over to the software-based trigger. The first one, HLT 1, reconstructs the final state partially by performing a track and primary vertex (PV) fit [153]. A selection of track quality, particle momentum and PV displacement is applied, optimised for b- and c-hadron decays. Muons are already identified in the HLT 1 step. The HLT 1 trigger reduces the rate to $\mathcal{O}(10)\,\mathrm{kHz}$.

In HLT 2, the events are reconstructed using the additional calorimeter and RICH responses. Furthermore, a more complete track reconstruction is performed. In Run 1, a simplified online reconstruction is followed by a more complete online reconstruction. In Run 2, the event reconstruction was performed fully online. To optimise the computational resources and to provide the needed computing time, events with positive HLT 1 decisions are saved to a buffer. The HLT 2 reconstruction and selection took place when the data-taking was on hold, *e.g.* in between the LHC fills or technical shutdowns [133]. Another advantage of the buffer introduced in Run 2 is that alignment and calibration tasks are run in "real-time", improving the HLT 2 reconstruction [133]. The HLT 2 selection is separated into *inclusive* and *exclusive* strategies. *Inclusive HLT 2 trigger lines* retain events with certain topologies, while *exclusive lines* are optimised for specific final states. In this thesis, the HLT 2 trigger lines are based on an *inclusive selection*. If the event or decay is selected in the HLT 2 step, it is saved to disk. During Run 1 the output rate was 5 kHz, while in Run 2 a rate of 12.5 kHz was allocated.

The selection of *inclusive lines* is broad, because of which the dataset is extensive. To prevent each analysis from running on all of the data, an offline preselection step is introduced, which is called *stripping*. The stripping selection ("line") used in the angular analysis of this thesis is optimised for selection of $\Lambda_b^0 \to pK^-\mu^+\mu^-$ decays, as explained in Sec. 3.2.2.

2.4 The upgraded LHCb detector

During Run 3 and 4, the instantaneous luminosity at the LHCb experiment is planned to be levelled at $2 \times 10^{33}\,\mathrm{cm}^{-2}\mathrm{s}^{-1}$. The higher luminosity levelling is supposed to cause an increase of the $\langle\mu\rangle$ value to 5.2. In preparation for Run 3, the LHCb detector underwent a major upgrade to keep up with the data acquisition rate and the radiation damage.

A considerable change is the removal of the hardware trigger by a fully software-based trigger, which aims to achieve similar efficiencies for hadrons and lepton. Bremsstrahlung photons are already attached in the HLT 1 trigger stage, which is beneficial for $b \to s\ell^+\ell^-$ analyses. The new trigger strategy is sketched in Fig. 2.20. The track reconstruction begins in a GPU-based HLT 1 trigger, implemented in the Allen software, which reads out the full detector. For this purpose, the front-end electronics of all subdetectors are replaced. The HLT 1 trigger decision is based on partially reconstructed events. Selected events are saved in a buffer, where the real-time alignment and calibration can be directly run and applied. Afterwards, the HLT 2 trigger, as part of the Moore software, takes over the full event reconstruction and the HLT 2 selection. If the HLT 2 trigger fires, the events are saved to tape. As for Run 1 and 2, an additional offline selection step is introduced for inclusive HLT 2 selections, which is called *sprucing*.

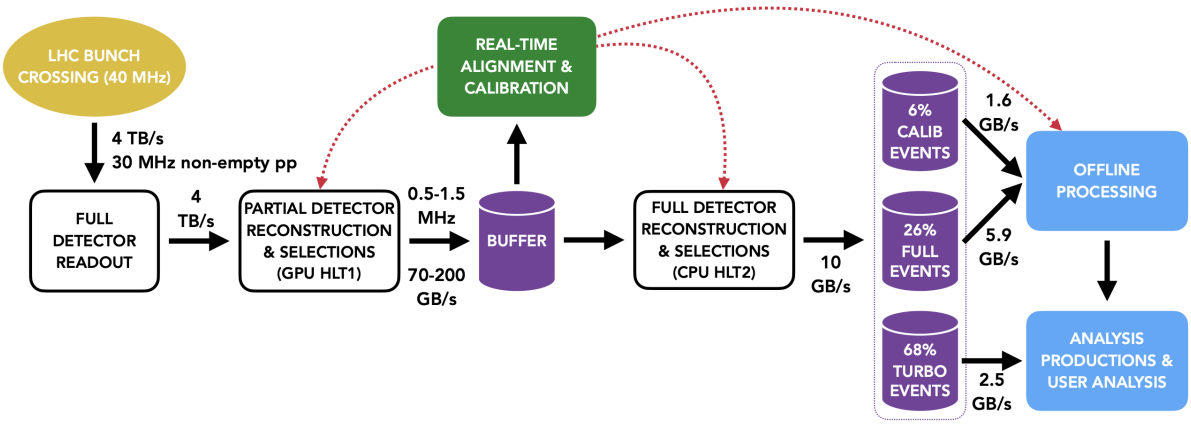

Figure 2.20 – Sketch of the trigger and offline analysis architecture during Run 3. Taken from Ref. [154].

The LHCb Upgrade I detector [155, 156] is equipped with a new vertex detector. This new vertex detector uses silicon pixels instead of silicon strips, permitting a better granularity for coping with the higher multiplicity and the increase of the ghost rate [157]. The modules are again split into A- and C-side, but constructed as L-shape. The modules

enclose the beam with a distance of 5.1 mm only. The positioning of the 26 layers is tuned to enhance the impact parameter resolution, which is improved by 40% for tracks possessing a first hit at $z > 300\,\text{mm}$ [157] and the track efficiencies, changing from 97.8% for long-tracks in Run 2 to 99.4% in Run 3 [3] [157].

In addition, the TT stations are planned to be replaced by the Upstream Tracker (UT), aimed to reduce the ghost rate and to improve the momentum resolution [158]. Its design is based on a finer granularity of the silicon strips and a stronger radiation hardness. However, the installation took place at the beginning of 2023, and, therefore, after the last weekend of data-taking in 2022, which is analysed in Ch. 5.

The IT and OT subdetectors are replaced by the Scintillating Fiber Tracker, which itself is composed of three stations. Instead of silicon strips, scintillating fibres are arranged in four layers slightly tilted towards each other. The detector aims a hit efficiency of 99% while keeping the noise rate down to 10% [158]. The hit resolution in the xz plane is planned to be less than $10\,\mu\text{m}$ [158].

Finally, the optics of the RICH 1 detector is renewed, which results in a larger image area and in a reduced peak occupancy [159]. To be able to read out the RICH detectors in time, the HPDs are exchanged by multi-anode photomultipliers.

At the time of the thesis writing, the LHCb Upgrade I detector is still in commissioning. However, first steps of an analysis of early Run 3 data has been conducted with the data collected in 2022 and will be presented in Ch. 5.

3. Note that in this calculation are performed with $B^0 \to K^*\mu^+\mu^-$ decays. In addition, the interactions per pp collision ν are 2 in the Run 2 case and 7.6 in the Run 3 case.

Chapter 3

Selection of $\Lambda_b^0 \to \Lambda(1520)\mu^+\mu^-$ decays

In order to improve the readers' experience, the analysis of $\Lambda_b^0 \to \Lambda(1520)\mu^+\mu^-$ decays is split into two chapters. The first one presents the selection of the signal process of interest and the second one covers the angular analysis itself.

In the first section, the analysis strategy is explained, describing the choice of the data and simulation samples. Afterwards, the q^2 binning is defined. Since a blinded analysis is performed, the blinding procedure is explained. Since the LHCb experiment records a myriad of decays, the dataset needs to be filtered in order to obtain the rare $\Lambda_b^0 \to \Lambda(1520)\mu^+\mu^-$ decays. The selection criteria are found in the second section of this chapter. Different background contributions are studied and eliminated when possible. Unfortunately, the simulation samples do not model perfectly well the recorded data. Therefore, corrections of the simulation samples are derived, which are explained in the third section. In the last section, the fit to the $pK^-\mu^+\mu^-$ invariant mass spectrum is shown, and the Λ_b^0 yields are estimated.

3.1 Analysis strategy

The following section is dedicated to clarifying the analysis idea and the strategy, including the q^2 binning and the blinding of the angular observables (explained in Sec. 3.1.2). Furthermore, the data and simulation samples used in this analysis are stated.

3.1.1 Summary of the analysis idea

To deal with the numerous overlapping Λ^* resonances in the pK^- invariant mass spectrum, the analysis focuses on the narrow and resonant $\Lambda(1520)$ peak, where theory

predictions are available [5, 6, 113]. A window of about ± 50 MeV/c^2 has been put in place around the $\Lambda(1520)$ pole mass. Nevertheless, the spin-1/2 Λ^* resonances and their interferences need to be considered in the angular fit.

This analysis aims to measure the angular observables A_{FB}^{ℓ} and S_{1cc}. Both are the *CP* averaged angular observables of the Λ_b^0 and $\overline{\Lambda_b^0}$ decay. The leptonic forward-backwards asymmetry has been found in Ref. [5,107] to be especially sensitive to NP effects. The existing predictions of the angular observables for the signal decay are presented in Fig. 1.19. Although different form factor predictions are used, the angular observable values are consistent with each other.

The well-known dataset of $\Lambda_b^0 \to pK^- J/\psi(\to \mu^+\mu^-)$ decays is used as a control mode of the analysis. Since the yields of the $\Lambda_b^0 \to pK^-\psi(2S)(\to \mu^+\mu^-)$ decay are closer to the rare mode, it is used as a control mode, too.

The background level in the signal mode is reduced by a dedicated selection. It includes the applied vetoes to reduce specific backgrounds and a multivariate analysis technique to suppress the combinatorial background. Instead of modelling the background distribution in the angular fit, the remaining combinatorial background is subtracted by the ${}_s\mathcal{W}eight$ technique [160]. Due to the different angular distributions of the Λ^* resonances and their interferences, the angular fit is the main challenge of the analysis. Fitting the background-subtracted angular distribution reduces the number of parameters in the angular fit.

3.1.2 Blinding strategy

An analysis result can be biased, even unconsciously, by expecting a particular outcome. To prevent this bias, blinded analyses are performed. The idea is not to "have a look" at the result until the analysis is frozen. Such a blind analysis is performed in this thesis.

To not unblind the BF measurement [60], which was done in parallel with this work, the high-q^2 bin and the efficiencies were blinded until permission to unblind was given. For the angular analysis, the angular fit values of A_{FB}^{ℓ} and S_{1cc} are kept blind in the rare mode. To do so, it was decided to perform the angular fit but keep the fit values and projections of the $\Lambda(1520)$ fit component blind. Unblinding the angular observables and fit projects can be asked for after freezing the analysis and studying the dominant systematic uncertainties.

3.1.3 Data and simulation samples

The analyzed dataset was collected by the LHCb experiment in *pp* collisions during Run 1 and Run 2, which correspond to the data-taking periods of 2011-12 and 2015-18.

The integrated luminosity and the centre-of-mass energy per data-taking year are given in table 3.1. The total integrated luminosity of the data-taking periods of Run 1 and 2 correspond to approximately 3 and 6 fb^{-1}. The total Run 1 and 2 dataset is used for the presented analysis.

Year	$\sqrt{s}$ [TeV]	$\mathcal{L}$ [fb^{-1}]
2011	7	1.1
2012	8	2.1
2015	13	0.3
2016	13	1.7
2017	13	1.7
2018	13	2.2

Table 3.1 – The centre-of-mass energy $\sqrt{s}$ and corresponding integrated luminosities $\mathcal{L}$ collected by the LHCb experiment are listed per year of data taking.

Simulation samples are necessary to evaluate the properties of a given process and their response in the LHCb detector. To correctly reproduce what is happening in the detector, the pp collisions and the quark hadronisation need to be generated. This is done using the Monte Carlo (MC) generator Pythia [161] with a configuration developed explicitly for the LHCb experiment [162]. The decay of the produced particles, in the signal case of the Λ_b^0 baryon, is modelled by EvtGen [163]. Photos adds Final-State radiation to the process [164]. All particles, which do not belong to the signal process, are only generated using Pythia. The interactions of the particles with the detector are described by the Geant4 software [165, 166]. To match the data, the generator-level simulated dataset needs to be reconstructed in the same way as the data sample. Therefore, the emulated detector response is digitised by the Boole package. The L0 and HLT trigger responses are mimicked by the Moore software. The reconstruction is performed in the simulation in the same way as in the data. The conceptual difference between data and simulation is that in simulation, the nature of generator-level particles is known.

Simulation samples of the signal process, $\Lambda_b^0 \to \Lambda(1520)(\to pK^-)\mu^+\mu^-$, are used in this analysis. Those are generated for the full Run 1 and 2 data taking. Since the theoretical prediction of this decay is form-factor-dependent and subject to recent changes, the analysis is based on phase space simulation samples. The phase space model describes a simulation procedure where the decay probability is constant in the helicity angles of the decay. [1] This means that after the generation, the distribution in the simulation sample is flat in each of the helicity angles of the decay. The flat generator-level distributions

1. The $\Lambda_b^0 \to pK^-\mu^+\mu^-$ decay angle definition in the helicity frame is sketched in Fig. 1.9. More details can be found in App. I.

of the helicity angles in the $\Lambda_b^0 \to \Lambda(1520)(\to pK^-)\mu^+\mu^-$ decay are shown in Fig. 3.1. Those simulation samples are important for selecting the signal decay, deciding on the Λ_b^0 mass shape model and extracting the angular acceptance. The simulation sample size corresponds to one million events per year during Run 1 and two million events per year for the Run 2 data taking. The selection and reconstruction is supposed to affect the phase-space simulation sample and the simulation sample with the theoretical prediction the same. However, a systematic uncertainty will be assigned for the change of the Λ_b^0 mass shape by using the simulation samples based on the theoretical prediction.

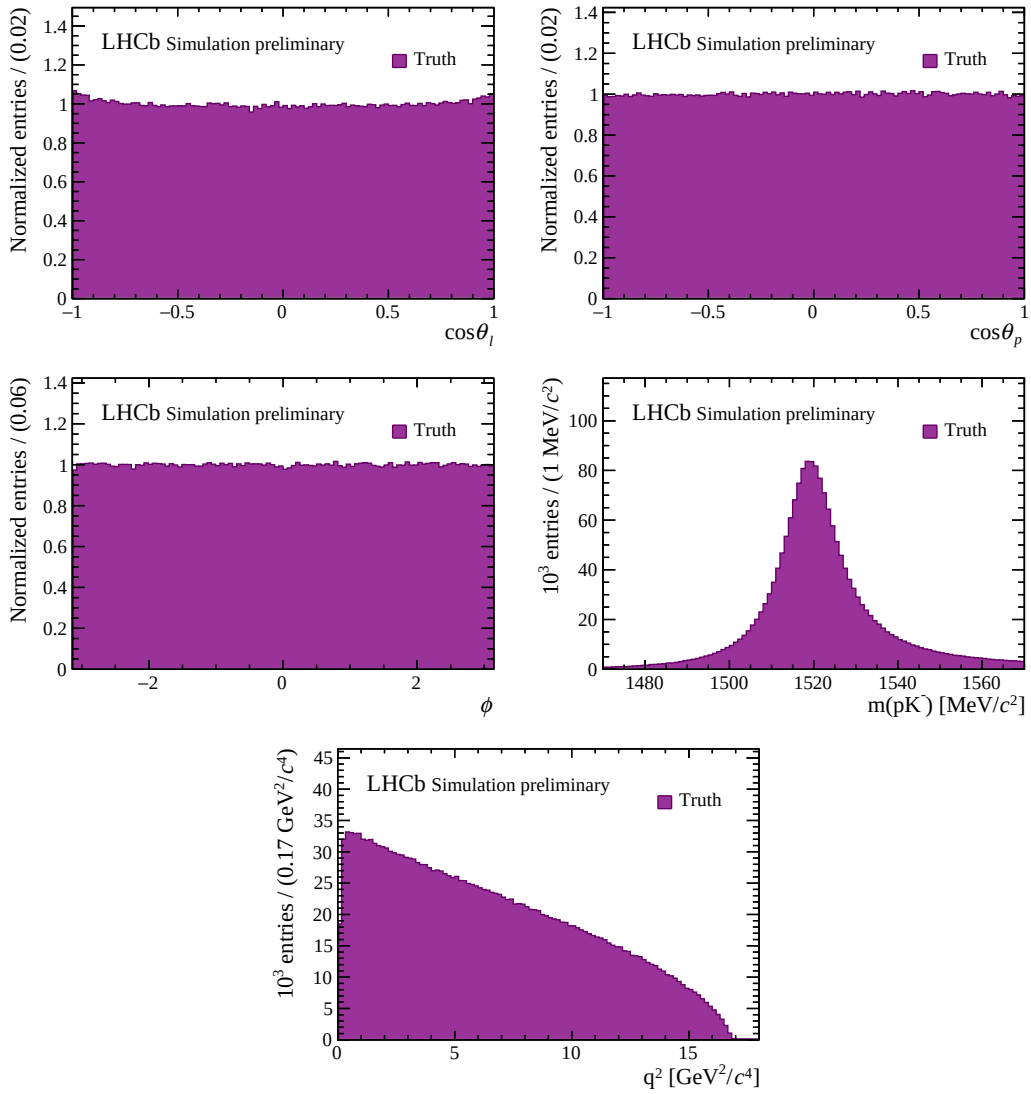

Figure 3.1 – Generator-level distributions in the $\Lambda_b^0 \to \Lambda(1520)(\to pK^-)\mu^+\mu^-$ phase space simulation sample, representing the data-taking period of 2016.

In the simulation samples, the true identity of the reconstructed particles is known. Therefore, the reconstructed particle can be truth-matched to the truth particle if they

share 70% of the hits in the detector. The same mass hypothesis needs to be assigned to the reconstructed particle as to the generated one [167]. Additionally, they are checked to originate from the same parent particle created in the pp collision. In this thesis, the truth-matching criterium translates into being associated with the correct true PID hypothesis and originating from an actual Λ_b^0 baryon. The proton and kaon are additionally asked to originate from a true $\Lambda(1520)$ resonance. This "truth matching" method is referred to as TrueID matching [167].

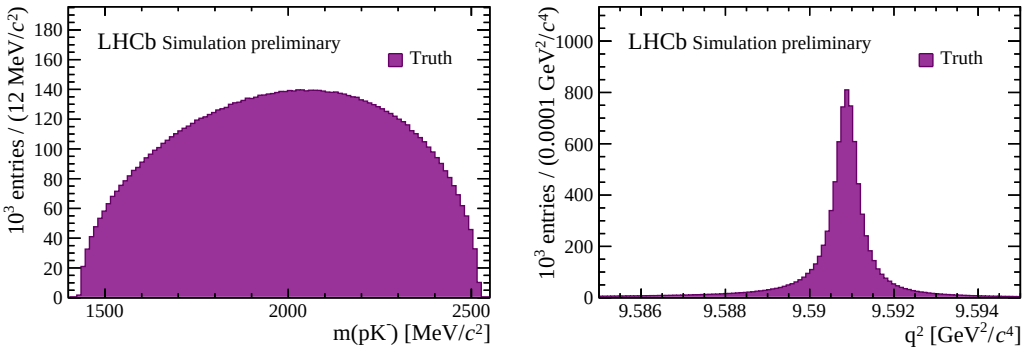

Figure 3.2 – Generator level distributions of the $\Lambda_b^0 \to pK^- J/\psi(\to \mu^+\mu^-)$ phase space 2016 simulation sample.

Simulation samples for the $\Lambda_b^0 \to pK^- J/\psi(\to \mu^+\mu^-)$ control mode are available for the entire data-taking period. $\Lambda_b^0 \to pK^-\psi(2S)(\to \mu^+\mu^-)$ samples are prepared for the data-taking years 2012 and 2016. Both control mode samples show a phase space distribution in the decay angles and the pK^- invariant mass, while the $c\bar{c}$ resonance is present in the dilepton system, as shown in Fig. 3.2. Samples with a phase space distribution in the Λ^* mass spectrum and the dimuon mass, denoted by $\Lambda_b^0 \to pK^-\mu^+\mu^-$ samples, are available for the data taking years 2012, 2017 and 2018. The resonant pK^- invariant mass structure is a priori not known in the rare, and the $\psi(2S)$ modes since no amplitude analysis has been performed with those decay modes yet. However, the spectrum is well-known in the J/ψ mode [4]. A dedicated model to reproduce the realistic resonant structure in the pK^- and pJ/ψ invariant mass spectra is available and calculated in subsection 3.4.1.

Simulation samples of the background decays are employed to estimate the size of the background contribution and extract the background shape of non-negligible contributions. A particular background is the double hadron swapped misidentification of the proton and kaon in the $\Lambda_b^0 \to pK^-\mu^+\mu^-$ decay as kaon and proton. A simulation sample is constructed by reconstructing the true protons, emerging from the Λ_b^0 signal decay, as kaons and vice versa.

To evaluate the background contribution from cascade decays, simulation samples of $\Lambda_b^0 \to \Lambda_c^+(\to pK^-\pi^+)\pi^-$ decays are found to be convenient and are available for the data-taking years 2012 and 2016. The Λ_c^+ baryon decay model includes the non-resonant decay, as well as decays via the K^{*0} and $\Delta(1232)^{++}$ resonances. In addition, $\Lambda_b^0 \to \Lambda_c^+(\to pK^-\pi^+)\mu^-\overline{\nu}_\mu$ decays are simulated to represent the data-taking in the year 2016. The $\Lambda_b^0 \to \Lambda_c^+(\to \Lambda(1520)(\to pK^-)\mu^+\nu_\mu)\pi^-$ simulation sample models decays via the $\Lambda(1520)$ resonance with the data-taking conditions during 2012.

Samples of $B^0 \to K^*(892)^0(\to K^+\pi^-)\mu^+\mu^-$ decays are simulated with the data-taking conditions of the year 2012. The resonant $B^0 \to K^*(892)^0 J/\psi$ and $B^0 \to K^*(892)^0\psi(2S)$ decays are generated and are available for the years 2012 and 2016. Non-resonant $K^+\pi^-$ decay can be studied with phase space 2012 and 2016 simulation samples in the J/ψ mode.

$B_s^0 \to K^+K^-\mu^+\mu^-$ simulation samples are produced with a K^+K^- phase space model for rare dimuon decays and via a J/ψ or $\psi(2S)$ resonance. The simulation samples modelling the resonant mode are available for the data-taking years 2012 and 2016. For rare $B_s^0 \to K^+K^-\mu^+\mu^-$ decays, only a simulation sample exists for the data-taking year 2012. More details about the simulation samples can be found in Appendix A.

3.1.4 The q^2 binning

In order to have comparable results, the q^2 binning is aligned between the angular analysis and the BF measurement [60]. The q^2 binning is listed in Tab. 3.2. Although the phase space ends at $q^2 \approx 16.8\,\mathrm{GeV}^2/c^4$, the upper limit of the high-q^2 bin is defined by $17.0\,\mathrm{GeV}^2/c^4$. This cut aims to prevent a reduction of the sample size by an inaccurate q^2 resolution. Since the BF measurement only measures 29 Λ_b^0 candidates in this bin [60], an angular fit is not feasible with this dataset. The tree-level $b \to c\bar{c}s$ decays dominate by far the electroweak penguin contribution. The q^2 bins of the $c\bar{c}$ resonances are defined to be broad, such that the bins contain their whole tails.

In supplementary, the measurement of the angular observables is planned in a broader q^2 bin to facilitate comparisons between decay modes. In this bin, the $\phi(1020)$ resonance is excluded [21], even though its contribution is found to be negligible, as seen in Fig. 3.3. The ϕ resonance is composed of a $s\bar{s}$ quark pair and possesses a mass and width of $m_\phi = 1019\,\mathrm{MeV}/c^2$ and $\Gamma_\phi = 4\,\mathrm{MeV}$ [21].

In Fig. 3.3, the resonant pK^- invariant mass spectrum is presented for the rare mode. The narrow and dominant $\Lambda(1520)$ resonance is distinguishable. Even though the combinatorial background is not fully removed, the resonant structure in the rare mode visually resembles the one measured in the J/ψ mode (see Fig. 1.15).

Bin	q^2 interval $[\,\mathrm{GeV}^2/c^4\,]$
below-J/ψ 1	$0.1 - 3.0$
below-J/ψ 2	$3.0 - 6.0$
below-J/ψ 3	$6.0 - 8.0$
J/ψ	$8.0 - 11.0$
mid-q^2	$11.0 - 12.5$
$\psi(2S)$	$12.5 - 15.0$
high-q^2	$15.0 - 17.0$
integrated	$1.1 - 6.0$

Table 3.2 – Dilepton invariant mass squared, q^2, bin definitions.

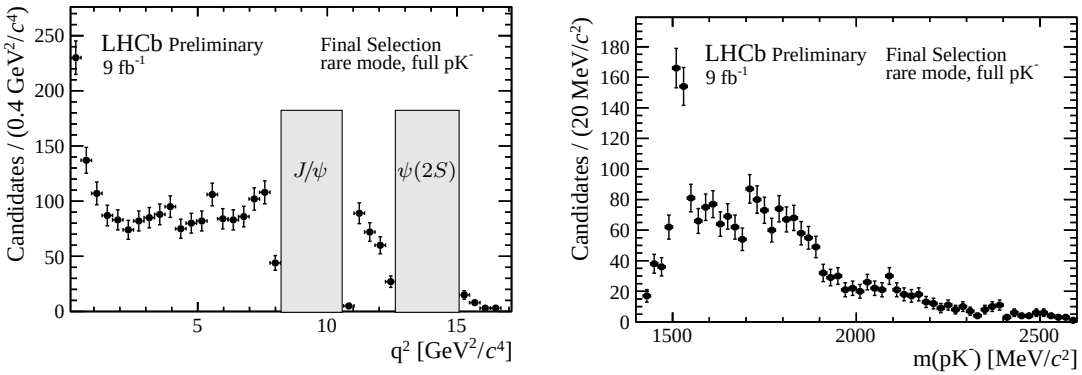

Figure 3.3 – The q^2 distribution in the rare mode after vetoing the J/ψ and $\psi(2S)$ mass regions is shown on the left. The corresponding pK^- invariant mass distribution is shown on the right. Apart from the cut on the pK^- invariant mass spectrum, the full selection is applied, which will be described later in this chapter. The $pK^-\mu^+\mu^-$ invariant mass is required to be within a mass window of $\pm 30\,\mathrm{MeV}/c^2$ around the Λ_b^0 pole mass in order to minimise the background contribution.

3.2 Signal candidate selection

The pp collisions at the LHC produce a multitude of different particles. Since the LHCb experiment cannot save all the events, interesting ones are selected. The tool that decides which events are interesting is called the trigger, and it is tuned to be as fast and versatile as possible. The trigger requirements for selecting the signal process are described in the first subsection. The preselection, mainly based on kinematic variables and loose PID criteria, is presented in the second subsection. Specific backgrounds are studied in the third subsection. The combinatorial background is suppressed by a multivariate classifier, which is presented in the fourth subsection.

3.2.1 Trigger requirements

During Run 1 and 2, the first trigger stage was the hardware trigger (L0). Its decision was based on the response of the calorimeter and the muon stations (see Ch.2). In the final state of the signal process, two muons, a proton and a kaon are present. In the control mode, the final state is identical, and therefore, the same trigger selection is used. Since muons have a clean signature in the LHCb detector, the L0 trigger decision is based on the muon system. For our mode of interest, it searches for high transverse momenta, p_{T}, muon or di-muon candidates in the muon stations [168]. The hardware and the software trigger decision is based on the signal particles (TOS = trigger on signal).

The first stage of the software trigger, denoted as High-Level Trigger (HLT) 1 (see Ch. 2.3.3), takes decisions based on the properties of tracks within the detector. It is optimised to retain b-hadron decay signatures, such as tracks, which are displaced from the primary vertex. The trigger selections, employed in the presented analysis, are listed in Tab. 3.3. The trigger lines, jargon for trigger selections, differ between Run 1 and 2. While in Run 1 events with a generic displaced track or muon track are picked by a cut-based selection, a multivariate analysis (MVA) is employed during Run 2 to select one- or two-track signatures. Through the re-optimisation between Run 1 and 2, a higher signal efficiency is achieved.

The HLT 2 trigger preserves events based on the event topology. During Run 1, a bonsai Boosted Decision Tree (BDT) [169] selected b-hadron decays to N particles. b-hadrons are long-lived due to the weak decays. Therefore, their decay vertex or *secondary vertex* (SV) is well separated from the collision point, the b-hadron production vertex or *primary vertex* (PV). N denotes two, three or four particles. Because of the presence of four particles in the final state, trigger lines with $N = 2, 3$ and 4 are considered connected with a logical "or". Looser displacement and kinematic criteria are applied by the HLT 2

Trigger	Run 1	Run 2
L0	Muon, DiMuon	
HLT 1	TrackAllL0, TrackMuon	TrackMVA, TwoTrackMVA
HLT 2	Topo(2,3,4)BodyBBDT, TopoMu(2,3,4)BodyBBDT	Topo(2,3,4)Body, TopoMu(2,3,4)Body

Table 3.3 – Trigger lines used to select the signal and control mode of the analysis.

trigger if at least one of those tracks is identified as a muon. The same principle is adopted in Run 2 by the MatrixNet algorithm [170, 171].

3.2.2 Preselection

After being retained by the trigger selection, the data are saved. Since individual analyses do not need the full dataset, another selection separates the data into different streams depending on its event properties. This preselection is called stripping. Events are saved on disk if selected by the stripping. In the following analysis, the stripping selection B2LLXBDT_Lb2mumuPKLine is used, which improves the purity by a BDT algorithm. The BDT classifier is trained on the square root of the significance of the impact parameter, computed as a difference of the χ^2 of the primary vertex fit with and without the probed track. The BDT is additionally trained on the logarithm of the transverse momenta of all involved particles. Furthermore, the square root of the significance of the Λ_b^0, J/ψ, and the Λ^* flight distances, being calculated as the χ^2 of the distance between the origin and decay vertex of the particle, are used in the training. Another input feature is the angle between the Λ_b^0 direction and the sum of the final-state particle four momenta. The stripping line requires the criteria specified in Tab. 3.4. The definitions of the employed variables are collected in the Glossary.

In the preselection, the particle identification (PID) requirements are tightened further via the ProbNN and DLL variables in order to suppress misidentification backgrounds. To ensure good particle identification, all final state particles are required to have hits in the RICH detector. Since protons can only be distinguished from charged kaons above the momentum threshold of 9.3 GeV/c, they are required to exceed the momentum threshold. Since the PID calibration samples are based on specific particle momenta, particles below the momenta cannot be calibrated. Therefore, they need to be aligned accordingly. The same selection requirements are applied on both of the muons in order not to disturb the symmetry of the angular distribution.

Particle	**Stripping**	**Preselection**	**Calibration sample**
μ	hasMuon, isMuon $\text{Prob}_{\text{ghost-track}} < 0.5$ $p_{\text{T}} > 200\,\text{MeV}/c$ $\chi^2_{\text{IP}} > 1$	hasRich ProbNNmu > 0.1 $p > 3\,\text{GeV}/c$ $\text{DLL}_{\mu\pi} > -5$	**Run 1:** $p_{\text{T}} > 800\,\text{MeV}/c$ $p > 3\,\text{GeV}/c$ **Run 2:** $p > 3\,\text{GeV}/c$
$\mu^+\mu^-$	$m < 5\,\text{GeV}/c^2$ $\chi^2_{\text{vertex}} < 16$ $\chi^2_{\text{DOCA}} < 30$		
p	ProbNNp > 0.05 $\text{Prob}_{\text{ghost-track}} < 0.4$ $p_{\text{T}} > 300\,\text{MeV}/c$ $\chi^2_{\text{IP}} > 4$	hasRich ProbNNp > 0.2 ProbNNk < 0.8 ProbNNpi < 0.7 $p > 9.3\,\text{GeV}/c$ $\text{DLL}_{p\pi} > -5$	**Run 1:** $p_{\text{T}} > 250\,\text{MeV}/c$ **Run 2:** -
K^-	ProbNNk > 0.1 $\text{Prob}_{\text{ghost-track}} < 0.4$ $p_{\text{T}} > 300\,\text{MeV}/c$ $\chi^2_{\text{IP}} > 4$	hasRich ProbNNk > 0.2 ProbNNp < 0.8 $p > 2\,\text{GeV}/c$ $\text{DLL}_{K\pi} > -5$	**Run 1+2:** $p > 2\,\text{GeV}/c$ $p_{\text{T}} > 250\,\text{MeV}/c$
pK^-	$m < 5.6\,\text{GeV}/c^2$ $\chi^2_{\text{vertex}} < 25$		
Λ_b^0	$m \in [4.0, 6.8]\,\text{GeV}/c^2$ $\chi^2_{\text{vertex}}/\text{ndof} < 25$ $\chi^2_{\text{IP}} < 400$ DIRA > 0.999 $\chi^2_{\text{decay-length}} > 0$	$p_{\text{T}} \in [1, 25]\,\text{GeV}/c$ $\chi^2_{\text{DTF}}/\text{ndof} < 100$	
General	Stripping BDT > -0.11 $n_{\text{PV}} \geq 1$		

Table 3.4 – The stripping and preselection criteria are specified. Since the PID calibration samples are cut on particle momenta, only particles with higher momenta can be calibrated.

3.3 Background studies

Decays of b hadrons are relatively clean experimentally due to their exceptionally long lifetime, which separates well hadrons from the pp interaction point and hadrons from b hadron decays. Therefore, most background sources are expected to originate from true b hadrons. Even if the background decays are mainly suppressed by the selection, they may be enhanced in comparison to the rarity of the signal decay, for example, because of a higher production fraction of the parent particle or higher rate of its decay at tree-level. To give the order of magnitude, $b \to s\ell^+\ell^-$ decays have BFs of the order 10^{-6} and $b \to c\ell^-\overline{\nu}_\ell$ transitions of the order 10^{-3}. This is the reason why all of the background sources need to be characterised precisely. Generally, four different background types are distinguished.

1. Random combinations of particle tracks are grouped under the term *combinatorial background*. As this background is the most abundant, several strategies are employed to reduce it.

2. The second background type is due to *misidentified particles*. Thanks to the clean signature of the muon tracks in the detector, lepton misidentification is supposed to be small and the misidentification of the involved hadrons is expected to be dominant. Mostly single, but also double misidentification occurs [2].

3. The third background type is composed by *over-reconstructed decays*. Although an actual b hadron decay is present, a random particle is attached to the b hadron decay vertex. Supplementary misidentification of the final state particles increases the probability of falling into the signal b hadron mass window.

4. The *partially reconstructed background* composes the fourth background category. It is emerging from multibody decays, where some particles are not reconstructed. The particularity of the partially reconstructed background is the missing energy in the decay. The difficulty of this background type is its final state being identical to the one of the signal decay.

In the following, each of the above-mentioned background types is studied in detail. The considered decays are specified, and their occurrence is quantified in the rare and resonant decay modes. Different strategies to suppress these backgrounds are employed.

2. The misidentification of more than two particles is rather unlikely, but would be tackled likewise by fighting against single and double misidentification backgrounds.

3.3.1 Combinatorial background

The combinatorial background denotes the combination of random tracks. Since in $\Lambda_b^0 \to pK^- J/\psi$ decays, strong constraints on the resonant masses are present, the combinatorial background is mainly composed by a true J/ψ or $\psi(2S)$ resonance combined with random hadrons. Above the $pK^-\mu^+\mu^-$ mass threshold, the combinatorial background distribution is continuous and not peaking. In the rare mode, the mass threshold value is $1643\,\mathrm{MeV}/c^2$ and in the J/ψ mode $4530\,\mathrm{MeV}/c^2$, due to the large mass of the J/ψ resonance.

In contrast to the $\Lambda_b^0 \to pK^- J/\psi$ decays, the origin and the momentum of the particles are not constrained in combinatorial background events. This property can be used to distinguish between signal and combinatorial background. Instead of cutting in the multidimensional variable space, a multivariate analysis technique (MVA) is employed to separate them. MVA techniques are more powerful than cut-based methods. The MVA technique used in this analysis is called Boosted Decision Tree (BDT) with Gradient boosting from the TMVA package [172], providing good discrimination with little tuning and a short processing time.

Concept of the Gradient Boosted Decision Tree technique

A BDT is a machine-learning technique [3], employed to solve binary classification problems. Representative samples of the signal and background classes are identified. The BDT is trained on the input variables of those samples, called features $\vec{x}$.

The working principle of decision trees is sketched in Fig. 3.4. In each node, the BDT splits the dataset into $x_i < c$ and $x_i > c$. The best-separating feature x_i and the best cut value c are calculated by a separation index. The range of each input feature is scanned, and the separation index is calculated. The index is weighted by the fraction of events present in the corresponding node. The splitting criterium is chosen according to the maximal separation index of the parent and child nodes. A stop criterion defines when the splitting stops. Stop criteria are, for example, the minimal fraction of events present in a node or the maximal depth of a tree. The final nodes are called *leaf nodes*. In those leaf nodes, the events are classified into signal and background depending on the most represented class.

The BDT technique does not rely on one tree only but on a forest, which is an ensemble of many trees. The aim is to improve the BDT performance and to achieve a higher resistance against statistical fluctuations. In the training of the succeeding tree, higher event weights are attributed to previously misclassified events. The final model response is the weighted sum of the different BDT output values. The gradient boost algorithm

3. This discussion is based on Ref. [172, 173].

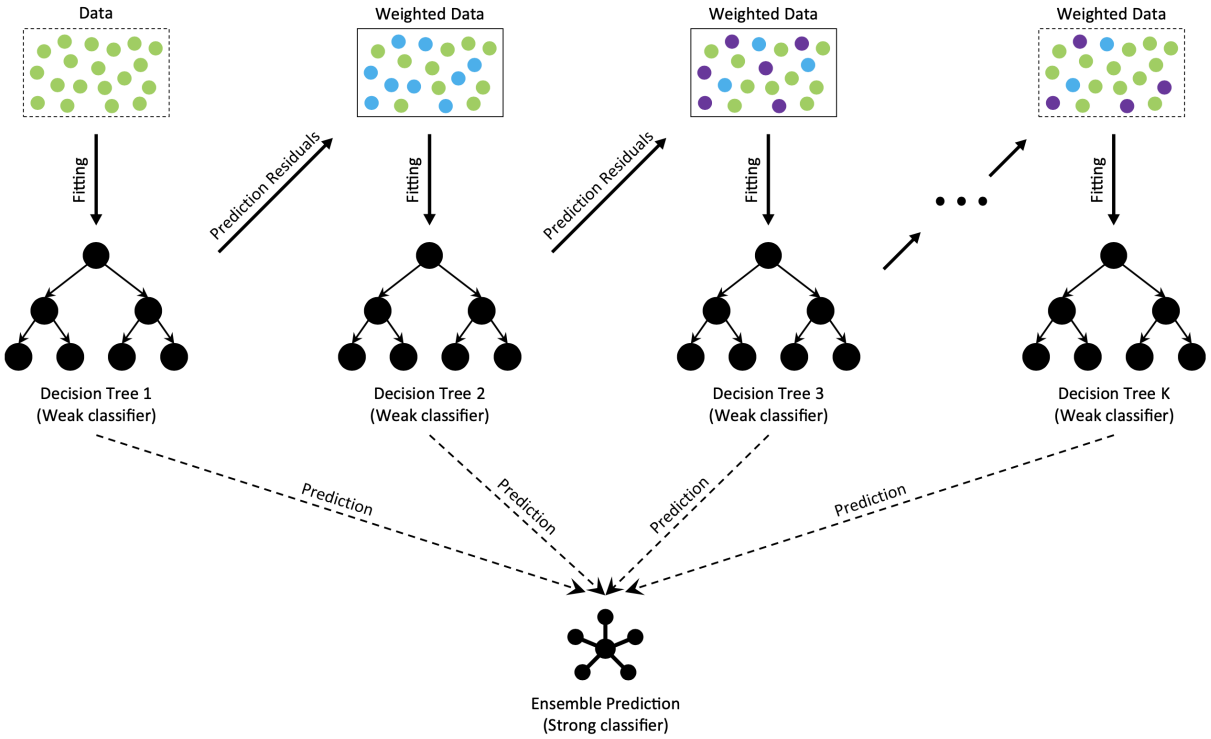

Figure 3.4 – The working principle of the Gradient Boosted Decision Tree technique (taken from Ref. [174]).

optimises the weights of the BDT outputs and the misclassified events in order to reduce the difference between the BDT response and the proper class inheritance. The BDT output value is situated between -1 an 1, corresponding to a classification of an event as background- and signal-like. The whole gradient boosted BDT training procedure is illustrated in Fig. 3.4.

The gradient boosted BDT algorithm is the further development of the AdaBoost algorithm, which is strongly influenced by outliers and mislabelled data events. Calculating the gradient of the binomial log-likelihood loss function makes the gradient boosted BDT algorithm more robust [172]. The robustness can be enhanced with smaller *shrinkage* values, which limits the learning rate in individual tree training.

A resampling procedure, called *stochastic gradient boosting*, is employed to improve the BDT classification. Random subsamples of the training dataset are used to grow the trees. The fraction of events added to each tree training can be indicated by the user. All the configuration parameters of the machine learning technique, which are set by the user, are grouped under the term *hyperparameters*. The separation index, the number of grid points and the stop criterion are some examples. A so-called model is composed of a set of features and hyperparameters.

The performance of the BDT is evaluated with an independent test sample. A good

BDT performs well on the training as on the test samples; neither under- nor overfitting should occur. While underfitting describes the choice of a too-simplistic model, which cannot account for the complexity of the data, a too-complex choice leads to overfitting, manifesting differences between the performance of the training and test samples. Both of them are non-optimal configurations. An appropriate capacity can be reached by optimizing the hyperparameters and the choice of features.

BDT training

The BDT of this analysis is shared with the differential branching fraction analysis of Ref. [60] in order to get comparable results. The 2016 $\Lambda_b^0 \to \Lambda(1520)\mu^+\mu^-$ simulation sample is chosen as a signal proxy. Partially reconstructed b-hadron decays are expected to be primarily present in the lower mass sideband of the Λ_b^0 peak. Therefore, the far upper mass sideband, defined as the $pK^-\mu^+\mu^-$ mass region above $6\,\mathrm{GeV}/c^2$, is a proxy for the combinatorial background. Both are processed using events passing the L0Muon hardware trigger and the PID requirements of Tab. 3.4. The stripping requirements are removed from the simulation sample since they already contain a BDT. Having an independently trained BDT against combinatorial background limits the potential problems. Because of the need to remove the stripping requirements, the training is only performed on one data-taking year, which is chosen to be one of the Run 2 years due to the higher integrated luminosity.

To remove the long background tail in the $\chi^2_{\mathrm{DTF}}/\mathrm{ndof}$ variable is required to be below 100. $\chi^2_{\mathrm{DTF}}/\mathrm{ndof}$ represents the quality of the decay-tree fit performed by the DecayTreeFitter algorithm. The same criterion is part of the preselection. The training is performed on the combined q^2 region of $[0.1, 8]$ and $[11, 12.5]\,\mathrm{GeV}^2/c^4$. The test and training samples are split randomly. In total, 0.1 million signal events and 0.7 million background events are used in the training.

The input features of the simulation sample are not corrected to match the data shape, which is expected to have a negligible effect. Input features, which separate signal and background, are chosen according to their separation power. An extensive set of kinematic and decay topological variables are tested. The final set is reduced to the most important features, listed in Tab. 3.5. The signal and background distributions of the input features are found in App. C.1.

The most important feature is the logarithm of the decay tree fit. The other features are χ^2 of the impact parameter of the track with respect to the PV, the flight distance with respect to the PV and the decay vertex quality. DIRA indicates the cosine of the direction angle between the vector pointing from the particle's production vertex to its decay vertex and the vector sum of the momenta of its decay particles.

Input features	Importance [$\times 10^{-2}$]
PV-constraint $\log \chi^2_{\mathrm{DTF}}/\mathrm{ndof}$	7.613
$\log p_{\mathrm{T}}(K^-)$	7.075
$\log p_{\mathrm{T}}(p)$	6.786
$\log \chi^2_{\mathrm{IP}}(\Lambda^*)$	6.151
$\log \chi^2_{\mathrm{IP}}(p)$	5.901
$\log \chi^2_{\mathrm{vertex}}(\Lambda_b^0)$	5.730
$\log \chi^2_{\mathrm{FD}}(\mu^+\mu^-)$	5.423
$\log \chi^2_{\mathrm{IP}}(K^-)$	5.377
$\log p_{\mathrm{T}}(\Lambda_b^0)$	5.375
$\log \chi^2_{\mathrm{IP}}(\Lambda_b^0)$	5.169
$\log \chi^2_{\mathrm{IP}}(\mu^+)$	5.166
$\log \chi^2_{\mathrm{IP}}(\mu^-)$	4.982
$\log \chi^2_{\mathrm{IP}}(\mu^+\mu^-)$	4.616
$\log \arccos \mathrm{DIRA}(\Lambda_b^0)$	4.295
$\log \chi^2_{\mathrm{FD}}(\Lambda_b^0)$	4.289
$\log \chi^2_{\mathrm{vertex}}(\Lambda^*)$	3.549
$\log \chi^2_{\mathrm{vertex}}(\mu^+\mu^-)$	3.207

Table 3.5 – The input features, which are used in the final BDT training, are listed with decreasing importance.

The correlation of the features is represented in Fig. 3.5 for the signal proxy. The correlation in the background dataset and the difference between the signal and background correlation is shown in App. C.2. A strong correlation can be seen in the signal dataset. Since the signal and background datasets show different correlation strengths, all the variables are kept, allowing an additional possibility to distinguish the two datasets.

It was seen that using the $\max\{p_{\mathrm{T}}(\mu^+), p_{\mathrm{T}}(\mu^-)\}$ feature in the training improves the BDT performance but introduces a non-negligible deformation of the angular distribution. A deformation of the angular distribution is preferred to be avoided when performing an angular analysis. This is the reason why this feature is removed. The optimised hyperparameters are listed in Tab. 3.6.

The output values of the BDT classifier for signal (red) and background events (blue) are shown in Fig. 3.6. The distributions are separated into training and test datasets. The indicated separation is determined depending on the number of signal N_{S} and background events N_{B} in each bin i, which is mathematically expressed as

$$S = \sum_{i=1}^{M} \frac{(N_{\mathrm{S}}(i) - N_{\mathrm{B}}(i))^2}{N_{\mathrm{S}}(i) + N_{\mathrm{B}}(i)}. \tag{3.1}$$

The separation power is compatible between the training and test datasets within one

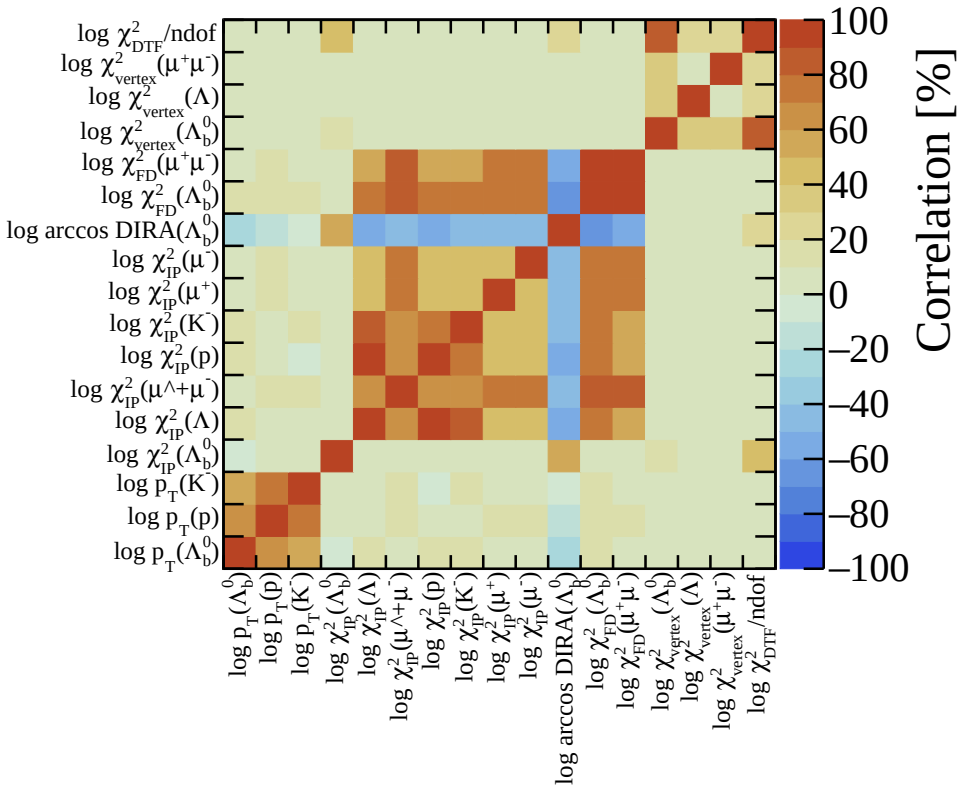

Figure 3.5 – The correlation of the features is presented for signal events. The correlation in the background sample and the difference between the signal and background are shown in Fig. C.4.

standard deviation. Therefore, no overtraining was detected.

In order to simplify the analysis, the same BDT classifier was used for all data-taking periods and q^2 bins. No k-folding was employed, but the same BDT is applied to the whole data and simulation dataset.

BDT optimisation

The signal efficiency, $\varepsilon_{\text{signal}}$, and background rejection rate, $1 - \varepsilon_{\text{bkg}}$, is calculated at different BDT output values. Everything above the cut value is interpreted as being signal, and everything below is classified as background. The curve relating the signal efficiency and the background rejection rate is called Receiver Operating Characteristics, abbreviated as the ROC curve. The area under the ROC curve (AUC) is a measure of the BDT performance. The best performance is characterised by a high signal efficiency while keeping a high background rejection rate. In other words, the higher the AUC, the better the BDT. The ROC curve of the final BDT is plotted in Fig. 3.7.

The optimal BDT cut value is evaluated by scanning the BDT output value range

Function	Hyperparameter	Value
Architecture	Number of trees	1000
Splitting	Separation index used to determine the best splitting	Gini index
	Number of grid points	20
Training	Signal to background ratio used in the training	1
	Learning rate per tree training	0.10
	Stochastic gradient boosting	True
	Fraction of events for random subsampling to grow trees	0.6
Stop criterion	Minimum percentage of events in a leaf node	2.5 %
	Maximal depth of trees	2

Table 3.6 – Hyperparameters of the BDT training [172].

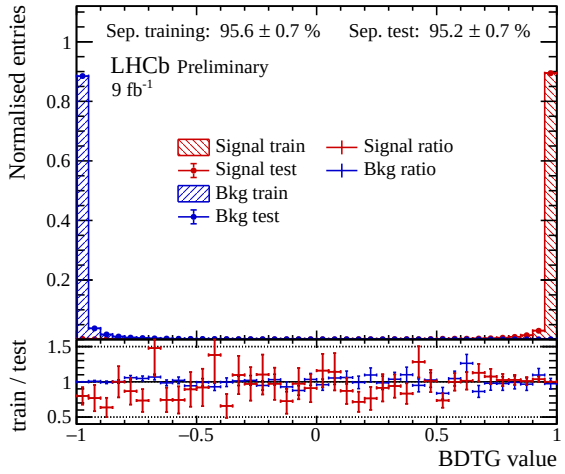

Figure 3.6 – The BDT output values for signal and background events, comparing the separation of the test and training samples. The separation power is comparable, and no overtraining is found.

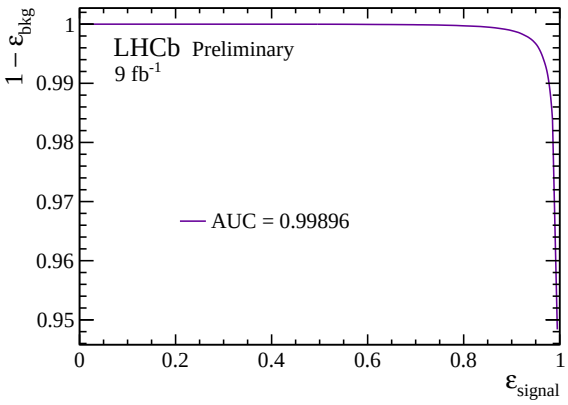

Figure 3.7 – ROC curve of the final BDT.

from 0.9 to 1 in steps of 0.002. The figure of merit,

$$FoM = \frac{N_{\mathrm{S}}}{\sqrt{N_{\mathrm{S}} + N_{\mathrm{B}}}}, \tag{3.2}$$

is calculated at each cut value. $N_{\mathrm{S,B}}$ denote the number of signal and background events passing the BDT requirement. The signal and background yields are obtained by a $pK^-\mu^+\mu^-$ invariant mass fit in data by applying a BDT cut value of 0.9. A double-sided Crystal Ball function models the Λ_b^0 mass peak, and the combinatorial background is described by an exponential. A scale factor is calculated by building a ratio between the BDT cut efficiency in the 2016 $\Lambda_b^0 \to \Lambda(1520)\mu^+\mu^-$ simulation sample and the signal yield in data. This scale factor is needed for obtaining the number of signal events at other BDT working points. After applying the BDT to all data-taking periods, the figure of merit is calculated and drawn in Fig. 3.8. The final cut value is chosen to be 0.99, which

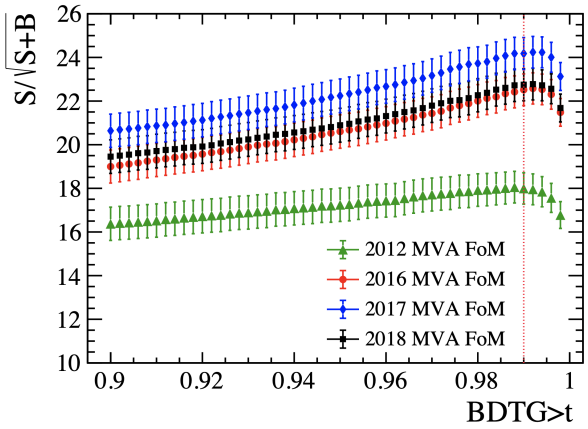

Figure 3.8 – The significance is drawn as a function of different BDT cut values for the data-taking years 2012, 2016, 2017 and 2018. The final cut value is highlighted as a red vertical line [60].

is close to the maximum of the figure of merit obtained for the data-taking years of Run 2 and just before the drop in the significance of the data-taking year 2012. The data-taking years are not retrained in order to prevent differences between the data-taking years. The figure of merit for 2011 and 2015 are not evaluated separately since the data sample sizes are the smallest. The BDT cut is applied in the following to reduce the combinatorial background and to visualise the remaining background components best. However, the combinatorial background is still not fully reduced and will be modelled in the mass fit.

3.3.2 Misidentification backgrounds

The different background contributions are studied with a data-driven approach, using the entire dataset collected during Run 1 and 2 by the LHCb detector. The *preselection* is applied, which includes the requirements listed in table 3.4 and the BDT cut. The samples are split into the *rare*, J/ψ and $\psi(2S)$ mode. To increase the statistics, the rare mode combines all the q^2 bins in the non-resonant region. The definition of the q^2 intervals is itemised in table 3.2.

Even though tight cuts on the invariant pK^- and $pK^-\mu^+\mu^-$ mass distributions are imposed in this analysis, for the purpose of this study, none of them is applied to better evaluate the background composition. Since the pK^- mass window of $[1470, 1570]\,\text{MeV}$ may reduce some of the backgrounds, its suppression power is evaluated during this section. The labels *full* pK^- and $\Lambda(1520)$ indicate the applied requirement on the pK^- invariant mass.

The background contributions are investigated by substituting the mass hypothesis of specific particles while preserving the measured momentum vector. A new invariant mass of a combination of the final state particles can be computed. Peaking structures point, in most cases, to physical backgrounds.

Hadron misidentification

The hadron misidentification background is mainly originating from the misidentification of one or both hadrons in the final state as protons, kaons or pions. The RICH detectors contribute to particle identification. However, in the low and high momentum regions, the information of the RICH detectors is less reliable. Since protons have the highest momentum threshold to create a Cherenkov ring in the RICH detectors, their identification is non-reliable at low momentum. Fig. 2.18 shows the misidentification probability of kaons and pions as protons against the correct identification rate of actual protons. Only above a momentum threshold of $9.3\,\text{GeV}/c$ the proton PID information is reliable. In the preselection, the proton is required to exceed this momentum threshold. Although the misidentification efficiency is expected to be the highest for protons, low- and high-momentum kaons can also be misidentified, as seen in Fig. 2.17.

Combining the different misidentification possibilities, the single and double misidentification backgrounds are listed in Tab. 3.7. Because of the higher probability of single misidentification background, it will be treated first. However, one has to keep in mind that the meson production fractions and branching fractions are often higher than the ones of the signal decay, which can cause a significant contribution. Only neutral b-hadron decays are considered in the table since the trace of charged b-hadron decays would be

Misidentification	Decay mode	Occurrence
$K \to p$	$B_s^0 \to K^+K^-\mu^+\mu^-$	Abundant. ϕ resonance vetoed.
$\pi \to p$	$\overline{B}^0 \to \pi^+K^-\mu^+\mu^-$	Rather abundant.
	$\overline{B}_s^0 \to \pi^+K^-\mu^+\mu^-$	Small, since CKM-suppressed.
$p \to K$	$B^0 \to p\bar{p}\mu^+\mu^-$	Rare, since $b \to d\mu^+\mu^-$ transition.
	$\overline{B}_s^0 \to p\bar{p}\mu^+\mu^-$	Rare, since suppressed by nature of QCD.
$\pi \to K$	$\Lambda_b^0 \to p\pi^-\mu^+\mu^-$	Rare, since $b \to d\mu^+\mu^-$ transition or via long-lived, weakly decaying Λ^0.
$p \leftrightarrow K$	$\overline{\Lambda}_b^0 \to K^+\bar{p}\mu^+\mu^-$	Present, but small.
$p \to K$, $\pi \to p$	$\overline{\Lambda}_b^0 \to \pi^+\bar{p}\mu^+\mu^-$	Rare, as above.
$\pi \to K$, $\pi \to p$	$B_s^0 \to \pi^+\pi^-\mu^+\mu^-$	Rare, since suppressed by nature of QCD.
	$B^0 \to \pi^+\pi^-\mu^+\mu^-$	Rare, since $b \to d\mu^+\mu^-$ transition.
$\pi \to K$, $K \to p$	$B^0 \to K^+\pi^-\mu^+\mu^-$	Small, since double misidentification.

Table 3.7 – The possible contributing background decay modes, due to hadron misidentification, are tabulated and their abundance is evaluated, implying the preselection requirements.

visible in the detector [4].

As a reminder, the ground state Λ baryon is decaying via the weak decay to $p\pi$ and is, thus, long-lived. Because of its long lifetime, it is expected to pass only rarely the selection criteria that require all four tracks to originate from the Λ_b^0 decay vertex.

The importance of all the hadron misidentification modes is listed in Tab. 3.7. The modes with the mention "rare" are seen to be negligible. In the following, only the misidentification decay modes are presented that have been classified as non-negligible. Hadron misidentification is supposed to be quasi-independent of the invariant mass spectrum of the leptons. Therefore, they are supposed to occur in the rare as in the resonant mode.

The $K \to p$ misidentification background is studied at first. In Fig. 3.9, the invariant $pK^-\ell^+\ell^-$ mass distribution by exchanging the proton mass hypothesis with the kaon mass is represented in the J/ψ and $\psi(2S)$ bins. The vertical band indicates the $\Lambda_b^0 \to pK^-\mu^+\mu^-$, and the horizontal line originates from $B_s^0 \to K^+K^-\mu^+\mu^-$ decays. The nominal BDT cut is removed for the plots in the top row and only applied to the bottom. The large lighter regions of the combinatorial background are significantly suppressed by the BDT.

Focusing on the K^+K^- mass spectrum in a window of $\pm 30\,\mathrm{MeV}/c^2$ around the B_s^0 mass and vetoing the Λ_b^0 signal and $B^0 \to K^{*0}\mu^+\mu^-$ decay, the distributions in Fig. 3.10

4. In principle, a charged b-hadron track could be misassigned to another vertex, which would lead to the mis-reconstruction of a neutral b-hadron decay. Because of the cleanness of the Λ_b^0 signal, this possibility has been neglected.

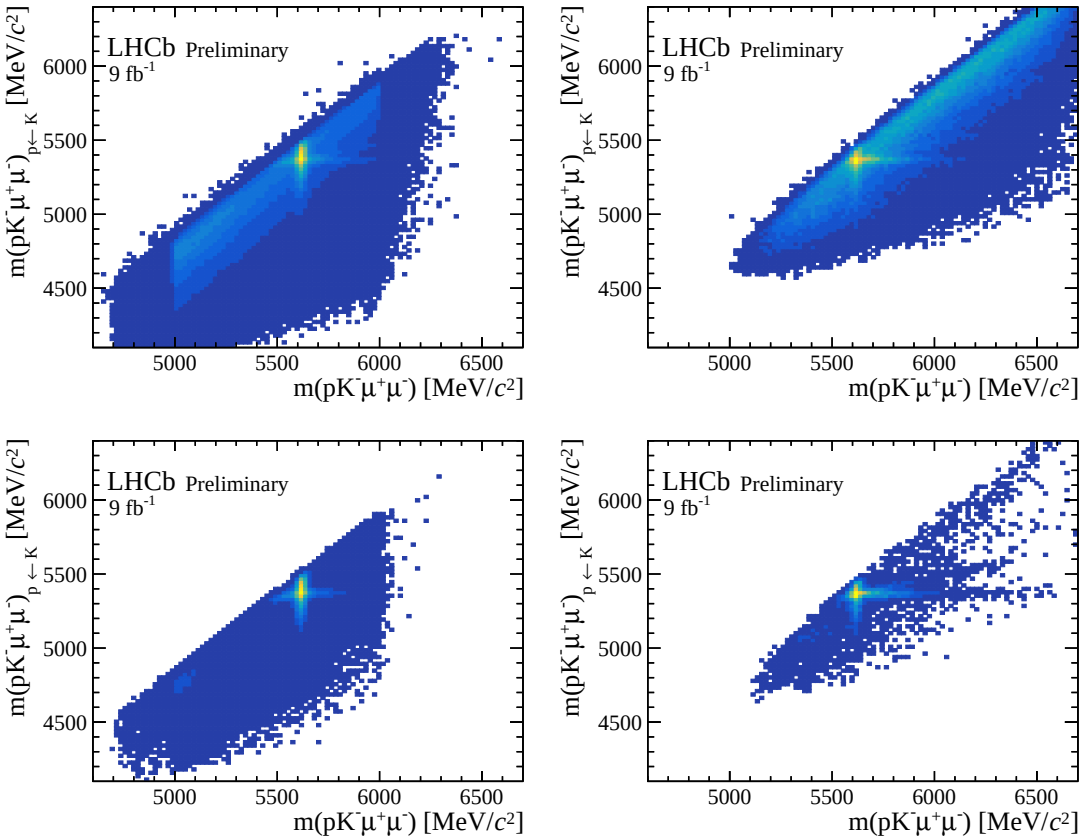

Figure 3.9 – Replacing the proton mass hypothesis by the kaon mass, the horizontal band of the B_s^0 decay appears. Because of the bigger sample size, the J/ψ (left) and the $\psi(2S)$ (right) bins are shown. No BDT requirement is applied on the top but is on the bottom row. The large continuous lighter regions originate from the combinatorial background and are shrinking with the nominal cut on the BDT output value.

are obtained. The J/ψ mode is represented in the total pK^- mass spectrum on the left and the rare mode in the $\Lambda(1520)$ mass window on the right. The $\phi(1020)$ resonance dominates the spectrum. In addition, the broader $f_2'(1525)$ resonance is present, but it is outside of the $\Lambda(1520)$ mass window.

Thanks to the abundant and narrow ϕ resonance, the decay can be vetoed with the requirement $|m(pK^-)_{p\leftarrow K} - 1020| > 12\,\mathrm{MeV}/c^2$. It needs to be noted that the tail of the ϕ resonance, the non-resonant decay and the decay via higher mass resonances remain. The ϕ resonance veto is applied in the following to improve the sensitivity to other misidentification backgrounds. The diagonal band in the lower right plot of Fig. 3.9 originates from the double misidentification of $K \to p$ and $\pi \to K$ in $B^0 \to K^+\pi^-\mu^+\mu^-$ decays.

Via $\pi \to p$ misidentification, $\overline{B}{}^0_{(s)} \to K^-\pi^+\mu^+\mu^-$ decays pass the selection criteria. Figure 3.11 shows the distribution of the invariant $pK^-\mu^+\mu^-$ mass, substituting the proton mass by a pion mass, against the invariant $pK^-\mu^+\mu^-$ mass. $\overline{B}{}^0_{(s)} \to K^-\pi^+\mu^+\mu^-$ decays appear as a horizontal band.

To investigate if the $\overline{B}{}^0_{(s)}$ decays can be vetoed, the $K^-\pi^+$ invariant mass distribution is exemplary for the J/ψ mode, drawn in Fig. 3.12. A tight cut around the $\overline{B}{}^0$ mass is applied. To ensure the presence of $\overline{B}{}^0 \to K^-\pi^+\mu^+\mu^-$ decays only, a veto of $\Lambda_b^0 \to pK^-\mu^+\mu^-$ and $B_s^0 \to K^+K^-\mu^+\mu^-$ decays is put in place. The mass windows and vetoes are always of ± 30 MeV/c^2 around the corresponding b-hadron mass.

Two resonances are particularly visible. These are namely the abundant $K^*(892)^0$ and the rarer $K_2^*(1430)^0$ resonance. The $K_2^*(1430)^0$ resonance is removed by applying the cut around the $\Lambda(1520)$ mass. In the $\psi(2S)$ bin, the $K^-\pi^+$ structure is the same. However, in the rare mode, no $K_2^*(1430)^0$ peak is visible due to the small sample size. A small effect of the implied mass requirements is visible in the low-mass region, originating from the ϕ veto.

The $\overline{B}{}^0_s \to K^-\pi^+\mu^+\mu^-$ decays are Cabibbo suppressed and expected to be rare. The invariant mass distributions of the $K^-\pi^+$ system are shown in Fig. 3.13. Both resonant q^2 bins are depicted. Again, their contribution is enriched by focusing on the $\overline{B}{}^0_s$ mass and vetoing the other decay modes. Nevertheless, much fewer events are present in the $\overline{B}{}^0_s$ than in the $\overline{B}{}^0$ mass window. The distribution has no strong peaking structure. Implying the pK^- mass requirements reduces its occurrence further.

A diagonal band appears in the 2D representation, mainly in the $\psi(2S)$ bin. This one results from $B_s^0 \to K^+K^-\mu^+\mu^-$ decays, even after vetoing the ϕ mass.

The $p \leftrightarrow K$ misidentification swap is a double misidentification background, which is expected to be small. Due to the final state being precisely the same as in the signal

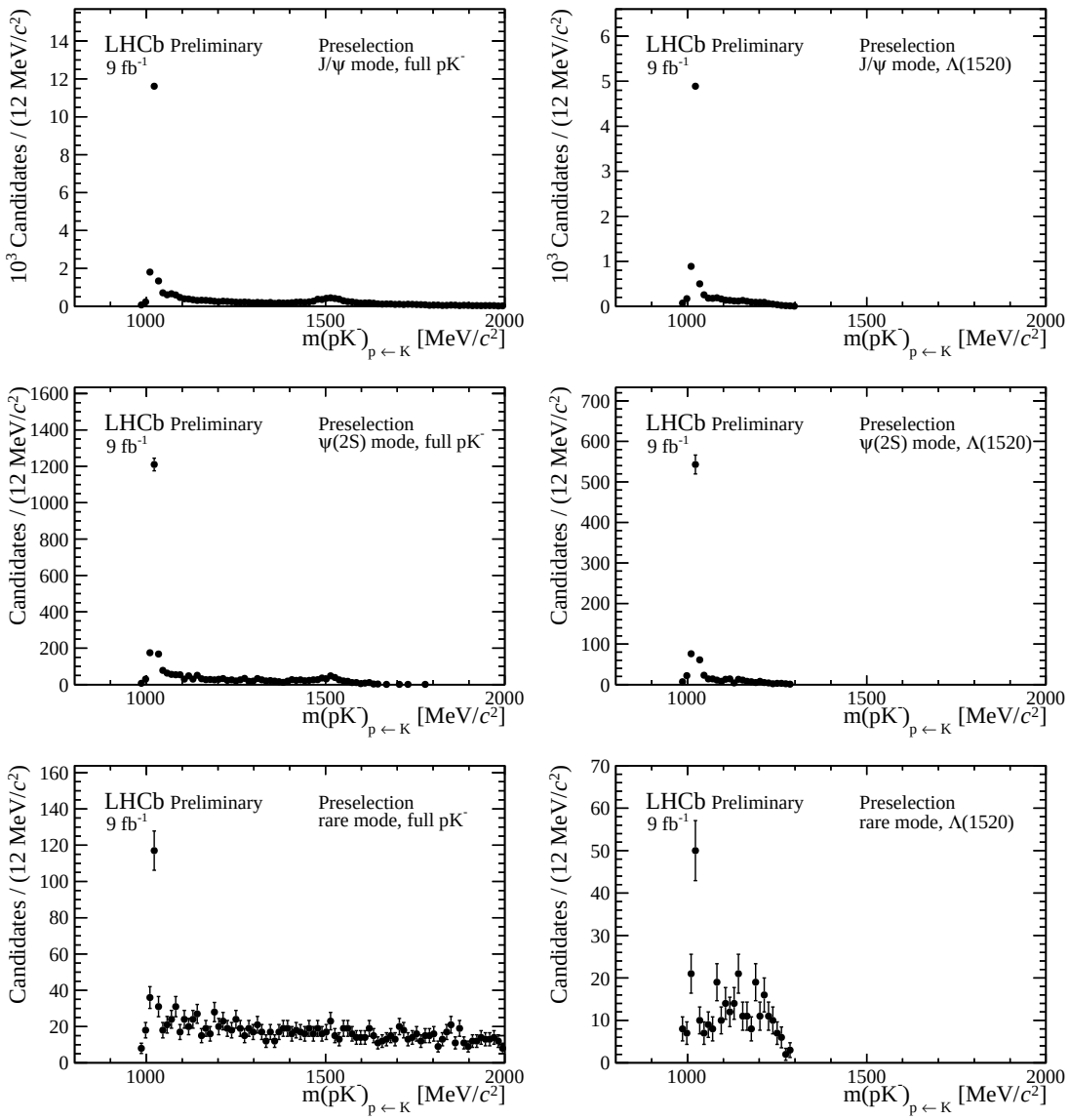

Figure 3.10 – In a window around the B_s^0 mass, with vetoed $\Lambda_b^0 \to pK^-\mu^+\mu^-$ and $B^0 \to K^{*0}\mu^+\mu^-$ contributions, the narrow ϕ resonance is distinguishable in the rare and resonant modes. The J/ψ (top), $\psi(2S)$ (middle) and the rare mode (bottom) are drawn. The high-mass K^+K^- structure, which is present in the full pK^- mass window (left), is reduced by requiring a window around the $\Lambda(1520)$ mass (right).

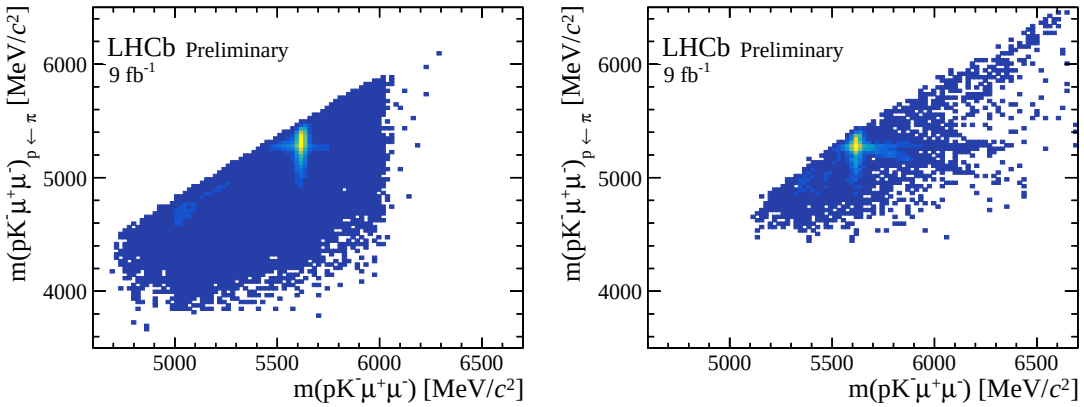

Figure 3.11 – The misidentified $\overline{B}{}^0_{(s)} \to K^-\pi^+\mu^+\mu^-$ background decays via the J/ψ (left) and $\psi(2S)$ (right) resonance are shown as horizontal bands. No requirement on the pK^- mass was made.

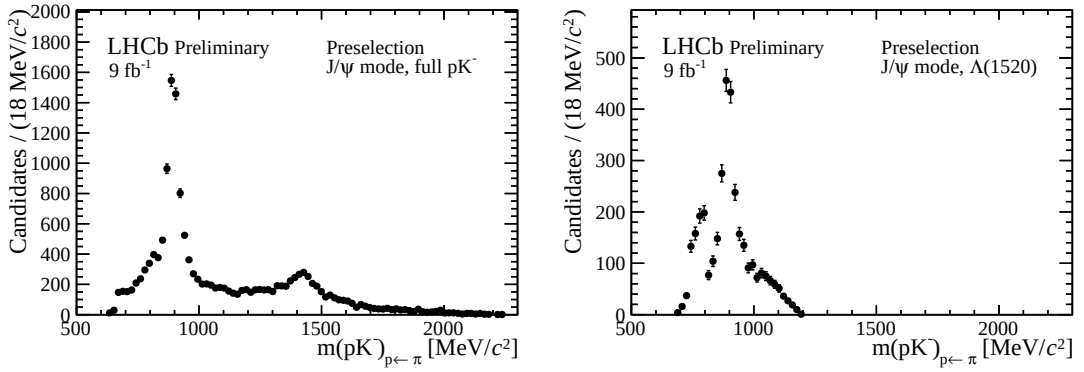

Figure 3.12 – $K^-\pi^+$ invariant mass distribution in a mass window around the $\overline{B}{}^0$ invariant mass. The $\Lambda_b^0 \to pK^-\mu^+\mu^-$ and $B_s^0 \to K^+K^-\mu^+\mu^-$ decays are vetoed.

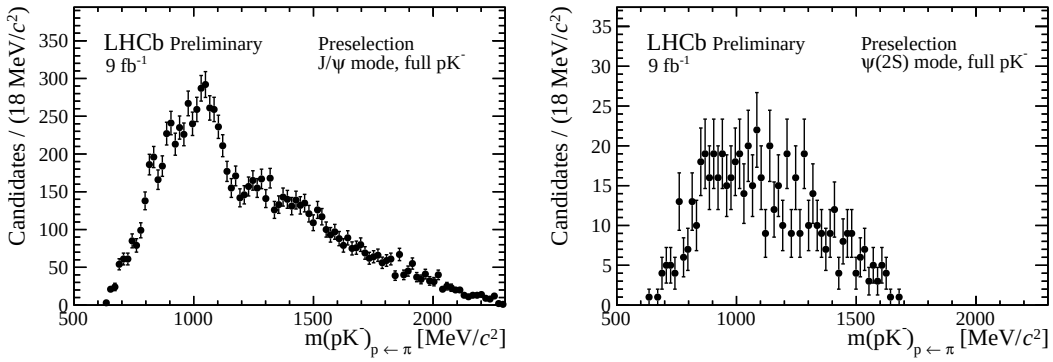

Figure 3.13 – The $m_{\pi^+K^-}$ spectrum of $\overline{B}{}^0_s \to K^-\pi^+\mu^+\mu^-$ decays in the J/ψ and $\psi(2S)$ bin. The distributions are obtained by selecting decays within the $\overline{B}{}^0_s \to K^-\pi^+\mu^+\mu^-$ mass window by vetoing $\Lambda_b^0 \to pK^-\mu^+\mu^-$ and $B_s^0 \to K^+K^-\mu^+\mu^-$ decays.

decay, it is a particularly dangerous background. Because of the big sample size of the J/ψ mode, the presence of the $p \leftrightarrow K$ swapped misidentification of the signal decay is the best distinguishable in this bin, as seen in Fig. 3.14. After applying the particle

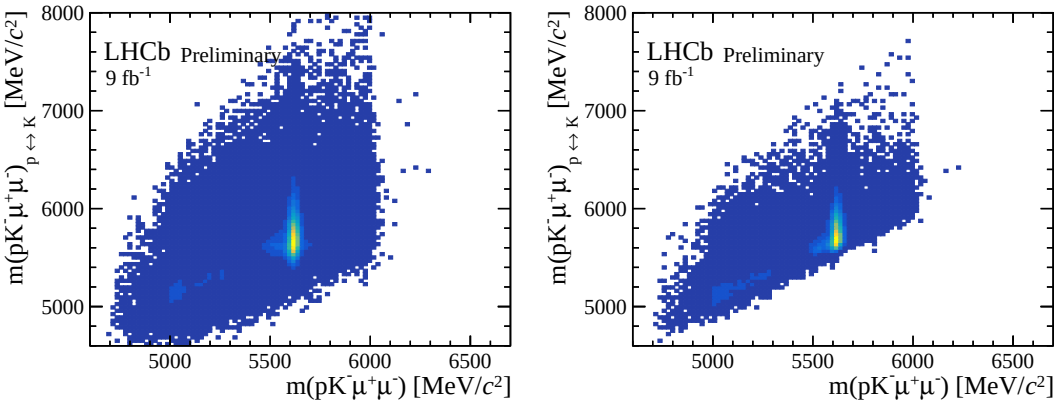

Figure 3.14 – The mass distribution of the $p \leftrightarrow K$ swapped misidentification of the signal decay is shown in the J/ψ bin in the full pK^- mass window (left) and in the $\Lambda(1520)$ mass window (right).

identification requirements, the contribution is small, and the requirement of the $\Lambda(1520)$ window suppresses the background additionally.

The $K \to p$ and $\pi \to K$ double misidentification background is contributing, too. While in the J/ψ and rare modes, the contribution is only slightly visible, a clear horizontal band appears in the $\psi(2S)$ mode, as illustrated in Fig. 3.15. By applying the $\Lambda(1520)$ mass window, the background contribution is significantly reduced.

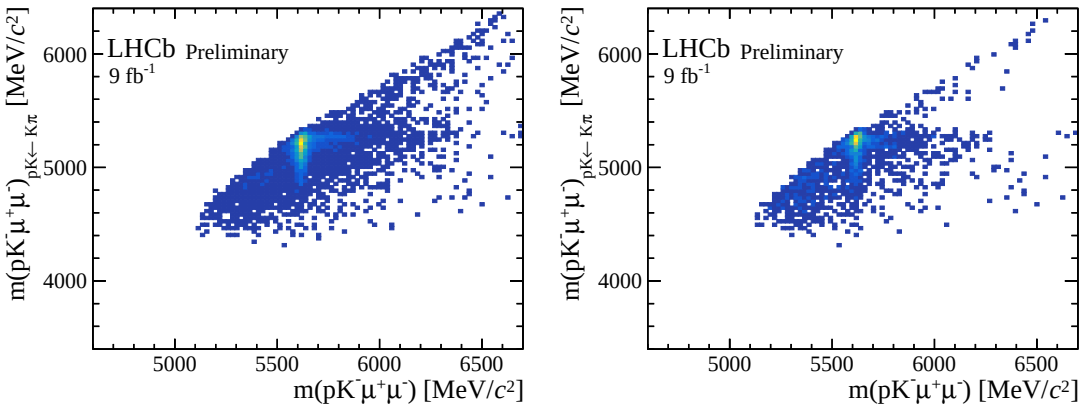

Figure 3.15 – The $B^0 \to K^+\pi^-\mu^+\mu^-$ double misidentification background is visible in the $\psi(2S)$ mode. The distribution is drawn in the full pK^- spectrum (left) and the $\Lambda(1520)$ mass window (right), which reduces its occurrence.

Lepton misidentification

In contrast to the hadron misidentification background, the lepton misidentification background is supposed to differ in the resonant and rare modes. Due to its abundance and the strict kinematic constraints of the J/ψ and $\psi(2S)$ mass, it is supposed to be negligible in the resonant regions but not in the rare mode.

Two different types of lepton misidentification backgrounds are listed in this chapter. The first type comes from $c\bar{c}$ resonances, where one of the muons is misidentified as a hadron. Those are separated into $K^- \to \mu^-$ and $p \to \mu^+$ misidentifications. The second group are the "cascade" decays, where two charged-current weak decays of the Λ_b^0 are succeeded. The decay is either into a semileptonic or purely hadronic final state. In the semileptonic case, missing energy due to the neutrino is present and causes a shift in the Λ_b^0 mass. This is the reason why the semileptonic decay is expected to be less problematic. The $\pi \to \mu$ misidentification results only in a slight mass shift, and a clear peak is supposed to be seen at the pole mass of the intermediate particle. In our case, the intermediate particle is either a Λ_c^+ baryon or a D^0 meson.

The $\mu^- \to K^-$ misidentification background is only appearing in the rare mode because of the tight mass constraints in the resonant q^2 bins. In Fig. 3.16, the J/ψ peak is present in the $m(K^-\mu^+)_{K\leftarrow\mu}$ distribution. After the $\Lambda(1520)$ mass cut, the contribution is significantly reduced. Nevertheless, the J/ψ mass is vetoed in the rare mode. The veto is expressed as $|m(K^-\mu^+)_{K\to\mu} - 3097| > 35\,\mathrm{MeV}/c^2$.

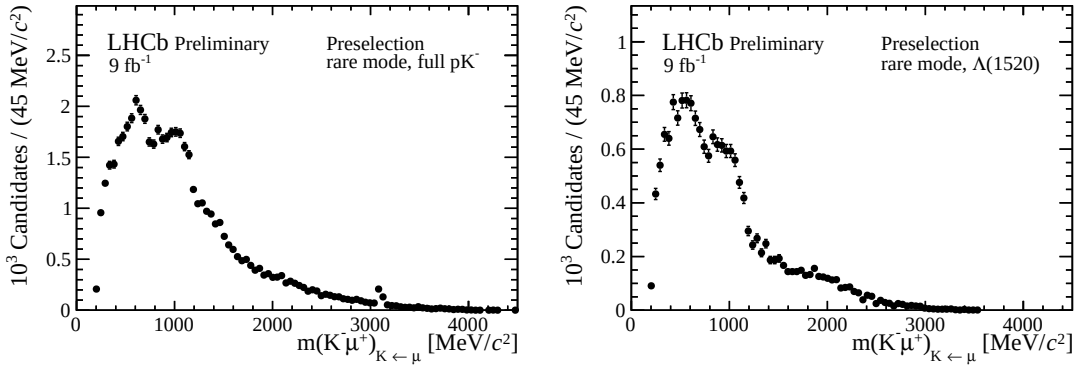

Figure 3.16 – The J/ψ peak is slightly visible in the $m(K^-\mu^+)_{K\leftarrow\mu}$ mass spectrum on the left, but disappearing by imposing the pK^- mass requirements on the right.

$\mu^+ \to p$ misidentification may lead to J/ψ peaks in the $m(p\mu^-)_{p\leftarrow\mu}$ distribution. The distribution is shown in Fig. 3.17. In the reduced pK^- mass window, the J/ψ peak

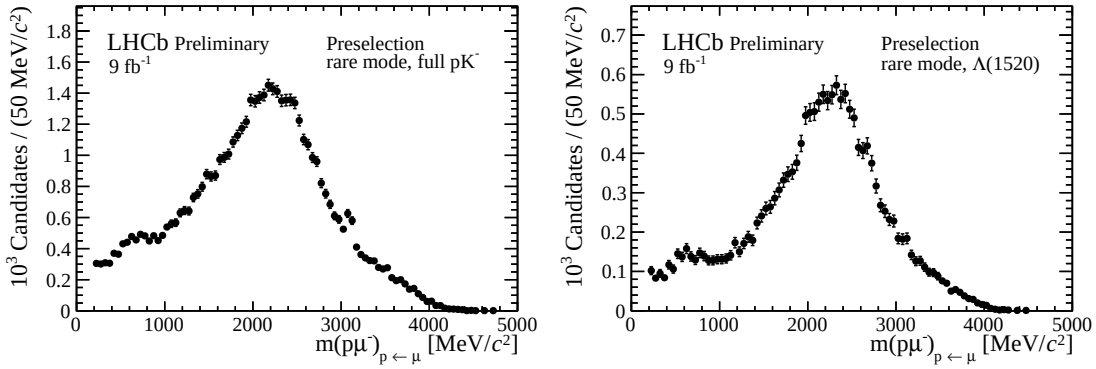

Figure 3.17 – The J/ψ peak is barely visible in the $m(p\mu^+)_{p\leftarrow\mu}$ mass spectrum on the left, but disappearing by imposing the pK^- mass requirements on the right.

is barely visible. Therefore, it is not vetoed.

Cascade Λ_b^0 decays via the Λ_c^+ baryon group together $\Lambda_b^0 \to \Lambda_c^+\pi^-$ and $\Lambda_b^0 \to \Lambda_c^+\mu^-\overline{\nu}_\mu$ decays. The Λ_c^+ baryon, itself, decays either into $pK^-\pi^+$ or $pK^-\mu^+\nu_\mu$. Hadronic decays, which pass the selection, have a pion misidentified as a muon. Hadronic Λ_c^+ decays are clearly visible as a straight line in the $pK^-\mu^+$ distribution. Fig. 3.18 presents the rare mode, where the Λ_c^+ baryon is the most abundant. Due to the missing energy of the neutrino, the semileptonic decays appear at lower $pK^-\mu^+$ masses. An enhancement is especially perceptible after cutting on the pK^- mass.

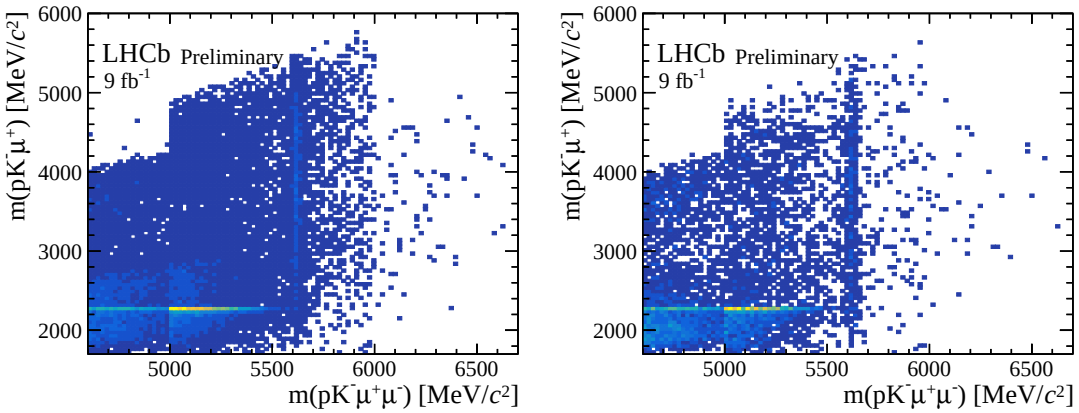

Figure 3.18 – The $pK^-\mu^+$ distribution reveals a horizontal band of hadronic Λ_c^+ decays as a function of the $pK^-\mu^+\mu^-$ mass in the full pK^- mass spectrum (left) and the $\Lambda(1520)$ mass window (right).

In the one-dimensional projection of the $pK^-\mu^+$ mass, drawn in Fig. 3.19, the narrow hadronic decay of the Λ_c^+ baryon is visible. Semileptonic decays cause a bulk at low $pK^-\mu^+$ masses. In the resonant q^2 bins, a tiny Λ_c^+ mass peak is perceptible in the one-dimensional distribution.

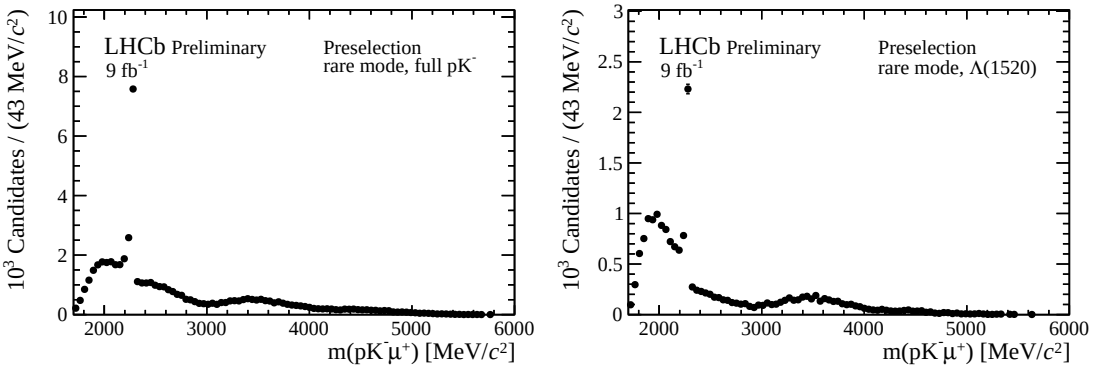

Figure 3.19 – In the rare mode, the $pK^-\mu^+$ mass distribution is clearly peaking at the Λ_c^+ baryon mass.

Cascade decays can arise in combination with $p \leftrightarrow K$ swapped misidentification. The corresponding $m(pK^-\mu^+)_{p\leftrightarrow K}$ distribution is shown in Fig. 3.20. No sharp Λ_c^+ mass peak is seen, neither in the 1D, nor in the 2D distribution, but potential semileptonic decays are supposed to be present in the left bulk.

The vetoes $m(pK^-\mu^+) > 2320\,\mathrm{MeV}/c^2$ and $m(pK^-\mu^+)_{p\leftrightarrow K} > 2320\,\mathrm{MeV}/c^2$ are proposed to suppress the hadronic and semileptonic decays of the Λ_c^+ baryon, without and with misidentification swap of the proton and kaon. The vetoes are investigated in sub-

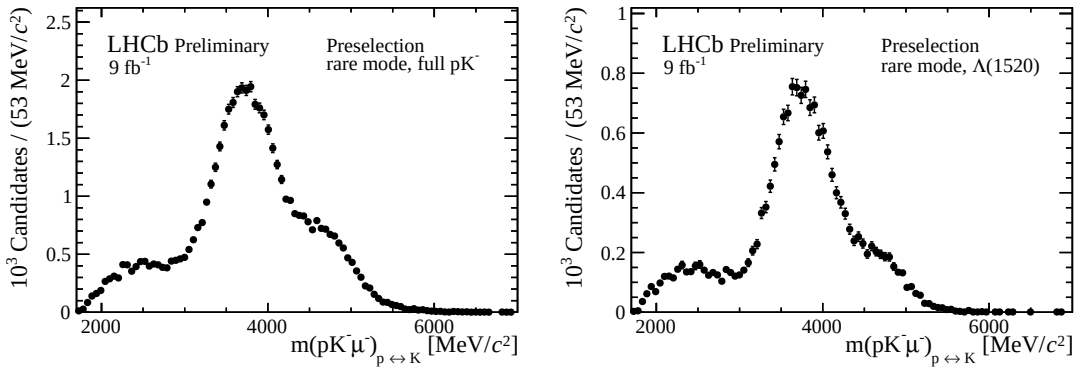

Figure 3.20 – The $pK^-\mu^-$ distribution combined with swapping the proton and kaon mass hypothesis is shown in the rare mode. The full pK^- mass window is shown on the left and the $\Lambda(1520)$ mass window is depicted on the right.

section 3.3.5.

Λ_b^0 cascade decays into the $pD^0\pi^-$ and $pD^0\mu\bar{\nu}_\mu$ final state are likewise considered. The D^0 meson can either decay into $K^-\pi^+$, where the pion is misidentified as a muon, or into $K^-\mu^+\nu_\mu$, where the missing neutrino causes an important energy loss. The $K^-\pi^+$ mass, substituting the muon mass hypothesis by a pion, is plotted in Fig. 3.21.

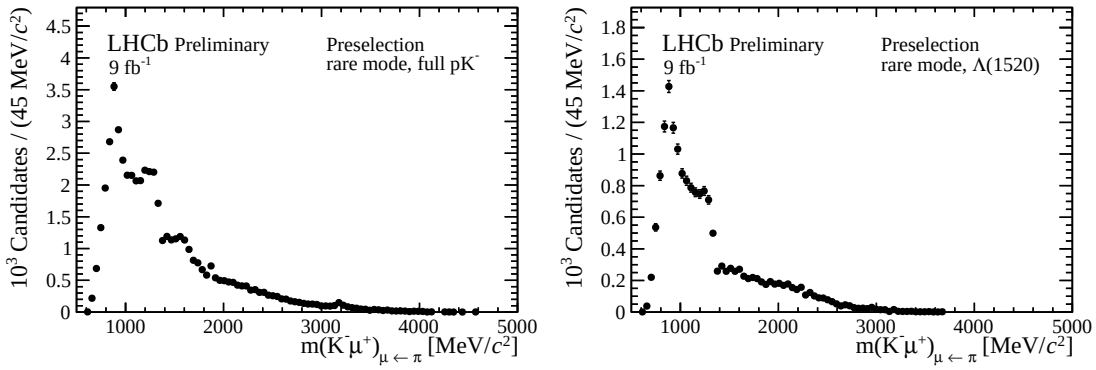

Figure 3.21 – The $K^-\mu^+$ mass distribution by replacing the muon mass hypothesis by a pion with (right) and without (left) the pK^- mass requirements.

The D^0 mass peak is only visible without pK^- mass requirements. In the same plot, the J/ψ mass peak appears at high masses. Implying the $\Lambda(1520)$ mass window removes both of them. In the resonant modes, the cascade decay is neither appearing in the 1D nor the 2D projections.

Since a veto on the lower mass sideband, would remove too much background, only a veto of the D^0 pole mass is applied. The veto is formulated as $|m(K^-\mu^+) - 1865| >$

20 MeV/c^2 and is only used in the rare mode. Semileptonic decays are supposed to be removed by requiring the $pK^-\mu^+\mu^-$ invariant mass to succeed 5500 MeV/c^2 and by imposing the $\Lambda(1520)$ mass window. The corresponding two-dimensional distribution is shown in Fig. 3.22.

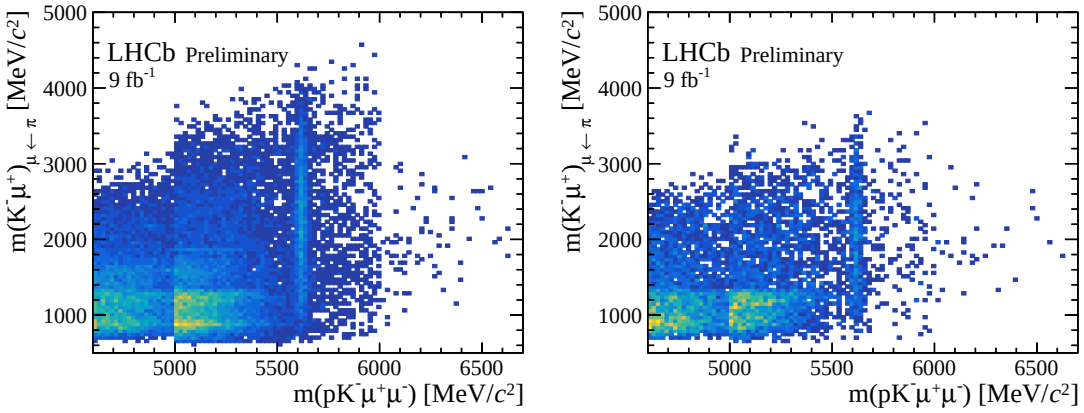

Figure 3.22 – The separation of the D^0 meson and the Λ_b^0 baryon mass with (right) and without (left) the pK^- mass requirements is presented in the rare mode.

3.3.3 Over-reconstructed background

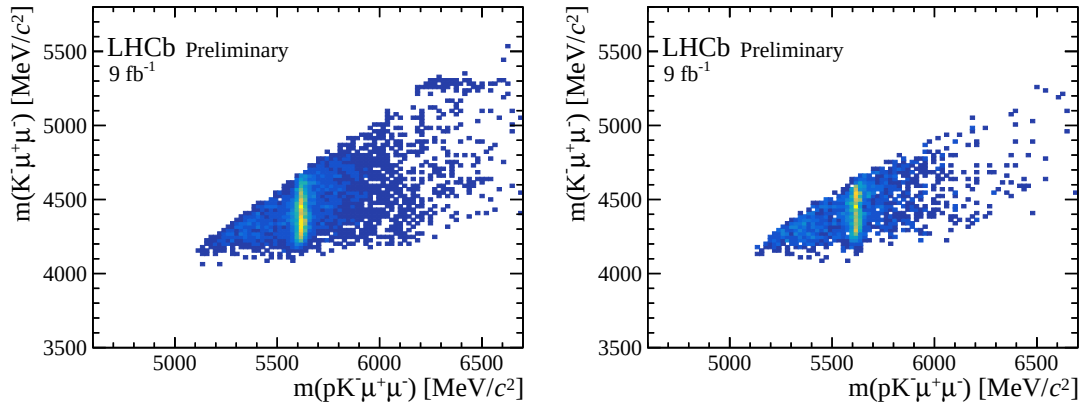

Figure 3.23 – $B^+ \to K^+\mu^+\mu^-$ decays associated with a random proton are present in the $\psi(2S)$ mode without requirements on the pK^- mass (left), but not in the $\Lambda(1520)$ mass window (right).

Decays of b hadrons that share the same final state as the signal decays due to a wrong association of an additional particle are referred to as "over-reconstructed backgrounds". A candidate for such a background is the $B^+ \to K^+\mu^+\mu^-$ decay, where a random proton is associated. This decay is only appearing in the $\psi(2S)$ mode, which is depicted in

Fig. 3.23. It is interesting to see that the horizontal band originating from $B^+ \to K^+\mu^+\mu^-$ decays disappears by requiring the $\Lambda(1520)$ mass window. Although the visible band in the $\psi(2S)$ bin is outside of the Λ_b^0 mass window, a veto of $m(K\mu^+\mu^-) < 5200\,\text{MeV}/c^2$ is suggested to remove all of those background contributions in all of the q^2 bins.

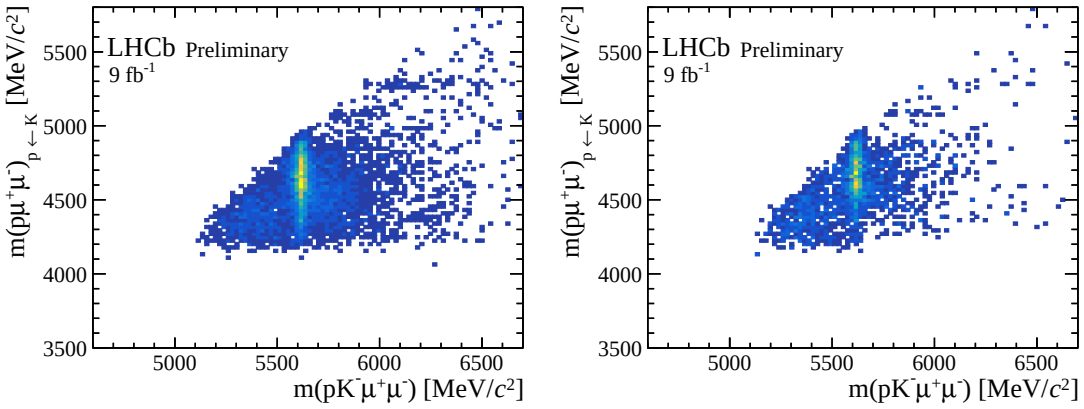

Figure 3.24 – Over-reconstructed $B^+ \to K^+\mu^+\mu^-$ decays combined with a $K \to p$ misidentification cause a horizontal band at the B^+ mass in the full pK^- window of the $\psi(2S)$ mode (left), which is disappearing in the $\Lambda(1520)$ mass window (right).

Over-reconstructed $B^+ \to K^+\mu^+\mu^-$ decays may appear combined with $K \to p$ misidentification. This background is investigated in Fig. 3.24. The background decay is again only visible in the $\psi(2S)$ mode within the whole pK^- mass window. To ensure the removal of those background events, a veto of $m(p\mu^+\mu^-)_{p\leftarrow K} < 5200\,\text{MeV}/c^2$ is proposed.

3.3.4 Partially reconstructed background

The partially reconstructed background includes all decays, where certain final state particles are lost, leading to a reconstructed final state identical to that of the signal. This can happen in case certain particles are not reconstructed or if they are outside of the LHCb acceptance. Usually, the lost final state particles are photons or neutral pions. However, it is also possible to lose a pair of charged particles. Loosing a single charged particle is not probable because of the Cabiboo-suppression of the rare $pK^-\pi^+\mu^+\mu^-$ decay, and the low production rate of Ξ_b^- and Ω_b^- decays [175–177]. Lost particles with masses higher than the pion mass are not considered due to the large shift in the $pK^-\mu^+\mu^-$ invariant mass.

Two types of partially reconstructed backgrounds are considered. The first one arises from the hadronic part of the decay, while the second one originates from the leptonic

system. As for the misidentification background, the hadronic partially reconstructed background is supposed to have similar properties in the rare and resonant modes. However, the partially reconstructed background emerging from the dilepton system is only present in the resonant mode.

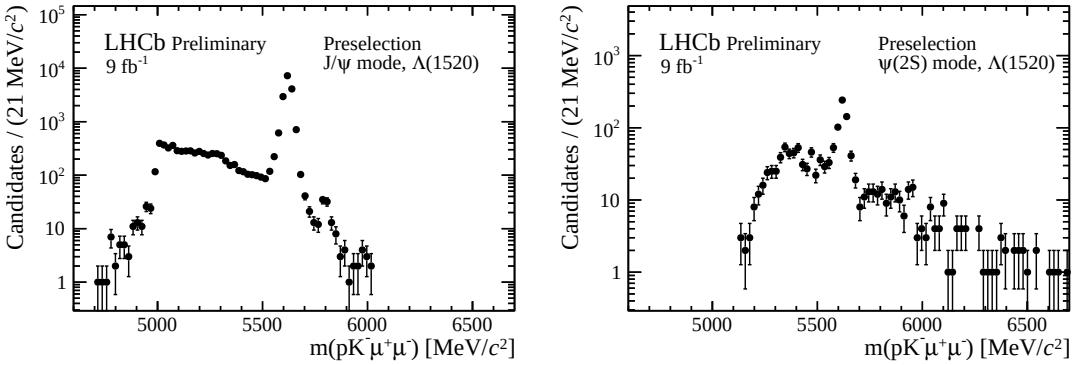

Figure 3.25 – The $pK^-\mu^+\mu^-$ invariant mass in the J/ψ and $\psi(2S)$ mode. On the J/ψ distribution, tight PID requirements are implied to visualise the $\Xi_b^0 \to pK^- J/\psi(\to \mu^+\mu^-)$ peak. The partially reconstructed background is mostly present in the low Λ_b^0 mass sideband.

In order to study better the partially reconstructed background, misidentification backgrounds are vetoed. In the J/ψ bin, the proton and the kaon are required to pass the tight PID cuts of ProbNNh > 0.8 ($h = p, K$). The partially reconstructed background is visible as a bump in the logarithmic scaled $pK^-\mu^+\mu^-$ mass distribution, depicted in Fig. 3.25. The step-function-like distribution in the J/ψ mode emerges probably from the variable ranges set in the BDT. In the J/ψ mode, Cabibbo-suppressed $\Xi_b^0 \to pK^- J/\psi(\to \mu^+\mu^-)$ decays are peaking close to the signal peak.

Partially reconstructed background originating from the hadronic system

The emission of an additional neutral pion or photon from the hadronic system is suppressed in non-resonant decays. Decays via a resonance, *e.g.* $\Lambda_b^0 \to pK^{*-}(K^-\pi^0)\mu^+\mu^-$ [5], might be enhanced with respect to the non-resonant case. Another resonant decay could contribute, namely the $\Lambda_b^0 \to \Delta^+(\to p\pi^0)K^-\mu^+\mu^-$ [6] decay. Potential contributions from higher excited Λ^* resonances to lower excited Λ^* resonances and a neutral pion are isospin suppressed.

Radiative decays of higher excited Λ^* or K^{*0} resonances to lower states are less probable because of the ample available phase space for strong decays. This is the reason why

5. This decay has not been observed yet. However, $b \to s\ell^+\ell^-$ decays with the K^{*-} resonance have been encountered in the R_K and R_{K^*} analyses [58, 94].

6. This decay has not been observed yet.

radiative contributions from the hadronic system are considered to be negligible.

To conclude, the highest probability of partially reconstructed backgrounds of hadronic nature have $\Lambda_b^0 \to pK^-\pi^0\mu^+\mu^-$ decays, where the π^0 arise from decays of excited K^{*-} resonances or Δ^+ baryons. All the other background decays are heavily suppressed.

Partially reconstructed background due to the dilepton system

Partially reconstructed background could arise from decays of higher charmonium resonances. In the J/ψ bin, the dominating contribution comes from $\chi_{c1,2} \to J/\psi\gamma$ and $\psi(2S) \to J/\psi\pi^+\pi^-$ decays, where the γ or the $\pi^+\pi^-$ are lost. Decays of higher charmonium(-like) resonances as $\chi_{c1}(3872)$ have invariant mass peaks significantly shifted from the Λ_b^0 mass peak. In Ref. [95], the peak has been situated in simulation to be below $4900\,\mathrm{MeV}/c^2$. In the $\psi(2S)$ mode, the $\psi(4360)$ and $\psi(4660)$ have been seen to decay into $\psi(2S)\pi^+\pi^-$ [21], but due to the energy conservation Λ_b^0 baryons cannot decay into $\Lambda(1520)$ and one of the excited ψ resonances. Photon radiation in the $J/\psi \to \mu^+\mu^-\gamma$ decays is the most probable for low-energetic photons. Because of the narrowness of the J/ψ mass peak in $\mu^+\mu^-$ invariant mass spectrum, it does not leak into the rare q^2 bins.

In summary, partially reconstructed background decays due to the dilepton system are supposed to be the most important in the J/ψ resonant mode and less critical in the $\psi(2S)$ mode. In the rare mode, it does not occur at all.

3.3.5 Impact of the vetoes on the angular distribution

The impact of the vetoes on the angular distribution is tested with the $\Lambda_b^0 \to \Lambda(1520)\mu^+\mu^-$ simulation sample. The simulation samples are fully corrected to match the data samples, according to section 3.4. The goal of this exercise is to evaluate if there is a distortion of the angular distribution and if the distortion can be described by the angular acceptance. For this study, the preselection, the BDT requirement and the $\Lambda(1520)$ mass window are requested.

At first, the veto on the ϕ resonance is applied. The angular distribution with the veto (blue) is shown in Fig. 3.26 and compared to the distribution without veto (yellow). The $\cos\theta_p$ distribution is distorted by the ϕ veto in the J/ψ, $\psi(2S)$ and rare mode. However, the distribution is not changing a lot, and the angular acceptance is therefore assumed to catch the distortion. The signal efficiency of the ϕ veto is about 94%.

Afterwards, the deformation with the Λ_c^+ veto with and without misidentification is investigated. The formulation of the corresponding vetoes is $m(pK^-\mu^+) > 2320\,\mathrm{MeV}/c^2$

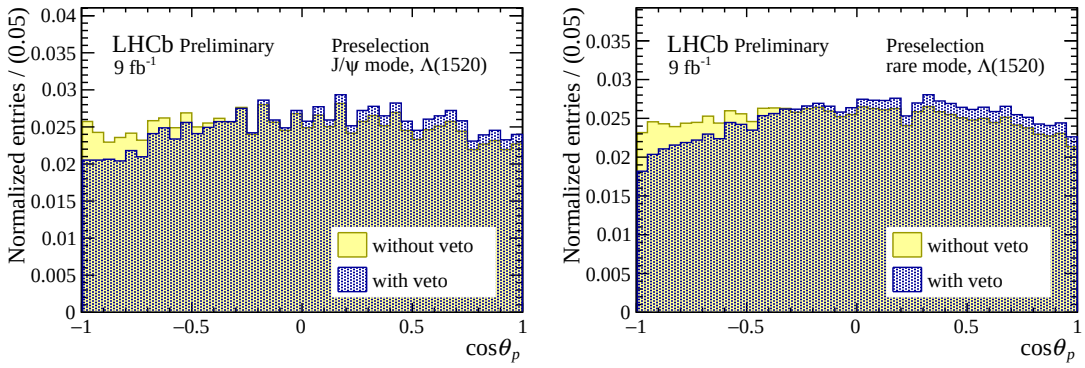

Figure 3.26 – Impact of ϕ veto on the $\cos\theta_p$ distribution, exemplary for the J/ψ (left) and rare mode (right).

and $m(pK^-\mu^+)_{p\leftrightarrow K} > 2320\,\text{MeV}/c^2$. The angular distribution of $\cos\theta_\ell$ before and after the application of the veto is plotted in Fig. 3.27. The Λ_c^+ veto without misidentification removes low values in the $\cos\theta_\ell$ distribution, while the Λ_c^+ veto with misidentification cuts away high $\cos\theta_\ell$ values. A fit would be, therefore, only possible in a reduced range of $-0.8 < \cos\theta_\ell < 0.8$. However, this reduces the sensitivity of the angular observables. In Fig. 3.18, the Λ_c^+ decays are mostly present at low $pK^-\mu^+\mu^-$ masses. Requiring $m(pK^-\mu^+\mu^-) > 5500\,\text{MeV}/c^2$ in addition to the $\Lambda(1520)$ mass window removes many hadronic and semileptonic decays of the Λ_c^+ baryon. Therefore, it was decided not to apply the Λ_c^+ veto in the following. The remaining yields are estimated in subsection 3.3.6.

The two following vetoes are only applied in the rare mode. Those are namely the J/ψ and the D^0 veto. By vetoing the J/ψ mass, originating from muon to kaon misidentification, the signal efficiency of the veto is 99%. A small deformation of $\cos\theta_p$ can be seen in Fig. 3.28. Since the deformation is so small, the angular acceptance should be able to catch the shape.

The D^0 veto impacts the angular distribution of $\cos\theta_\ell$, too. However, it removes only a few events, and the change of the distribution is supposed to be modelled by the angular acceptance. The $\cos\theta_\ell$ distribution can be seen in Fig. 3.28. The signal efficiency of the veto is about 98% in the rare q^2 region.

The last veto removes overreconstruced background decays combined with and without hadron misidentification. Since the background decays are situated at higher $pK^-\mu^+\mu^-$ masses, the veto does not impact the angular distribution. The signal efficiency is, thus, 100%.

In summary, the ϕ, J/ψ and the D^0 veto disturb the angular distribution. However, the deformation is expected to be eventually modelled by the angular acceptance, and

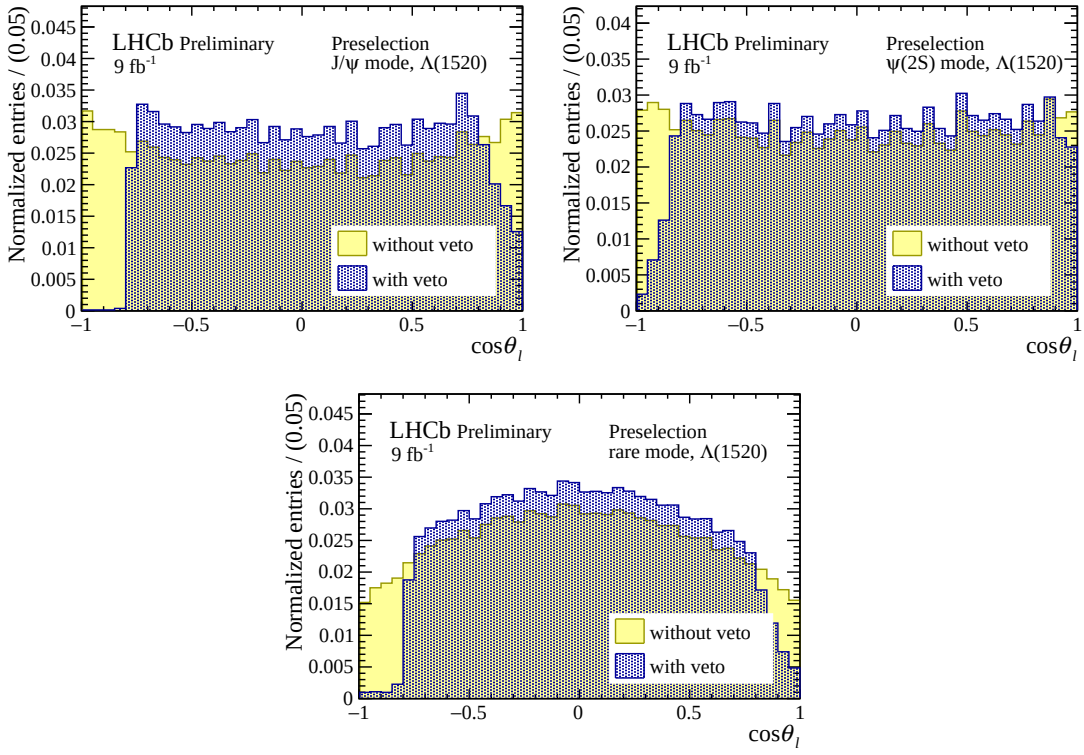

Figure 3.27 – Impact of the Λ_c^+ veto on the $\cos\theta_\ell$ distribution in the J/ψ, $\psi(2S)$ and the rare mode. The Λ_c^+ veto without misidentification is responsible for the removal of low $\cos\theta_\ell$ values, while the Λ_c^+ veto combined with the hadron misidentification swap removes high $\cos\theta_\ell$ values.

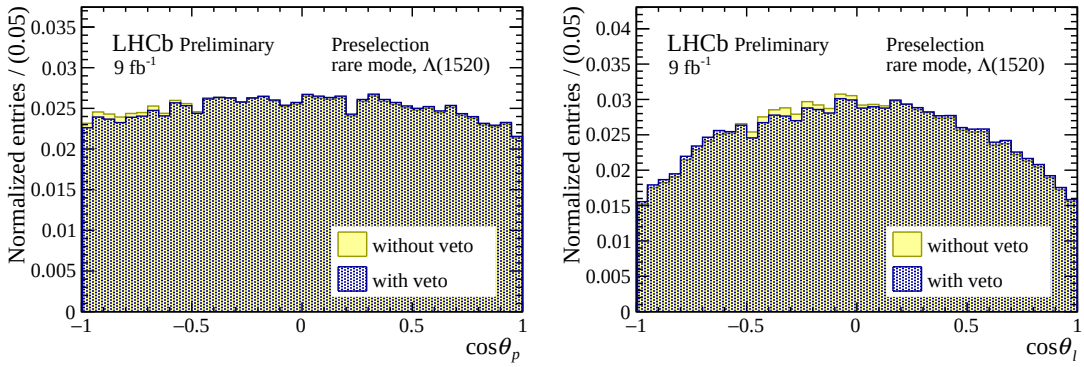

Figure 3.28 – The J/ψ (left) and the D^0 (right) vetoes deform the angular distribution of the rare mode only slightly.

therefore the vetoes are maintained. The total efficiency amounts to about 94% in the resonant modes and 91% in the rare q^2 bin. Λ_c^+ decays cannot be vetoed safely without introducing the need for a cut on the $\cos\theta_\ell$ distribution, but they are seen to be situated mostly outside of the Λ_b^0 mass window.

3.3.6 Background yield estimation

After having sighted all the contributing backgrounds, the question of how many background events will still be present within the Λ_b^0 and $\Lambda(1520)$ mass window is addressed in this subsection. The equation to calculate the yield is written as

$$N_{\text{decay}} = \mathcal{L} \times 2\sigma_{b\bar{b}} \times f_{X_b} \times \mathcal{B}(\text{decay}) \times \varepsilon_{\text{tot}}(\text{decay}). \tag{3.3}$$

Since the $b\bar{b}$ cross section, $\sigma_{b\bar{b}}$, is used in the formula above, the possibility of b baryon and b antibaryon production has to be accounted for by multiplying it with a factor of two. The b hadron production fraction f_{X_b} describes the probability of the b quark to hadronise into a b hadron X_b.

A large uncertainty comes from the production cross-section of $b\bar{b}$ pairs. It is, thus, advantageous to calculate the yield by a ratio of two different background decay modes, in which the cross-section $\sigma_{b\bar{b}}$ and the luminosity, $\mathcal{L}$, cancels out. The J/ψ control mode is chosen to act as the normalisation channel. The background yield is expressed as

$$N_{\text{decay}} = \frac{N^{\text{data}}_{\Lambda_b^0 \to pK^- J/\psi(\to \mu^+\mu^-)}}{\varepsilon_{\text{tot}}(\Lambda_b^0 \to pK^- J/\psi(\to \mu^+\mu^-))} \frac{f_{X_b}}{f_{\Lambda_b^0}} \frac{\varepsilon_{\text{tot}}(\text{decay})\mathcal{B}_{\text{tot}}(\text{decay})}{\mathcal{B}_{\text{tot}}(\Lambda_b^0 \to pK^- J/\psi(\to \mu^+\mu^-))}. \tag{3.4}$$

The number of data events in the $\Lambda_b^0 \to pK^- J/\psi(\to \mu^+\mu^-)$ decay are evaluated in the full pK^- mass window in order to match the measured branching fraction $\mathcal{B}(\to pK^- J/\psi)$. $\mathcal{B}_{\text{tot}}$ represents the BF of the full decay chain. Similarly, ε_{tot} denotes the total efficiencies. All of the components are explained in the following.

Efficiencies

Efficiencies are extracted with the help of the simulation samples. The total efficiencies are calculated via

$$\varepsilon_{\text{tot}} = \varepsilon_{\text{geom}} \times \varepsilon_{\text{filt}} \times \varepsilon_{\text{reco}} \times \varepsilon_{\text{sel}}. \tag{3.5}$$

The geometrical efficiency $\varepsilon_{\text{geom}}$ depends on the number of tracks in the detector. Since neutrinos do not leave a track, they are ignored. Photons originating from Final-State Radiation are simulated in the simulation samples by PHOTOS, but they are not recon-

structed. The studied backgrounds have the same number of tracks as the control mode, because of which the geometrical efficiency drops out in the ratio. To save disk space, simulation samples can be filtered by the stripping selection while removing the PID requirements. The PID cuts can, thus, be evaluated more precisely using data-driven techniques. The filtering efficiency is noted with $\varepsilon_{\text{filt}}$. Most of the samples are unfiltered. The only filtered simulation sample consists of $\Lambda_b^0 \to \Lambda_c^+(\to pK^-\pi^+)\mu^-\overline{\nu}_\mu$ decays. The filtering efficiency is provided by the LHCb simulation group and values $\varepsilon_{\text{filt}} = 4.03\%$. The product of the reconstruction and selection efficiency $\varepsilon_{\text{reco}} \times \varepsilon_{\text{sel}}$ is evaluated together with the help of the formula

$$\varepsilon_{\text{reco}} \times \varepsilon_{\text{sel}} = \frac{N_{\text{reco}}^{\text{truth-matched, selected, reweighted}}}{N_{\text{truth}}^{\text{reweighted}}}. \tag{3.6}$$

The multiple candidate removal is applied to the reconstructed samples before extracting the yields. Since this section aims to estimate the number of background events, the background samples are not reweighted. In general, the kinematics and topology of b-mesons are better described in the simulation than for b-baryons. Neglecting the reweighting for the backgrounds is supposed to have a negligible effect.

As a reminder, all of the simulation samples used to calculate the reconstruction and selection efficiencies are presented in the subsection 3.1.3 of this chapter and in appendix A. The resulting total efficiencies, ε_{tot}, extracted from these simulation samples, are listed in Tab. 3.8.

To simplify the decay description, the J/ψ and $\psi(2S)$ resonances are imposed to decay into a muon pair. Similarly, the decays $\Lambda(1520) \to pK^-$ and $K^*(892)^0 \to K^+\pi^-$ are implicitly meant.

The efficiencies in the $\psi(2S)$ signal mode are expected to be higher than in the J/ψ mode since high energetic muons are passing easier the selection criteria. The amount of the $p \leftrightarrow K$ misidentification swapped $\Lambda_b^0 \to \Lambda(1520)\psi(2S)$ decays is about 3.5% of the not misidentified decays in the year 2012 and 0.6% in the year 2016. The average over the total Run 1 and 2 datasets lead to a percentage of about 1.6%, which is neglected.

The efficiencies of zero result from the PID requirements on the muons, which reject all misidentified pions. The $\Lambda_b^0 \to \Lambda_c^+(\to \Lambda(1520)\mu^+\nu_\mu)\pi^-$ decay has a higher efficiency, due to the true $\Lambda(1520)$ resonance. Therefore, this decay is not impacted by the requirements on the pK^- mass, contrary to the induced efficiency loss for simulation samples, showing a phase space distribution in the pK^- invariant mass spectrum.

Decay mode	$\varepsilon_{\text{tot},2012}$ $[10^{-5}]$	$\varepsilon_{\text{tot},2016}$ $[10^{-5}]$	$\varepsilon_{\text{tot},2017}$ $[10^{-5}]$
$\Lambda_b^0 \to pK^-J/\psi$	2237.10 ± 29.81	2819.70 ± 8.76	2995.37 ± 14.26
$\Lambda_b^0 \to \Lambda(1520)\psi(2S)$	696.60 ± 5.36	717.27 ± 3.87	-
$\Lambda_b^0 \to \Lambda(1520)\psi(2S)$, $p \leftrightarrow K$ misID	24.04 ± 1.07	4.64 ± 0.34	-
$\Lambda_b^0 \to \Lambda_c^+(\to pK^-\pi^+)\pi^-$	0.0	0.0	-
$\Lambda_b^0 \to \Lambda_c^+(\to pK^-\pi^+)\mu^-\overline{\nu}_\mu$	-	0.0	-
$\Lambda_b^0 \to \Lambda_c^+(\to \Lambda(1520)\mu^+\nu_\mu)\pi^-$	0.59 ± 0.34	-	-
$B^0 \to K^+\pi^-\mu^+\mu^-$	-	-	0.33 ± 0.19
$B^0 \to K^*(892)^0 J/\psi$	10.61 ± 0.34	17.02 ± 0.41	-
$B^0 \to K^+\pi^- J/\psi$	1.35 ± 0.18	1.93 ± 0.42	-
$B^0 \to K^*(892)^0\psi(2S)$	7.43 ± 0.47	14.04 ± 0.64	-
$B_s^0 \to K^+K^-\mu^+\mu^-$	2.78 ± 0.46	2.57 ± 0.46	-
$B_s^0 \to K^+K^- J/\psi$	25.81 ± 1.44	15.49 ± 0.46	-
$B_s^0 \to K^+K^-\psi(2S)$	80.14 ± 3.29	37.65 ± 1.78	-

Table 3.8 – The total efficiencies, ε_{tot}, are given in order of 10^{-5} for the data-taking periods 2012, 2016 and 2017. The total efficiencies are the input of the background yield calculation.

Branching fractions

To get reliable results, the same decay should be used for the efficiency calculation and the measured branching fraction. However, this is not always feasible because of missing measurements and a complicated resonant structure. The $B^0 \to K^+\pi^-\mu^+\mu^-$, the $B_s^0 \to K^+K^-\mu^+\mu^-$ and the $B_s^0 \to K^+K^-\psi(2S)$ decay are simulated with a phase space model, but the BFs are only known for the decay via the $K^*(892)^0$ and ϕ resonance. In those cases, the resonant BFs are used.

The BFs are taken from Ref. [21] when available. If the BF is not available in Ref. [21], the determination is explained explicitly. In the rare mode, the BF measurement are performed usually in bins of q^2. The measurement of the $B^0 \to K^*\mu^+\mu^-$ BF in the $[1.0, 6]\,\text{GeV}^2/c^4$ bin is used since it covers a wide q^2 region and is comparable to the q^2 bin of $[1.1, 6.0]\,\text{GeV}^2/c^4$, which is intended to be explored in this analysis. The BF of the $B_s^0 \to \phi\mu^+\mu^-$ decay is not part of Ref. [21]. However, the BF in the $q^2 in [1.1, 6]\,\text{GeV}^2/c^4$ bin is published in Ref. [66].

Since the $\Lambda_b^0 \to \Lambda_c^+\ell\overline{\nu}_\ell$ BF is measured in Ref. [21] for the electronic and muonic decay mode together, the BF of the muonic decay only is approximated by half of the above-cited measurement. The BF of the $\Lambda_c^+ \to \Lambda(1520)e^+\nu_e$ decay has been determined in Ref. [178]. Because of the lack of other measurements, it is approximated to be the same in the muonic decay mode.

The total BFs are summarised in Tab. 3.9. Rates of all subsequent decays are multiplied by each other.

Decay mode	$\mathcal{B}_{\text{tot}}$
$\Lambda_b^0 \to pK^- J/\psi$	$(1.91 \pm 0.37) \cdot 10^{-5}$
$\Lambda_b^0 \to \Lambda(1520)\psi(2S)$	$(5.28 \pm 1.36) \cdot 10^{-7}$
$\Lambda_b^0 \to \Lambda_c^+(\to pK^-\pi^+)\pi^-$	$(3.08 \pm 0.41) \cdot 10^{-4}$
$\Lambda_b^0 \to \Lambda_c^+(\to pK^-\pi^+)\mu^-\overline{\nu}_\mu$	$(1.95 \pm 0.54) \cdot 10^{-3}$
$\Lambda_b^0 \to \Lambda_c^+(\to \Lambda(1520)\mu^+\nu_\mu)\pi^-$	$(1.13 \pm 0.68) \cdot 10^{-6}$
$B^0 \to K^+\pi^-\mu^+\mu^-$	$(1.148 \pm 0.073) \cdot 10^{-7}$
$B^0 \to K^*(892)^0 J/\psi$	$(5.0 \pm 1.0) \cdot 10^{-5}$
$B^0 \to K^+\pi^- J/\psi$	$(6.86 \pm 0.34) \cdot 10^{-5}$
$B^0 \to K^*(892)^0\psi(2S)$	$(3.11 \pm 0.44) \cdot 10^{-6}$
$B_s^0 \to K^+K^-\mu^+\mu^-$	$(1.41 \pm 0.25) \cdot 10^{-10}$
$B_s^0 \to K^+K^- J/\psi$	$(4.71 \pm 0.44) \cdot 10^{-8}$
$B_s^0 \to K^+K^-\psi(2S)$	$(2.04 \pm 0.52) \cdot 10^{-7}$

Table 3.9 – The total branching fractions of the considered decay modes are collected in the table.

Production fractions

Another property is needed to calculate the background yields. The missing part is the fraction of b quarks, which hadronise into a specific b hadron. The production fractions $f_{\Lambda_b^0}$ and f_s have been measured by the LHCb collaboration in Ref. [126], as discussed in Ch. 2.2, and particularly in Eq. 2.3 and 2.2. These fractions are averaged over the kinematics of the hadrons. By assuming isospin symmetry in B mesons, the production fractions f_u and f_d are equal. Since the ratio of the production fractions is needed, they are obtained via

$$\frac{f_d}{f_{\Lambda_b^0}} = \frac{1}{2}\left(\frac{f_{\Lambda_b^0}}{2f_d}\right)^{-1} = \frac{1}{2}\left(\frac{f_{\Lambda_b^0}}{f_u + f_d}\right)^{-1}, \tag{3.7}$$

$$\frac{f_s}{f_{\Lambda_b^0}} = \left(\frac{f_s}{f_u + f_d}\right)\left(\frac{f_{\Lambda_b^0}}{f_u + f_d}\right)^{-1}. \tag{3.8}$$

Yields

The estimation of the background yields is based on the knowledge of the $\Lambda_b^0 \to pK^- J/\psi$ yield. The yields are extracted from data by fitting the $pK^-\mu^+\mu^-$ invariant

mass in the J/ψ bin. Using Eq. 3.4, the signal and background yields are estimated. The final yields are collected in tab 3.10.

Decay mode	2012	2016	2017
$\Lambda_b^0 \to pK^-J/\psi$ (measured)	$18,735 \pm 157$	$31,130 \pm 199$	$31,848 \pm 201$
$\Lambda_b^0 \to \Lambda(1520)\psi(2S)$	162 ± 44	220 ± 60	-
$\Lambda_b^0 \to \Lambda(1520)\psi(2S)$, $p \leftrightarrow K$ misID	6 ± 2	1.4 ± 0.4	-
$\Lambda_b^0 \to \Lambda_c^+(\to pK^-\pi^+)\pi^-$	0.0 ± 0.0	0.0 ± 0.0	-
$\Lambda_b^0 \to \Lambda_c^+(\to pK^-\pi^+)\mu^-\overline{\nu}_\mu$	-	0.0 ± 0.0	-
$\Lambda_b^0 \to \Lambda_c^+(\to \Lambda(1520)\mu^+\nu_\mu)\pi^-$	0.3 ± 0.2	-	-
$B^0 \to K^+\pi^-\mu^+\mu^-$	-	-	0.04 ± 0.02
$B^0 \to K^*(892)^0 J/\psi$	451 ± 93	951 ± 196	-
$B^0 \to K^+\pi^- J/\psi$	79 ± 19	148 ± 44	-
$B^0 \to K^*(892)^0\psi(2S)$	20 ± 5	49 ± 11	-
$B_s^0 \to K^+K^-\mu^+\mu^-$	0.0 ± 0.0	0.0 ± 0.0	-
$B_s^0 \to K^+K^- J/\psi$	0.25 ± 0.06	0.20 ± 0.05	-
$B_s^0 \to K^+K^-\psi(2S)$	3.4 ± 0.9	2.1 ± 0.5	-

Table 3.10 – The $\Lambda_b^0 \to pK^-J/\psi$ yields are obtained with a fit to data. Having those yields, the signal and background yields are estimated.

The contributions of the cascade decays are negligible due to the mass and PID requirements. As stated before, the signal decay with $p \leftrightarrow K$ misidentification swap is of only 1.7%, by extrapolating to the full Run 1 and 2 datasets. Similarly, $B_s^0 \to K^+K^-\mu^+\mu^-$ decays are negligible in the rare, J/ψ and $\psi(2S)$ modes. However, it needs to be kept in mind that the simulation here is based on a phase space model in the K^+K^- mass rather than the ϕ tail, which is mostly present in data.

In the rare mode, the $B^0 \to K^+\pi^-\mu^+\mu^-$ yield is negligible. Since the $\Lambda_b^0 \to pK^-J/\psi$ yield is measured in the full pK^- mass window, the measured yield in the $\Lambda(1520)$ mass window is taken as a comparison. Then, the $B^0 \to K^*(892)^0 J/\psi$ yield is about 7% of the signal yield in the year 2012 and 9% in the year 2016. In the $\psi(2S)$ mode, the contribution is estimated to be about 14% and 20%. The contribution of $B^0 \to K^+\pi^-\mu^+\mu^-$ decays is negligible in the rare mode. Therefore, the B^0 decay needs to be modelled in the pK^-J/ψ and $pK^-\psi(2S)$ invariant mass fits.

3.3.7 Summary of the background treatment

To conclude, the hadron misidentification backgrounds are the main backgrounds in this analysis. The dominant one is the $B_s^0 \to \phi(\to K^+K^-)\mu^+\mu^-$ background, which can be vetoed. The veto is applied to all of the bins. The $B^0 \to K^*\mu^+\mu^-$ background is the second important background. While the yields are negligible in the rare mode, they are not in the resonant modes.

The lepton misidentification backgrounds are mostly important in the rare mode. The J/ψ peak in the $K^-\mu^+$ invariant mass spectrum can be vetoed. Similarly, the cascade backgrounds are strongly reduced by the PID requirements on the muons. Semileptonic Λ_b^0 decays via a D^0 resonance are vetoed. However, the veto of semileptonic Λ_b^0 decays via a Λ_c^+ resonance cuts away the endpoints of the $\cos\theta_\ell$ spectrum and is therefore not applied. It was seen to have a small contribution only due to the presence at small $pK^-\mu^+\mu^-$ masses.

Which decay?	*Veto formulation?*	*Which mode?*
$B_s^0 \to \phi(\to K^+K^-)\mu^+\mu^-$	$\lvert m(pK^-)_{p\leftarrow K} - 1020\rvert > 12\,\text{MeV}/c^2$	all
J/ψ peak in $K^-\mu^+$	$\lvert m(K^-\mu^+)_{K\to\mu} - 3097\rvert > 35\,\text{MeV}/c^2$	rare mode
Cascade Λ_b^0 via $D^0 \to K^-\pi^+$	$m(K^-\mu^+) \pm 20\,\text{MeV}/c^2$	rare mode
$B^+ \to K^+\mu^+\mu^-$	$m(K\mu^+\mu^-) < 5200\,\text{MeV}/c^2$	all
$B^+ \to K^+\mu^+\mu^-$, $K \to p$ misID	$m(p\mu^+\mu^-)_{p\leftarrow K} < 5200\,\text{MeV}/c^2$	all

Table 3.11 – Summary of the employed vetoes.

Over-reconstructed backgrounds are vetoed, even if they are mostly outside of the mass windows. The same procedure is repeated for over-reconstructed backgrounds combined with misidentification. All of the vetoes are summarised in Tab. 3.11. Applying them removes 5.5% of the signal candidates in the resonant mode and 8.2% in the rare mode.

Partially reconstructed backgrounds, being produced in the hadronic system, are suspected to arise dominantly from Λ_b^0 decays, where a π^0 arises from the decay of an excited K^{*-} resonance or a Δ^+ baryon. The dilepton system can be a source of partially reconstructed backgrounds, but only in the resonant mode. A photon or a charged pion pair, coming from the decay of a higher charmonium resonance, could be lost. The partially reconstructed backgrounds are expected to be present mostly at low $pK^-\mu^+\mu^-$ masses.

Finally, the combinatorial background is strongly reduced by a BDT. Nevertheless, some of it remains and will be modelled in the Λ_b^0 mass fit.

3.4 Simulation sample corrections

In the previous chapter, the efficiencies are estimated with simulation samples by using correction weights. Those correction weights are important to get a perfect agreement between data and simulation samples in the signal decay, as well as in the control mode. Besides the luminosity weight, the corrections of the simulation samples are shared with Ref. [60]. All of them are applied sequentially. The first correction improves the description of the Dalitz structure in $\Lambda_b^0 \to pK^-J/\psi$ decays. Since the $\Lambda_b^0 \to pK^-J/\psi$ simulation samples are generated with a phase space model, they need to be corrected for the resonant structure in the pK^- and pJ/ψ mass.

Other corrections are necessary to have the most precise data description possible. Since the lifetime and transverse momentum of the Λ_b^0 baryon are known to deviate in the simulation sample, each of them has a correction weight, which is determined in a data-driven way. External factors such as the track multiplicity can influence the response and are corrected, too. Since the three variables are linearly uncorrelated, the correction order is not important.

The particle identification has slightly different behaviour in the data than in the simulation samples. Therefore, instead of placing cuts on the PID variables in the $\Lambda_b^0 \to \Lambda(1520)\mu^+\mu^-$ and $\Lambda_b^0 \to pK^-J/\psi$ simulation samples, special PID weights are determined to model the PID response in data.

Another correction is needed for the hardware trigger response. The discrepancies are corrected with the TISTOS method [179]. All of the weights are determined in the signal and control mode for the generator and reconstruction level simulation samples.

Before adding the simulation samples of different years together, a luminosity weight is introduced to scale the sample to the correct luminosity ratio. Each of the corrections is further described in this section.

3.4.1 Decay model correction

The resonant structure in the pK^- and pJ/ψ invariant mass is well known, thanks to the amplitude analysis of Ref. [4]. Based on the so-called pentaquark analysis, weights are calculated as a function of the truth particle four-momenta. The weights are extracted for the generator and reconstruction level simulation samples. These weights can only be determined in the J/ψ mode. The complex two-dimensional structure obtained in the pentaquark analysis is presented in Fig. 1.15. It can be compared to the distributions obtained with the decay model correction, shown in Fig. 3.29.

The rare mode simulation samples do not need a weight since they are generated for the $\Lambda(1520)$ resonance. Unfortunately, the pK^- invariant mass distribution is not

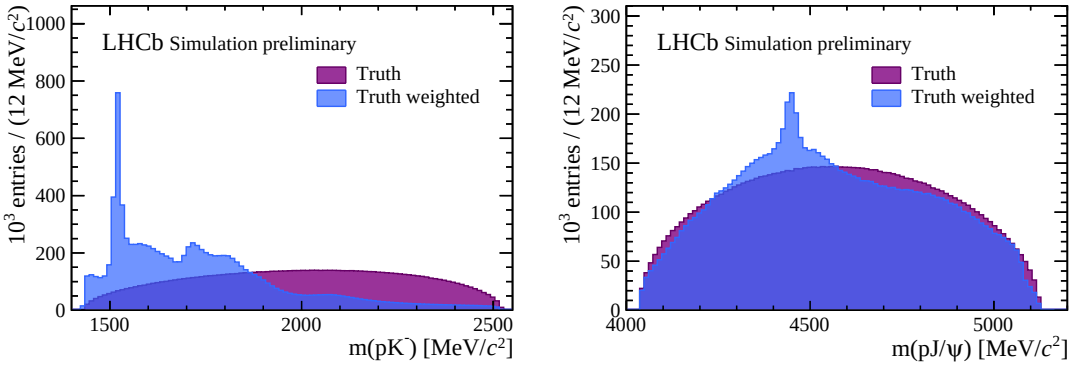

Figure 3.29 – Generator level distributions of the $\Lambda_b^0 \to pK^- J/\psi(\to \mu^+\mu^-)$ of the 2016 simulation sample with and without decay model correction weights.

measured in the $\psi(2S)$ mode. Therefore, the phase space pK^- invariant mass cannot be reweighted in the $\Lambda_b^0 \to pK^-\psi(2S)$ simulation samples.

3.4.2 The Λ_b^0 baryon lifetime correction

In the generation of the simulation samples, a certain value of the Λ_b^0 lifetime, $\tau_{\Lambda_b^0}$, is implied. The generated lifetime values differ from the latest measurements, reported in the PDG [21]. The different lifetime values are summarised in tab 3.12.

$\tau_{\Lambda_b^0}$ [fs]	2011	2012	2015	2016	2017	2018
$\Lambda_b^0 \to pK^- J/\psi$	1451.000	1424.702	1451.000	1451.000	1451.000	1451.000
$\Lambda_b^0 \to \Lambda(1520)\mu^+\mu^-$	1424.702	1424.702	1451.000	1451.000	1451.000	1451.000
PDG	1464.316					

Table 3.12 – Λ_b^0 lifetimes used in the generation of the different simulation samples, compared to the latest measurements in the PDG [21].

The simulation samples are reweighted by the weight $w(t)$, which is a function of the simulated lifetimes τ_{sim} and the PDG value τ_{PDG}. It is defined as

$$w(t) = \frac{\frac{1}{\tau_{\text{PDG}}} \exp\left(-\frac{t}{\tau_{\text{PDG}}}\right)}{\frac{1}{\tau_{\text{sim}}} \exp\left(-\frac{t}{\tau_{\text{sim}}}\right)}. \tag{3.9}$$

The Λ_b^0 lifetime is reweighted in the generator and reconstruction level simulation samples.

3.4.3 Event multiplicity correction

The event multiplicity is known to be described incorrectly in the simulation. Usually, the number of tracks in an event, nTracks, or the number of hits in the scintillating pad detector, nSPDHits, is taken as a proxy to correct for these discrepancies. The nSPDHits variable is an input of the hardware trigger lines L0Muon and L0DiMuon. Correcting the nSPDHits variable introduces even higher discrepancies in other multiplicity variables because of the data simulation mismatch of the M1 muon station modelling. This is the reason, why the correction was performed, based on the nTracks variable.

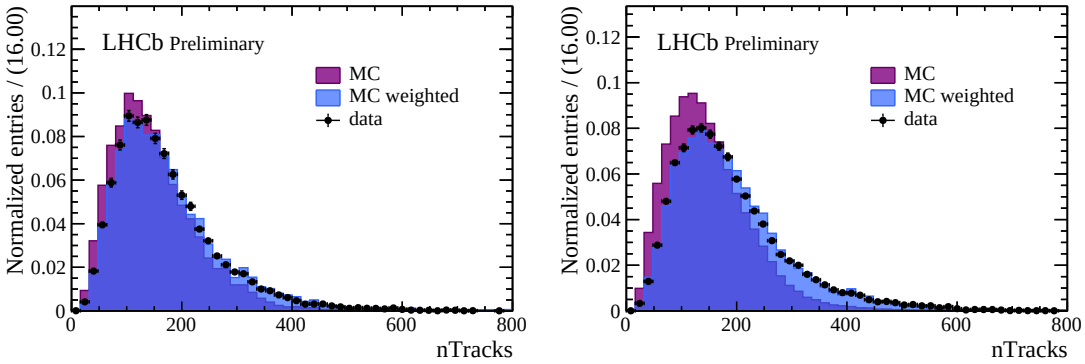

Figure 3.30 – The raw and corrected nTracks distribution of the $\Lambda_b^0 \to pK^-J/\psi$ simulation sample are drawn. Those are compared to the ${}_s\mathcal{W}eight$ted data distributions for the years 2012 (left) and 2016 (right).

The nTracks distribution differs between the different data taking years and is, thus, calculated per year. Fig. 3.30 shows the discrepancy of the nTracks distribution in the simulation samples and the data, for the years 2012 and 2016. A correction is calculated after applying the preselection, the decay model and the lifetime correction on the simulation samples. The corrected nTracks distribution matches better the data.

Since the generator level distributions of the signal and control mode simulation samples are found to be similar, the corrections, derived from the control mode, are applied to the signal decay, as well. The corresponding distributions are shown in appendix D.1. Splitting the events, selected by the L0Muon and L0DiMuon trigger line, reveals a discrepancy between the two distributions. Since the measurement is performed in the two categories together, the small sample size, and in order to follow the same strategy as the BF measurement [60], the corrections are chosen to be identical.

3.4.4 Kinematic correction

The transverse momentum of the Λ_b^0 is another variable, which is known to be mismodelled in the simulation. Especially the dependence of the Λ_b^0 production fraction on the transverse Λ_b^0 momentum is badly described in simulation [126]. Consequently, correction weights are derived for the Λ_b^0 transverse momenta in simulation for each of the data taking years, based on the ${}_s\mathcal{W}eight$ted $\Lambda_b^0 \to pK^-J/\psi(\to \mu^+\mu^-)$ data. The weights, calculated for the control mode, are applied to the signal mode, too. The advantage of this procedure is the availability of large sample size and the statistical independence of the J/ψ mode with respect to the signal data sample.

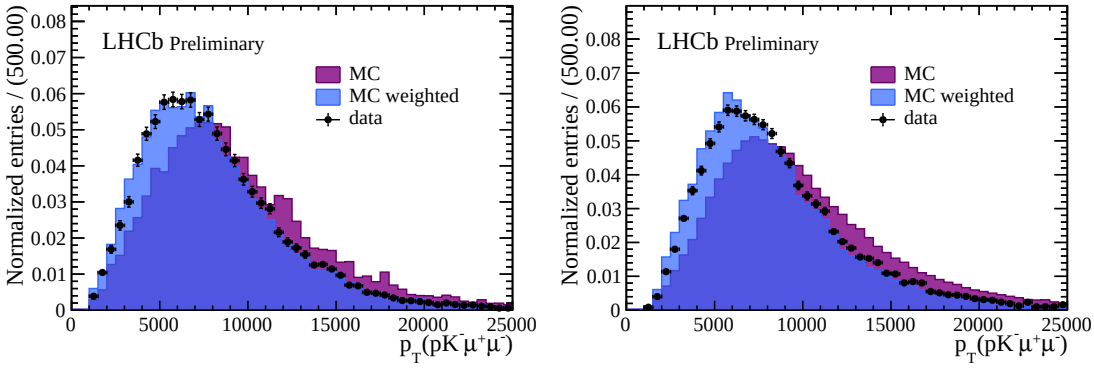

Figure 3.31 – The data distribution of the $p_{\mathrm{T}}(\Lambda_b^0)$ is compared to the distributions of the corrected and uncorrected simulation samples of the data-taking year 2012 (left) and 2016 (right).

The effect of the correction weights on the $p_{\mathrm{T}}(\Lambda_b^0)$ distribution is illustrated in Fig. 3.31. More comparisons can be found in App. D.2.

3.4.5 Correction of the particle identification response

The fifth quantity, which needs to be corrected, is the particle identification (PID) response. The difference in the PID performance in simulation and in data is due to the RICH detector and μ station response, in particular, due to detector misalignments and under-estimated multiplicity of secondary particles in the simulation. The PIDCalib package [180] provides the calibration samples to evaluate the efficiency of the final state particle identification.

Clean samples of two- or three-body decays are collected in parallel to the regular data taking. Strict requirements on the "tag" particle ensure the cleanness of the sample, while the PID efficiency is tested on the "probe" particle which has no prior PID requirements applied. The background is subtracted via the ${}_s\mathcal{P}lot$ technique [160]. The number of

events in the ${}_s\mathcal{W}eight$ted data sample, passing the PID requirements, with respect to the initial ${}_s\mathcal{W}eight$ted sample, indicates the PID efficiency. The simulation sample is extended by per-event weights, accounting for the PID efficiency. Those PID weights can be extracted as a function of kinematic variables if the size of the calibration sample allows.

Calibration samples

Crucial for the PID correction is the choice of the calibration sample. The kinematic range of the particles in the signal sample has to overlap sufficiently with those of the calibration sample. The calibration samples are listed in Tab. 3.13.

Particle	Run 1 sample	Run 2 sample	Decay description
p	Lam0 (default)	P (default)	$\Lambda^0 \to p\pi^-$
	IncLc	IncLc	$\Lambda_c^+ \to pK^-\pi^+$ inclusive
	-	P_LcfB	$\Lambda_b^0 \to \Lambda_c^+(\to pK^-\pi^+)\ell^-\overline{\nu}_\ell$
K	Dst (default)	K (default)	$D^{*+} \to D^0(\to K^-\pi^+)\pi^+$
	-	K_DsPhi	$D_s^+ \to \phi(\to K^+K^-)\pi^+$
μ	Jpsi (default)	Mu_B_Jpsi	$J/\psi \to \mu^+\mu^-$ from b hadron decays
	-	Mu (default)	$J/\psi \to \mu^+\mu^-$ decays
	-	Mu_nopt	$J/\psi \to \mu^+\mu^-$ without p_T cuts

Table 3.13 – Name and decay description of the PID calibration samples, collected to correct the simulation samples of Run 1 and Run 2.

The kinematic requirements of the calibration samples are summarised in Tab. 3.4. Since particles outside of this kinematic range cannot be calibrated, the selection is aligned with those requirements present in the calibration samples.

In the default proton calibration sample, protons emerge far from the primary vertex, due to the long flight distance of the Λ^0 baryons. In the signal decay, the Λ^* resonances have a much shorter flight distance and the protons are produced earlier. The proton production region impacts the PID efficiency. This is the reason why protons are calibrated with inclusive $\Lambda_c^+ \to pK^-\pi^+$ samples. Because of the lack of calibration samples for the data-taking year 2015, calibrations are exceptionally calculated based on $\Lambda_b^0 \to \Lambda_c^+(\to pK^-\pi^+)\ell^-\overline{\nu}_\ell$ decays, despite its smaller sample size.

In Run 2, low-momentum protons with $p_\mathrm{T} < 1000\,\mathrm{MeV}/c$ are not covered by the employed calibration sample. Therefore, the corrections of low-momentum protons are calculated with the default Λ^0 sample. A corresponding systematic uncertainty for the calibration with the Λ^0 sample in this particular case will enter the systematic uncertainties due to the simulation correction, as described in Sec. 4.3.

The kaon PID calibration is performed with the default kaon calibration samples. During Run 1, the muon PID efficiencies are extracted from the default muon calibration sample. For Run 2, the $J/\psi \to \mu^+\mu^-$ calibration sample without p_{T} requirements is chosen. For the analysis, the availability of many low momentum muons is important since such requirements have a large impact on the deformation of the $\cos\theta_\ell$ distribution.

The PID of muons with low transverse momentum of $p_{\mathrm{T}} < 800\,\mathrm{MeV}/c$ cannot be calibrated in Run 1 with the above-listed calibration samples. The PID efficiency corrections are, thus, calculated with an artificial sample, as explained later in this section.

Efficiency map binning

The PID response is a function of the particle properties, in particular the momentum and pseudo-rapidity of the particle, as well as the event multiplicity [7]. Because of the mismodelling of the nTracks variable, no multiplicity variable has been used in the binning. Moreover, the event multiplicity of the signal sample should be similar to the one of the calibration sample, as both are b-hadron decays and, thus, using the average PID efficiency should be sufficient. The PID efficiency is calculated as a two-dimensional map of momentum p and pseudorapidity η. Dividing the calibration sample in a three-dimensional map would decrease the statistical power in each bin and lead to an increase in uncertainties. Nevertheless, the corrected PID efficiencies are plotted in bins of the nTracks variable, as presented in Fig. 3.32.

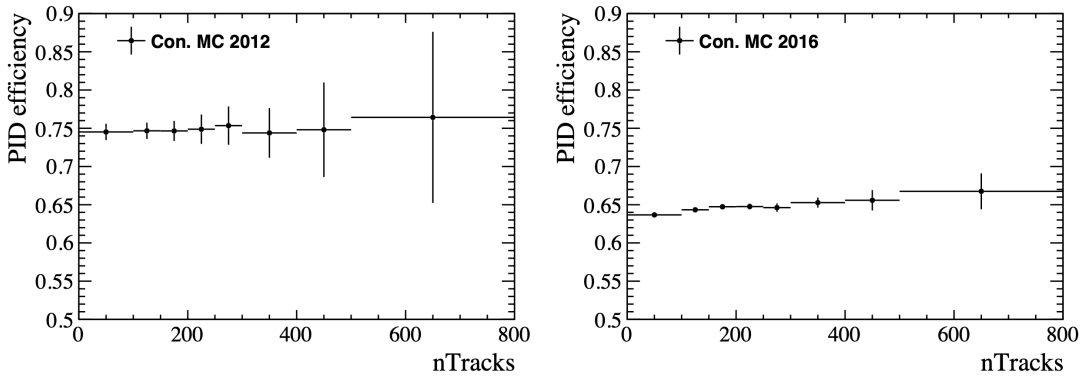

Figure 3.32 – The total PID efficiency for $\Lambda_b^0 \to pK^-J/\psi$ decays are shown as a function of the nTracks distribution.

The binning is optimised with the PIDCalib Binning Scheme Optimiser. It balances describing the efficiency variations well enough while keeping the amount of data per

7. The higher the event multiplicity, the more difficult is the association of the Cherenkov photons to the original particle, especially when the Cherankov rings are overlapping or when the subdetectors are misaligned.

bin large enough to avoid fluctuations. The binning procedure used in this analysis starts with N isopopulated bins. If the efficiency difference between two bins is smaller than 3σ, the bins are merged. A complementary binning procedure is considered to calculate the systematic uncertainties. The difference to the previous method is the initialisation with equally-sized bins. The PID efficiency maps, as well as the prerequirements on the calibration samples, are listed in App. D.4 and App. D.3. To be consistent with the preselection requirement on the proton momentum, a boundary at $p = 9.3\,\text{GeV}/c$ is set by hand in the final proton binning scheme.

PID calibration for low momentum muons in Run 1

Low transverse momentum muons have no calibration sample in Run 1. The stripping line StrippingLowPTMuIDJpsiFromBLowPT was designed to study PID efficiencies of low-momentum muons in Run 1. However, it was not yet part of the official PIDCalib package, but it was used to reproduce a PID calibration efficiency map.

Particle	Requirement
Probe μ	$\chi^2_{\text{IP}} > 25$
Tag μ	isMuon $== 1$ $p_{\text{T}} > 1000\,\text{MeV}/c$ $\chi^2_{\text{IP}} > 45$
J/ψ	$\lvert m - 3096.92\rvert < 200\,\text{MeV}/c^2$ $\chi^2_{\text{vertex}}/\text{ndof} < 5$ $\chi^2_{\text{FD}} > 225$ DIRA > 0.9995

Table 3.14 – Selection criteria of the LowPTMuIDJpsiFromBLowPT stripping line, which was used to calibrate the PID response for low-momentum muons.

The stripping requirements, listed in Tab. 3.14, show that the probe muon is not required to pass a transverse momentum requirement. In general, loose criteria are applied on the probe muon and strict ones on the tag muon. $J/\psi \to \mu^+\mu^-$ decays, originating from b hadrons, are extracted with the ${}_s\mathcal{P}lot$ technique [160]. The signal component is described by a double-sided Crystal-ball (DSCB) function, while the combinatorial background is modelled by an exponential. The tail parameters of the DSCB are fixed after the fit to the simulation sample. The data fits are shown in Fig. 3.33.

The kinematic ranges of the $\Lambda_b^0 \to \Lambda(1520)\mu^+\mu^-$ and the $\Lambda_b^0 \to pK^-J/\psi(\to \mu^+\mu^-)$ samples are checked against the range of the calibration sample. The comparison is plotted in Fig. 3.34.

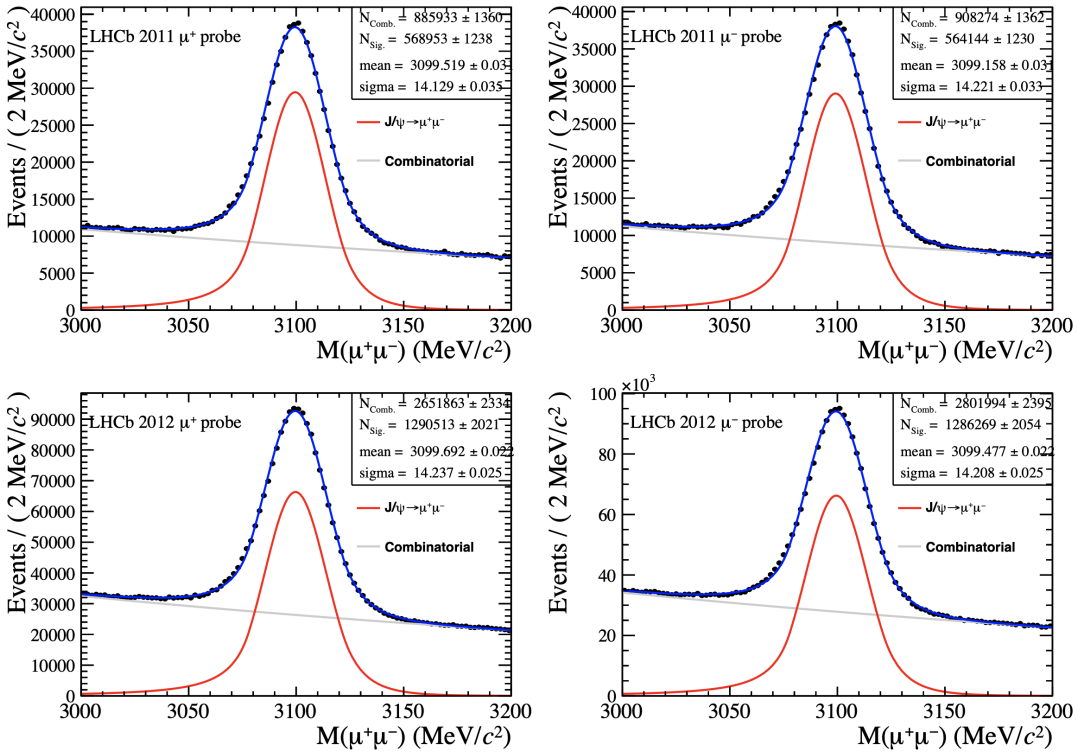

Figure 3.33 – The data fit of $J/\psi \to \mu^+\mu^-$ decays from b hadrons is shown. A stripping line without p_{T} requirements on the probe muon are used to study the PID efficiencies of low momentum muons. The fits are performed separately per muon charge and data-taking year.

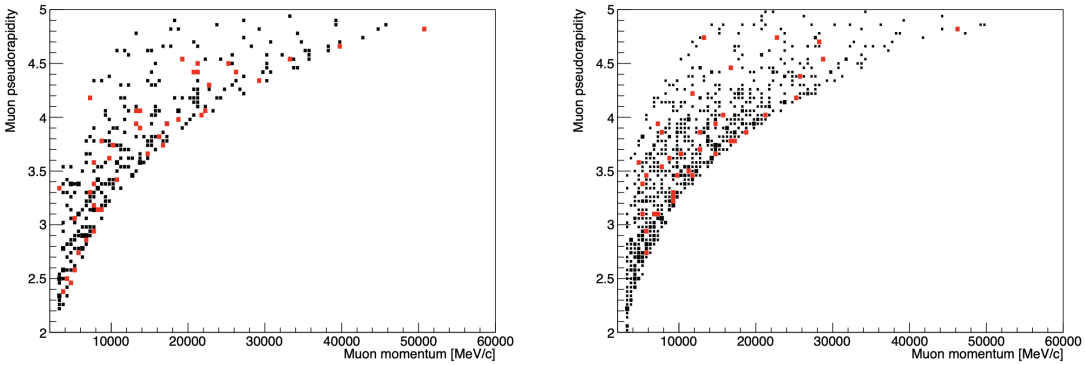

Figure 3.34 – The muon pseudorapidity and momentum are plotted for the $\Lambda_b^0 \to \Lambda(1520)\mu^+\mu^-$ and the $\Lambda_b^0 \to pK^-J/\psi(\to \mu^+\mu^-)$ sample with the condition of $p_{\mathrm{T}}(\mu) < 800$ in red. Muons from the artificial calibration sample are represented in black. On the left (right) side, the distribution is shown for the data-taking year 2011 (2012). For better visualisation, only a subsample of the calibration events is plotted.

The kinematic regions of the two decay modes overlap. Therefore, calibrating the $\Lambda_b^0 \to \Lambda(1520)\mu^+\mu^-$ decay with the $\Lambda_b^0 \to pK^-J/\psi(\to \mu^+\mu^-)$ decay mode is judged to be applicable. Therefore, the PID efficiencies of the low-momentum muons are calculated in bins of the momentum p and the pseudorapidity η with the formula

$$\varepsilon_{\text{PID}} = \frac{\sum_i w_i(\text{after PID cut applied on probe})}{\sum_i w_i(\text{before PID cut applied on probe})}. \tag{3.10}$$

The ${}_s\mathcal{P}lot$ weights w_i are extracted before and after the combination of the PID cuts MC12TuneV3_ProbNNmu > 0.1, PIDmu > -5 and IsMuon $== 1$ by a logical "and". PID efficiency maps are filled with the obtained ε_{PID} in the same muon binning scheme as before by separating them depending on the magnet polarity.

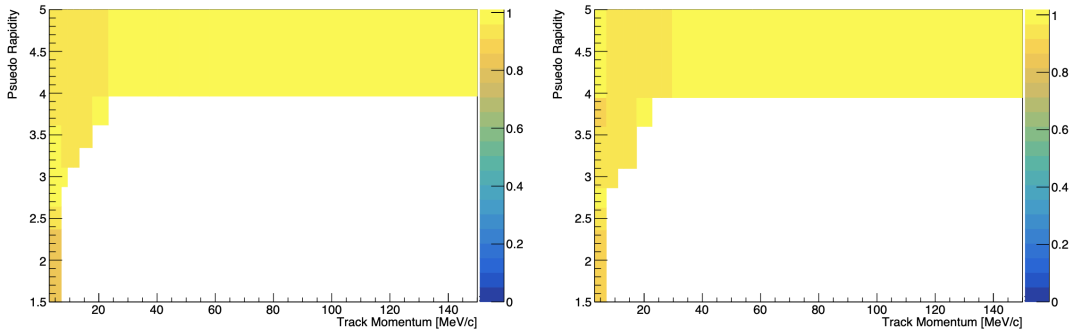

Figure 3.35 – The PID efficiency maps (MagDown) to calibrate low p_{T} muons are shown for the year 2011 (left) and 2012 (right).

To check the reliability of the obtained PID efficiency maps, the muon PID efficiency is compared in the overlapping bins. The comparison is made between the PIDCalib procedure, presented in Sec. D.4, and the one with the artificial calibration sample, shown in Fig. 3.35. The efficiency ratio is drawn in Fig. 3.36.

3.4.6 Hardware trigger correction

In the simulation samples, the emulation of a single L0 trigger threshold is applied per year. However, the L0 trigger threshold varies in data over time, following the rate of the LHC collisions. The mismodelling of the hardware trigger response is corrected in a data-driven way by the TISTOS method [179]. Therefore, the number of events, which are triggered independently of the signal decay N_{TIS} are evaluated [8]. The events out of the N_{TIS} subsample, being triggered on the signal decay, $N_{\text{TIS\&\&TOS}}$, are measured, too [9].

8. The requirement on the Λ_b^0 is translated into «L0MuonTIS || L0PhotonTIS || L0HadronTIS || L0ElectronTIS».

9. The corresponding criteria are «L0MuonTOS || L0DiMuonTOS».

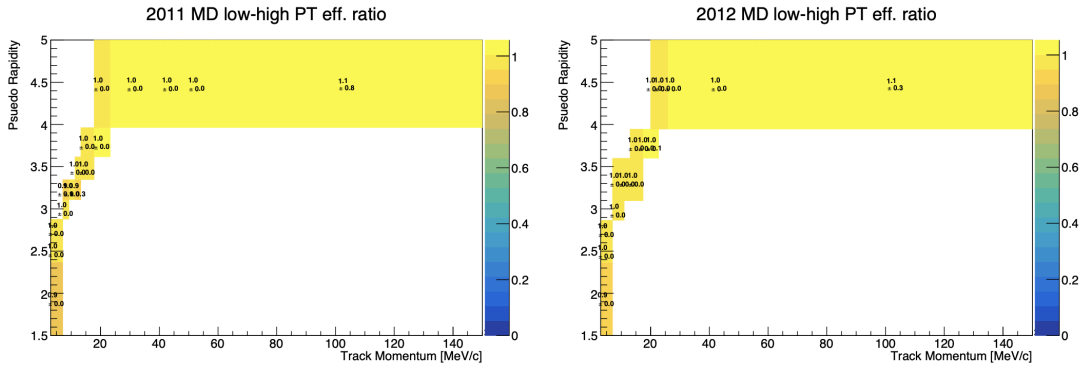

Figure 3.36 – The ratio of the muon PID efficiencies between the PID maps from the PIDCalib package and the corrections from the artificial calibration sample in the overlapping bins.

The efficiency is built as the ratio of the number of events, written as

$$\varepsilon_{\mathrm{TOS}} = \frac{N_{\mathrm{TIS\&\&TOS}}}{N_{\mathrm{TIS}}}. \tag{3.11}$$

N_{TIS} is obtained by fitting the pK^-J/ψ invariant mass. The number of TOS events in this subsample is obtained from the sum of their ${}_s\mathcal{W}eights$s. The efficiency $\varepsilon_{\mathrm{TOS}}$ is extracted on data and simulation, applying the full selection on both. The correction weights are used in the simulation sample. The dependence of the efficiency on kinematic variables is checked. The final correction is defined as the ratio

$$w_{L0} = \frac{\varepsilon^{\mathrm{data}}_{\mathrm{TOS}}}{\varepsilon^{\mathrm{MC}}_{\mathrm{TOS}}}. \tag{3.12}$$

Since the trigger response is a function of the muon momentum, the hardware trigger correction is calculated in bins of $\max\{p_{\mathrm{T}}(\mu^+), p_{\mathrm{T}}(\mu^-)\}$. The binning is chosen to be one-dimensional only. Another choice would be a two-dimensional binning in $p_{\mathrm{T}}(\mu^+)$ and $p_{\mathrm{T}}(\mu^-)$. The advantage is a larger sample size in the low $\max\{p_{\mathrm{T}}(\mu^+), p_{\mathrm{T}}(\mu^-)\}$ bins, where the data-MC difference is the largest. However, a systematic uncertainty is attributed to the different binning schemes, entering the systematic budget of the simulation corrections (see Sec.4.3). The final corrections are shown in Fig. 3.37.

After applying the hardware trigger corrections, the TISTOS efficiencies of the HLT 1 and HLT 2 triggers are calculated in the $\Lambda_b^0 \to pK^-J/\psi$ simulation and data sample, which are found to be compatible. The HLT 1 and HLT 2 efficiencies are presented in Fig. 3.38 and Fig. 3.39. The trend of the HLT 1 efficiency in Run 1 is the same in data as in simulation, but an overall shift of 3% is observed. Given that the HLT 2 efficiencies are well represented without correcting for the shift in the HLT 1 efficiencies, no systematic

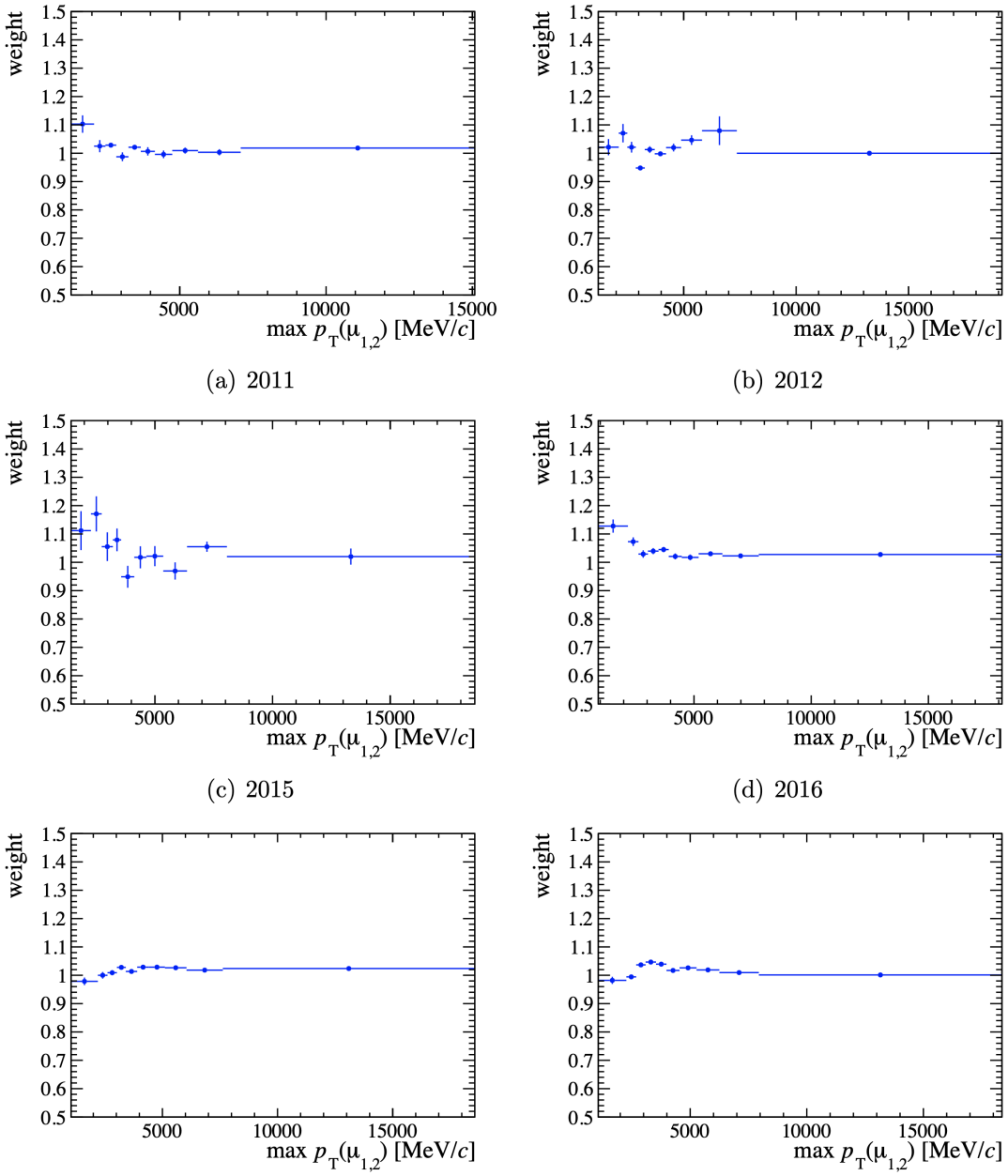

(a) 2011 (b) 2012

(c) 2015 (d) 2016

(e) 2017 (f) 2018

Figure 3.37 – Hardware trigger correction weights as a function of the maximal muon momentum for the different data taking years.

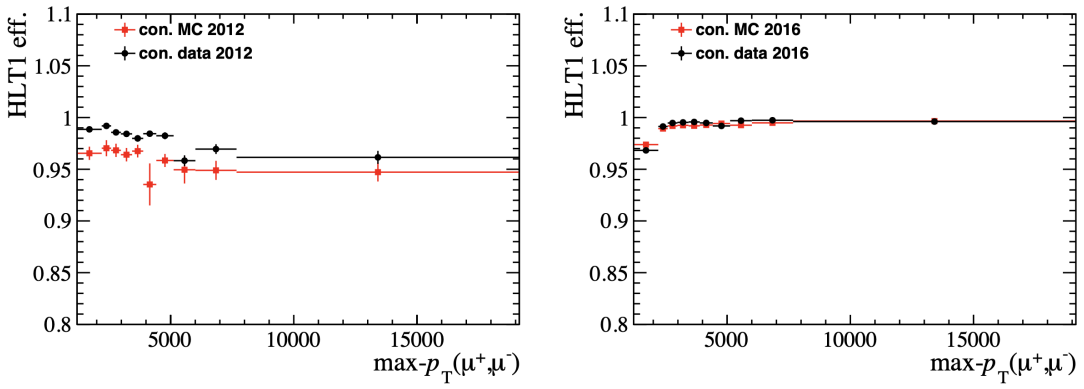

Figure 3.38 – Comparison of the HLT 1 efficiency in the control mode in data (black) and simulation (red).

uncertainty is assigned for this effect.

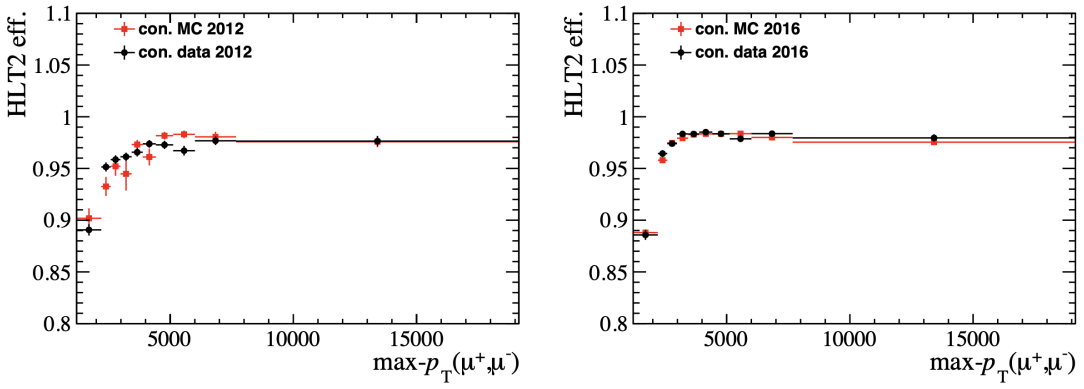

Figure 3.39 – Comparison of HLT 2 efficiencies in the control mode in data (black) and simulation (red).

3.4.7 Luminosity weight

Small differences in the invariant mass of the Λ_b^0 candidate have been seen in the signal simulation samples between the different Run periods, as visible in Fig. 3.40. Those can originate from higher pile-up conditions, which lead to worse momentum and impact parameter resolution. In addition, differences in the particle reconstruction cause changes of the Λ_b^0 mass tails. Therefore, it was decided to introduce weights, which scale the simulation samples from different year periods as it is expected from the luminosity for each year $\mathcal{L}_y$, given in Tab.3.1. The weights are then calculated as

$$w_y = \frac{\mathcal{L}_y}{\sum_i \mathcal{L}_i} \times \frac{N_y}{\sum_j N_j}. \tag{3.13}$$

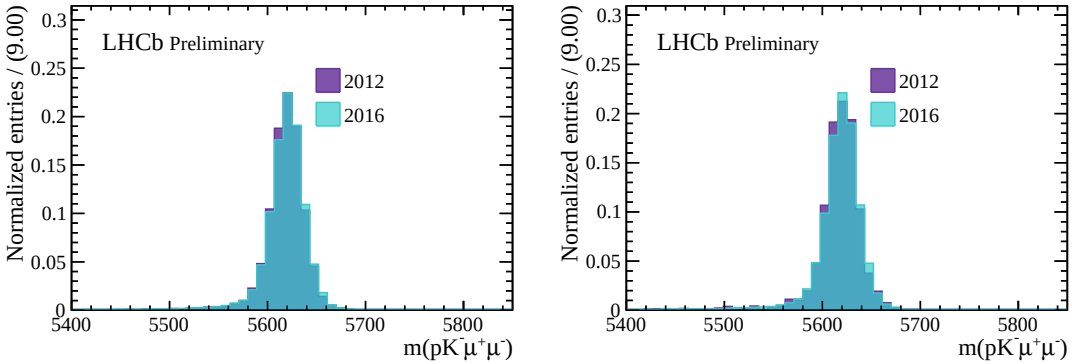

Figure 3.40 – Comparison of Λ_b^0 invariant mass distribution in the rare q^2 region of the $\Lambda_b^0 \to pK^-\mu^+\mu^-$ simulation samples (left) and the J/ψ bin of the $\Lambda_b^0 \to pK^- J/\psi$ samples (right).

N_y denotes the number of entries in the specific simulation sample.

For most of the background simulation samples, only the years 2012 and 2016 are available. For most of the decays, there is no big difference between the two years. Only for the $B_s^0 \to K^+K^- J/\psi$ and $B_s^0 \to K^+K^- \psi(2S)$ simulation samples an important discrepancy is visible, as shown in Fig. 3.41. This discrepancy is probably due to the lower momentum of the protons in Run 1 than in Run 2, because of the center-of-mass energy. Moreover, the aerogel was employed in Run 1. Therefore, the proton PID differs at low momentum, causing a difference between the 2012 and 2016 simulation samples.

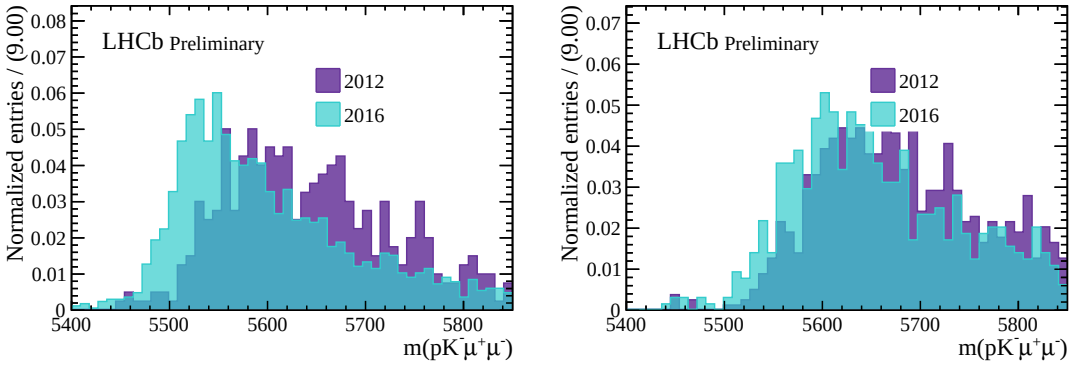

Figure 3.41 – Comparison of Λ_b^0 invariant mass distribution in the background simulation samples of the $B_s^0 \to K^+K^- J/\psi$ (left) and the $B_s^0 \to K^+K^- \psi(2S)$ (right) decay for the years 2012 and 2016.

The comparisons for other decays can be found in the App.B. Nevertheless, the luminosity weights are calculated for all samples to be consistent. The luminosity weight

calculation is this time formulated as

$$w_{2012} = \frac{\mathcal{L}_{\text{Run 1}}}{\sum_i \mathcal{L}_i} \times \frac{N_{2012}}{\sum_{j\in\{2012,2016\}} N_j}, \tag{3.14}$$

$$w_{2016} = \frac{\mathcal{L}_{\text{Run 2}}}{\sum_i \mathcal{L}_i} \times \frac{N_{2016}}{\sum_{j\in\{2012,2016\}} N_j}. \tag{3.15}$$

Because of the small data sample size, the data and simulation samples for different data-taking years are merged. The sizes of the simulation samples are initially not scaled to the expected luminosity. Therefore, it is essential to use the luminosity weight.

3.4.8 Impact of the correction weights on the angles

In this section, the impact of the correction weights on the angular distributions is studied. The first weight is the decay model weight, which exists only for the J/ψ mode. Its application has a large impact on the angular distributions, as shown in Fig. 3.42. The decay model weight needs to be applied on both generator and reconstruction level samples. However, since these weights modify the assumption of flat generated angles, the decay model weights are not taken into account in the calculation of the angular acceptance.

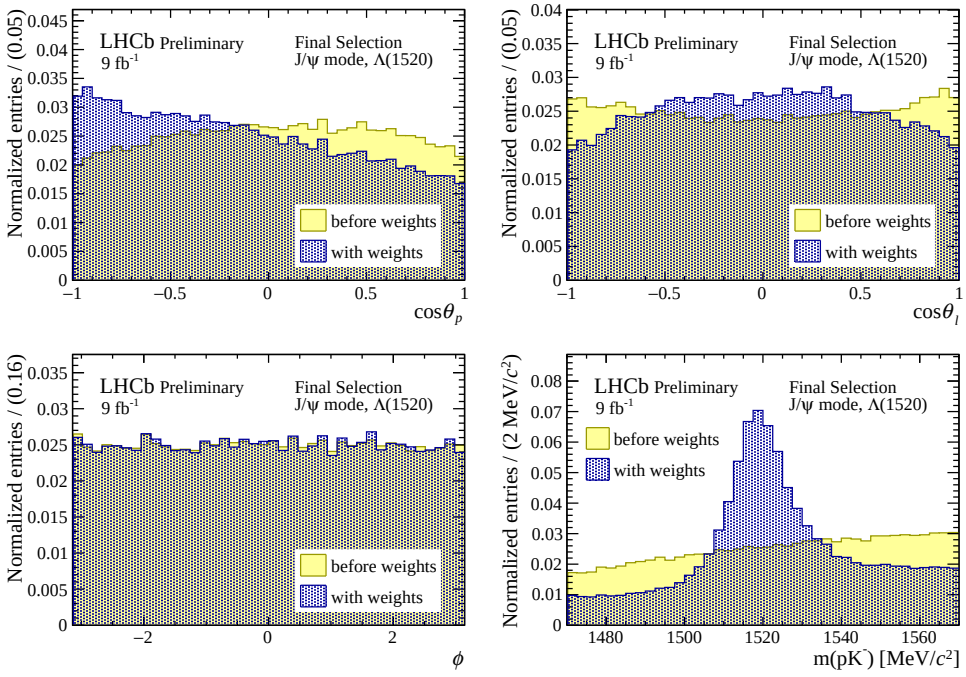

Figure 3.42 – Effect of the decay model correction weights on the angular and pK^- invariant mass distributions in the J/ψ mode.

All the other correction weights are tested on $\Lambda_b^0 \to \Lambda(1520)\mu^+\mu^-$ and $\Lambda_b^0 \to pK^- J/\psi$

phase space simulation samples. In summary, the correction weights have only a tiny impact on the angular distributions. Neither the lifetime weights, the hardware trigger weights, the PID weights nor the multiplicity weights have an impact on the angles. The correction of the Λ_b^0 transverse momentum causes a slight change of the $\cos\theta_p$ distribution. The impact is represented in Fig. 3.43, where it is exemplarily shown for the rare mode.

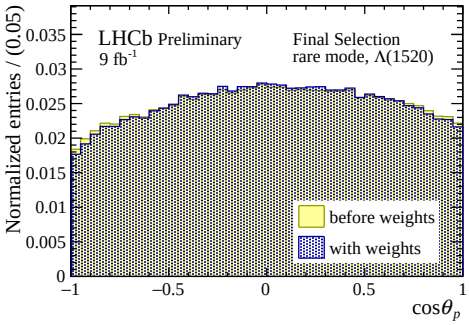

Figure 3.43 – Effect of the $p_{\mathrm{T}}(\Lambda_b^0)$ correction weights on the $\cos\theta_p$ distribution, which is checked with the $\Lambda_b^0 \to \Lambda(1520)\mu^+\mu^-$ simulation sample in the rare q^2 region.

The last weight is the luminosity weight, which impacts the $\cos\theta_p$ and $\cos\theta_\ell$ distributions slightly, as seen in Fig. 3.44. All of the weights are applied consecutively. The effect of the correction weights on the angular distributions is considered in the angular acceptance calculation, presented in Ch. 4.1.

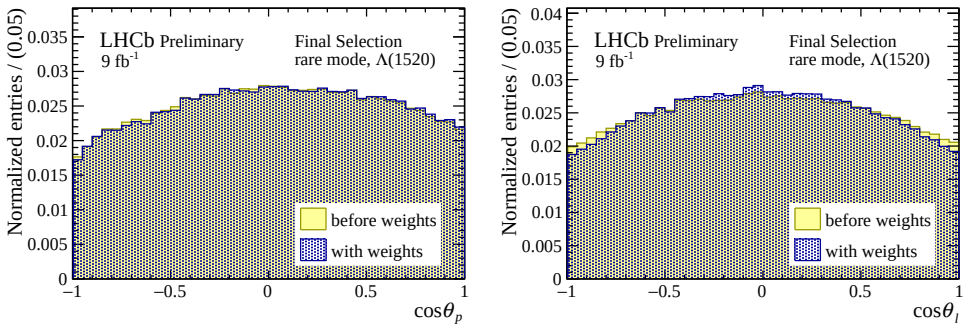

Figure 3.44 – Effect of the luminosity correction weights on the $\cos\theta_p$ and $\cos\theta_\ell$ distributions, plotted with the $\Lambda_b^0 \to \Lambda(1520)\mu^+\mu^-$ simulation sample in the rare q^2 region.

3.5 The Λ_b^0 mass fit

As discussed in section 3.3, certain background decays cannot be vetoed. Therefore, they must be modelled in the unbinned maximum likelihood fit of the $pK^-\mu^+\mu^-$ invariant mass. The shapes of the background components are extracted from simulation samples, which are assumed to model the data well, and subsequently fixed in fits to data. Each of the components is described in the following.

3.5.1 Signal component

The model of $\Lambda_b^0 \to \Lambda(1520)\mu^+\mu^-$ decays is called "signal component", in the following. Since the same model is used to describe $\Lambda_b^0 \to \Lambda(1520)J/\psi$ and $\Lambda_b^0 \to \Lambda(1520)\psi(2S)$ decays, they are exceptionally included under the term "signal", even they are control modes.

The Hypatia 2 function [9] describes the signal, which is composed of a generalised hyperbolic core and two Crystal-Ball-like tails. The Hypatia function has been seen to describe the $pK^-\mu^+\mu^-$ invariant mass distribution in simulation slightly better than the double-sided Crystal-Ball function: the pulls, defined as

$$\text{Pull} = \frac{y_i^{\text{data}} - y_i^{\text{fit}}}{\Delta y_i}, \tag{3.16}$$

are closer to zero. The data points are marked as y_i^{data} and have an uncertainty Δy_i. The fit value at the same point is represented by y_i^{fit}. Nevertheless, the Crystal-Ball function gives a good description, too. Therefore, it will be used as an alternative model for the systematic uncertainty estimation of the Λ_b^0 mass modelling in Ch. 4.3.

The hyperbolic core of the Hypatia 2 function has a mean μ and a width parameter σ, which depends on the asymmetry parameter β. The core shape is defined by λ and ζ. The shape parameter ζ is fixed to the value 0.1 because of the strong correlation to the other parameters. Each of the tails has a parameter defining their start α and their shape n.

J/ψ mode

In the J/ψ and $\psi(2S)$ modes, the dilepton invariant mass can be constrained explicitly to the known mass of the respective $c\bar{c}$ resonance, which improves the mass resolution significantly. The J/ψ constraint improves the resolution of the lepton momenta, which propagates to the J/ψ resolution and consequently the Λ_b^0 resolution. The fits to the pK^-J/ψ invariant mass with and without J/ψ constraint are compared in Fig. 3.45. The

fully corrected $\Lambda_b^0 \to pK^- J/\psi$ simulation samples are used for this comparison.

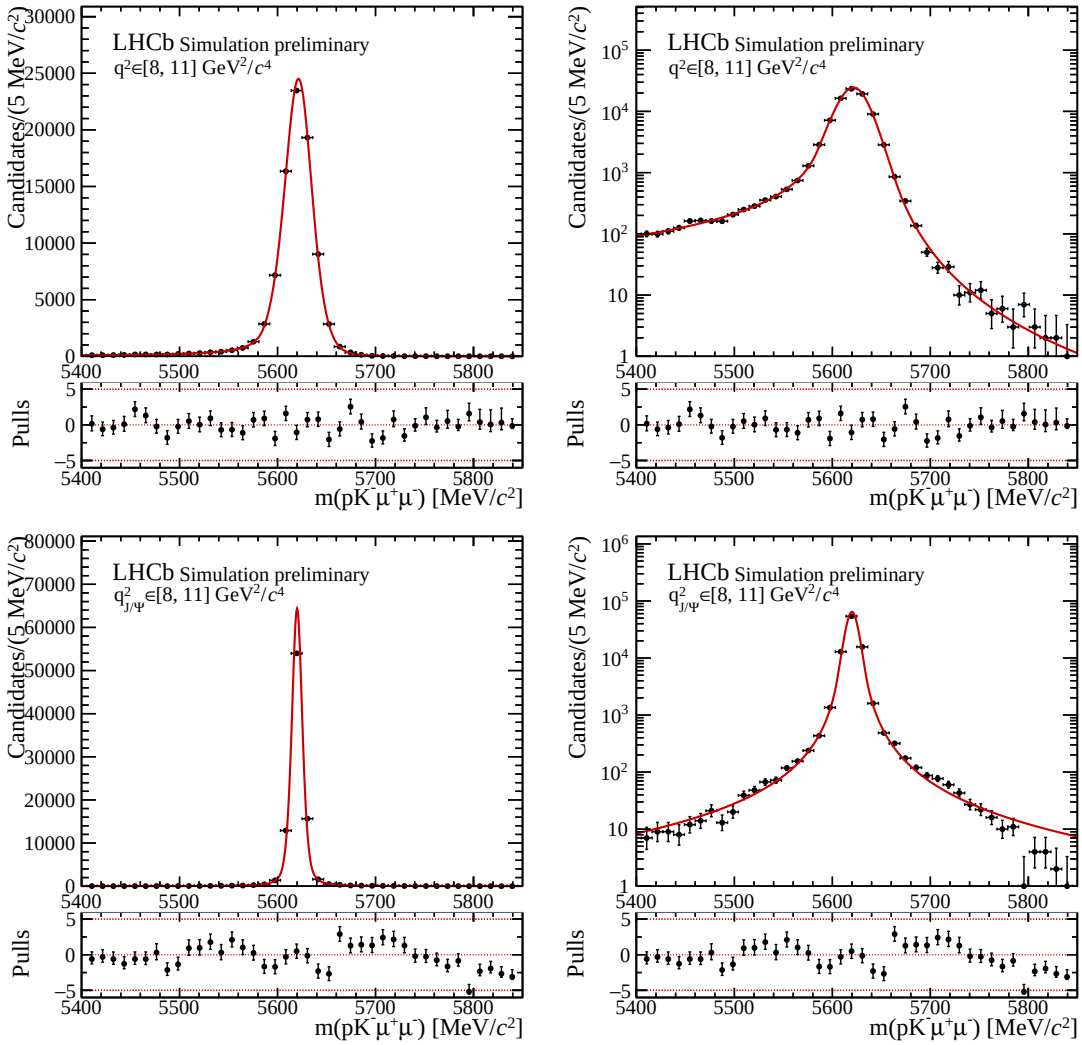

Figure 3.45 – The J/ψ-unconstrained (top) and J/ψ-constrained (bottom) $pK^-\mu^+\mu^-$ invariant mass fits to the fully corrected $\Lambda_b^0 \to pK^- J/\psi$ simulation sample are shown in the J/ψ bin. The scale of the y axis is linear on the left plot and logarithmic on the right plot.

The pulls of the unconstrained fit are all situated close to zero. Therefore, the signal model describes well the signal peak in the simulation sample. The pulls of the J/ψ-constrained fit are more spread. The kink in the distribution of the simulation sample at 5720 MeV/c^2 is not well described by the fit.

The resulting fit parameter values of the two fits are collected in Tab. 3.15. Since it is a weighted unbinned maximum likelihood fit, the parameter errors are estimated by using the asymptotic error calculation [181]. The resolution is, as expected, significantly reduced in the constrained fit. In addition, a shift in the mean value of the Λ_b^0 mass can be perceived. The tail parameters are for both fits of the same order of magnitude.

Parameter	J/ψ-unconstrained	J/ψ-constrained
μ [MeV/c^2]	5623.42 ± 0.27	5620.00 ± 0.08
σ [MeV/c^2]	17.33 ± 0.18	7.11 ± 0.09
α_L	2.22 ± 0.04	2.11 ± 0.05
n_L	1.19 ± 0.04	1.90 ± 0.05
α_R	2.32 ± 0.14	1.93 ± 0.05
n_R	3.27 ± 0.28	2.00 ± 0.05
λ	-3.18 ± 0.19	-2.50 ± 0.13
β	-0.01139 ± 0.00110	-0.00163 ± 0.00213

Table 3.15 – The rounded resulting fit parameter values of the J/ψ-unconstrained and J/ψ-constrained Λ_b^0 mass fits in the J/ψ mode are listen in this table.

However, it needs to be noted that the parameters of the J/ψ-unconstrained Λ_b^0 mass fit have larger uncertainties than in the J/ψ-constrained case. The value of β indicates a higher asymmetry in the unconstrained fit.

$\psi(2S)$ mode

Due to the lack of decay model weights for the $\Lambda_b^0 \to pK^-\psi(2S)$ simulation sample, the $\Lambda_b^0 \to \Lambda(1520)\mu^+\mu^-$ simulation sample served to model the unconstrained Λ_b^0 mass peak in the $\psi(2S)$ mode. The $\psi(2S)$-constrained Λ_b^0 mass fit is performed on the $\Lambda_b^0 \to pK^-\psi(2S)$ simulation sample. The fits are depicted in Fig. 3.46. Both fits describe well the mass distribution of the simulated sample. The $\psi(2S)$ distributions visually resemble those of the J/ψ mode. The similarity is especially visible in the unconstrained fit, which underlines that the $\Lambda_b^0 \to \Lambda(1520)\mu^+\mu^-$ sample provides in the $\psi(2S)$ mass region a good description of the Λ_b^0 mass peak, originating from $\Lambda_b^0 \to \Lambda(1520)\psi(2S)$ decays.

For the fit, the asymmetry parameter β is fixed to the value obtained in the J/ψ mode fit, such that the resolution can be compared between the two q^2 bins. The resulting parameter values are collected in Tab. 3.16. The values of the tail parameters are similar between the constrained and unconstrained fits, up to a slight difference in the n_L parameter. The mean of the $\psi(2S)$ fits is of the same order of magnitude as the J/ψ fits. The resolution is better in the constrained case and similar in the unconstrained case.

Rare mode

In the rare q^2 bins, the $\Lambda_b^0 \to \Lambda(1520)\mu^+\mu^-$ simulation sample is used for the fits, although the fits are performed in each of the q^2 bins separately. The fits of the simulated $pK^-\mu^+\mu^-$ invariant mass in the rare q^2 bins are presented in Fig. 3.47. The resulting fit

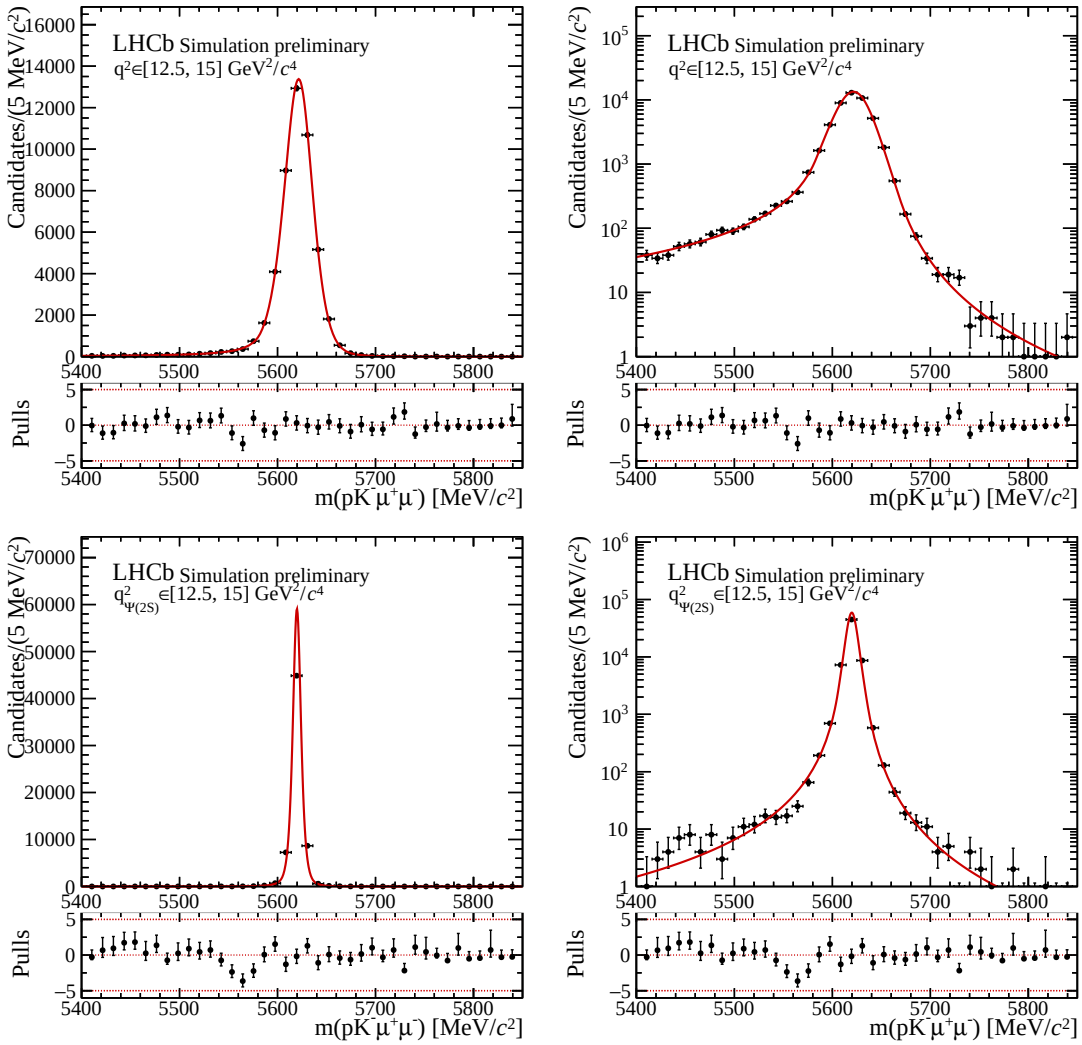

Figure 3.46 – The $pK^-\mu^+\mu^-$ invariant mass fits to the fully corrected $\Lambda_b^0 \to \Lambda(1520)\mu^+\mu^-$ simulation sample in the $\psi(2S)$ bin and the fit of the $\psi(2S)$-constrained Λ_b^0 mass to the $\Lambda_b^0 \to pK^-\psi(2S)$ simulation sample are shown.

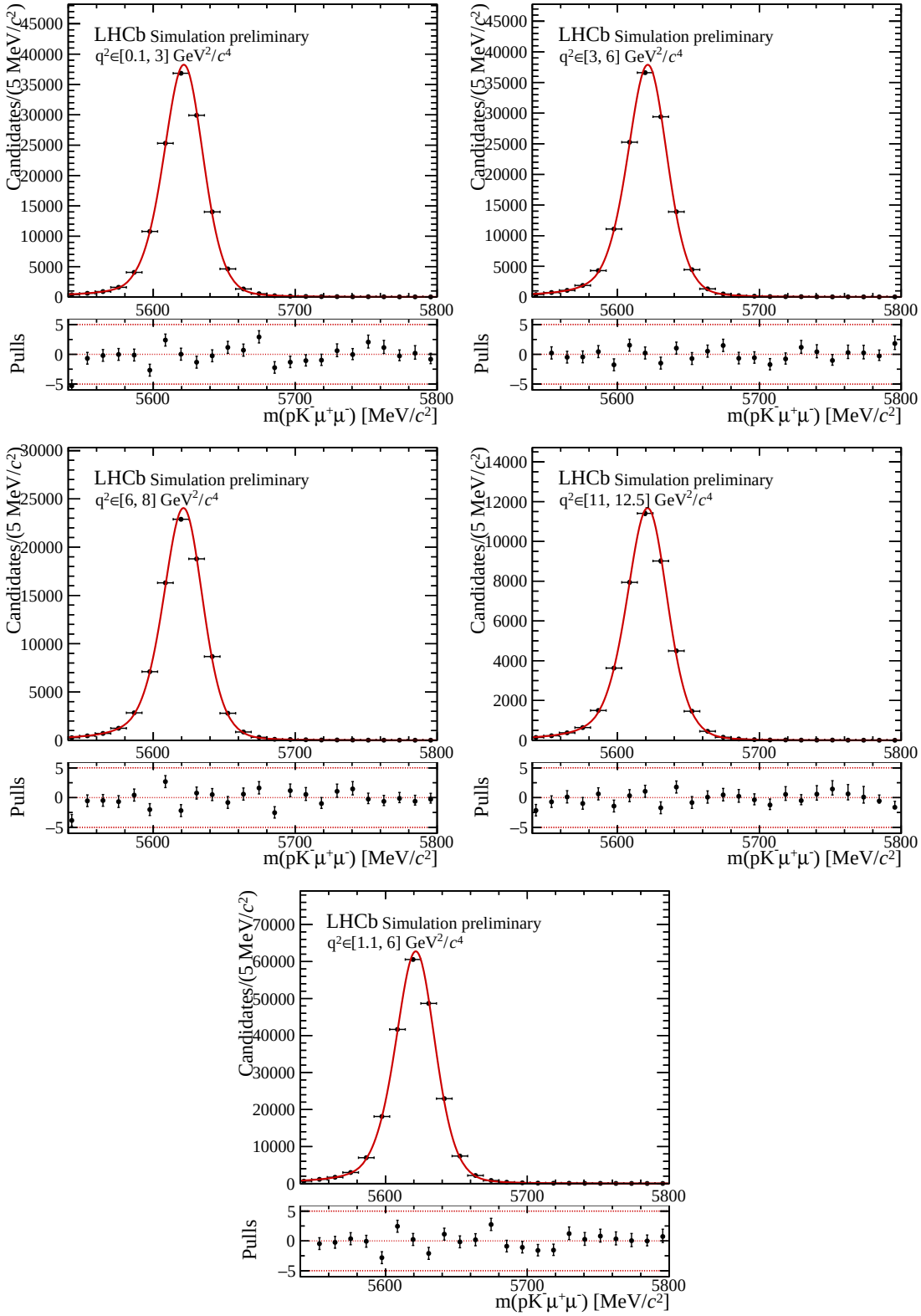

Figure 3.47 – The $pK^-\mu^+\mu^-$ invariant mass fits of the fully corrected $\Lambda_b^0 \to \Lambda(1520)\mu^+\mu^-$ simulation sample are shown. The fits are performed in all q^2 bins of the rare mode.

Parameter	$\psi(2S)$-unconstrained	$\psi(2S)$-constrained
μ [MeV/c^2]	5623.71 ± 0.08	5619.82 ± 0.02
σ [MeV/c^2]	17.91 ± 0.22	6.26 ± 0.10
α_L	2.27 ± 0.06	2.26 ± 0.11
n_L	1.40 ± 0.07	2.38 ± 0.10
α_R	2.51 ± 0.11	2.64 ± 0.23
n_R	2.94 ± 0.31	2.97 ± 0.20
λ	-3.10 ± 0.22	-1.88 ± 0.07
β	fixed to -0.01139	fixed to -0.00163

Table 3.16 – The rounded fit parameter values of the Λ_b^0 mass in simulation in the $\psi(2S)$ bin are listen in this table. A $\psi(2S)$ constraint is applied on the Λ_b^0 mass for comparison.

values are listed in the tables 3.17 and 3.18.

Parameter	$q^2 \in [0.1, 3]\,\mathrm{GeV}^2/c^4$	$q^2 \in [3, 6]\,\mathrm{GeV}^2/c^4$	$q^2 \in [6, 8]\,\mathrm{GeV}^2/c^4$
μ [MeV/c^2]	5623.54 ± 0.05	5623.38 ± 0.05	5623.24 ± 0.07
σ [MeV/c^2]	16.84 ± 0.15	17.09 ± 0.12	17.38 ± 0.25
α_L	2.49 ± 0.08	2.13 ± 0.03	2.079 ± 0.006
n_L	1.16 ± 0.16	1.75 ± 0.11	1.91 ± 0.06
α_R	2.32 ± 0.05	2.35 ± 0.05	2.52 ± 0.51
n_R	2.11 ± 0.12	2.31 ± 0.12	2.26 ± 0.57
λ	-3.55 ± 0.22	-3.38 ± 0.15	-3.12 ± 0.70
β	fixed to -0.01139	fixed to -0.01139	fixed to -0.01139

Table 3.17 – The resulting parameter values from the $pK^-\mu^+\mu^-$ invariant signal mass fit in the low q^2 bins. In the fit to data, the shape parameters are fixed to these values.

The resolution, σ, and mean, μ, values are all of the same order of magnitude. The absolute Λ_b^0 mass mean is slightly shifted with respect to the known world-average value [21]. The shape parameters are fixed in the fit to the data, while the mean and the resolution remain free-floating.

3.5.2 The $B^0 \to K^{*0}\mu^+\mu^-$ background component

As seen in Ch. 3.3.6, the $B^0 \to K^{*0}J/\psi$ contribution cannot be neglected in the $\Lambda_b^0 \to \Lambda(1520)J/\psi$ decay. Therefore, a one-dimensional kernel estimation PDF models this background by a superposition of Gaussian, which is also called `RooKeysPdf`. The

Parameter	$q^2 \in [1, 6]\,\mathrm{GeV}^2/c^4$	$q^2 \in [11, 12.5]\,\mathrm{GeV}^2/c^4$
μ [MeV/c^2]	5623.42 ± 0.04	5623.34 ± 0.09
σ [MeV/c^2]	17.15 ± 0.10	17.73 ± 0.23
α_L	2.29 ± 0.04	2.04 ± 0.06
n_L	1.44 ± 0.10	2.09 ± 0.25
α_R	2.40 ± 0.04	2.48 ± 0.12
n_R	2.17 ± 0.10	2.77 ± 0.35
λ	-3.27 ± 0.12	-3.22 ± 0.25
β	fixed to -0.01139	fixed to -0.01139

Table 3.18 – The resulting parameter values of $pK^-\mu^+\mu^-$ signal fit in the larger low q^2 bin and the bin between the two $c\bar{c}$ resonances. In the fit to data, the shape parameters are fixed to these values.

shape of this background is extracted from $B^0 \to K^{*0}J/\psi$ simulation samples, as drawn in Fig. 3.48. To prevent edge effects, when fitting to these simulated samples, the mass

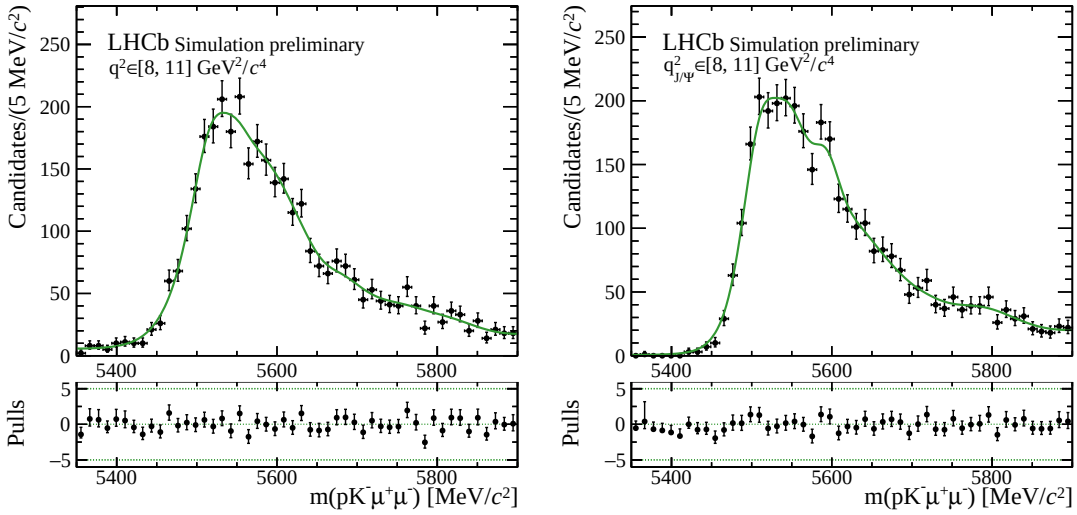

Figure 3.48 – Extraction of the shape of the $B^0 \to K^*J/\psi$ background contribution from $B^0 \to K^*J/\psi$ simulation samples in the J/ψ-unconstrained (left) and J/ψ-constrained (right) $pK^-\mu^+\mu^-$ invariant mass fit.

range is chosen to be broader than in the signal fit, and the MirrorBoth option is turned on. This background shape is used later in the fit to data, where only the yields stay free floating. Therefore, the normalisation of the distribution can change, but no mass shift be introduced.

This background needs to be modelled in the $\psi(2S)$ bin as well. The shape of the $B^0 \to K^{*0}\psi(2S)$ contribution is extracted from simulation samples, following a similar

procedure. The final shape is shown in Fig. 3.49. In the $\psi(2S)$ mode, the B^0 bump in

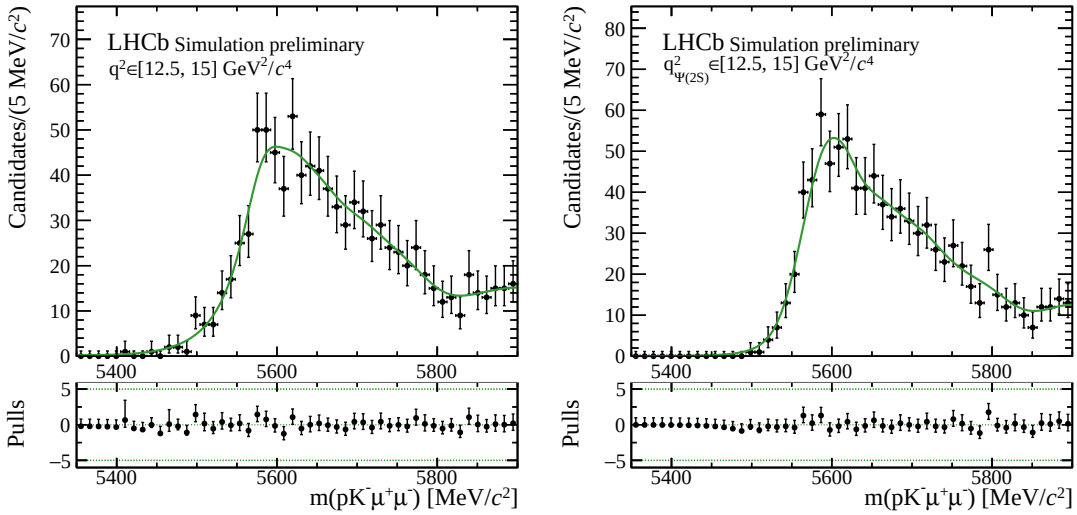

Figure 3.49 – Extraction of the shape of the $B^0 \to K^*\psi(2S)$ background contribution from $B^0 \to K^*\psi(2S)$ simulation samples in the $\psi(2S)$-unconstrained (left) and $\psi(2S)$-constrained (right) $pK^-\mu^+\mu^-$ invariant mass fit.

the $pK^-\mu^+\mu^-$ spectrum is moving closer to the Λ_b^0 mass peak than in the J/ψ bin.

In the BF analysis of $\Lambda_b^0 \to \Lambda(1520)\mu^+\mu^-$ decays [60], the misidentification background is not accounted for in the nominal fit. However, the difference between the nominal fit and the fit, including the misidentification background modelling, contributes as systematic uncertainty. In this analysis, the background is chosen to be modelled in the control mode because of the contribution calculated in Tab. 3.10, while it is obtained to be negligible in the rare mode.

3.5.3 The $B_s^0 \to K^+K^-\mu^+\mu^-$ background component

After including the $B^0 \to K^{*0}J/\psi$ background component, the fit of the pK^-J/ψ invariant mass did not converge. Enlarging the ϕ veto to $\pm 30\,\mathrm{MeV}/c^2$ around the resonance helps the convergence of the fit with a $B^0 \to K^{*0}J/\psi$ component. Unfortunately, employing such a veto leads to an 8.8% loss of signal efficiency. Although the core of the ϕ resonance is vetoed, the tail of this resonance cannot be neglected. This is the reason why it is concluded that the $B_s^0 \to K^+K^-J/\psi$ background needs to be modelled in the J/ψ mode.

The background shape is extracted from $B_s^0 \to K^+K^-J/\psi$ simulation samples and modeled by a `RooKeysPdf`. The final result can be seen in Fig. 3.50. The similar component is also modelled in the $\psi(2S)$ mode, since the contribution is expected to be higher due to its larger relative branching fraction in the $\psi(2S)$ mode. The $B_s^0 \to K^+K^-\psi(2S)$

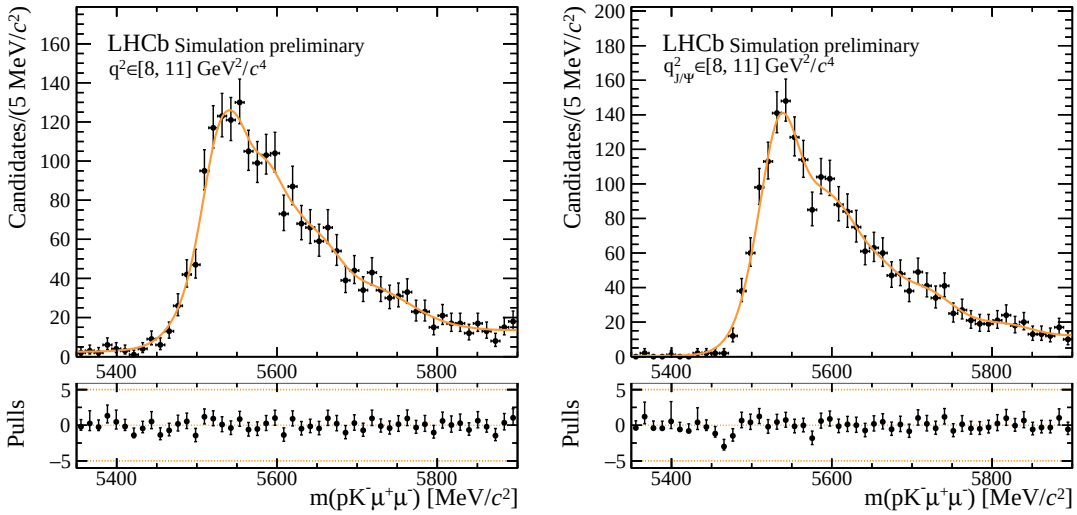

Figure 3.50 – Extraction of the shape of the $B_s^0 \to K^+K^-J/\psi$ background contribution from $B_s^0 \to K^+K^-J/\psi$ simulation samples in the J/ψ-unconstrained (left) and J/ψ-constrained (right) $K^+K^-\mu^+\mu^-$ invariant mass fit.

shape is presented in Fig. 3.51. Similarly to the B^0 case, the B_s^0 bump moves closer to the Λ_b^0 mass peak.

3.5.4 Combinatorial background component

To prevent the misidentification background from catching up some of the combinatorial background, the combinatorial background shape is evaluated in five bins of the BDT. The low BDT region $[-1.0, -0.9]$ is excluded since other backgrounds populate it, and the shape is not exponential anymore. In the high BDT region of $[0.9, 1.0]$, the $B_s^0 \to K^+K^-\mu^+\mu^-$ and the $B^0 \to K^{*0}\mu^+\mu^-$ backgrounds are present. Therefore, this region is also excluded from the background evaluation.

The Λ_b^0 mass is described by a bifurcated Crystal-Ball distribution. The shape parameters and the resolution are fixed to those obtained from the fit to the simulation sample. The Λ_b^0 mean stays free-floating in the J/ψ fits and is fixed in the $\psi(2S)$ fits to the value obtained from the J/ψ fit due to a lower amount of Λ_b^0 decays. The combinatorial background is modelled with an exponential. The fits are performed in a $pK^-\mu^+\mu^-$ invariant mass window of $[5350, 5900]\,\mathrm{MeV}/c^2$.

The fits of the $\psi(2S)$-constrained $pK^-\mu^+\mu^-$ invariant mass are presented in Fig. 3.52. The fits to the J/ψ-constrained mass are collected in App. F, in addition to the fits to the unconstrained $pK^-\mu^+\mu^-$ invariant mass in J/ψ and $\psi(2S)$ bins.

The resulting slope values, τ, of the exponential are collected in Tab. 3.19 for the fits

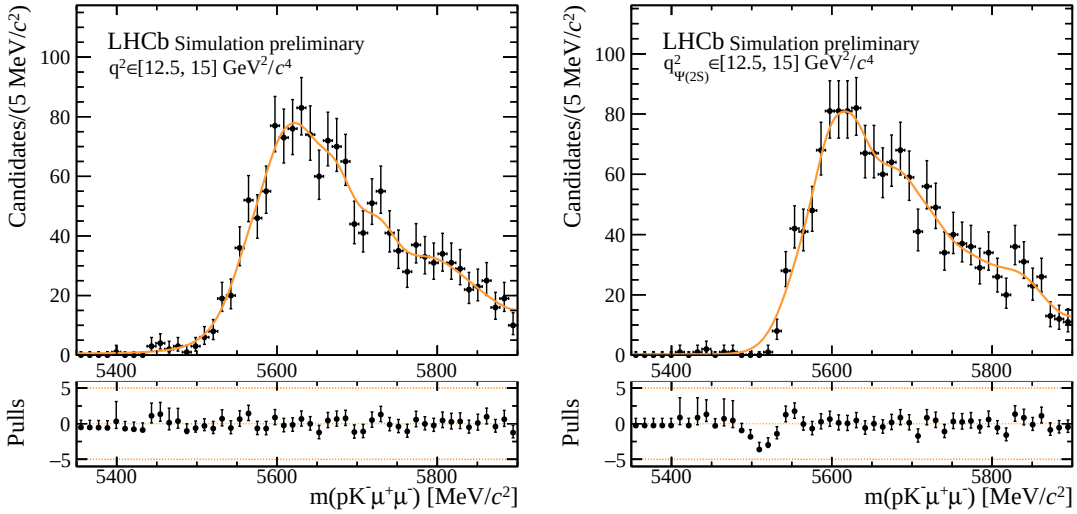

Figure 3.51 – Extraction of the shape of the $B_s^0 \to K^+K^-\psi(2S)$ background contribution from $B_s^0 \to K^+K^-\psi(2S)$ simulation samples in the $\psi(2S)$-unconstrained (left) and $\psi(2S)$-constrained (right) $K^+K^-\mu^+\mu^-$ invariant mass fit.

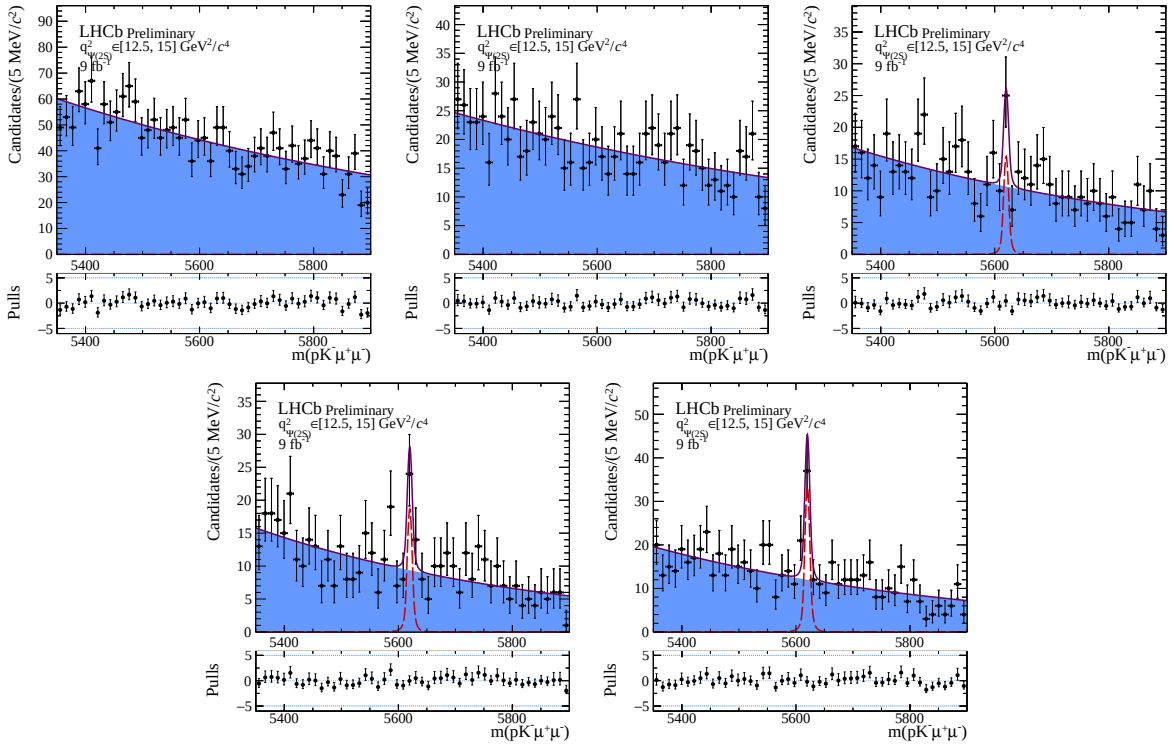

Figure 3.52 – Combinatorial background shape in the $\psi(2S)$-constrained bin is obtained by fitting the $\psi(2S)$-constrained $pK^-\mu^+\mu^-$ invariant mass in bins of the BDT. The fit results per each BDT bins are listed in Tab. 3.20.

in the J/ψ mode. The τ parameters obtained from the J/ψ-constrained and unconstrained fits are compatible with each other within one standard deviation.

BDT bin	$\tau_{J/\psi}\,[\frac{c^2}{\text{MeV}}]$	$\tau_{J/\psi\text{-constrained}}\,[\frac{c^2}{\text{MeV}}]$
$[-0.9, -0.6]$	-0.00176 ± 0.00007	-0.00177 ± 0.00007
$[-0.6, -0.2]$	-0.00187 ± 0.00010	-0.00190 ± 0.00010
$[-0.2, 0.2]$	-0.00198 ± 0.00012	-0.00192 ± 0.00012
$[0.2, 0.6]$	-0.00223 ± 0.00012	-0.00207 ± 0.00012
$[0.6, 0.9]$	-0.00222 ± 0.00010	-0.00221 ± 0.00010

Table 3.19 – The resulting τ parameter values, by fitting the combinatorial background in different bins of the BDT. The fits to the J/ψ-constrained and unconstrained $pK^-\mu^+\mu^-$ invariant mass are performed in the J/ψ bin.

The resulting slope values, τ, of the $\psi(2S)$ mode fits are collected in Tab. 3.20. The τ parameters from the $\psi(2S)$-constrained and unconstrained fits have larger discrepancies at low BDT output values than the τ values in the J/ψ case. However, compatibility of at most two standard deviations is reached. The $\psi(2S)$ bins contain a smaller data sample size than the J/ψ bin and a larger fluctuation, which are the origin of larger uncertainties of the τ parameters.

BDT bin	$\tau_{\psi(2S)}\,[\frac{c^2}{\text{MeV}}]$	$\tau_{\psi(2S)\text{-constrained}}\,[\frac{c^2}{\text{MeV}}]$
$[-0.9, -0.6]$	-0.00103 ± 0.00014	-0.00112 ± 0.00014
$[-0.6, -0.2]$	-0.00078 ± 0.00021	-0.00111 ± 0.00021
$[-0.2, 0.2]$	-0.00160 ± 0.00028	-0.00168 ± 0.00027
$[0.2, 0.6]$	-0.00174 ± 0.00029	-0.00193 ± 0.00029
$[0.6, 0.9]$	-0.00189 ± 0.00027	-0.00182 ± 0.00026

Table 3.20 – The resulting τ parameter values, by fitting the combinatorial background in different bins of the BDT. A fit of the $\psi(2S)$-constrained and unconstrained $pK^-\mu^+\mu^-$ invariant mass is performed in the $\psi(2S)$ bin.

The resulting τ values are plotted in Fig. 3.53 for the different q^2 bins. A fit is performed to the τ values as a function of the BDT value, which permits to extrapolate the τ parameter to the signal region in the BDT $\in [0.99, 1.0]$ bin. The resulting values are listed in Tab. 3.21.

The τ values in J/ψ-constrained and unconstrained bins are compatible within one standard deviation. Their uncertainty is 2-3 times smaller than for the $\psi(2S)$ bins. The τ values in the $\psi(2S)$-constrained and unconstrained bins are compatible within one standard deviation. The τ value will be fixed in the $\psi(2S)$ fit to these extrapolated values.

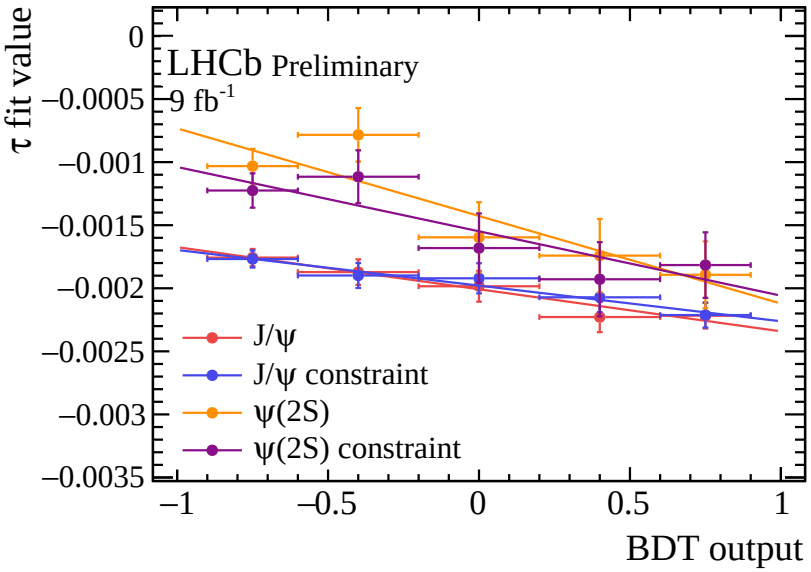

Figure 3.53 – The τ parameters, obtained by fitting the combinatorial background in bins of the BDT, are drawn.

Bin	Extrapolated τ value $[\frac{c^2}{\text{MeV}}]$
J/ψ	-0.00234 ± 0.00014
J/ψ-constrained	-0.00226 ± 0.00013
$\psi(2S)$	-0.00212 ± 0.00032
$\psi(2S)$-constrained	-0.00206 ± 0.00030

Table 3.21 – The extrapolated τ values in the different q^2 bins. They are obtained by fitting the τ values in the different BDT bins and extrapolating it to the interval of BDT $\in [0.99, 1.0]$.

It will be seen in the data fits that the resulting τ value of the J/ψ-unconstrained fit agrees within one standard deviation with the extrapolated value. In contrast, a discrepancy of six standard deviations is seen in the J/ψ-constrained case.

3.5.5 Data fits

In data, the ratio of the signal and background components depends on the q^2 bin. This is the reason why the fit strategy is explained separately for each of the q^2 regions.

J/ψ mode

Fits to the J/ψ-constrained and unconstrained $pK^-\mu^+\mu^-$ invariant mass distribution are performed. Both of them are composed of a signal component and an exponential for the combinatorial background component. The yield and the slope of the exponential are free-floating. Furthermore, $B^0 \to K^{*0}J/\psi$ and $B_s^0 \to K^+K^-J/\psi$ decays are part of the fit model. Their relative yields are extracted from data.

To extract the relative yields of the misidentification backgrounds, the proton mass hypothesis is substituted in the fully selected data sample, and separate fits are performed to the J/ψ-constrained invariant mass distributions of the $K^-\pi^+\mu^+\mu^-$, $K^+K^-\mu^+\mu^-$ and the $p \leftrightarrow K$ swapped misidentification decays. $\Lambda_b^0 \to pK^-J/\psi$ decays are vetoed, as well as other misidentification backgrounds. For example, in the fit to the $K^+\pi^-J/\psi$ distribution, an additional veto of $B_s^0 \to K^+K^-J/\psi$ decays is implemented. Each of the vetoes is of about $\pm 30\,\text{MeV}$ around the known respective b-hadron mass. For the swapped double hadron misidentification background, both of the B meson background decays are vetoed.

In App. E, the fits to the B^0 and the B_s^0 misidentification backgrounds, as well as the pK^- swapped double misidentification background, are shown. The resulting relative yields are

$$r_{B_s^0}^{J/\psi} = \frac{N_{B_s^0 \to K^+K^-J/\psi}}{N_{B^0 \to K^{*0}J/\psi}} = 0.72 \pm 0.04, \tag{3.17}$$

$$r_{p\leftrightarrow K}^{J/\psi} = \frac{N_{p\leftrightarrow K}}{N_{\Lambda_b^0 \to pK^-J/\psi}} = 0.0211 \pm 0.0014. \tag{3.18}$$

The fraction $r_{B_s^0}^{J/\psi}$ above obtained is smaller than the one obtained in the R_{pK} analysis [95] and the BF analysis [60], which are extrapolated to the full Run 1 and 2 dataset 1.25 ± 0.12 and 0.98 ± 0.09. Since the PID variables were retrained for Run 2, the ratio could differ between Run 1 and 2. Particularly in Ref. [97, 98], a difference between the background compositions in Run 1 and 2 has been observed. It needs to be kept in mind that imposing

the pK^- mass window removes the contribution of the $f_2'(1525)$, as it was seen in Sec. 3.3. However, for the two referenced analyses, a contribution of $f_2'(1525)$ is present. Due to the similar shape of the two contributions, it is better to fix their relative fraction $r_{B_s^0}^{J/\psi}$ in the data fits to the number obtained in Eq. 3.17.

The fraction $r_{p\leftrightarrow K}^{J/\psi}$ is compatible within two standard deviations with the fraction obtained by the R_{pK} analysis, extrapolated to the full Run 1 and 2 dataset [95]. An extrapolation is performed because of the different proton PID requirements in the R_{pK} analysis and yields a value of 0.0190 ± 0.0013. Therefore, the tighter PID requirements in the R_{pK} analysis are compensated by the narrower pK^- mass window in this analysis. Combining the obtained fractions of the BF measurement [60] for the Run 1 and 2 dataset leads to a fraction of $r_{p\leftrightarrow K}^{J/\psi} = 0.033 \pm 0.002$. This fraction is expected to be bigger than ours due to the wider pK^- mass window. Because this fraction is at 2% level, it is neglected in the final fit.

The data fits of the Λ_b^0 mass distribution are presented in Fig. 3.54. The J/ψ-constrained and unconstrained mass fits are both plotted. The fit to the unconstrained mass describes well the data distribution. In the fit to the J/ψ-constrained Λ_b^0 mass, a peak of the Ξ_b^0 baryon is slightly visible. However, the misidentification background shapes represent less good the data shape since it has pulls deviating from zero at around $5500\,\mathrm{MeV}/c^2$ and $5850\,\mathrm{MeV}/c^2$. The deviation seems to originate from an imprecise background shape modelling.

Parameter	J/ψ-unconstrained	J/ψ-constrained
μ [MeV/c^2]	5623.96 ± 0.10	5619.81 ± 0.04
σ [MeV/c^2]	19.94 ± 0.12	7.97 ± 0.04
N_{sig}	44302 ± 251	43373 ± 222
N_{combi}	9196 ± 256	8639 ± 233
N_{B^0}	4798 ± 162	5755 ± 129
$N_{B_s^0}$	3455 ± 225	4144 ± 248
$N_{\Xi_b^0}$	-	84 ± 27
τ [$\frac{c^2}{\mathrm{MeV}}$]	-0.00240 ± 0.00013	-0.00310 ± 0.00016

Table 3.22 – The resulting parameter values and yields are listed separately for the results of the J/ψ-unconstrained and J/ψ-constrained Λ_b^0 mass fits in data.

The fit values are summarised in Tab. 3.22. The Λ_b^0 mass mean is in the unconstrained case about 4 MeV/c^2 away from the mass in the PDG [21], while in the constrained case, the difference is of only about $0.2\,\mathrm{MeV}/c^2$. As expected, the mass resolution is significantly worse in the unconstrained case. The slope of the exponential is compatible within one standard deviation with the extrapolated τ for the J/ψ-unconstrained fit. The τ value of

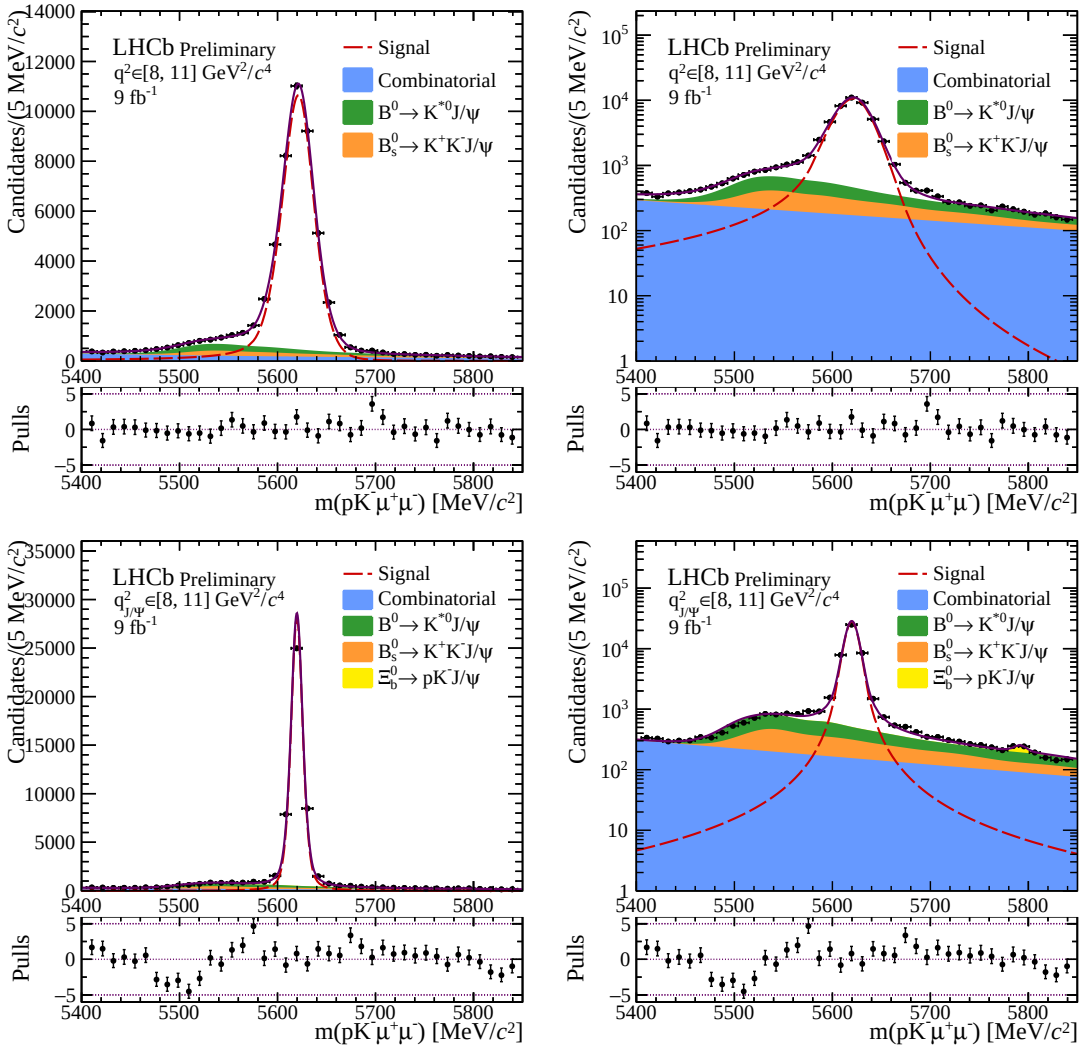

Figure 3.54 – The fits of the J/ψ-unconstrained (top) and J/ψ-constrained (bottom) $pK^-\mu^+\mu^-$ data samples are shown. The scale is linear on the left and logarithmic on the right.

the J/ψ-constrained fit is six standard deviations away from the extrapolated value. The reason for this is probably that the left shoulder of the misidentification background does fit the data worse, which is observable by the spikes in the pull distribution. Due to the worse background shape modelling, the B^0 and the B_s^0 background yields are higher in the J/ψ-constrained fit. To compensate, the signal and combinatorial background yields are about four standard deviations lower. Nevertheless, the yield difference is only about 2% with respect to the signal yield.

In the J/ψ-unconstrained fit, the yield of the combinatorial background is measured to be 20% of the signal yield. As expected, it is the dominant background. The yield of the $B^0 \to K^{*0} J/\psi$ decay is about 11% of the signal decay yield, and the $B_s^0 \to K^+K^- J/\psi$ decays 8%. These numbers are slightly higher than their estimation. In the following, the J/ψ-unconstrained Λ_b^0 mass fit is used predominantly as the control mode. The decision is based on better mass fit modelling and the similarity of the procedure with the one employed in the rare mode. Despite the different procedures in extracting ${}_s\mathcal{W}eights$, the angular distributions should be similar.

Although the fit convergence is optimised with the negative log-likelihood, the final fit quality is evaluated by the χ^2 per degree of freedom. The χ^2/ndof value of the J/ψ-unconstrained Λ_b^0 mass fit is 1.08 and 2.09 in the constrained case. Both of them are reasonably close to unity. However, the closeness of the χ^2/ndof value of the unconstrained fit to unity reflects the excellent fit quality.

$\psi(2S)$ mode

It is an interesting cross-check to test the fitting procedure in the $\psi(2S)$ bin since it is a resonant mode but with lower yields. The fitting procedure is similar to the J/ψ mode.

The relative fraction of $B^0 \to K^{*0}\psi(2S)$ yields has been calculated in this chapter to be higher than in the J/ψ mode. Therefore, this background is not negligible. Therefore, the fraction of background decays is extracted in data and calculated to be of

$$r_{B_s^0}^{\psi(2S)} = \frac{N_{B_s^0 \to K^+K^-\psi(2S)}}{N_{B^0 \to K^{*0}\psi(2S)}} = 1.2 \pm 0.2, \tag{3.19}$$

$$r_{p\leftrightarrow K}^{\psi(2S)} = \frac{N_{p\leftrightarrow K}}{N_{\Lambda_b^0 \to pK^-\psi(2S)}} = 0.023 \pm 0.012. \tag{3.20}$$

The interplay of a higher branching fraction of the $B_s^0 \to K^+K^-\psi(2S)$ decay and a lower branching fraction of the $B^0 \to K^{*0}\psi(2S)$ with comparison to the J/ψ mode, a higher $r_{B_s^0}^{\psi(2S)}$ value is expected. The fraction $r_{p\leftrightarrow K}^{\psi(2S)}$ is compatible within one standard deviation with the $r_{p\leftrightarrow K}^{J/\psi}$ fraction. Since it is measured to be very small, the swapped misidentification of the proton and kaon background is not part of the fit model.

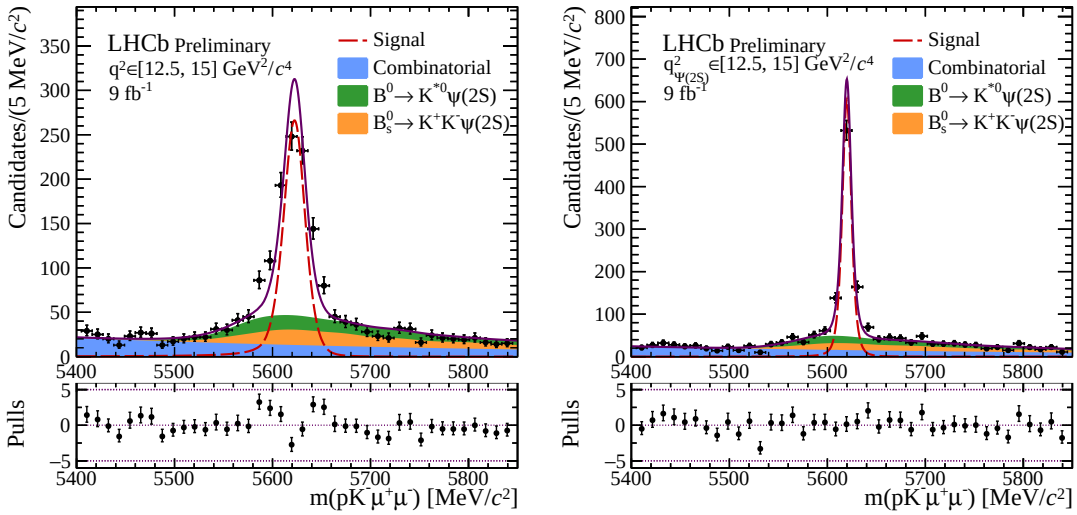

Figure 3.55 – The data fit of the $pK^-\mu^+\mu^-$ invariant mass spectrum with (right) and without (left) $\psi(2S)$ constraint is shown in the $\psi(2S)$ bin.

Both the $B_s^0 \to K^+K^-\psi(2S)$ and the $B^0 \to K^{*0}\psi(2S)$ decays are modelled in the fit. Their relative fraction is fixed to the data-driven fraction estimation in Eq. 3.19. The slope of the combinatorial background is fixed to the value calculated in Tab. 3.21, in order to ensure the correct background yield calculation.

As shown in App. G.2, the resolution of the Λ_b^0 in the $\psi(2S)$ unconstrained $pK^-\mu^+\mu^-$ invariant mass fit, is as broad as in the J/ψ unconstrained fit. Because of the reduced phase-space, a smaller resolution is expected. This is why the resolution of the $\psi(2S)$-unconstrained fit, $\sigma_{\psi(2S)}$, has been fixed to a function of the resolution of the J/ψ-unconstrained fit, $\sigma_{J/\psi}$, which is expressed as

$$\sigma_{\psi(2S)} = \sigma_{J/\psi}\sqrt{\frac{m_{\Lambda_b^0} - m_p - m_{K^-} - m_{\psi(2S)}}{m_{\Lambda_b^0} - m_p - m_{K^-} - m_{J/\psi}}} = 13.54 \tag{3.21}$$

The final fit projection is drawn in Fig. 3.55. The resulting yields are summarised in Tab. 3.23. The signal yields are compatible within one standard deviation. The individual background yields are compatible within up to three standard deviations. The resolutions of the constrained fits in the J/ψ, and $\psi(2S)$ regions are difficult to compare since the DecayTreeFitter algorithm adapts the momenta of the final state particles in the J/ψ mode, while this algorithm is not used in the $\psi(2S)$ constraint.

The ratio of the Λ_b^0 yields in the $\psi(2S)$ mode and the J/ψ mode are for the constrained and unconstrained fit of $(1.67 \pm 0.07)\%$ and $(1.67 \pm 0.08)\%$. The ratio is compared to the results of previous analyses in Tab. 3.24. As can be seen, this analysis has a smaller $\Lambda_b^0 \to pK^-\psi(2S)$ yield than the previous analyses. Compared to the others, this analysis

Parameter	$\psi(2S)$-unconstrained	$\psi(2S)$-constrained
μ [MeV/c^2]	5623.68 ± 0.70	5619.87 ± 0.26
σ [MeV/c^2]	fixed to 13.52	6.98 ± 0.38
N_{sig}	741 ± 35	724 ± 32
N_{combi}	701 ± 50	814 ± 50
N_{B^0}	341 ± 26	306 ± 24
$N_{B_s^0}$	409 ± 75	367 ± 68
τ [$\frac{c^2}{\text{MeV}}$]	fixed to -0.00212	fixed to -0.00206

Table 3.23 – The resulting parameter values and yields of the unconstrained and constrained $pK^-\psi(2S)$ invariant mass fit in data are listed in this table.

focuses on the $\Lambda(1520)$ resonance, while the others analyze the full pK^- invariant mass spectrum. In addition, the full Run 1 and 2 datasets are analyzed.

	Run1	2016
Ref. [95]	$(2.48 \pm 0.12)\%$	$(2.43 \pm 0.12)\%$
Ref. [182]	$(2.74 \pm 0.13)\%$	
Ref. [60]	$(2.62 \pm 0.16)\%$ (2012)	$(2.64 \pm 0.13)\%$
This analysis	$(1.67 \pm 0.08)\%$	

Table 3.24 – Ratio of $\Lambda_b^0 \to pK^-\psi(2S)$ yields over the $\Lambda_b^0 \to pK^-J/\psi$ yields.

The χ^2/ndof of the fit to the unconstrained $pK^-\psi(2S)$ invariant mass distribution is 1.29, and in the constrained fit it is about 0.92, which are both reasonably close to one.

Rare q^2 bins

The dominant background in the rare mode is the combinatorial one, which is modelled by an exponential. Contributions from $B^0 \to K^+\pi^-\mu^+\mu^-$ and $B_s^0 \to K^+K^-\mu^+\mu^-$ decays are calculated to be negligible, but their yield uncertainties are large in comparison to their yields. It has been decided to choose the lower bound of the Λ_b^0 mass window to be $5540\,\text{MeV}/c^2$, such that the exponential could eventually include contributions from B^0 and B_s^0 decays in the bins below the J/ψ resonance. Due to the small data sample size, the expected tininess of the background contribution and the large uncertainties of the theoretical predictions in this q^2 region, the description is acceptable.

The width of the Hypatia 2 function, describing the signal, is found to vary in the different q^2 bins. Thanks to the large data sample size in the J/ψ bin, the resolution of the Λ_b^0 mass peak is well-known in this bin. However, the Λ_b^0 mass resolution depends

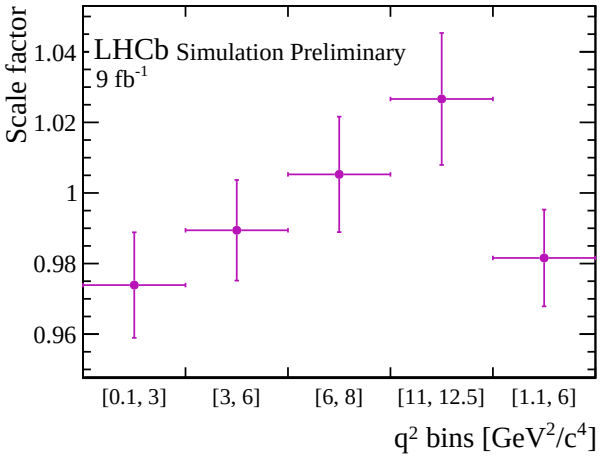

Figure 3.56 – The scale factor α of the ratio of the Λ_b^0 mass width in the different q^2 bins in the simulation sample.

on the available phase space and has, therefore, to be scaled by a scale factor. The scale factor α is the ratio of the Λ_b^0 mass resolutions of the simulation samples, which has been calculated as shown in Fig. 3.56. The full formula is written as

$$\sigma_{\text{rare}}^{\text{data}} = \alpha \sigma_{J/\psi}^{\text{data}}, \tag{3.22}$$

$$\alpha = \frac{\sigma_{\text{rare}}^{\text{MC}}}{\sigma_{J/\psi}^{\text{MC}}}. \tag{3.23}$$

In the data fits to the rare mode, the mean of the Λ_b^0 mass distribution changed depending on the different q^2 bin. Since there is no physical reason for this variation, the mean has been fixed to the value obtained in the J/ψ bin. This effect is accounted for as systematic uncertainty.

The projections of the fit in data can be seen in Fig. 3.57. The pulls in all these fits are close to zero. In the q^2 bin between 6 and 8 GeV^2/c^4, a statistical fluctuation is the reason why the Λ_b^0 mass peak in data seems to be a bit lower than the maximum of the total fit lineshape. The corresponding fit parameter values and yields are listed in Tab. 3.25 and 3.26.

The slope of the exponential, τ, is compatible within one standard deviation between all of the bins. The χ^2 of the fits are all below unity, in-between 0.43 and 0.92. This means that the fit tends to describe the data slightly too well for the available data sample size.

In summary, the $pK^-\mu^+\mu^-$ invariant mass is fitted in the rare, J/ψ and $\psi(2S)$ mode. All of the fits describe well the data. The J/ψ and $\psi(2S)$-constrained and unconstrained fits are compared with each other. The J/ψ-unconstrained fit has pulls closer to zero, which is the reason why the unconstrained fits are retained as a reference.

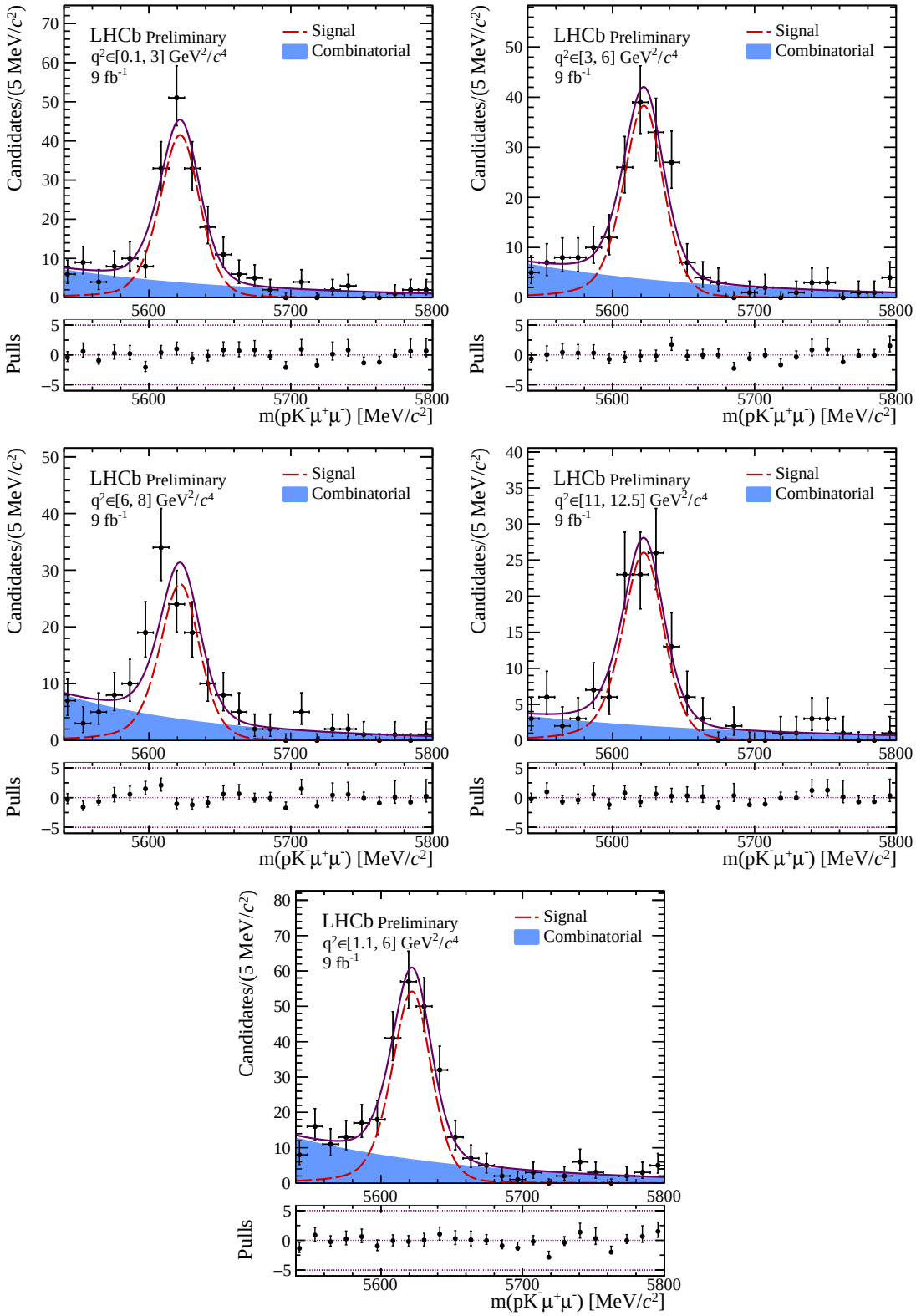

Figure 3.57 – The $pK^-\mu^+\mu^-$ invariant mass fits performed on data, separately for each of the q^2 bins in the rare mode.

Parameter	$q^2 \in [0.1, 3]\,\mathrm{GeV}^2/c^4$	$q^2 \in [3, 6]\,\mathrm{GeV}^2/c^4$	$q^2 \in [6, 8]\,\mathrm{GeV}^2/c^4$
$\mu\ [\,\mathrm{MeV}/c^2\,]$	fixed to 5623.96	fixed to 5623.96	fixed to 5623.96
$\sigma\ [\,\mathrm{MeV}/c^2\,]$	fixed to 16.80	fixed to 17.07	fixed to 17.34
N_{sig}	145 ± 14	135 ± 14	97 ± 13
N_{bkg}	335 ± 116	332 ± 113	452 ± 166
$\tau\ [\frac{c^2}{\mathrm{MeV}}]$	-0.0074 ± 0.0018	-0.0073 ± 0.0018	-0.0092 ± 0.0019

Table 3.25 – The resulting parameter values and yields of the $pK^-\mu^+\mu^-$ fit in data are shown for the low q^2 bins in the non-resonant region.

Parameter	$q^2 \in [1.1, 6]\,\mathrm{GeV}^2/c^4$	$q^2 \in [11, 12.5]\,\mathrm{GeV}^2/c^4$
$\mu\ [\,\mathrm{MeV}/c^2\,]$	fixed to 5623.96	fixed to 5623.96
$\sigma\ [\,\mathrm{MeV}/c^2\,]$	fixed to 16.93	fixed to 17.71
N_{sig}	189 ± 17	94 ± 11
N_{bkg}	656 ± 166	156 ± 69
$\tau\ [\frac{c^2}{\mathrm{MeV}}]$	-0.0079 ± 0.0014	-0.0061 ± 0.0024

Table 3.26 – The resulting parameter values and yields of the $pK^-\mu^+\mu^-$ fit in data are shown for the larger bin in the low q^2 region and the q^2 bin in-between the two $c\bar{c}$ resonances.

The $pK^-\mu^+\mu^-$ invariant mass fits are used to assign ${}_s\mathcal{W}eight$s, which are per-event-weights, corresponding to the signal probability of each of these events. With these ${}_s\mathcal{W}eight$s, the backgrounds can be subtracted from the data distributions, which are not correlated to the $pK^-\mu^+\mu^-$ invariant mass. The correlation with the $pK^-\mu^+\mu^-$ invariant mass is checked in the following section.

3.5.6 Correlations with the $pK^-\mu^+\mu^-$ invariant mass

Performing an angular fit on the ${}_s\mathcal{W}eight$ted data [160] is only valid if the correlations are negligible between the $pK^-\mu^+\mu^-$ invariant mass, where the ${}_s\mathcal{W}eight$s are extracted, and the variables of the angular fit. Therefore, the linear correlation is estimated in data by calculating the Pearson coefficient in each of the q^2 bins.

The absolute value of the correlation between the $pK^-\mu^+\mu^-$ invariant mass and the angles is in all bins smaller or equal to 1%. The corresponding correlation plots are in App. H. The biggest correlation is between the $pK^-\mu^+\mu^-$ and the pK^- invariant mass, due to the momentum resolution of the hadrons. Over- or under-estimating the momentum of one of the hadrons leads to a higher value of $m(pK^-\mu^+\mu^-)$ and the $m(pK^-)$. The corresponding correlation is at most 3%. The two-dimensional histograms, which are used to calculate the correlation, are shown in Fig. 3.58.

The correlations are judged to be small enough to perform an angular fit on the ${}_s\mathcal{W}eight$ed dataset. Consequently, ${}_s\mathcal{W}eight$s are calculated for all bins and added to the data distributions.

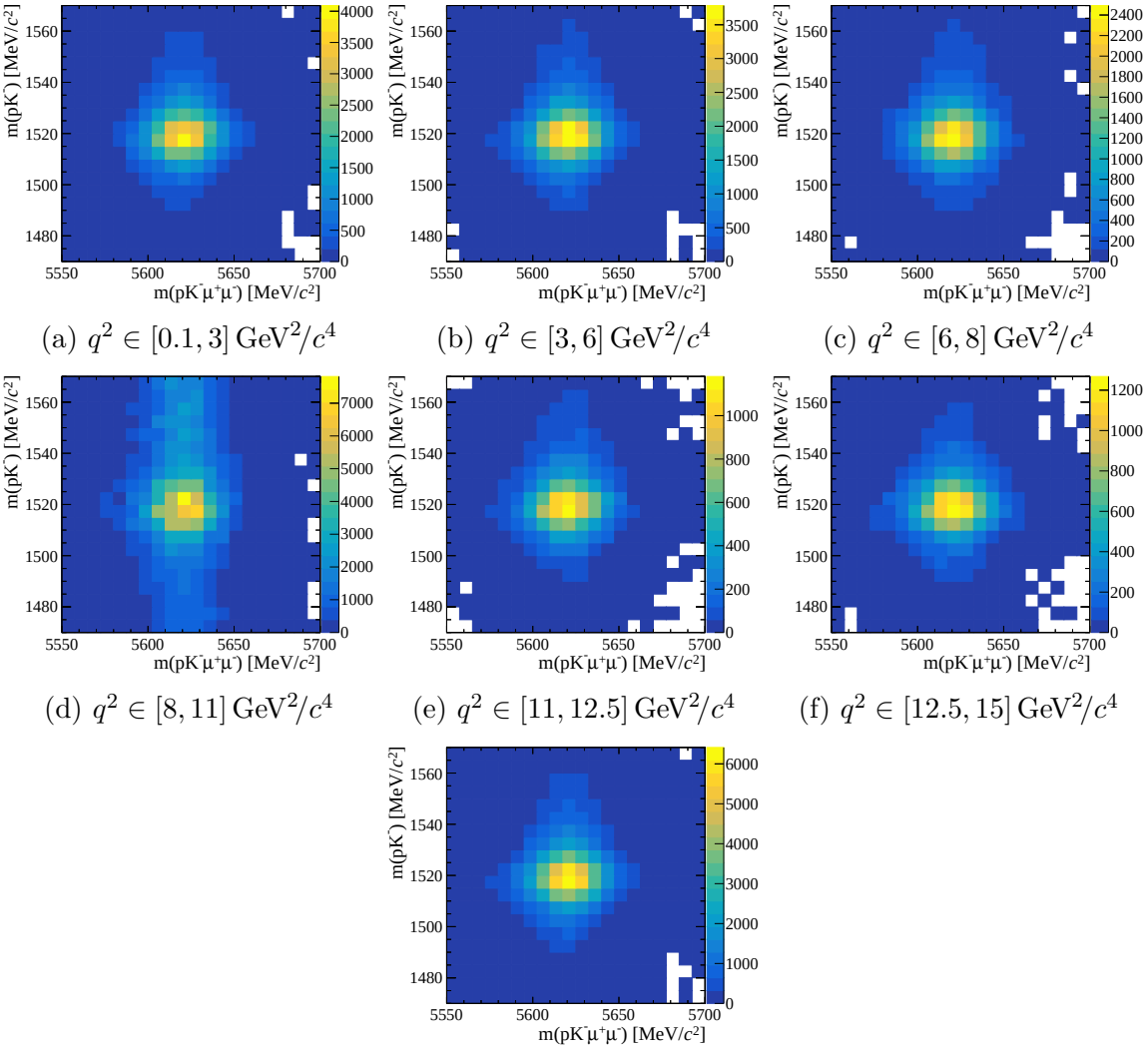

(a) $q^2 \in [0.1, 3]\,\mathrm{GeV}^2/c^4$ (b) $q^2 \in [3, 6]\,\mathrm{GeV}^2/c^4$ (c) $q^2 \in [6, 8]\,\mathrm{GeV}^2/c^4$

(d) $q^2 \in [8, 11]\,\mathrm{GeV}^2/c^4$ (e) $q^2 \in [11, 12.5]\,\mathrm{GeV}^2/c^4$ (f) $q^2 \in [12.5, 15]\,\mathrm{GeV}^2/c^4$

(g) $q^2 \in [1.1, 6]\,\mathrm{GeV}^2/c^4$

Figure 3.58 – The two-dimensional distributions of the $pK^-\mu^+\mu^-$ and pK^- invariant masses are plotted in the different q^2 bins. No strong correlation is found between the two mass distributions.

Chapter 4

Angular analysis of $\Lambda_b^0 \to \Lambda(1520)\mu^+\mu^-$ decays

This chapter focuses on the development and set-up of the angular analysis. The final aim is to measure observables in data such as $A_{\rm FB}^{\ell}$ and S_{1cc} in bins of q^2. The prerequisite is a fully selected and background-substracted data sample, which has been obtained as described in the previous chapter. The trigger, reconstruction and selection introduce a deformation of the angular distribution referred to as "angular acceptance". This distortion is accounted for with dedicated event weights, also described in this chapter.

The angular fit is developed based on our current knowledge of theoretical predictions. The angular fit is composed of many building blocks. The first blocks come from our theory predictions of the $\Lambda_b^0 \to \Lambda(1520)\mu^+\mu^-$ transition. However, one also needs to account for additional spin 1/2 resonances. Furthermore, it is crucial to account for the interferences between the different Λ^* resonances as they impact the shape of the angular distributions and, ultimately, the observables which will be measured, as shown later in this chapter. There are no theoretical predictions of the values of the possible interferences between the different Λ^* resonances. Therefore, dedicated Monte-Carlo samples with different interference schemes are employed to study these effects and their impact on the angular observables. Finally, it is also essential to state that the development of the angular fit is very much an iterative process and far from being a linear one.

4.1 Angular acceptance

The angular acceptance denotes the angular shape, which is introduced by requirements such as trigger, reconstruction and selection of the $\Lambda_b^0 \to \Lambda(1520)\mu^+\mu^-$ decay. For

example, selections on the transverse momentum of the muons have been identified to distort heavily the distribution of the $\cos\theta_\ell$ angle. As a result, the angular acceptance is extracted separately for each of the studied q^2 bins.

The distortion of the angular shape can be easily extracted from phase-space simulation samples, which are produced to be flat in the helicity angles $\cos\theta_\ell$, $\cos\theta_p$ and ϕ. The $\Lambda_b^0 \to \Lambda(1520)\mu^+\mu^-$ phase-space simulation sample is used in the rare mode. In the $\psi(2S)$ mode, two different approaches are studied. The angular acceptance is extracted from the $\Lambda_b^0 \to pK^-\psi(2S)$ simulation samples when applying the background subtraction weights, ${}_s\mathcal{W}eights$, from the $\psi(2S)$-constrained Λ_b^0 mass fit. If the ${}_s\mathcal{W}eights$ are obtained in the $\psi(2S)$ bin from the unconstrained Λ_b^0 mass fit, the angular acceptance is extracted from the $\Lambda_b^0 \to \Lambda(1520)\mu^+\mu^-$ simulated samples. This procedure is employed due to the lack of $\Lambda_b^0 \to \Lambda(1520)\psi(2S)$ simulation samples and to cross-check the two approaches. The angular acceptance in the J/ψ bin is calculated from the $\Lambda_b^0 \to pK^-J/\psi$ phase-space simulation sample. No decay model weights are applied since they distort the angular distribution, as seen in Ch. 3.4.8.

4.1.1 Angular acceptance model

An acceptance model treating the correlation between the angles correctly is set up, although a linear correlation of at most 2% between the decay angles has been calculated. The non-factorised angular acceptance is calculated via the Method of Moments (MoM) [183]. The advantage of this method, in comparison to likelihood fits, is an unbiased result, even with a small sample size.

In the following, the principle of the MoM and the extraction of the angular acceptance with the MoM are explained. The input for the calculation is the data points x_i from a distribution P, which depend on the parameter θ. The mean of the sample tends towards its expectation value with increasing sample size as

$$\overline{x} = \frac{1}{n}\sum_{i=1}^{n} y_i \xrightarrow{n\to\infty} \langle x\rangle = \int_{-\infty}^{+\infty} xP(x|\theta)dx = k(\theta). \tag{4.1}$$

$k(\theta)$ represents a function of θ. Equating the sample mean $\overline{x}$ and its expectation value $\langle x\rangle$ results into

$$\overline{x} = k(\hat{\theta}), \tag{4.2}$$

where $\hat{\theta}$ is the estimate of the parameter θ. The idea of the method is to get $\hat{\theta}$ by calculating the mean of a certain distribution.

The method can be extended to a function of the data points $f(x)$, which translates

into studying the distribution of one variable y. The mean of a function $f(x)$ is then written out as

$$\langle y \rangle = \langle f(x) \rangle = \int_{-\infty}^{+\infty} f(x) P(x|\theta) dx. \tag{4.3}$$

This described technique can be used to extract the angular acceptance ε. It depends on the three angles $\vec{\Omega} = (\cos\theta_p, \cos\theta_\ell, \phi)$ and the q^2 region. The sample mean is now denoted by M and is calculated as

$$\langle M \rangle = \int f(\cos\theta_p, \cos\theta_\ell, \phi, q^2) \varepsilon(\cos\theta_p, \cos\theta_\ell, \phi, q^2 | c_{k,l,m,n}) d\vec{\Omega} dq^2. \tag{4.4}$$

The angular acceptance can be expressed in terms of Legendre Polynomials P_L as

$$\varepsilon(\cos\theta_p, \cos\theta_\ell, \phi, q^2 | c_{k,l,m,n}) = \sum_{k,l,m,n} c_{k,l,m,n} P_{L,k}(\cos\theta_p) P_{L,l}(\cos\theta_\ell) P_{L,m}(\phi) P_{L,n}(q^2). \tag{4.5}$$

As a result, the correlations between the different variables are considered correctly. The function $f(x)$ is expressed by Legendre Polynomials in $\cos\theta_p$, $\cos\theta_\ell$, ϕ and q^2. The advantage of this choice is that the orthogonality relation of Legendre Polynomials,

$$\int_{-1}^{1} P_{L,m}(x) P_{L,m'}(x) dx = \frac{2}{2m+1} \delta_{m,m'}, \tag{4.6}$$

can be used to simplify the expression in Eq. 4.5 to

$$\langle M_{k,l,m,n} \rangle = \frac{1}{\sum_i w_i} \sum_{i=1}^{N} w_i P^i_{L,k}(\cos\theta_p) P^i_{L,l}(\cos\theta_\ell) P^i_{L,m}(\phi) P^i_{L,n}(q^2) \tag{4.7}$$

$$= \left(\frac{2}{2k+1}\right)\left(\frac{2}{2l+1}\right)\left(\frac{2}{2m+1}\right)\left(\frac{2}{2n+1}\right) c_{k,l,m,n}. \tag{4.8}$$

In conclusion, a product of Legendre Polynomials of the angles and q^2 is calculated for all data points. By summing over all data points N, an estimate of the parameters $c_{k,l,m,n}$ can be accessed. With those parameters, the angular acceptance is reconstructed.

Fourier polynomials can be used as an alternative for Legendre polynomials to parametrise the angular acceptance. The Fourier polynomials can be written as

$$P_{F,m}(x) = \begin{cases} \cos\frac{mx}{2} & \text{if } m \text{ is even} \\ \sin\frac{(m+1)x}{2} & \text{if } m \text{ is odd.} \end{cases} \tag{4.9}$$

The order of the Fourier polynomials m is a non-negative integer. Their advantage is the periodicity, which is important for the ϕ angle. The integral over the product of two

Fourier polynomials reads

$$f_{mm'} = \int_{-\pi}^{\pi} P_{F,m}(x) P_{F,m'}(x) dx = \begin{cases} 0 & \text{if } m \neq m' \\ \pi & \text{if } m = m' \neq 0 \\ 2\pi & \text{if } m = m' = 0. \end{cases} \tag{4.10}$$

Therefore, the Fourier polynomials are still orthogonal but not normalised to one.

The final angular acceptance parameters are, thus, expressed as

$$c_{k,l,m,n} = \frac{1}{\sum_i w_i} \sum_{i=1}^{N} w_i \Bigg[P^i_{L,k}(\cos\theta_p) P^i_{L,l}(\cos\theta_\ell) P^i_{F,m}(\phi) P^i_{L,n}(q^2) \\ \times \left(\frac{2k+1}{2}\right) \left(\frac{2l+1}{2}\right) f_{mm'} \left(\frac{2n+1}{2}\right) \Bigg]. \tag{4.11}$$

The advantage of the described acceptance parametrisation is the need for fewer polynomials to describe the ϕ shape sufficiently.

4.1.2 Extraction of the angular acceptance event weights

The nominal angular acceptance model contains Legendre polynomials up to order eight for describing the shape of the $\cos\theta_p$ variable. The $\cos\theta_\ell$ angle is described by even Legendre polynomials up to order four. The ϕ distribution is modelled by even Fourier polynomials up to order four. The angular acceptance is extracted in bins of q^2. Since the bins are relatively small, the q^2 distribution is not included in the acceptance model.

The angular shapes of the fully selected and corrected $\Lambda_b^0 \to \Lambda(1520)\mu^+\mu^-$ and $\Lambda_b^0 \to pK^-J/\psi$ phase space simulation samples are presented in Fig. 4.1, exemplarily for one of the rare q^2 bin and the J/ψ bin. The projections of the angular acceptance model are illustrated as a red line. The acceptance models in all the other q^2 bins are shown in App. M.1. The angular acceptance is calculated for each data event, and the inverse is saved in the data sample as per event weight. To cross-check the angular acceptance, the angular acceptance weights are calculated for the simulation sample, too. In this case, the inverse of the acceptance weights is called "correction weights" to distinguish it from the data sample.

Applying the correction weights on the simulation samples should lead to a flat distribution. In Fig. 4.2, the phase space simulation samples with the entire selection and all the corrections are shown for two q^2 bins. All the other q^2 bins are listed in App. M.2. The application of the correction weights leads, as expected, to a flat distribution.

In conclusion, the angular acceptance is extracted from phase space simulation samples. The event weights have been validated and will be used in the angular fit on data.

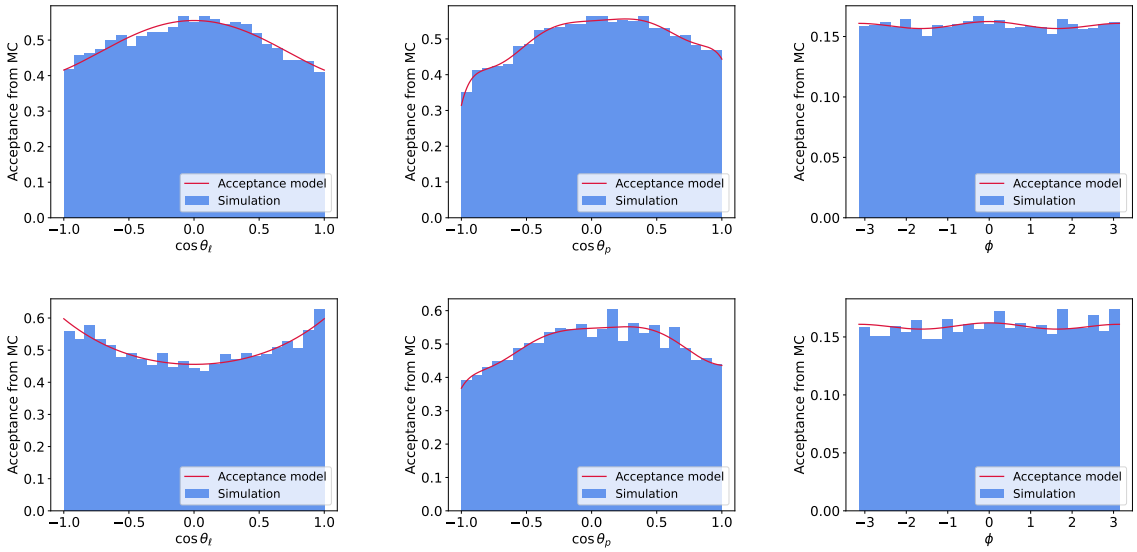

Figure 4.1 – The distributions of the $\Lambda_b^0 \to \Lambda(1520)\mu^+\mu^-$ phase space simulation samples after the full selection and the corrections are shown in blue for the $q^2 \in [3,6]\,\mathrm{GeV}^2/c^4$ bin in the top row. On the bottom row, the angular acceptance of the J/ψ bin is shown, which is extracted from the $\Lambda_b^0 \to pK^-J/\psi$ phase space simulation sample. The projections of the angular acceptance model are drawn as a red line.

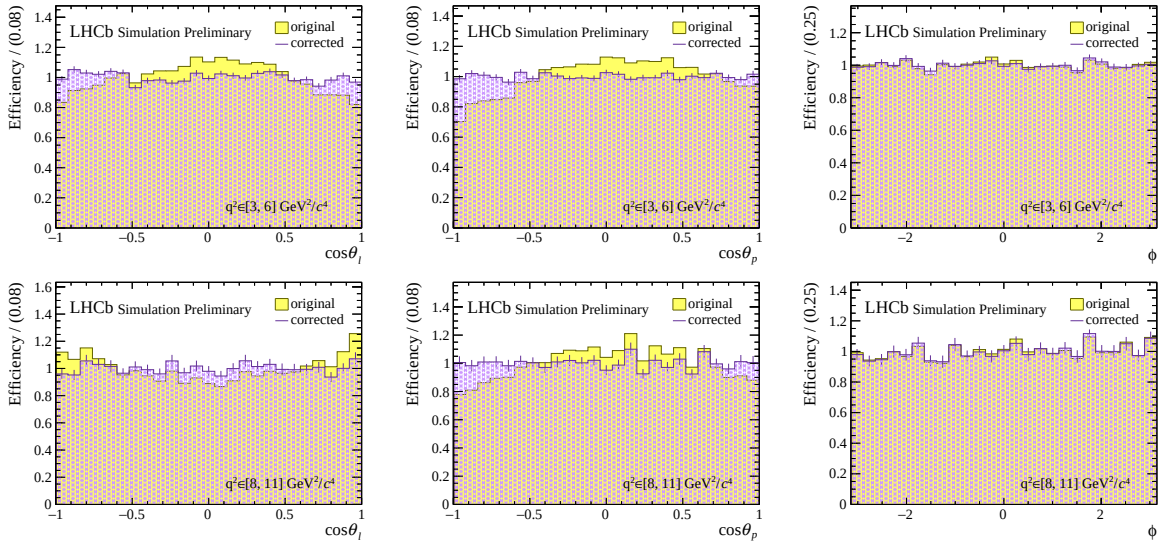

Figure 4.2 – The angular distributions of phase space simulation samples after the selection and corrections are shown in yellow. The angles with the correction weights are drawn in violet. On the top, the $q^2 \in [3,6]\,\mathrm{GeV}/c^2$ bin is drawn, and the J/ψ bin is on the bottom.

4.2 Development of the angular fit model

In this section, the angular fit model is developed step by step. It starts with the description and simplification of the angular fit component describing $\Lambda_b^0 \to \Lambda(1520)\mu^+\mu^-$ decays. The second section treats the inclusion of the spin-1/2 Λ^* resonances. Finally, the interferences between the Λ^* resonances are accounted for in the fit model.

4.2.1 Angular fit model of $\Lambda_b^0 \to \Lambda(1520)\mu^+\mu^-$ decays

The first building block to construct the angular fit model of the $\Lambda_b^0 \to \Lambda(1520)\mu^+\mu^-$ decays is the differential decay width, stated in Eq. 1.57 in Sec. 1.3.3. Since the Λ_b^0 and $\bar{\Lambda}_b^0$ decays are measured together, the differential decay width is *CP* averaged. The leptonic forward-backwards asymmetry, A_{FB}^{ℓ}, referred to as $A_{FB,3/2}$ in the rest of the text, is the main observable of interest as it carries the highest sensitivity to NP. The differential decay width in the heavy-quark limit (see Ch.1.3.3) is expressed as

$$\begin{aligned}\frac{8\pi}{3}\frac{d^4(\Gamma+\bar{\Gamma})}{dq^2 d\cos\theta_\ell d\cos\theta_p d\phi} &\simeq \frac{1}{4}\left(S_{1ss}\sin^2\theta_\ell + S_{1cc}\cos^2\theta_\ell + \frac{4}{3}A_{FB,3/2}^{\ell}\cos\theta_\ell\right) \\ &\quad\times\left(1+3\cos^2\theta_p\right). \end{aligned} \tag{4.12}$$

The final fit model is a normalised probability density function (PDF). As a result, the observables S_{1ss} can be expressed as a function of S_{1cc}. The angular PDF of the $\Lambda_b^0 \to \Lambda(1520)\mu^+\mu^-$ decay is written as

$$\begin{aligned}\mathrm{PDF}_{\mathrm{ang},3/2} = \frac{1}{4}&\left(\left(1-\frac{1}{2}S_{1cc}\right)\left(1-\cos^2\theta_\ell\right) + S_{1cc}\cos^2\theta_\ell + \frac{4}{3}A_{FB,3/2}^{\ell}\cos\theta_\ell\right) \\ &\times\left(1+3\cos^2\theta_p\right). \end{aligned} \tag{4.13}$$

The angular observables, which are aimed to be extracted, are marked in red. The derived angular PDF is based on the assumption to be within the heavy quark limit (see Ch. 1.2.2). The PDF is tested on Monte-Carlo samples, which are generated with the full angular differential decay width. The quark model form factors were used in the generation [6]. The values of the angular observables are fixed to the computed FLAVIO values in order to check the consistency with the data points. The plots are shown on the left in Fig. 4.3. The pulls show a good agreement between the dedicated MC sample, generated with the full differential decay width, and the angular PDF in the heavy-quark limit, where the angular observables are fixed to the values obtained by FLAVIO.

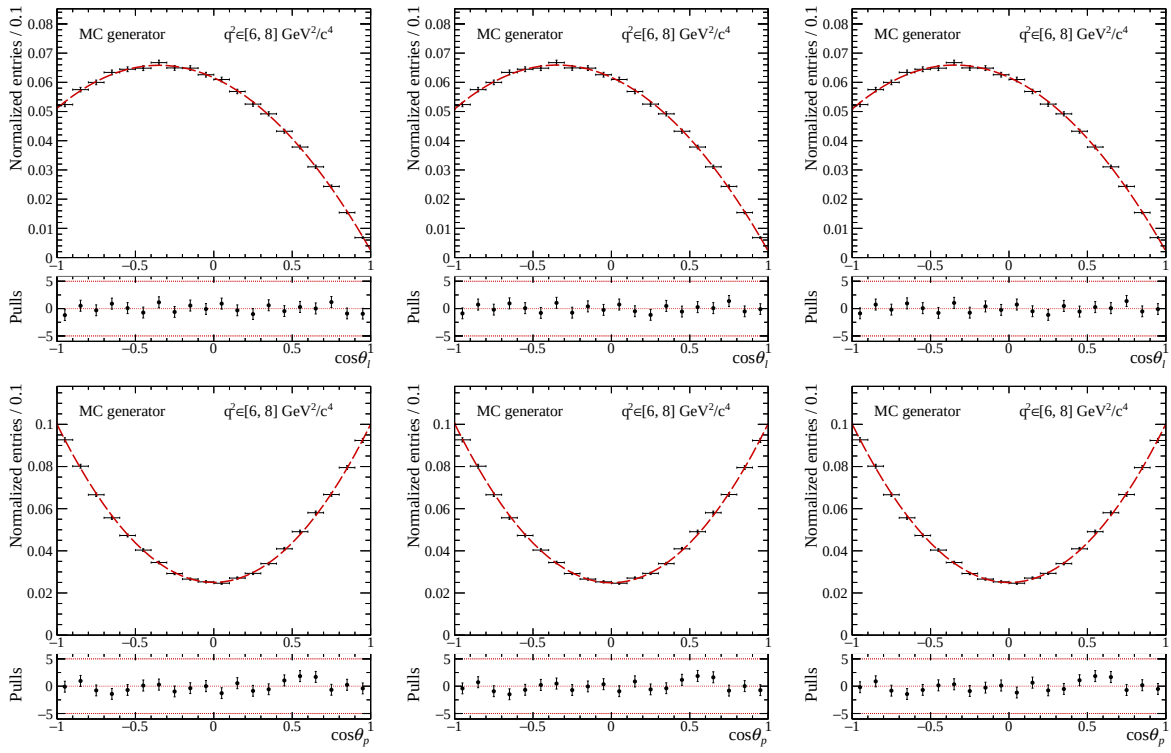

Figure 4.3 – The dedicated MC samples of the $\Lambda_b^0 \to \Lambda(1520)\mu^+\mu^-$ decays are compared to three different fit models, where the observable values are fixed to the theoretical prediction. The fit models are the angular PDF in the heavy-quark limit (left), the full PDF integrated over ϕ (middle) and the full PDF integrated over ϕ, but with ϵ_3 set to zero (right). The distributions are in the q^2 bin in the interval of $[3, 6]\,\mathrm{GeV}^2/c^4$.

Two alternative models have been tested. Instead of assuming the heavy-quark limit, both models are obtained by integrating the full differential decay width over the ϕ angle to reduce the number of observables and to obtain a better fit stability. The calculation is described in App. J. The ϕ integrated PDF is written as

$$\begin{aligned}\mathrm{PDF}_{\mathrm{ang},3/2} \quad &= \pi\left(\frac{1}{8}(6-2S_{1ss}-S_{1cc})+\frac{1}{3}(2A^{\ell}_{FB,3/2}+\epsilon_3)\cos\theta_\ell\right)\\ &+\frac{\pi}{8}(6-10S_{1ss}+S_{1cc})\cos^2\theta_\ell\\ &+\pi\left(\frac{3}{8}(6S_{1ss}+S_{1cc}-2)+(2A^{\ell}_{FB,3/2}-\epsilon_3)\cos\theta_\ell\right)\cos^2\theta_p\\ &+\frac{3\pi}{8}\left(5S_{1cc}-2S_{1ss}-2\right)\cos^2\theta_\ell\cos^2\theta_p. \end{aligned} \tag{4.14}$$

The full ϕ integrated PDF represents the second configuration. It depends on the observables S_{1cc}, S_{1ss}, $A^{\ell}_{FB,3/2}$ and ϵ_3. However, the most NP-sensitive observable remains $A^{\ell}_{FB,3/2}$. The same check has been performed as before. Fixing the angular observables to the FLAVIO values, the angular distributions correspond to the distributions of the MC samples generated with the full differential decay width. The full PDF integrated over the ϕ angle is shown in the centre plots in Fig. 4.3. Again, a good agreement is seen between the distribution in the MC sample and the PDF integrated of the ϕ angle.

We have shown in the previous chapter that with the current Run 1 and 2 datasets, we typically expect about a hundred candidates in each q^2 bin. With this in mind, we have to make sure that we reduce the complexity of the fit *i.e.* the number of free parameters, as much as possible. Hence, the values of ϵ_3, from Eq. 4.14, have been calculated with the FLAVIO implementation, listed in Tab. 4.1. In each of the bins, the ϵ_3 value is smaller or

q^2 bin $[\,\mathrm{GeV}^2/c^4\,]$	ϵ_3 value
$q^2 \in [0.1, 3]$	-0.0001 ± 0.0003
$q^2 \in [3, 6]$	-0.0006 ± 0.0083
$q^2 \in [6, 8]$	-0.0012 ± 0.0055
$q^2 \in [11, 12.5]$	-0.0035 ± 0.0033
$q^2 \in [1.1, 6]$	-0.0004 ± 0.0006

Table 4.1 – The SM prediction of the ϵ_3 values, using the FLAVIO implementation with the quark model form factors. They are compatible with zero within two Standard deviations.

equal to 1% of the $A^{\ell}_{FB,3/2}$ prediction. In addition, the ϵ_3 values are compatible with zero within at most two standard deviations. This is why ϵ_3 is set to zero in a third angular PDF configuration. The test with the full PDF integrated over the ϕ angle and setting ϵ_3 to zero is shown on the right in Fig. 4.3. The MC sample and the PDF integrated over

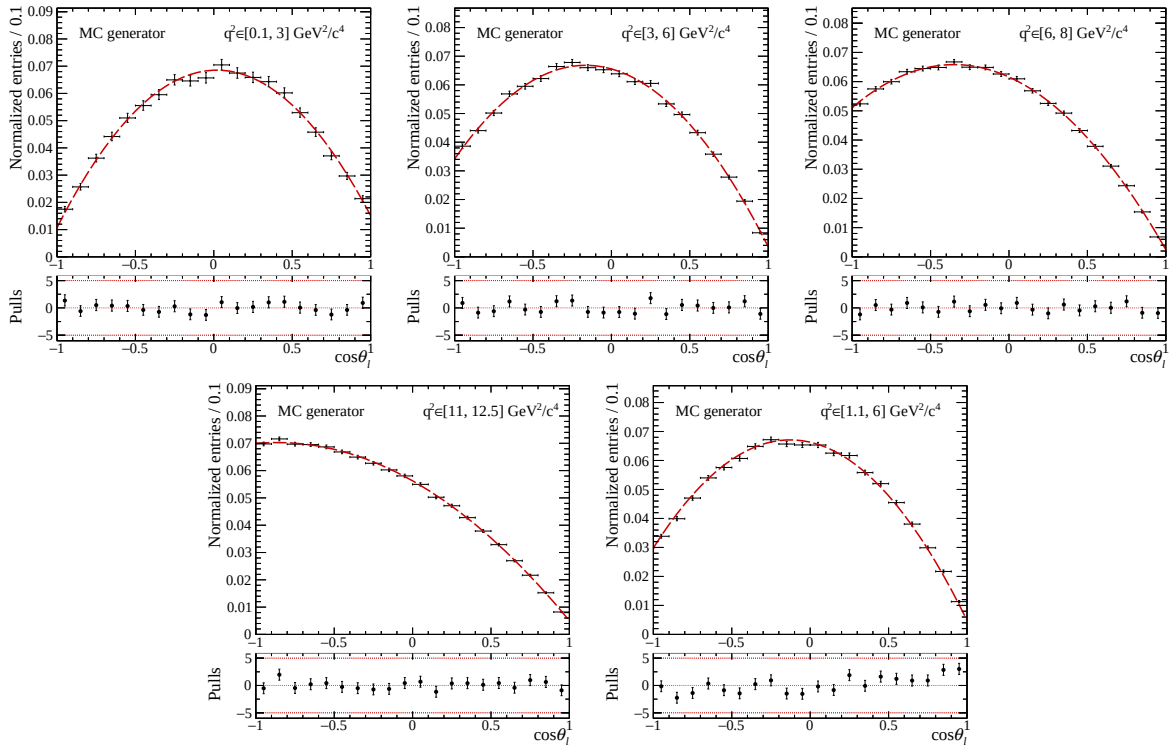

Figure 4.4 – The $\cos\theta_\ell$ contribution of the dedicated $\Lambda_b^0 \to \Lambda(1520)\mu^+\mu^-$ MC samples are shown for the different q^2 bins in the rare mode.

the ϕ angle, and setting ϵ_3 to zero, are agreeing well.

All three fit models describe well the Monte-Carlo sample. The angular PDF in the heavy-quark limit, Eq. 4.13, is chosen to be the default model since the number of free parameters is the smallest. The angular fit in the heavy quark limit is performed in all of the rare q^2 bins. The corresponding $\cos\theta_\ell$ and $\cos\theta_p$ projections are presented in Fig. 4.4 and 4.5. The angular fit is only performed in the rare q^2 bins because the angular distribution in the J/ψ and $\psi(2S)$ control mode is a priori not known and the MC samples do not describe the $c\bar{c}$ contribution.

4.2.2 Inclusion of other Λ^* resonances in the fit model

In the pK^- mass window around the $\Lambda(1520)$ resonance which carries a spin 3/2, several other Λ^* resonances contribute. In Ref. [4], these have been identified to be mainly the $\Lambda(1405)$ and the $\Lambda(1600)$ resonance, as visible in Fig. 1.15. A small contribution of the $\Lambda(1800)$ is visible, too. However, all of those resonances possess a spin of 1/2. For simplification, it was decided to treat the spin-1/2 Λ^* resonances together in one fit component.

To the best of our knowledge, no theoretical predictions are available for Λ^* 1/2

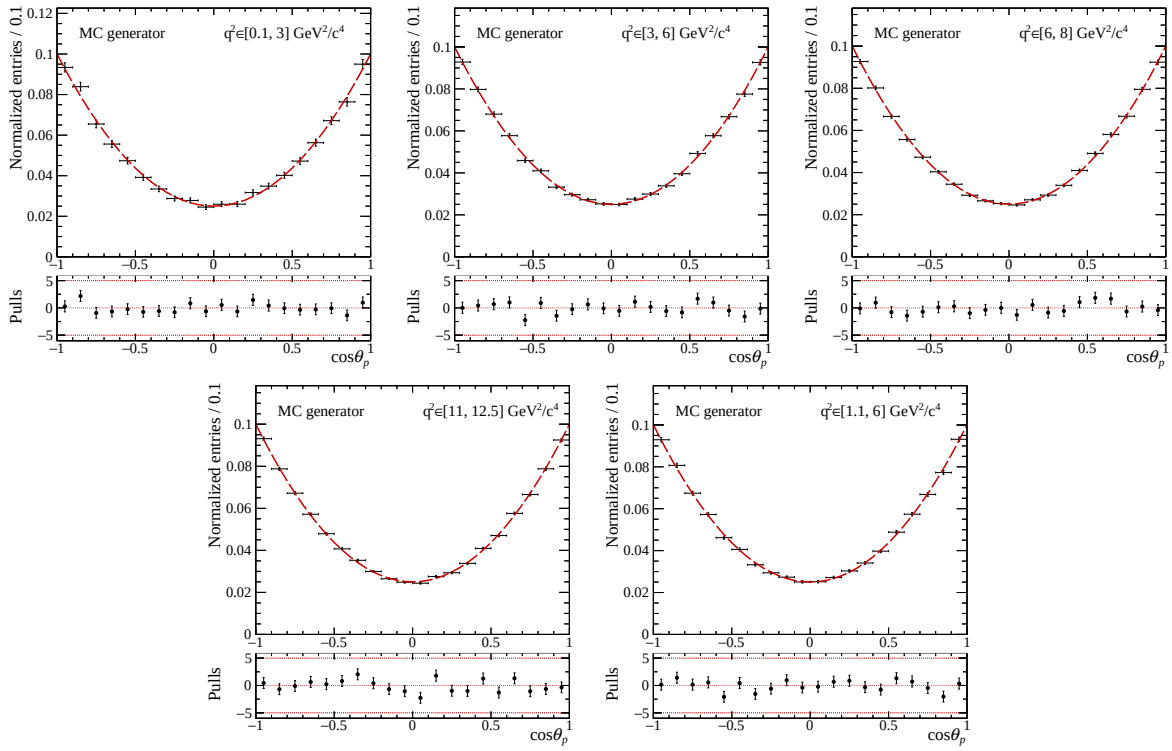

Figure 4.5 – The $\cos\theta_p$ contribution of the dedicated $\Lambda_b^0 \to \Lambda(1520)\mu^+\mu^-$ MC samples are shown for the different q^2 bins in the rare mode.

resonances, decaying strongly into a proton and a kaon. The only prediction is the differential decay width of $\Lambda_b^0 \to \Lambda^0\ell^+\ell^-$ decays with the weakly decaying ground state Λ^0 [10], which is written as

$$\begin{aligned}\frac{8\pi}{3}\frac{d^4\Gamma}{dq^2 d\cos\theta_\ell d\cos\theta_p d\phi} &= \left(K_{1c}\cos\theta_\ell + K_{1cc}\cos^2\theta_\ell + K_{1ss}\sin^2\theta_\ell\right) \\ &+ \left(K_{2c}\cos\theta_\ell + K_{2cc}\cos^2\theta_\ell + K_{2ss}\sin^2\theta_\ell\right)\cos\theta_p \\ &+ \left(K_{3sc}\sin\theta_\ell\cos\theta_\ell + K_{3s}\sin\theta_\ell\right)\sin\theta_p\sin\phi \\ &+ \left(K_{4sc}\sin\theta_\ell\cos\theta_\ell + K_{4s}\sin\theta_\ell\right)\sin\theta_p\cos\phi. \end{aligned} \tag{4.15}$$

The K_i terms represent the angular coefficients. Since the strongly decaying Λ^* resonances are studied, the differential decay width can be simplified. All the angular coefficients dependent on the weak decay parameter α vanish. K_{1ss}, K_{1cc} and K_{1c} are the only non-vanishing angular coefficients.

As before, the differential decay width is *CP* averaged and normalised. In addition, the forward-backwards asymmetry of the spin-1/2 Λ^* resonances $A^\ell_{FB,1/2}$ is introduced. The angular PDF, describing the $\Lambda_b^0 \to \Lambda^*_{J=1/2}\mu^+\mu^-$ contribution is expressed as

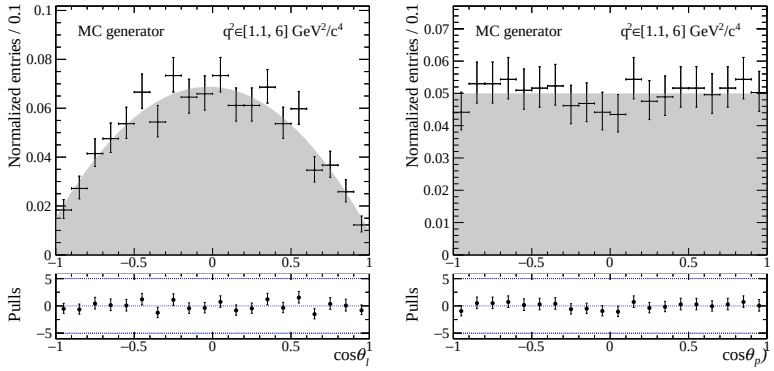

Figure 4.6 – Testing the fit model of the spin-1/2 Λ^* resonances on the mixture of the Monte-Carlo samples of $\Lambda_b^0 \to \Lambda(1405)\mu^+\mu^-$ and $\Lambda_b^0 \to \Lambda(1600)\mu^+\mu^-$ decays.

$$\mathrm{PDF}_{\mathrm{ang},1/2} = \frac{1}{2}\left(1 - K_{1cc}\right)\sin^2\theta_\ell + K_{1cc}\cos^2\theta_\ell + \frac{2}{3}A^\ell_{FB,1/2}\cos\theta_\ell. \tag{4.16}$$

For convenience, even after *CP* averaging, the observable name K_{1cc} is kept, in order to distinguish it from S_{1cc}. Compared to the $\Lambda(1520)$ contribution, the distribution of $\cos\theta_p$ is flat. It is essential to keep in mind that both of the PDFs are symmetric in $\cos\theta_p$.

Monte-Carlo samples are generated for the $\Lambda(1405)$ and $\Lambda(1600)$ resonances. As they are treated together, the fit model is tested on the merged $\Lambda(1405)$ and $\Lambda(1600)$ MC samples. A fit has been performed in Fig. 4.6. The $\Lambda^*_{J=1/2}$ fit model describes well the shape of the joint MC samples.

Adding the pK^- invariant mass to the fit model

The angular PDFs in Eq. 4.13 and 4.16 have a similar shape in $\cos\theta_\ell$. Only the $\cos\theta_p$ distributions differ. To help the fit distinguish the resonances, it is necessary to introduce another fit dimension. Thanks to the pK^- invariant mass, the fit entangles the $\Lambda(1520)$ and the $\Lambda^*_{J=1/2}$ contribution. Therefore, the fraction of the Λ^* resonances $f_{3/2}$ is well known.

The $\Lambda(1520)$ resonance is modelled with a relativistic Breit-Wigner distribution (BW), which describes the mass distribution of unstable intermediate resonant states [21, 184, 185]. This complex mass distribution is introduced in order to describe well the shape of the $\Lambda(1520)$ resonance. However, the BW is only a valid description for narrow resonances situated far from the mass thresholds and other resonances with the same quantum

numbers, which is the case for the $\Lambda(1520)$ resonance. The relativistic BW amplitude is written as

$$\mathrm{BW}(m_{pK}) = \frac{1}{M^2_{\Lambda^*} - m^2_{pK} - iM_{\Lambda^*}\Gamma(m_{pK})}, \tag{4.17}$$

where

$$\Gamma(m_{pK}) = \Gamma_{\Lambda^*}\left(\frac{p(m_{pK})}{p(M_{\Lambda^*})}\right)^{2L_{\Lambda^*\to pK}+1} \frac{M_{\Lambda^*}}{m_{pK}} F^2_{\Lambda^*\to pK}(p(m_{pK}), p(M_{\Lambda^*})). \tag{4.18}$$

The BW pole mass is marked as M_{Λ^*} and its pole width with Γ_{Λ^*}. The BW pole mass and width only agree with the resonance mass and width if the resonances are narrow and well separated from other resonances. The $\Lambda(1520)$ resonance is close to the $\Lambda(1405)$ and $\Lambda(1600)$ resonances, which can affect the BW pole mass and width.

The relativistic Breit-Wigner contains barrier factors, which act as an angular momentum barrier of low angular momenta of the decay products. Those momenta are namely the Λ^* momentum in the Λ_b^0 restframe, denoted as p, and the K^- momentum in the Λ^* restframe, expressed with q. Those barrier factors are the ratio of the momentum at a certain pK^- mass value with respect to the momentum at the pole mass. Those are scaled by the orbital angular momentum L. $L_{\Lambda^*\to pK}$ denotes the orbital angular momentum difference between the proton and kaon in the $\Lambda^* \to pK^-$ decay. The orbital angular momentum between the Λ^* and the dimuon system in the $\Lambda_b^0 \to \Lambda^*\mu^+\mu^-$ decay is written as $L_{\Lambda_b\to\Lambda^*\mu\mu}$.

Positive values of the orbital angular momentum L cause rapid growth with increasing momenta p and q. This growth is stopped with the help of the Blatt-Weisskopf form factors F [186]. The Blatt-Weisskopf form factors are a function of the momenta of the decay products and the interaction radius of the decaying particle r.

Due to the choice of rectangular phase-space variables $(m_{pK}, \cos\theta_\ell, \cos\theta_p, \phi)$, the relativistic Breit-Wigner formula needs to be multiplied by the momenta p and q. Those daughter momenta in the rest frame of the mother particle are calculated via the formula

$$p(m_{pK}) = \frac{\sqrt{(m^2_{pK} - M_1^2 - M_2^2)^2 - 4M_1^2M_2^2}}{2m_{pK}}, \tag{4.19}$$

where $M_{1,2}$ denote the masses of the daughters.

The full relativistic BW lineshape is written as

$$\mathrm{BW}_{\mathrm{rel}}(m_{pK})^2 = q(m_{pK})p(m_{pK})\left[\left(\frac{q(m_{pK})}{q(M_{\Lambda^*})}\right)^{L_{\Lambda_b\to\Lambda^*\mu\mu}}\left(\frac{p(m_{pK})}{p(M_{\Lambda^*})}\right)^{L_{\Lambda^*\to pK}} \times F_{\Lambda_b\to\Lambda^*\mu\mu}(q(m_{pK}), q(M_{\Lambda^*}), r_{\Lambda_b})\frac{F_{\Lambda^*\to pK}(p(m_{pK}), p(M_{\Lambda^*}), r_{\Lambda^*})}{M^2_{\Lambda^*} - m^2_{pK} - iM_{\Lambda^*}\Gamma(m_{pK})}\right]^2. \quad (4.20)$$

The fit of the pK^- invariant mass distribution of the dedicated $\Lambda_b^0 \to \Lambda(1520)\mu^+\mu^-$ simulation samples with the real part of the full relativistic BW lineshape is shown in Fig. 4.7.

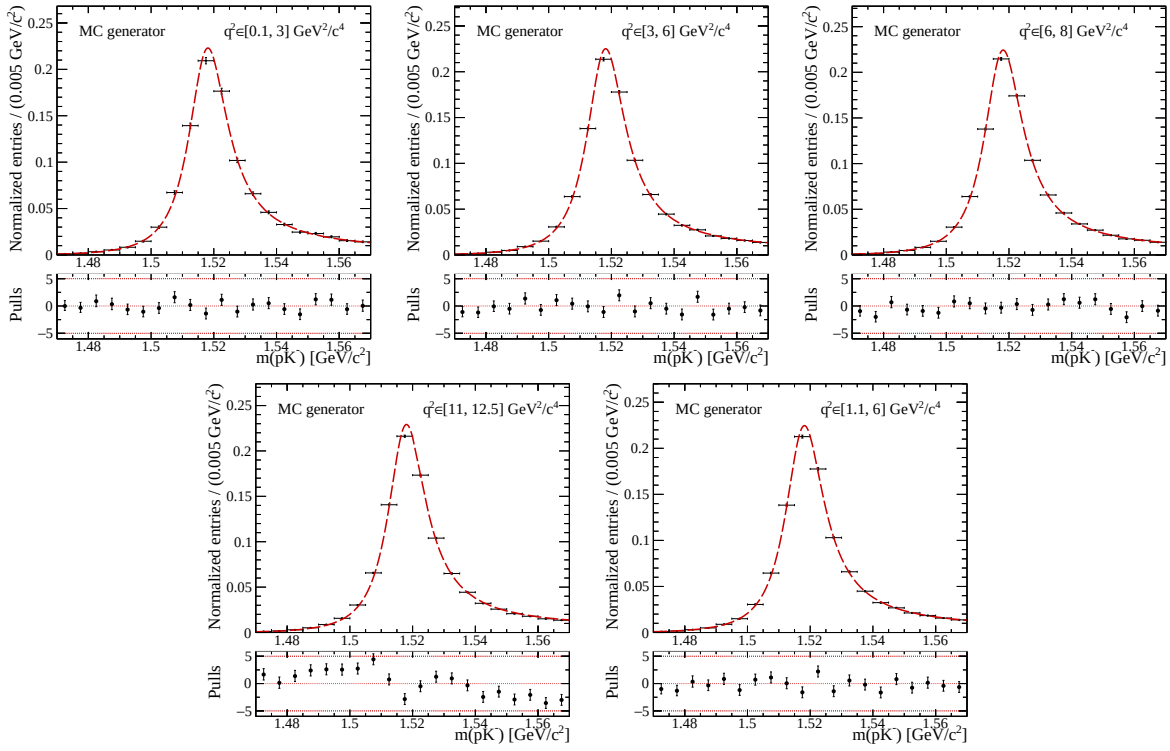

Figure 4.7 – The pK^- invariant mass distribution of the dedicated $\Lambda_b^0 \to \Lambda(1520)\mu^+\mu^-$ simulation samples is fitted by the full relativistic Breit-Wigner in different q^2 bins in the rare mode.

The $\Lambda(1520)$ mass peak is especially well described in the q^2 bins below the J/ψ resonance since the pulls are close to zero. The $\Lambda(1520)$ mass peak in the q^2 bin in-between the two $c\bar{c}$ resonances, the pulls follow an s-like distribution within +5 and -5σ.

For large data samples, the fitting algorithm has no problem finding the mean, $M_{\Lambda(1520)}$, and the width of the resonance $\Gamma_{\Lambda(1520)}$. However, with a smaller sample size, a simplified BW function converges better. In this simplified BW version, the barrier factors, the Blatt-Weisskop form factors and the momentum factors are replaced by the pK^- invariant

mass and the $\Gamma(m_{pK})$, which can be written as

$$\mathrm{BW}_{\mathrm{rel}}(m_{pK})^2 = \frac{m_{pK}\Gamma(m_{pK})}{[M^2_{\Lambda^*} - m^2_{pK} - iM_{\Lambda^*}\Gamma(m_{pK})]^2}. \tag{4.21}$$

The fits of the pK^- invariant mass distribution with the simplified BW are shown in Fig. 4.8. The pulls are slightly farther from zero than in the complete description. However, given the size of the data samples that we will be fitting for, the overall size of the discrepancy observed in these pulls is likely to be negligible.

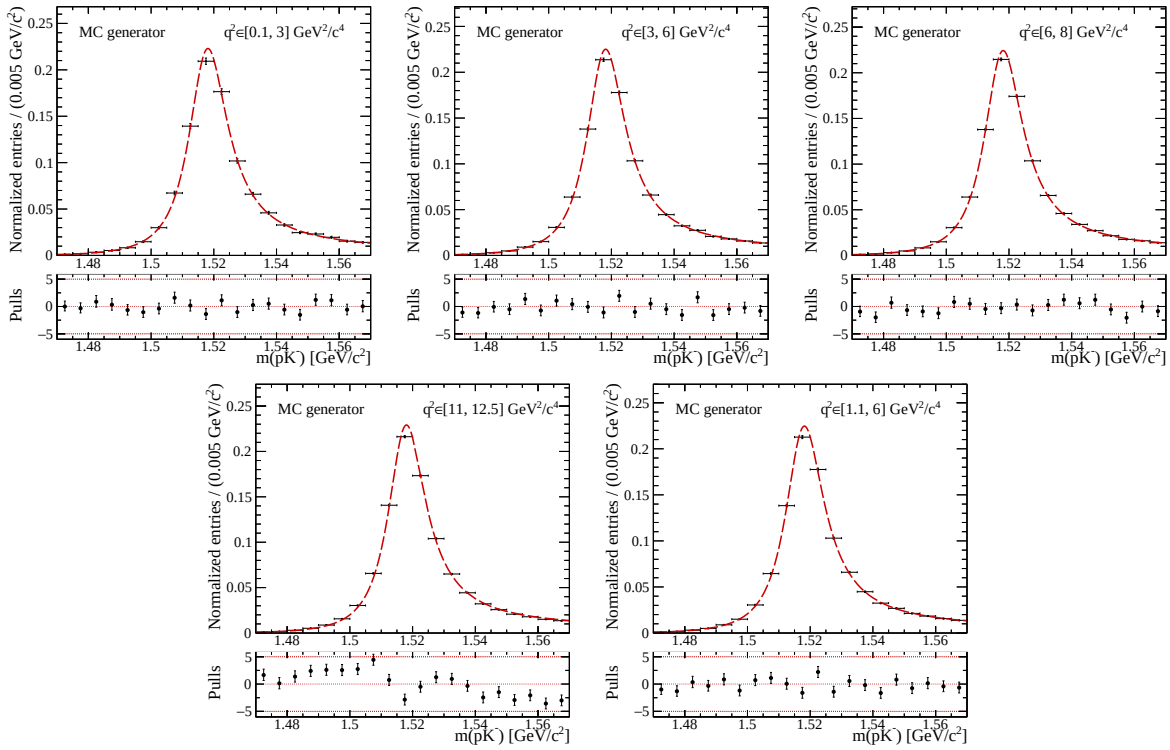

Figure 4.8 – The pK^- invariant mass distribution of the realistic $\Lambda_b^0 \to \Lambda(1520)\mu^+\mu^-$ samples is fitted by the simplified relativistic Breit-Wigner.

As in the generator `EvtGen`, the interaction radii of $r_{\Lambda_b} = 0.003$ and $r_{\Lambda^*} = 0.005\,\mathrm{MeV}^{-1}$ are fixed. The orbital angular momentum $L_{\Lambda^*\to pK}$ can only take the value of two. $L_{\Lambda_b\to\Lambda^*\mu\mu}$ can take the integer values 0, 1 and 2. Only the lowest orbital angular momentum is retained and fixed in the future. The same was done in the generation of the dedicated Monte-Carlo samples [187]. The pole mass and width of the $\Lambda(1520)$ resonance stay free-floating.

The spin-1/2 Λ^* resonances are modelled with Chebyshev polynomials, which have the advantage of being orthogonal. The dedicated simulation samples have a large sample size, because of which a polynomial up to order three is used. For the fit of real data, a

polynomial with fewer orders can model the pK^- invariant mass distribution.

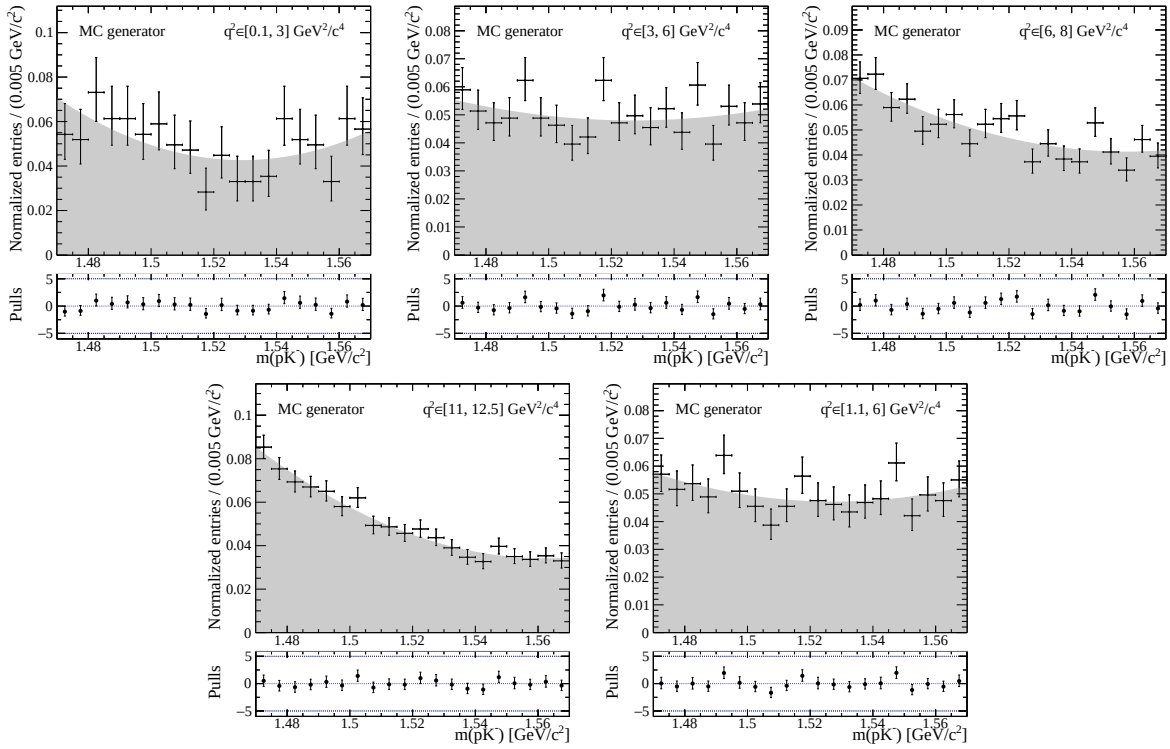

Figure 4.9 – The pK^- invariant mass distribution of the two spin-1/2 Λ^* resonance mixture in the dedicated MC samples.

The pK^- invariant mass distribution in the dedicated MC samples is plotted in Fig. 4.9, where the $\Lambda(1405)$ and the $\Lambda(1600)$ resonances are mixed. Their occurrence is generated according to the differential branching fractions of the specific $\Lambda_b^0 \to \Lambda^* \mu^+ \mu^-$ decays using the Quark Model form factors [6] (described in Ch. 1.3.3). The branching fraction of the $\Lambda^* \to pK^-$ decays is taken from Ref. [21]. However, as it will be seen in Fig. 4.14, the fraction of $\Lambda(1520)$ resonances in the pK^- invariant mass window varies significantly across the different q^2 bins, which implies that the composition of $\Lambda(1405)$ and $\Lambda(1600)$ resonances could differ in the different q^2 bins.

Fit model combining $\Lambda(1520)$ and $\Lambda^*_{J=1/2}$ resonances

Combining the $\Lambda(1520)$ with the spin-1/2 Λ^* resonances, the total fit model for the pK^- invariant mass is written as

$$\mathrm{PDF}_{pK\mathrm{mass}} = f_{3/2} |\mathrm{BW}_{\mathrm{rel}}(m_{pK})|^2 + (1 - f_{3/2}) \mathrm{Polynomial}(m_{pK}). \tag{4.22}$$

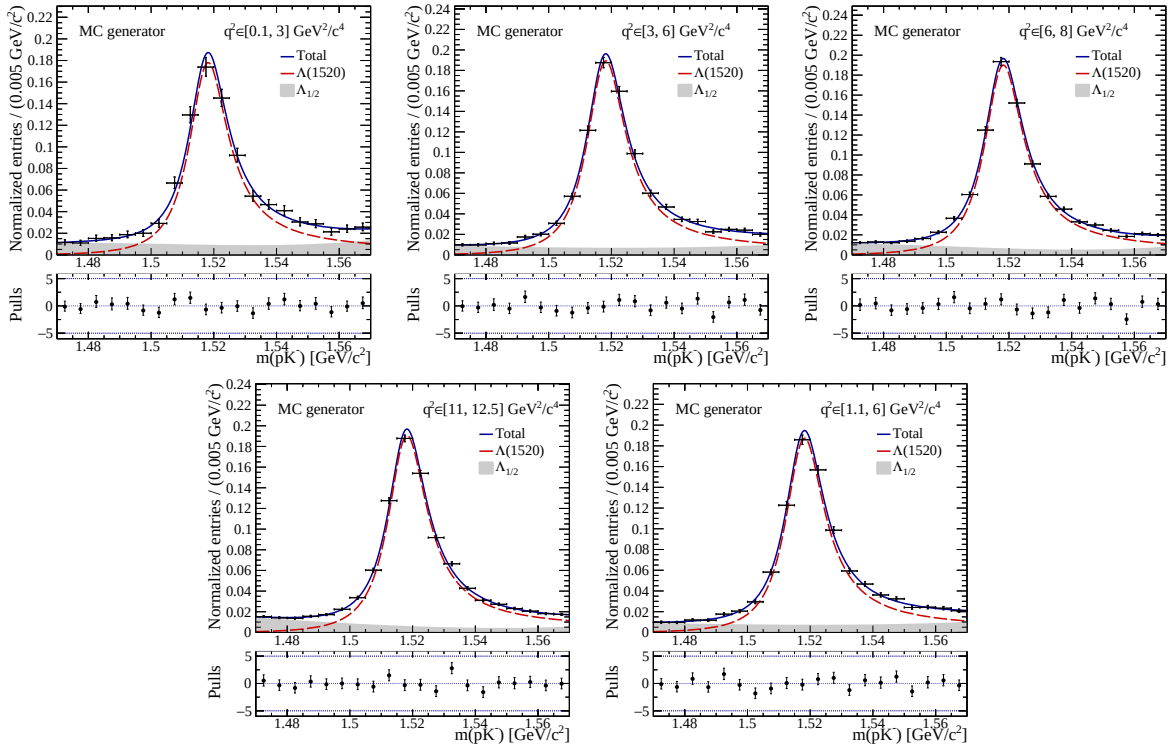

Figure 4.10 – The projections of the pK^- invariant mass fit to the dedicated MC samples in the different q^2 bins.

To test the fit model, the individual MC samples of the $\Lambda(1405)$, $\Lambda(1520)$ and $\Lambda(1600)$ resonances have been added together, without considering possible interferences. The fraction of $\Lambda(1520)$ resonances is kept to be approximately 80%, as it was extrapolated from the pK^- mass spectrum in Fig. 1.15. Fitting the dedicated MC samples in the different q^2 bins yields the fit projections drawn in Fig. 4.10.

The pK^- mass distribution is well described by the new fit model. The resulting fit parameters of the polynomial are shown in Tab. 4.2. The fraction of $\Lambda(1520)$ decays varies

q^2 bin $[\,\mathrm{GeV}^2/c^4\,]$	$f_{3/2}$	a_1	a_2	a_3
$[0.1, 3]$	0.794 ± 0.027	0.06 ± 0.12	0.13 ± 0.16	0.08 ± 0.11
$[3, 6]$	0.845 ± 0.015	0.03 ± 0.08	0.15 ± 0.12	0.021 ± 0.08
$[6, 8]$	0.849 ± 0.012	-0.28 ± 0.07	0.21 ± 0.10	0.10 ± 0.07
$[11, 12.5]$	0.853 ± 0.009	-0.58 ± 0.07	0.25 ± 0.08	0.03 ± 0.05
$[1.1, 6]$	0.837 ± 0.013	0.04 ± 0.07	0.13 ± 0.10	0.022 ± 0.07

Table 4.2 – The resulting values of the fraction of $\Lambda(1520)$ decays and the shape of the polynomial in the different q^2 bins.

slightly in the different q^2 bins. The shape parameter a_2 and a_3 are compatible with zero

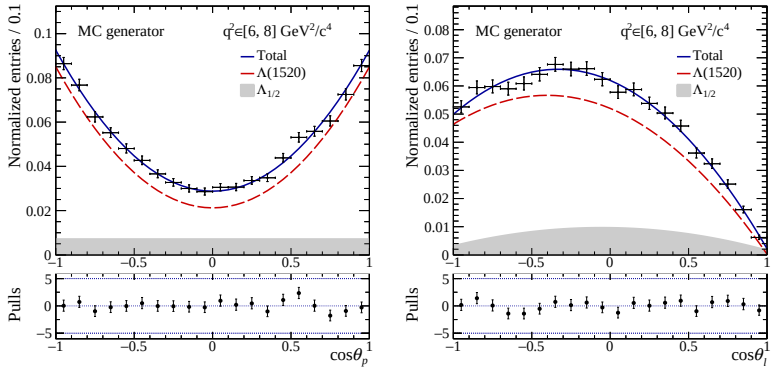

Figure 4.11 – The projections of the angular fit to the dedicated MC samples without interference effects in the $q^2 \in [6, 8]\,\mathrm{GeV}^2/c^4$ bin.

within four standard deviations. However, the sample size is much larger in the dedicated MC sample, where one million events are present than the sample size of approximately 100 events expected in the less populated q^2 bins in the data.

The total angular PDF can be constructed in the same way. It appears as

$$\begin{aligned}\mathrm{PDF}_{\mathrm{ang}} = \frac{f_{3/2}}{4}\left(\left(1-\frac{1}{2}S_{1cc}\right)\left(1-\cos^2\theta_\ell\right)+S_{1cc}\cos^2\theta_\ell+\frac{4}{3}A^{\ell}_{FB,3/2}\cos\theta_\ell\right)\left(1+3\cos^2\theta_p\right)\\ +(1-f_{3/2})\left(\frac{1}{2}\left(1-K_{1cc}\right)\left(1-\cos^2\theta_\ell\right)+K_{1cc}\cos^2\theta_\ell+\frac{2}{3}A^{\ell}_{FB,1/2}\cos\theta_\ell\right)\end{aligned} \tag{4.23}$$

The angular terms K_{1cc} and $A^{\ell}_{FB,1/2}$ carry the information of all the remaining spin 1/2 resonances. Given the size of the available data samples, as discussed before, we do not attempt to have an individual description of the spin 1/2 resonances and they are all treated together.

The angular coefficients depend on the q^2 bin. The different dependencies of the $\Lambda(1520)$ and the spin-1/2 Λ^* resonances on the $\cos\theta_p$ variable is not enough to separate the two components. Therefore the pK^- invariant mass is introduced as an additional fit dimension. Instead of fitting all three dimensions at once (m_{pK}, $\cos\theta_\ell$, $\cos\theta_p$) in bins of q^2, the fit is performed independently in each q^2 bin, in order to prevent a potential bias of the $f_{3/2}$ fraction. The fit is executed in the following order:

1. Fit the pK^- mass spectrum with the $\mathrm{PDF}_{pK\mathrm{mass}}$ to extract the fraction of $\Lambda_b^0 \to \Lambda(1520)\mu^+\mu^-$ decays, namely $f_{3/2}$.
2. Fit the angles $\cos\theta_\ell$ and $\cos\theta_p$ with the $\mathrm{PDF}_{\mathrm{ang}}$ to extract the angular observables of interest, as well as the interferences.

The fit projections are shown in Fig. 4.11, for instance in the $q^2 \in [6, 8]\,\mathrm{GeV}^2/c^4$ bin.

As indicated by the pulls, the fit describes well the angular distribution.

To conclude, the angular fit model including spin-1/2 resonances and the $\Lambda(1520)$ resonance has been developed. The pK^- invariant mass is fitted first to determine the fraction of $\Lambda(1520)$ resonances. By naively combining the individual samples with the different resonances, the fit describes well the dedicated simulation samples. However, the interference effects are not considered in the fit.

4.2.3 Interferences between the Λ^* resonances

Due to the presence of different Λ^* resonances, it is not sufficient to only model the resonances. It is important to consider the overlap of their amplitudes, which is expressed via interference terms. This overlap cannot be predicted by theory, but only be determined by experiments. A "dedicated" generator has been developed in parallel with this work by LHCb colleagues [187]. It was employed to generate samples with different interference schemes and allow us to establish how they must be accounted for in the angular fit as will be shown in this chapter.

Generation of dedicated simulation samples

For the generation of dedicated simulation samples, the full differential decay width of $\Lambda_b^0 \to \Lambda^* \ell^+ \ell^-$ decays, including Λ^* resonances up to spin $\frac{5}{2}$ and their interferences, has been worked out in Ref. [187].

Since the strength of the interference terms is not predicted by theory, a Monte-Carlo generator was developed [187]. Random combinations of the strong phase differences $e^{\pm i(\varphi_{\Lambda(1520)} - \varphi_{\Lambda(X)})}$ are generated to test the different interference hypotheses. In table 4.3, the values of the different phase differences $\Delta\varphi_X := \varphi_{\Lambda(1520)} - \varphi_{\Lambda(X)}$ are listed.

Phase combination	$\Delta\varphi_{1405}$	$\Delta\varphi_{1600}$
0	0.00π	0.00π
1	1.38π	1.93π
2	1.10π	1.61π
3	0.43π	0.62π
4	0.06π	1.38π
5	1.41π	0.70π

Table 4.3 – Monte Carlo samples are generated based on the following random phase combinations, which are defined as two phases $\Delta\varphi_{1405}$ and $\Delta\varphi_{1600}$ with respect to the $\Lambda(1520)$ resonance.

The Monte-Carlo distributions of the different phase combinations are shown in Fig. 4.12.

The distributions of the Monte-Carlo samples, which are mixtures of different Λ^* states,

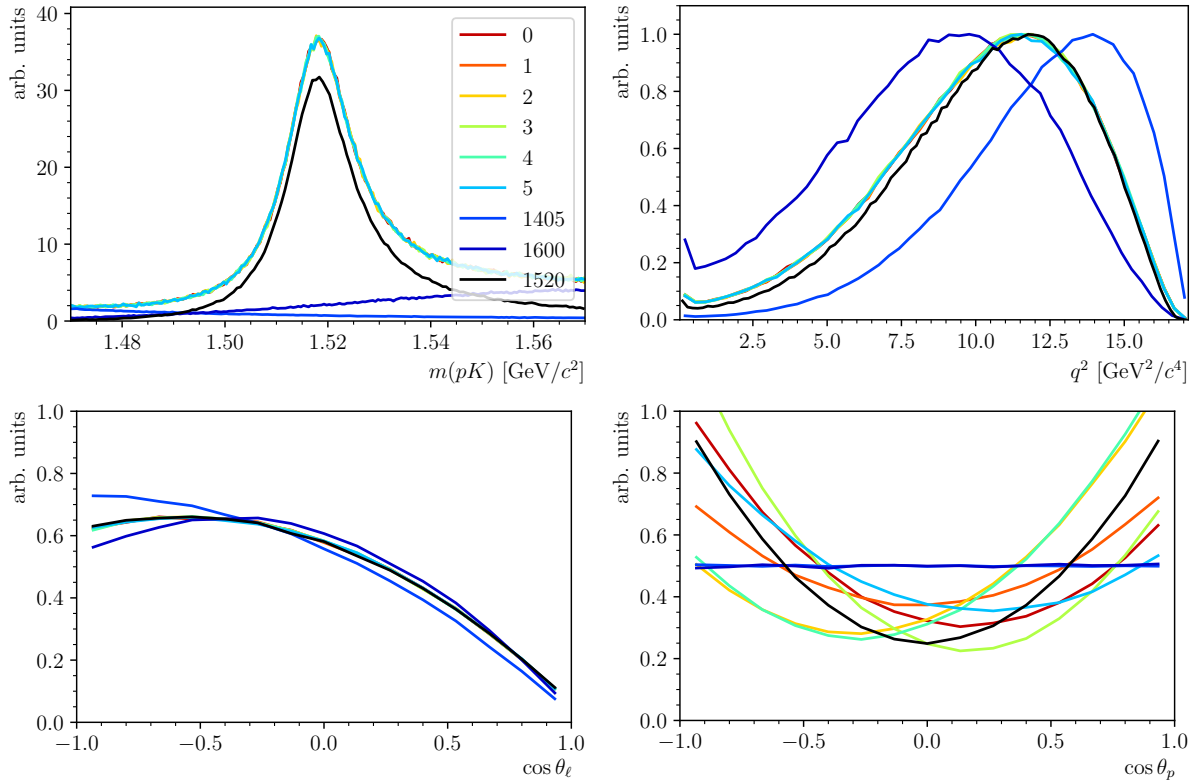

Figure 4.12 – The m_{pK}, q^2, $\cos\theta_\ell$ and $\cos\theta_p$ distributions are drawn for the different Monte-Carlo samples with interfering $\Lambda(1405)$, $\Lambda(1520)$ and $\Lambda(1600)$ resonances, which are generated with random phase combinations $0-5$.

overlap in the m_{pK}, q^2 and $\cos\theta_\ell$ distribution. In the mass distributions, only interference terms between resonances with the same spin and parity appear. However, the distribution of $\cos\theta_p$ changes significantly depending on the sample. This demonstrates that the interference terms cannot be neglected, but need to be considered in the angular fit model.

Fit model with interferences

Interferences occur in-between the two spin-1/2 resonances as well as between one of the spin-1/2 and the $\Lambda(1520)$ resonance. These interference effects introduce a shift of the $\cos\theta_p$ distribution, as shown in Fig. 4.12. In Ref. [187], it was worked out that the interference terms can be constant, linear and quadratic in $\cos\theta_p$.

Since interferences appear between the three resonances, the best approach would be to have a third component for the interference effects. Since this parametrisation requires many interference parameters and the expected data sample size, it was decided to include

the interference terms in one of the two PDFs. The following three different configurations have been tested.

1. The first strategy is to multiply the interference terms to the $\text{PDF}_{\text{ang},1/2}$. Taking into account the normalisation of the interference terms, the PDF can be expressed as

$$\begin{aligned}
&\text{PDF}_{\text{ang}}^{\text{Int}1/2} \\
&= f_{3/2}\left(\left(1-\frac{1}{2}S_{1cc}\right)\left(1-\cos^2\theta_\ell\right)+S_{1cc}\cos^2\theta_\ell+\frac{4}{3}A_{FB,3/2}^{\ell}\cos\theta_\ell\right) \\
&\times\left(\frac{1}{4}+\frac{3}{4}\cos^2\theta_p\right) \\
&+(1-f_{3/2})\left(\frac{1}{2}\left(1-K_{1cc}\right)\left(1-\cos^2\theta_\ell\right)+K_{1cc}\cos^2\theta_\ell+\frac{2}{3}A_{FB,1/2}^{\ell}\cos\theta_\ell\right) \\
&\times\left(\frac{3-i_2}{3}+i_1\cos\theta_p+i_2\cos^2\theta_p\right). \qquad (4.24)
\end{aligned}$$

2. The second configuration includes the interference terms in the $\text{PDF}_{\text{ang},3/2}$. After taking into account the normalisation of the interference terms, the PDF takes the shape of

$$\begin{aligned}
\text{PDF}_{\text{ang}}^{\text{Int}3/2} &= f_{3/2}\left(\left(1-\frac{1}{2}S_{1cc}\right)\left(1-\cos^2\theta_\ell\right)+S_{1cc}\cos^2\theta_\ell+\frac{4}{3}A_{FB,3/2}^{\ell}\cos\theta_\ell\right) \\
&\times\left(\left(\frac{1}{4}-\frac{j_2}{3}\right)+j_1\cos\theta_p+\left(\frac{3}{4}+j_2\right)\cos^2\theta_p\right) \qquad (4.25) \\
&+(1-f_{3/2})\left(\frac{1}{2}\left(1-K_{1cc}\right)\left(1-\cos^2\theta_\ell\right)+K_{1cc}\cos^2\theta_\ell+\frac{2}{3}A_{FB,1/2}^{\ell}\cos\theta_\ell\right).
\end{aligned}$$

The two configurations above require that both of the angular PDFs of the spin-1/2 and the $\Lambda(1520)$ component stay individually positive. Given that the size of the interference effects can a priori be large, the requirement of the positivity of the individual interferences is not necessarily guaranteed.

3. In this third option, the $\textbf{PDF}_{\textbf{ang}}^{\textbf{Int}1/2}$ of Eq. 4.25 is taken, but instead of implementing two separated PDFs, the **entire PDF is coded in one file**[1]. The advantage of this procedure is that the fit is able to converge even with large interference parameters.

1. Instead of using `RooAddPDF`, everything is encoded in one `RooAbsPDF`.

The fits with each of those configurations are tested in the following on the dedicated Monte-Carlo samples.

Fit of dedicated simulation samples with the fit configuration 1

At first, the pK^- invariant mass fit has been performed on the dedicated Monte-Carlo samples with the different phase differences. An example of phase combination 0 is shown in Fig. 4.13. A polynomial of order three is used. The pulls are close to zero. The

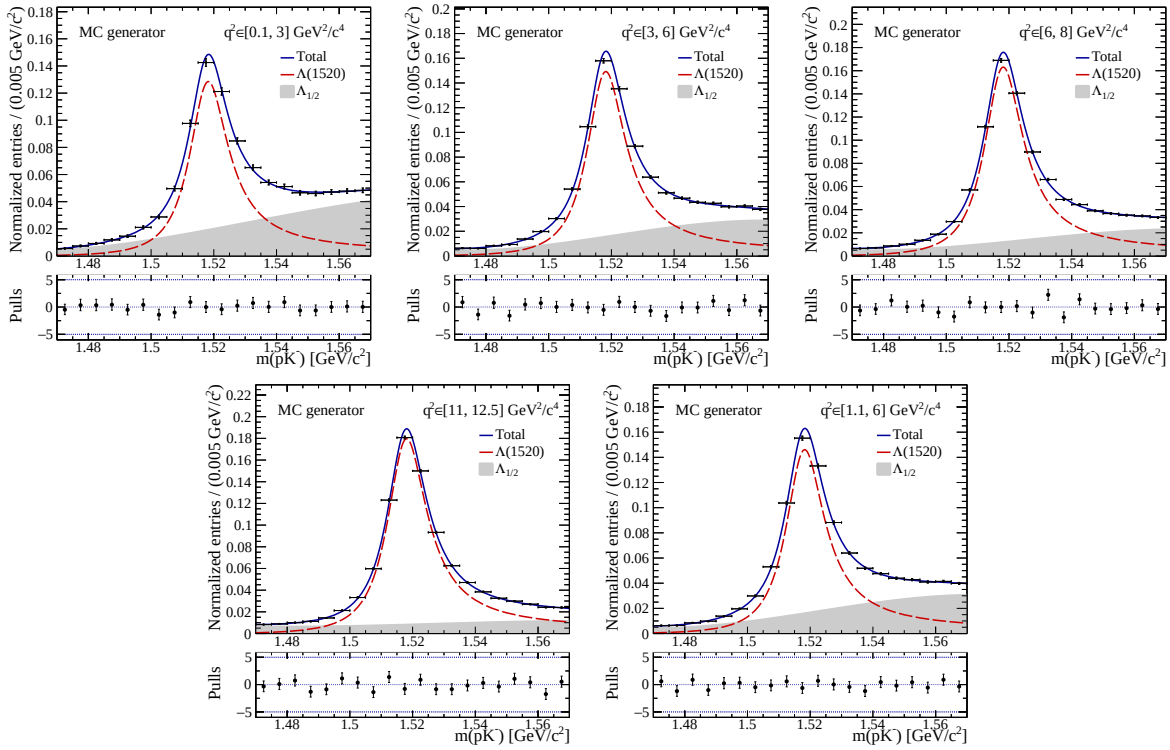

Figure 4.13 – The projections of the pK^- invariant mass fit of the dedicated MC samples with the phase combination 0 in the different q^2 bins.

pK^- mass shape of the spin-1/2 Λ^* resonances seem predominantly linear, which could be used later to simplify the model when fitting samples of smaller sizes. The resulting fit parameters, by fitting the dedicated samples with different phase combinations, are collected in Fig. 4.14.

First, it is visible that the fit results of the different phase combinations are compatible. The interferences do not change the pK^- mass distribution. This is the reason why the fit results are supposed to be compatible with each other. The fraction of $\Lambda(1520)$ resonances seems primarily compatible with the generated value.

Interestingly, $f_{3/2}$ depends strongly on the q^2 bin. a_1 differs between the different q^2 bins, while a_2 and a_3 are mostly constant between the different bins. The polynomial

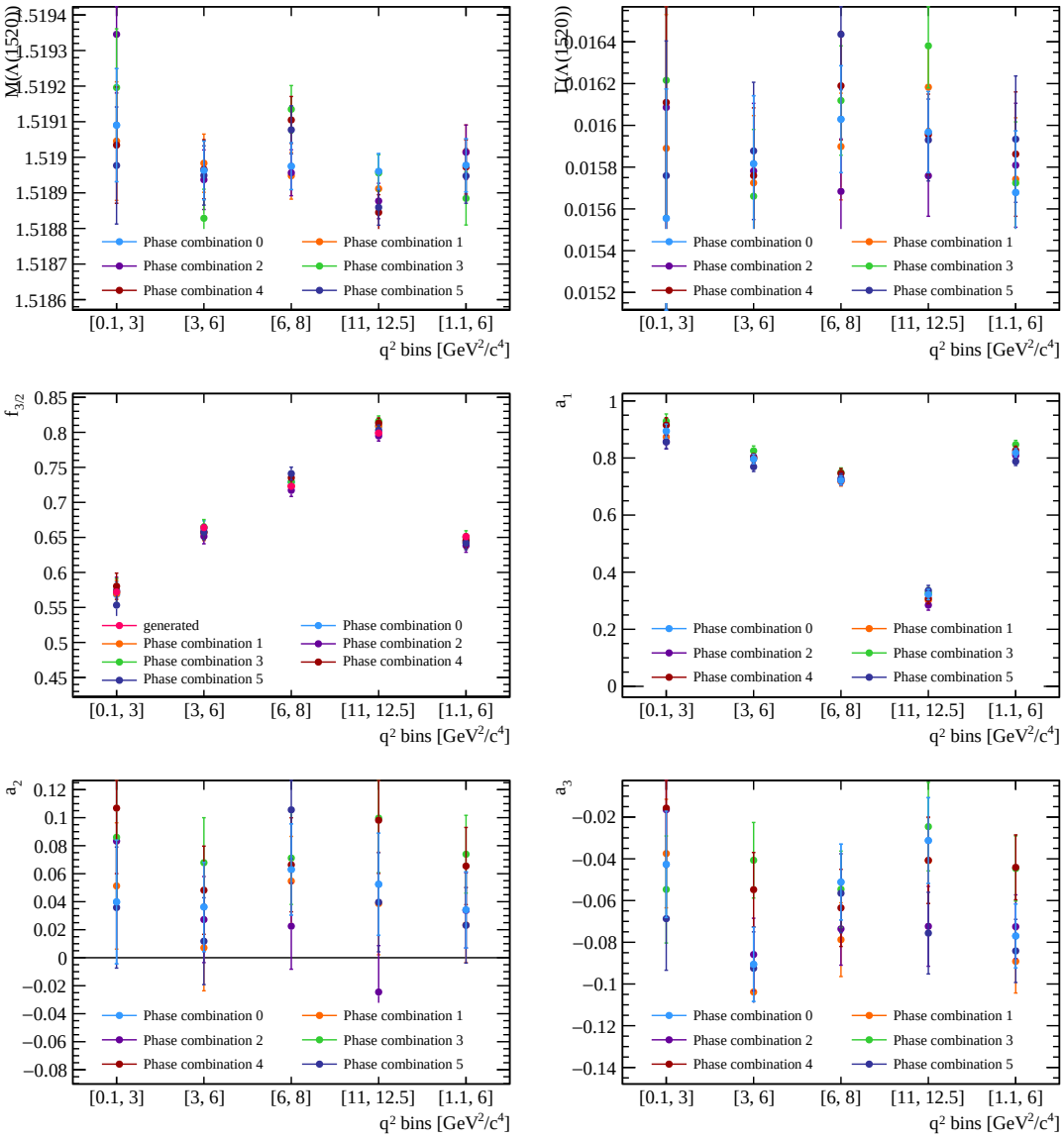

Figure 4.14 – Plot of the resulting mass parameter in the different q^2 bins by fitting the dedicated Monte Carlo samples with the different interference hypotheses.

parameter a_1 is distributed between 0.95 and 0.25, while the absolute values of the polynomial parameters a_2 and a_3 are smaller or equal to 0.1. These values are judged to be negligible in comparison to the a_1 parameter. The error bars are based on the large Monte Carlo sample size and are not scaled to the smaller realistic yields expected in data. Therefore, an increase in the error bars is expected as compatibility with zero.

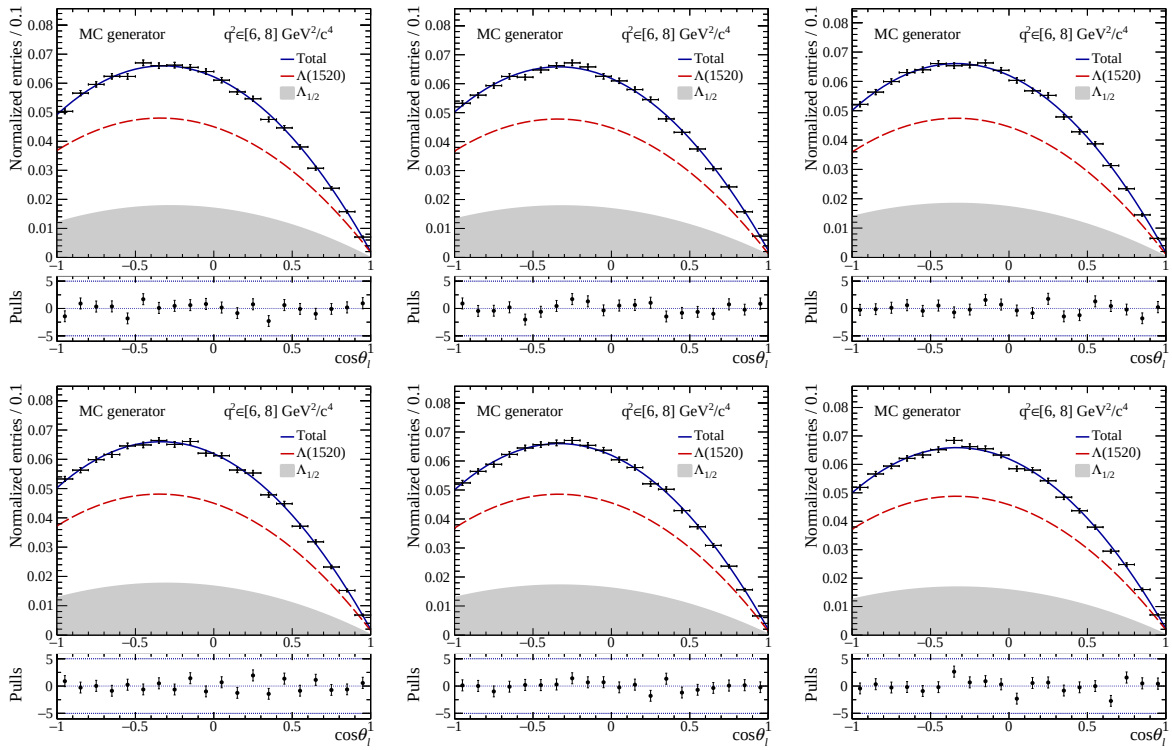

Figure 4.15 – The $\cos\theta_\ell$ projections of the fit to the dedicated MC samples with the interference hypotheses 0 (top left) to 5 (bottom right) in the $q^2 \in [6,8]\,\mathrm{GeV}^2/c^4$ bin. Fit model 1 is used, in which the interference terms are part of the spin-1/2 PDF.

After extracting the $f_{3/2}$ parameter, the angular fit is performed. Exemplarily, the angular distributions are shown in Fig. 4.15 and 4.16 for the $q^2 \in [6,8]\,\mathrm{GeV}^2/c^4$ bin. The angular fit projections of all the other q^2 bins are shown in App. K.1. The $\cos\theta_\ell$ distribution stays as seen previously, the same in the different q^2 bins. The projection of the $\Lambda_{1/2}$ contribution and the $\Lambda(1520)$ contribution has the same shape. This is the reason why a fit has difficulties in separating them.

The interferences have an impact on the $\cos\theta_p$ distribution. While in this configuration, the $\Lambda(1520)$ contributions stay symmetric, the spin-1/2 PDF is now accounting for the shift of the distribution. To correctly describe the shape, the spin-1/2 PDF, including the interference terms, takes negative values in some projections. This behaviour under-

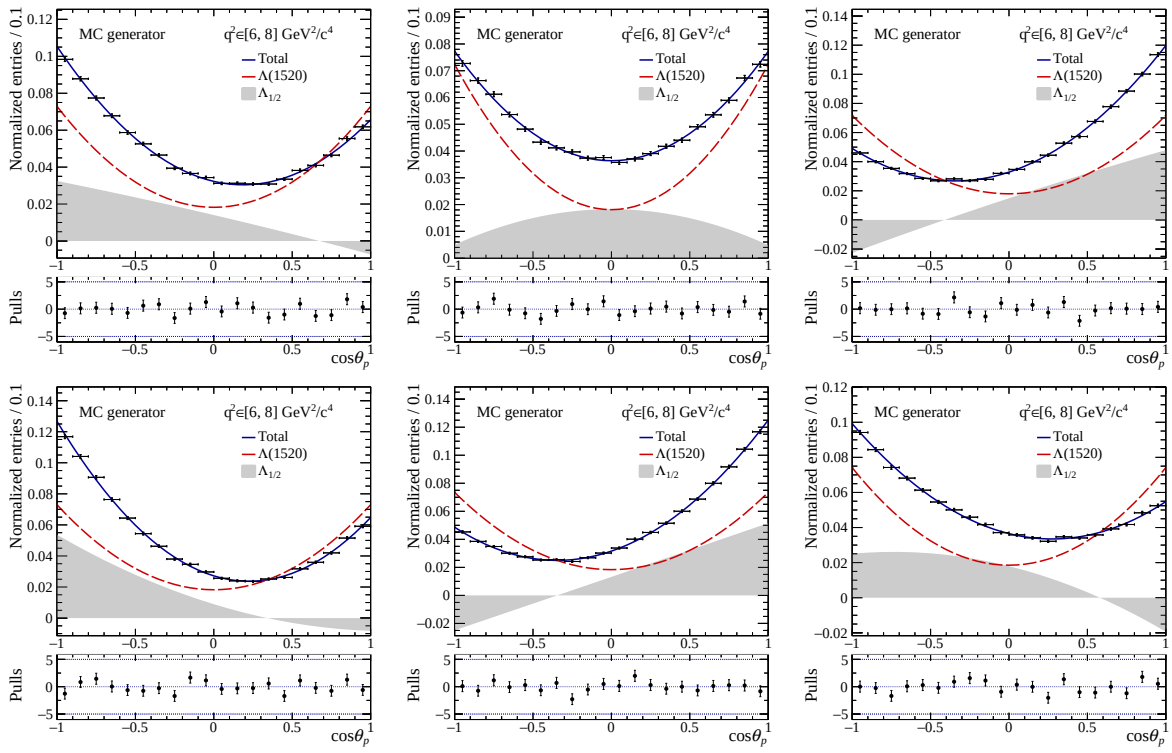

Figure 4.16 – The $\cos\theta_p$ projections of the fit to the dedicated MC samples with the interference hypotheses 0 (top left) to 5 (bottom right) in the $q^2 \in [6, 8]\,\mathrm{GeV}^2/c^4$ bin. Fit model 1 is used, in which the interference terms are multiplied with the spin-1/2 PDF.

lines the strength of the interference parameters. This observation motivated adding the interference terms to the PDF describing the $\Lambda(1520)$ resonance.

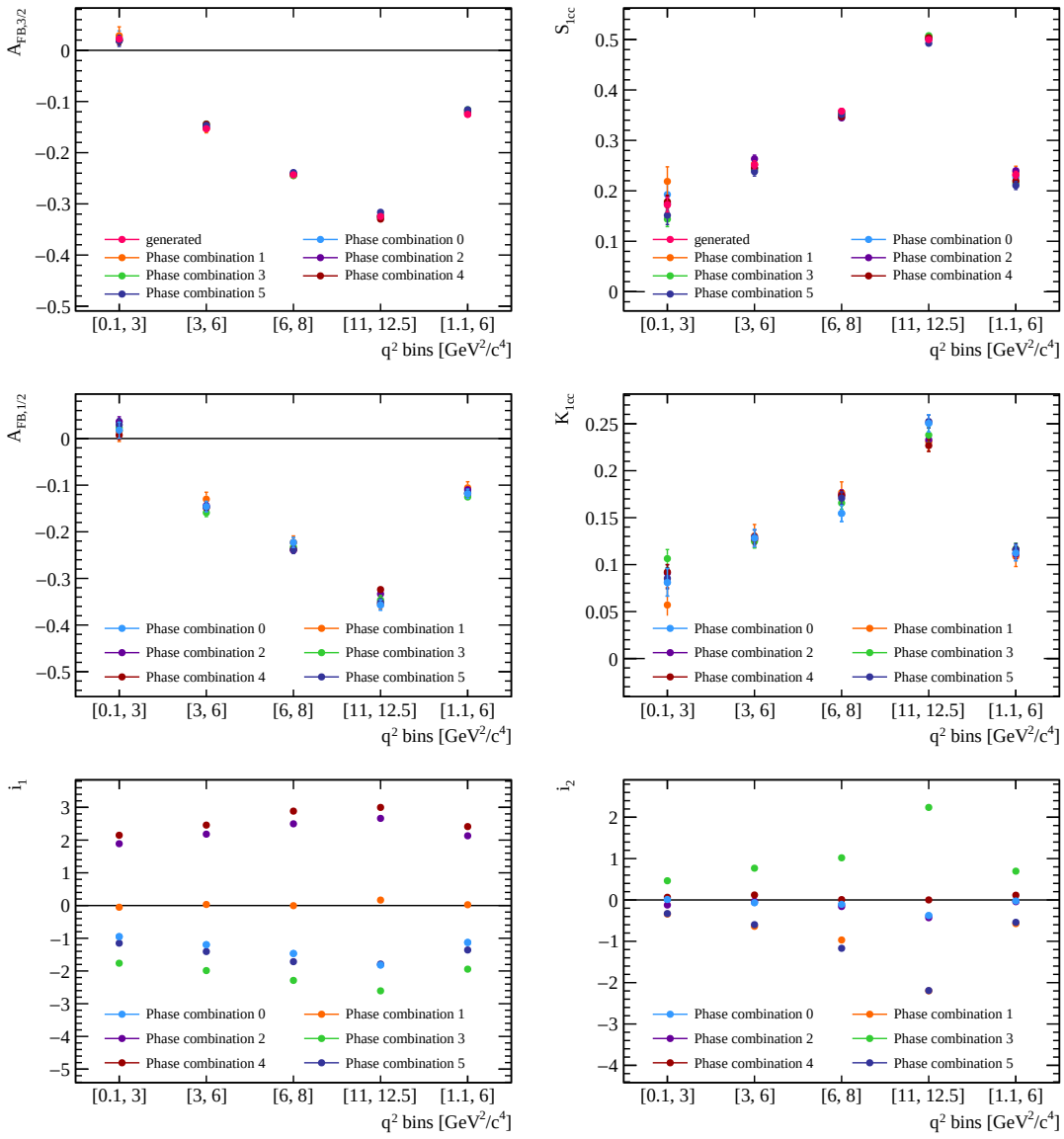

Figure 4.17 – The resulting fit parameters of the angular fit with the fit model 1, which multiplies the interference terms to the PDF of the spin-1/2 Λ^* resonances.

The resulting parameter values of the fit to the dedicated Monte-Carlo samples with different interference hypotheses are plotted in Fig. 4.17. The fit results of the most important parameter, A_{FB}^{ℓ}, are close to the generated values. This closeness can be seen for all of the q^2 bins. The uncertainties are minor because of the huge Monte-Carlo sample size. The fit values of the parameter S_{1cc} are close to the generated values.

The generated value of the fit parameters of the spin-1/2 PDF, $A_{\mathrm{FB},1/2}$ and K_{1cc}, are not precisely known since it is a mixture of different resonances and only in a reduced

pK^- mass window. However, the fit values are compatible with each other. By eye, the maximum number of standard deviations is five.

The interference parameter can get high strength values of up to three. Since the interference parameters are not at all compatible with zero, the necessity to take the interferences into account is underlined again.

To conclude, the fit results of this configuration are coherent with the generated values and each other. Unfortunately, the fits of the J/ψ and $\psi(2S)$ control modes did not converge. The source seems to come from the high values of the interference parameters and the negative spin-1/2 PDF.

Fit of dedicated simulation samples with the fit configuration 2

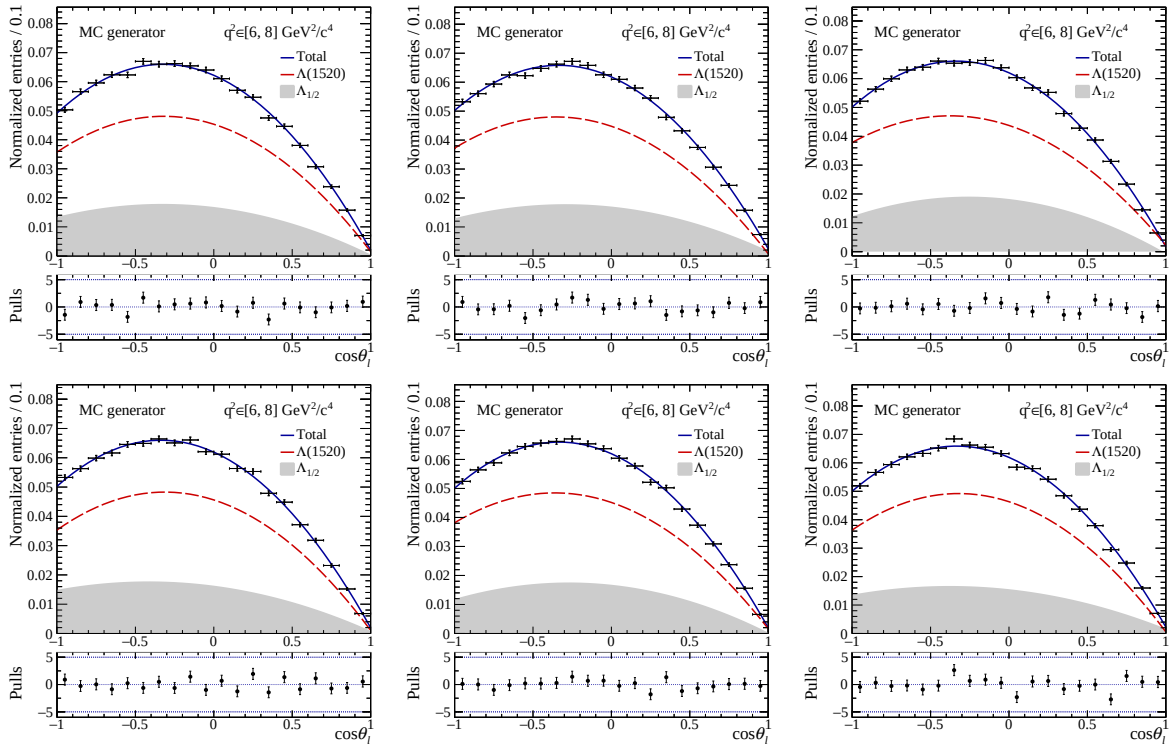

Figure 4.18 – The $\cos\theta_\ell$ projections of the fit to dedicated simulation samples with the interference hypotheses 0 (top left) to 5 (bottom right) in the $q^2 \in [6, 8]\,\mathrm{GeV}^2/c^4$ bin. Fit model number 2 is used, in which the interference terms are included in the $\Lambda(1520)$ angular PDF.

In configuration 2, the dedicated Monte-Carlo samples are fit with the $\mathrm{PDF}_{\mathrm{ang}}^{\mathrm{Int3/2}}$, defined in Eq. 4.25. The dedicated Monte-Carlo samples are fitted again. The projections in the $q^2 \in [6, 8]\,\mathrm{GeV}^2/c^4$ bin are shown in Fig. 4.18 and 4.19. The remaining q^2 bins are presented in App. K.2.

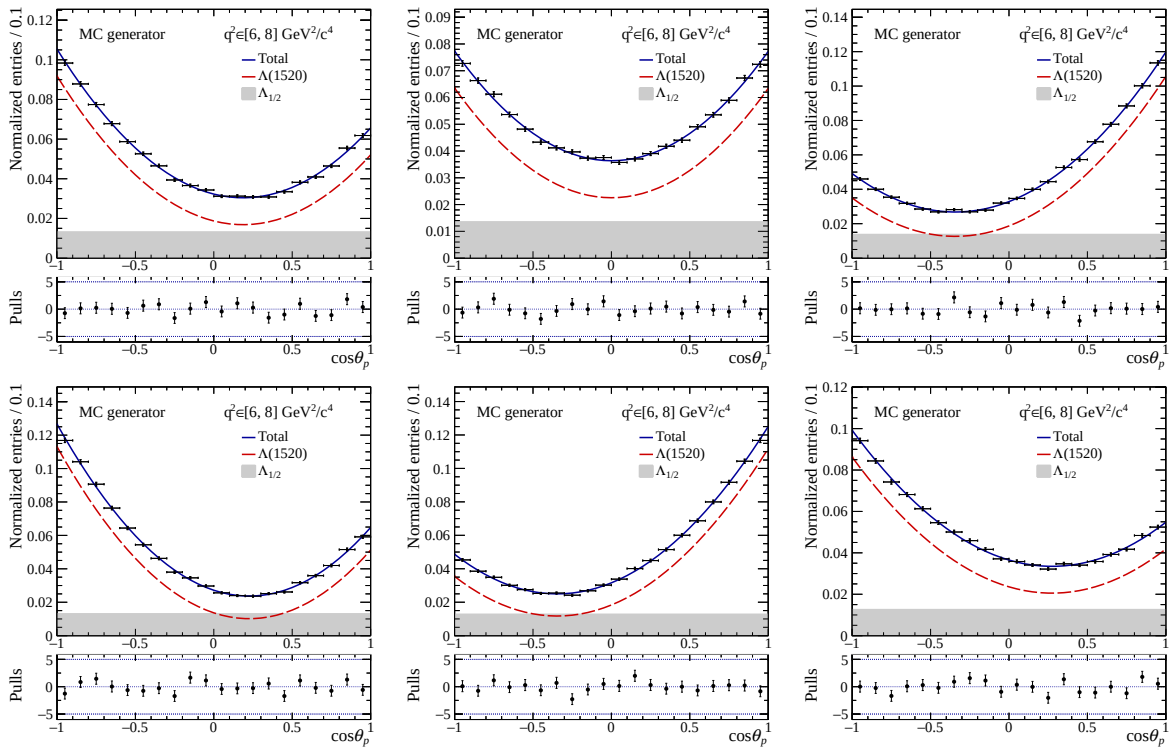

Figure 4.19 – The $\cos\theta_p$ projections of the fit to the dedicated simulation samples with the interference hypotheses 0 (top left) to 5 (bottom right) in the $q^2 \in [6, 8]\,\mathrm{GeV}^2/c^4$ bin. Fit model number 2 is used, in which the interference terms are included in the $\Lambda(1520)$ angular PDF.

The pulls of the projections in $\cos\theta_\ell$ and $\cos\theta_p$ are both distributed around zero. In this fit configuration, the PDF of the $\Lambda_{1/2}$ contributions is flat. Since the interference terms are part of the more common $\Lambda(1520)$ contribution, none of the PDFs get negative. The fit values are shown in Fig. 4.20.

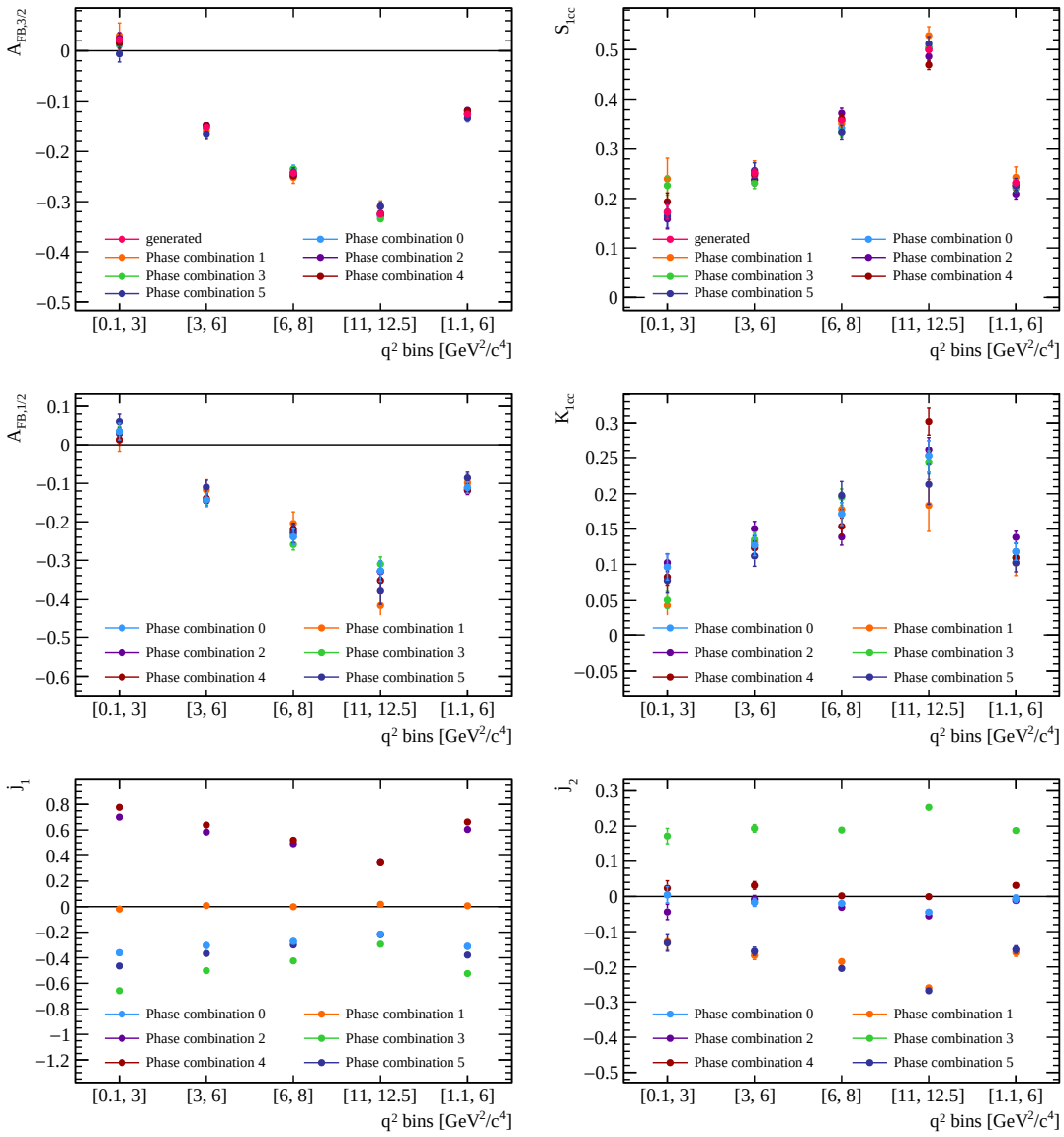

Figure 4.20 – The resulting fit parameters of the angular fit with the fit model 2, which includes the interference terms in the PDF of the $\Lambda(1520)$ resonance.

Generally, the fit values of the fit parameters A_{FB}, $A_{\mathrm{FB},1/2}$, S_{1cc} and K_{1cc} are the same between the two configuration. The fit parameter values are still close to the generated values, but the values are slightly more distributed and have larger uncertainties. This behavior is especially visible for the S_{1cc} and K_{1cc} observables. As expected, the values of the interference parameters j_1 and j_2 are different from the i_1 and i_2 parameters.

To conclude, the parametrisation of the angular fit model with the $\mathrm{PDF}_{\mathrm{ang}}^{\mathrm{Int3/2}}$ has the advantage that none of the PDFs are getting negative in the presence of large interference contributions. The drawback of this parametrisation is the existence of larger uncertainties than for the fit configuration 1.

Fit of dedicated simulation samples with the fit configuration 3

The idea of the third fit configuration is to use the best working fit model, which is model 1, and adapt it such that none of the PDFs can get negative. This is done by coding the full PDF as one singular PDF, avoiding constraints on the positivity of its components. The disadvantage of this method is that the components cannot be separated and only the total PDF is drawn.

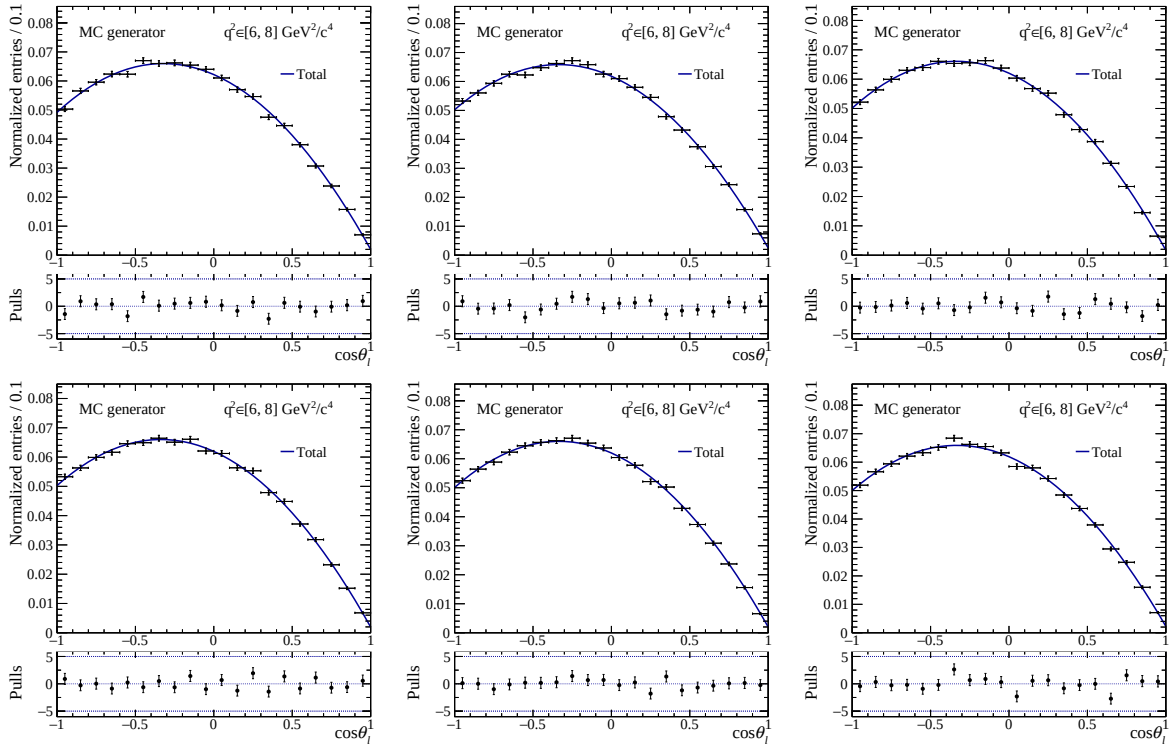

Figure 4.21 – The $\cos\theta_\ell$ projection of the angular fit in the $q^2 \in [6, 8]\,\mathrm{GeV}^2/c^4$ bin. The dedicated Monte-Carlo samples with the interference hypotheses 0 (top left) to 5 (bottom right) are drawn. The fit model number 3 is chosen, because of which the only projection is the total one.

The fit projections are shown in Fig. 4.21 and 4.22 for the $q^2 \in [6, 8]\,\mathrm{GeV}^2/c^4$ bin. The projections of the angular fits in the remaining q^2 bins are shown in App. K.2. The fit projections in $\cos\theta_\ell$ and $\cos\theta_p$ describe well the dedicated Monte-Carlo samples with the different interference hypotheses.

The resulting fit parameters are plotted in Fig. 4.23. A good agreement between the

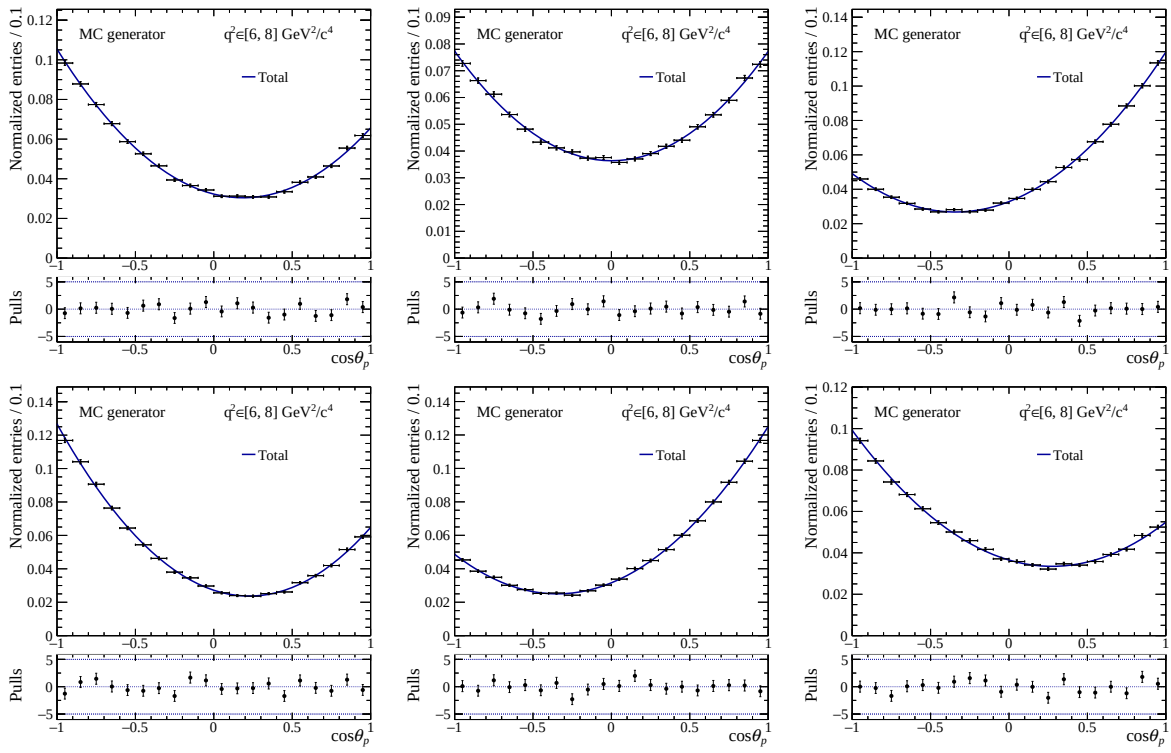

Figure 4.22 – The $\cos\theta_p$ projection of the angular fit in the different q^2 bins. The dedicated Monte-Carlo samples with the interference hypothesis 0 are drawn. The fit model number 3 is chosen, because of which the only projection is the total one.

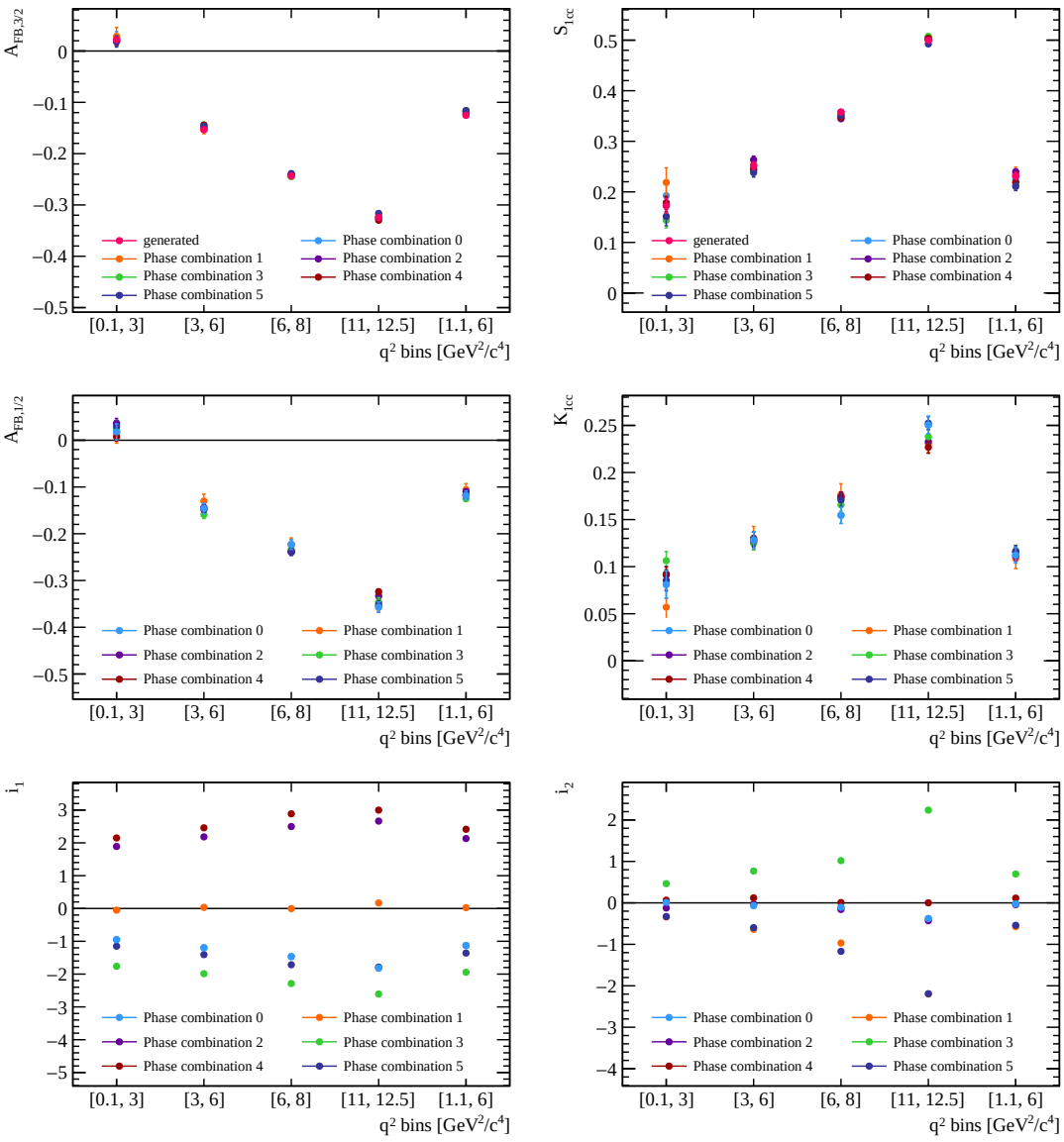

Figure 4.23 – The resulting parameter values by fitting the dedicated Monte-Carlo samples with the fit model 3.

fit parameters, $A^{\ell}_{FB,3/2}$ and S_{1cc}, and their generated values is found. The fit values of the nuisance parameter, $A^{\ell}_{FB,1/2}$ and K_{1cc}, agree within one standard deviation. In general, the resulting fit values are comparable to the ones of the other two fit models, especially the ones obtained with the fit configuration 1.

In summary, the third fit configuration describes well the Monte-Carlo simulations. It is worth emphasising that from this study, one can conclude that the values of the lepton asymmetries remain stable with respect to different interferences schemes, as shown in fig 4.23. Compared to model 1, the advantage of this third configuration is that the spin-1/2 PDF does not become negative. Therefore, this fit configuration will be used as a baseline for the rest of this thesis.

4.2.4 Two-dimensional scan of the angular PDF

Since probabilities cannot be negative, the angular PDF has to be positive in the full phase space spanned by $\cos\theta_p$ and $\cos\theta_\ell$. If the PDF becomes negative, `RooFit` [188] the fitting framework used in this analysis, which is built on top of `Minuit` [189], "struggles" to find a minimum. This is the reason why the sign of the angular PDF is scanned.

For this scan, the observable values are set to those received by the fit to the dedicated simulation samples with phase combination 0. Then, two observables are varied in 101 equidistant steps between the minimum and maximum. At each observable value, $\cos\theta_p$ and $\cos\theta_\ell$ are scanned using a grid of 101 equidistant points in each of the angles. If the PDF stays positive for the whole scan, the value one is assigned. A negative PDF value is represented by the value zero.

The PDF scan in the $q^2 \in [6, 8]\,\mathrm{GeV}^2/c^4$ bin is shown in Fig. 4.24 and 4.25. The scans in all the other rare q^2 bins are presented in App. L. The negative PDF regions are marked in grey and the initial observable values are drawn as red dots.

The scan of the angular PDF shows that minor variations of the observable values result in a negative PDF. The $A^{\ell}_{FB,3/2}$ versus S_{1cc} plot shows an especially closeness to the physical boundary. This behaviour complicates the convergence of the fitting algorithm.

4.2.5 Data fits of the control modes

The studies on the dedicated Monte-Carlo samples allowed us to establish a good model for the m_{pK} line shape as well as the angles. The next step is to test our setup on data by taking into account backgrounds and angular acceptances. The control mode fit is a crucial test in order to determine the fit convergence on a large data sample, before fitting the rare signal.

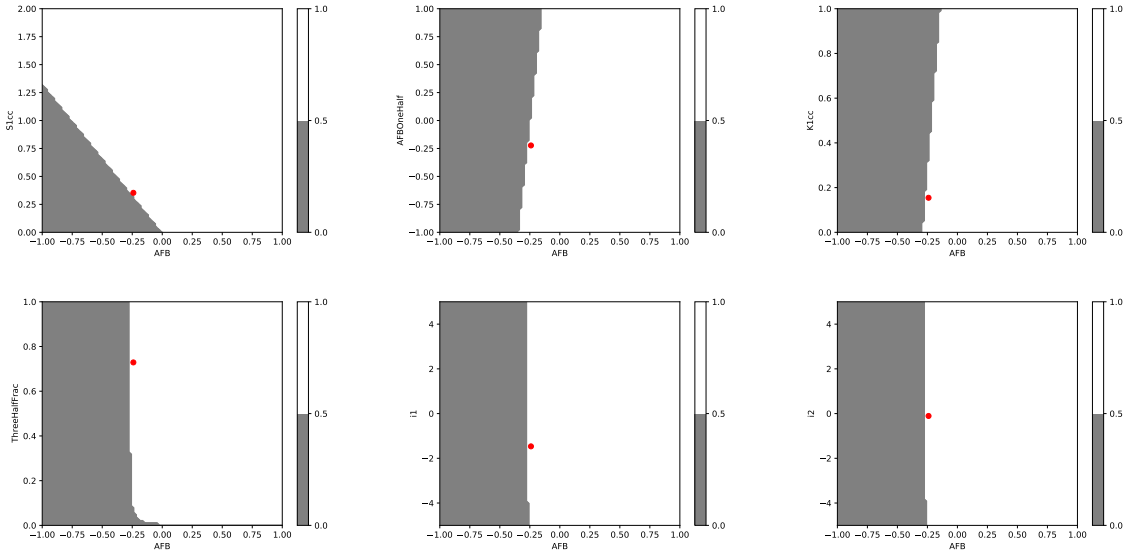

Figure 4.24 – The first part of the two-dimensional scan of the angular PDF of the fit configuration 3. The starting values are taken from the fit result of the dedicated simulation samples with phase combination 0 in the $q^2 \in [6, 8]\,\mathrm{GeV}^2/c^4$ bin, which is marked in red. The grey zone corresponds to the region, where the angular PDF gets negative.

Applying the ${}_s\mathcal{W}eight$s on the data yields a background subtracted distribution. By adding, then, the angular acceptance weights on the data corrects for the shape introduced by the trigger, selection and corrections weights. This enables to perform a maximum likelihood fit on the ${}_s\mathcal{W}eight$ted and acceptance corrected dataset [190]. The angular fit is tested on both control modes *i.e.* $\Lambda_b^0 \to \Lambda(1520)J/\psi$ and $\Lambda_b^0 \to \Lambda(1520)\psi(2S)$. Given that the leptonic part of the control modes occurs via well-known very narrow resonances (J/ψ or $\psi(2S)$), mass constraints can be applied to these resonances when computing the Λ_b^0 invariant mass fit and thus improving the mass resolution of the $\Lambda_b^0 \to \Lambda(1520)J/\psi$ and $\Lambda_b^0 \to \Lambda(1520)\psi(2S)$ distributions. Given that it is not expected that the angular observables of interest vary when running the final angular fit on these two configurations, it is interesting to perform both fits as additional cross-checks.

Angular fit of the $\Lambda_b^0 \to \Lambda(1520)J/\psi$ control mode

In the previous chapter, the third fit configuration is determined to work the best. This third fit configuration is, thus, tested to fit the pK^- invariant mass and the angular distribution in the ${}_s\mathcal{W}eight$ted and acceptance corrected data. Two data fits are compared. To the first one, ${}_s\mathcal{W}eight$s from the J/ψ-constrained Λ_b^0 mass fit are applied on the data, while in the second case, the data is background subtracted with ${}_s\mathcal{W}eight$s from

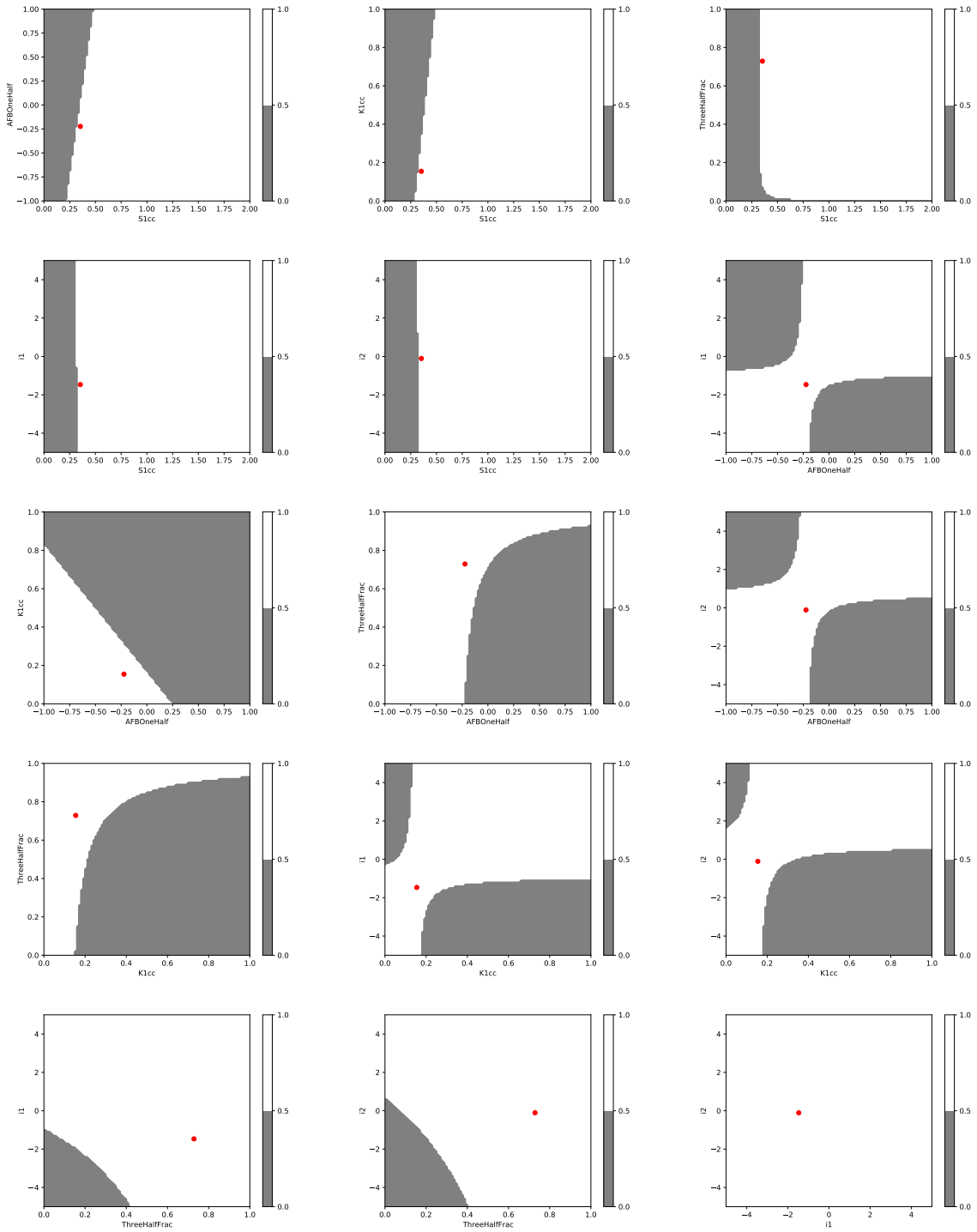

Figure 4.25 – The second part of the two-dimensional scan of the angular PDF of the fit configuration 3. The starting values are taken from the fit result of the dedicated simulation samples in the $q^2 \in [6, 8]\,\mathrm{GeV}^2/c^4$ bin, which is marked in red. The grey zone corresponds to the region where the angular PDF gets negative.

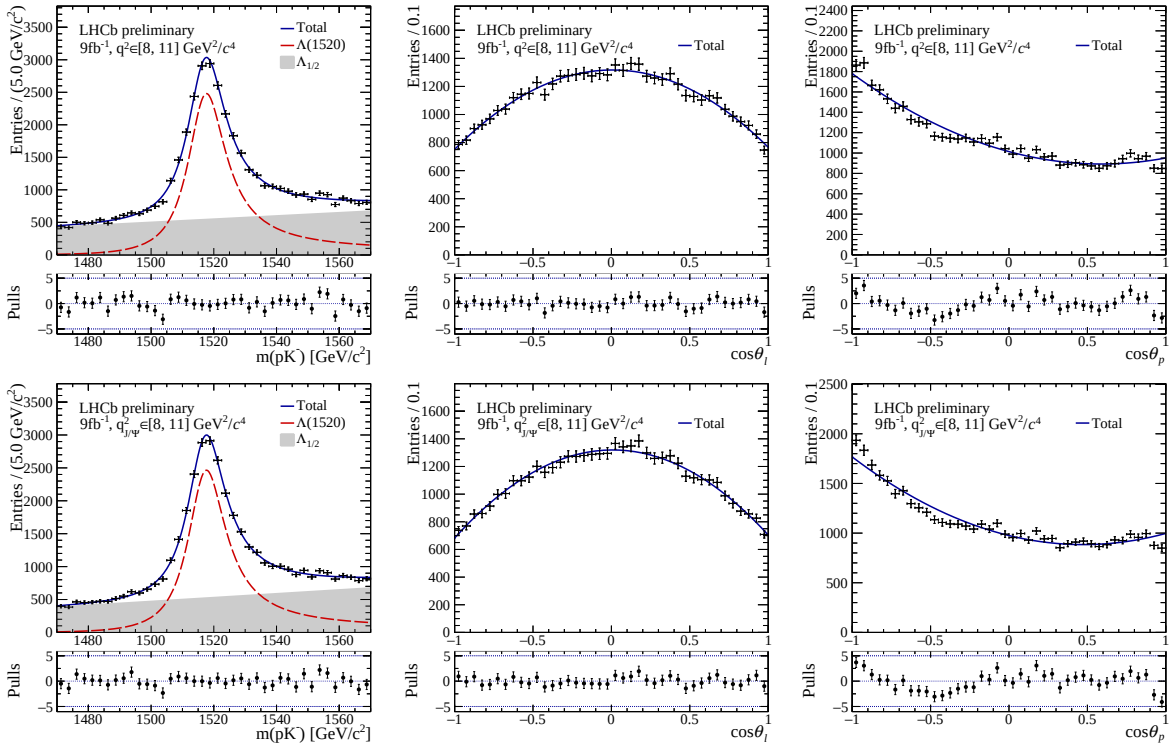

Figure 4.26 – The $m(pK^-)$, $\cos\theta_\ell$ and $\cos\theta_p$ fit projections are drawn. The fit is performed in the J/ψ bin, with ${}_s\mathcal{W}eights$ from the J/ψ-constrained (bottom) and unconstrained (top) $pK^-\mu^+\mu^-$ invariant mass fit.

the J/ψ-unconstrained Λ_b^0 mass fit.

As described previously, a fit to the pK^- mass spectrum is performed first to get the fraction of $\Lambda(1520)$ resonances. To avoid any bias of the $f_{3/2}$ fraction, the Breit-Wigner pole mass and width are fixed in the pK^- mass fit to the values used in Ref. [191] and [60]. However, a tiny bias is seen in the pseudo-experiments later in this section, and its size is evaluated in App. N.3. This bias has been corrected before fitting the angular observables.

The final fit projections are drawn in Fig. 4.26. The pulls of the $m(pK^-)$, $\cos\theta_\ell$ and $\cos\theta_p$ fit projections are distributed around zero. While the shape of the pK^- invariant mass fit and the $\cos\theta_p$ fit projection are similar between the two fits, the shape of the $\cos\theta_\ell$ distribution has small differences. The $\cos\theta_\ell$ distribution with the ${}_s\mathcal{W}eights$ from the J/ψ unconstrained fit case is relatively flat and slightly parabolic in the constrained case. The values of the K_{1cc} and S_{1cc} observables are a bit different in the two cases.

The fit parameter values are collected in Tab. 4.4. The goal of the pK^- invariant mass fit is the extraction of the fraction of $\Lambda(1520)$ resonances. Consequently, it is reassuring that both fits yield $f_{3/2}$ fractions, which are compatible with each other within

Parameter	J/ψ unconstrained	J/ψ constrained
M_{Λ^*} [MeV/c^2]	fixed to 1518.5	fixed to 1518.5
Γ_{Λ^*} [MeV]	fixed to 15.7	fixed to 15.7
$f_{3/2}$	0.493 ± 0.005	0.500 ± 0.005
a_1	0.220 ± 0.014	0.270 ± 0.014
$A^{\ell}_{\mathrm{FB},3/2}$	0.010 ± 0.008	0.008 ± 0.008
S_{1cc}	0.642 ± 0.015	0.609 ± 0.014
$A^{\ell}_{\mathrm{FB},1/2}$	-0.004 ± 0.009	0.001 ± 0.009
K_{1cc}	0.354 ± 0.008	0.332 ± 0.008
i_1	-0.387 ± 0.016	-0.364 ± 0.016
i_2	-2.180 ± 0.031	-2.137 ± 0.032

Table 4.4 – The resulting parameter values and yields of the mass and angular fits in the J/ψ bin are listed in this table. The fits are performed by applying the ${}_s\mathcal{W}eight$s extracted from the J/ψ-unconstrained (left) and J/ψ-constrained (right) $pK^-\mu^+\mu^-$ invariant mass fits in data.

one standard deviation. In the SM, the $b \to c\bar{c}s$ transitions are expected to possess vanishing leptonic forward-backwards asymmetries. In the J/ψ mode, the measured forward-backwards asymmetries, $A^{\ell}_{FB,3/2}$ and $A^{\ell}_{FB,1/2}$, are compatible with zero within two standard deviations. This holds for the angular fits with both ${}_s\mathcal{W}eight$ configurations, obtained from the J/ψ constrained and unconstrained Λ^0_b mass. The interference parameters $i_{1,2}$ are incompatible with zero, which highlights the importance of taking them into account.

While the A^{ℓ}_{FB} asymmetries in the two ${}_s\mathcal{W}eight$ configurations are compatible with each other within one standard deviation, the observables S_{1cc} and K_{1cc} are three standard deviations away in both configurations, which could be explained by a strong correlation of the two observables (see Tab. 4.6). The interference terms agree within two standard deviations. In Tab. 4.5, the linear correlation coefficients between the pK^- mass fit parameters in the J/ψ bin are given. The fraction $f_{3/2}$ is nearly uncorrelated from the coefficient of the first-order polynomial term, a_1, which describes the spin-1/2 Λ^* resonance contribution.

The strongest correlations of the angular fit parameters, which are in the following case anti-correlations, are mostly between the asymmetries $A^{\ell}_{FB,3/2}$ and $A^{\ell}_{FB,1/2}$, and between the observables S_{1cc} and K_{1cc}. Both pairs show the same $\cos\theta_\ell$ dependence in the $\mathrm{PDF}_{\mathrm{ang},3/2}$ and $\mathrm{PDF}_{\mathrm{ang},1/2}$. The correlations in the J/ψ-constrained case show similar behaviour. A fit with decorrelated observables was tested but did not show any improvement. Therefore, the previously described fit remains the baseline.

	$f_{3/2}$	a_1
$f_{3/2}$	1.000	-0.141
a_1	-0.141	1.000

Table 4.5 – The linear correlation coefficients, derived by `Minuit` [189], between the different pK^- invariant mass fit parameters are listed exemplarily for the fit in the J/ψ mode. The employed ${}_s\mathcal{W}eights$ are obtained from the J/ψ-unconstrained Λ_b^0 mass fit.

	$A^{\ell}_{FB,3/2}$	S_{1cc}	$A^{\ell}_{FB,1/2}$	K_{1cc}	i_1	i_2
$A^{\ell}_{FB,3/2}$	1.000	-0.017	-0.414	0.017	-0.016	0.012
S_{1cc}	-0.017	1.000	0.017	-0.417	-0.035	0.033
$A^{\ell}_{FB,1/2}$	-0.414	0.017	1.000	-0.014	0.020	-0.008
K_{1cc}	0.017	-0.417	-0.014	1.000	0.053	-0.047
i_1	-0.017	-0.036	0.020	0.053	1.000	-0.120
i_2	0.012	0.033	-0.008	-0.047	-0.120	1.000

Table 4.6 – The linear correlation coefficients, derived by `Minuit` [189], between the different angular fit parameters are given exemplarily for the fit in the J/ψ mode. The employed ${}_s\mathcal{W}eights$ are obtained from the J/ψ-unconstrained Λ_b^0 mass fit.

The fit stability can be tested by generating Monte-Carlo (MC) samples based on the data fit results. To distinguish those MC samples from other simulation samples, they are called "pseudo-datasets". Those pseudo-datasets are fitted in the same way as the data, and the pulls are calculated according to Eq. 3.16. A large number of such pseudo-experiments are performed to quantify the fit stability. The pull distribution itself is fitted with a Gaussian. An unbiased fit has a Gaussian mean compatible with zero. A Gaussian width compatible with one indicates a good coverage of the confidence interval.

Such pseudo-experiments have been performed in the J/ψ bin, while the fit results are obtained by applying ${}_s\mathcal{W}eights$ from the J/ψ-unconstrained Λ_b^0 mass fit. The results with ${}_s\mathcal{W}eights$ from the J/ψ-constrained Λ_b^0 mass fit can be looked up in App. N.1. In total, 1000 pseudo-experiments are performed. The size of the pseudo-dataset corresponds to the Λ_b^0 yield in the corresponding J/ψ bin. At first, the pK^- invariant mass fit parameters are tested, as shown in Fig. 4.27.

The fraction $f_{3/2}$ is biased by 5σ, while the a_1 slope is well estimated. Since the $f_{3/2}$ value is part of the angular fit, the value needs to be corrected. The parameter uncertainties are well covered. A test has been performed by generating pseudo-experiments with the J/ψ mass parameters combined with the $\psi(2S)$ yield. The pulls of the $f_{3/2}$ fraction are well-behaved, as seen in App. N.3. This cross-check indicates the smallness of the

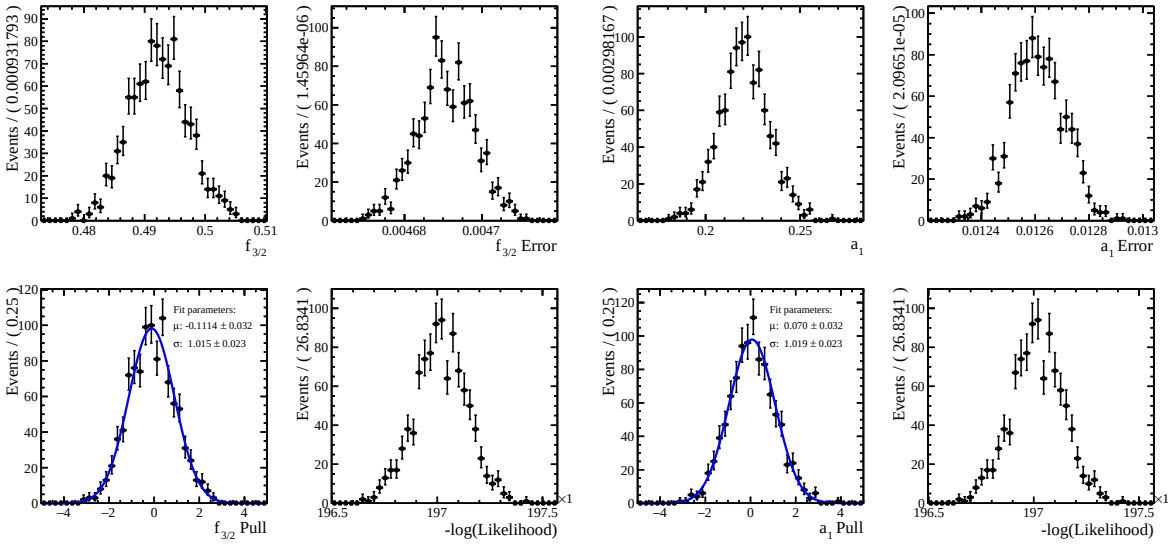

Figure 4.27 – The pull distributions of the pK^- invariant mass fit parameters, based on the fit results in the J/ψ bin. One thousand pseudo-experiments are generated. The pulls of the fraction $f_{3/2}$ and the slope parameter a_1 are plotted.

observed bias.

In the second step, pseudo-experiments are generated to test the angular fit. In the generation of each pseudo-dataset, the fraction $f_{3/2}$ is fixed to the value obtained in the previous pK^- invariant mass fit. The angular fit results in the J/ψ bin serve as starting values for generating the angular pseudo-datasets. The pull distributions of the angular observables are shown in Fig. 4.28.

The pulls of the forward-backwards asymmetries, $A^{\ell}_{FB,3/2}$ and $A^{\ell}_{FB,1/2}$, are well behaved. The S_{1cc} observable is unbiased, but the uncertainties are slightly underestimated. The remaining nuisance parameters are reasonably well estimated.

In summary, the angular fit model has been validated on data in the J/ψ bin, which has a large data sample size. The angular fit has been performed on the ${}_s\mathcal{W}eight$ted, and acceptance corrected data sample, while the ${}_s\mathcal{W}eight$s are extracted from the J/ψ-constrained and unconstrained Λ_b^0 mass fit. The forward-backwards asymmetries $A^{\ell}_{FB,3/2}$ and $A^{\ell}_{FB,1/2}$ vanish in both configurations, as expected. A bias of the fraction $f_{3/2}$ is observed, which has been corrected before performing the angular fit. The size of the bias has been tested to be tiny and not visible with a sample size corresponding to the $\psi(2S)$ yield. The pull distributions of the angular observables are well-behaved.

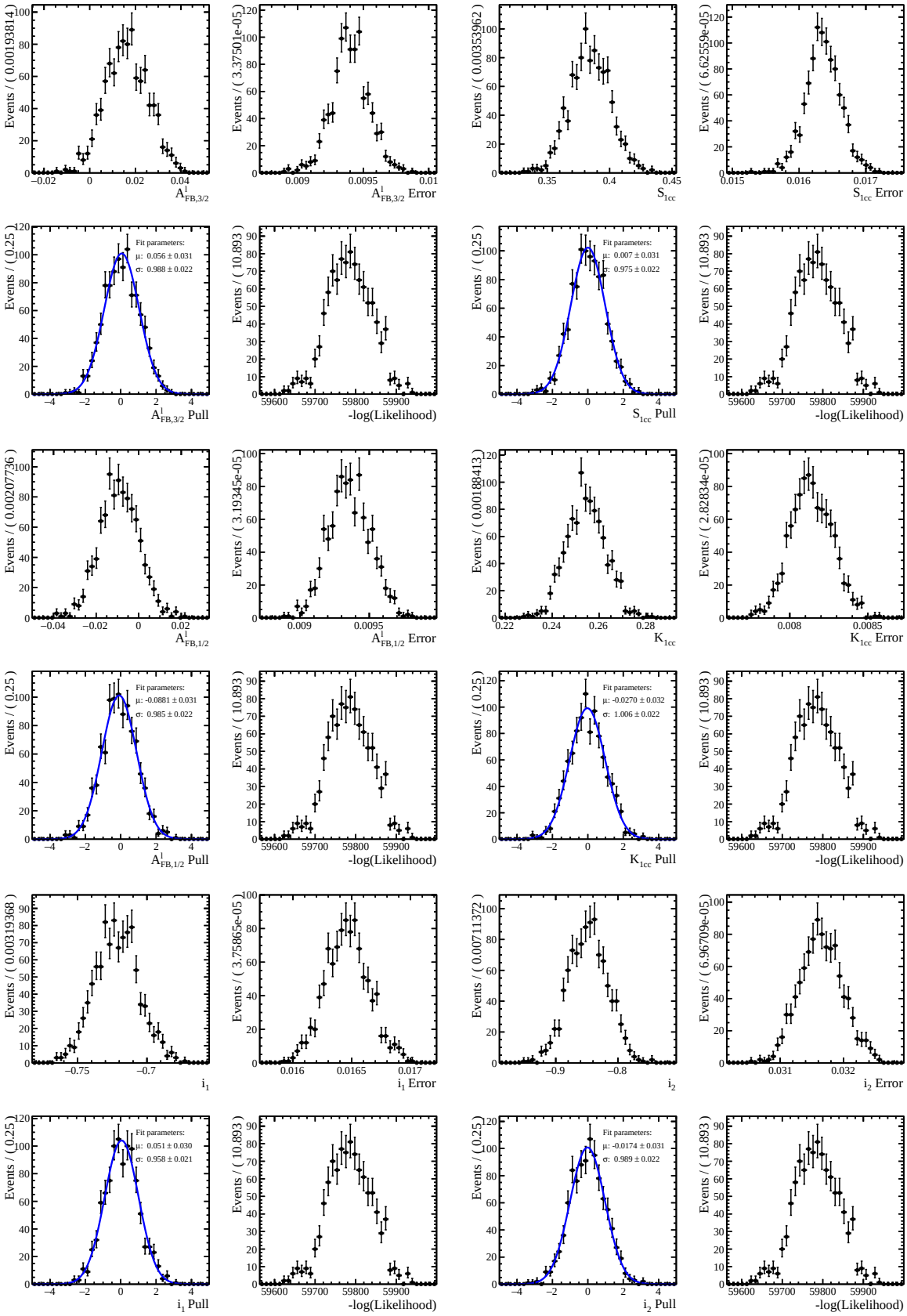

Figure 4.28 – The pull distributions of the angular observables are shown. One thousand pseudo-experiments are generated based on the angular fit results in the J/ψ bin.

Angular fit of the $\Lambda_b^0 \to \Lambda(1520)\psi(2S)$ control mode

The fit procedure of the $\Lambda_b^0 \to \Lambda(1520)\psi(2S)$ decay is similar to the one of the J/ψ mode. Testing the fit procedure on the $\psi(2S)$ mode is interesting since the data sample size is closer to the rare mode. The angular distribution in the ${}_s\mathcal{W}eight$ted and acceptance corrected data is fitted by applying ${}_s\mathcal{W}eight$s obtained in the $\psi(2S)$-unconstrained and constrained Λ_b^0 mass fit. The angular fits of both configurations are shown in Fig. 4.29.

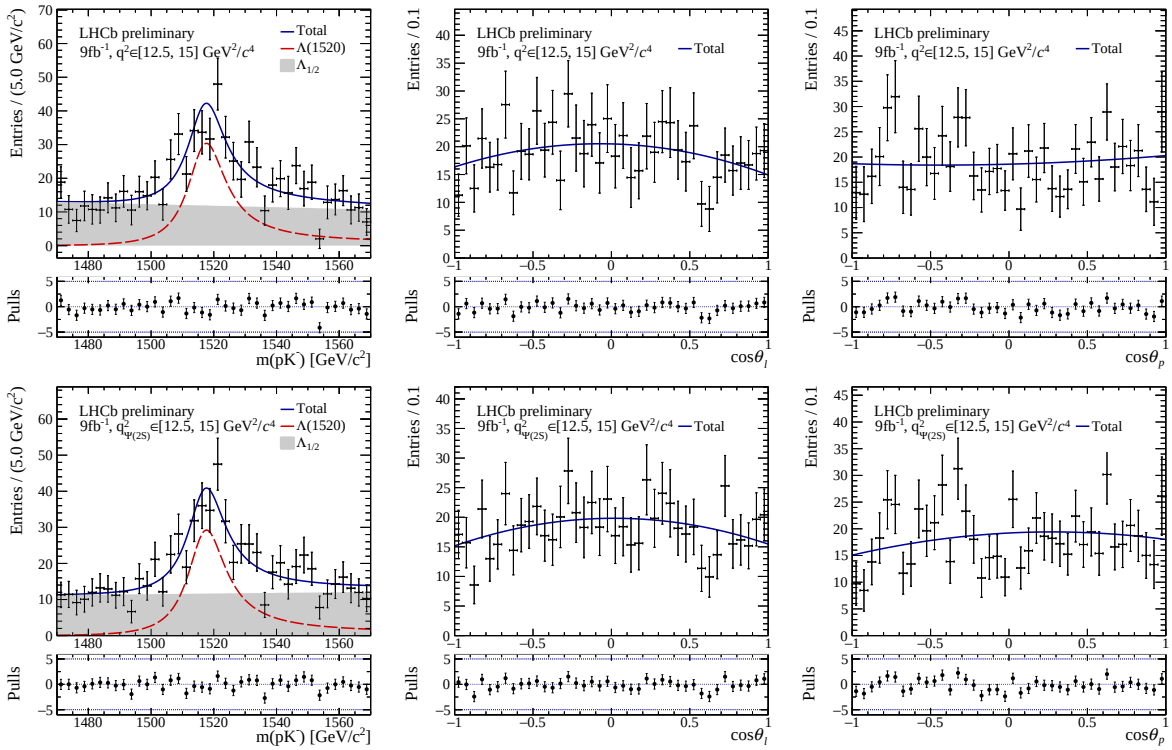

Figure 4.29 – The $m(pK^-)$, $\cos\theta_\ell$ and $\cos\theta_p$ fit projections are drawn for the fit of the $\psi(2S)$ control mode. On the top, the ${}_s\mathcal{W}eight$s are extracted from the $pK^-\mu^+\mu^-$ unconstrained invariant mass fit and on the bottom, from the $\psi(2S)$ constrained mass fit.

Both $\psi(2S)$ fits look visually similar. For both fit configurations, the pulls are consistent with zero. The corresponding fit results are listed in Tab. 4.7. All fit parameters are compatible in the two ${}_s\mathcal{W}eight$ configurations within one standard deviation. The forward-backwards asymmetries, $A^\ell_{FB,3/2}$ and $A^\ell_{FB,1/2}$, are consistent with zero within at most two standard deviations. While the interference parameter i_1 is compatible with zero, i_2 is ten standard deviations away from being negligible. Although the interference parameter i_2 takes in the J/ψ and $\psi(2S)$ mode a value of about -2, the strength of the interference terms cannot be extrapolated to the rare q^2 bins since the fraction of $\Lambda(1405)$ versus $\Lambda(1600)$ resonances may change and impact the interference parameter values.

Parameter	$\psi(2S)$ unconstrained	$\psi(2S)$ constrained
M_{Λ^*} [MeV/c^2]	fixed to 1518.5	fixed to 1518.5
Γ_{Λ^*} [MeV]	fixed to 15.7	fixed to 15.7
$f_{3/2}$	0.361 ± 0.043	0.365 ± 0.040
a_1	-0.095 ± 0.110	0.031 ± 0.097
$A^{\ell}_{\mathrm{FB},3/2}$	-0.143 ± 0.094	-0.053 ± 0.124
S_{1cc}	0.454 ± 0.146	0.455 ± 0.252
$A^{\ell}_{\mathrm{FB},1/2}$	0.055 ± 0.067	0.048 ± 0.072
K_{1cc}	0.478 ± 0.056	0.464 ± 0.071
i_1	0.016 ± 0.097	0.024 ± 0.116
i_2	-1.909 ± 0.211	-1.952 ± 0.210

Table 4.7 – The resulting parameter values and yields of the pK^- invariant mass fit and the angular fit in the $\psi(2S)$ bin are listed in this table. The fits are performed by applying the ${}_s\mathcal{W}eights$ extracted from the $\psi(2S)$-unconstrained (left) and $\psi(2S)$-constrained (right) $pK^-\mu^+\mu^-$ invariant mass fits in data.

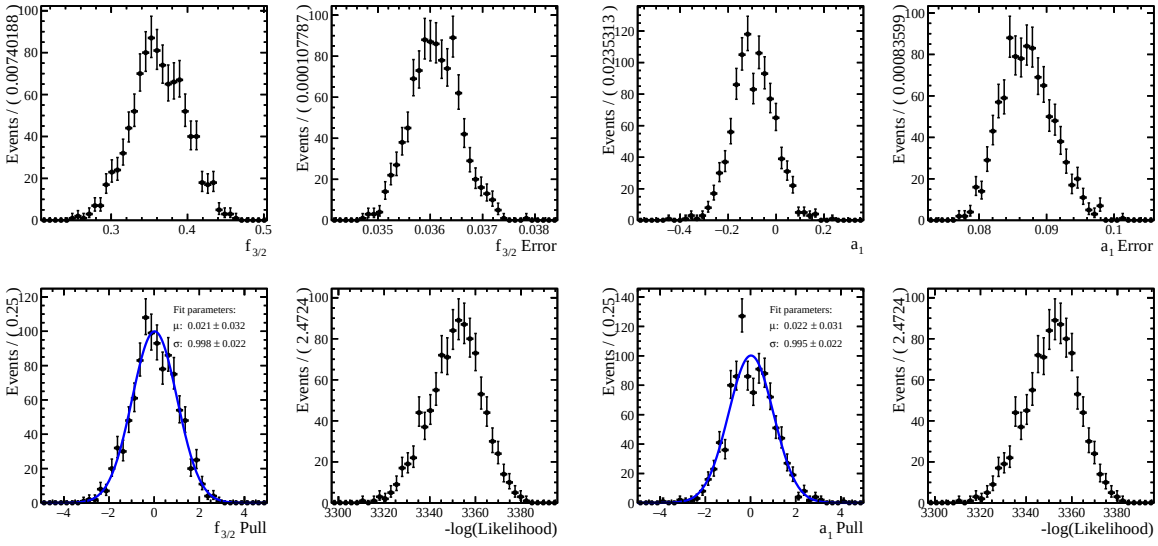

Figure 4.30 – Pseudo-experiments are generated based on the pK^- invariant mass fit in the $\psi(2S)$ bin in data, employing the ${}_s\mathcal{W}eights$ from the unconstrained Λ_b^0 mass fit. The pull distributions of the $f_{3/2}$ fraction and the a_1 parameter are drawn.

The pK^- invariant mass fit is tested by performing pseudo-experiments. The ${}_s\mathcal{W}eight$ configuration without a $\psi(2S)$-constraint is shown in this section, while the $\psi(2S)$-constrained case is added to App. N.2. The resulting pull distributions are shown in Fig. 4.30. The pull of the $f_{3/2}$ fraction has a Gaussian mean and width compatible with zero and one, respectively, within one standard deviation. The polynomial parameter a_1 is unbiased, and its uncertainty is well estimated.

Pseudo-experiments are also performed for the angular fit in the $\psi(2S)$ bin, in the same manner as in the J/ψ mode (see above in Sec. 4.2.5). The results are shown in Fig. 4.31. The pull distributions of the angular observables $A_{FB,3/2}$ and S_{1cc} show a Gaussian mean two and three standard deviations away from zero. The confidence intervals of the angular observables are well-covered. The same trend can be seen in the pulls of the nuisance parameters.

To conclude, the angular fit to the ${}_s\mathcal{W}eight$ted and acceptance corrected data converges in the $\psi(2S)$ bin. However, the angular observables $A_{FB,3/2}$ and S_{1cc} are slightly biased.

4.2.6 The ${}_s\mathcal{W}eight$ted data fits in the rare mode

In this section, the angular fit procedure is applied in the rare q^2 bins. The fit is performed on ${}_s\mathcal{W}eight$ted and acceptance corrected data, but the angular observables are kept blind. This procedure has been chosen because of the observed fit convergence problems.

All of the pK^- invariant mass fits converge reliably. On the contrary, the angular fit terminates in most of the q^2 bins with a fit status of 4, indicating that Migrad did not converge. In the $q^2 \in [3,6]\,\mathrm{GeV}^2/c^4$ bin, the fit terminates without any problem, but one of the fit parameter values reaches the parameter limit. The resulting fit projections are shown in Fig. 4.32 and 4.33

Although the non-convergence, the pulls are distributed around zero. Due to the small sample size, some bins become negative. For checking if the problem arises from unexpected behaviour of the ${}_s\mathcal{W}eight$s and acceptance weights, their distributions are examined. The ${}_s\mathcal{W}eight$ and acceptance weight distributions are shown in App. M.5 and M.3. It can be seen that the negative entries result from the ${}_s\mathcal{W}eight$s, needed to subtract the background contribution. No surprisingly high weight could be found neither in the ${}_s\mathcal{W}eight$ nor the acceptance weight distribution.

For testing purposes, a constant shift was added independently to the weights. While a shift of the acceptance weights does not change anything, a shift of the ${}_s\mathcal{W}eight$s by at least 0.8 helps the fit to converge properly. The fits are illustrated in Fig. 4.34 and 4.35.

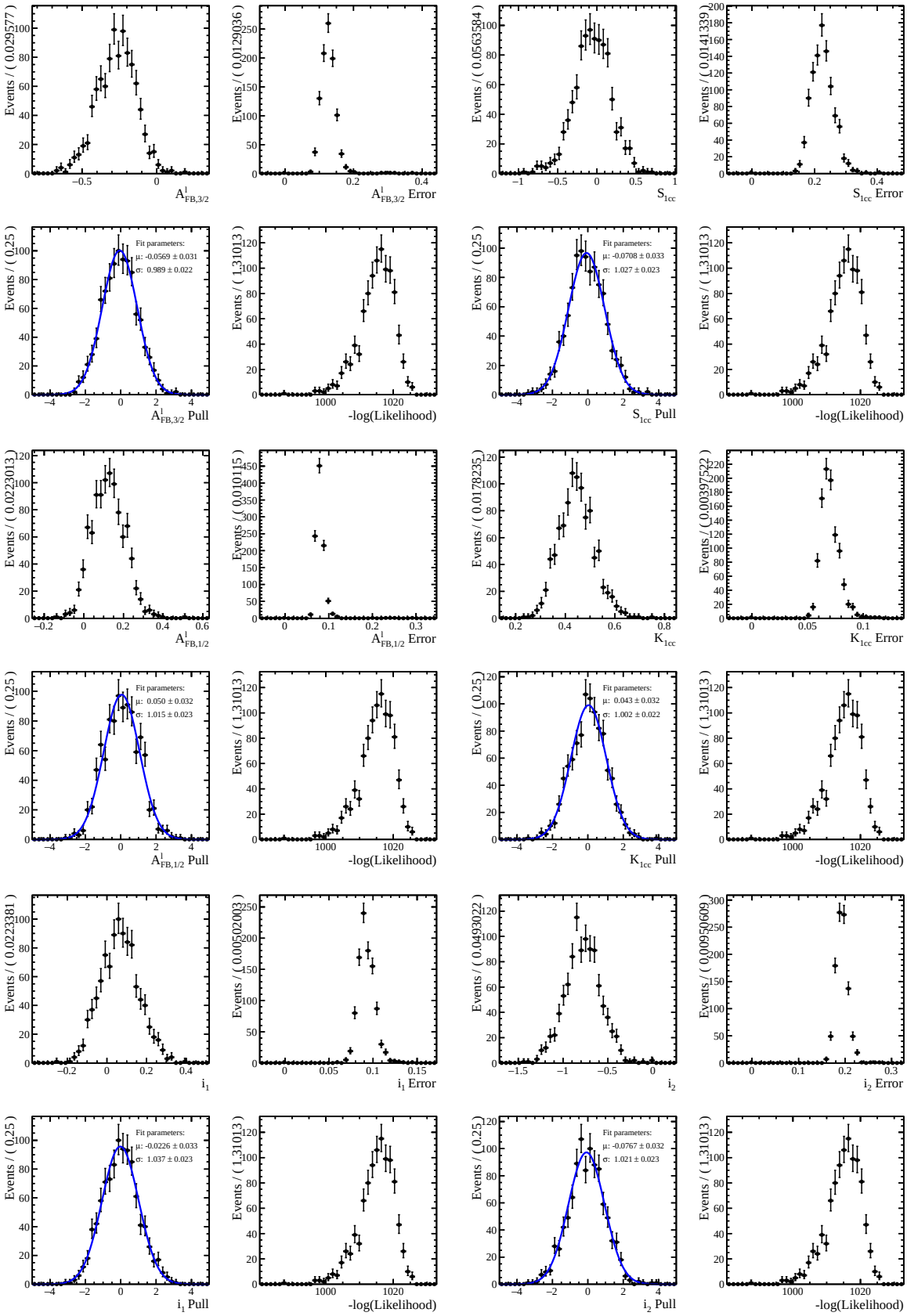

Figure 4.31 – The pull distributions of the angular observables after generating 1000 pseudo-experiments in the $\psi(2S)$ bin, using the ${}_s\mathcal{W}eight$s from the unconstrained Λ_b^0 mass fit, are shown.

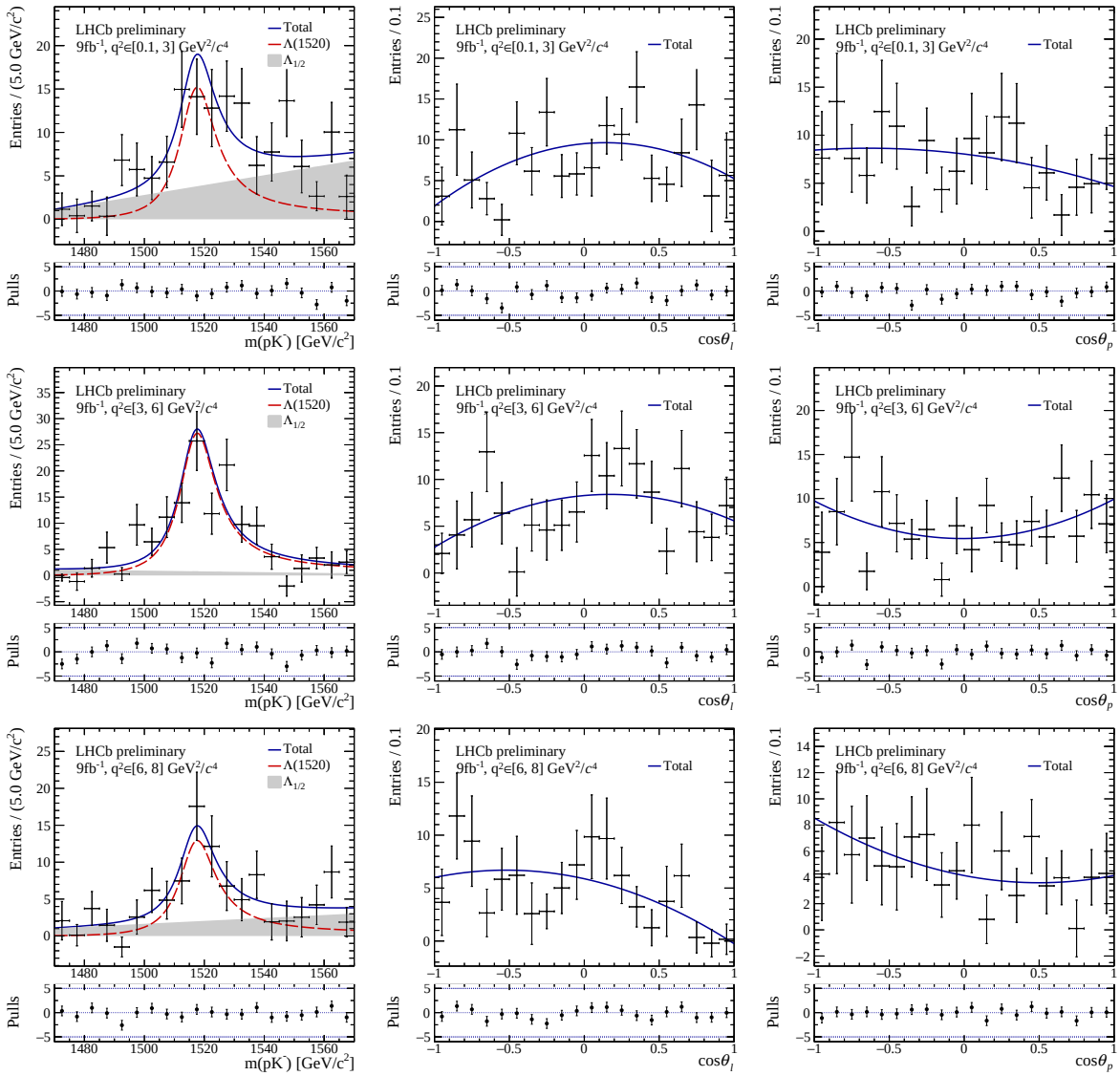

Figure 4.32 – The fit projections of the pK^- invariant mass, $\cos\theta_\ell$ and $\cos\theta_p$ angles for the three narrow q^2 bins below the J/ψ resonance.

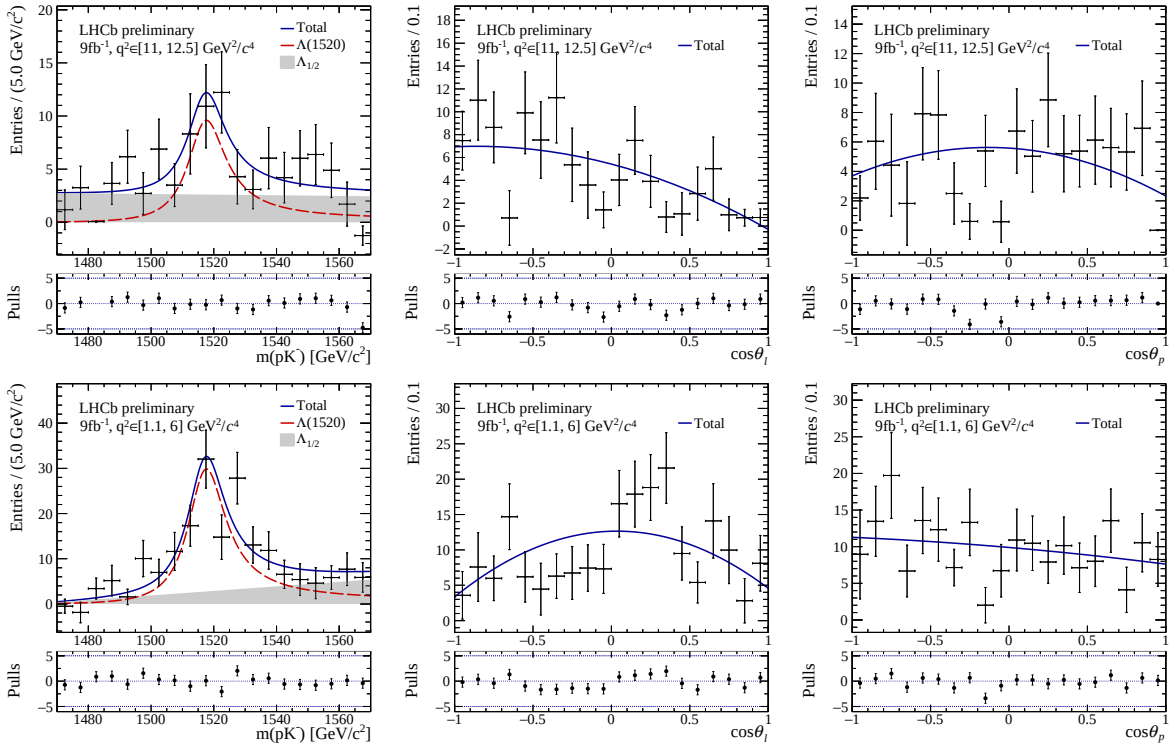

Figure 4.33 – The fit projections of the pK^- invariant mass, $\cos\theta_\ell$ and $\cos\theta_p$ angles for the q^2 bin in-between the $c\bar{c}$ resonances and the large q^2 bin.

From this check, it has been concluded that the convergence problem results from the combination of the small data sample size, the negative ${}_s\mathcal{W}eights$ and the angular PDF getting easily negative, which is shown in sec 4.2.4. What probably happens is that when the fit gets stuck in forbidden regions of the phase space, the negative entries and the small data sample size are not powerful enough to pull the fit into a stable and positive region. The change of the angular shape by applying ${}_s\mathcal{W}eights$ and acceptance weights on data have been checked in App. M.5, but no unexpected behaviour has been spotted.

4.2.7 Rethinking of the combinatorial background treatment in the rare mode

Another possibility to perform an angular fit avoiding ${}_s\mathcal{W}eights$ is to model the combinatorial background. The high sideband of the $pK^-\mu^+\mu^-$ invariant mass above 5700 GeV/c^2 in data is used as a proxy of the combinatorial background. In Fig. 4.36, it can be seen that the combinatorial background sample size is small by using the nominal selection. To increase the size of the combinatorial background sample, and consequently the fit stability, the BDT cut is loosened to 0.9. The pK^- invariant mass shape of this sample is shown in Fig. 4.37 for the different q^2 bins in the rare mode.

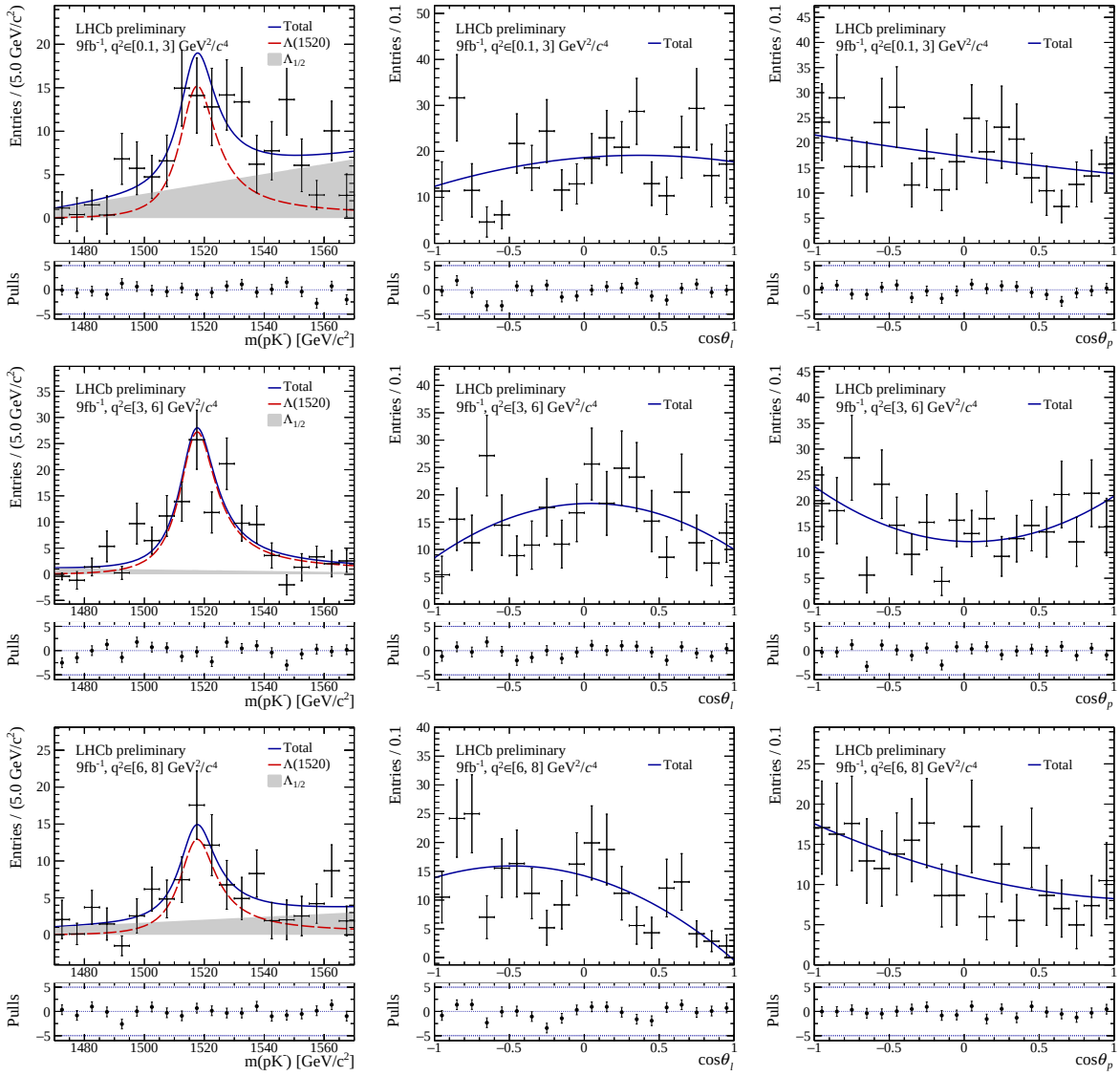

Figure 4.34 – The fit projections of the pK^- invariant mass and angles in the narrow q^2 bins below the $c\bar{c}$ resonances, which converge after applying a shit of 0.8 to the ${}_s\mathcal{W}eights$.

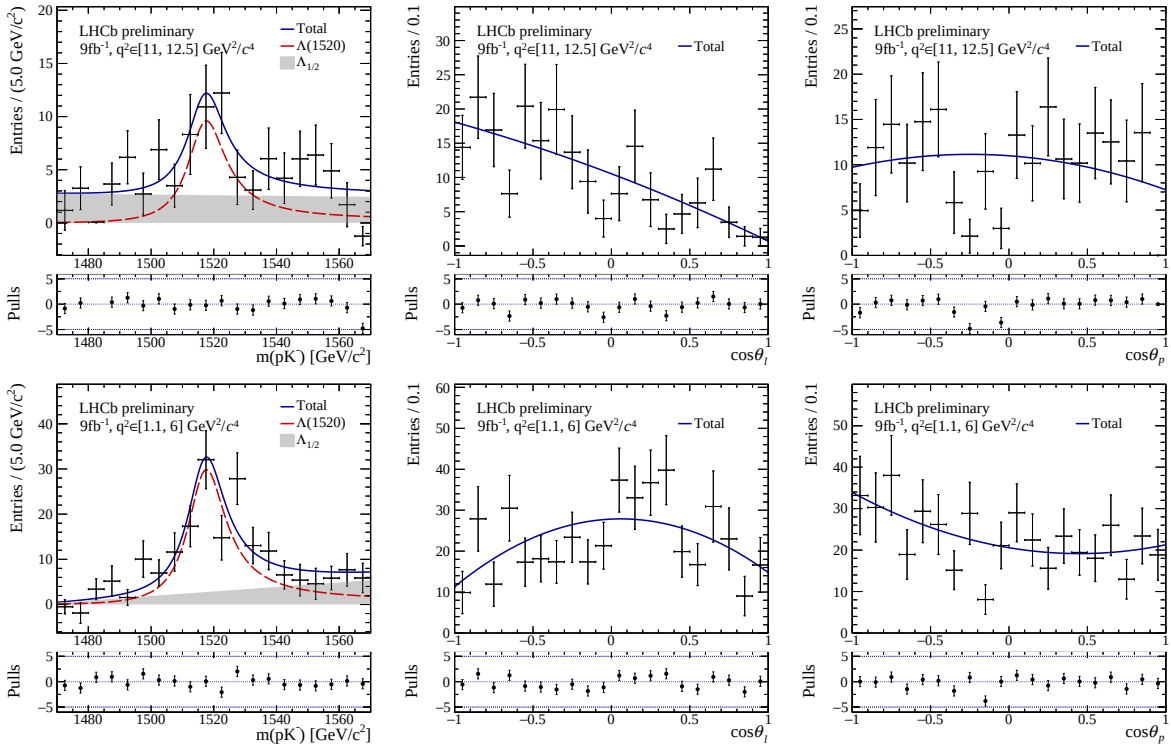

Figure 4.35 – The projections of the pK^- invariant and angular fits in the q^2 bin between the $c\bar{c}$ resonances and the large q^2 bin, which are converging after applying a shit of 0.6 to the ${}_s\mathcal{W}eights$.

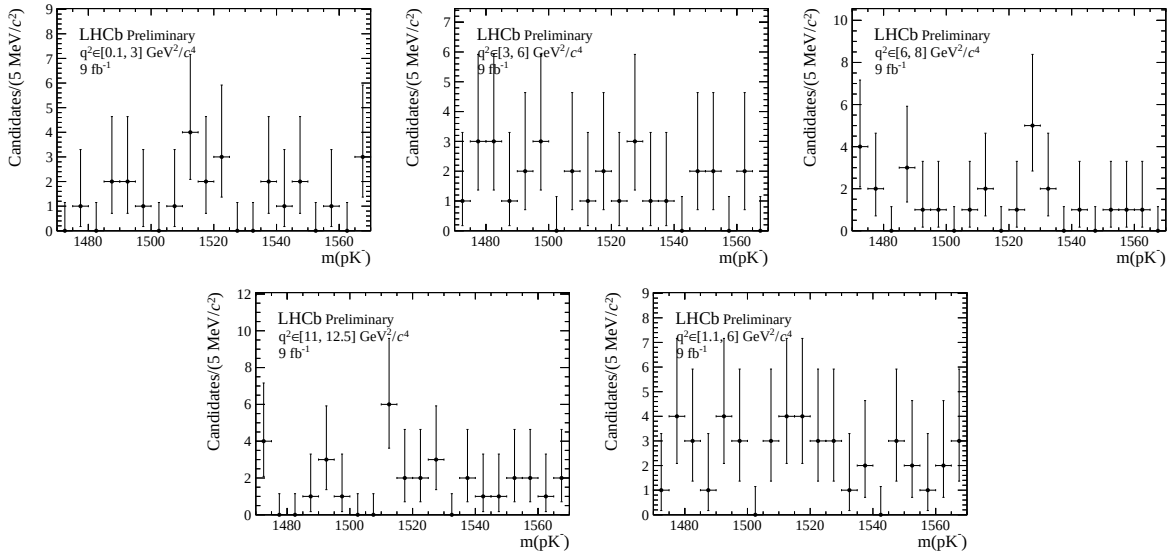

Figure 4.36 – With the nominal BDT cut, keeping only events above 0.99, the data sample size of the combinatorial background is tiny in all q^2 bins in the rare mode.

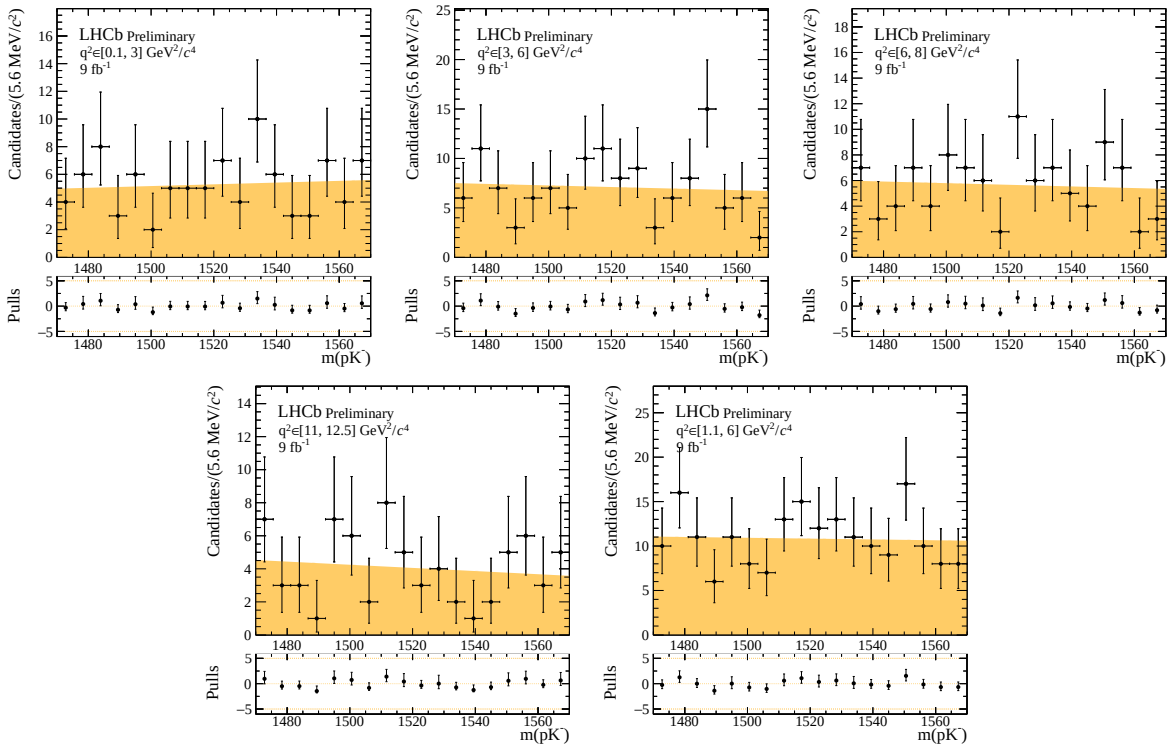

Figure 4.37 – The pK^- invariant mass model for the combinatorial background in the different rare q^2 bins. The BDT cut is loosened to 0.9 in order to increase the data sample size.

A first-order polynomial was chosen to model the combinatorial background's pK^- invariant mass shape. The values of the Chebyshev polynomial parameter c_1 are listed in Tab. 4.8 for the different q^2 bins. Four different BDT cut values between -0.99 and 0.5 are tested to extract the c_1 parameter, in order to cross-check the validity of loosening the BDT cut, as well as the consistency with other cut values. The resulting values are checked to be consistent within, at most, two standard deviations. The BDT cut value of 0.9 has been picked, by balancing the increase of the data sample size with the closeness of the nominal BDT cut, with which the background contributions were evaluated.

	c_1
$q^2 \in [0.1, 3]\,\mathrm{GeV}^2/c^4$	0.06 ± 0.17
$q^2 \in [3, 6]\,\mathrm{GeV}^2/c^4$	-0.06 ± 0.16
$q^2 \in [6, 8]\,\mathrm{GeV}^2/c^4$	-0.06 ± 0.18
$q^2 \in [11, 12.5]\,\mathrm{GeV}^2/c^4$	-0.12 ± 0.19
$q^2 \in [1.1, 6]\,\mathrm{GeV}^2/c^4$	-0.02 ± 0.13

Table 4.8 – The value of the first order polynomial parameter describing the combinatorial background's pK^- invariant mass shape in the different rare q^2 bins.

Since the combinatorial background is supposed to possess uncorrelated $\cos\theta_\ell$ and $\cos\theta_p$ distributions, the angular shape of the combinatorial background is modelled by a product of two Chebyshev polynomials. Both polynomials are restricted to order two, thanks to good modelling of the angular shape in the different q^2 bins. The full model can be written out as

$$\mathrm{PDF}_{\mathrm{combi}} = \mathrm{Poly}_{\mathcal{O}2}(\cos\theta_p) \times \mathrm{Poly}_{\mathcal{O}2}(\cos\theta_\ell). \tag{4.26}$$

The shape is again extracted from the high $pK^-\mu^+\mu^-$ invariant mass sideband in data, but the angular acceptance weights are applied in this case. The angular shapes of the combinatorial background in $\cos\theta_\ell$ and $\cos\theta_p$ are drawn in Fig. 4.38 and 4.39. The binning is chosen in order to minimise the number of empty bins.

The pulls of the angular projections are within an interval of $\pm 5\sigma$. The angular shape parameters to model the combinatorial background are listed in Tab. 4.9.

The combinatorial background component is included in the fit model by fixing the shape parameters to the values presented in Tab. 4.9. Its fraction f_{combi} is fixed in the different q^2 bins to the value listed in Tab. 4.10. The fraction of combinatorial background is calculated from the Λ_b^0 mass fits, shown in Fig. 3.57 and described in Sec. 3.5.5.

The pK^- invariant mass and angular fit projections, including the combinatorial background and the signal component, are drawn in Fig. 4.40 and 4.41. With this new fit

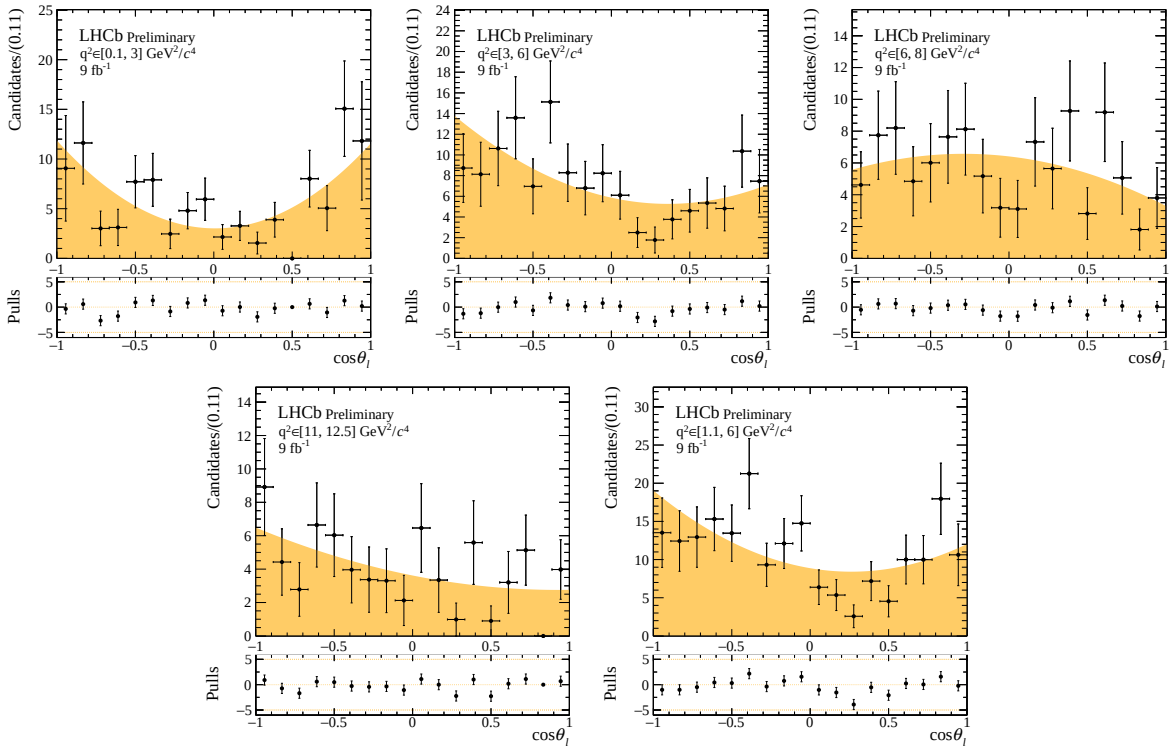

Figure 4.38 – The $\cos\theta_\ell$ projection of the combinatorial background shape in the different rare q^2 bins.

	$c_{\ell,1}$	$c_{\ell,2}$	$c_{p,1}$	$c_{p,2}$
$q^2 \in [0.1, 3]\,\mathrm{GeV}^2/c^4$	-0.02 ± 0.19	0.59 ± 0.11	-0.16 ± 0.20	-0.16 ± 0.20
$q^2 \in [3, 6]\,\mathrm{GeV}^2/c^4$	-0.41 ± 0.15	0.28 ± 0.13	-0.56 ± 0.14	0.21 ± 0.13
$q^2 \in [6, 8]\,\mathrm{GeV}^2/c^4$	-0.21 ± 0.17	-0.18 ± 0.19	-0.52 ± 0.16	0.15 ± 0.15
$q^2 \in [11, 12.5]\,\mathrm{GeV}^2/c^4$	-0.45 ± 0.18	0.12 ± 0.18	-0.38 ± 0.22	-0.17 ± 0.23
$q^2 \in [1.1, 6]\,\mathrm{GeV}^2/c^4$	-0.29 ± 0.13	0.27 ± 0.11	-0.35 ± 0.12	0.03 ± 0.12

Table 4.9 – The values of the angular shape parameters to describe the combinatorial background in the different rare q^2 bins are shown in this table.

	f_{combi}
$q^2 \in [0.1, 3]\,\mathrm{GeV}^2/c^4$	0.24 ± 0.105
$q^2 \in [3, 6]\,\mathrm{GeV}^2/c^4$	0.24 ± 0.010
$q^2 \in [6, 8]\,\mathrm{GeV}^2/c^4$	0.31 ± 0.14
$q^2 \in [1.1, 6]\,\mathrm{GeV}^2/c^4$	0.29 ± 0.09
$q^2 \in [11, 12.5]\,\mathrm{GeV}^2/c^4$	0.21 ± 0.11

Table 4.10 – The values of the combinatorial background fractions in the different q^2 bins are summarised in this table.

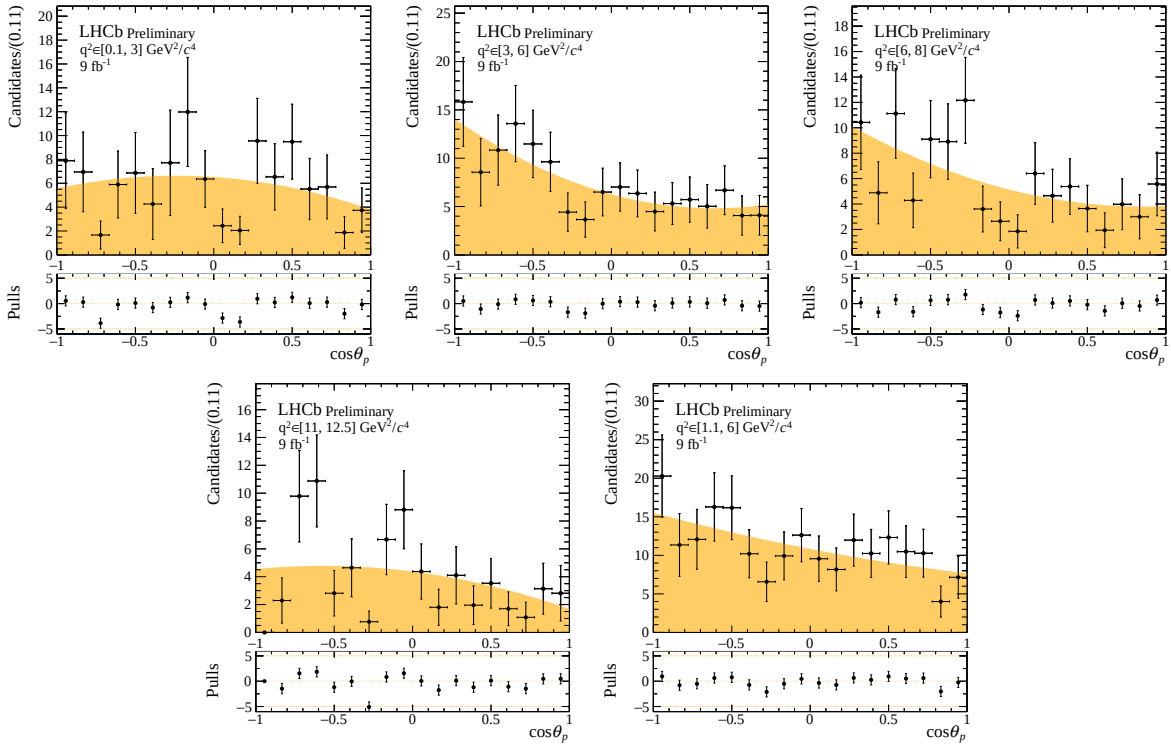

Figure 4.39 – The shape of the combinatorial background in $\cos\theta_p$ is plotted for the different rare q^2 bins.

model, the angular fit converges in all the q^2 bins. The pulls of the fit projections are distributed around zero for all the different q^2 bins.

Pseudo-experiments are performed for this new fit model in the rare mode. Up to now, the combinatorial background shape and the fraction of the combinatorial background, which are extracted from data, are fixed in the pseudo-experiment generation. As for the control modes, pseudo-experiments are first generated for the pK^- invariant mass. The resulting value of the $f_{3/2}$ fraction from each pK^- mass pseudo-experiment is then injected in the generation of the angular pseudo-dataset. The pull distributions of the a_1 parameter and the $f_{3/2}$ fraction are shown in Fig. 4.42 - 4.46.

The $f_{3/2}$ fraction is well-behaved in the $q^2 \in [0.1, 3]\,\mathrm{GeV}^2/c^4$ and the $q^2 \in [3, 6]\,\mathrm{GeV}^2/c^4$ bin. In the $q^2 \in [3, 6]\,\mathrm{GeV}^2/c^4$ bin, the pull distribution of the nuisance parameter a_1 does not follow a Gaussian distribution, as visible in Fig. 4.43. The source of this large distribution could be the small amount of spin-1/2 Λ^* resonances in this q^2 bin. The wide parameter value distribution causes many events to end up at the parameter limit. The parameter error cannot be well estimated there and is probably the origin of the second peak in the a_1 error distribution.

Enlarging the ranges of the a_1 parameter and the $f_{3/2}$ fraction leads to the parameter

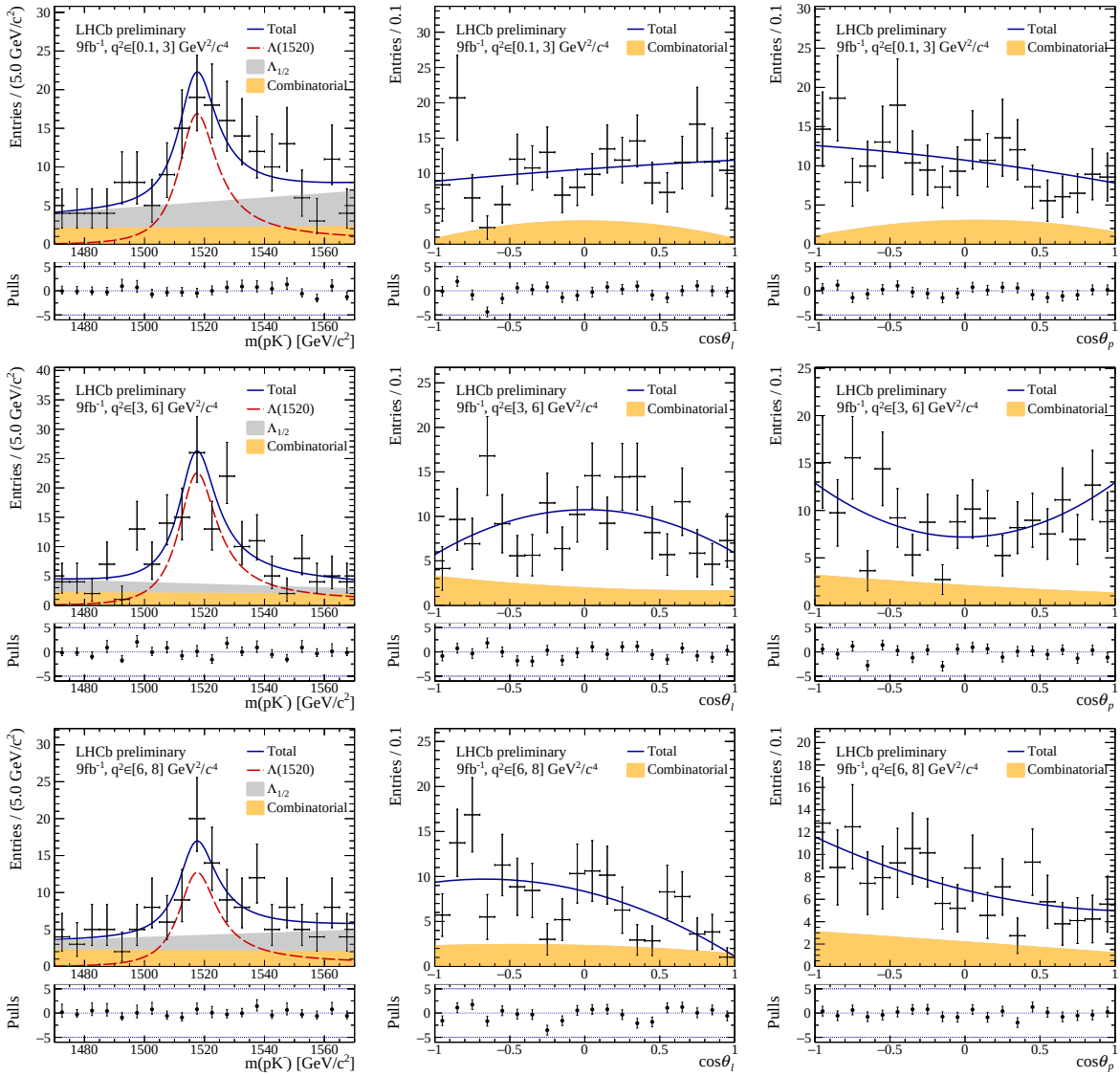

Figure 4.40 – The projections of the pK^- invariant mass and angular fits in the narrow q^2 bin below the $c\bar{c}$ resonances. In the fit model, a component of the combinatorial background is added to the description of the $\Lambda(1520)$ and spin-1/2 Λ^* resonances.

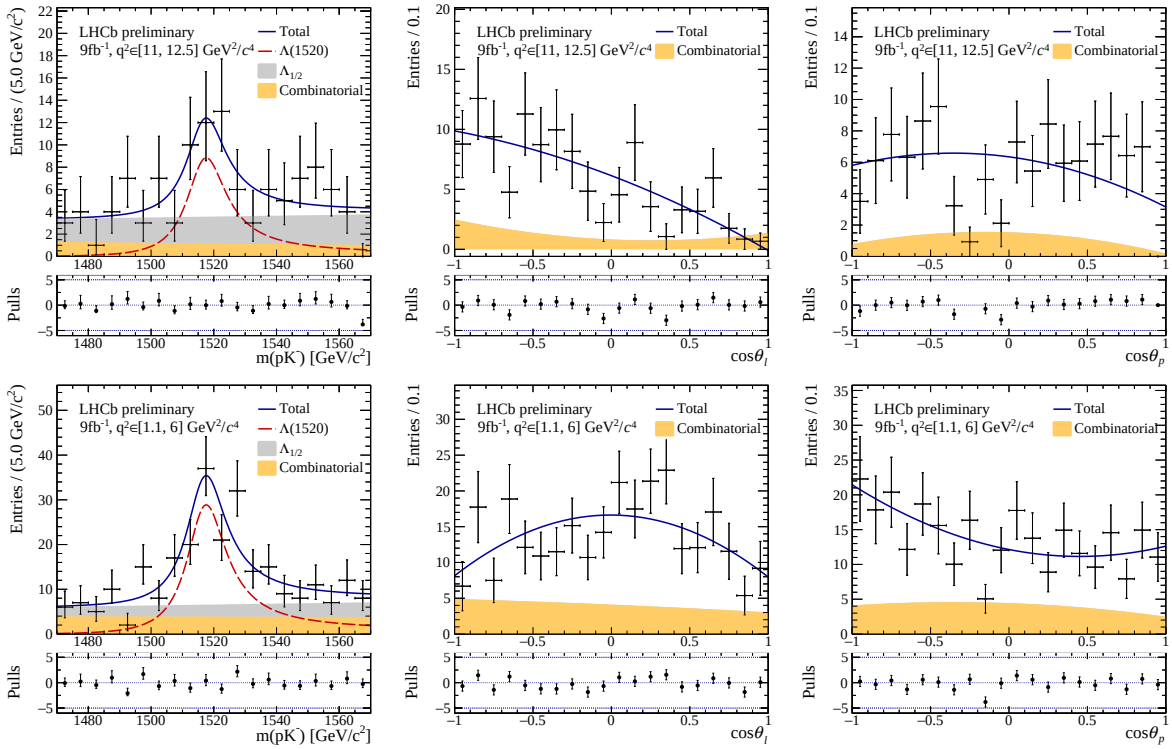

Figure 4.41 – The projections of the pK^- invariant mass and angular fit projections in the q^2 bin between the $c\bar{c}$ resonances and the large q^2 bin. In the fit model, a component of the combinatorial background is added to the description of the $\Lambda(1520)$ and spin-1/2 Λ^* resonances.

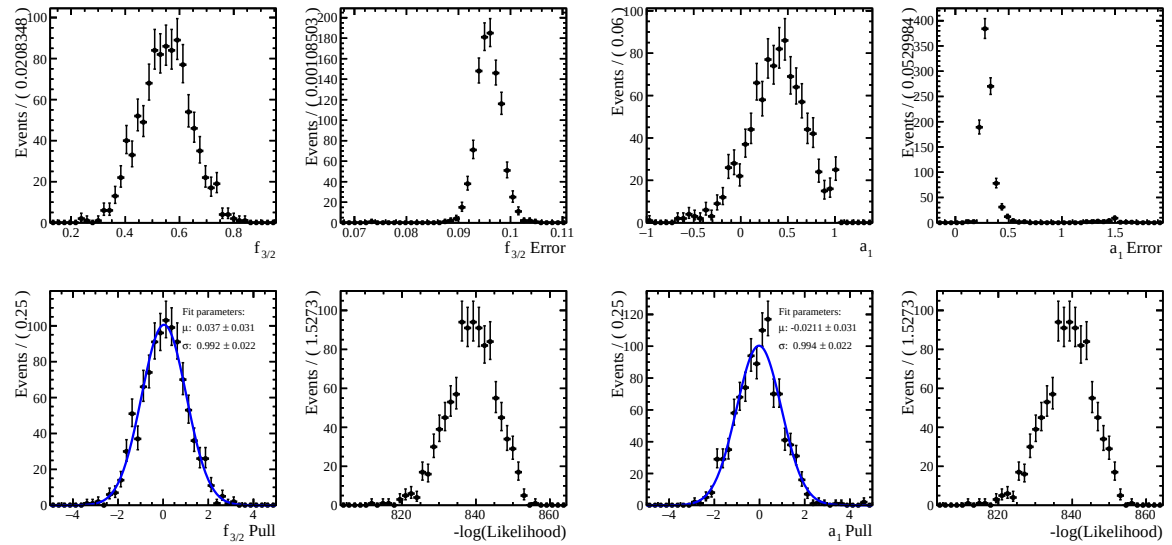

Figure 4.42 – The pull distributions of the mass parameters after generating 1000 pseudo-experiments are shown. The initial parameter values are taken from the fit result in the $q^2 \in [0.1, 3]\,\mathrm{GeV}^2/c^4$ bin.

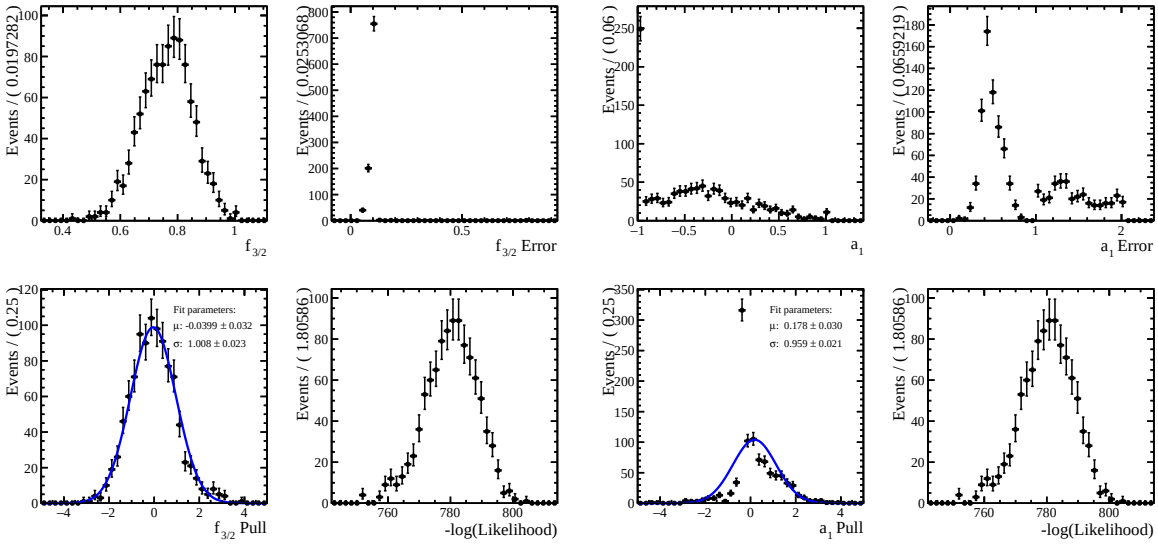

Figure 4.43 – The pull distributions of the mass parameters after generating 1000 pseudo-experiments are shown. The initial parameter values are taken from the fit result in the $q^2 \in [3, 6]\,\mathrm{GeV}^2/c^4$ bin.

and error distributions in Fig. N.7, in App. N.4. The parameter and error distributions are more Gaussian-like. However, a strong bias and a misestimation of the uncertainty of the $f_{3/2}$ fraction are observed. Since the angular fit is based on a good knowledge of the $f_{3/2}$ fraction, the larger parameter range option has been discarded.

The pull distribution of Fig. 4.44 indicates a good estimation of the $f_{3/2}$ value and slight underestimation of the uncertainty in the $q^2 \in [6, 8]\,\mathrm{GeV}^2/c^4$ bin. In the contrary, the nuisance parameter a_1 is less well estimated in this q^2 bin. Fig. 4.45 shows that the $f_{3/2}$ fraction is unbiased in the $q^2 \in [11, 12.5]\,\mathrm{GeV}^2/c^4$ bin. The uncertainties are slightly underestimated. The pull distribution of the a_1 nuisance parameter is reasonable. In the $q^2 \in [1.1, 6]\,\mathrm{GeV}^2/c^4$ bin, the central value of the $f_{3/2}$ fraction is well estimated, but its uncertainty is slightly underestimated. The nuisance parameter a_1 is unbiased but has overestimated uncertainties.

In the second step, pseudo-experiments are generated to evaluate the angular fit. Since the initial observable values are taken from the angular fit result, the parameter plots are removed in order to keep the angular observable values blind. The pull distributions can be seen in Fig. 4.47 - 4.51. The Gaussian fit of the pull distributions has been removed because it did not converge.

In the $q^2 \in [0.1, 3]\,\mathrm{GeV}^2/c^4$ bin, the pull distributions of the angular observables $A^{\ell}_{FB,3/2}$ and S_{1cc} follow a Gaussian-like distribution. Visually a strong bias of both angular observables is visible. The width of S_{1cc} pull distribution is large, which indicates an additional

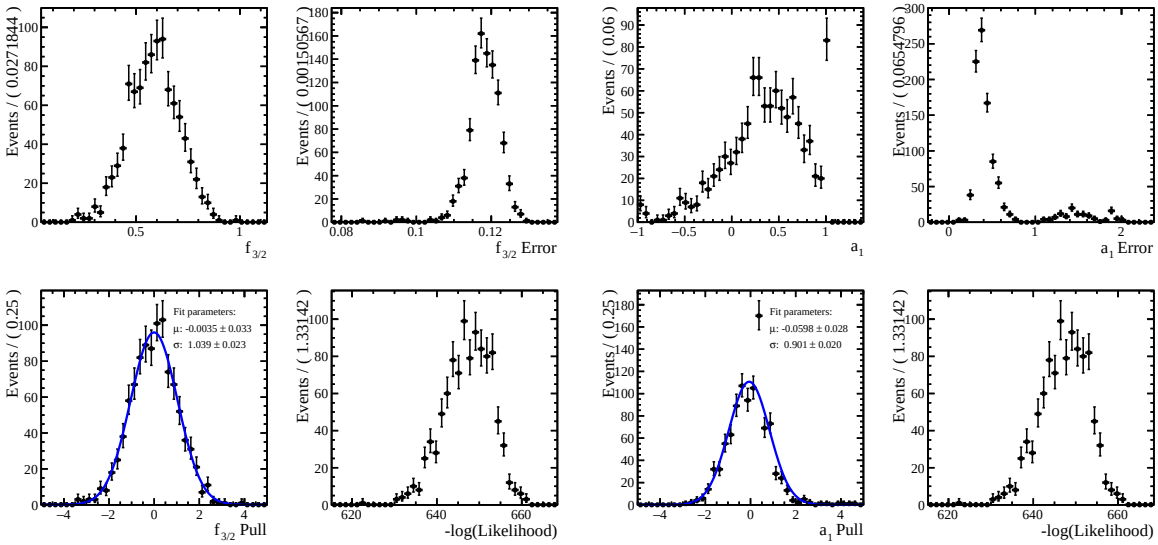

Figure 4.44 – The pull distributions of the mass parameters after generating 1000 pseudo-experiments are shown. The initial parameter values are taken from the fit result the $q^2 \in [6, 8]\,\mathrm{GeV}^2/c^4$ bin.

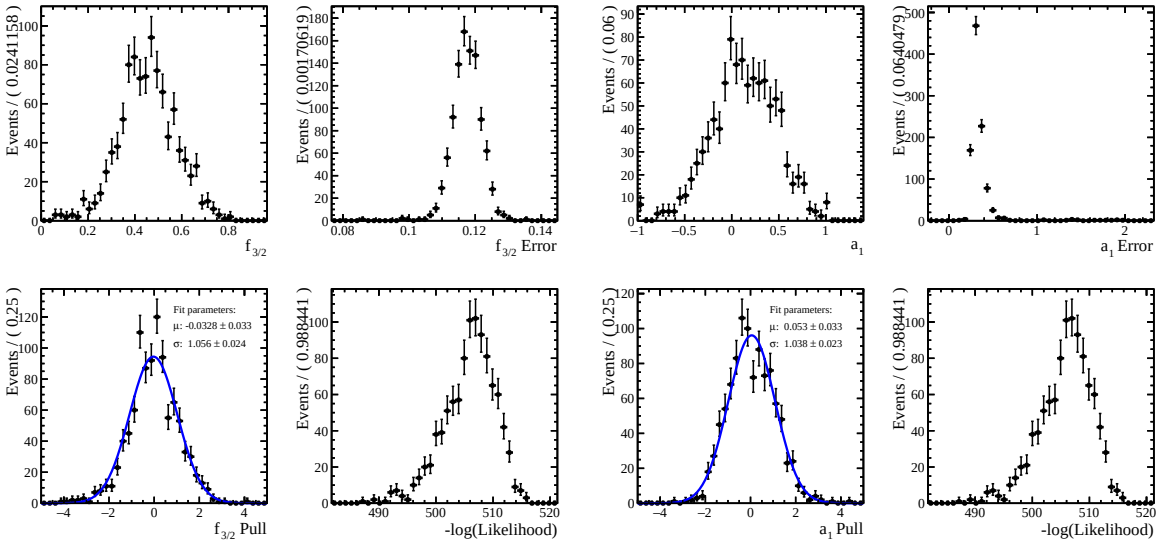

Figure 4.45 – The pull distributions of the mass parameters after generating 1000 pseudo-experiments are shown. The initial parameter values are taken from the fit result in the $q^2 \in [11, 12.5]\,\mathrm{GeV}^2/c^4$ bin.

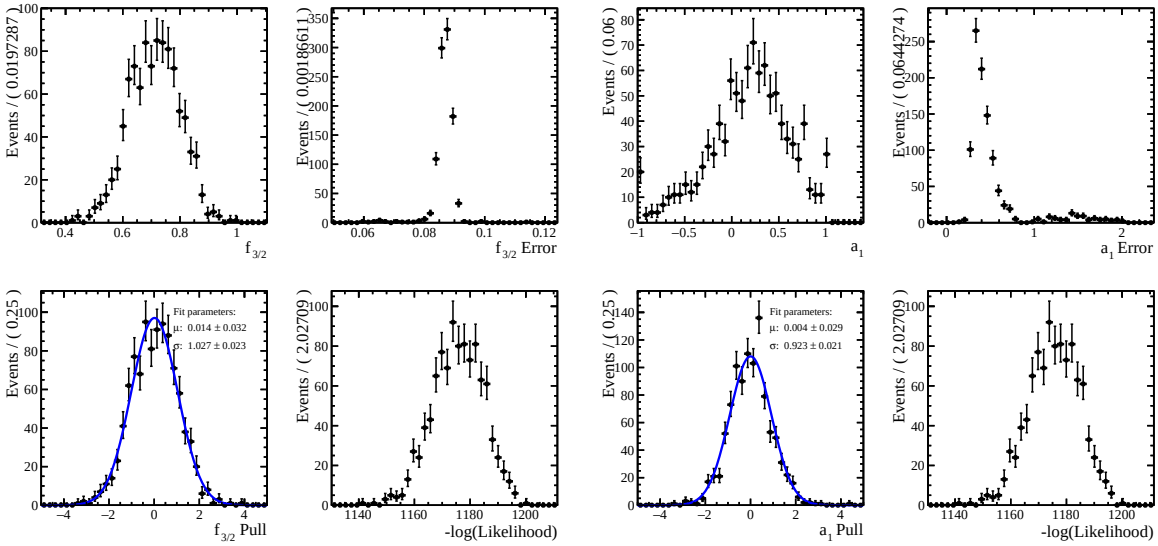

Figure 4.46 – The pull distributions of the mass parameters after generating 1000 pseudo-experiments are shown. The initial parameter values are taken from the fit result in the $q^2 \in [1.1, 6]\,\mathrm{GeV}^2/c^4$ bin.

underestimation of its uncertainties. Fig. 4.48 shows the pull distributions of the angular observables in the $q^2 \in [3, 6]\,\mathrm{GeV}^2/c^4$ bin. Visually the pull distributions of the angular observables $A^{\ell}_{FB,3/2}$ and S_{1cc} seem to be centred around zero and have a width close to one. However, a bias of the nuisance parameters is observed. The pull distributions of the angular fit in the $q^2 \in [6, 8]\,\mathrm{GeV}^2/c^4$ bin are evaluated. The angular observables $A^{\ell}_{FB,3/2}$ and S_{1cc} seem visually to be a bit biased. In the $q^2 \in [11, 12.5]\,\mathrm{GeV}^2/c^4$ bin, the pull distribution of the $A^{\ell}_{FB,3/2}$ observable looks Gaussian-like, the S_{1cc} pull distribution shows some peaking structure. This could indicate the existence of several minima. The nuisance parameter distributions are Gaussian-like but seem to be strongly biased. In the $q^2 \in [1.1, 6]\,\mathrm{GeV}^2/c^4$ bin, pseudo-experiments are generated based on the angular fit result, too. The pull distributions of the $A^{\ell}_{FB,3/2}$ and S_{1cc} observables follow a Gaussian distribution, and a small bias is visually distinguishable.

To conclude, the angular fits on the ${}_s\mathcal{W}eight$ted and acceptance corrected data have convergence problems in the rare q^2 bins. The convergence issues arise due to the negative ${}_s\mathcal{W}eight$s and the small data sample size. The angular PDF seems to get lost in negative PDF regions and does not find a stable minimum. To overcome the issue, an offset was added to the ${}_s\mathcal{W}eight$s, which leads to converging angular fits. Up-to-date, no analysis in LHCb was published with a similar data sample size and a fit of ${}_s\mathcal{W}eight$ted data. Instead of ${}_s\mathcal{W}eight$ing the data, the combinatorial background is modelled in the rare mode. With this additional component in the fit model, the angular fits converge in all

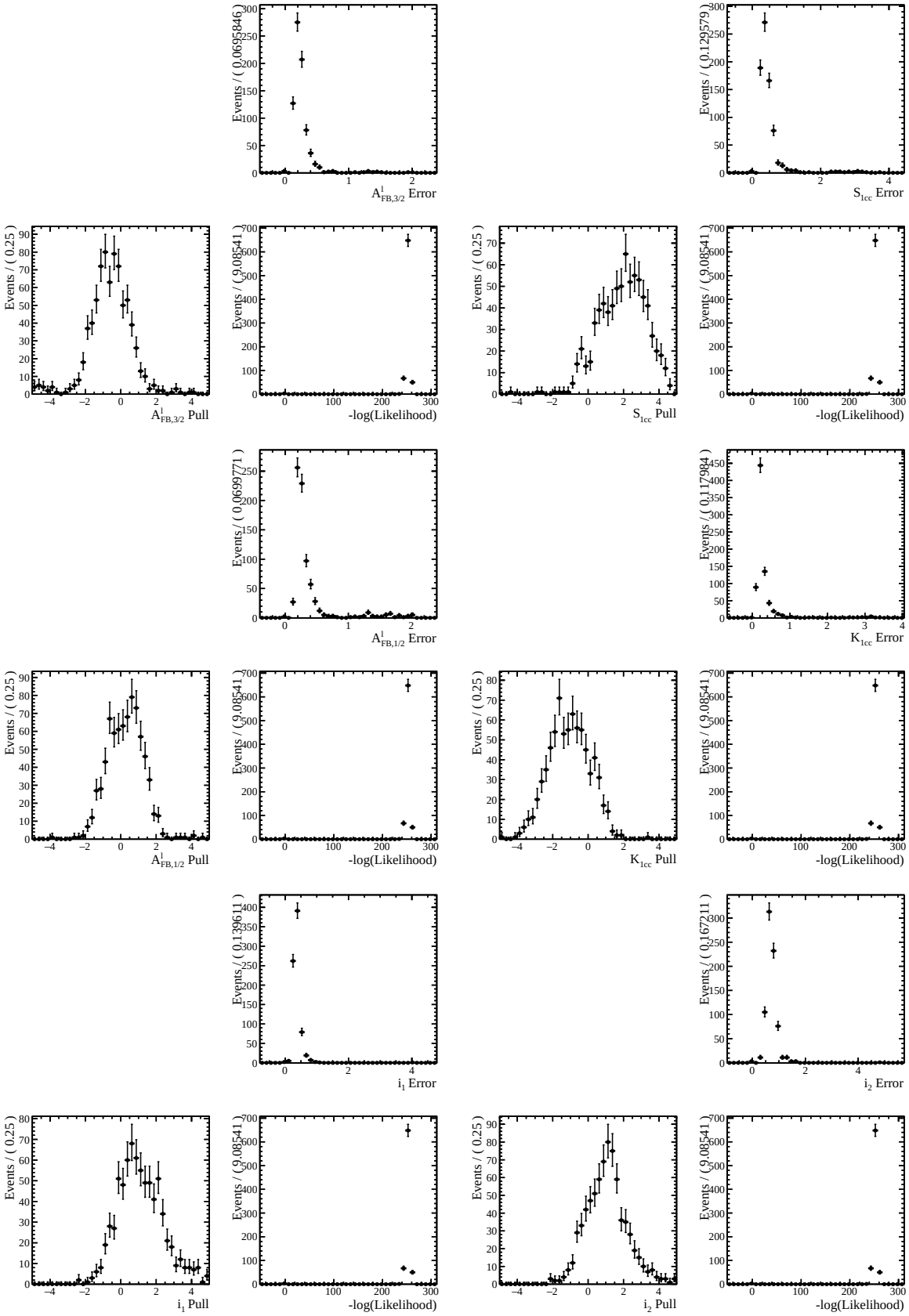

Figure 4.47 – The pull distributions of the angular fit parameters are shown. One thousand pseudo-experiments are generated with the initial parameter values from the angular fit in the $q^2 \in [0.1, 3]\,\mathrm{GeV}^2/c^4$ bin.

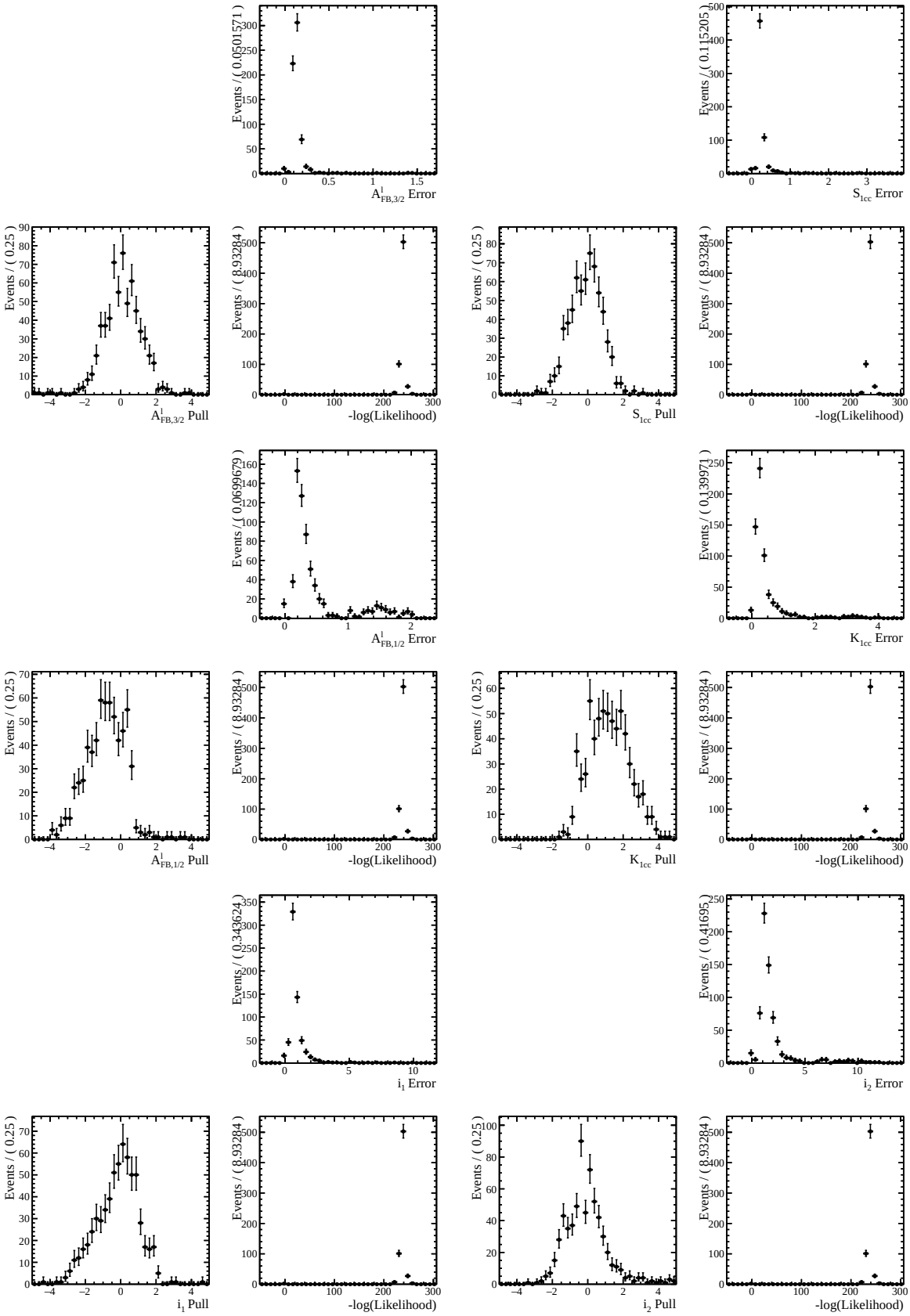

Figure 4.48 – The pull distributions of the angular fit parameters are shown. One thousand pseudo-experiments are generated with the initial parameter values from the angular fit in the $q^2 \in [3, 6]\,\mathrm{GeV}^2/c^4$ bin.

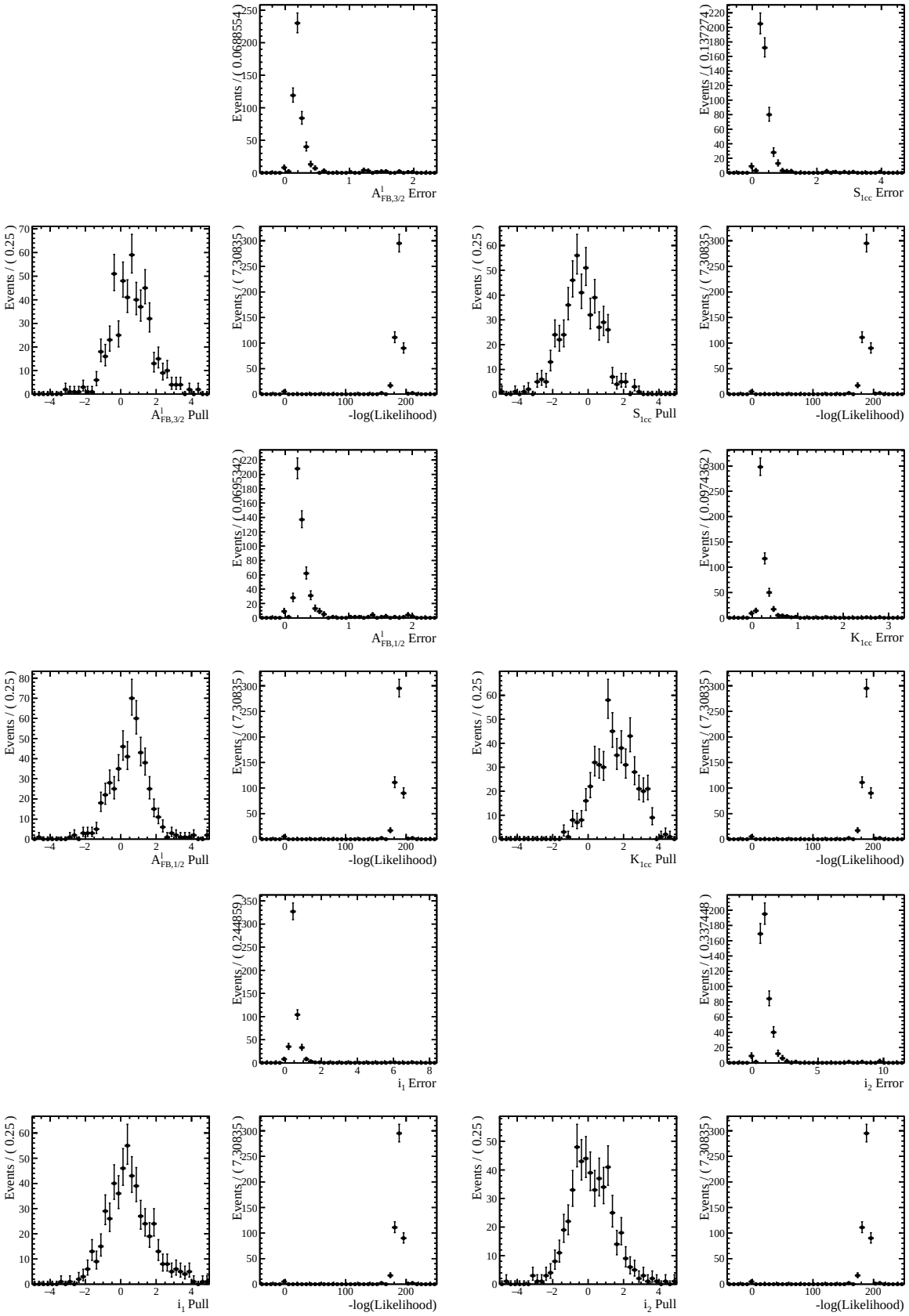

Figure 4.49 – The pull distributions of the angular fit parameters are shown. One thousand pseudo-experiments are generated with the initial parameter values from the angular fit in the $q^2 \in [6, 8]\,\mathrm{GeV}^2/c^4$ bin.

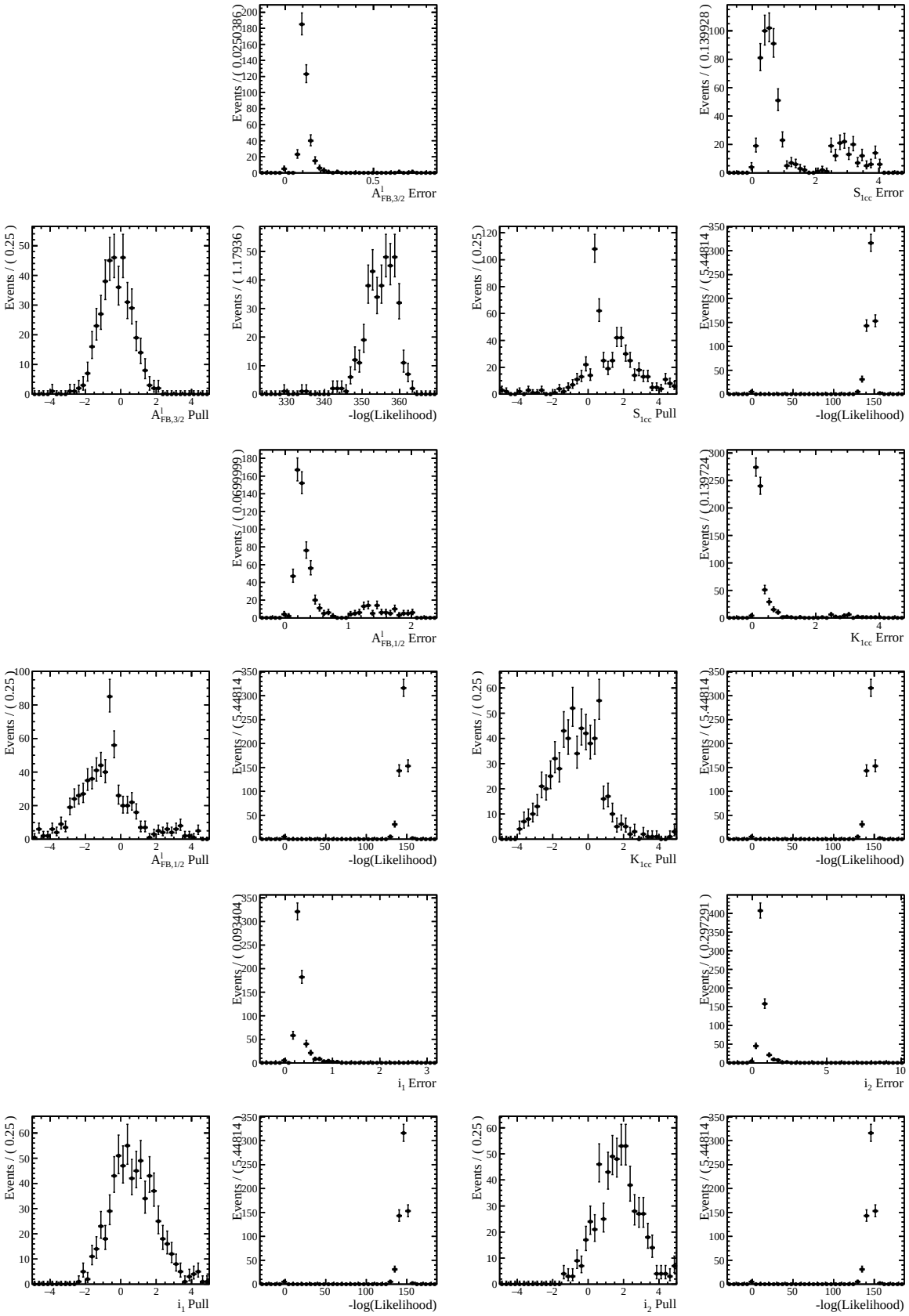

Figure 4.50 – The pull distributions of the angular fit parameters are shown. One thousand pseudo-experiments are generated with the initial parameter values from the angular fit in the $q^2 \in [11, 12.5]\,\mathrm{GeV}^2/c^4$ bin.

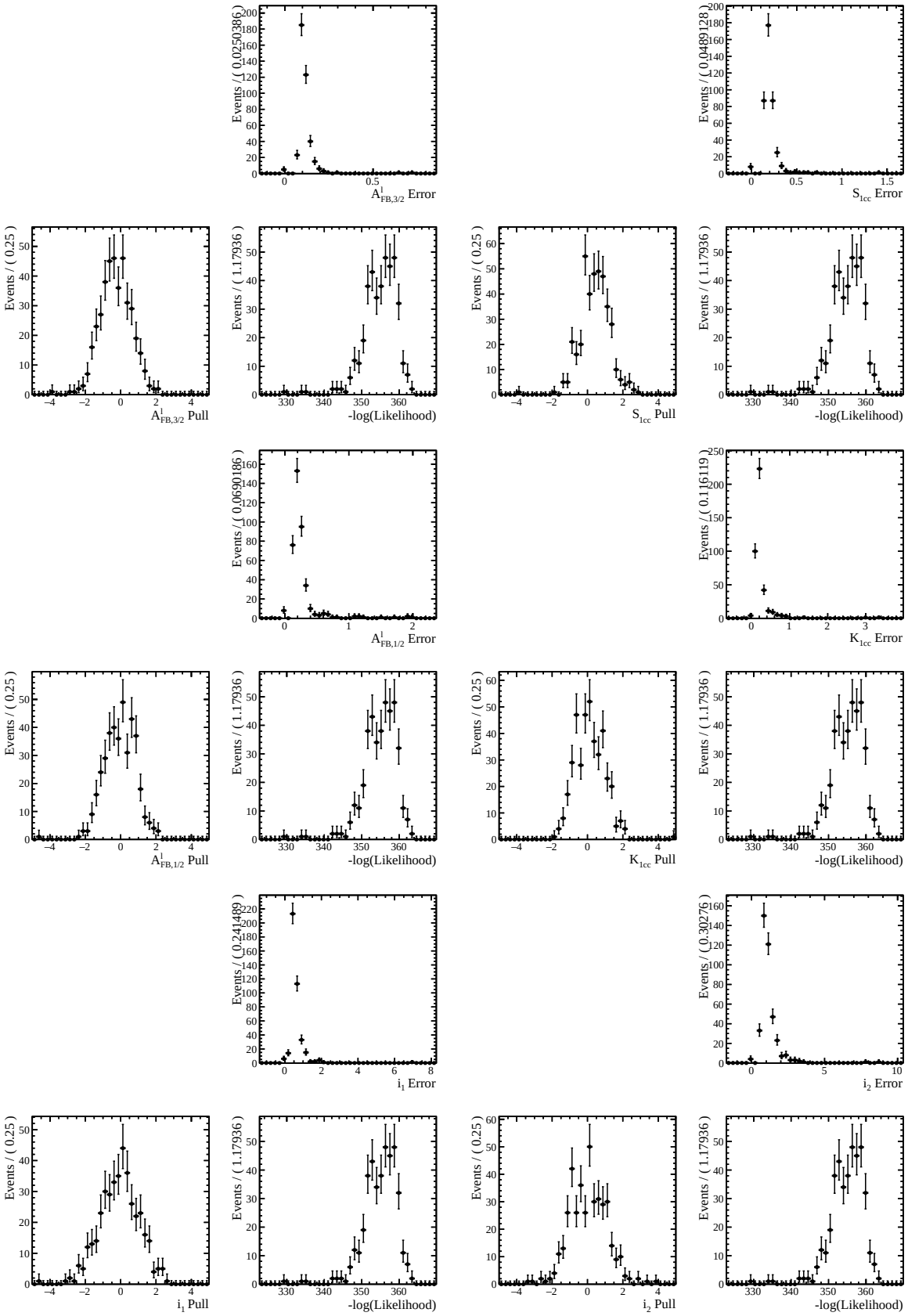

Figure 4.51 – The pull distributions of the angular fit parameters are shown. One thousand pseudo-experiments are generated with the initial parameter values from the angular fit in the $q^2 \in [1.1, 6]\,\mathrm{GeV}^2/c^4$ bin.

the rare q^2 bins.

For the analysis, a good estimation of the $f_{3/2}$ fraction is crucial. A tiny bias of the $f_{3/2}$ fraction is observed in the narrow q^2 bins below the $c\bar{c}$ resonances. A slight underestimation of the $f_{3/2}$ uncertainties is seen in three rare q^2 bins. Due to the small sample size and the fact that the angular PDF gets easily negative, the angular observables are strongly biased, and their uncertainties are underestimated. Further statistical treatments will be necessary to correct the biases and properly evaluate the uncertainties. For example, techniques such as Feldman Cousins scans [192] may be employed for estimating the statistical uncertainties.

4.3 Systematic uncertainties

The performed measurement could be potentially biased. The bias is evaluated in the systematic uncertainties. While statistical uncertainties decrease with a more extensive data sample size, systematic uncertainties do not necessarily decrease. In the described analysis, systematic uncertainties are introduced through the Λ_b^0 baryon mass fit, the angular acceptance and the angular fit.

The systematic uncertainties, which are collected in the **Λ_b^0 baryon mass fit** category, originate from eventually contributing peaking backgrounds, as $B_s^0 \to K^+K^-\mu^+\mu^-$ and $B^0 \to K^*\mu^+\mu^-$ decays. Another source is the model of the Λ_b^0 mass peak, which could be changed. For an alternative Λ_b^0 mass peak modelling, a Crystal-ball function can be used instead of a Hypatia 2 function. Another possibility would be a Λ_b^0 mass model by two Crystal-ball functions with a shared mean.

Systematic uncertainties could arise from the **angular acceptance**. Possible effects could be the choice of the order of the angular acceptance modelling and properties related to the imperfections of the simulation sample. The imperfections mainly arise from the limited simulation sample size and the simulation-data corrections. Alternative angular acceptance models are planned to be tested. The orders of the Polynomial and Fourier functions can be changed. In addition, the requirement on the angles $\cos\theta_\ell$ and ϕ to be symmetric could be lifted. Different angular acceptances are obtained by applying alternative corrections to the simulation samples. A different binning scheme for the L0 trigger correction and another PID efficiency map could be used. However, as seen in Sec. 3.4.8, the change of the angular shape due to the simulation corrections is small.

The systematic uncertainties linked to the **angular fit** include the modelling of the

combinatorial background. Simplifying the angular PDF, which describes the $\Lambda(1520)$ resonance in the heavy-quark limit, has been checked in Ch. 4.2.1 not to cause any deviation. However, the assumption of this test is that the QM form factors describe well the angular distribution. Another systematic effect could be caused by the interference model. The effect of the resonances depend on their spin and parity. Since a component describing the spin-1/2 resonances is implemented in the angular fit model, eventual contributions of additional spin-1/2 resonances would be treated correctly. Spin-3/2 resonances, heavier than the $\Lambda(1520)$ resonance, could contribute. The closest one is the $\Lambda(1690)$. Since the spin and the parity of the $\Lambda(1690)$ resonance are the same as the $\Lambda(1520)$, the angular fit model accommodates it. Contributions of higher spin resonances are not included in the angular fit. However, the lightest ones are, according to Ref. [193], the $\Lambda(1820)$, $\Lambda(1830)$ and the $\Lambda(2080)$ resonances, which are supposed to be well separated from the $\Lambda(1520)$ mass window, as shown in Fig. 1.15. However, interference effects between the included resonances with the spin-5/2 resonance could impact the angular distribution. The remaining bias of the angular observables is evaluated with pseudo-experiments.

The angular shape of the combinatorial background can be alternatively described by a two-dimensional `RooKeysPDF` distribution. Furthermore, the proxy of the combinatorial background can be changed by modifying the BDT requirement and the $pK^-\mu^+\mu^-$ invariant mass threshold to define the high Λ_b^0 mass sideband.

The importance of the systematic uncertainties is estimated based on the published results of the angular analysis in $B_s^0 \to \phi\mu^+\mu^-$ decays [80]. The similarity of the angular analysis of B_s^0 decays and the $\Lambda_b^0 \to \Lambda(1520)\mu^+\mu^-$ decays is that in both cases, an angular fit of a neutral b-hadron decay is performed. In particular, the wide $q^2 \in [1.1, 6]\,\mathrm{GeV}^2/c^4$ bin is chosen as a reference.

The estimated magnitudes of the systematic uncertainties with respect to the statistical uncertainties are listed in Tab. 4.11. The maximal uncertainty fraction for all of the angular observables in the $q^2 \in [1.1, 6]\,\mathrm{GeV}^2/c^4$ bin is presented. Assuming the same systematic effect as in the $B_s^0 \to \phi\mu^+\mu^-$ analysis, the highest systematic uncertainty arises from the simulation corrections, which change the angular acceptance shape. The acceptance order, the PID correction and the limited simulation statistics cause an inferior effect.

The second highest systematic uncertainty is due to the Λ_b^0 mass peak modelling, which impacts the ${}_s\mathcal{W}eights$ or the fraction of the combinatorial background, f_{combi}. A systematic uncertainty will have to be evaluated for the modelling of the Λ (1520) Breit-Wigner as well as the underlying shape of the spin 1/2 resonances.

Contributions of additional Λ^* resonances and their interferences could cause a system-

Source	$\Delta u_{sys}/\Delta u_{stat}$ [%]
Signal mass model	6.2
Angular acceptance order	0.3
Simulation correction	9.6
PID correction	1.1
Angular background model	5.6

Table 4.11 – The dominating sources of systematic uncertainties expected to contribute are listed. Their maximal systematic uncertainty with respect to the statistical uncertainty, called $\Delta u_{sys}/\Delta u_{stat}$, is taken from Ref. [80] in the $q^2 \in [1.1, 6]\,\mathrm{GeV}^2/c^4$ bin. The sources are separated into those related to the mass fit (1st section), the angular acceptance (2nd section) and the angular fit (3rd section).

atic bias. In the presented analysis, Λ^* resonances of spin 5/2 and higher are neglected. While their occurrence is expected to be tiny in the $\Lambda(1520)$ mass window, interferences with the spin-5/2 resonances could cause a systematic deviation. However, the importance of this effect cannot be estimated with the $B_s^0 \to \phi\mu^+\mu^-$ analysis.

Another significant contribution is supposed to originate from the modelling of the angular background shape.

Considering that a proper evaluation of the systematic uncertainties will follow, a first comparison with similar, previously published analysis is useful. In summary, by comparing the angular analysis of $B_s^0 \to \phi\mu^+\mu^-$ decays, the highest systematic uncertainty arises from the simulation corrections, which impact the angular acceptance. The second highest systematic uncertainty is estimated to originate from the signal mass model. The third important acceptance originates from the background model in the angular fit. From this it can be concluded that the measurement discussed in this thesis will be dominated by statistical uncertainties.

4.4 Implications and prospects

In this chapter, the angular PDF describing the angular shape of the $\Lambda(1520)$ resonance has been implemented for the first time. Since the spin-1/2 resonances, namely $\Lambda(1405)$ and $\Lambda(1600)$ resonances, cannot be fully separated from $\Lambda(1520)$ resonance, they must be modelled as well. The corresponding PDF is developed and included in the angular fit model. Due to the resemblance of the two PDFs, the pK^- invariant mass is used to help with the separation between the Λ^* contributions. The interferences between the

resonances have been studied and cause a non-negligible effect. Therefore, additional interference terms are introduced in the angular PDF in order to cope with the observed change in the $\cos\theta_p$ distribution.

The ${}_s\mathcal{W}eight$ method is used to subtract the backgrounds in data. In the control modes, the data fits converge on the ${}_s\mathcal{W}eight$ted and acceptance corrected data. However, the angular fits suffer in the rare bins from the small data sample size. Furthermore, the SM predictions of the angular observables are situated close to the negative limit of the angular PDF, with which the fit has difficulties to cope with. This is why the fit strategy in the rare mode is changed. The ${}_s\mathcal{W}eight$ method is replaced by introducing low levels of combinatorial background and modelling it in the angular distributions. With the combinatorial background model, the fit converges in all the q^2 bins in the rare mode. The pseudo-experiments indicate possible biases of the angular observable values, which need to be corrected.

In the future, more data will be needed to increase the precision of the angular observables measurements and test accurately the possible presence of New Physics effects in this decay. Additionally with more data, one could also consider deriving an angular PDF without using the Heavy Quark limit model, for instance, or exploring information from the other resonances that populate the $\Lambda_b^0 \to pK^-\mu^+\mu^-$ spectrum.

Chapter 5

First look at 2022 data

The 5th of July 2022 marked the official launch of the LHC Run 3, starting pp collisions with an unprecedented world record centre-of-mass energy of $\sqrt{s} = 13.6\,\text{TeV}$. To cope with the increase of the instantaneous luminosity from $\mathcal{L} = 2{-}4{\times}10^{32}\,\frac{1}{\text{cm}^2\text{s}}$ in Run 1 and 2 by an order of magnitude to $\mathcal{L} = 2 \times 10^{33}\,\frac{1}{\text{cm}^2\text{s}}$ in Run 3, the LHCb detector underwent a major upgrade. During the year 2022, the installation of most of the upgraded subdetectors took place.

Analyses of data collected at the start of Run 3 are necessary to help the commissioning of the upgraded detector and to spot problems or missing features as early as possible. Since the upgraded LHCb detector is operated without a hardware trigger, Early Measurements (EMs) are especially important for testing the Real-Time-Analysis trigger and reconstruction at 30 MHz.

In the scope of this thesis, 2022 data are analysed in order to prepare a measurement of the $R_{\psi(2S)}$ ratio, asserting lepton flavour universality between electrons and muons in tree-level b meson decays. The utility of this measurement is further explained in Sec. 5.1 of this chapter. The Upgrade simulation samples and their conditions are described in Sec. 5.2. Due to the change in the trigger strategy, new trigger selections ("lines") have been implemented for Run 3. The efficiency of several Run 3 trigger lines has been compared in Sec. 5.3. Before analysing the data, a preselection is applied, as explained in Sec. 5.4. It includes the description of the employed multivariate classifier, which is trained to discriminate between the abundant combinatorial background and signal. Having obtained the fully selected data sample, the e^+e^- and $K^+e^+e^-$ invariant mass peaks are fitted. ${}_s\mathcal{W}eights$ are extracted based on these fits, with which the background can be statistically subtracted from the data. This technique enables a direct comparison of Run 3 data and simulation, which is presented in Sec. 5.6.

5.1 Role of the $R_{\psi(2S)}$ measurement for Lepton Flavour Universality tests

Lepton Flavour Universality (LFU) tests examine the coupling of the electroweak bosons to different lepton families. Because of the rarity of $b \to s\ell^+\ell^-$ decays and the additional experimental challenge to reconstruct τ leptons, LFU tests in electroweak penguin decays at LHCb are usually performed as ratios of the muonic over electronic decay modes. The robustness of these analyses is validated with the abundant tree-level $b \to c\bar{c}s$ transitions, where the $c\bar{c}$ resonance decays either to e^+e^- or to $\mu^+\mu^-$.

In this thesis, an EM is prepared testing LFU using resonant $B^+ \to K^+\ell^+\ell^-$ decays. In order to demonstrate the understanding of the reconstruction and selection efficiencies in the muonic and electronic final states, existing LFU measurements [58,94] perform the measurement of

$$r_{J/\psi} = \frac{\mathcal{B}(B^+ \to K^+ J/\psi(\to \mu^+\mu^-))}{\mathcal{B}(B^+ \to K^+ J/\psi(\to e^+e^-))}. \tag{5.1}$$

Since the branching fractions of the $J/\psi \to \mu^+\mu^-$ and the $J/\psi \to e^+e^-$ decays are measured to be equal [21], the $r_{J/\psi}$ ratio has to be unity.

At LHCb LFU tests are measured as double-ratios of the rates of muonic over electronic $b \to s\ell^+\ell^-$ decays, normalised by the $r_{J/\psi}$ ratio. The double ratio approach, enabled by the established LFU in $J/\psi \to \ell^+\ell^-$ decays, permits the cancellation of most of the systematic uncertainties. Another validation step performed in LFU tests is to measure the double-ratio of branching fractions involving resonant $\psi(2S)$ decays instead of the rare signal decays. This double-ratio is called $R_{\psi(2S)}$ ratio and can be written as

$$R_{\psi(2S)} = \frac{\mathcal{B}(B^+ \to K^+\psi(2S)(\to \mu^+\mu^-))}{\mathcal{B}(B^+ \to K^+ J/\psi(\to \mu^+\mu^-))} \Bigg/ \frac{\mathcal{B}(B^+ \to K^+\psi(2S)(\to e^+e^-))}{\mathcal{B}(B^+ \to K^+ J/\psi(\to e^+e^-))}. \tag{5.2}$$

Since no NP is expected to be present in the $\psi(2S) \to e^+e^-$ and $\psi(2S) \to \mu^+\mu^-$ decay modes, the $R_{\psi(2S)}$ double-ratio is expected to be equal to unity. Through the $R_{\psi(2S)}$ measurement, the stability of the double-ratio approach and the understanding of the reconstructed data in a different kinematic region is demonstrated.

The measurement of the $R_{\psi(2S)}$ double-ratio is planned to be performed with "early data" because it is a crucial test of the electron and muon efficiencies. As described in Ch. 2.4, the PS and SPD subdetectors are removed in Run 3, due to the replacement of the L0 hardware trigger and their minor role in the fully software-based trigger. Since coincidence in the SPD, PS, and the ECAL was used to improve electron-photon separation in Run 1 and 2, it is crucial to demonstrate that electron identification in Run 3

does not suffer from this change. The foreseen benefit of the fully software-based trigger is the efficient triggering of decay modes with electrons in the final state by eliminating the hardware trigger that searched for signatures in the electromagnetic calorimeter with high transversal energy E_{T}. However, the occupancy of the electromagnetic calorimeter is higher than that of the muon stations, which is mainly due to abundant production of π^0s in the pp collisions. This is illustrated by the p_{T} thresholds for electrons [1] that were about 2700 MeV/c in 2012 and 2400 MeV/c in 2016, while muons were triggered with p_{T} of only 1700 MeV/c in 2012 and 1800 MeV/c in 2016 [194, 195]. One change in the fully software-based trigger in Run 3 is that electrons are triggered via the tracking stations, not the electromagnetic calorimeter [195], which permits lowering the E_{T} threshold and would be beneficial for LFU measurements. Another advantage for electrons is that bremsstrahlung photons are already attached at the HLT 1 step, leading to an expected improvement in the electron trigger efficiency in Run 3 compared to Run 1 and 2 due to the recovery of the lost energy.

Another motivation to perform the $R_{\psi(2S)}$ measurement on data is that tree-level $b \to c\bar{c}s$ decays possess a significantly larger branching fraction than rare $b \to s\ell^+\ell^-$ decays. Therefore, these decays can be measured even with a comparably small amount of accumulated data. With a very rough back-of-the-envelope computation, it was shown that a dataset corresponding to an integrated luminosity of about 2 fb^{-1} would be needed to improve the world average precision on the $R_{\psi(2S)}$ measurement. Furthermore, the $R_{\psi(2S)}$ measurement establishes the successful operation of the trigger system and a significant part of the analysis chain since the rare and resonant decay modes pass through the same Run 3 trigger selections.

5.2 2022 simulated samples

To prepare the analysis of the 2022 data, Upgrade simulation samples generated with the Run 3 conditions are necessary. Because LHCb is still in the commissioning phase at the time when this thesis is being written, the data-taking conditions are not stable yet. Typically, it is expected that many versions of the simulation will be produced as the understanding of the new detector develops. For completeness and whenever possible, the software versions are specified.

1. For better comparison with the muon p_T trigger threshold, the electron p_T threshold is calculated by considering $m_e c^2 << E_{\mathrm{T}}$.

5.2.1 Upgrade simulation and data samples

Simulated $B^+ \to K^+ J/\psi(\to \ell^+\ell^-)$ and $B^+ \to K^+\psi(2S)(\to \ell^+\ell^-)$ decays are generated for the electronic and muonic final states. The event types of the different samples are summarised in Tab. 5.1. The signal decay is a sequential decay of a scalar particle S to

Event type	Decay mode
12153001	$B^+ \to K^+ J/\psi(\to e^+e^-)$
12143001	$B^+ \to K^+ J/\psi(\to \mu^+\mu^-)$
12153012	$B^+ \to K^+\psi(2S)(\to e^+e^-)$
12143020	$B^+ \to K^+\psi(2S)(\to \mu^+\mu^-)$

Table 5.1 – Event types of the different signal simulation samples.

a vector V and a scalar, where the vector decays to two leptons L. The employed model is abbreviated by SVS and VLL.

The simulation samples are generated with version 10aU1. Collisions at a centre-of-mass energy of $\sqrt{s} = 14\,\text{TeV}$ are simulated with both magnet polarities, which is higher than the actual centre-of-mass energy of $\sqrt{s} = 13.6\,\text{TeV}$ reached in Run 3. The average number of visible proton-proton interactions per bunch crossing, μ, is estimated to be around 5.3. The time in between two bunch crossings is set to 25 ns in order to emulate the conditions in the pp collisions. The HLT trigger selection of the Moore software version v54r0 produces the simulation samples. The final nTuples are produced by the DaVinci software with version v63r0.

During the last weekend of the data taking in 2022, pp collisions at $\sqrt{s} = 13.6\,\text{TeV}$ were recorded for both magnet polarities. Only the runs that are flagged to be of good quality were used in this analysis. A number of features listed below made this data sample "special". The average number of visible proton-proton interactions per bunch crossing is 2.2, which is lower than the one used in the simulation sample and data-taking conditions foreseen for Run 3. The integrated luminosity of this dataset corresponds to $27\,\text{pb}^{-1}$. The detector-alignment conditions AlignmentV10_2023_05_09_LHCP, which were the latest ones at the time of this thesis, were used.

One difference between simulation and data is that the Upgrade simulation samples were originally generated, including the Upstream Tracker (UT) reconstruction. Due to delays in its production, the UT could only be installed at the beginning of 2023. Two reconstruction algorithms for long tracks without the UT information were developed by LHCb colleagues to operate the detector reconstruction in the absence of the UT. The data used in this thesis are reconstructed with the forward tracking algorithm without

UT [196] [2]. The tracking efficiency without the UT worsens only by 1 - 2% for long tracks. The main impact of missing the UT studied in Ref. [196], is found to be predominantly the rate of misreconstructed tracks. This "ghost rate", estimated using $B_s^0 \to \phi(\to K^+K^-)\phi(\to K^+K^-)$ decays, increases by a factor of 2 - 3, which is shown in Fig. 5.1.

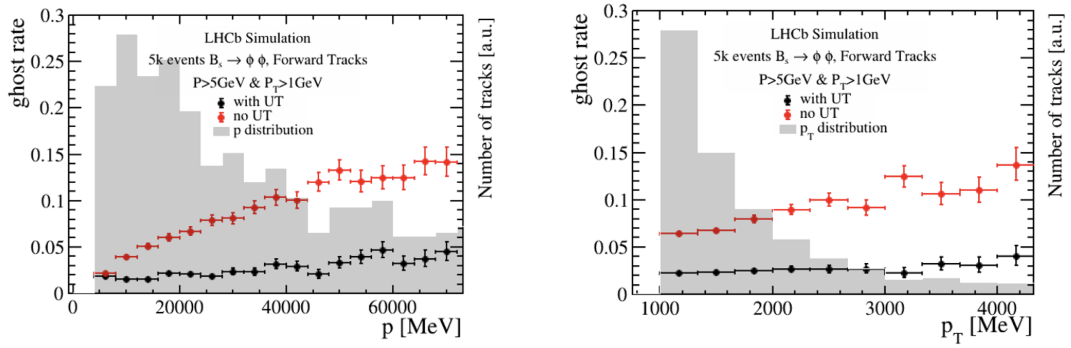

(a) (b)

Figure 5.1 – A comparison of the forward tracking algorithm with and without UT as (a) a function of the momentum p and (b) the transverse momentum p_{T}. Taken from Ref. [196].

The VELO detector was fully closed around the beam during the last data-taking weekend in 2022. A drift of one side of the VELO was observed during a short data-taking period. A dedicated alignment procedure was applied and updated frequently to correct for this effect at the first level trigger HLT 1.

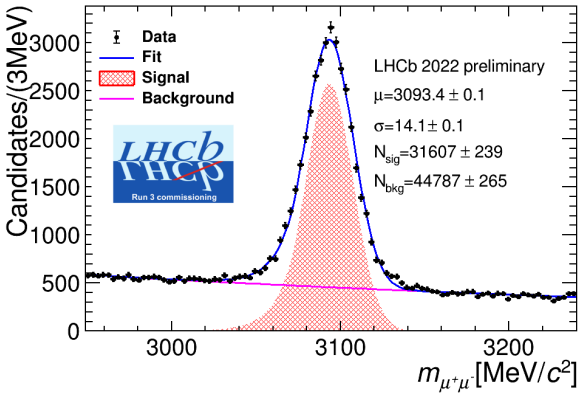

Figure 5.2 – The fit of the prompt di-muon invariant mass spectrum with Run 3 data in the vicinity of the J/ψ resonance. Taken from Ref. [197].

Unfortunately, the muon stations were not fully time-aligned during those runs. The misalignment of the readout time with respect to the bunch crossing and propagation

2. This is indicated in the Run database by the activity tag "PHYSICS|TrackingForward".

time through the detector leads to a loss in the overall muon hit efficiency. For illustration, the fit to the prompt $J/\psi \to \mu^+\mu^-$ decays are presented in Fig. 5.2. The obtained $J/\psi \to \mu^+\mu^-$ yield is roughly estimated to be in the run 8404, a factor 50 smaller than expected. The latest improvement in the tracking-system alignment enables obtaining a resolution on the J/ψ mass which is comparable to but slightly worse than the resolution of $(11.55 \pm 0.05)\,\mathrm{MeV}/c^2$ in Run 1 and 2 [198]. The total yields in this dataset were too low to observe individual fully-reconstructed b-hadron decays. This is why the decay modes that include muons were not yet analysed in the context of this work.

In summary, the main differences (comparisons will be shown in Sec. 5.6) between the data and simulation samples are attributed to originate from the use of the UT in the reconstruction algorithm, the not-yet-optimal general detector performance, the imperfect detector alignment and the different μ value. The change in the centre-of-mass energy is expected to have minor impacts on the descriptive quality of the simulation. Due to the suboptimal time alignment of the muon stations, b decays with muons in the final state were not studied yet.

5.3 Trigger and reconstruction in Run 3

The physics program at the LHCb experiment extends from measuring the properties of high-transverse-momentum jets to the study of soft QCD, such as the production of K^0_S and Λ^0 particles. The difficulty of the trigger task is to cover a wide range of physics while keeping a high efficiency on each of the signal decays and coping with the limitations of the processable bandwidth.

The Run 1 and 2 trigger system causes saturation of the hadron yields for large instantaneous luminosities, which is inappropriate for the instantaneous luminosities foreseen for Run 3. During Run 1 and 2, the hardware trigger was based on the calorimeter system and muon station information. Dropping the hardware trigger allows the tracking system information to be used additionally in Run 3, which enables to trigger not only on signatures with high (transverse) particle momenta and energies but also the displacements of the secondary vertices with respect to the primary vertices.

5.3.1 Overview of the processing chain in Run 3

At the start of this analysis, the simulated signal decays are produced following the processing steps indicated below. This allows the reprocessing of the simulation samples based on the improvements of the trigger software. Nowadays, the software changes are

less frequent, allowing "central" productions of the LHCb simulation samples. While the simulated signal decays follow the processing chain:

$$\text{xDigi} \xrightarrow[\text{Allen}]{\textbf{HLT 1}} \text{DST} \xrightarrow[\text{Moore}]{\textbf{HLT 2}} \text{DST} \xrightarrow[\text{Moore}]{\textbf{Sprucing}} \text{DST} \xrightarrow[\text{DaVinci}]{\textbf{Tupling}} \text{.root},$$

the processing chain of the data sample reads:

$$\text{RAW} \xrightarrow[\text{Allen}]{\textbf{HLT 1}} \text{MDF} \xrightarrow[\text{Moore}]{\textbf{HLT 2}} \text{MDF} \xrightarrow[\text{Moore}]{\textbf{Sprucing}} \text{DST} \xrightarrow[\text{DaVinci}]{\textbf{Tupling}} \text{.root}\ .$$

The data samples are reconstructed with the Moore version v54r7 and produced with the DaVinci version v63r4.

5.3.2 HLT 1 lines

The HLT 1 lines are optimised to maintain high b hadron efficiencies and at the same time to fulfil the bandwidth requirements. As a result, it is essential to test the HLT 1 efficiencies for different decays, in order to discover inefficiencies at an early stage. In this work, the HLT 1 efficiency to select $B^+ \to K^+ J/\psi(\to e^+e^-)$ decays is studied. A total of five lines are compared, which trigger either on the final state electrons or the overall event topology. All of the lines employ first a requirement on the global event, only accepting events where the occupancy in the tracking stations is below a given threshold [3], which $(75.9 \pm 0.8)\%$ of the events pass [196].

The `DisplacedDielectron` line focuses on displaced electron tracks that can be combined to form one secondary vertex with a significant displacement from any primary vertex in the event. The `SingleHighPtElectron` line isolates single tracks that are consistent with being of electron type and that have high transverse momenta. Furthermore, there are three different lines that employ multivariate techniques. The `TrackElectronMVA` line uses a classifier trained specifically on electron tracks coming from b hadron decays. A more inclusive approach is followed by the `TrackMVA` line [199], which works similarly to the former but does not specifically use electron tracks as training input. Lastly, there is the `TwoTrackMVA` line that specifically uses a combination of two tracks as input [199]. All the MVA lines are trained to utilise tracking information related to reconstruction quality and kinematics in order to obtain a positive trigger decision.

The efficiency of the lines is evaluated both on simulated signal decays and real data collected by the LHCb experiment during the last weekend of data-taking in 2022. The

3. Currently the global event cut is enforced using information from the SciFi, after the UT installation, high-occupancy events in the UT are planned to be removed, too.

efficiencies determined on simulation are computed without truth matching the simulation, therefore the numbers could be subject to small changes. Their orders of magnitude are, however, to be trusted.

In data, the percentage of signal events triggered by each of the different trigger lines is calculated after applying the full selection, discussed in the following section. In order to subtract contributions from backgrounds, such as random combinations of tracks that form the same final state as the signal, a statistical subtraction of these events is performed using the ${}_s\mathcal{W}eight$ method. This allows to study the fraction of events that are exclusively triggered by a single trigger line.

Tab. 5.2 summarises the efficiencies for the different trigger lines found from simulated signal decays and the fractions of events triggered by different lines in real data. The multivariate lines are found to be most efficient in selecting the signal decays. Their architecture allows to utilise most information about the event and therefore are best at accepting signal decays. The MVA lines will be the most important lines discussed in the following.

Line	efficiency on simulation [%]	(exclusive) fraction in data [%]
`DisplacedDielectron`	16.5 ± 0.7	27% (2%)
`SingleHighPtElectron`	5.7 ± 0.4	15% (2%)
`TrackElectronMVA`	34.9 ± 0.9	62% (15%)
`TrackMVA`	26.9 ± 0.8	45% (5%)
`TwoTrackMVA`	38.7 ± 0.9	65% (14%)

Table 5.2 – Summary of HLT 1 efficiencies for the different lines, discussed in the text. The efficiencies are determined using simulated signal decays and real data, where on real data the percentage of background subtracted candidates triggered (exclusively) by the given line is quoted.

5.3.3 HLT 2 lines and sprucing

As part of my role as Real-Time-Analysis and Early Measurement Task Force liaison of the Rare Decays (RD) Working Group (WG), I acted as link between the physics WG and the RD WG, informing the physics WG about the changes and progress with respect to Run 3. With the liaison team, our duty was to review the HLT 2 trigger and sprucing lines. The lines needed to be optimised to achieve a high efficiency while limiting the rates to a processable level. A total of 335 HLT 2 and 88 sprucing lines were commissioned, which cover the full RD physics program.

In order to have a consistent selection on the signal and control modes, the same trigger and sprucing lines select $B^+ \to K^+ J/\psi(\to e^+e^-)$ and $B^+ \to K^+\psi(2S)(\to e^+e^-)$

decays as the $B^+ \to K^+e^+e^-$ decays. For validation purposes and redundancy in one of the most important decay modes, two strategies exist to select the electronic B^+ decays via a $c\bar{c}$ resonance.

The first one is the **inclusive selection strategy**. An inclusive HLT 2 line, selecting three-body decays with two electrons in the final state. A sprucing line selecting the specific signal decay is followed. The employed lines are listed below.

1. `Hlt2_InclDetDiElectron(_3Body)` is the name of the inclusive HLT 2 line in full stream, which saves the full event and not only the triggered particles. It is a neural network trained on detached dielectron signatures. The second line exploits additionally the three-body decay topology.
2. The `SpruceRD_BuToKpEE` sprucing line is a cut-based selection line, optimised for retaining specifically $B^+ \to K^+e^+e^-$ decays.

The advantage of the inclusive procedure is that decays, which are not triggered by an exclusive line, can be recuperated at a later stage. This includes improving the trigger efficiencies on standard candle modes such as $B^+ \to K^+\ell^+\ell^-$ but can extend to flavour tagging or studying new decay modes with novel analysis techniques as they are being developed.

The second one is the **exclusive selection strategy**. An exclusive HLT 2 line is employed, selecting specifically $B^+ \to K^+e^+e^-$ decays.

1. The corresponding HLT 2 line is called `Hlt2RD_BuToKpEE`, which applies a cut-based selection.
2. Afterwards, the event is processed via a pass-through sprucing line. The pass-through line does not perform another selection; its implementation permits to treat inclusively and exclusively selected events in the same way.

While the inclusive HLT 2 lines are kept as generic as possible, the exclusive HLT 2 lines are adapted to the specific decay mode. The advantage of this strategy is a higher signal efficiency given a lower bandwidth, but the downside is a higher risk in case of problems since isolation information, additional candidates, including bremsstrahlung photons, or flavour tagging cannot be recovered.

This is the reason why the performances of both strategies are evaluated. In the simulation samples, 13% of the $B^+ \to K^+J/\psi(\to e^+e^-)$ decays pass the exclusive selection. The 20% of the signal decays are selected by the inclusive HLT 2 line, but only 56% of them pass the sprucing. Therefore, the inclusive strategy with a total efficiency of 11% is

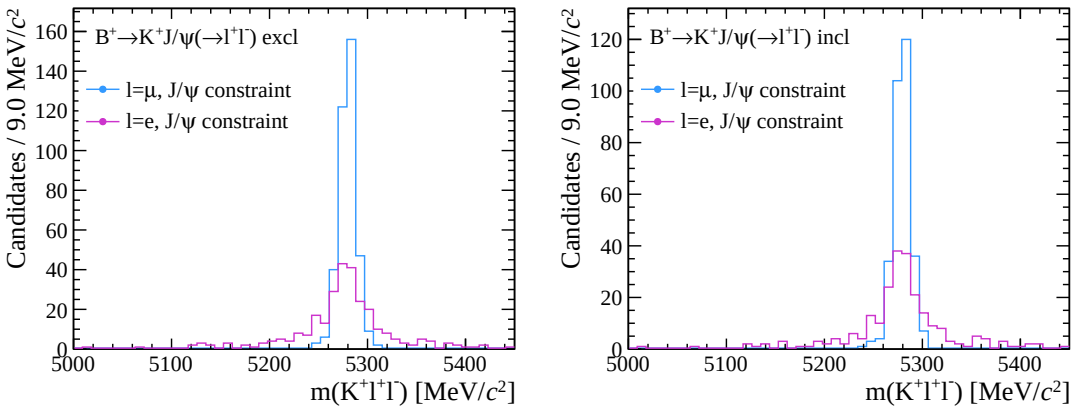

Figure 5.3 – Invariant mass of the $K^+\ell^+\ell^-$ system for the electronic and muonic $B^+ \to K^+J/\psi$ decays is compared after applying the full selection to the simulation samples. On the left, the exclusive selection is shown, whereas the right side depicts the inclusive strategy.

inferior to the exclusive selection. This can be explained by the fact that the selections of the sprucing lines are not optimised yet.

The $K^+\ell^+\ell^-$ invariant mass distributions of the simulation samples are illustrated for the different selection strategies in Fig. 5.3. The electronic and muonic $B^+ \to K^+J/\psi$ decay modes are compared and, as expected, the decay modes with muons in the final state have a better $m(K^+\ell^+\ell^-)$ resolution. Note, that the invariant mass peaks are plotted by applying a J/ψ constraint in the reconstruction.

5.4 Selection

This section outlines the selection used to purify the collected data. It is identical for the $B^+ \to K^+J/\psi(\to e^+e^-)$ and $B^+ \to K^+\psi(2S)(\to e^+e^-)$ decays in order to keep differences between the kinematic regions at a minimum. The selection is split into two parts: a preselection stage and a BDT, employed to suppress the combinatorial background contribution specifically.

5.4.1 Preselection

The preselection focuses on selecting characteristic properties of the B^+ decays while retaining a high signal efficiency and removing specific background sources discussed hereafter. Mainly the selection employs cuts on the final-state particle momenta and a loose kaon PID condition. A challenging background is formed by so-called clone tracks that appear if a given set of VELO hits is associated with different sets of hits in the tracking

stations. This effectively creates two tracks in the detector from one track in the VELO. Since the bremsstrahlung emission and multiple scattering in the detector material cause a comparatively poor track quality, decays with electrons are subject to many clone contributions. Clone tracks typically have a very small opening angle between two tracks, as their VELO segment is shared. Requiring an opening angle between two tracks superior to 0.5 mrad in the lab frame aims to remove the clone track contribution. All of the requirements are listed in Tab. 5.3. Electron PID requirements are avoided at this stage because the PID variables are not optimised yet and as it will be shown in Fig. 5.15 and 5.16, the $\mathrm{DLL}_{e\pi}$ variable differs between data and simulation.

Preselection	Requirement
$p_{\mathrm{T}}(e^{\pm})$	$> 500\,\mathrm{MeV}/c$
$p_{\mathrm{T}}(K^{+})$	$> 400\,\mathrm{MeV}/c$
$\mathrm{DLL}_{K-\pi}(K^{-})$	> 5
$\theta(e^{+}, e^{-})$	$> 0.5\,\mathrm{mrad}$
$\theta(e^{+}, K^{+})$	$> 0.5\,\mathrm{mrad}$
$\theta(K^{+}, e^{-})$	$> 0.5\,\mathrm{mrad}$

Table 5.3 – The preselection criteria, based on particle momenta, kaon PID and clone track removal.

The truth information is accessible in the simulation samples. The so-called "truth-matching" procedure checks if the assigned particle hypothesis matches the known generated true particle ID. Not only correctly matched decays are retained, but also correctly identified particles, where radiative losses are missed, are allowed. In the simulation sample, this category appears to contribute about 1/3 of the pure signal category.

5.4.2 Multivariate selection to remove combinatorial background

A BDT, based on the XGBoost algorithm, is employed to suppress the combinatorial background. The $B^{+} \to K^{+}J/\psi(\to e^{+}e^{-})$ simulation sample serves as the signal proxy. The combinatorial background is represented by the high B^{+} mass sideband, defined as $m(K^{+}e^{+}e^{-}) > 5600$ MeV/c^2. The distributions of the input features for discriminating between signal and background are sketched in Fig. 5.4. The signal and combinatorial background distributions are drawn in blue and red, respectively.

The BDT training is performed separately on the odd and even event numbers. The respective other sample is used to test the BDT performance, on which the training is then applied. The advantage of this method is that the BDT output is not applied to the same sample which was used for its training. The relative importance of the input features in

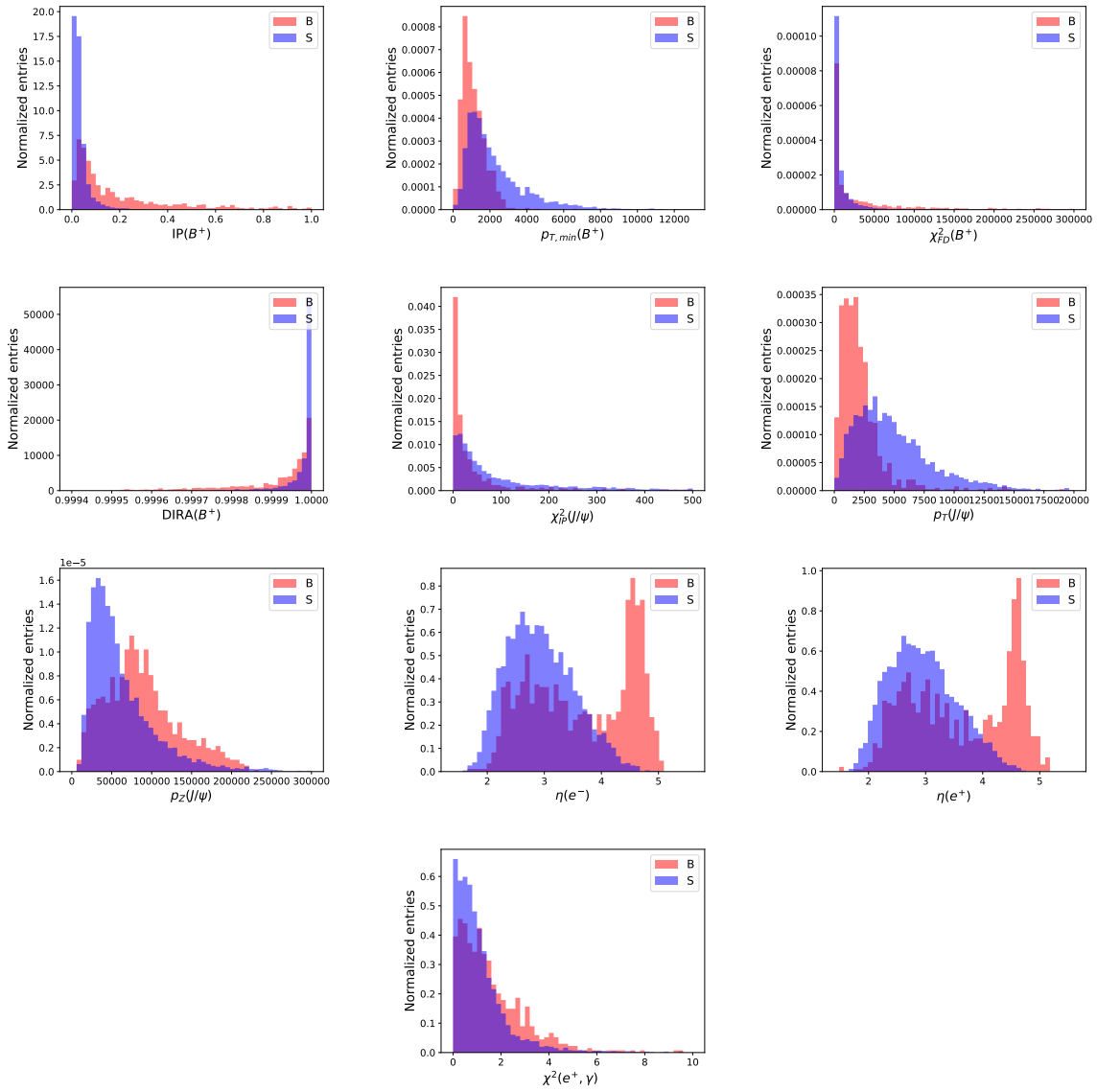

Figure 5.4 – The $B^+ \to K^+ J/\psi(\to e^+e^-)$ signal (S) and combinatorial background (B) distributions of the input features are drawn. The training is shown, which is composed of events with even event numbers.

the BDT training is detailed in App. P.1, the most important features are the significance of the flight distance and the impact parameter of the B^+. The hyperparameters are optimised to be the ones in Tab. 5.4.

Function	Hyperparameter	Value
Architecture	Number of trees	100
Training	Tree construction algorithm	exact
	Feature selector	cyclic
	Signal to background ratio used in the training	1
	Learning rate per tree training	0.1
	Evaluation metric minimised during gradient boosting	NLL
	Fraction of events for random subsampling to grow trees	0.75
Stop criterion	Maximal depth of trees	2

Table 5.4 – The hyperparameter values set in the BDT training. NLL stands for negative log-likelihood.

The ROC curves of the training and testing of the two BDTs are shown in Fig. 5.5. The training curves have an area under the curve (AUC) score of around 0.984 and 0.985, while the AUC of the testing curves are about 0.01 less than in the training. This indicates a slightly worse performance of the BDTs on the training sample. However, the AUC values are consistent between the two BDTs.

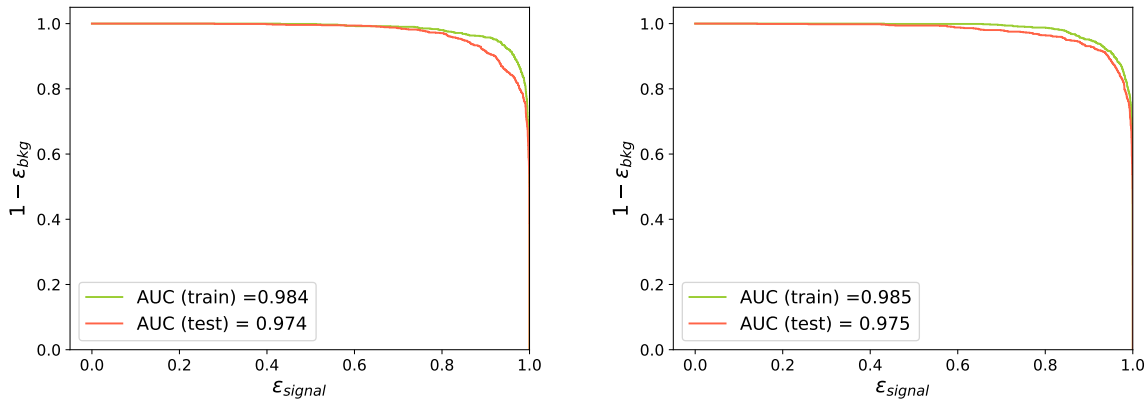

Figure 5.5 – The training and testing ROC curves of the BDTs trained on even (left) and odd event numbers (right). The area under the curve (AUC) is marked, too.

The signal and background distributions of the BDT output value are presented in Fig. 5.6, indicating that the training and testing performances are similar. With the help

of Fig. 5.6, the BDT cut value has been chosen to be 0.7 in order to preserve the majority of the signal while rejecting most of the background.

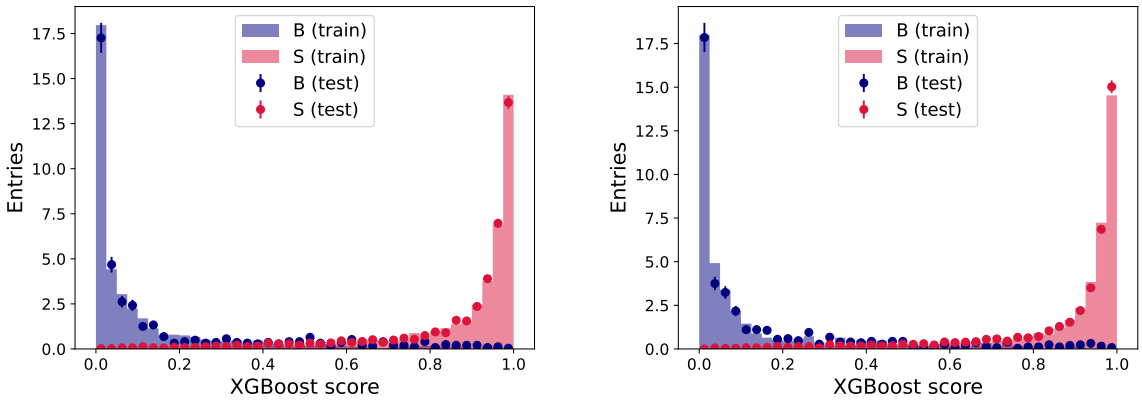

Figure 5.6 – The train and testing distributions of the BDTs trained on even (left) and odd event numbers (right).

5.5 Invariant mass fits

After applying the full selection, the number of decays retained is evaluated by an invariant mass fit. At first, decay candidates involving displaced J/ψ and $\psi(2S)$ vertices, called secondary J/ψ or $\psi(2S)$, are isolated in the data. The majority of these originate from the decay of a b- or c-hadron, as discussed in Ch. 2.2 and are therefore containing the signal of interest for this work. Afterwards, extended unbinned maximum likelihood fits of the B^+ mass are performed in the J/ψ and $\psi(2S)$ mass-constrained $K^+e^+e^-$ invariant mass spectra.

The bremsstrahlung emission of the electrons and its subsequent recovery impact the shape of the mass peaks. Therefore, the fits are usually performed per bremsstrahlung category separately. The "Brem 0" category denotes that no bremsstrahlung photon was recovered for either the electron or for the positron. If either the electron or positron receives one recovered bremsstrahlung photon, the event is part of the "Brem 1" category. Finally, the "Brem 2" category designates events where a bremsstrahlung photon is assigned to the electron and the positron. All three bremsstrahlung sub-categories together are denoted by "all Brem".

5.5.1 Secondary $J/\psi \to e^+e^-$ and $\psi(2S) \to e^+e^-$ decays

In the fit of the e^+e^- invariant mass spectrum, the J/ψ and $\psi(2S)$ mass peaks are modelled by a double-sided Crystal-Ball function and the combinatorial background is described by an exponential. The same model is used for fitting the spectrum in different bremsstrahlung categories. In order to illustrate the goodness of fit for the chosen model, an unbinned maximum likelihood fit to the e^+e^- invariant mass in simulation is presented in Fig. 5.7.

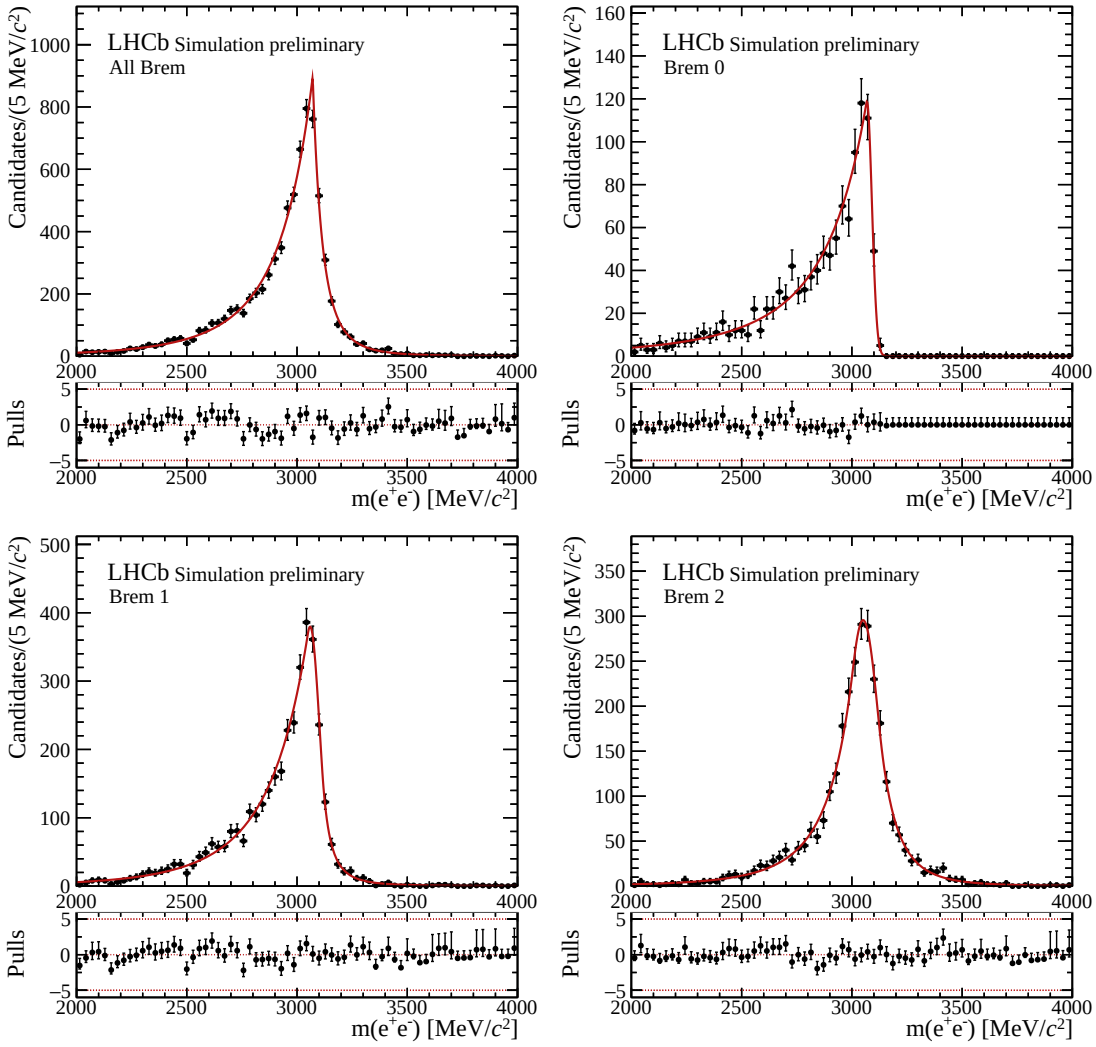

Figure 5.7 – The fit of the e^+e^- invariant mass in the $B^+ \to K^+J/\psi(\to e^+e^-)$ simulation sample is shown for the different bremsstrahlung categories.

The $B^+ \to K^+J/\psi(\to e^+e^-)$ simulation sample is used to fix the shape parameters of the double-sided Crystal-Ball distribution. The parameter values are listed in Tab. 5.5. The mean of the J/ψ peak determined in the Brem sub-categories is consistent within two standard deviations with the value found in the "all Brem" category. The resolution of

Parameter	"All Brem"	"Brem 0"	"Brem 1"	"Brem 2"
$m_{J/\psi}$ [MeV/c^2]	3058 ± 3	3068 ± 5	3059 ± 5	3051 ± 4
$\sigma_{J/\psi}$ [MeV]	43 ± 5	23 ± 3	43 ± 6	72 ± 9
α_L	0.29 ± 0.04	0.12 ± 0.03	0.24 ± 0.04	0.63 ± 0.10
n_L	4.6 ± 0.6	3.7 ± 1.3	6 ± 2	4.4 ± 0.9
α_R	0.93 ± 0.10	5 ± 5	1.3 ± 0.2	1.0 ± 0.2
n_R	3.5 ± 0.3	10 ± 26	2.9 ± 0.5	4.8 ± 1.3

Table 5.5 – The values of the shape parameters of the J/ψ mass peak in the $B^+ \to K^+ J/\psi(\to e^+e^-)$ simulation sample are tabulated. The fit is performed separately in different bremsstrahlung categories.

the J/ψ resonance, σ, is the smallest for the "Brem 0" category. The resolution increases by nearly a factor of two for the "Brem 1" category and a factor of 3 for the "Brem 2" category. This behaviour is attributed to the change of the behaviour of the right tail depending on the bremsstrahlung category. While it is really sharp in the "Brem 0" category, it evolves to be nearly symmetric to the left tail in the "Brem 2" category.

The $\psi(2S)$ resonance is modelled using the same mass model as the J/ψ, with its centre shifted according to the mass difference obtained from Ref. [21]. Owing to the small number of $\psi(2S)$ decays in the data, the resolution of the signal shape for the $\psi(2S)$ model is shared with the J/ψ. The remaining background is modelled by an exponential. The fits to the data are visualised in Fig. 5.8. The pulls are distributed around zero, indicating the good quality of the fit. In order to account for the known differences between simulation and data, a shift of the mean of the J/ψ mass peak with respect to the parameter determined from simulation is introduced. This shift is observed to be about $10\,\mathrm{MeV}/c^2$, indicating the discussed misalignment between data and simulation. The results of the fits in the different bremsstrahlung categories are listed in Tab. 5.6. The sum

Parameter	"All Brem"	"Brem 0"	"Brem 1"	"Brem 2"
$N_{J/\psi}$	1356 ± 41	192 ± 14	618 ± 27	558 ± 27
$N_{\psi(2S)}$	118 ± 17	18 ± 6	48 ± 11	56 ± 12
N_{bkg}	103 ± 28	12 ± 7	70 ± 19	6 ± 2
$m_{J/\psi}$ [MeV/c^2]	3048 ± 2	3071 ± 4	3052 ± 3	3029 ± 6
$\sigma_{J/\psi}$ [MeV]	33.7 ± 1.4	13.0 ± 1.4	30 ± 2	78 ± 5
τ [$10^{-5} \frac{c^2}{\mathrm{MeV}}$]	0 ± 3	0 ± 41	0 ± 6	0 ± 55

Table 5.6 – The J/ψ and $\psi(2S)$ fit results are listed for the different bremsstrahlung categories.

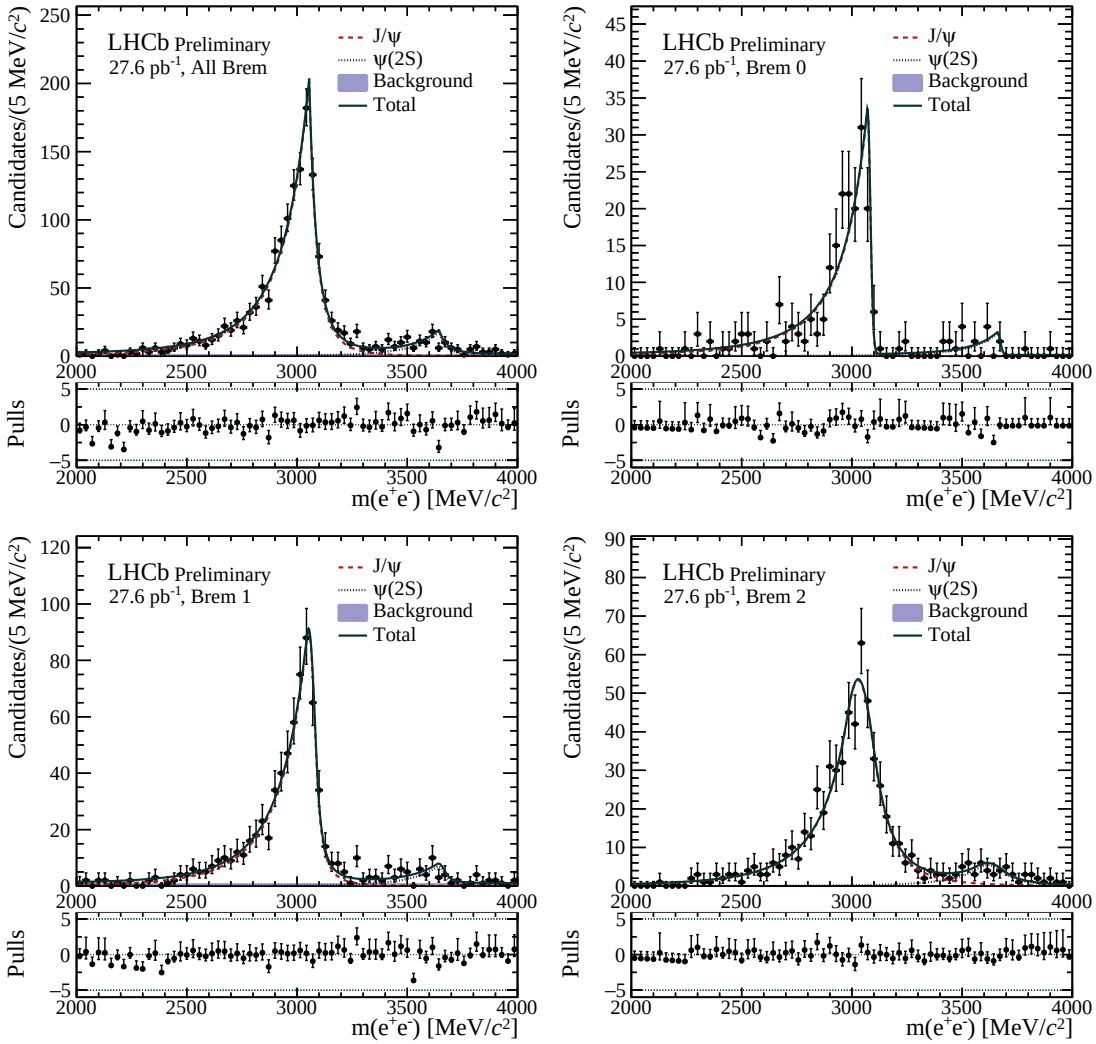

Figure 5.8 – The fit of the e^+e^- invariant mass in data is shown for the different bremsstrahlung categories.

of the individual yields in the "Brem 0 – 2" categories is consistent within one standard deviation with the yield in the "all Brem" category. The ratio of the $\psi(2S) \to e^+e^-$ yield with respect to the $J/\psi \to e^+e^-$ yield is measured to be 0.087 ± 0.012. Note that the ratio is not corrected for the reconstruction and selection efficiencies in the different kinematic ranges.

5.5.2 $B^+ \to K^+ J/\psi(\to e^+e^-)$ decays

This section presents the analysis of $B^+ \to K^+ J/\psi(\to e^+e^-)$ decays in the Run 3 LHCb dataset. To select the J/ψ resonance, the squared invariant mass of the dilepton system, q^2, is required to be within $[6, 11]\,\mathrm{GeV}^2/c^4$. The q^2 bin employed here is broader than the corresponding one in the angular analysis of the $\Lambda_b^0 \to \Lambda(1520)J/\psi$ decays (see Ch. 3). This choice is made in order to account for the radiative tails caused by missing or over-reconstructing bremsstrahlung photons, as by the imperfect resolution of the electromagnetic calorimeter. The $K^+e^+e^-$ invariant mass is modelled by a double-sided Crystal-Ball function. The excellent description of the mass spectrum when using this model is presented in Fig. 5.9. The model parameters are obtained through an unbinned maximum likelihood fit to the $B^+ \to K^+ J/\psi(\to e^+e^-)$ simulation sample.

Parameter	"All Brem"	"Brem 0"	"Brem 1"	"Brem 2"
m_{B^+} [MeV/c^2]	5274.9 ± 0.7	5274 ± 2	5275.3 ± 1.0	5275.1 ± 0.8
σ_{B^+} [MeV]	16.8 ± 1.1	15 ± 2	15 ± 2	18.6 ± 1.4
α_L	0.62 ± 0.05	0.48 ± 0.11	0.53 ± 0.08	0.77 ± 0.08
n_L	4.9 ± 0.5	6 ± 2	4.8 ± 0.7	4.8 ± 0.8
α_R	1.02 ± 0.08	1.15 ± 0.18	0.94 ± 0.13	1.06 ± 0.11
n_R	3.9 ± 0.4	3.0 ± 0.7	3.5 ± 0.5	5.0 ± 1.0

Table 5.7 – The parameter values of the B^+ mass peak in the $B^+ \to K^+ J/\psi(\to e^+e^-)$ simulation sample are listed. The fit is performed separately in different bremsstrahlung categories.

The result of the fit to simulation is presented in Tab. 5.7. The tail parameters of the B^+ mass-peak model are fixed in the fit to data, while the B^+ mass mean and its resolution stay free-floating, allowing to account for differences between simulation and data. Up to now, the considered backgrounds constitute only combinatorial background, originating from random combinations of tracks that form the same final state as the signal. The combinatorial background is modelled by an exponential function. Partially reconstructed backgrounds and misidentified backgrounds are neglected at this early stage. The fits to the B^+ mass in data are depicted in Fig. 5.10.

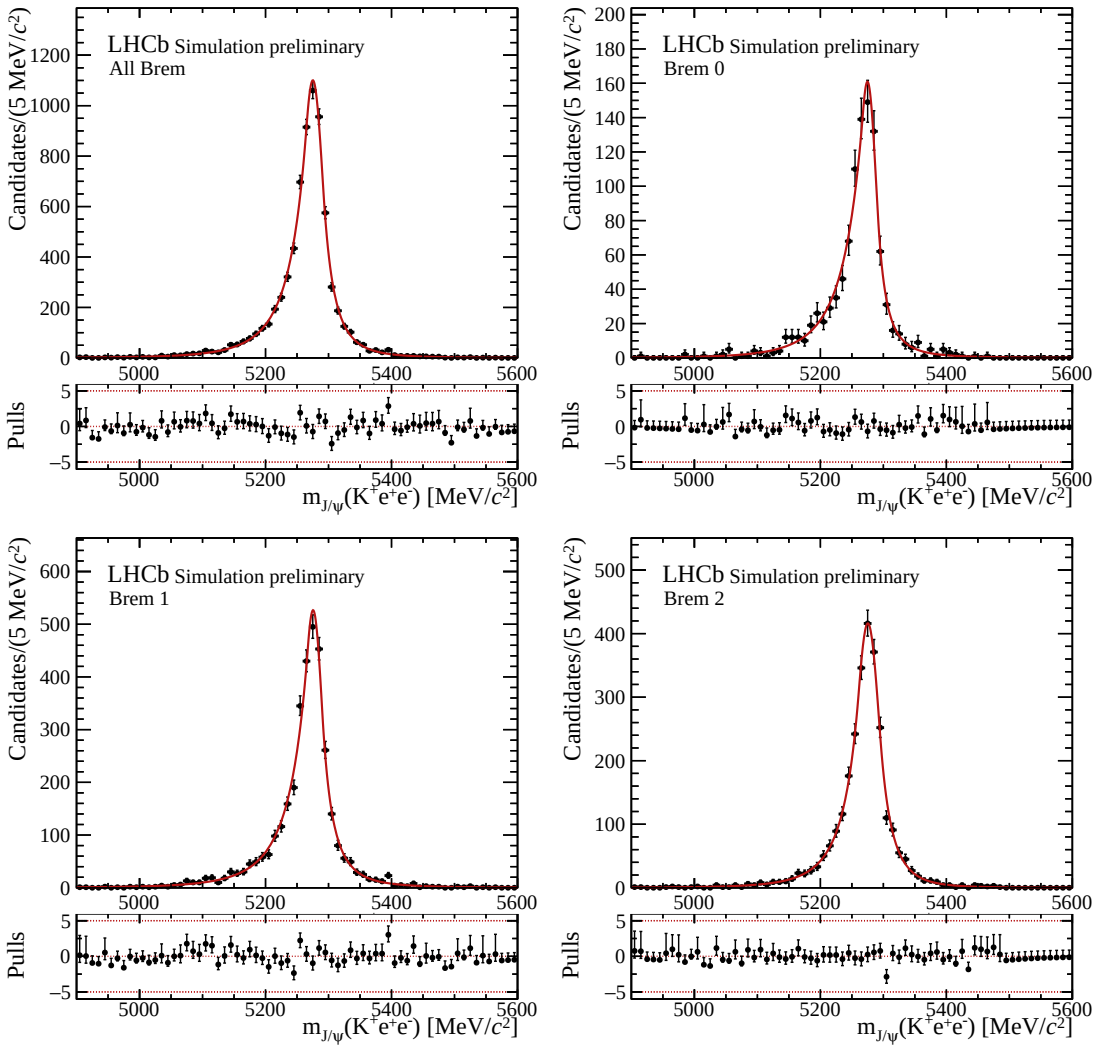

Figure 5.9 – The fits to the J/ψ mass-constrained $K^+e^+e^-$ invariant mass in the $B^+ \to K^+J/\psi(\to e^+e^-)$ simulation sample are shown for the different bremsstrahlung categories.

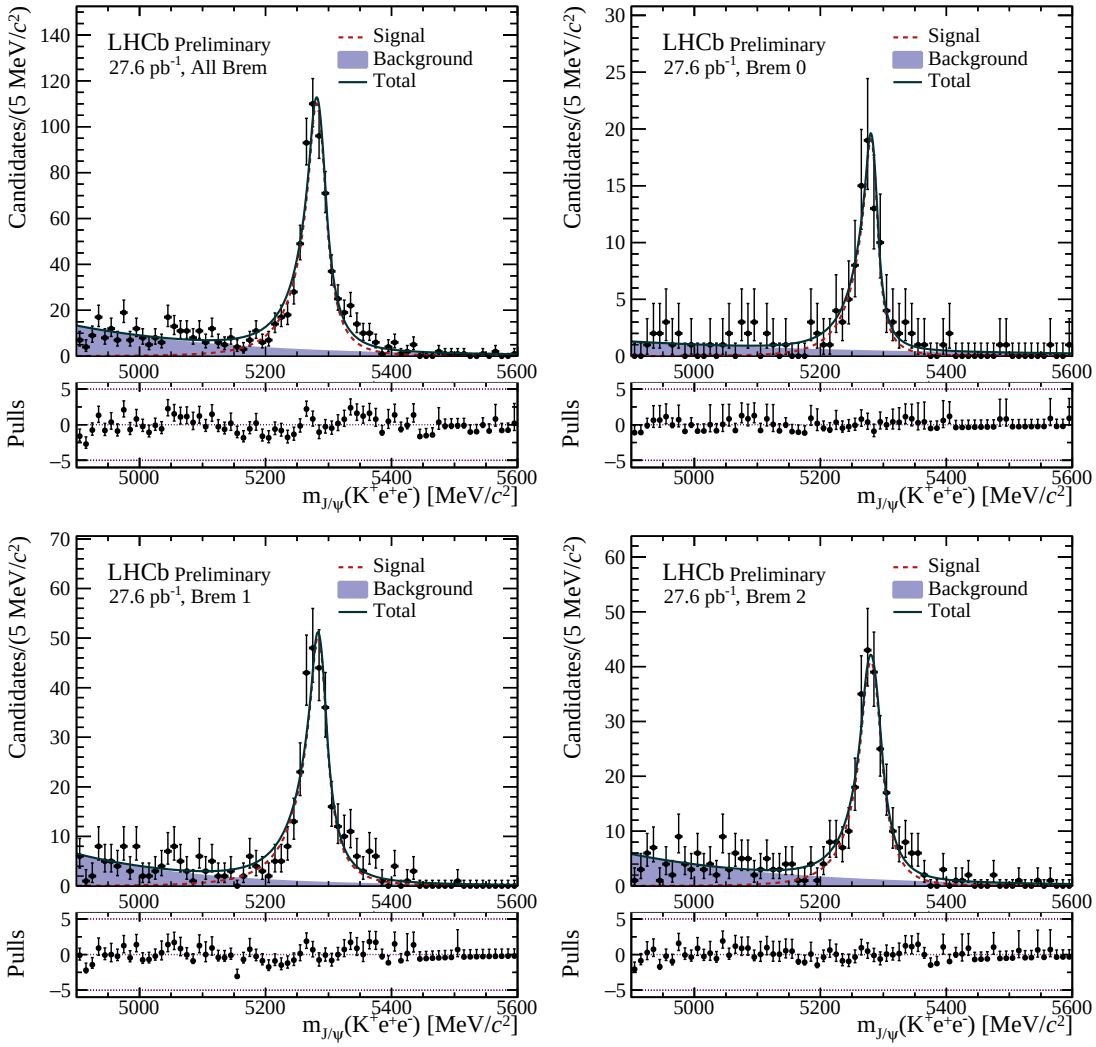

Figure 5.10 – The fit to the J/ψ-constrained $K^+e^+e^-$ invariant mass in data, shown for the different bremsstrahlung categories.

The goodness of fit is illustrated by the pulls of the data fits that are distributed randomly around zero. The only minor imperfection is given by a bump at approximately 5320 MeV/c^2 that appears in the "all Brem" and "Brem 1" categories only. A larger data sample is needed to identify its origin.

The fit parameter values for the different bremsstrahlung categories are listed in Tab. 5.8. The sum of the yields in the "Brem 0 – 2" categories is consistent with the fit in the "all Brem" category within one standard deviation. The mean of the B^+ mass distribution is consistent between the different Brem categories within three standard deviations. However, bremsstrahlung losses impact the B^+ mean and can, in principle, differ in the different Brem categories. The signal peak resolution and the exponential slope parameter are consistent in the Brem subcategories within two standard deviations with the respective values in the "all Brem" category, confirming the observed behaviour in simulation.

Parameter	"All Brem"	"Brem 0"	"Brem 1"	"Brem 2"
N_{B^+}	632 ± 30	94 ± 11	299 ± 21	241 ± 18
N_{bkg}	320 ± 24	46 ± 9	129 ± 17	143 ± 15
m_{B^+} [MeV/c^2]	5277 ± 2	5281 ± 3	5283 ± 2	5280 ± 2
σ_{B^+} [MeV]	14.8 ± 1.0	12 ± 2	14 ± 2	17 ± 2
τ [$10^{-3} \frac{c^2}{\text{MeV}}$]	-4.0 ± 0.4	-2.3 ± 0.9	-4.7 ± 0.9	-4.1 ± 0.6

Table 5.8 – Yields and resulting parameter values of the $K^+e^+e^-$ invariant mass fit in data. The fits are performed in the J/ψ bin and separated into different bremsstrahlung categories.

5.5.3 $B^+ \to K^+\psi(2S)(\to e^+e^-)$ decays

In this section, the $B^+ \to K^+\psi(2S)(\to e^+e^-)$ decays are studied. They are isolated by changing the q^2 requirement to be within $[11, 15]\,\text{GeV}^2/c^4$. Because of the lack of a large $B^+ \to K^+\psi(2S)(\to e^+e^-)$ simulation sample, the $K^+e^+e^-$ mass shape is determined by an unbinned maximum likelihood fit to the J/ψ-constrained $B^+ \to K^+J/\psi(\to e^+e^-)$ simulation sample, as discussed in the previous section. After fixing the shape parameters, a fit to the $\psi(2S)$-constrained $K^+e^+e^-$ mass is performed. The fit to the data is visualised in Fig. 5.11 and its results summarised in Tab. 5.9. Despite the challenges connected to the small data sample size, the fit converges and describes the data well.

The ratio of the $B^+ \to K^+\psi(2S)$ over the $B^+ \to K^+J/\psi$ yields gives a fraction of 0.027 ± 0.008, which is not efficiency-corrected up to now. Ref. [58, 94] quotes a ratio of 0.0745 ± 0.0010 analysing the full Run 1 and 2 datasets, including all trigger categories.

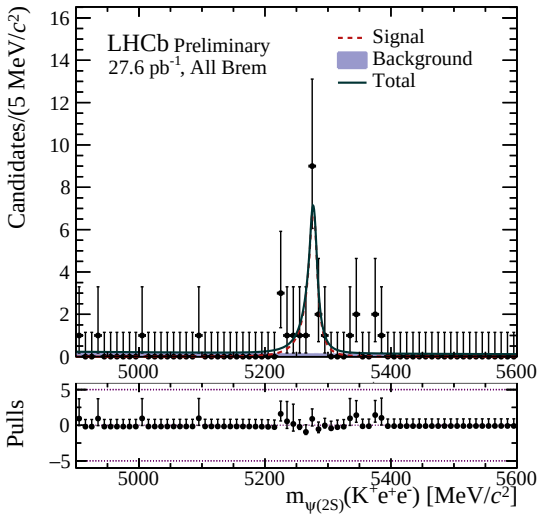

Figure 5.11 – The $\psi(2S)$-constrained $K^+e^+e^-$ invariant mass fitted in data. Since the amount of data is so small, the B^+ mass fit is only performed in all Brem categories together.

The measured ratio in the Run 3 dataset is 6σ away from the published ratio. A difference could originate from a better trigger efficiency in Run 2 for the $\psi(2S)$ mode than for the J/ψ mode. In Run 3, the trigger on low p_{T} electrons is improved. Those are supposed to be more abundant in the J/ψ mode due to the smaller phase space. Such a big difference, however, is not explained by the trigger efficiency, highlighting the importance of double-checking this ratio with a larger dataset.

Parameter	Fit value
N_{B^+}	17 ± 5
N_{bkg}	12 ± 5
m_{B^+} $[\mathrm{MeV}/c^2]$	5277 ± 2
σ_{B^+} $[\mathrm{MeV}]$	6 ± 4
τ $[\frac{c^2}{\mathrm{MeV}}]$	-0.0010 ± 0.0002

Table 5.9 – The resulting parameter values and yields of the $\psi(2S)$-constrained $K^+e^+e^-$ invariant mass fit in data.

In summary, 1356 ± 41 secondary $J/\psi \to e^+e^-$ decays are found in the "all Brem" category of the 2022 data. This yield is more than double the number of $B^+ \to K^+J/\psi(\to e^+e^-)$ decays observed in the data sample. A small contribution of $\psi(2S) \to e^+e^-$ decays is found, too. The yield of $B^+ \to K^+\psi(2S)(\to e^+e^-)$ amounts to about 14% of all

observed $\psi(2S) \to e^+e^-$ decays in 2022 data.

5.6 Comparison of variable distributions in simulation and ${}_s\mathcal{W}eight$ted data

In order to evaluate the quality of the descriptive power of the simulation used to generate $B^+ \to K^+J/\psi(\to e^+e^-)$ decays, a comparison between the simulation and data is performed. For this purpose, ${}_s\mathcal{W}eight$s are extracted from the fit to the $K^+J/\psi(\to e^+e^-)$ invariant mass spectrum in the "all Brem" category. The ${}_s\mathcal{W}eight$s allow subtracting the background component from the data distributions, enabling a comparison of the data and the simulation. Plotting the distributions in simulation and ${}_s\mathcal{W}eight$ted data results in the distributions shown in Fig. 5.12 - 5.16. A full overview of comparisons also in other variables is presented in App. P.2. The comparison starts with variables related to the B^+ meson and continues with the Kaon, the J/ψ, and finishes discussing the electrons.

The variable distributions related to the $\boldsymbol{B^+}$ **meson** are presented in Fig. 5.12. Immediately noticeable is that the PV positions in x and y direction (x_{PV}, y_{PV}) are shifted by $(\Delta x, \Delta y) = (1, 0.45)\,\mathrm{mm}$ in the data with respect to the simulation sample. This is due to the fact that during the data taking, the beam was off-axis, while the VELO was almost centred around the beam, shifted by only 0.1 mm. The distribution of the PV position in z-direction, z_{PV} is thinner in the data than in the simulation sample, potentially originating from the smaller value of μ.

The distributions of the flight distance, FD(B^+), and the decay time of the B^+ meson, $\tau(B^+)$, are well represented in the simulation sample. The impact parameter χ^2 distribution (χ^2_{IP}) shows slight differences at low values, but more data is needed to evaluate if this is a statistical effect.

The mean of the distributions of the z-component of the momentum, $p_z(B^+)$, as well as the energy of the B^+ meson, $E(B^+)$, seem to be situated at higher values in the data sample compared to simulation, but more data is needed to quantify the effect. It will be seen later that the detector had been less efficient in data than in simulation. The shift in energy and p_z indicates that only more energetic events passed the trigger selection.

The distributions of η ($\eta(B^+)$) and the x-, y-projections of the momentum ($p_x(B^+)$, $p_y(B^+)$) are slightly shifted in data, which could be related to an acceptance effect from the off-axis beam. It should be noted that the accurate simulation of the kinematics of B^+ mesons is challenging in the kinematic region covered by LHCb, being known to underestimate average momenta also in Run 2 simulation. This highlights the importance of further tuning the Pythia generator when moving forward with Run 3.

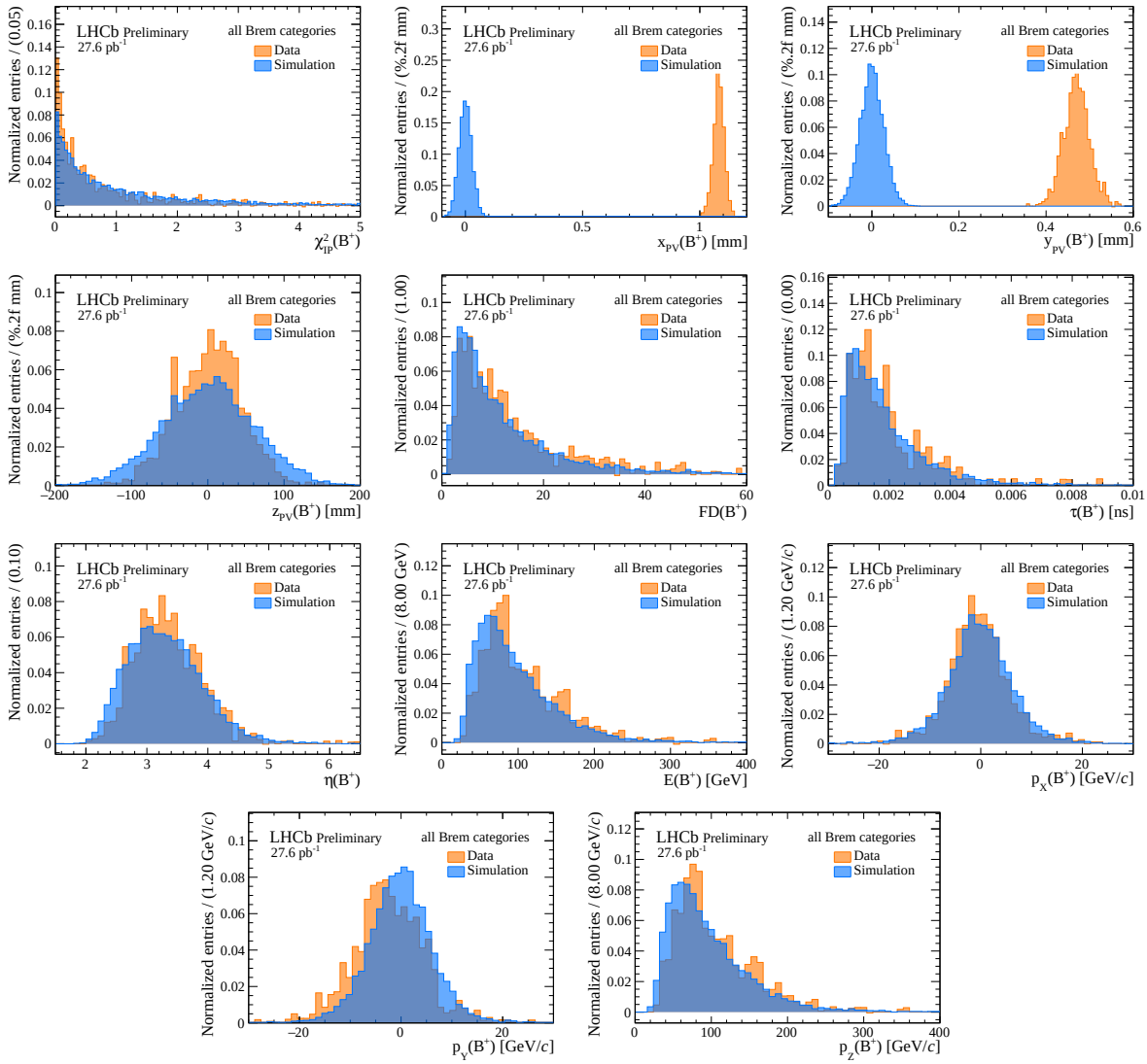

Figure 5.12 – Comparison of the variable distributions related to the B^+ meson in the $B^+ \to K^+ J/\psi(\to e^+e^-)$ simulation sample and the ${}_s\mathcal{W}eight$ted data.

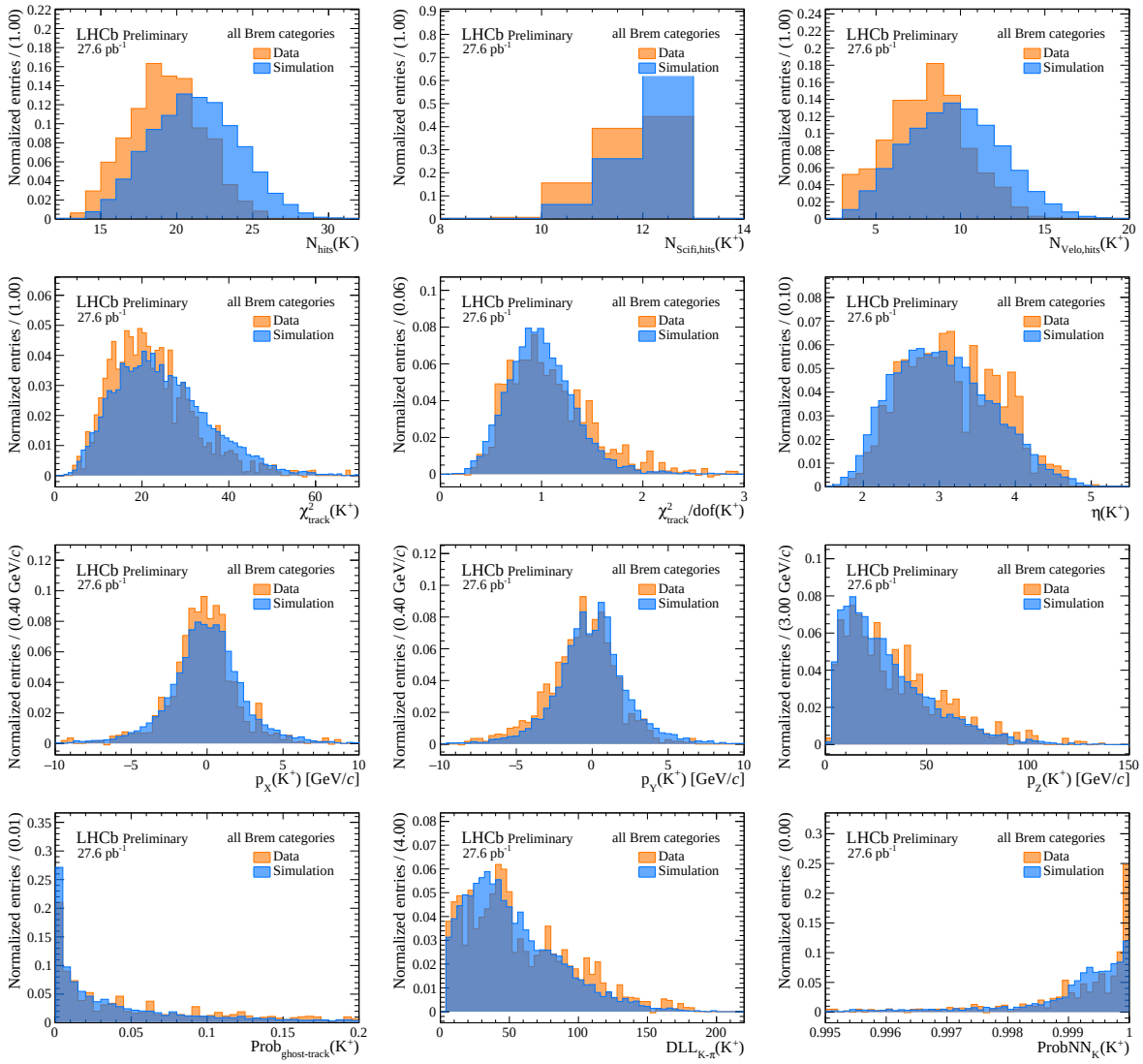

Figure 5.13 – Comparison of the variable distributions related to the K^+ meson in the $B^+ \to K^+ J/\psi(\to e^+e^-)$ simulation sample and the ${}_s\mathcal{W}eight$ted data.

The properties of the detected $\boldsymbol{K^+}$ **mesons** from B^+ decays are shown in Fig. 5.13. The discussion of the modelling starts with parameters related to the track reconstruction. The number of hits associated to the K^+ track, $N_{\text{hits}(K^+)}$, features a smaller mean in the data sample. On the one hand, fewer hits are caused by the missing UT. On the other hand, the SciFi and VELO subdetectors are less efficient in real data taking, which can be seen in the numbers of SciFi and VELO hits ($N_{\text{Scifi,hits}}(K^+)$, $N_{\text{Velo,hits}}(K^+)$), peaking in data at lower values. The observed smaller efficiency in data is induced from certain modules in the VELO detector being off, as well as tracker misalignment. Also, the track χ^2 distribution, $\chi^2_{\text{track}}(K^+)$, is peaking at lower values in the data sample, which could be induced by the lower number of hits in the detector. The $\chi^2_{\text{track}}/\text{ndof}(K^+)$ is peaking, as expected, at one, and its width seems to be slightly smaller in the simulation sample, which is expected to scale with $1/\sqrt{\text{ndof}}$. This strengthened the hypothesis of missing hits in data compared to the simulation sample.

Similar to the B^+, the η, p_x and p_y distributions are slightly shifted in data. However, the p_z distribution is consistent between data and simulation. Therefore, it is likely that the observed shift of the B^+ p_z originates from the electrons.

Even though the performance of the PID variables is not optimised yet, the distributions of $\text{Prob}_{\text{ghost-track}}$, $\text{DLL}_{K-\pi}$ and ProbNN_K are similar in data and simulation. The ProbNN_K distribution in simulation has a second bump at 0.9991, while it seems in data, given the sample size, to be purely exponential. Experience has shown that the accurate simulation of the PID response is a particularly challenging part of the simulation at LHCb, which is crucial since the PID information is used broadly across analyses. The effect of the second peak needs to be re-evaluated after the PID optimisation and using a larger data sample.

The variables related to the $\boldsymbol{J/\psi}$ **resonance** are presented in Fig. 5.14. The fractions of the Brem categories are similar in data and simulation. The data has a fraction of about 0.018 dielectron pairs less in the "Brem 0" category, about 0.025 events less are present in the "Brem 1" category, and approximately 0.007 more entries are situated in the "Brem 2" category. The effect of the higher "Brem 2" category is probably due to the better identification of electrons when radiated bremsstrahlung photons are recovered. The lower efficiency in the "Brem 1" category is explained by the loss of the bremsstrahlung photon, combined with a lower electron identification efficiency. The additional events in the "Brem 0" category could indicate a small fraction of misidentification backgrounds which end up in this category.

The q^2 distribution, which is $m^2_{J/\psi}$, is peaking at slightly lower values in data and possesses a shorter right tail. The same effect has been seen by fitting the e^+e^- invariant

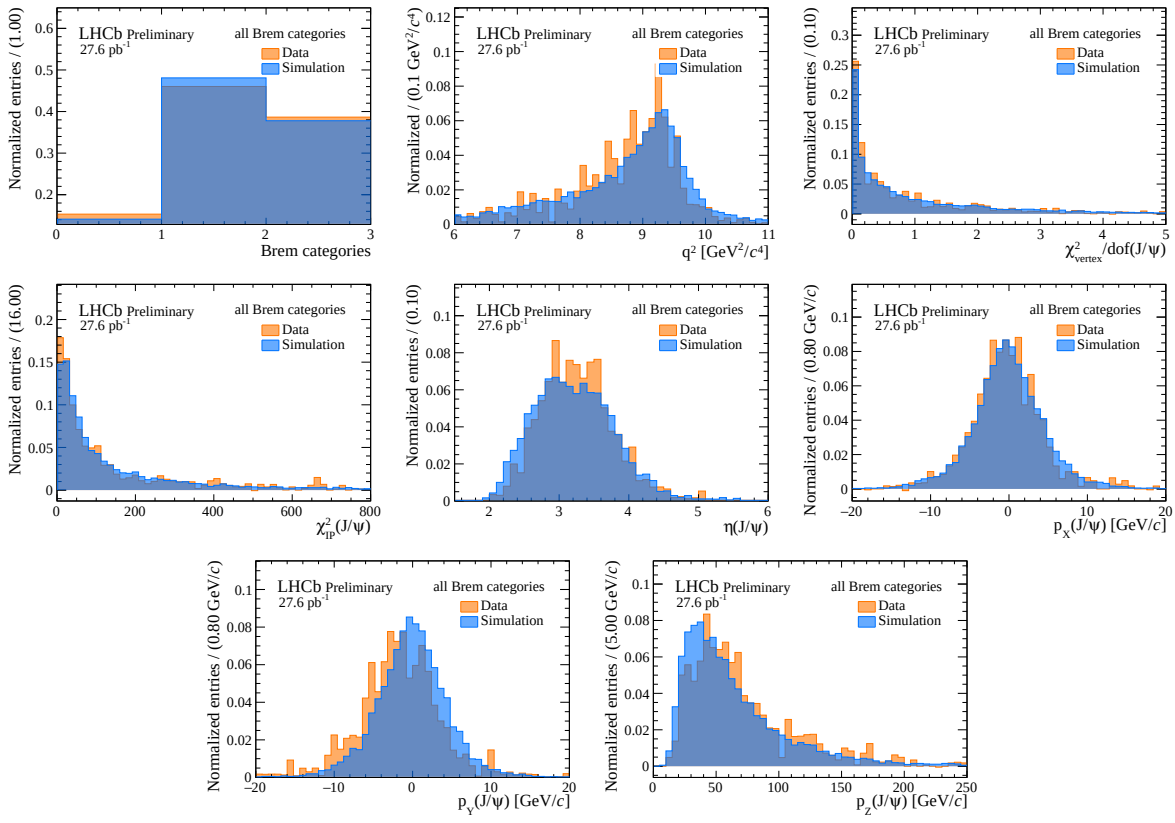

Figure 5.14 – Comparison of the variable distributions related to the J/ψ resonance in the $B^+ \to K^+ J/\psi(\to e^+e^-)$ simulation sample and the ${}_s\mathcal{W}eight$ted data.

mass in data, which is situated at approximately 10 MeV/c^2 lower values than in the simulation sample.

The χ^2_{vertex}/ndof and the χ^2_{IP} of the dielectron candidates are well represented in the simulation sample. Also, the J/ψ momenta and pseudorapidity are subject to a shift in simulation relative to data. The p_x distribution, however, is well represented. The p_z distribution is shifted to higher values and is, thus, expected to be the reason for the shift in the p_z distribution for the B^+ meson.

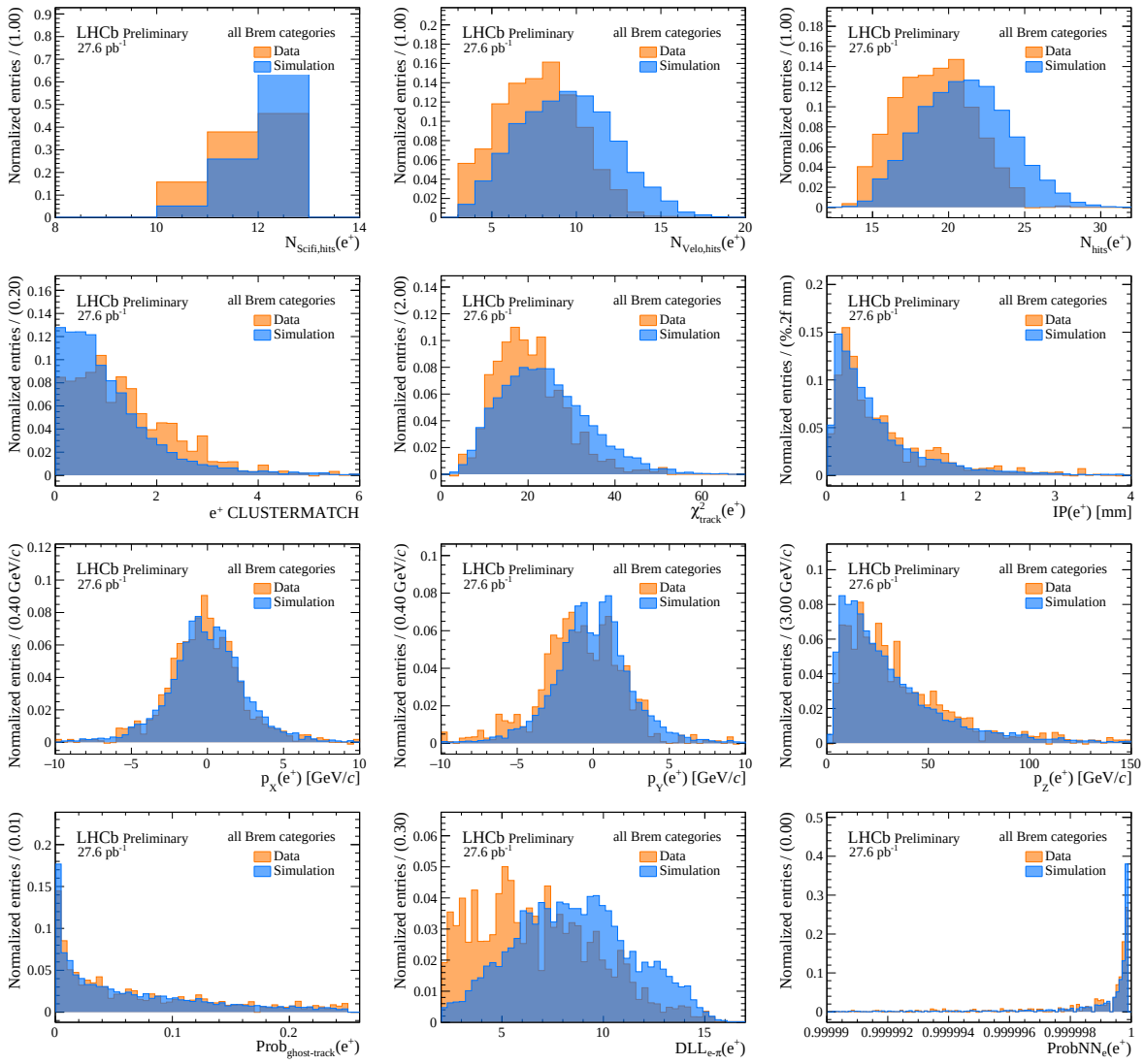

Figure 5.15 – Comparison of the variable distributions related to the e^+ in the $B^+ \to K^+ J/\psi(\to e^+e^-)$ simulation sample and the ${}_s\mathcal{W}eight$ted data.

The detector hits of the electron and positron tracks in Fig. 5.15 and Fig. 5.16 underline the not-yet optimised detector efficiency. The CLUSTERMATCH variable is derived by

calculating the two-dimensional χ^2 value of a reconstructed track matched to a calorimeter cluster. It is crucial to the accuracy of the simulated PID variables, as they utilise this information among others. The distributions of the CLUSTERMATCH variable in data and in simulation differ, with a bigger disagreement observed in the positron case. This can be identified as a good starting point to improve the description of electron and positron PID in simulation. In a future iteration of this analysis, the BDT suppressing the combinatorial background explained in Sec. 5.4.2 should not be trained on this poorly modelled variable.

The electron and positron χ^2_{track} variables possess a peak at lower values in data than in simulation. The impact parameter distributions of the electron and positron are similar in data and simulation. The momentum in x-direction has a Mexican hat shape in the electron distribution and is peaking at zero for the positron. Since the distribution in the simulation sample is the same for $p_x(e^-)$ and $p_x(e^+)$ and in between the two shapes, the difference in the data sample seems to be only a statistical effect. The shape of the positron and electron momenta distribution in y-direction are both Mexican-hat-like. For the electron and positron, the p_z distribution peaks at higher values in data, causing the shift in the p_z momenta of the J/ψ and the B^+.

The electron and positron PID variables $\text{Prob}_{\text{ghost-track}}$ and ProbNN_e are well modelled, while the $\text{DLL}_{e-\pi}$ differs in data and simulation. This could be explained by the $\text{DLL}_{e-\pi}$ being directly related to the badly described CLUSTERMATCH variable, whereas the ProbNN_e variables combine more information into a PID score.

In conclusion, the performance of the Upgrade I LHCb detector in 2022 data is in a reasonably good state, given the many challenges faced at the moment. Many topological and kinematic variables have matching distributions in data and simulation within the statistical limitation of the current study. What needs to be optimised in the future is the spatial and time alignment, as well as the performances of the individual sub-detectors. The off-axis position of the beam could affect the acceptance of the decay topology but will need to be studied further with corresponding simulation samples. The PID variables agree overall in simulation and data, except for the particularly challenging $\text{DLL}_{e-\pi}$ variable, which could be improved by a better description of the CLUSTERMATCH variable.

5.7 Outlook

The results from this analysis are dominated by the statistical precision of the 2022 dataset. Therefore, it is of central importance to collect more data in order to clarify some of the posed questions in this work. The data-taking in 2023 was subject to a couple of

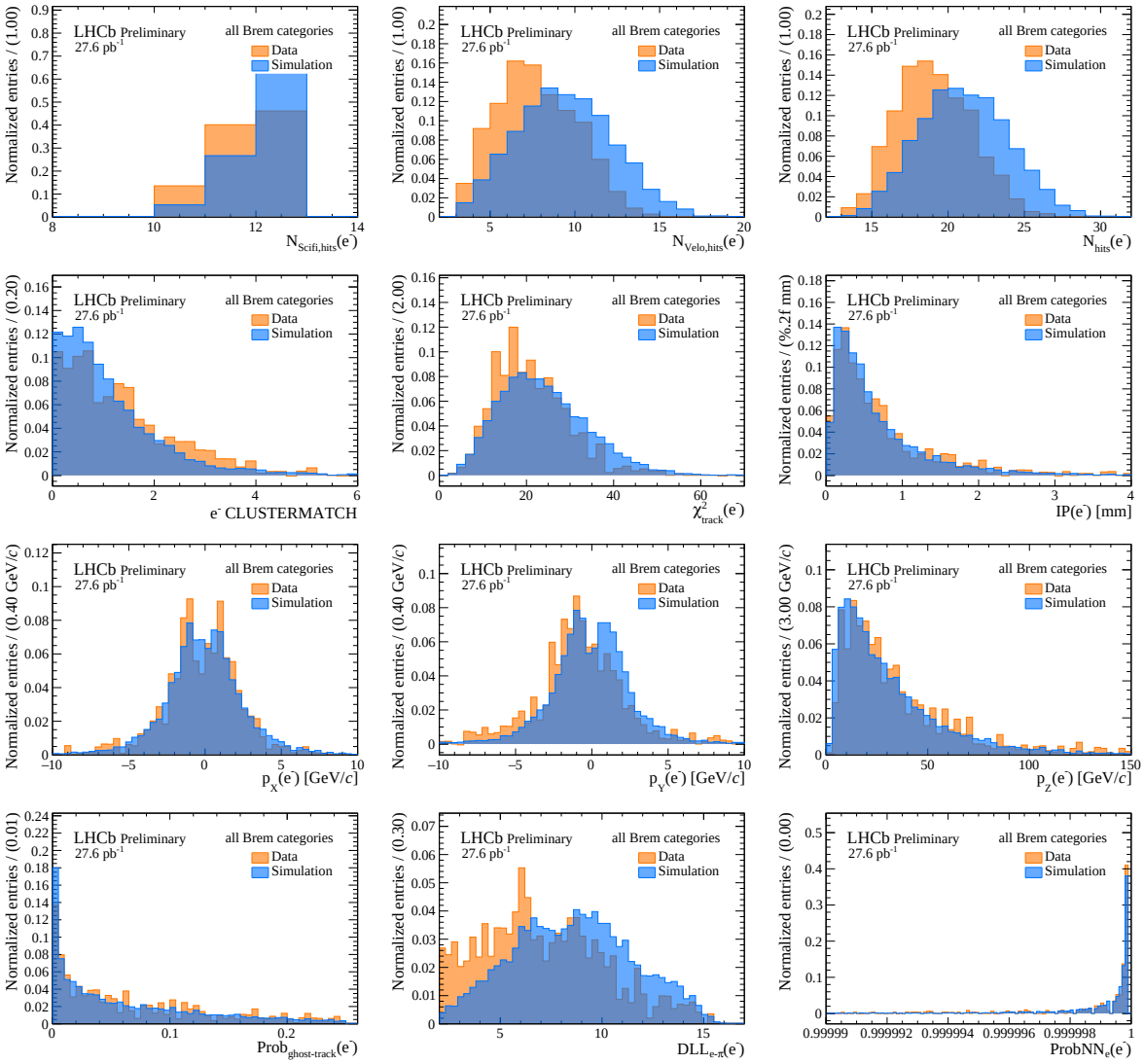

Figure 5.16 – Comparison of the variable distributions related to the e^- in the $B^+ \to K^+ J/\psi(\to e^+e^-)$ simulation sample and the ${}_s\mathcal{W}eight$ted data.

unforeseen challenges, outlined in the following.

At the beginning of 2023, an incident occurred involving the VELO detector. Before the LHC declares stable beams, the VELO detector is normally in an open position for safety reasons. It is situated in a secondary vacuum, which is isolated from the beam vacuum by a thin RF foil. A safety system balances the vacuum to be within -5 and +2 mbar with respect to the beam vacuum. In case of a pressure difference between the two vacuums of more than 10 mbar, the safety system is supposed to balance. This limit has been reached by warming the VELO detector. A defect in the relay caused a malfunctioning of the protection system. The vacuum was balanced in the wrong direction, leading to a pressure difference of about 200 mbar between the two vacuums. The high pressure caused a permanent plastic deformation of the RF foil towards the beam vacuum.

The VELO detector is luckily not damaged by the incident. However, a tomography of the RF foil showed that closing of up to 32 mm distance to the beam was safe in order to prevent the RF-boxes from A- and C-side from touching each other. As a reference, the closed detector has an opening of a 5 mm distance from the beam.

Moreover, a movement of the VELO motion system of about $1 - 2$ mm in x and y direction has been detected, which is caused by a loose screw. As a result, the VELO was kept constantly in a half-closed position, which is 24.5 mm far from the beam. This incident and its repercussions have sensitively affected the operations of LHCb in 2023, resulting in a reduced acceptance due to the VELO being in a half-open position.

During the 2022 data-taking, the muon stations were not time aligned precisely, and the reconstruction efficiency of final states with muons was lower than expected. During 2023, the muon station time alignment is progressing, enabling the extension of the analysis to the muon modes. In addition, the UT subdetector was installed in the year and technical stop and is now undergoing commissioning. The UT will help this analysis by suppressing the rate of ghost tracks.

In 2023, about $40\,\mathrm{pb}^{-1}$ of data with reasonable quality has been recorded with a $\mu = 1.1$. On July 17, 2023 an incident occurred at the LHC, which stopped the data taking. The collaboration investigates what measurements can be performed with this "peculiar" dataset.

To sum up, the commissioning of the Run 3 detector is ongoing. Nevertheless, there is already much useful information obtained with 2022 and soon with 2023 data. The hope is that 2024 will not be subject to incidents, and LHCb will be able to move to physics data taking. The continuation of this analysis will then be able to offer valuable insights into the quality of the data and how to improve the simulation of the new LHCb detector.

Chapter 6

Conclusion and future prospects

While in the past decades, the Standard Model of Particle Physics was shown to be a very powerful theory, as of today, it can not explain the matter-antimatter asymmetry observed in our universe, the hierarchy problem or the nature of Dark Matter. The solution to those problems is searching for New Physics models (NP) and completing the SM. Indirect searches in $b \to s\ell^+\ell^-$ decays are particularly sensitive to NP since their potential contributions could contribute significantly to the loop-suppressed SM processes.

The main goal of this thesis is to perform an angular analysis of the $\Lambda_b^0 \to pK^-\mu^+\mu^-$ decays, which gives an insight into $b \to s\ell^+\ell^-$ decays of b baryons and probes different spin-structures than analyses of B meson decays. The leptonic forward-backward asymmetry, $A_{FB,3/2}^{\ell}$, and the angular observable S_{1cc} are aimed to be measured in five bins of the dimuon invariant mass squared, q^2. The presented analysis exploits the Run 1 and 2 datasets collected by the LHCb experiment. Given the data sample size and the available theoretical predictions, the focus is set on the $\Lambda(1520)$ resonance.

In the presented analysis, the angular distribution of the $\Lambda(1520)$ resonance has been implemented. Previous measurements indicate underlying contributions of spin-1/2 Λ^* resonances in the studied pK^- invariant mass spectrum, namely from the $\Lambda(1405)$ and $\Lambda(1600)$ resonances. Their contribution is included in the angular fit model. The pK^- invariant mass helps in discriminating between the spin-3/2 and spin-1/2 resonances. Due to the presence of several Λ^* resonances, interference effects could occur. The interferences cause a non-negligible shift in the $\cos\theta_p$ distribution, which has been incorporated in the angular fit model.

The data have been corrected for angular acceptance, and the remaining backgrounds are suppressed using the ${}_s\mathcal{W}eight$ technique. The angular fit of the ${}_s\mathcal{W}eight$ted and

acceptance-corrected data is exercised on the $\Lambda_b^0 \to \Lambda(1520)J/\psi$ and $\Lambda_b^0 \to \Lambda(1520)\psi(2S)$ control modes, and A_{FB}^{ℓ} values of 0.008 ± 0.008 and -0.053 ± 0.124 are found, respectively. The measured values are found to be compatible with zero, as one would expect.

The angular fit in the rare mode turned out to be very challenging because of the small sample size and the presence of the SM observables that are close to the negative limit. The modelling of the combinatorial background component in the angular fit, instead of applying ${}_s\mathcal{W}eights$, added stability to the fit model and helped with the fit convergence issues. Pseudo-experiments indicate possible biases which will be studied more precisely in the future.

According to previously published analyses of similar decays with datasets of equal size, the analysis is expected to be statistically dominated. As a consequence, the precision of the angular observables will be improved with a more extensive dataset, as the ones which will hopefully be available in future runs of the LHC. In addition, the angular fit could be performed without the heavy quark limit approximation, enabling the access of supplementary angular observables. Finally, another possibility would be to enlarge the pK^- invariant mass spectrum and to include more resonances in the angular fit model.

The increase in the instantaneous luminosity will be beneficial for the statistically limited $b \to s\ell^+\ell^-$ decays. The fully software-based trigger employed in Run 3 is intended to achieve higher electron efficiencies by triggering on the electron tracks by recovering the bremsstrahlung photons already at the first trigger step. However, excellent control of the electron and muon efficiencies is crucial for LFU measurements and needs to be validated, especially after the removal of the SPD and PS detectors. For this purpose, a study of $B^+ \to K^+J/\psi(\to e^+e^-)$ and $B^+ \to K^+\psi(2S)(\to e^+e^-)$ decays has been prepared. These decays are selected by the same trigger requirements as the rare decays, allowing to validate the new trigger strategy. The secondary $\psi(2S) \to e^+e^-$ and $B^+ \to K^+\psi(2S)(\to e^+e^-)$ yields are determined for the first time with 2022 data, and compared with the J/ψ yields. These studies enable the comparison of relevant distributions in the simulation samples and the background-subtracted data.

In summary, a fairly good agreement is found in the topological and kinematic variables in data and simulation samples. While most of the PID variables match overall in data and simulation, the $\mathrm{DLL}_{e\pi}$ variable shows large disagreements. An improvement of the spatial and time alignment of the LHCb Upgrade I detector is desirable to exploit its full potential. This analysis will then be beneficial to monitor the data quality and to improve the simulations of the upgraded LHCb detector.

Appendix A

Event types of the simulation samples

The event types and simulation versions of the different simulation samples is listed in Tab. A.1. To simplify the decay descriptor, some decays are not stated explicitly. However, the J/ψ and $\psi(2S)$ resonances are always decaying into a muon pair. Similarly, the decays $\Lambda(1520) \to pK^-$ and $K(892)^{*0} \to K^+\pi^-$ are imposed implicitly.

Decay mode	Event type	Simulation version (Sim)					
		2011	2012	2015	2016	2017	2018
$\Lambda_b^0 \to \Lambda(1520)\mu^+\mu^-$	15114001	09k	09k	09h	09h	09h	09h
$\Lambda_b^0 \to pK^-\mu^+\mu^-$	15114011	-	09k	-	-	09h	09h
$\Lambda_b^0 \to pK^-J/\psi$	15144001	09b	08i	09b	09b	09h	09h
$\Lambda_b^0 \to pK^-\psi(2S)$	15144011	-	08e	-	09b	-	-
$\Lambda_b^0 \to \Lambda_c^+(\to pK^-\pi^+)\pi^-$	15364010	-	09d	-	09l	-	-
$\Lambda_b^0 \to \Lambda_c^+(\to pK^-\pi^+)\mu^-\overline{\nu}_\mu$	15574001	-	-	-	09c	-	-
$\Lambda_b^0 \to \Lambda_c^+(\to \Lambda(1520)\mu^+\nu_\mu)\pi^-$	15574005	-	09l	-	-	-	-
$B^0 \to K^+\pi^-\mu^+\mu^-$	11114000	-	-	-	-	09h	-
$B^0 \to K^*(892)^0J/\psi$	11144001	-	08f	-	09b	-	-
$B^0 \to K^+\pi^-J/\psi$	11144050	-	09k	-	09h	-	-
$B^0 \to K^*(892)^0\psi(2S)$	11144011	-	09i	-	09i	-	-
$B_s^0 \to K^+K^-\mu^+\mu^-$	13114007	-	09b	-	-	-	-
$B_s^0 \to K^+K^-J/\psi$	13144041	-	09h	-	09b	-	-
$B_s^0 \to K^+K^-\psi(2S)$	13144044	-	09k	-	09k	-	-

Table A.1 – Event types and simulation versions of the different simulation samples.

Appendix B

Comparison of background simulation samples between different years

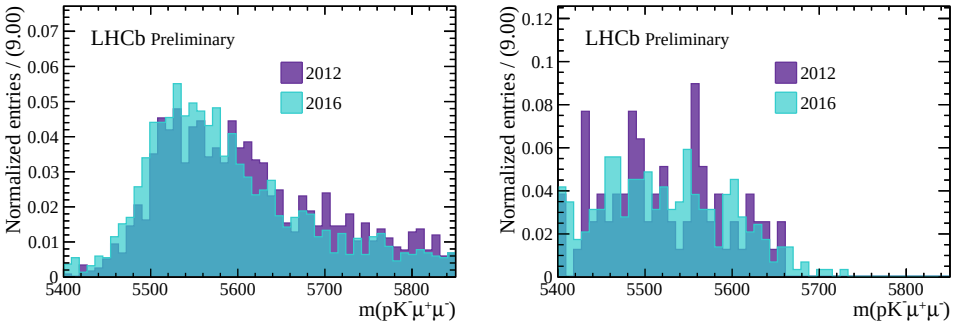

Figure B.1 – Comparison of the $B^0 \to K^{*0} J/\psi$ (left) and the pK^- swapped misidentification background simulation sample (right) for the years 2012 and 2016 in the J/ψ bin.

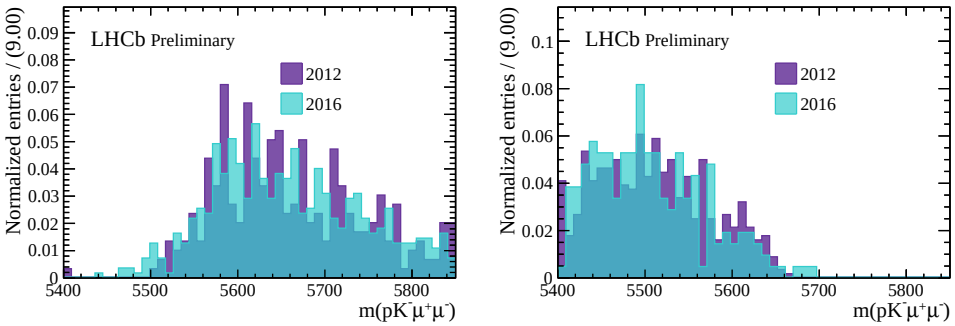

Figure B.2 – Comparison of the $B^0 \to K^{*0}\psi(2S)$ (left) and the pK^- swapped misidentification background simulation samples (right) for different years in the $\psi(2S)$ bin.

Appendix C

Additionnal plots related to the BDT training

C.1 Features of the BDT training

The different input variables used in the BDT training are shown in Fig. C.1, C.2 and C.3. The signal and background distributions in the BDT training are compared. The definition of the different variables is reminded in the Glossary.

C.2 Correlations between the features in the BDT training

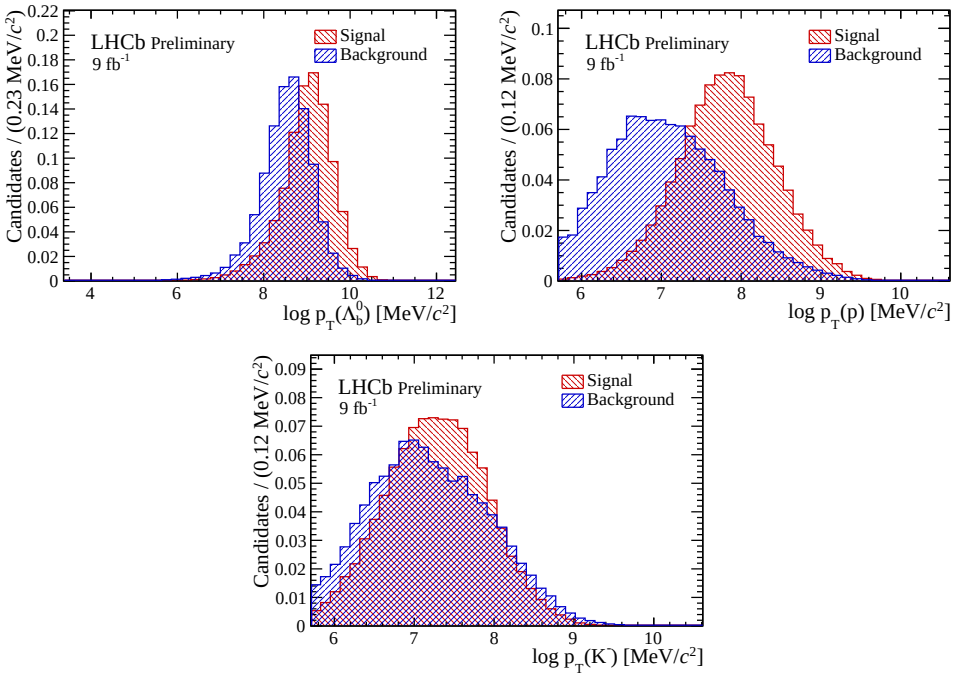

Figure C.1 – Features in the BDT related to the kinematics of the particles.

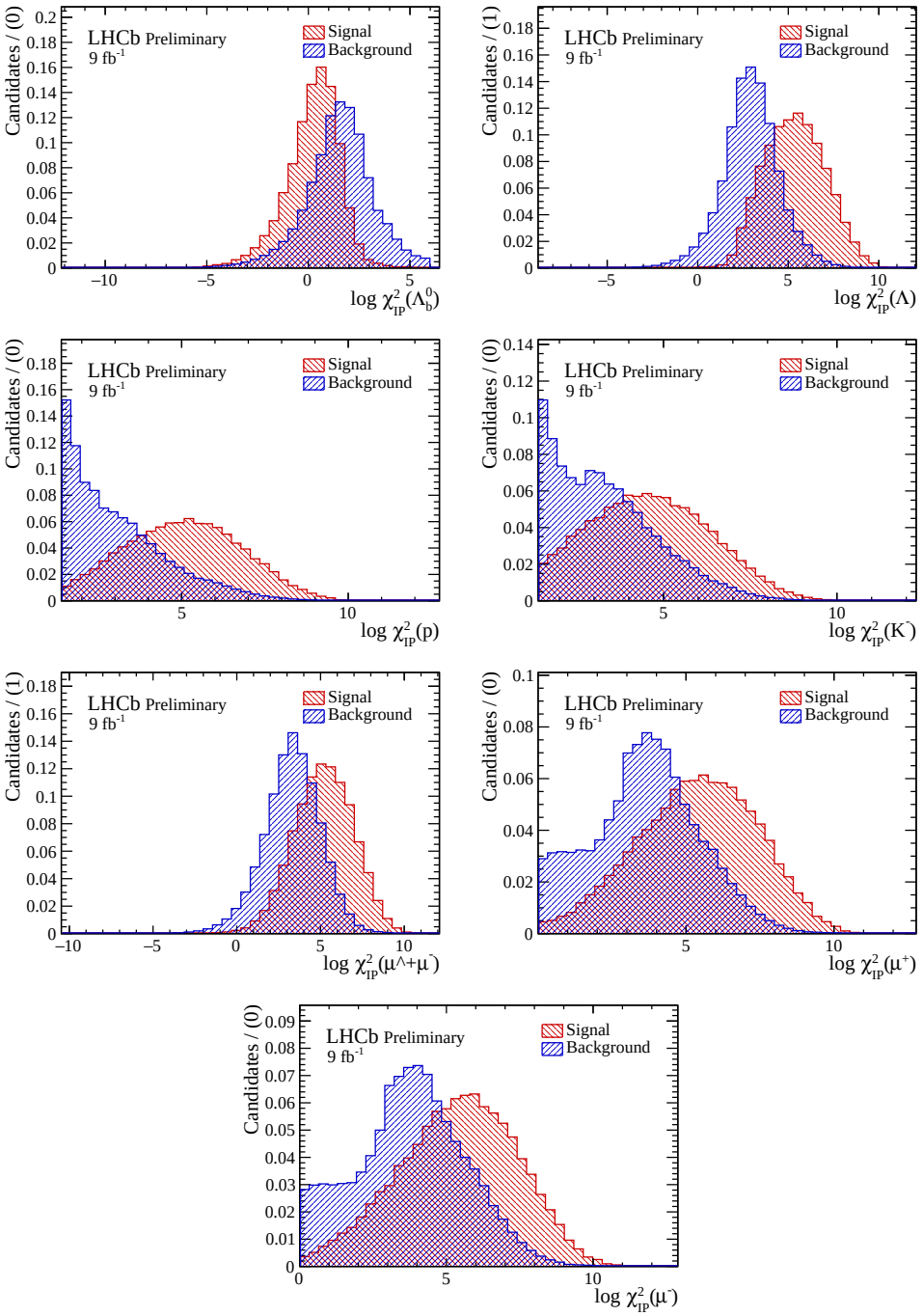

Figure C.2 – Features in the BDT using the logarithm of the impact parameter χ^2 distribution for the different particles.

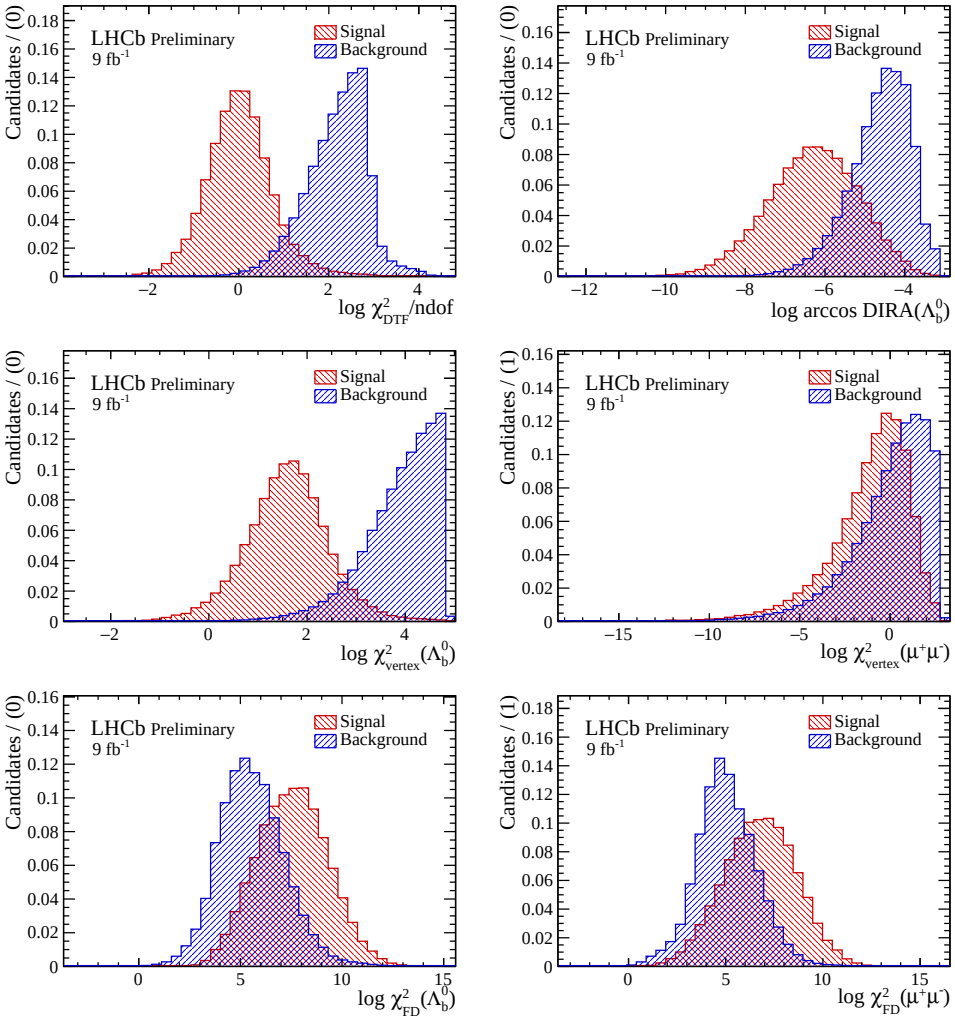

Figure C.3 – Features in the BDT related to the event topology.

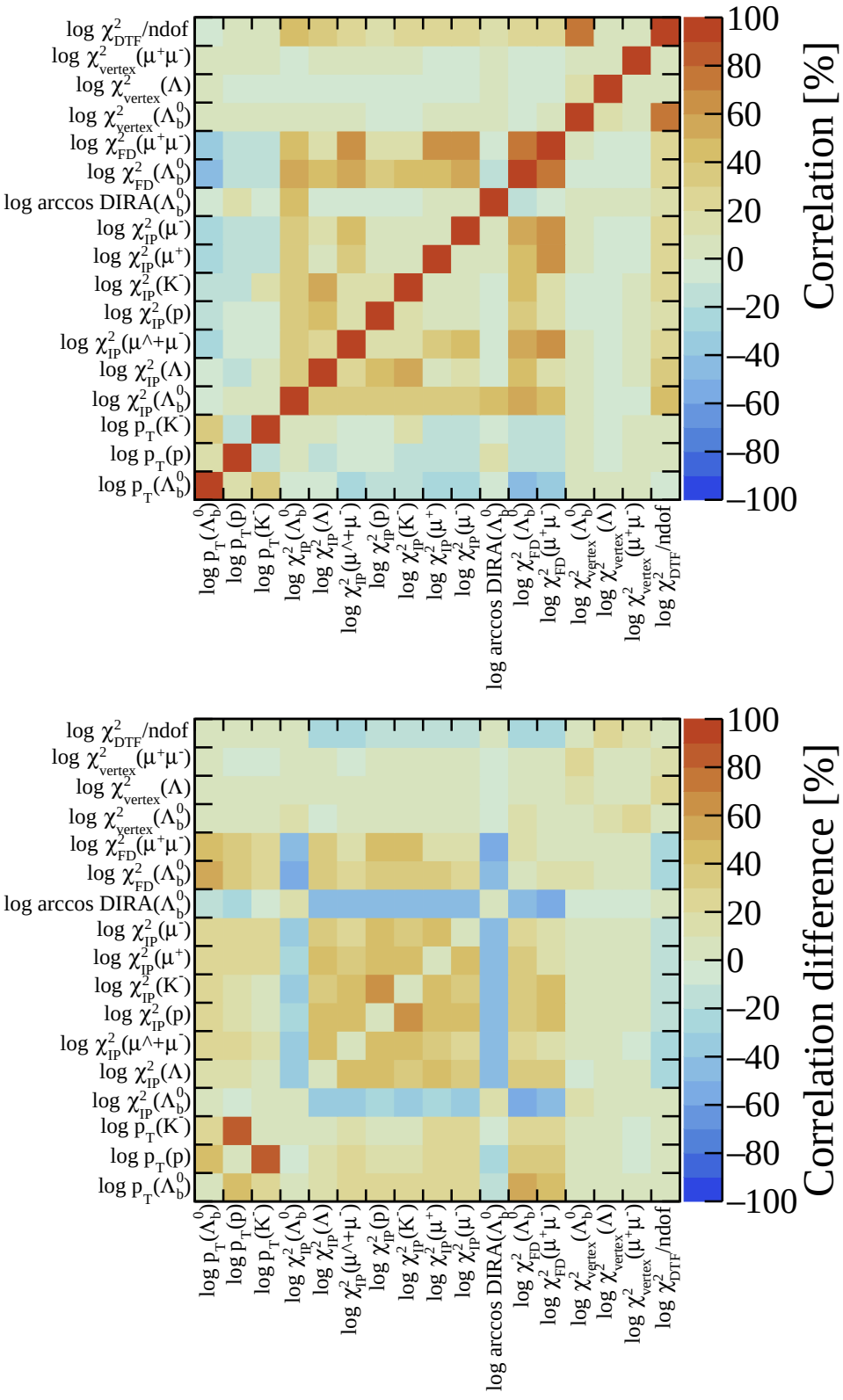

Figure C.4 – The correlation of the features for the background proxy is shown on the top. Those are defined as the $pK^-\mu^+\mu^-$ high mass sideband. The difference between the signal and background correlations is shown in the bottom plot.

Appendix D

Simulation correction plots

D.1 Multiplicity corrections

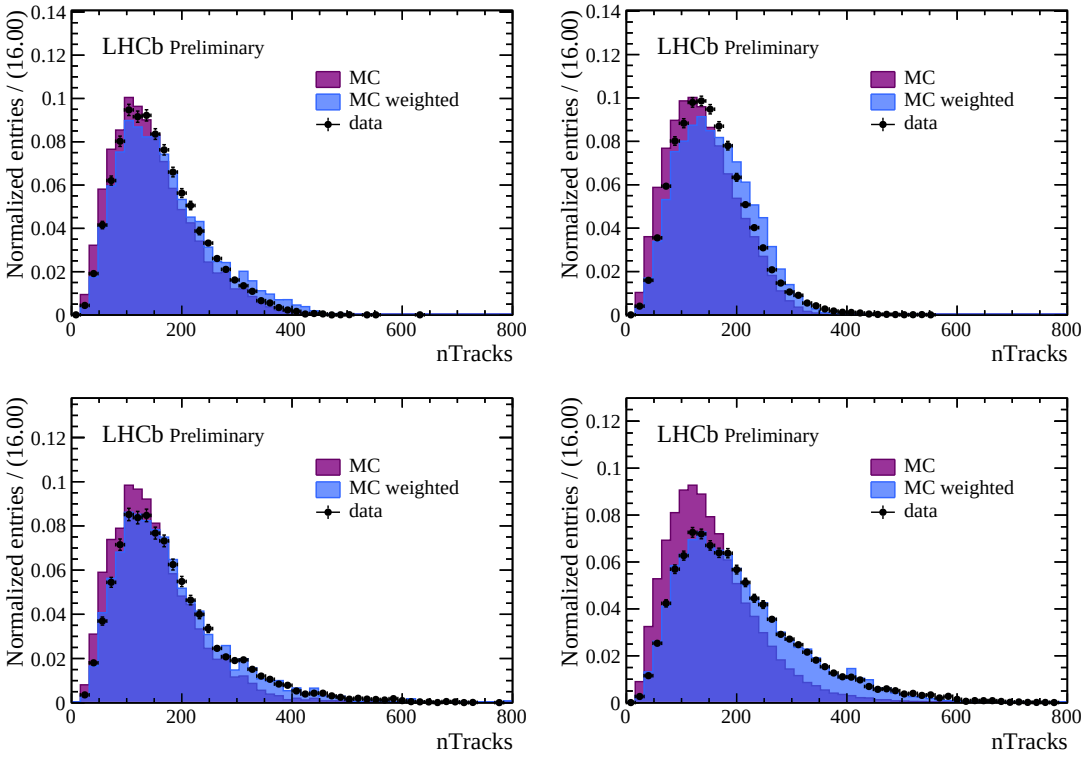

Figure D.1 – nTracks distribution for the data taking year 2012 (left) and 2016 (right) in $\Lambda_b^0 \to pK^- J/\psi$ simulation and data by focusing on events triggered by the L0Muon (top) and L0DiMuon (bottom) hardware trigger.

The simulation data difference of event triggered by the L0Muon trigger and the L0DiMuon trigger are shown in Fig. D.1. The shape of the data and simulation distributions differ between the two trigger lines. Since the analysis is performed by combining the two categories and in order to align the procedure with the one in the BF measurement [60], the corrections are chosen to be identical.

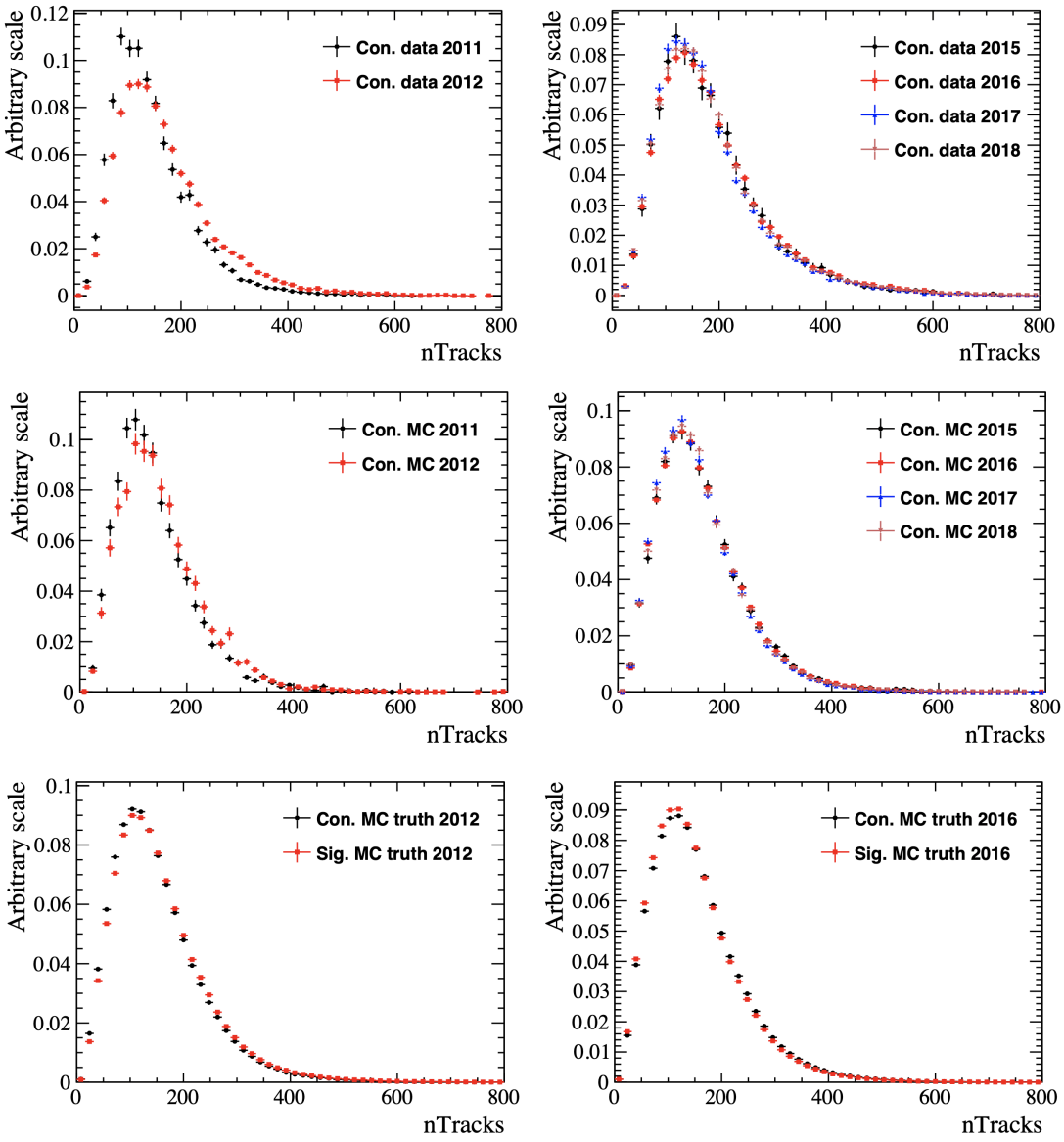

Figure D.2 – Comparison of the nTracks distribution for all data taking years in $\Lambda_b^0 \to pK^-J/\psi$ data (top) and simulation (middle) are shown, as well as the generator level distributions for the signal and control mode for 2012 and 2016 (bottom).

In Fig. D.2, the nTracks distribution is compared for the different years in data and simulation. In addition, the generator level distribution of the $\Lambda_b^0 \to \Lambda(1520)\mu^+\mu^-$ and

the $\Lambda_b^0 \to pK^- J/\psi$ distributions are compared for the years 2012 and 2016. Both of them are quite similar.

D.2 Kinematic corrections

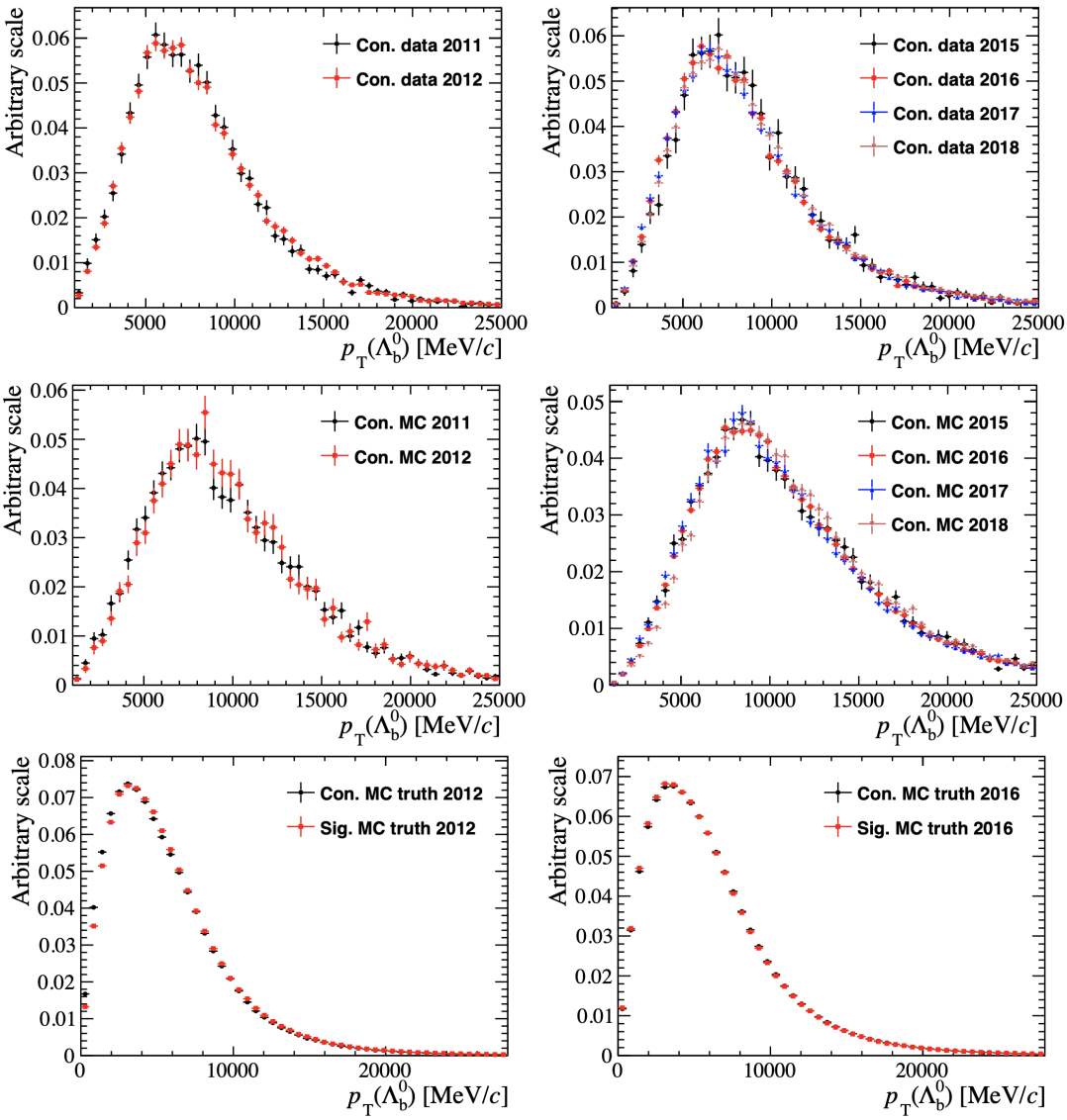

Figure D.3 – The corrected Λ_b^0 transversal momenta in data (top) and simulation (middle) for all years is compared. Furthermore, the $p_(T)(\Lambda_b^0)$ distribution is shown on generator level for signal and control mode (bottom) for the years 2012 and 2016.

D.3 Requirements on the PID calibration samples

Particle	PID requirements	Initial conditions
p	MC12TuneV3_ProbNNp>0.2 MC12TuneV3_ProbNNK<0.8 MC12TuneV3_ProbNNpi<0.7 DLLp>-5.0	PT>300 P>2000 hasRich==1
K	MC12TuneV3 ProbNNK>0.2 MC12TuneV3_ProbNNp<0.8 DLLK>-5.0	PT>300 P>2000 hasRich==1
μ	MC12TuneV3_ProbNNmu>0.1 DLLmu>-5.0 IsMuon==1	PT>800 P>3000 hasRich==1 InMuonAcc==1

Table D.1 – PIDCalib requirements applied on the calibration samples for Run 1 and connected by a logical "&&".

D.4 PID efficiency maps

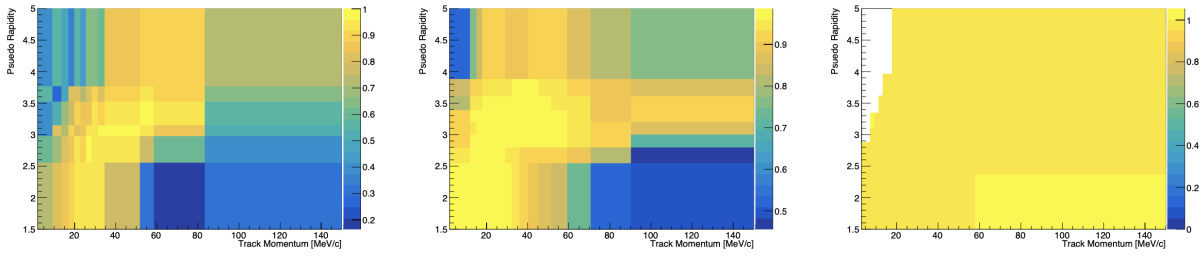

(a) Proton (b) Kaon (c) Muon

Figure D.4 – PID efficiency maps for the year 2011 with the MagUp magnet polarisation.

Particle	PID requirements	Initial conditions
p	Brunel_MC15TuneV1_ProbNNp>0.2 Brunel_MC15TuneV1_ProbNNK<0.8 Brunel_MC15TuneV1_ProbNNpi<0.7 Brunel_DLLp>-5.0	Brunel_PT>1000 Brunel_P>2000 Brunel_HasRich==1.0
K	Brunel_MC15TuneV1_ProbNNK>0.2 Brunel_MC15TuneV1_ProbNNp<0.8 Brunel_DLLK>-5.0	Brunel_PT>300 Brunel_P>2000 Brunel_HasRich==1.0
μ	Brunel_MC15TuneV1_ProbNNmu>0.1 Brunel_DLLmu>-5.0 Brunel_IsMuon==1.0	Brunel_PT>200 Brunel_P>3000 Brunel_HasRich==1.0 Brunel_InMuonAcc==1.0

Table D.2 – PIDCalib requirements applied on the calibration samples for Run 2 and connected by a logical "&&".

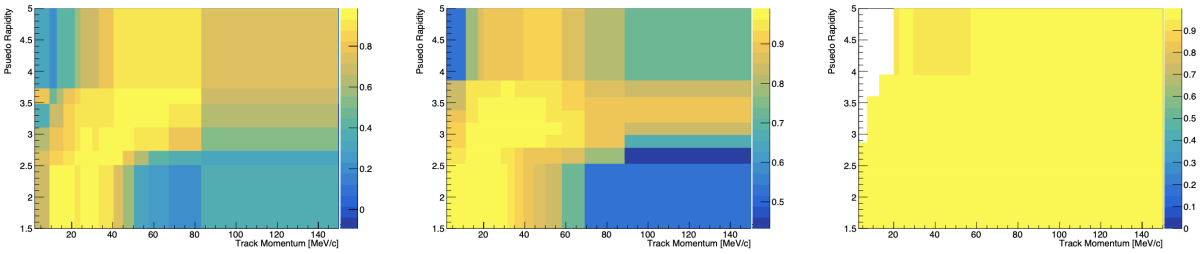

(a) Proton (b) Kaon (c) Muon

Figure D.5 – PID efficiency maps for the year 2012 with the MagUp magnet polarisation.

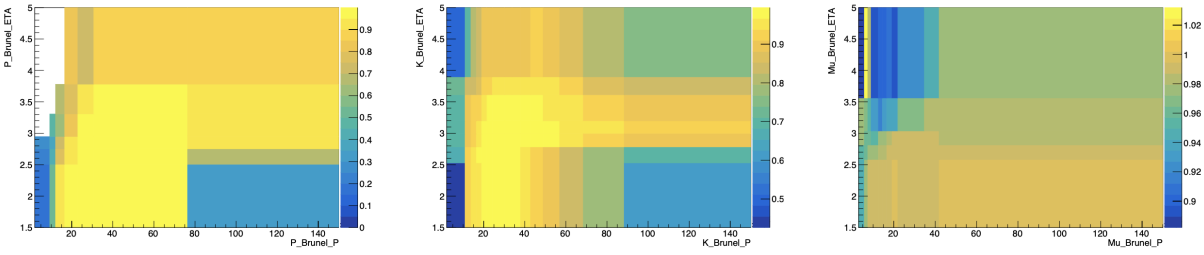

(a) Proton (b) Kaon (c) Muon

Figure D.6 – PID efficiency maps for the year 2015 with the MagUp magnet polarisation.

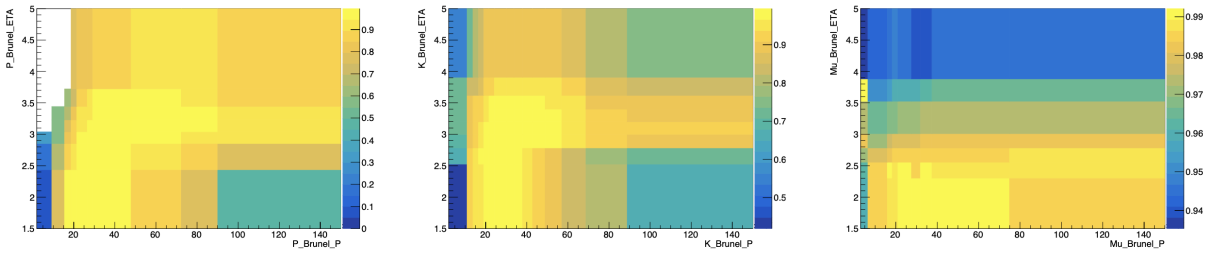

(a) Proton (b) Kaon (c) Muon

Figure D.7 – PID efficiency maps for the year 2016 with the MagUp magnet polarisation.

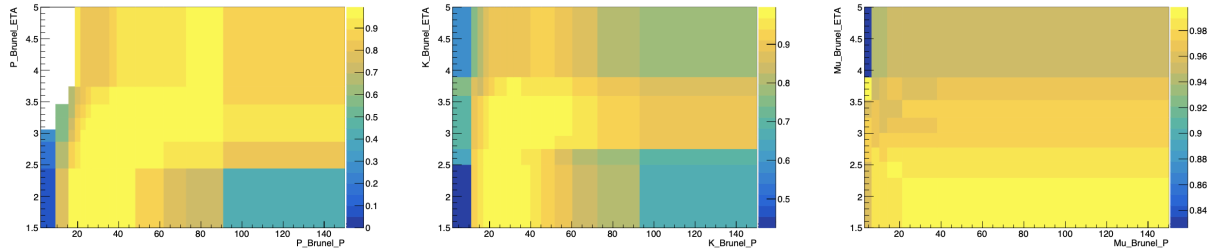

(a) Proton (b) Kaon (c) Muon

Figure D.8 – PID efficiency maps for the year 2017 with the MagUp magnet polarisation.

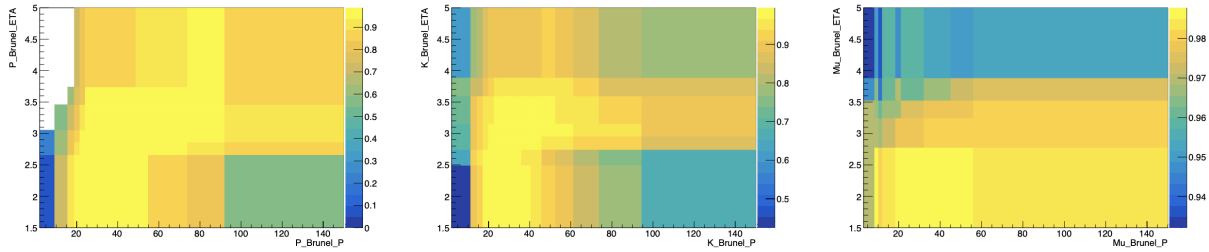

(a) Proton (b) Kaon (c) Muon

Figure D.9 – PID efficiency maps for the year 2018 with the MagUp magnet polarisation.

Appendix E

Background fraction estimation from data

A fit of the B^0 and the B_s^0 masses are performed, as visible in the top plots in Fig. E.1. In the bottom plot, the yield of the pK^- swapped double misidentification is shown. The background is described by an exponential. The signal components are modeled by a Hypatia 2 function, which shape is extracted from the $B^0 \to K^{*0}J/\psi$, the $B_s^0 \to K^+K^-J/\psi$ and the $\Lambda_b^0 \to pK^-J/\psi$ simulation samples and fixed in the data fit.

The fraction of $B_s^0 \to K^{*0}J/\psi$ decays compared to $B^0 \to K^{*0}J/\psi$ decays is

$$r_{B_s^0/B^0}^{K^{*0}J/\psi} = \frac{N_{B_s^0 \to K^{*0}J/\psi}}{N_{B^0 \to K^{*0}J/\psi}} = 0.20 \pm 0.02, \tag{E.1}$$

which is rather small considering the $B^0 \to K^{*0}J/\psi$ yield. This the reason why $B_s^0 \to K^{*0}J/\psi$ decays are neglected. In a similar manner, the fraction of $B^0 \to K^+K^-J/\psi$ decays is calculated with respect to the yield of $B_s^0 \to K^+K^-J/\psi$ decays. Its value of

$$r_{B^0/B_s^0}^{K^+K^-J/\psi} = \frac{N_{B^0 \to K^+K^-J/\psi}}{N_{B_s^0 \to K^+K^-J/\psi}} = 0.17 \pm 0.03 \tag{E.2}$$

is again tiny and, thus, negligible.

To be able to extrapolate the yields to the vetoed region, the veto efficiency needs to be comparable. The veto efficiency has been checked in the simulation sample. For the $B^0 \to K^{*0}J/\psi$ simulation sample, the veto efficiency is about $(34.3 \pm 0.8)\%$, by taking the statistical error of the yield after the veto as an error. The $B_s^0 \to K^+K^-J/\psi$ sample has a veto efficiency of $(42 \pm 3)\%$. Therefore, the veto efficiency agrees within 3σ with each other. For the proton kaon swapped misidentification background, the veto efficiency is of factor two higher, which is numbers $(82 \pm 4)\%$.

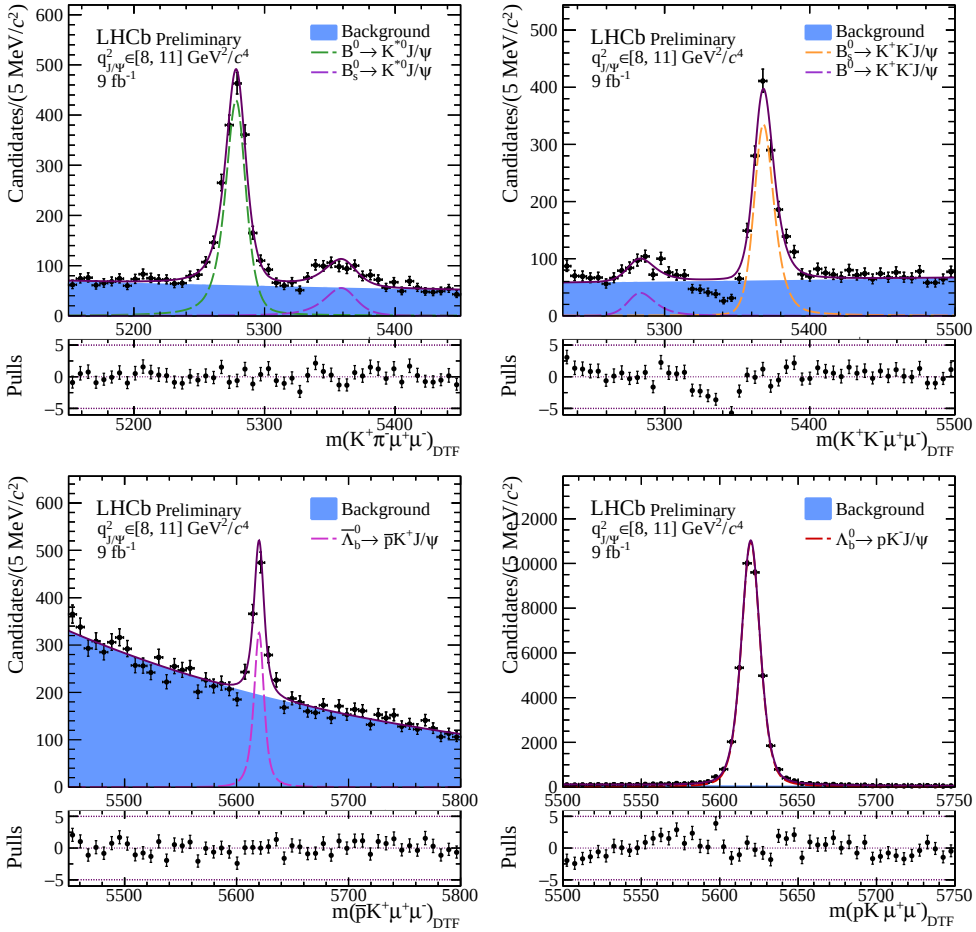

Figure E.1 – In order to estimate the relative fraction of $B^0_s \to K^+K^-J/\psi$ against $B^0 \to K^{*0}J/\psi$ decays and proton kaon swapped misidentification background versus signal events, they are estimated in data by fitting the background components in the Λ^0_b mass sidebands and by vetoing other backgrounds.

For the $\psi(2S)$ mode, the same procedure as in the J/ψ mode is followed. The value of the background contributions in data is shown in Fig. E.2. The proton kaon swapped

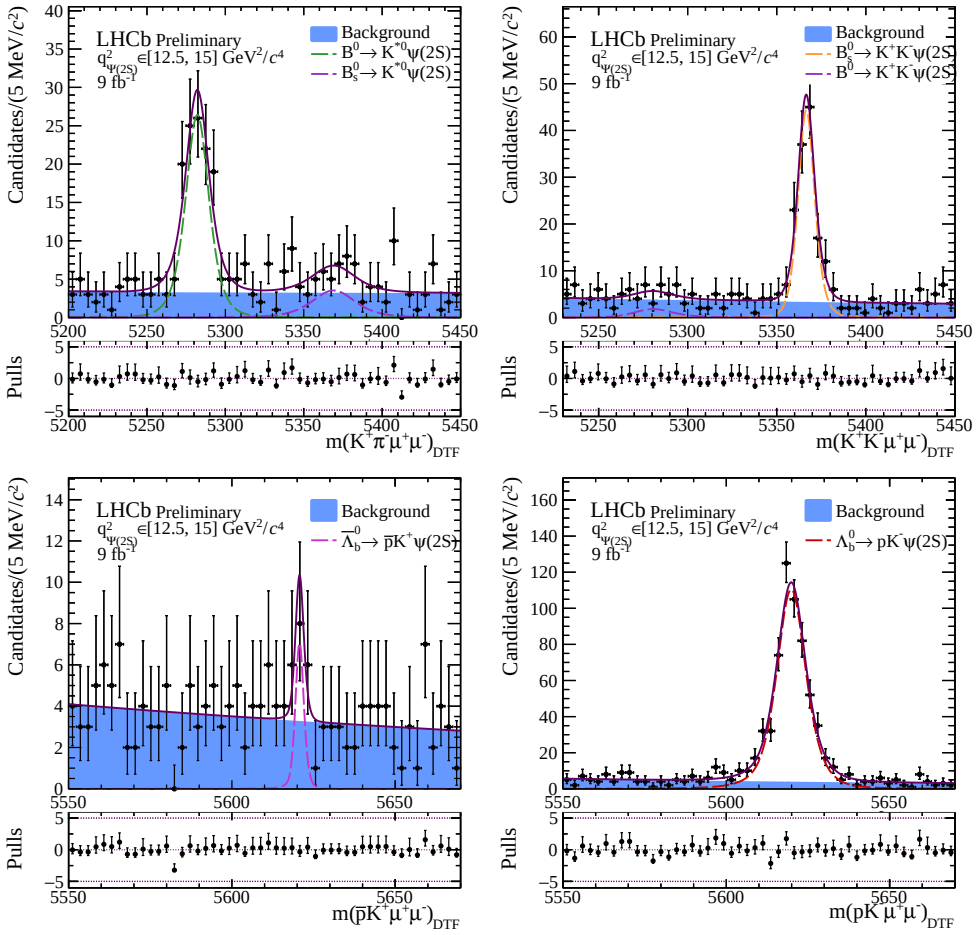

Figure E.2 – In order to estimate the relative fraction of $B^0_s \to K^+K^-\psi(2S)$ versus $B^0 \to K^{*0}\psi(2S)$ decays, and proton kaon swapped misidentification background versus signal events, they are estimated in data by fitting the background components in the Λ^0_b mass sidebands and by vetoing other backgrounds.

misidentification background is small in the plots. Its yield is of 11 ± 5 candidates, which is compatible with zero within three standard deviations. Since, in addition, the yield of the $B^0_s \to K^{*0}\psi(2S)$ decays is 103 ± 13, ten times bigger than the double misidentification background, the swapped misidentification background is neglected.

The contribution of $B^0_s \to K^{*0}\psi(2S)$ decays in comparison to the decay of the B^0 to the same final state is

$$r^{K^{*0}\psi(2S)}_{B^0_s/B^0} = \frac{N_{B^0_s \to K^{*0}\psi(2S)}}{N_{B^0 \to K^{*0}\psi(2S)}} = 0.09 \pm 0.08, \tag{E.3}$$

which is compatible with zero within two standard deviations and, thus, negligible. Similarly, the the ratio of $B^0 \to K^+K^-\psi(2S)$ decays with respect to the $B_s^0 \to K^+K^-\psi(2S)$ decays is

$$r_{B^0/B_s^0}^{K^+K^-\psi(2S)} = \frac{N_{B^0\to K^+K^-\psi(2S)}}{N_{B_s^0\to K^+K^-\psi(2S)}} = 0.25 \pm 0.10. \tag{E.4}$$

This fraction is neglected since it is compatible with zero within three standard deviations.

The efficiency of the different background vetos is calculated with the use of the simulation samples. The veto efficiency is in the $B^0 \to K^{*0}\psi(2S)$ simulation sample of $(40 \pm 5)\%$. This value is compatible within two standard deviations with the veto efficiency in the J/ψ mode and the efficiency of $B_s^0 \to K^+K^-\psi(2S)$ decays, which is $(49 \pm 3)\%$. It has to be noted that for the J/ψ and the $\psi(2S)$ mode, the veto efficiency of $B_s^0 \to K^+K^-\mu^+\mu^-$ decays is slightly higher than the one of $B^0 \to K^{*0}\mu^+\mu^-$ decays. The veto efficiency of the double misidentification background is $(82 \pm 3)\%$, which is the double of the b-meson efficiencies. Although the high veto efficiency, the background yield in data is small, which is another reason for neglecting this background.

Appendix F

Combinatorial background shape extraction

To evaluate the shape of the combinatorial background in bins of the BDT, the combinatorial background is fitted with an exponential in bins of the BDT. The J/ψ unconstrained and constrained $pK^-\mu^+\mu^-$ invariant mass fits in the different BDT intervals are shown in Fig. F.1 and F.2.

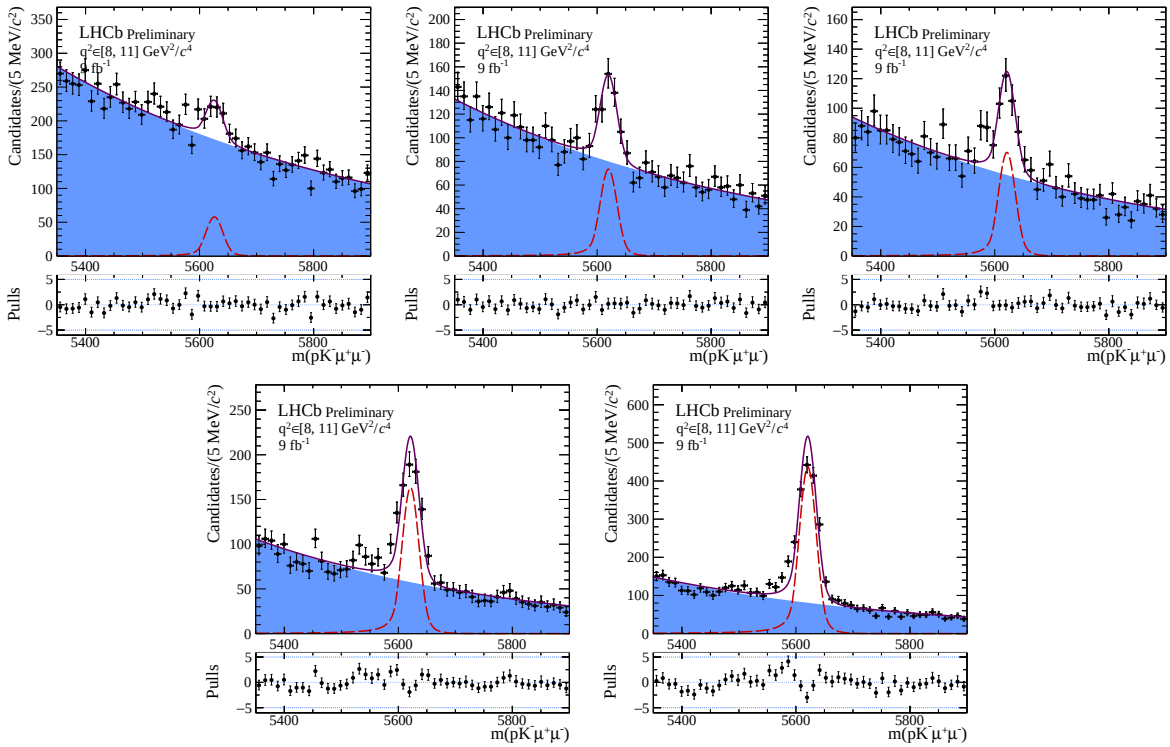

Figure F.1 – Combinatorial background shape in the J/ψ bin is obtained by fitting the $pK^-\mu^+\mu^-$ invariant mass in bins of the BDT, listed in Tab. 3.19.

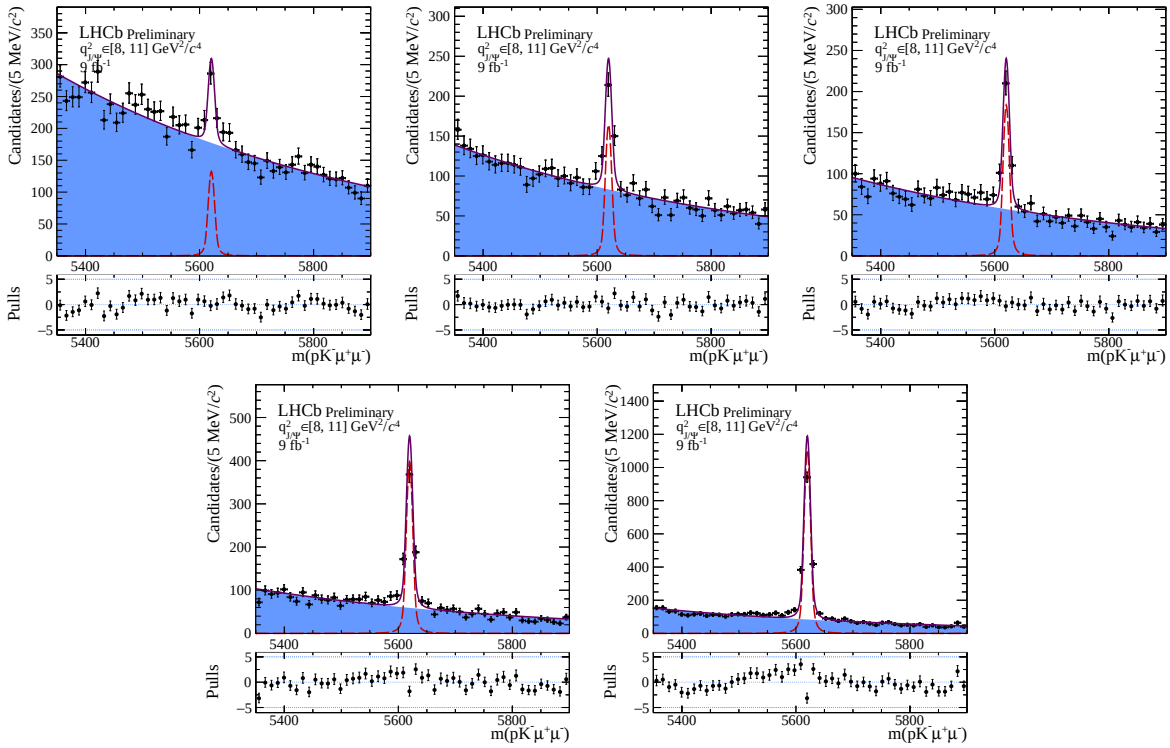

Figure F.2 – Combinatorial background shape in the J/ψ constrained bin by fitting the J/ψ constrained $pK^-\mu^+\mu^-$ invariant mass in each of the BDT bins.

The same fits are performed on the $pK^-\mu^+\mu^-$ invariant mass in the $\psi(2S)$ bin. They are presented in Fig. F.3

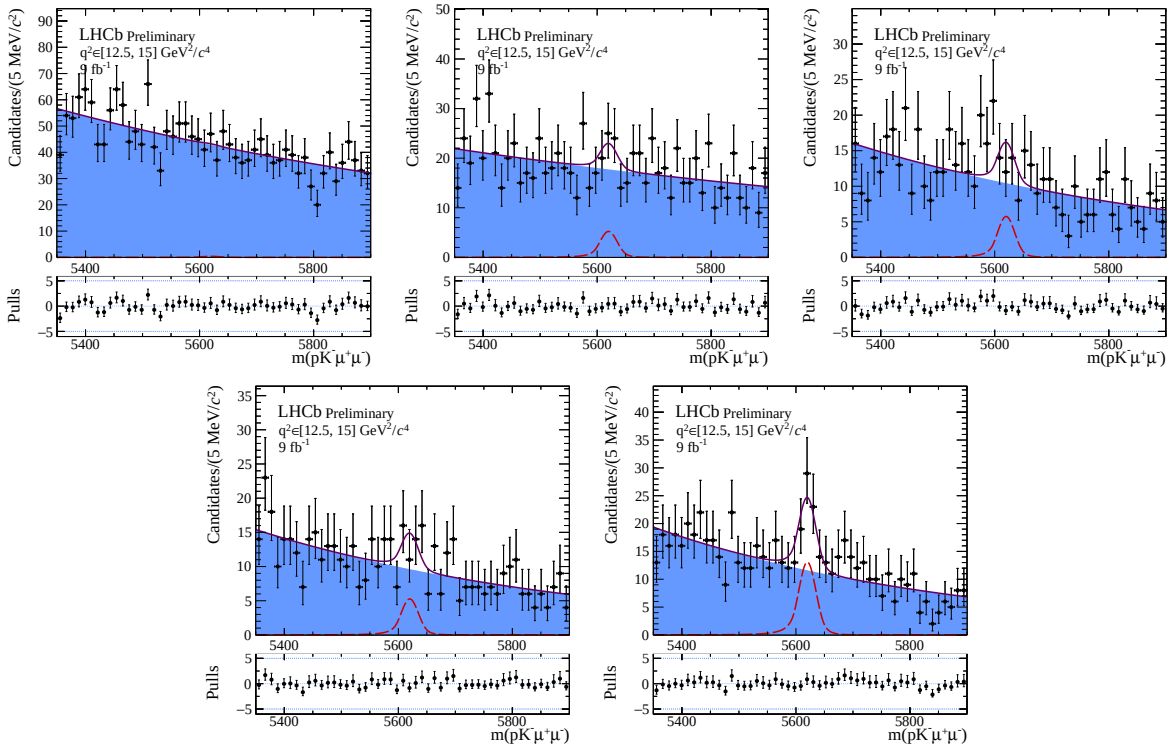

Figure F.3 – Combinatorial background shape in the $\psi(2S)$ bin is obtained by fitting the unconstrained $pK^-\mu^+\mu^-$ invariant mass in the $\psi(2S)$ bin. The fit results per each BDT bins are listed in Tab. 3.20.

Appendix G

Additionnal Λ_b^0 mass fits

G.1 Λ_b^0 mass fit in the full pK^- mass range

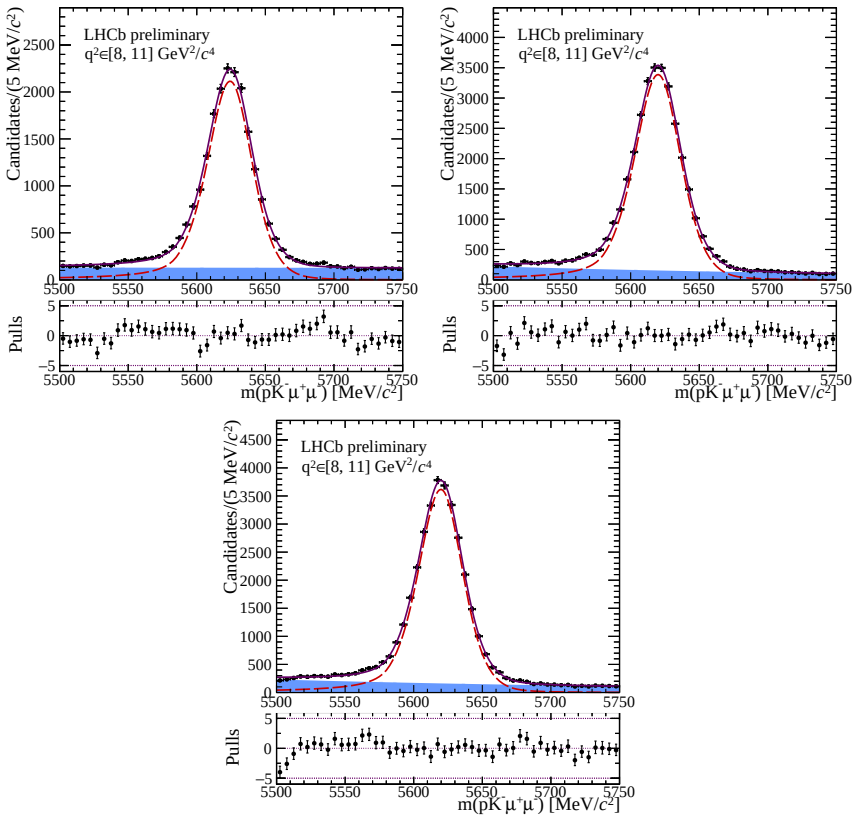

Figure G.1 – The data fit of the $pK^-\mu^+\mu^-$ invariant mass in the J/ψ bin for the years 2012, 2016 and 2017.

The mass fits of the $pK^-\mu^+\mu^-$ invariant mass in the J/ψ bin are needed to calculate the background yields. Those fits are performed on the 2012, 2016 and 2017 datasets in Fig. G.1 without any requirement on the pK^- invariant mass.

G.2 $pK^-\psi(2S)$ unconstrained fit in data without fixing the resolution

The $pK^-\psi(2S)$ unconstrained fit in data has been tested with a free-floating resolution. The corresponding fit is shown in Fig. G.2.

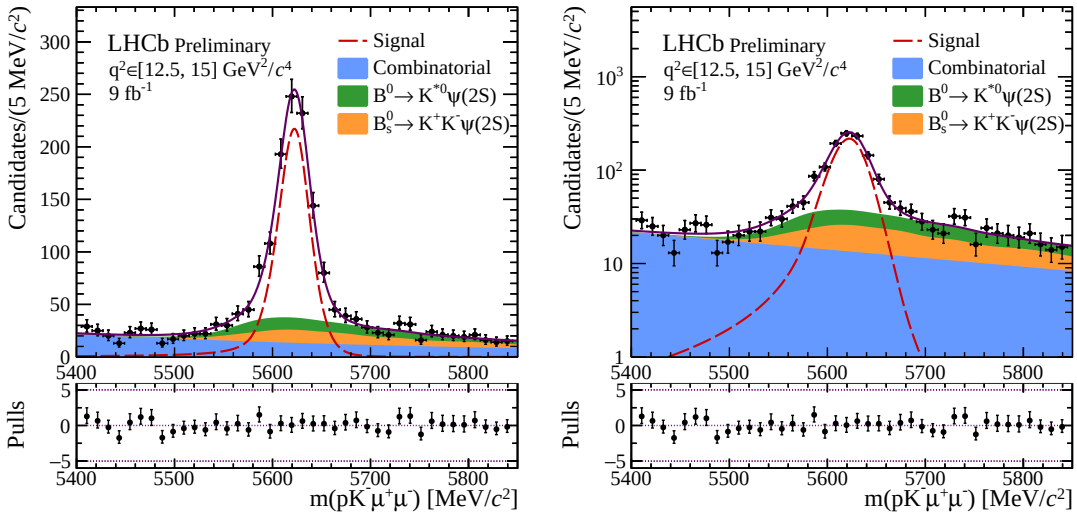

Figure G.2 – The $pK^-\mu^+\mu^-$ invariant mass fits are performed on data in the $\psi(2S)$ mode, letting the resolution free floating.

The corresponding parameters are listed in Tab. G.1. The resolution is supposed to

Parameter	$\psi(2S)$ unconstrained
μ [MeV/c^2]	5625.15 ± 0.86
σ [MeV/c^2]	20.18 ± 1.00
N_{sig}	909 ± 44
N_{combi}	717 ± 52
N_{B^0}	245 ± 28
τ	fixed to -0.00212

Table G.1 – The resulting parameter values and yields of the unconstrained $pK^-\psi(2S)$ invariant mass fit in data are listed in this table.

be smaller than in the J/ψ fit, due to the reduced phase-space. However, in this fit, the resolution takes a large value. This is the reason why the resolution was decided to be fixed in the nominal data fit, as shown in Ch. 3.5.5.

Appendix H

Correlation between the angles and the $pK^-\mu^+\mu^-$ invariant mass

The linear correlation between the $pK^-\mu^+\mu^-$ invariant mass and the angles are shown for the different q^2 bins in Fig. H.1, H.2 and H.3. The absolute value of the linear correlation coefficient between the $pK^-\mu^+\mu^-$ invariant mass and the angles is in all of the bins smaller or equal to 1%.

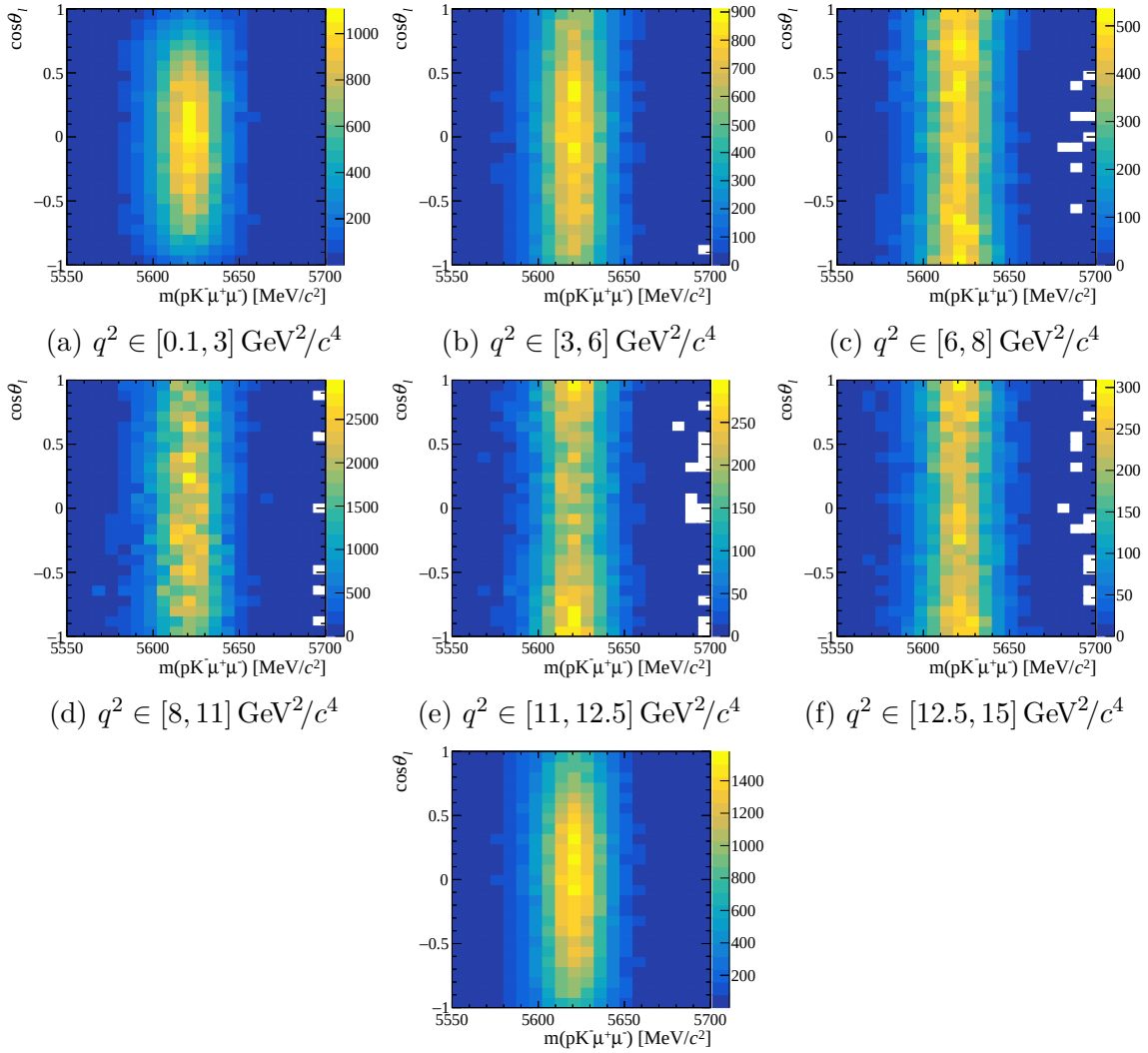

(a) $q^2 \in [0.1, 3]\,\mathrm{GeV}^2/c^4$ (b) $q^2 \in [3, 6]\,\mathrm{GeV}^2/c^4$ (c) $q^2 \in [6, 8]\,\mathrm{GeV}^2/c^4$

(d) $q^2 \in [8, 11]\,\mathrm{GeV}^2/c^4$ (e) $q^2 \in [11, 12.5]\,\mathrm{GeV}^2/c^4$ (f) $q^2 \in [12.5, 15]\,\mathrm{GeV}^2/c^4$

(g) $q^2 \in [1.1, 6]\,\mathrm{GeV}^2/c^4$

Figure H.1 – The two-dimensional distributions of the $pK^-\mu^+\mu^-$ invariant mass and $\cos\theta_\ell$ are plotted in the different q^2 bins.

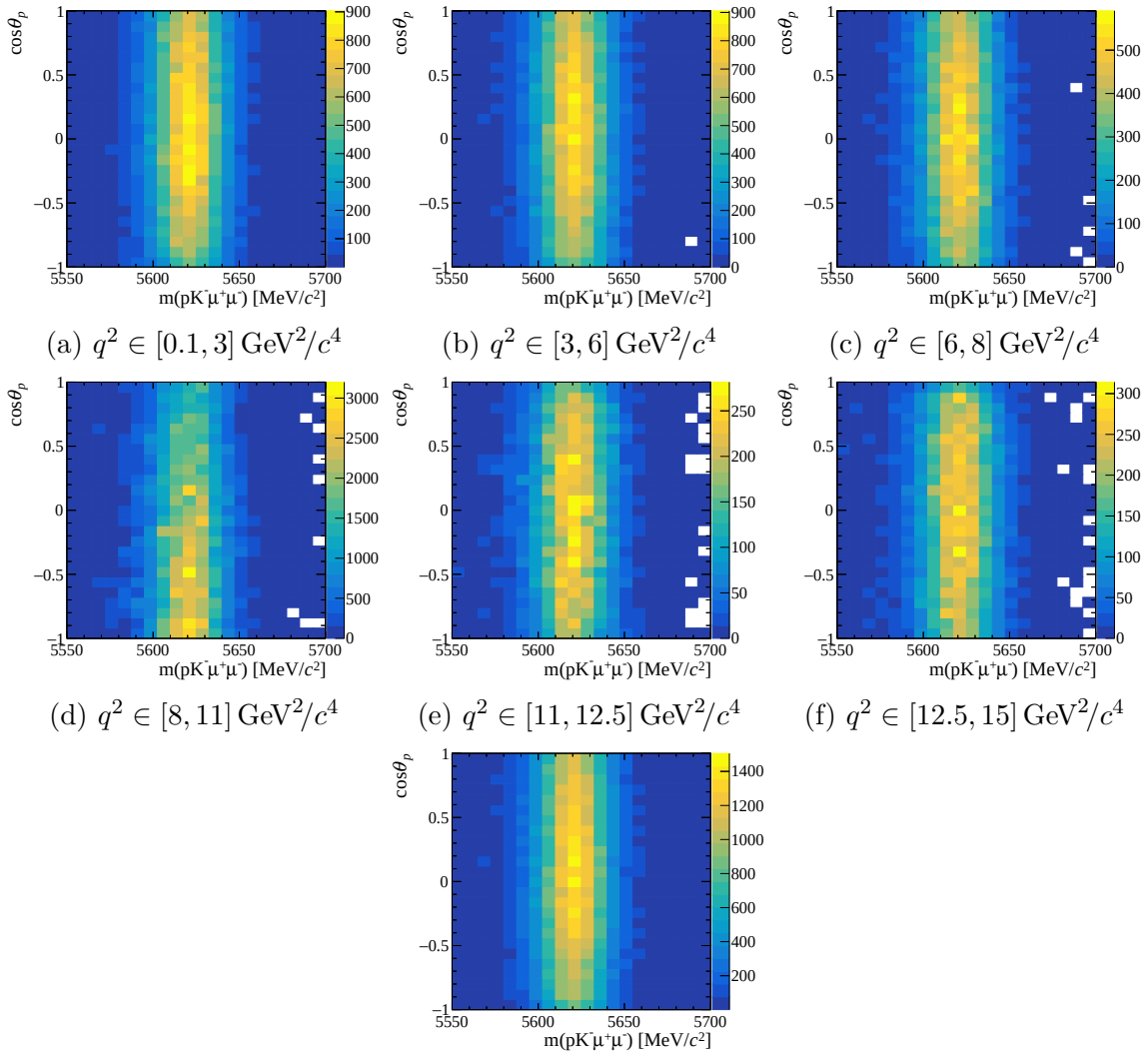

(a) $q^2 \in [0.1, 3]\,\mathrm{GeV}^2/c^4$ (b) $q^2 \in [3, 6]\,\mathrm{GeV}^2/c^4$ (c) $q^2 \in [6, 8]\,\mathrm{GeV}^2/c^4$

(d) $q^2 \in [8, 11]\,\mathrm{GeV}^2/c^4$ (e) $q^2 \in [11, 12.5]\,\mathrm{GeV}^2/c^4$ (f) $q^2 \in [12.5, 15]\,\mathrm{GeV}^2/c^4$

(g) $q^2 \in [1.1, 6]\,\mathrm{GeV}^2/c^4$

Figure H.2 – The two-dimensional distributions of the $pK^-\mu^+\mu^-$ invariant mass and $\cos\theta_p$ are plotted in the different q^2 bins.

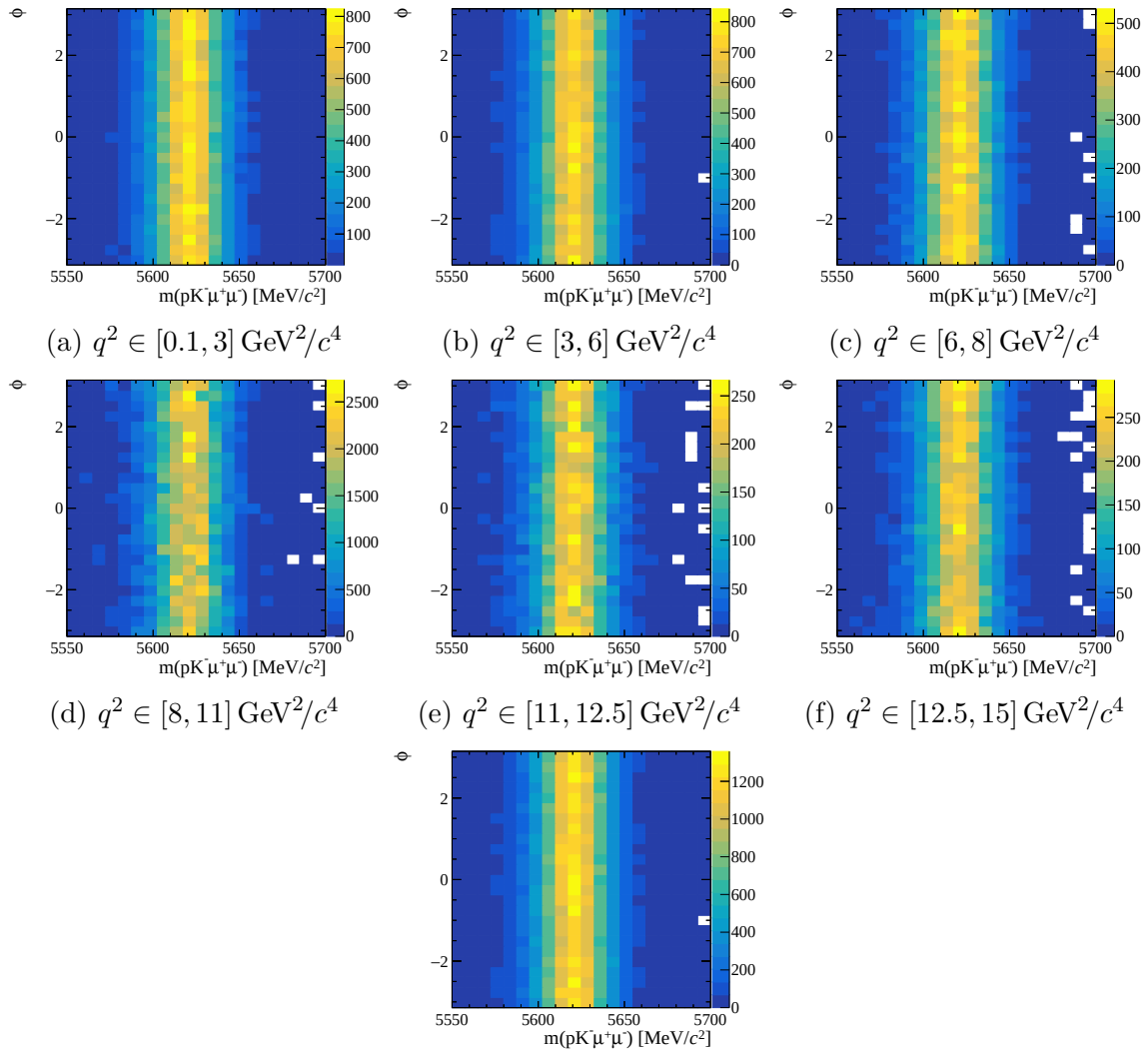

(a) $q^2 \in [0.1, 3]\,\mathrm{GeV}^2/c^4$ (b) $q^2 \in [3, 6]\,\mathrm{GeV}^2/c^4$ (c) $q^2 \in [6, 8]\,\mathrm{GeV}^2/c^4$

(d) $q^2 \in [8, 11]\,\mathrm{GeV}^2/c^4$ (e) $q^2 \in [11, 12.5]\,\mathrm{GeV}^2/c^4$ (f) $q^2 \in [12.5, 15]\,\mathrm{GeV}^2/c^4$

(g) $q^2 \in [1.1, 6]\,\mathrm{GeV}^2/c^4$

Figure H.3 – The two-dimensional distributions of the $pK^-\mu^+\mu^-$ invariant mass and ϕ are plotted in the different q^2 bins.

Appendix I

Angle definition in the helicity frame

The decay angles to describe the $\Lambda_b^0 \to pK^-\mu^+\mu^-$ decay are defined in the helicity basis, following the definition in Ref. [65, 109, 111]. A sketch of the angle definition is shown in Fig. 1.9.

The angle θ_p is defined as the angle between proton direction in the Λ^* rest frame and the flight direction of the Λ^*-baryon in the Λ_b^0 rest frame. The angle θ_ℓ is measured from the μ^+ flight direction in the di-lepton rest frame and the flight direction of the di-lepton pair in the Λ_b^0 rest frame.

For calculating the angle in-between the plane spanned by the final state hadrons and the one defined by the four vectors of the two muons, the normal vectors of the planes are calculated. The cross product of the Λ^* direction in the Λ_b^0 rest frame and the proton unit vector in the Λ^* rest frames defines the normal vector of the pK^- plane. The normal vector of the dilepton plane is calculated accordingly. The scalar product of the two normal vectors are called the cosinus of the ϕ angle. The cross product of the normal vector of the muon plane and the pK^- plane gives the sinus of the ϕ angle. Therefore, the ambiguity can be solved and the ϕ angle set to $+\arccos\cos\phi$ for $\sin\phi > 0$ and in the contrary to $\phi := -\arccos\cos\phi$.

Appendix J

Simplification of the full $\Lambda_b^0 \to \Lambda(1520)\ell^+\ell^-$ decay width by ϕ integration

The differential decay rate of the decay through a Λ^{*0}-resonance with spin $J = \frac{3}{2}$ has been calculated in Ref. [5] and is presented in equation 1.53.

$$\begin{aligned}
&\frac{8\pi}{3}\frac{d^4\Gamma}{dq^2 d\cos\theta_\ell d\cos\theta_p d\phi} \\
&\quad = \cos^2\theta_p\left(L_{1c}\cos\theta_\ell + L_{1cc}\cos^2\theta_\ell + L_{1ss}\sin^2\theta_\ell\right) \\
&\qquad + \sin^2\theta_p\left(L_{2c}\cos\theta_\ell + L_{2cc}\cos^2\theta_\ell + L_{2ss}\sin^2\theta_\ell\right) \\
&\qquad + \sin^2\theta_p\left(L_{3ss}\sin^2\theta_\ell\cos^2\phi + L_{4ss}\sin^2\theta_\ell\sin\phi\cos\phi\right) \\
&\qquad + \sin\theta_p\cos\theta_p\cos\phi(L_{5s}\sin\theta_\ell + L_{5sc}\sin\theta_\ell\cos\theta_\ell) \\
&\qquad + \sin\theta_p\cos\theta_p\sin\phi(L_{6s}\sin\theta_\ell + L_{6sc}\sin\theta_\ell\cos\theta_\ell).
\end{aligned} \tag{J.1}$$

It can be described with the angles $(\theta_\ell, \theta_p, \phi)$ and the dilepton invariant mass q^2. After the integration, the equation simplifies to

$$\begin{aligned}
&\frac{8\pi}{3}\frac{d^4\Gamma}{dq^2 d\cos\theta_\ell d\cos\theta_p} \\
&\quad = \pi\cos^2\theta_p\left(2L_{1c}\cos\theta_\ell + 2L_{1cc}\cos^2\theta_\ell + 2L_{1ss}\sin^2\theta_\ell\right) \\
&\qquad + \pi\sin^2\theta_p\left(2L_{2c}\cos\theta_\ell + 2L_{2cc}\cos^2\theta_\ell + (2L_{2ss} + L_{3ss})\sin^2\theta_\ell\right).
\end{aligned} \tag{J.2}$$

By defining $L_{23} := 2L_{2ss} + L_{3ss}$ and using the relation $\sin^2\theta = 1 - \cos^2\theta$, the probablitiy density function gets

$$\frac{8\pi}{3}\frac{d^4\Gamma}{dq^2 d\cos\theta_\ell d\cos\theta_p}$$
$$= \pi\left(L_{23} + 2L_{1c}\cos\theta_\ell + (2L_{2cc} - L_{23})\cos^2\theta_\ell\right)$$
$$+\pi\cos^2\theta_p\,(2L_{1ss} - L_{23} + (2L_{1c} - 2L_{2c})\cos\theta_\ell)$$
$$+\pi\cos^2\theta_p\,(2L_{1cc} - 2L_{1ss} - 2L_{2cc} + L_{23})\cos^2\theta_\ell. \tag{J.3}$$

The angular coefficients L_i show linear dependence of each other, which can be expressed as :

$$L_{2c} = \frac{1}{4}(L_{1c} + \epsilon_3) \tag{J.4}$$
$$\epsilon_3 := -6\mathcal{B}_{\Lambda^{*0}}(\mathrm{Re}(B^L_{\perp 1}B^{L*}_{\parallel 1}) - (L \leftrightarrow R))$$
$$L_{2cc} = \frac{1}{4}(L_{1cc} + \epsilon_1) \tag{J.5}$$
$$\epsilon_1 := 3\mathcal{B}_{\Lambda^{*0}}(|B^L_{\parallel 1}|^2 + |B^L_{\perp 1}|^2 + (L \leftrightarrow R))$$
$$L_{3ss} = \frac{\sqrt{3}}{2}\mathcal{B}_{\Lambda^{*0}}\left(\mathrm{Re}(B^L_{\parallel 1}A^{L*}_{\parallel 1}) - \mathrm{Re}(B^L_{\parallel 1}A^{L*}_{\parallel 1}) + (L \leftrightarrow R)\right) \tag{J.6}$$
$$L_{2ss} = \frac{1}{8}(2L_{1ss} + \epsilon_1 - 4L_{3ss}) \tag{J.7}$$

The angular coefficient ϵ_1 appears in equation J.7 and in J.5. Rearranging both equations and setting ϵ_1 equal, one gets the following relation

$$L_{1cc} - 2L_{1ss} - 4L_{2cc} + 4L_{23} = 0. \tag{J.8}$$

The expression $L_{23} := 2L_{2ss} + L_{3ss}$ is used for further simplify the equation.

Fitting a distribution is better by using a normalised PDF. For this, after integrating out the angles the angular PDF $\frac{d\Gamma}{dq^2}$, which is written explicitly in equation 1.54, has to be equal to 1. The second important equation can be expressed as

$$L_{1cc} + 2L_{1ss} + 2L_{2cc} + 2L_{23} = 3. \tag{J.9}$$

The value for the forward-backward asymmetry can additionally be simplified by using the normalisation condition.

$$A^\ell_{FB} = \frac{1}{2}(L_{1c} + 2L_{2c}) = \frac{1}{4}(3L_{1c} + \epsilon_3) \tag{J.10}$$

Using the expressions in J.8 and J.9, two angular coefficients can be expressed by the

other ones. In this case, L_{2cc} and L_{23} is expressed as seen in equation J.11 - J.12.

$$L_{2cc} = \frac{1}{8}(6 - 6L_{1ss} - L_{1cc}) \tag{J.11}$$

$$L_{23} = \frac{1}{8}(6 - 2L_{1ss} - 3L_{1cc}) \tag{J.12}$$

Using this re-expression of the angular coefficients, the over ϕ integrated PDF can be simplified to the one shown in equation J.3. This PDF in only dependent on the observables L_{1cc}, L_{1ss}, A_{FB}^{ℓ} and ϵ_3.

$$\begin{aligned}
&\frac{8\pi}{3}\frac{d^4\Gamma}{dq^2 d\cos\theta_\ell d\cos\theta_p} \\
&\quad = \pi\left(\frac{1}{8}(6 - 2L_{1ss} - L_{1cc}) + \frac{1}{3}(2A_{FB}^{\ell} + \epsilon_3)\cos\theta_\ell\right) \\
&\qquad + \frac{\pi}{8}(6 - 10L_{1ss} + L_{1cc})\cos^2\theta_\ell \\
&\qquad + \pi\left(\frac{3}{8}(6L_{1ss} + L_{1cc} - 2) + (2A_{FB}^{\ell} - \epsilon_3)\cos\theta_\ell\right)\cos^2\theta_p \\
&\qquad + \frac{3\pi}{8}(5L_{1cc} - 2L_{1ss} - 2)\cos^2\theta_\ell\cos^2\theta_p
\end{aligned} \tag{J.13}$$

Since in LHCb, we are only measuring the *CP*-averaged differential decay rate, the angular coefficients, become the *CP*-averaged observables S_{1cc}, S_{1ss} and A_{FB}^{ℓ}, as shown in Eq. 4.14.

Appendix K

The angular fit of dedicated simulation samples

K.1 Angular fit with the fit model 1

The fit projections of the angular fit with the fit model 1 in the remaining q^2 bins are shown in Fig. K.1 - K.4.

K.2 Angular fit with the fit model 2

The fit projections of the angular fit with the fit model 2 in the remaining q^2 bins are shown in Fig. K.5 - K.8.

K.3 Angular fit with the fit model 3

The fit projections of the angular fit with the fit model 3 in the remaining q^2 bins are shown in Fig. K.9 - K.12.

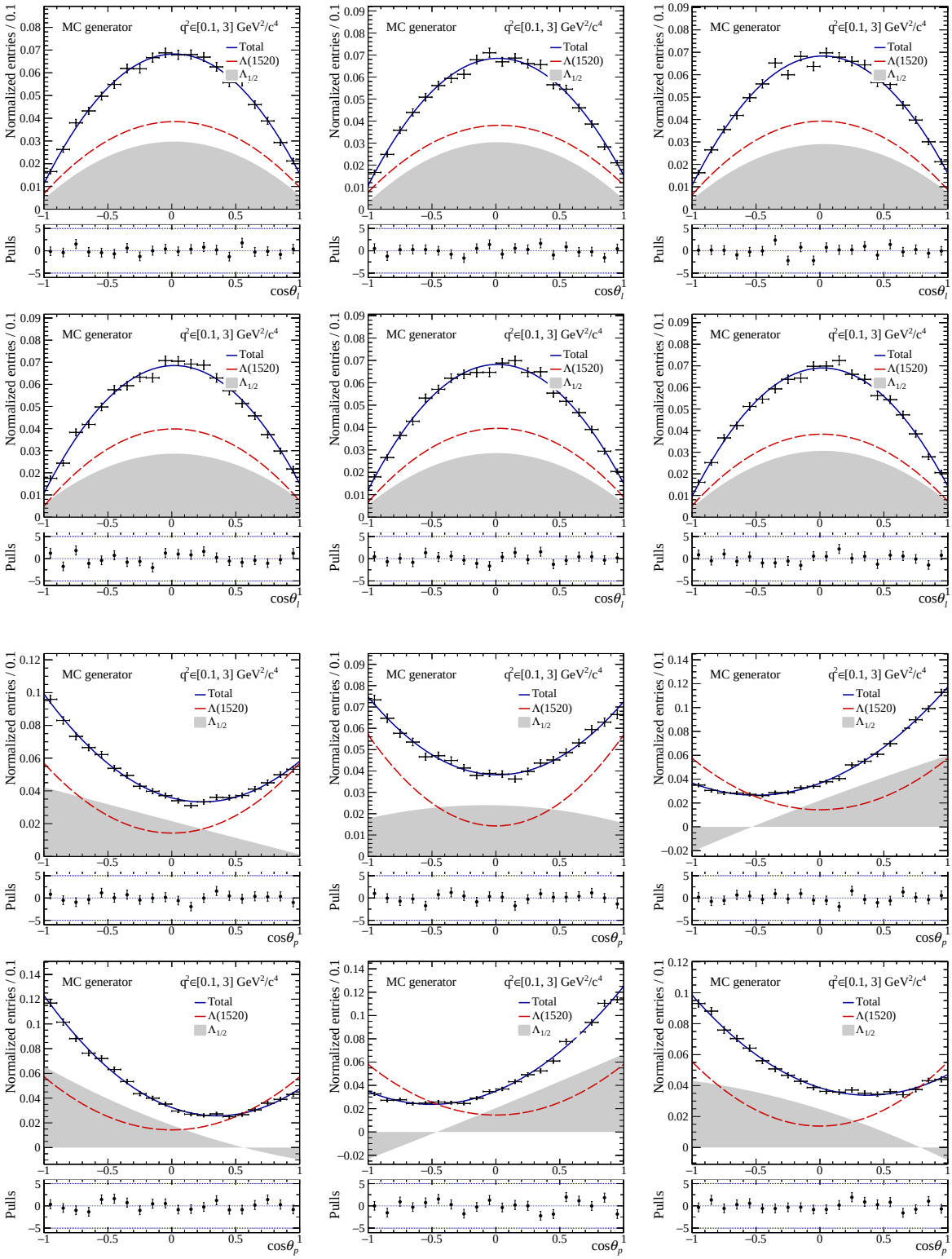

Figure K.1 – The $\cos\theta_\ell$ (1st and 2nd row) and $\cos\theta_p$ (3rd and 4th row) projections of the angular fit with model 1 to the dedicated MC samples with the interference hypotheses 0 (top left) to 5 (bottom right) in the $q^2 \in [0.1, 3]\,\mathrm{GeV}^2/c^4$ bin.

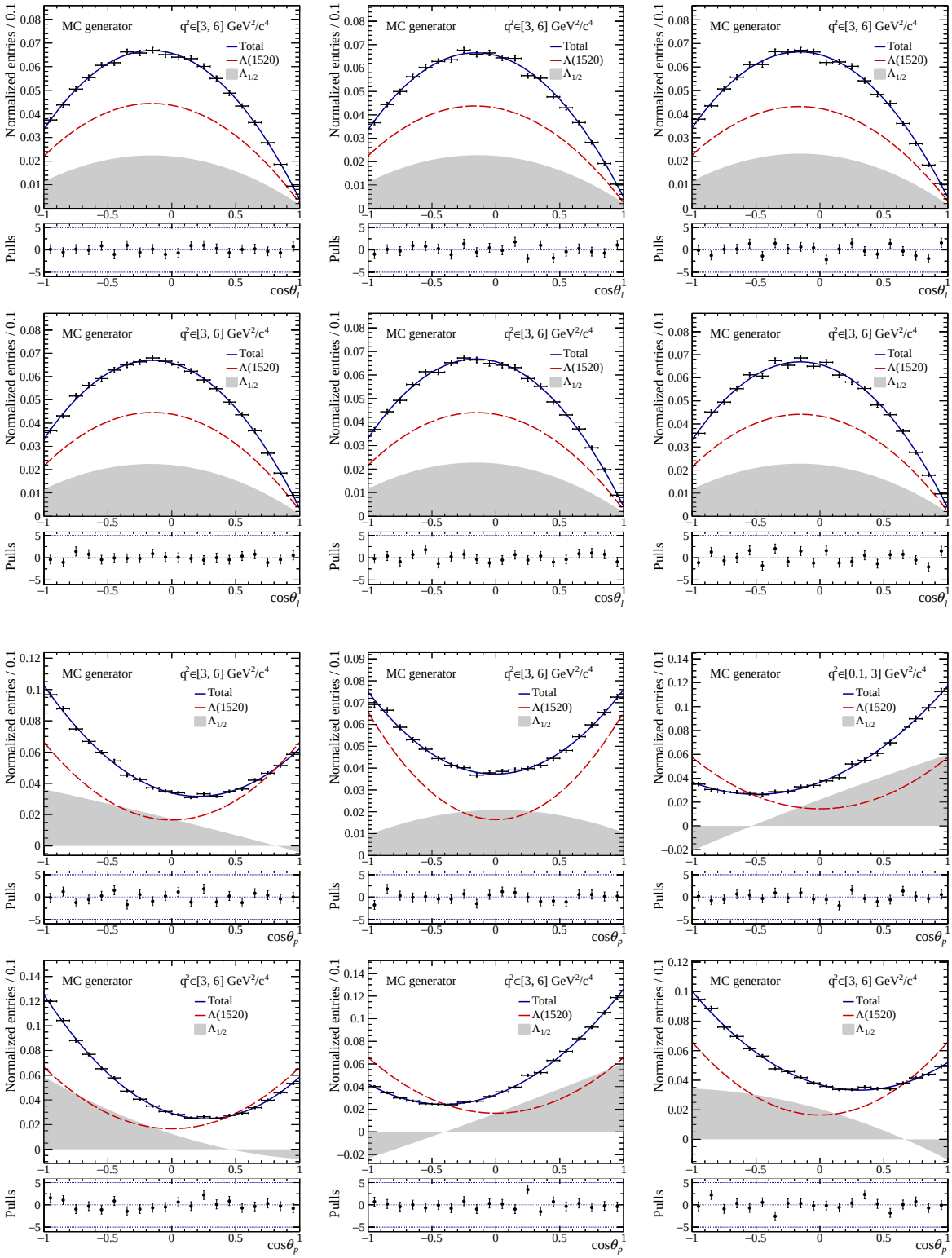

Figure K.2 – The $\cos\theta_\ell$ (1$^{\text{st}}$ and 2$^{\text{nd}}$ row) and $\cos\theta_p$ (3$^{\text{rd}}$ and 4$^{\text{th}}$ row) projections of the angular fit with model 1 to the dedicated MC samples with the interference hypotheses 0 (top left) to 5 (bottom right) in the $q^2 \in [3, 6]\,\text{GeV}^2/c^4$ bin.

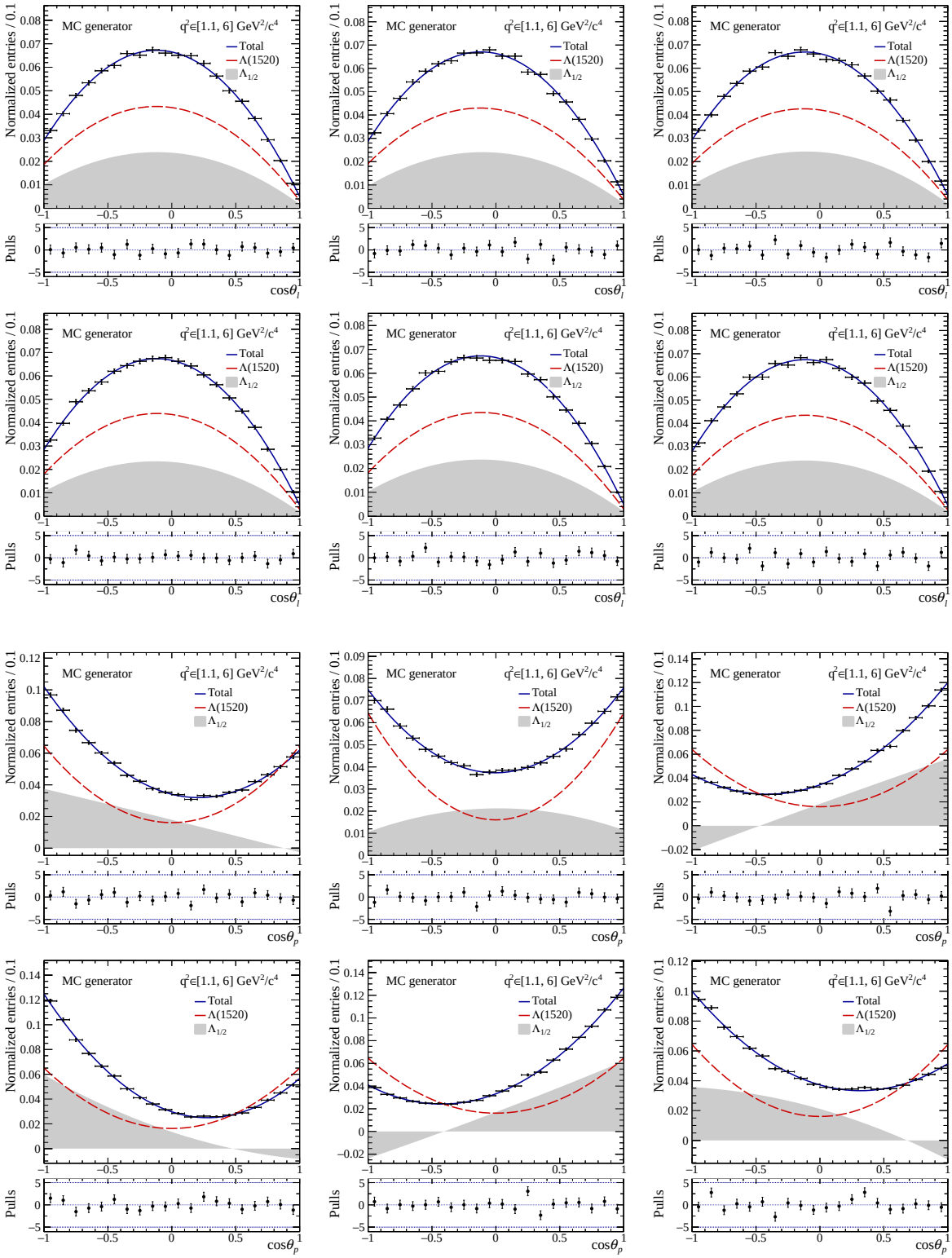

Figure K.3 – The $\cos\theta_\ell$ (1st and 2nd row) and $\cos\theta_p$ (3rd and 4th row) projections of the angular fit with model 1 to the dedicated MC samples with the interference hypotheses 0 (top left) to 5 (bottom right) in the $q^2 \in [1.1, 6]\,\mathrm{GeV}^2/c^4$ bin.

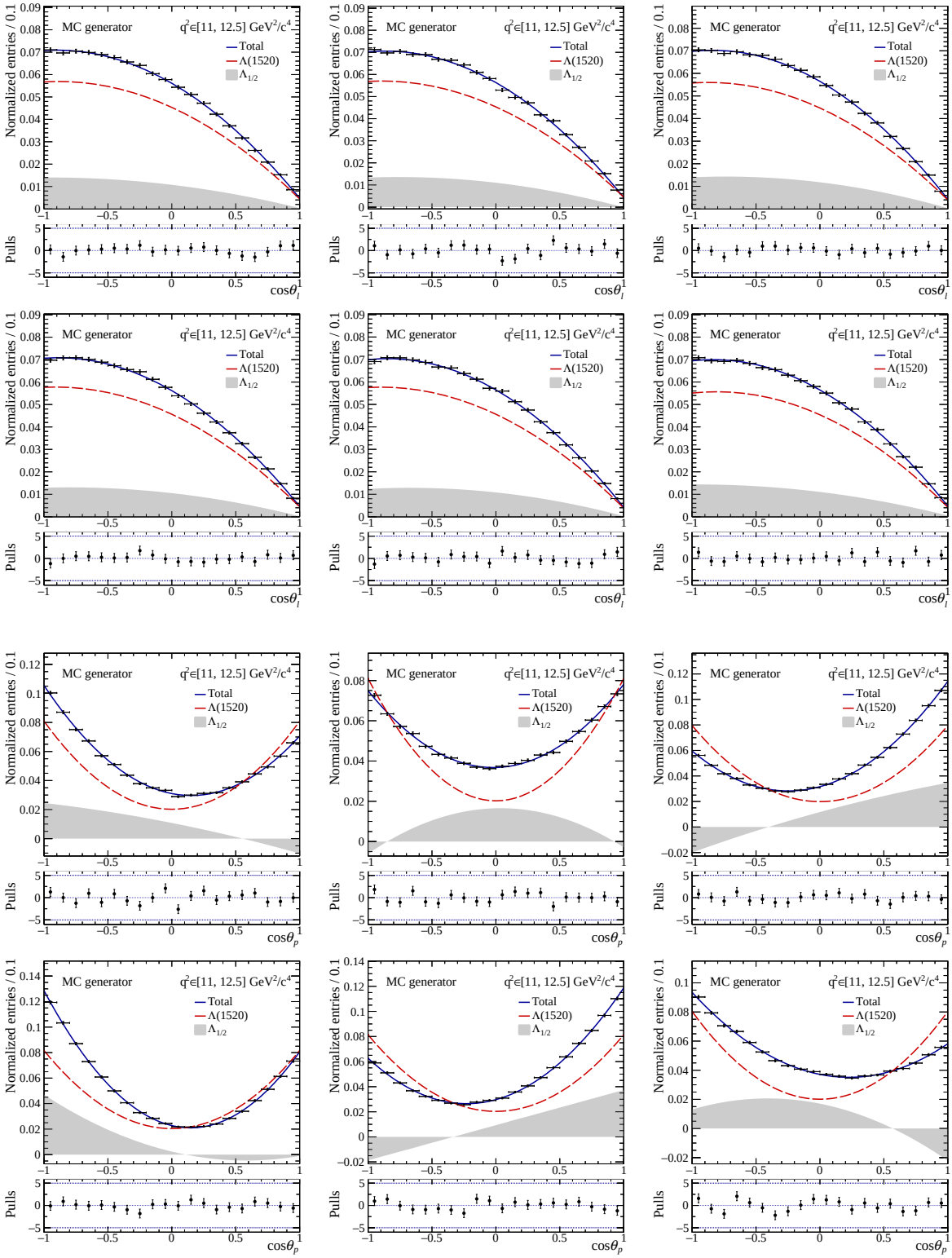

Figure K.4 – The $\cos\theta_\ell$ (1$^{\text{st}}$ and 2$^{\text{nd}}$ row) and $\cos\theta_p$ (3$^{\text{rd}}$ and 4$^{\text{th}}$ row) projections of the angular fit with model 1 to the dedicated MC samples with the interference hypotheses 0 (top left) to 5 (bottom right) in the $q^2 \in [11, 12.5]\,\text{GeV}^2/c^4$ bin.

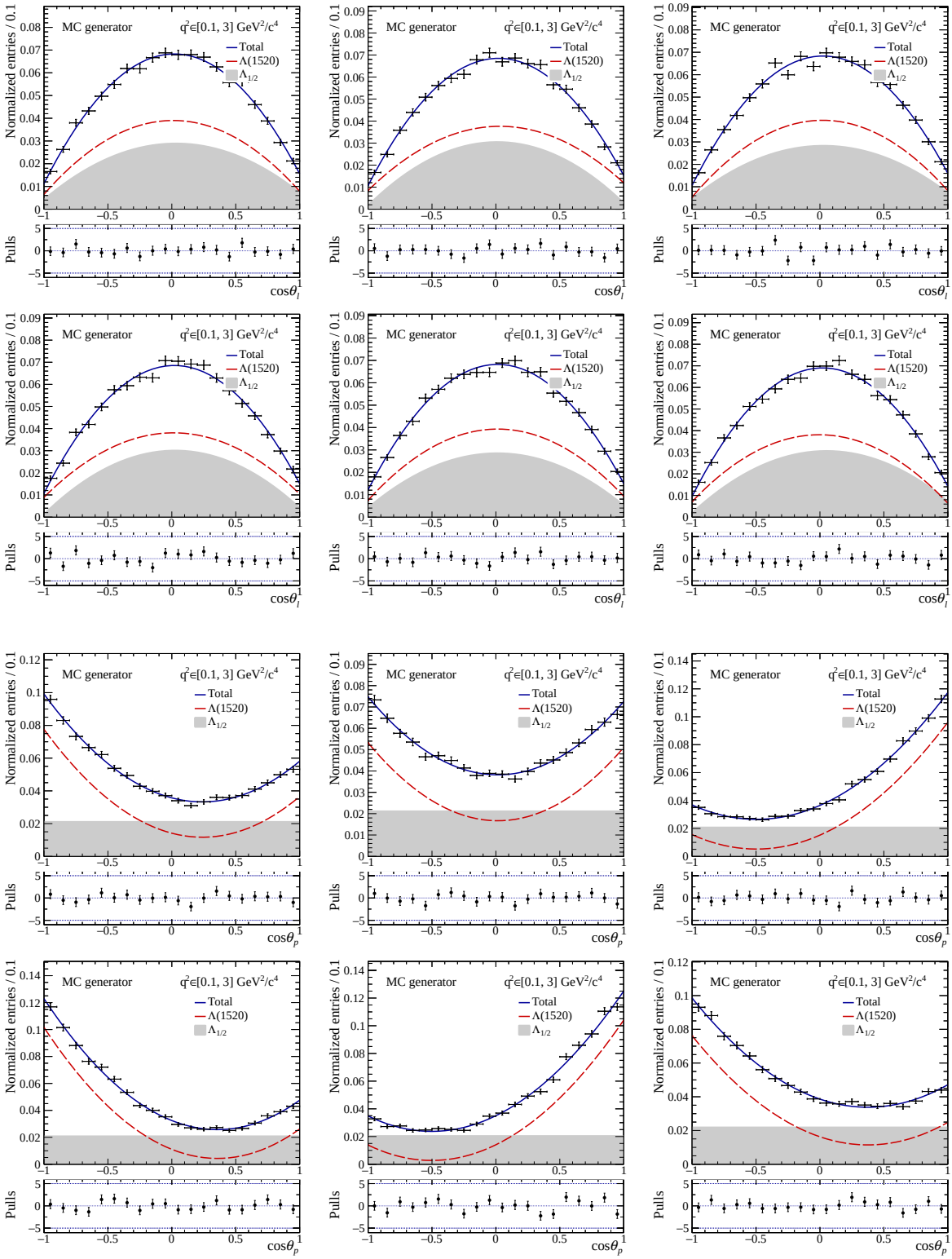

Figure K.5 – The $\cos\theta_\ell$ (1st and 2nd row) and $\cos\theta_p$ (3rd and 4th row) projections of the angular fit with model 2 to the dedicated MC samples with the interference hypotheses 0 (top left) to 5 (bottom right) in the $q^2 \in [0.1, 3]\,\mathrm{GeV}^2/c^4$ bin.

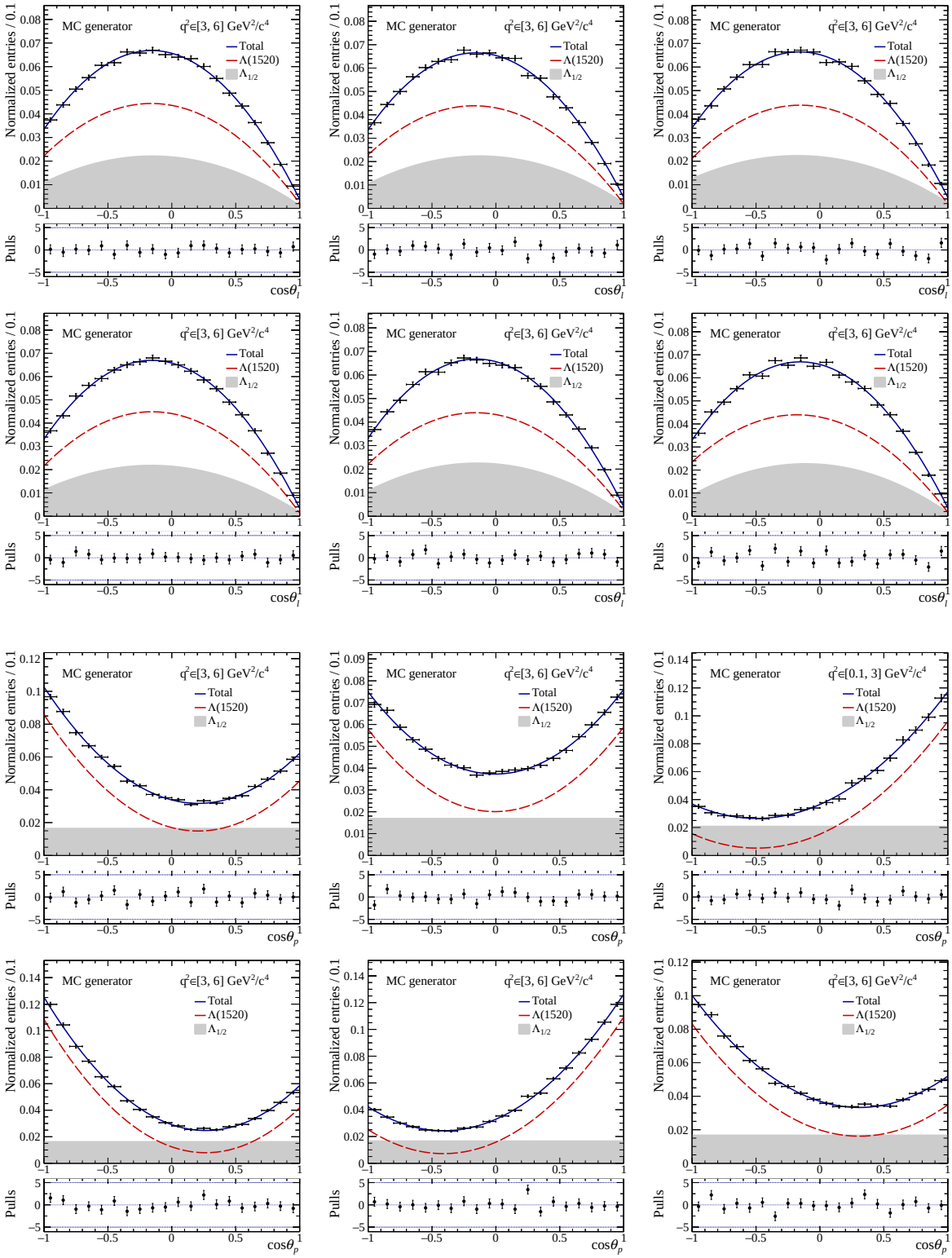

Figure K.6 – The $\cos\theta_\ell$ (1st and 2nd row) and $\cos\theta_p$ (3rd and 4th row) projections of the angular fit with model 2 to the dedicated MC samples with the interference hypotheses 0 (top left) to 5 (bottom right) in the $q^2 \in [3, 6]\,\mathrm{GeV}^2/c^4$ bin.

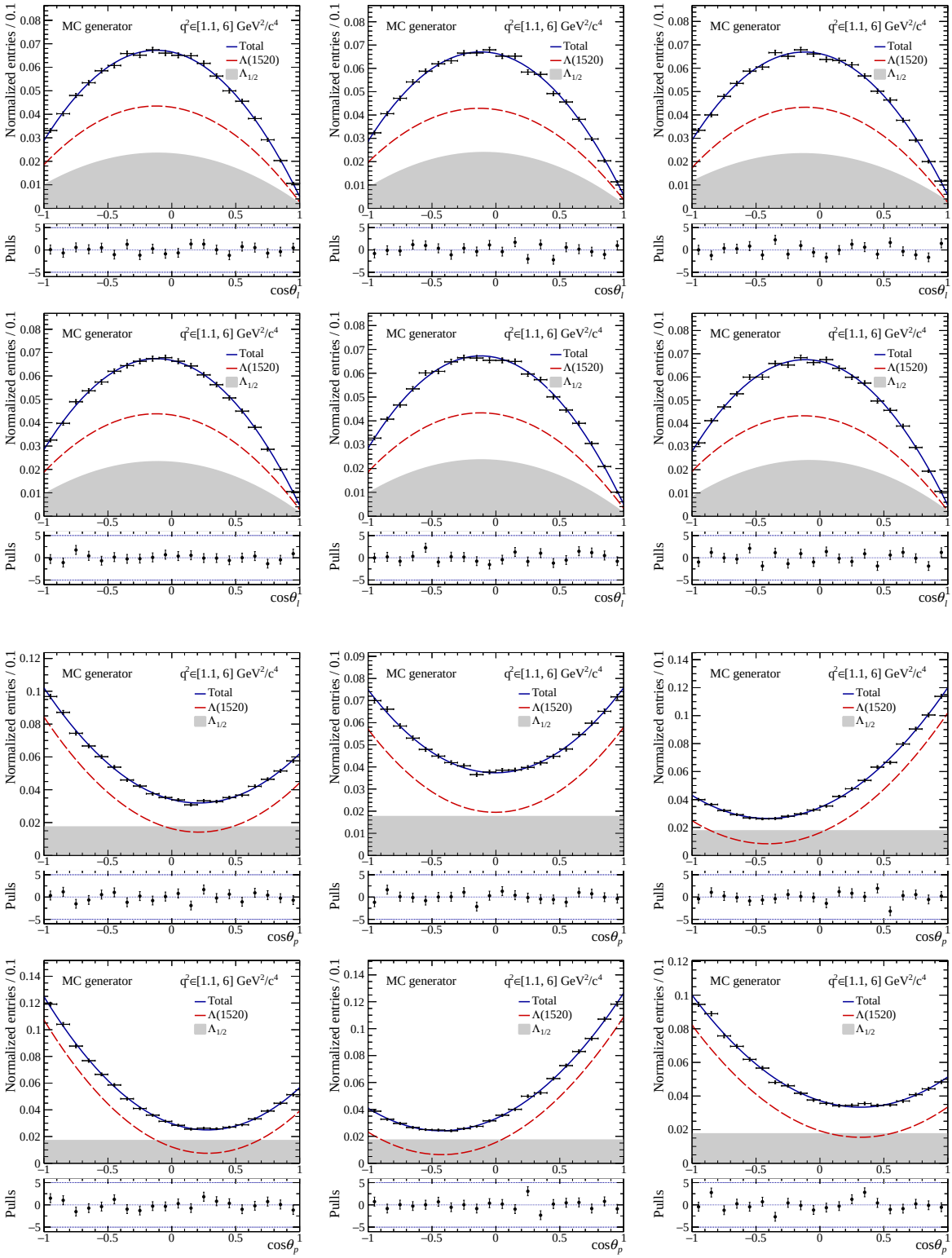

Figure K.7 – The $\cos\theta_\ell$ (1st and 2nd row) and $\cos\theta_p$ (3rd and 4th row) projections of the angular fit with model 2 to the dedicated MC samples with the interference hypotheses 0 (top left) to 5 (bottom right) in the $q^2 \in [1.1, 6]\,\mathrm{GeV}^2/c^4$ bin.

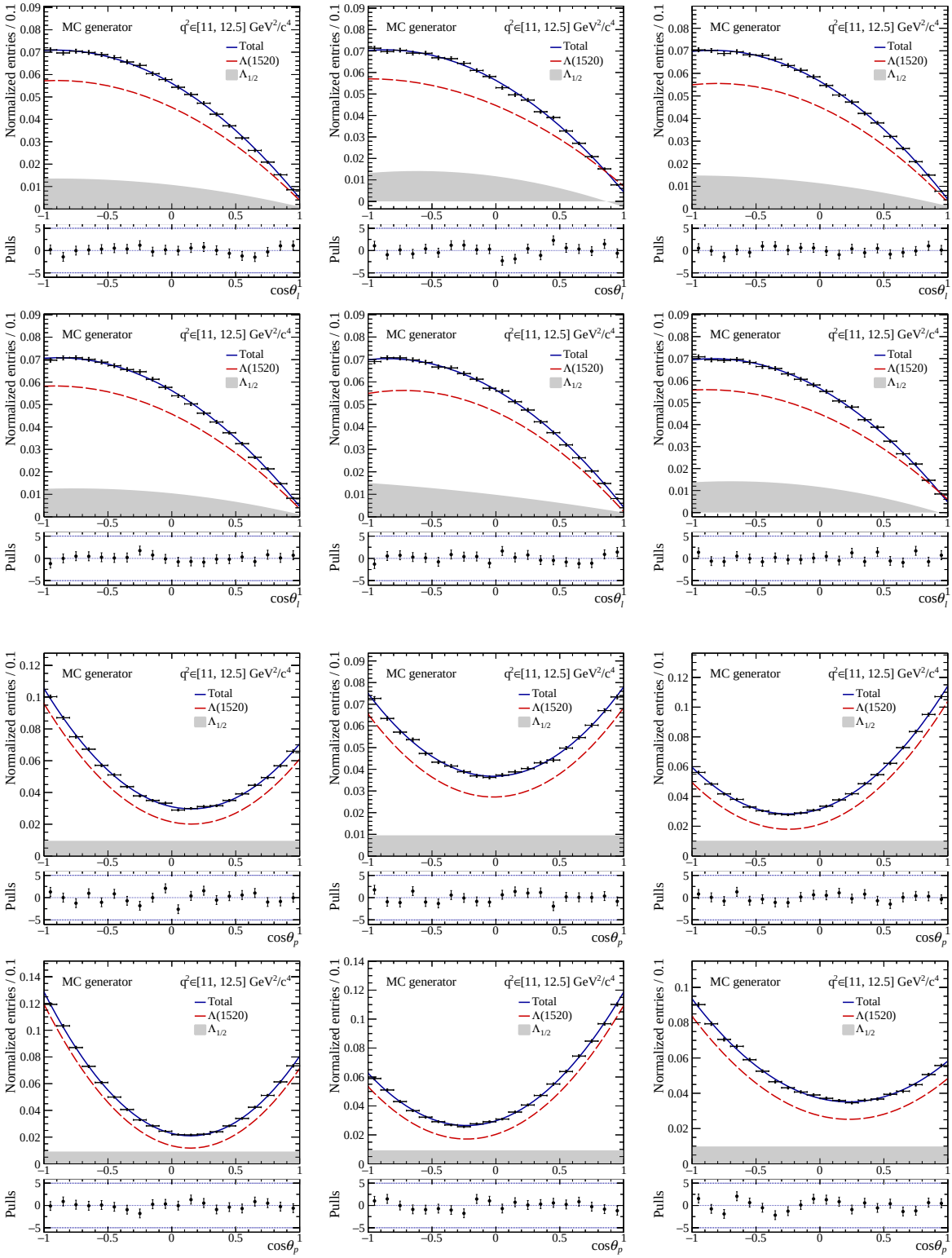

Figure K.8 – The $\cos\theta_\ell$ (1$^{\text{st}}$ and 2$^{\text{nd}}$ row) and $\cos\theta_p$ (3$^{\text{rd}}$ and 4$^{\text{th}}$ row) projections of the angular fit with model 2 to the dedicated MC samples with the interference hypotheses 0 (top left) to 5 (bottom right) in the $q^2 \in [11, 12.5]\,\text{GeV}^2/c^4$ bin.

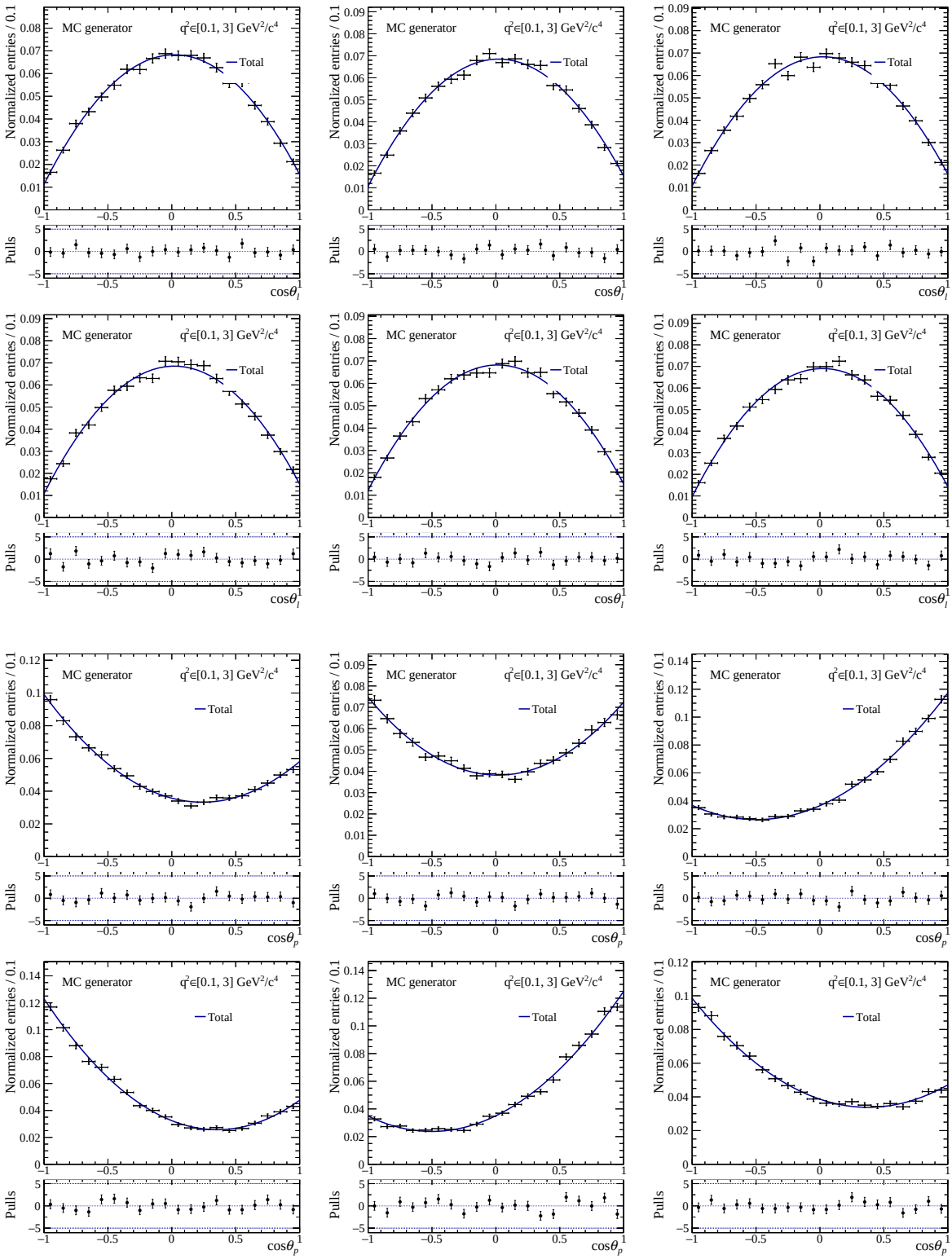

Figure K.9 – The $\cos\theta_\ell$ (1st and 2nd row) and $\cos\theta_p$ (3rd and 4th row) projections of the angular fit with model 3 to the dedicated MC samples with the interference hypotheses 0 (top left) to 5 (bottom right) in the $q^2 \in [0.1, 3]\,\mathrm{GeV}^2/c^4$ bin.

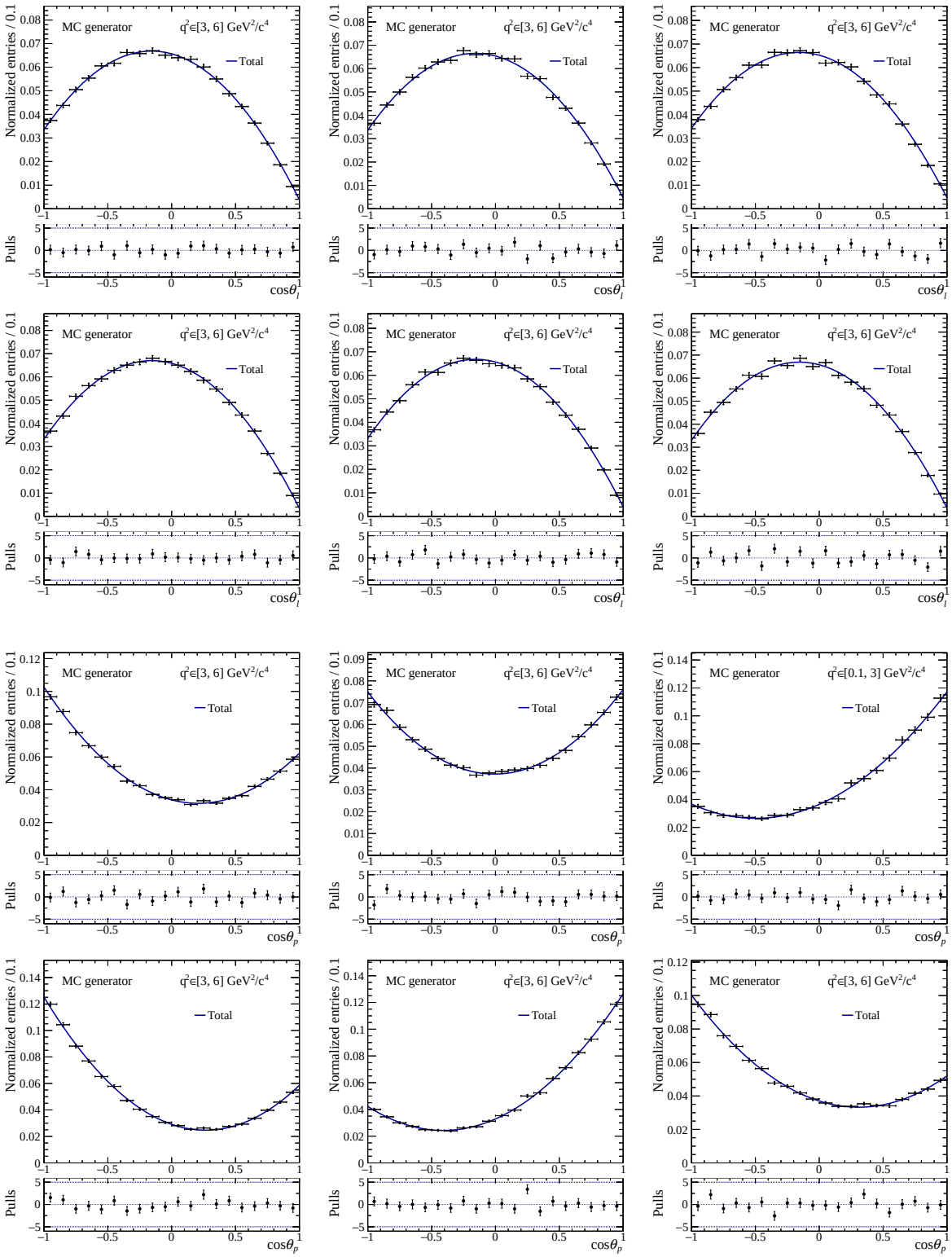

Figure K.10 – The $\cos\theta_\ell$ (1st and 2nd row) and $\cos\theta_p$ (3rd and 4th row) projections of the angular fit with model 3 to the dedicated MC samples with the interference hypotheses 0 (top left) to 5 (bottom right) in the $q^2 \in [3, 6]\,\mathrm{GeV}^2/c^4$ bin.

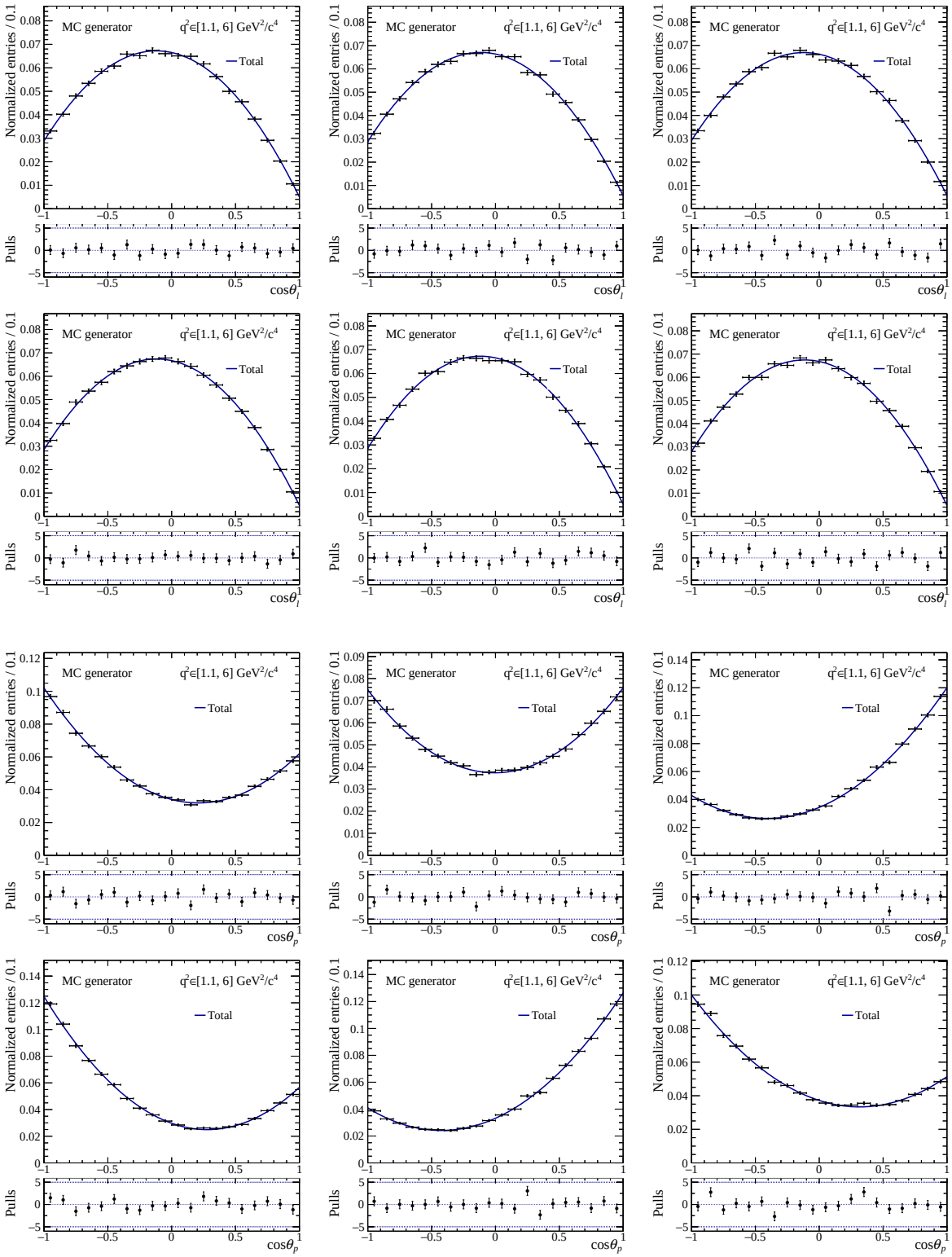

Figure K.11 – The $\cos\theta_\ell$ (1st and 2nd row) and $\cos\theta_p$ (3rd and 4th row) projections of the angular fit with model 3 to the dedicated MC samples with the interference hypotheses 0 (top left) to 5 (bottom right) in the $q^2 \in [1.1, 6]\,\mathrm{GeV}^2/c^4$ bin.

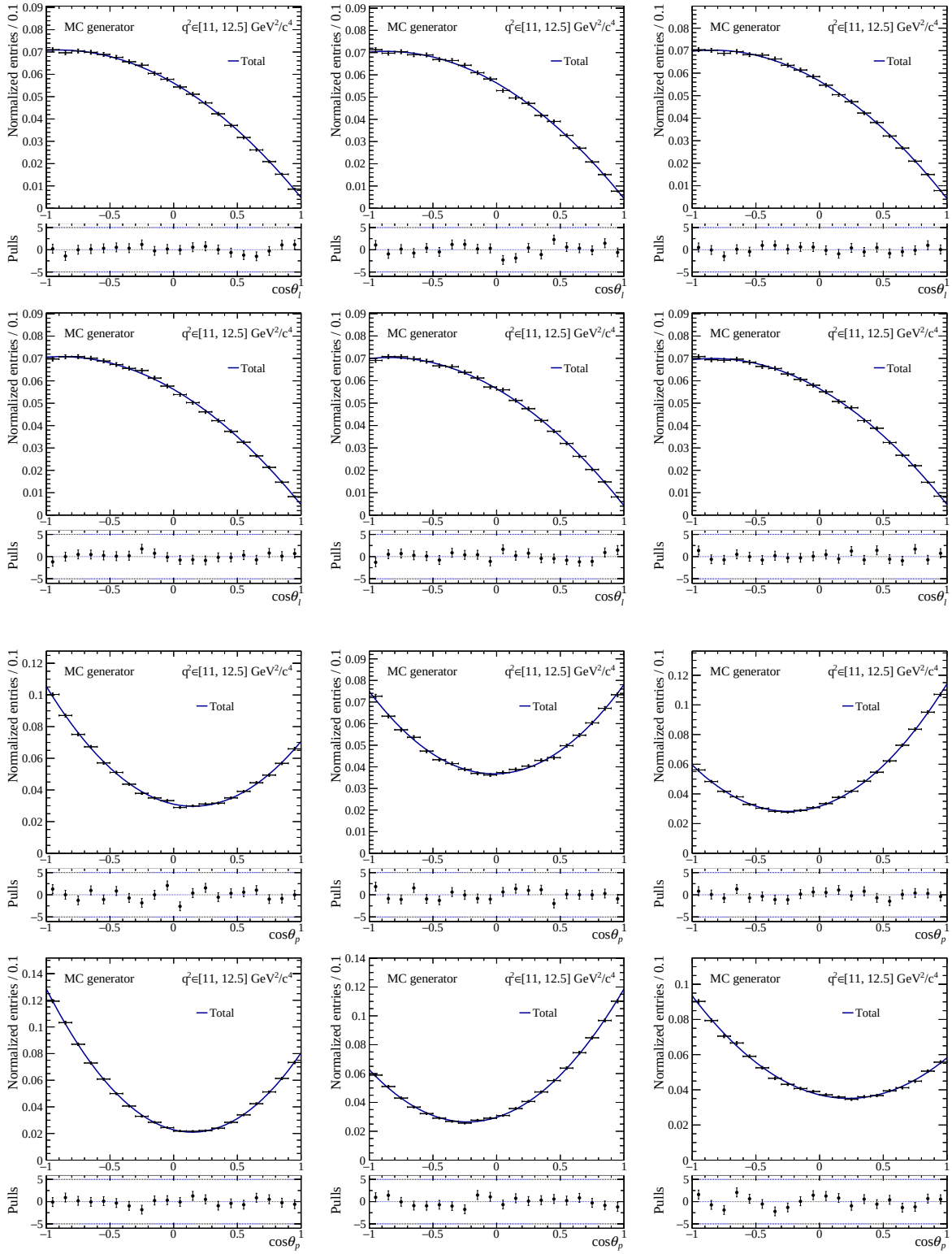

Figure K.12 – The $\cos\theta_\ell$ (1st and 2nd row) and $\cos\theta_p$ (3rd and 4th row) projections of the angular fit with model 3 to the dedicated MC samples with the interference hypotheses 0 (top left) to 5 (bottom right) in the $q^2 \in [11, 12.5]\,\mathrm{GeV}^2/c^4$ bin.

Appendix L

Two dimensional scan of the angular PDF in the rare q^2 bins

As explained in Ch. 4.2.4, a two-dimensional scan of the angular PDF with the fit configuration 3 is performed. The starting values are taken from the fit result of the dedicated simulation samples with phase combination 0 (shown in Fig. 4.23) in the corresponding q^2 bin, which is marked in red. The grey zone corresponds to the region where the angular PDF gets negative. The scan has been shown for the $q^2 \in [3, 6]\,\mathrm{GeV}^2/c^4$ in Fig. 4.24 and 4.25. The PDF scans in all the other rare q^2 bins are presented in this section.

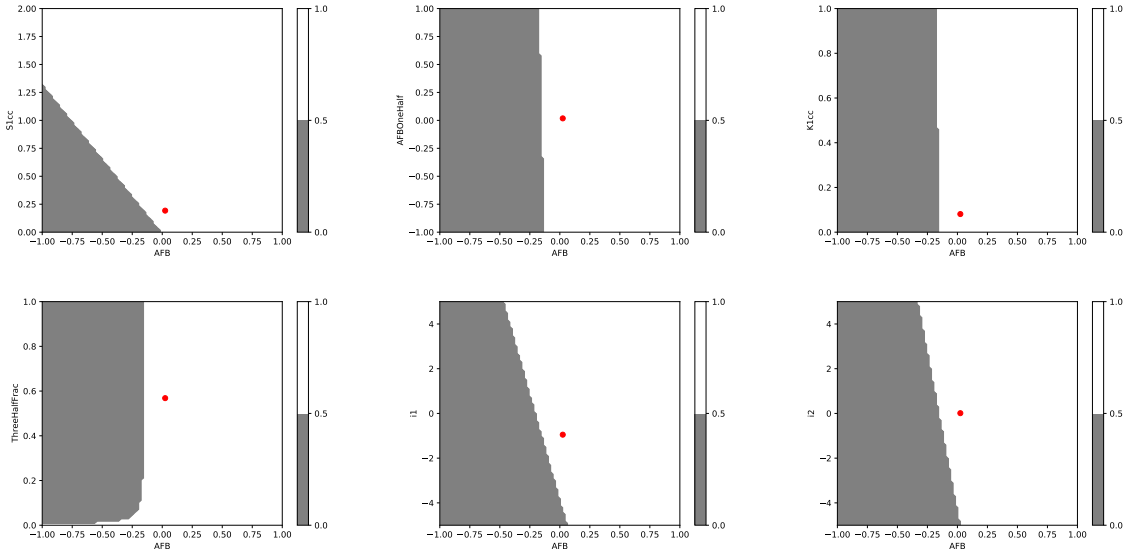

Figure L.1 – First part of the two-dimensional scan of the PDF in the $q^2 \in [0.1, 3]\,\mathrm{GeV}^2/c^4$ bin.

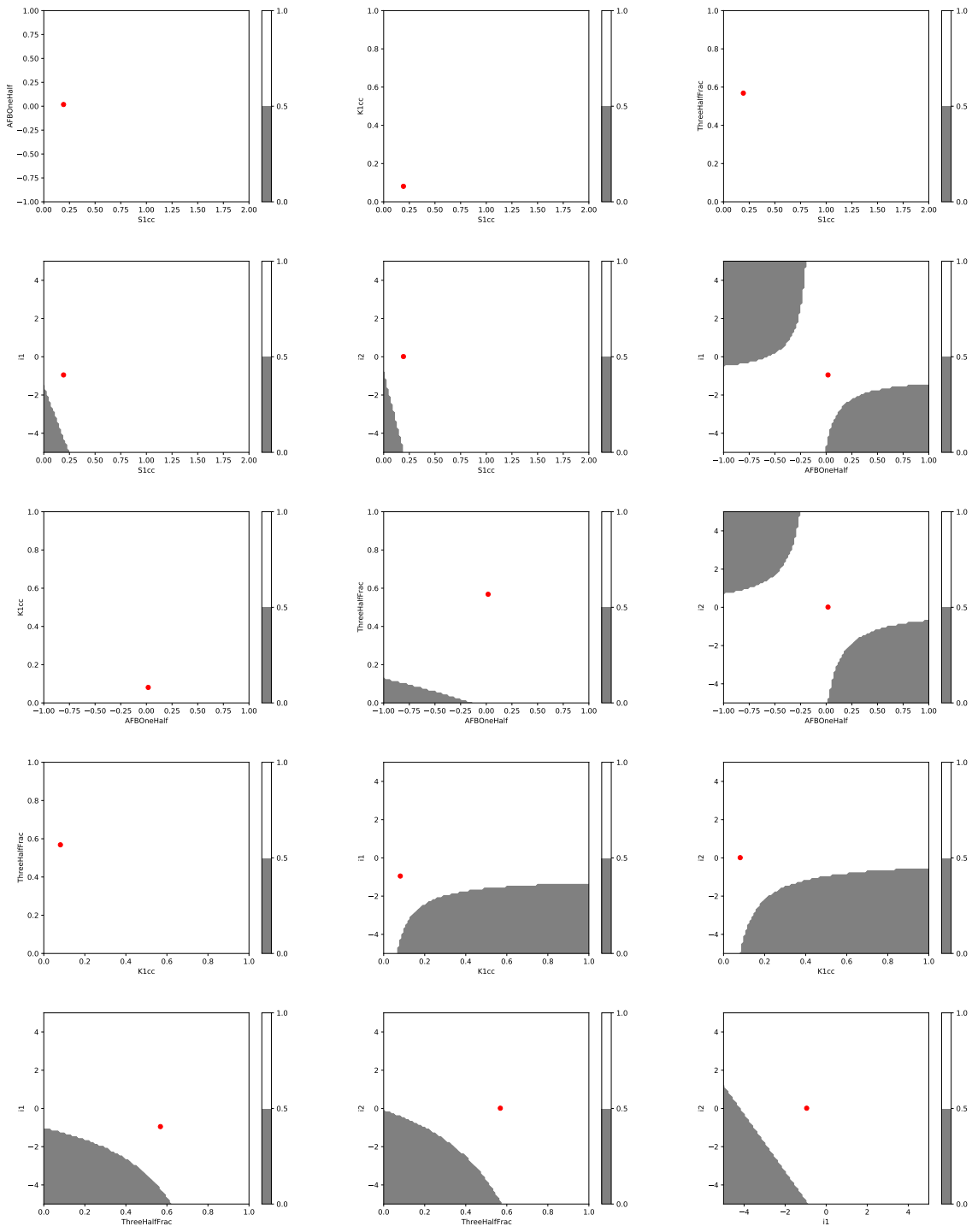

Figure L.2 – Second part of the two-dimensional scan of the PDF in the $q^2 \in [0.1, 3]\,\mathrm{GeV}^2/c^4$ bin.

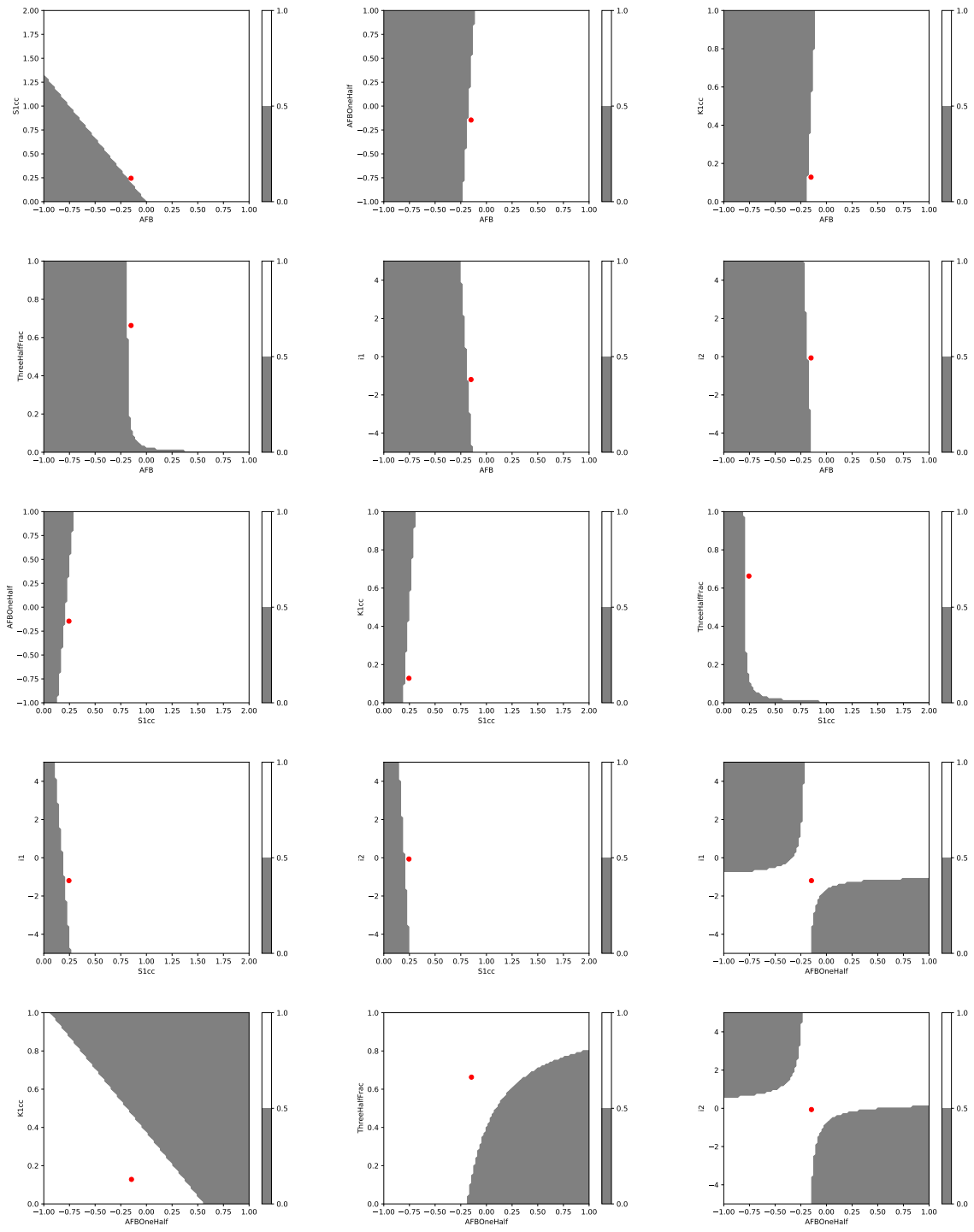

Figure L.3 – First part of the two-dimensional scan of the PDF in the $q^2 \in [3, 6]\,\mathrm{GeV}^2/c^4$ bin.

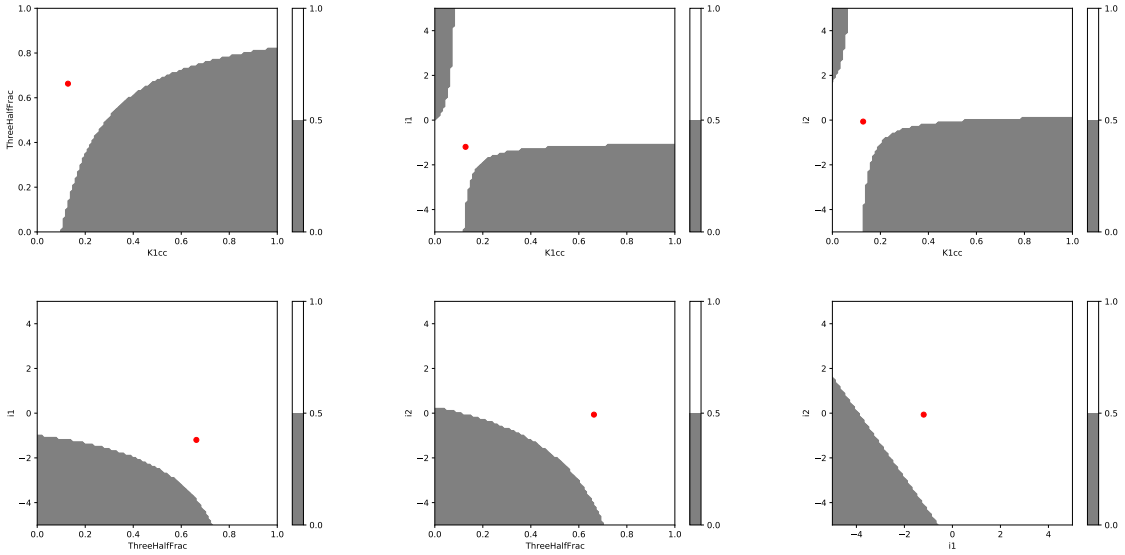

Figure L.4 – Second part of the two-dimensional scan of the PDF in the $q^2 \in [3, 6]\,\mathrm{GeV}^2/c^4$ bin.

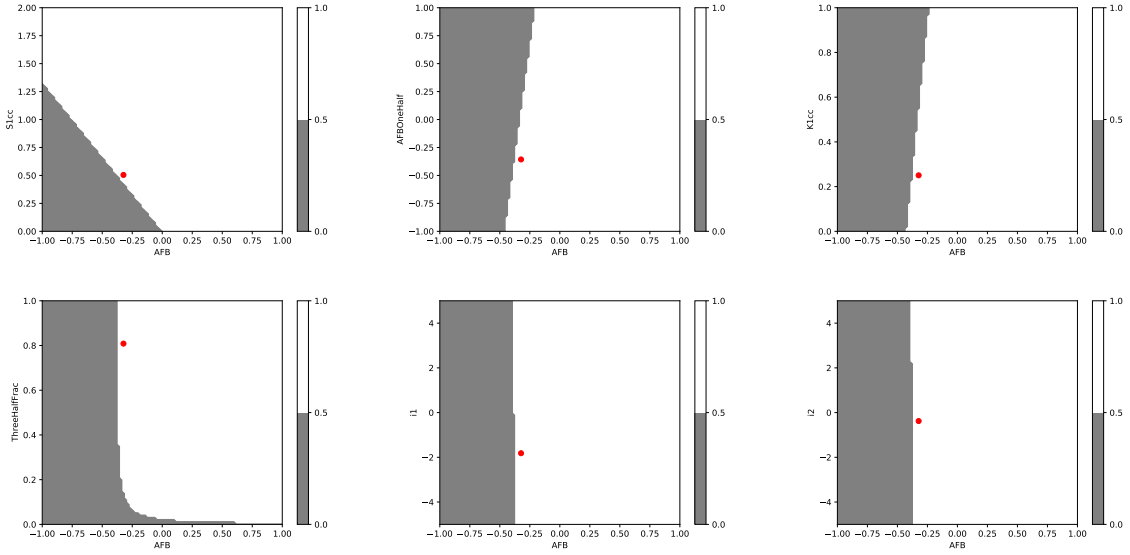

Figure L.5 – First part of the two-dimensional scan of the PDF in the $q^2 \in [11, 12.5]\,\mathrm{GeV}^2/c^4$ bin.

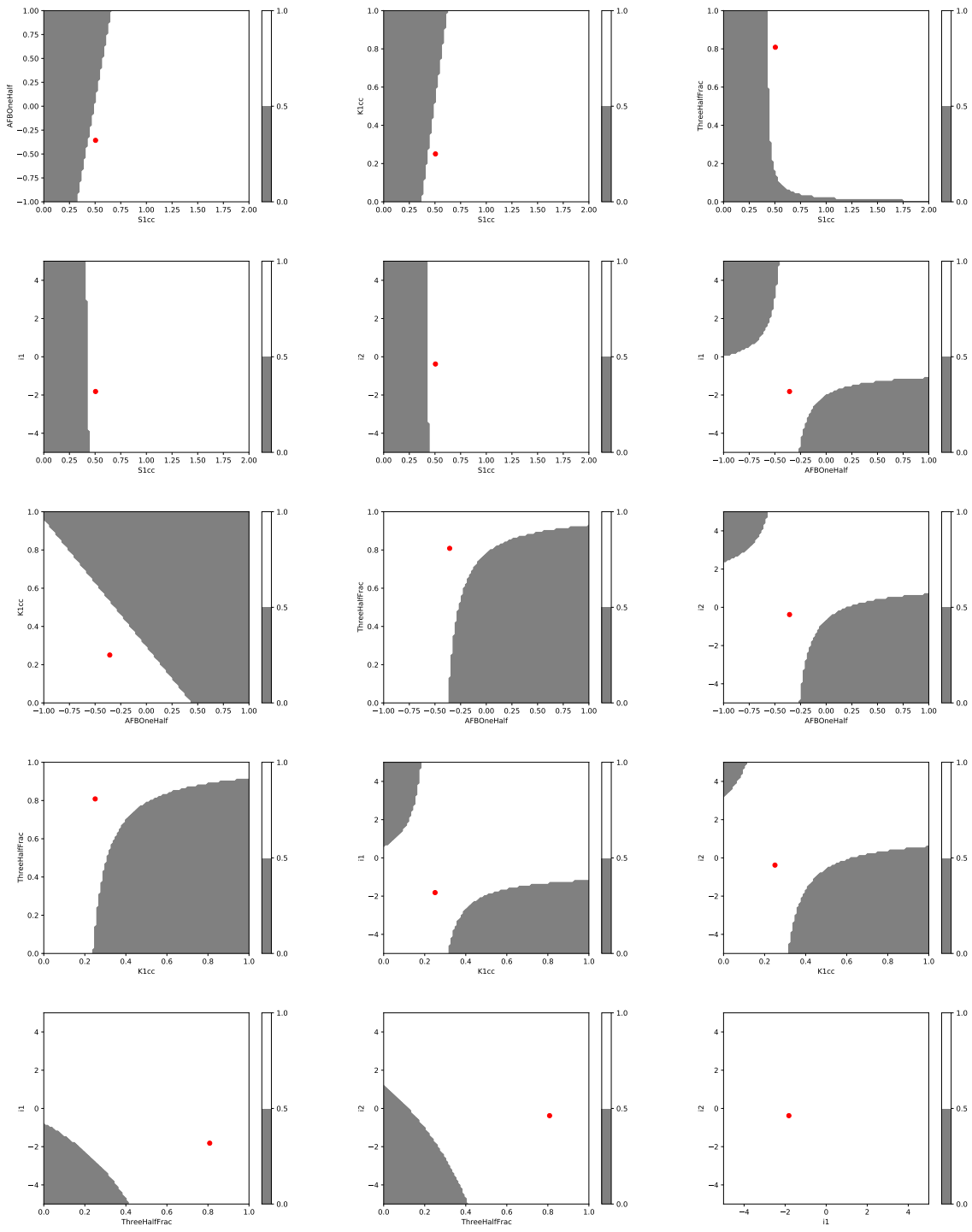

Figure L.6 – Second part of the two-dimensional scan of the PDF in the $q^2 \in [11, 12.5]\,\mathrm{GeV}^2/c^4$ bin.

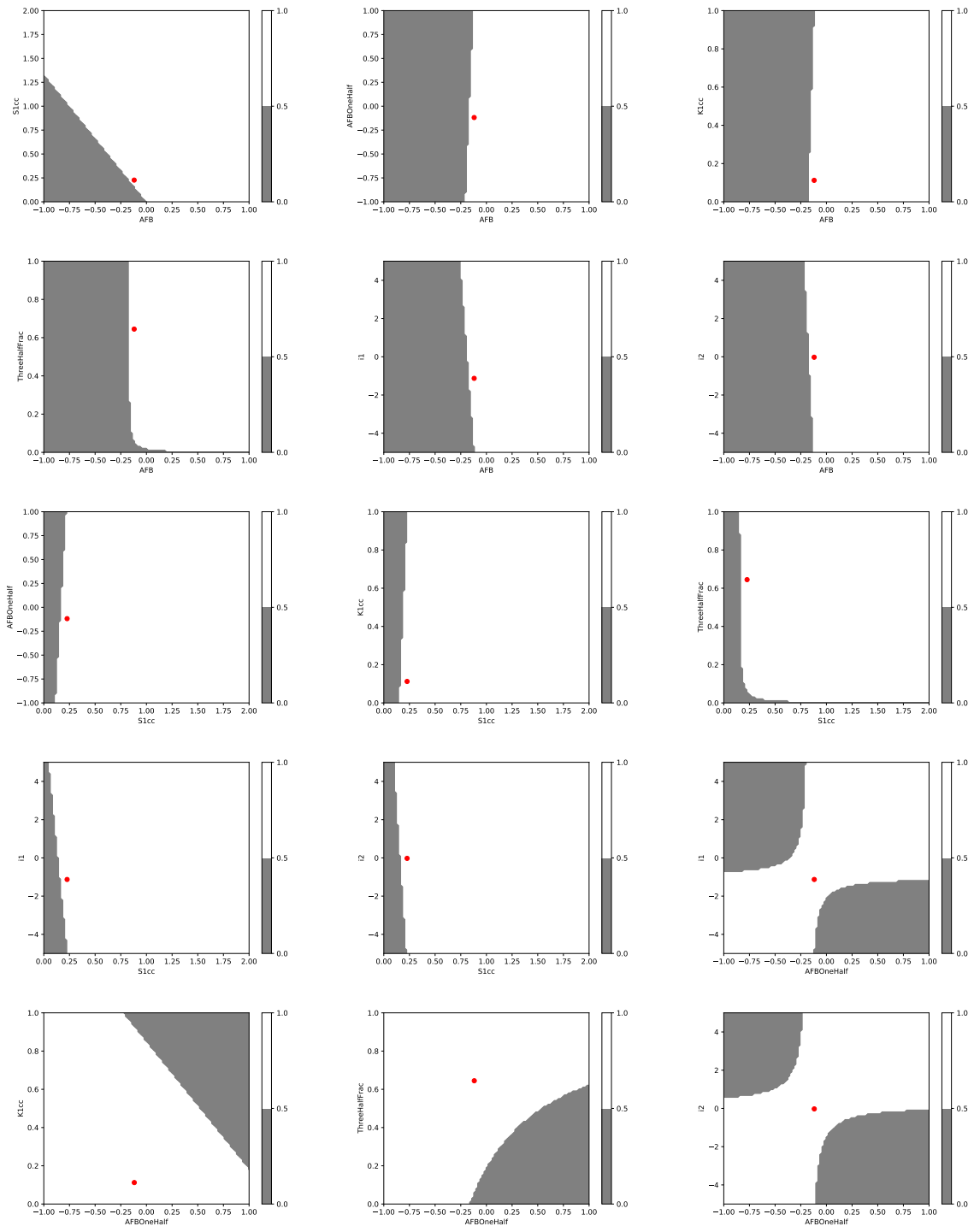

Figure L.7 – First part of the two-dimensional scan of the PDF in the $q^2 \in [1.1, 6]\,\mathrm{GeV}^2/c^4$ bin.

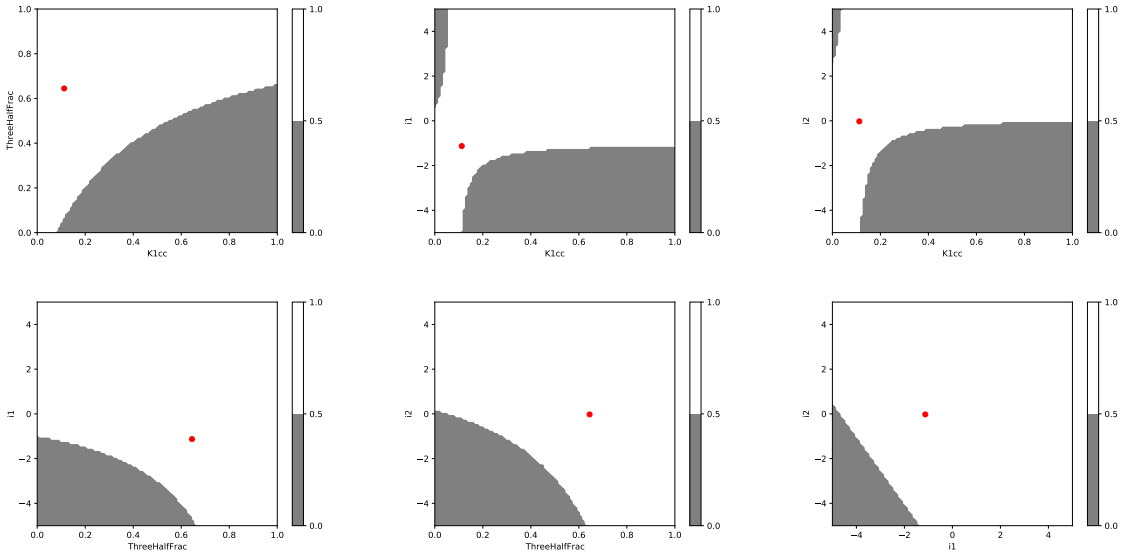

Figure L.8 – Second part of the two-dimensional scan of the PDF in the $q^2 \in [1.1, 6]\,\mathrm{GeV}^2/c^4$ bin.

Appendix M

Distributions of ${}_s\mathcal{W}eight$s and acceptance weights

M.1 Acceptance models in the remaining q^2 bins

The extraction of the acceptance model is described in Ch. 4.1.2. Only the $q^2 \in [3,6]\,\mathrm{GeV}^2/c^4$ bin and the J/ψ bin are shown in Fig. 4.1. This is the reason why all the other q^2 bins are presented in Fig. M.1.

The distributions of the $\Lambda_b^0 \to \Lambda(1520)\mu^+\mu^-$ phase space simulation samples after the full selection and the corrections are shown in blue and the projections of the angular acceptance model are drawn as a red line. The acceptance model describes well the distribution in the simulation sample.

M.2 Correction weights in the remaining q^2 bins

Fig. 4.2 in Ch. 4.1.2 is a cross check of the acceptance weights. This test is performed in the $q^2 \in [3,6]\,\mathrm{GeV}/c^2$ and J/ψ bin, while all of the other bins are listed in Fig. M.2.

The angular distributions of phase space simulation samples after the selection and corrections are shown in yellow. The angles with the correction weights are drawn in violet. As expected, the distribution of the simulation sample gets flat by applying the correction weights.

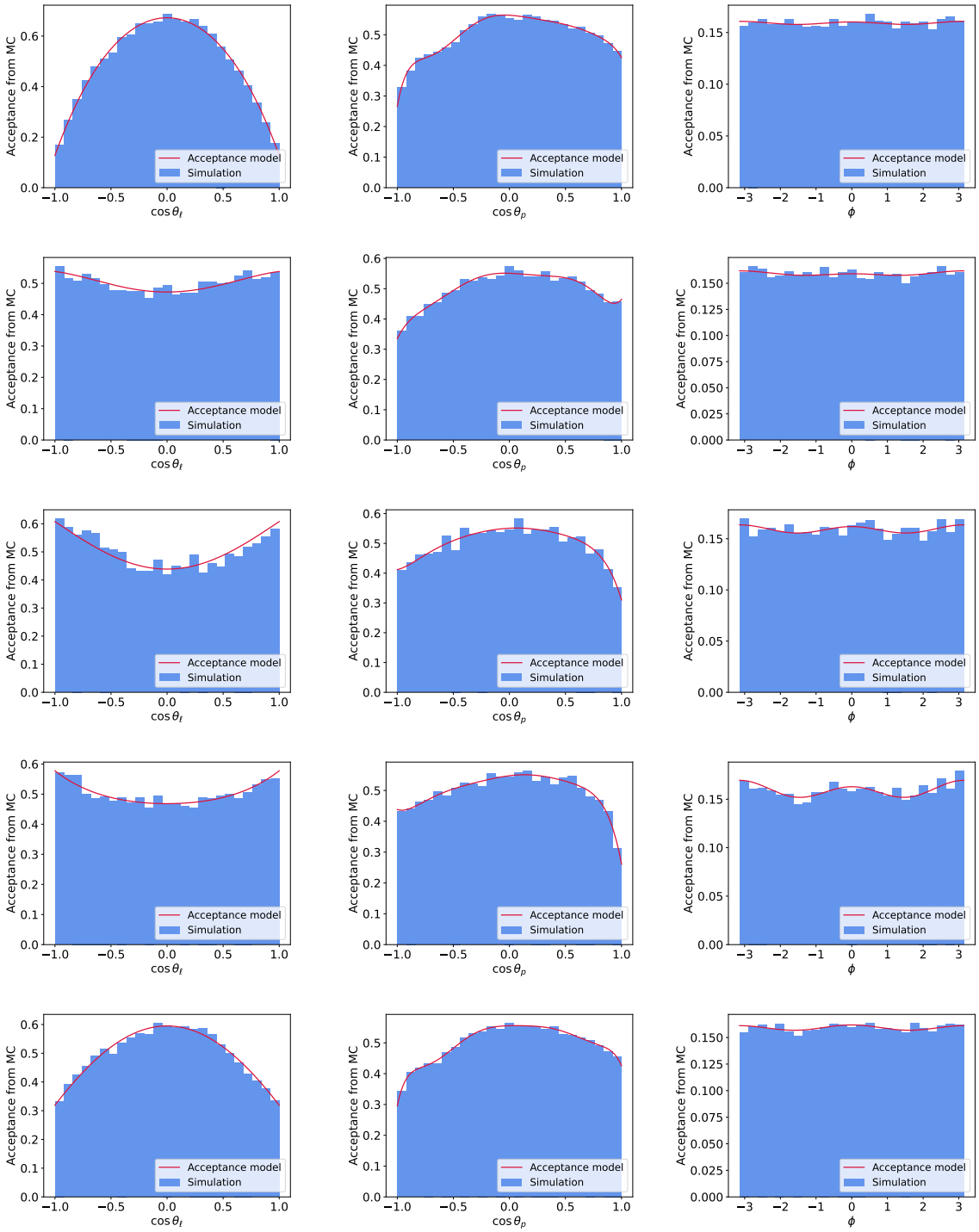

Figure M.1 – The acceptance models in the $q^2 \in [0.1, 3]\,\mathrm{GeV}^2/c^4$ (1^{st} row), $q^2 \in [6, 8]\,\mathrm{GeV}^2/c^4$ (2^{nd} row), $q^2 \in [11, 12.5]\,\mathrm{GeV}^2/c^4$ (3^{rd} row), $\psi(2S)$ (4^{th} row) and $q^2 \in [1.1, 6]\,\mathrm{GeV}^2/c^4$ bin (5^{th} row) are plotted.

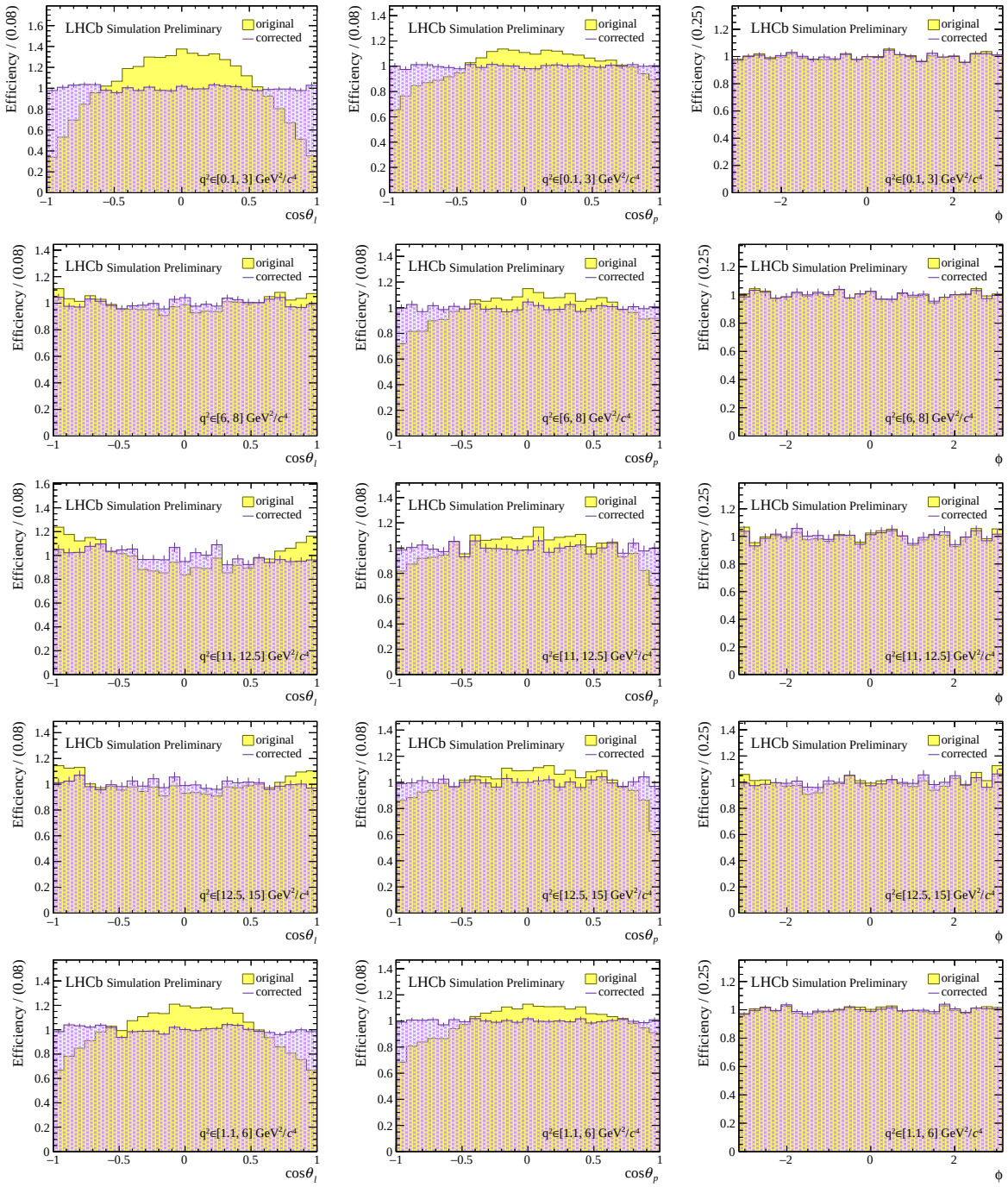

Figure M.2 – The simulation sample with and without corrections weights is plotted in the $q^2 \in [0.1, 3]\,\mathrm{GeV}^2/c^4$ (1^{st} row), $q^2 \in [6, 8]\,\mathrm{GeV}^2/c^4$ (2^{nd} row), $q^2 \in [11, 12.5]\,\mathrm{GeV}^2/c^4$ (3^{rd} row), $\psi(2S)$ (4^{th} row) and $q^2 \in [1.1, 6]\,\mathrm{GeV}^2/c^4$ bin (5^{th} row).

M.3 The distribution of the acceptance weights

The distribution of acceptance weights is drawn in Fig. M.3. The acceptance weights do not have any unreasonable high value and are all positive.

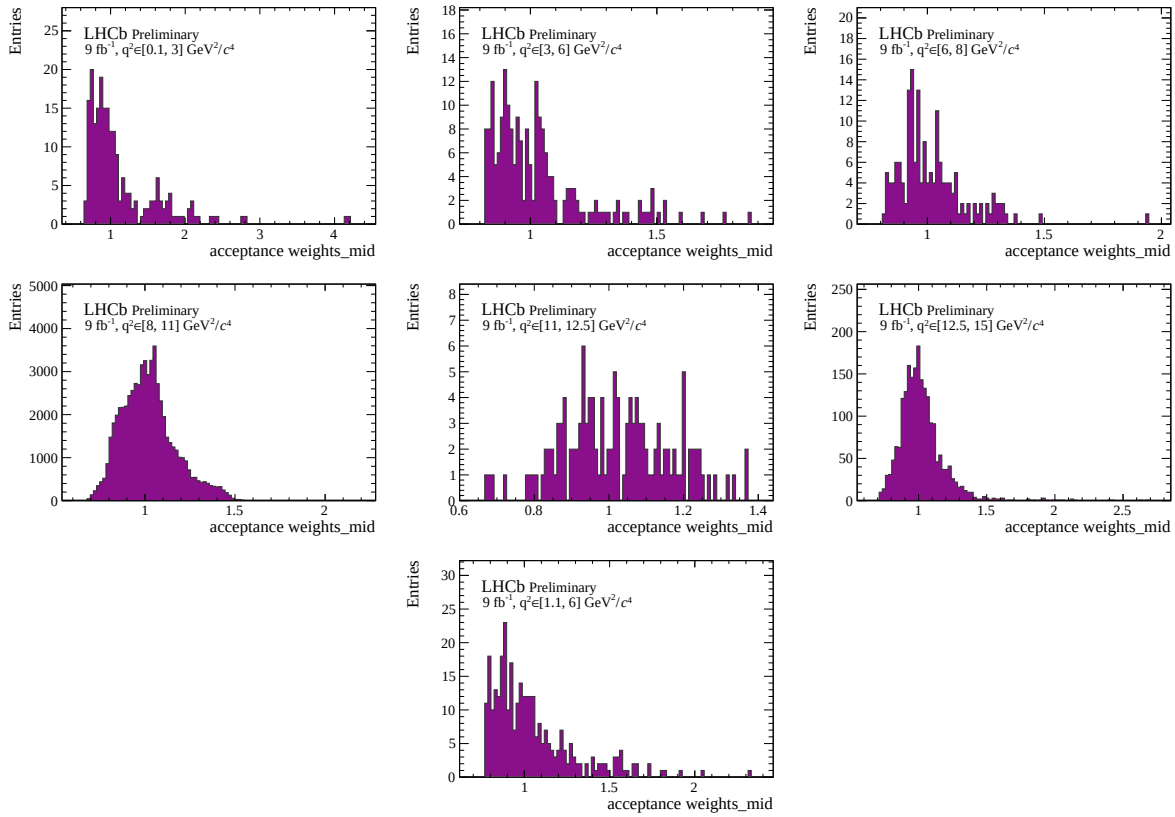

Figure M.3 – The distribution of the acceptance weights in the different q^2 bins.

M.4 The distribution of the ${}_s\mathcal{W}eights$

The values of the ${}_s\mathcal{W}eights$ are presented in Fig. M.4. Events in the signal region do have values around one. The events in the background dominated mass region obtain small or even negative weights.

M.5 Application of the weights to the pK^- invariant mass and the angles in data

The ${}_s\mathcal{W}eights$ and acceptance weights are applied to the pK^- invariant mass distribution in data to see the change of the distribution. The corresponding normalised plots

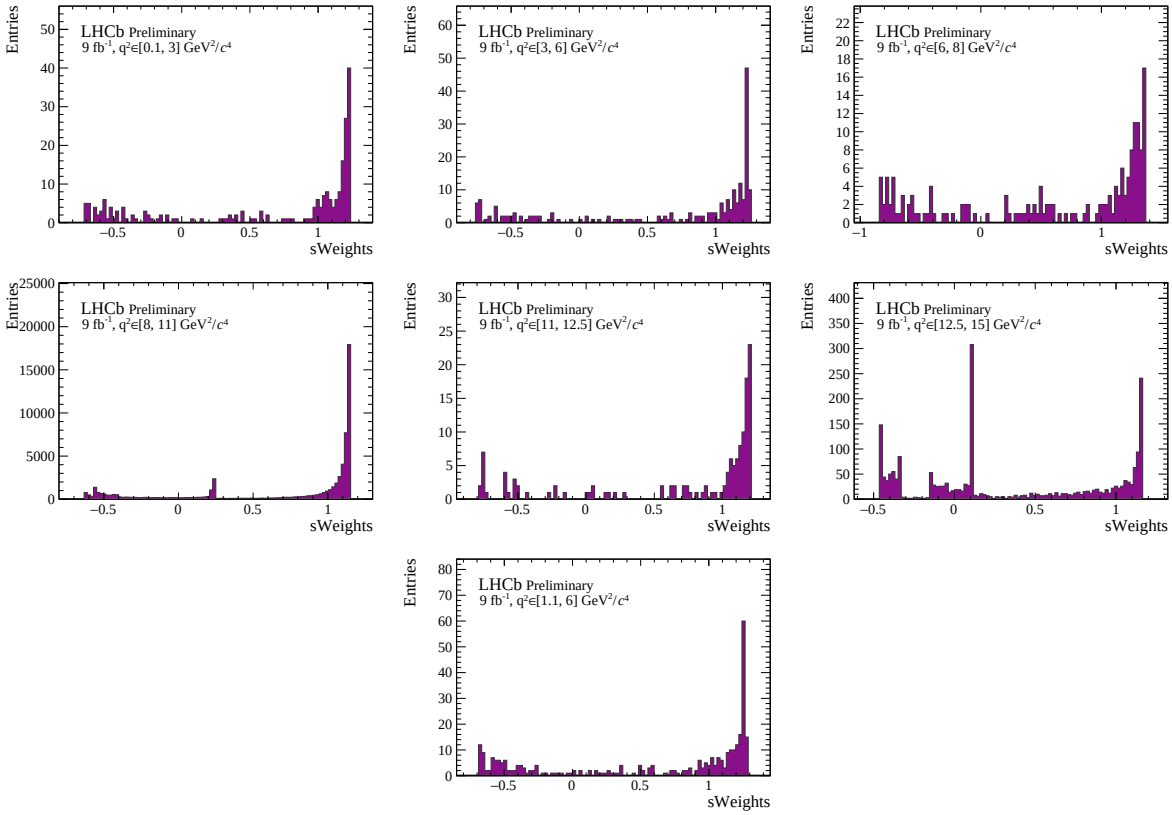

Figure M.4 – The distribution of the ${}_s\mathcal{W}eights$s in the different q^2 bins.

are drawn in Fig. M.5. The acceptance weights do not change the pK^- invariant mass

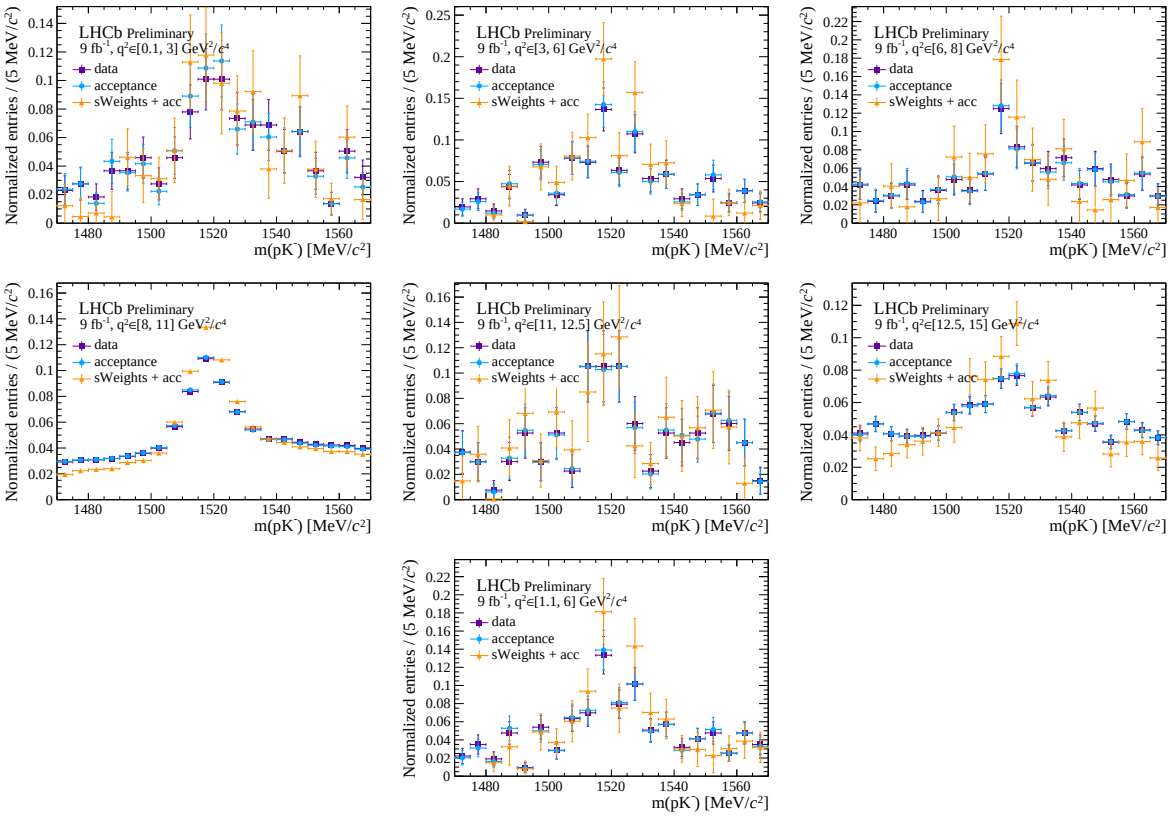

Figure M.5 – The application of the ${}_s\mathcal{W}eights$ and acceptance weights to the pK^- invariant mass distribution in data.

distribution, which is reassuring. The ${}_s\mathcal{W}eights$ have, as expected, an impact on the pK^- invariant mass distribution.

The same exercise is performed on the angles, which are shown in Fig. M.6 and M.7. In the J/ψ bin, the angular acceptance weights have the strongest impact on the angular distributions, while the change of the distributions due to the ${}_s\mathcal{W}eights$ is negligible. With smaller data sample sizes, the ${}_s\mathcal{W}eights$ introduce a more significant effect. This can be seen in the $\psi(2S)$ and the rare mode. However, the ${}_s\mathcal{W}eighted$ data points are within two standard deviations compatible with the initial and acceptance corrected data distributions.

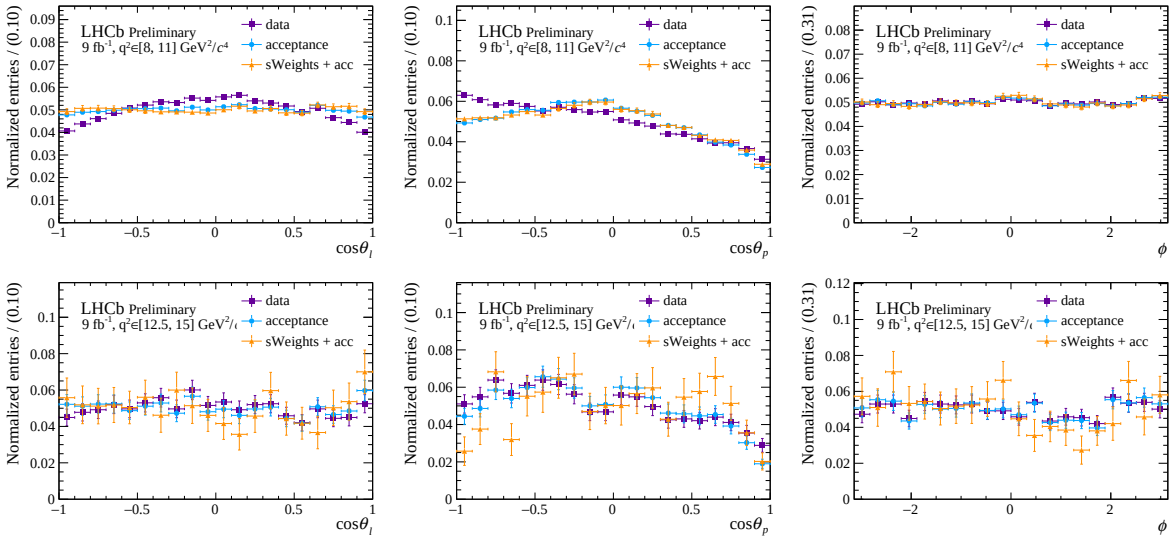

Figure M.6 – The change of the angular data distribution in the control mode by applying ${}_s\mathcal{W}eight$s and acceptance weights.

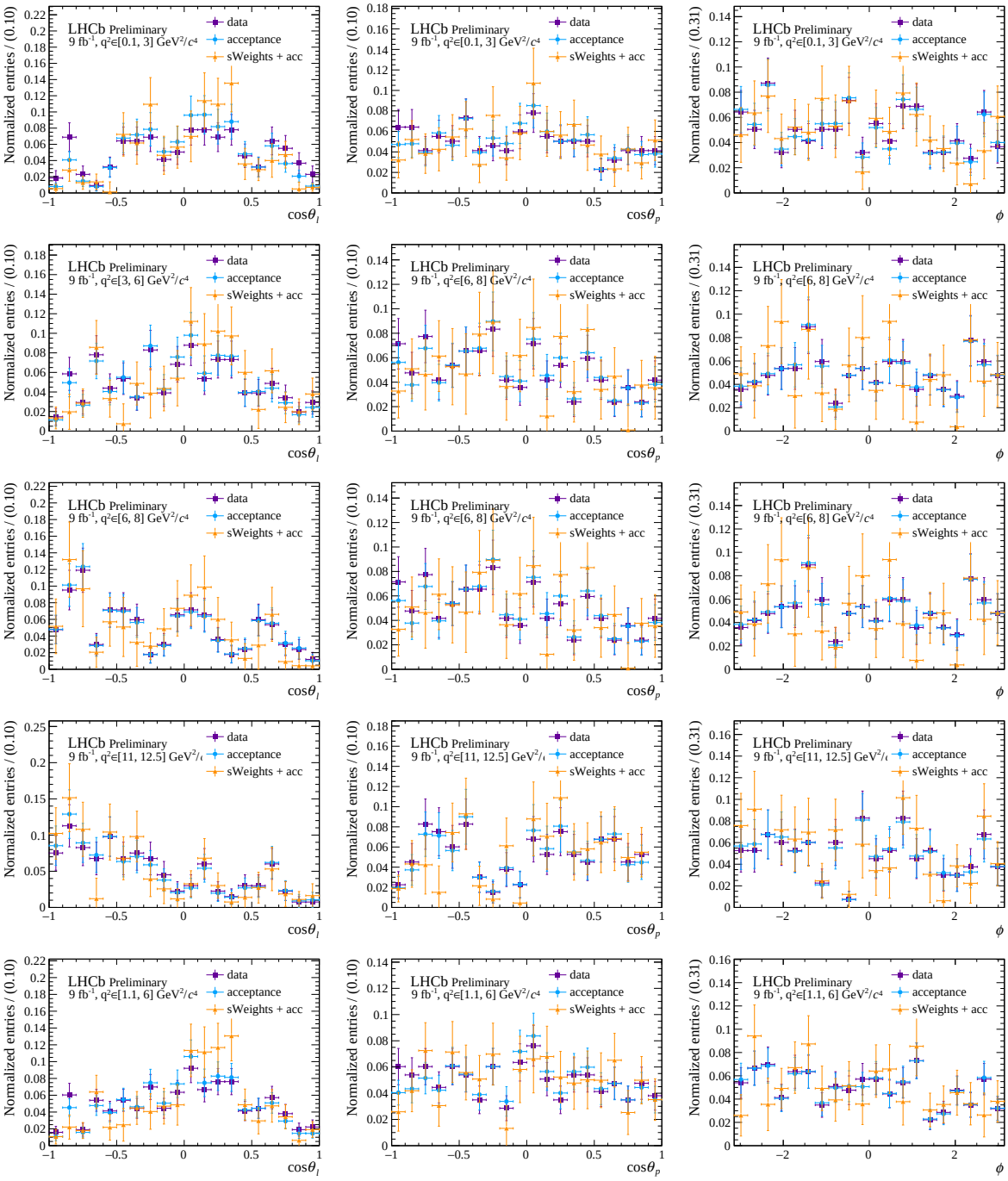

Figure M.7 – The change of the angular data distribution in the rare q^2 bins by applying ${}_s\mathcal{W}eights$ and acceptance weights.

Appendix N

Angular fit validation

N.1 Angular fit validation in the J/ψ bin

The angular data fits in the J/ψ mode are shown in Ch. 4.2.5. Pseudo-experiments are generated for the case, where the ${}_s\mathcal{W}eights$ are obtained from the J/ψ unconstrained Λ_b^0 mass fit. The pseudo-experiments for the angular fit with the ${}_s\mathcal{W}eights$ from the J/ψ constrained Λ_b^0 mass fit, are shown in this section.

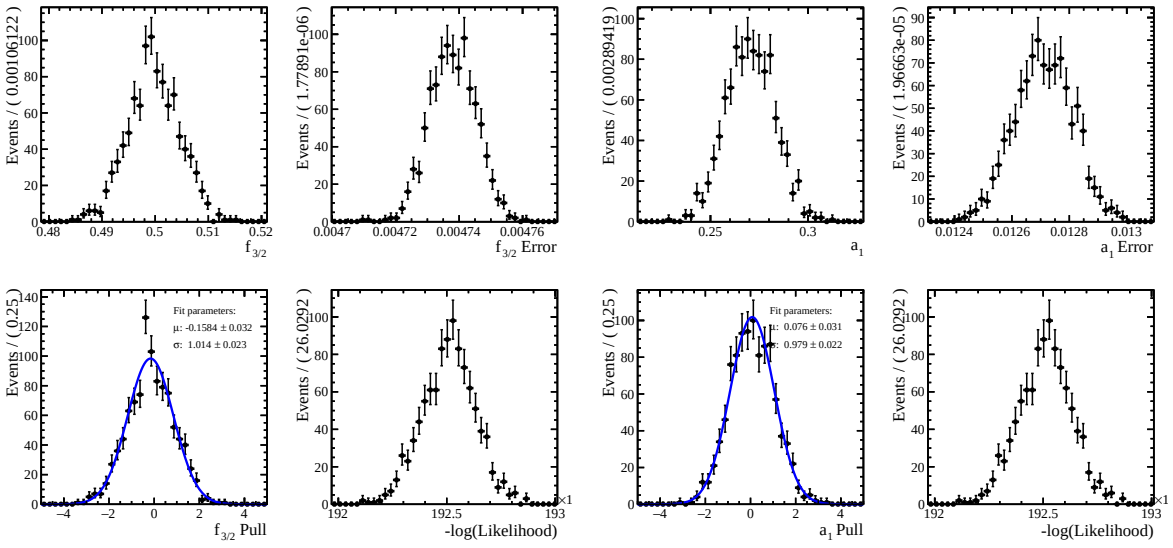

Figure N.1 – The pK^- mass parameter distributions after generating 1000 pseudo-experiments in the J/ψ bin, where the ${}_s\mathcal{W}eights$ are obtained from the J/ψ constrained Λ_b^0 mass fit. The pulls of the parameters $f_{3/2}$ and a_1 are plotted.

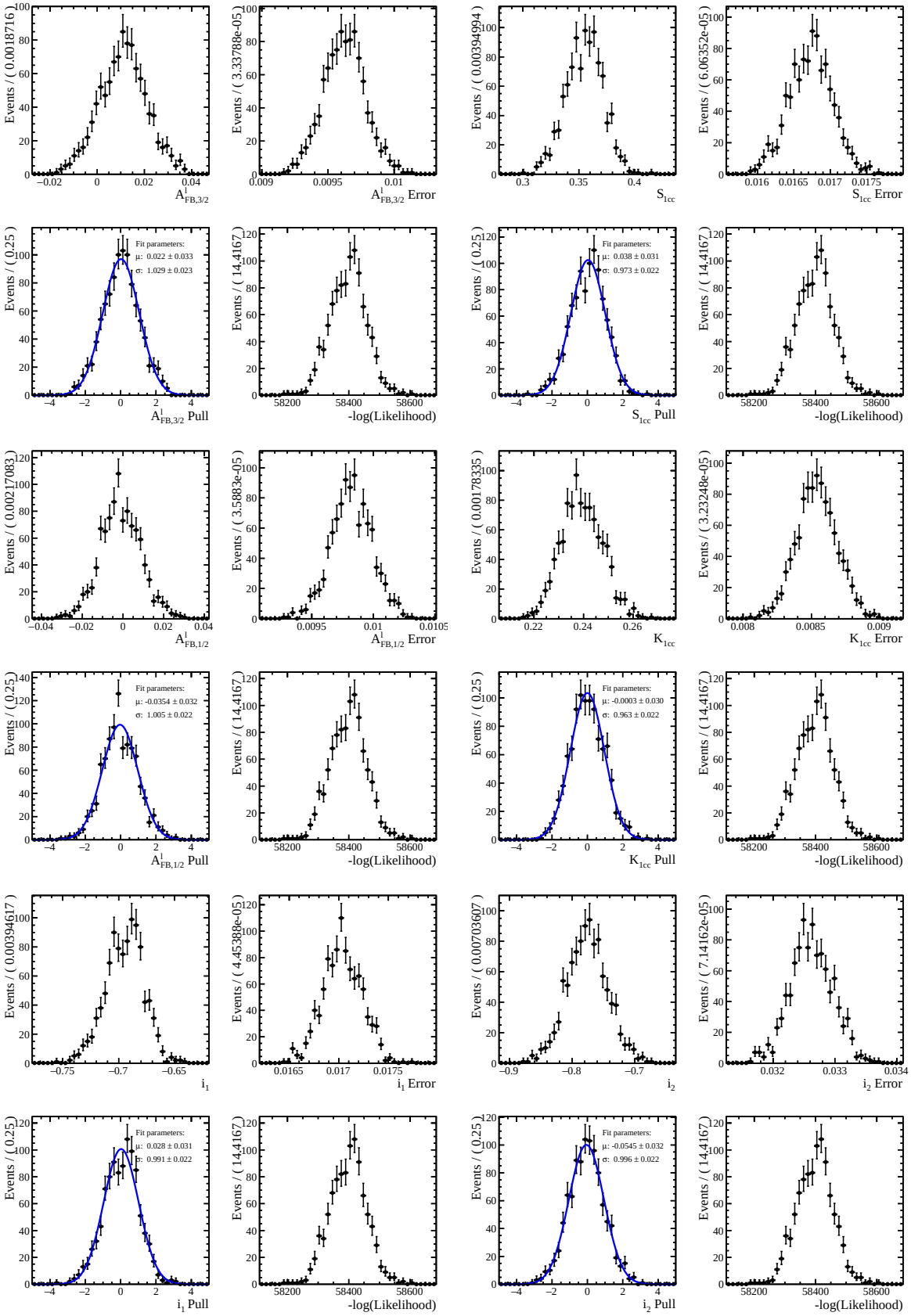

Figure N.2 – The distributions of the angular observables after generating 1000 pseudo-experiments in the J/ψ bin, where the ${}_s\mathcal{W}eights$ are obtained from the J/ψ constrained Λ_b^0 mass fit.

N.2 Angular fit validation in the $\psi(2S)$ bin

The angular data fit in the $\psi(2S)$ mode are shown in Ch. 4.2.5. Pseudo-experiments are generated for the case, where the ${}_s\mathcal{W}eights$ are obtained from the $\psi(2S)$ unconstrained Λ_b^0 mass fit. The pseudo-experiments for the angular fit with the ${}_s\mathcal{W}eights$ from the $\psi(2S)$ constrained Λ_b^0 mass fit, are shown in this section.

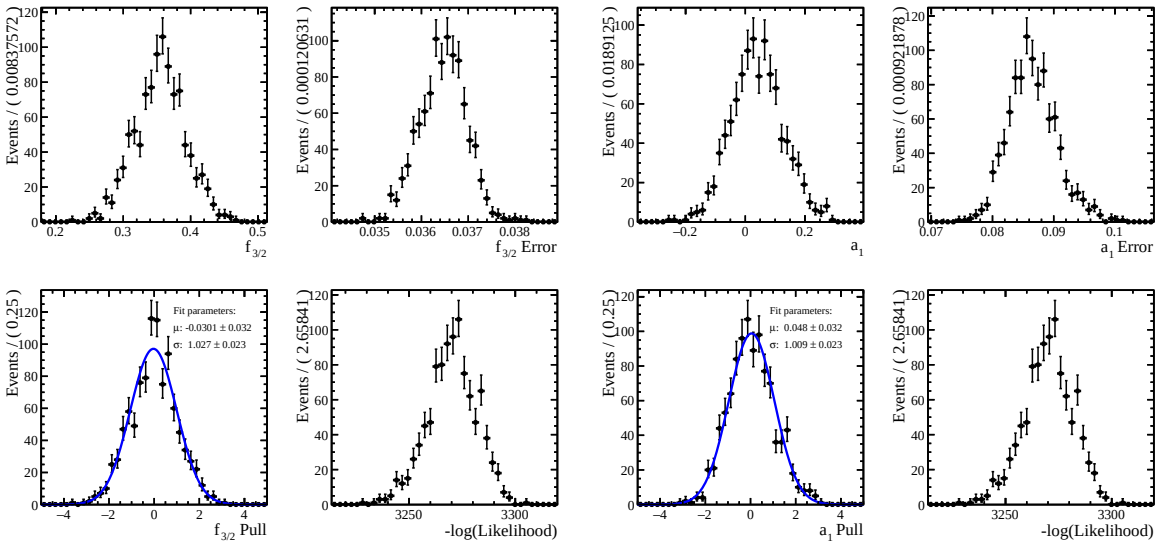

Figure N.3 – The pK^- mass parameter distributions after generating 1000 pseudo-experiments in the $\psi(2S)$ bin, where the ${}_s\mathcal{W}eights$ are obtained from the $\psi(2S)$ constrained Λ_b^0 mass fit. The pulls of the parameters $f_{3/2}$ and a_1 are plotted.

N.3 Size of $f_{3/2}$ bias in J/ψ bin

Pseudo-experiments are generated with the J/ψ parameter values but using the $\psi(2S)$ yields. This test is performed to check the bias on the $f_{3/2}$ fraction with a lower yield. The pull distributions are shown in Fig. N.5. The pulls are well-behaved without any bias, which shows that the bias is only a tiny effect at high yields.

N.4 Fit validation of the rare mode fits with larger mass parameter range

Pseudo-experiments are performed in the rare mode with a larger range of the a_1 parameter and $f_{3/2}$ fraction in order to prevent the pulls from becoming asymmetric. The pull distributions are shown in Fig. N.6 - N.10.

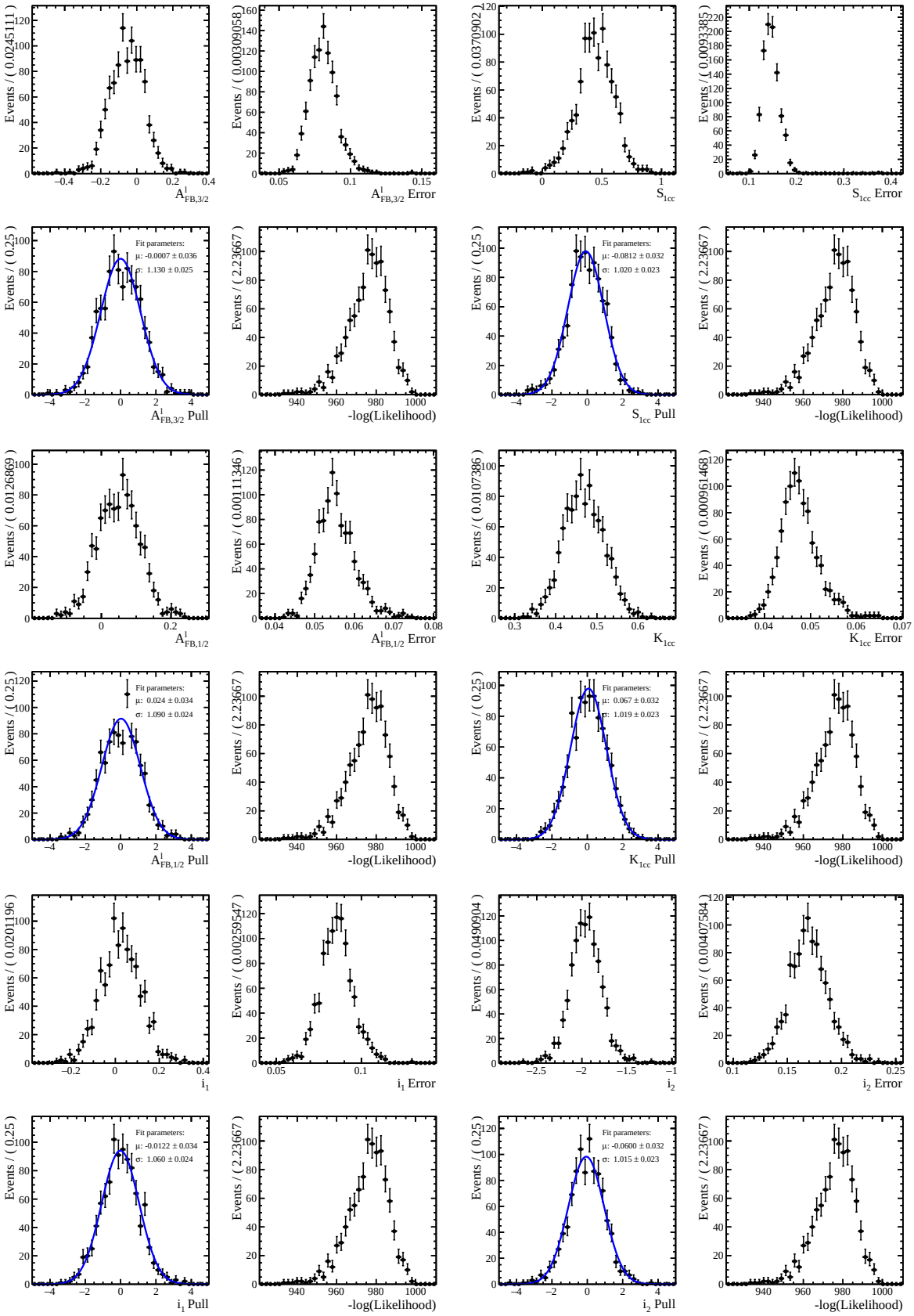

Figure N.4 – The distributions of the angular observables after generating 1000 pseudo-experiments in the $\psi(2S)$ bin, where the ${}_s\mathcal{W}eights$ are obtained from the $\psi(2S)$ constrained Λ_b^0 mass fit.

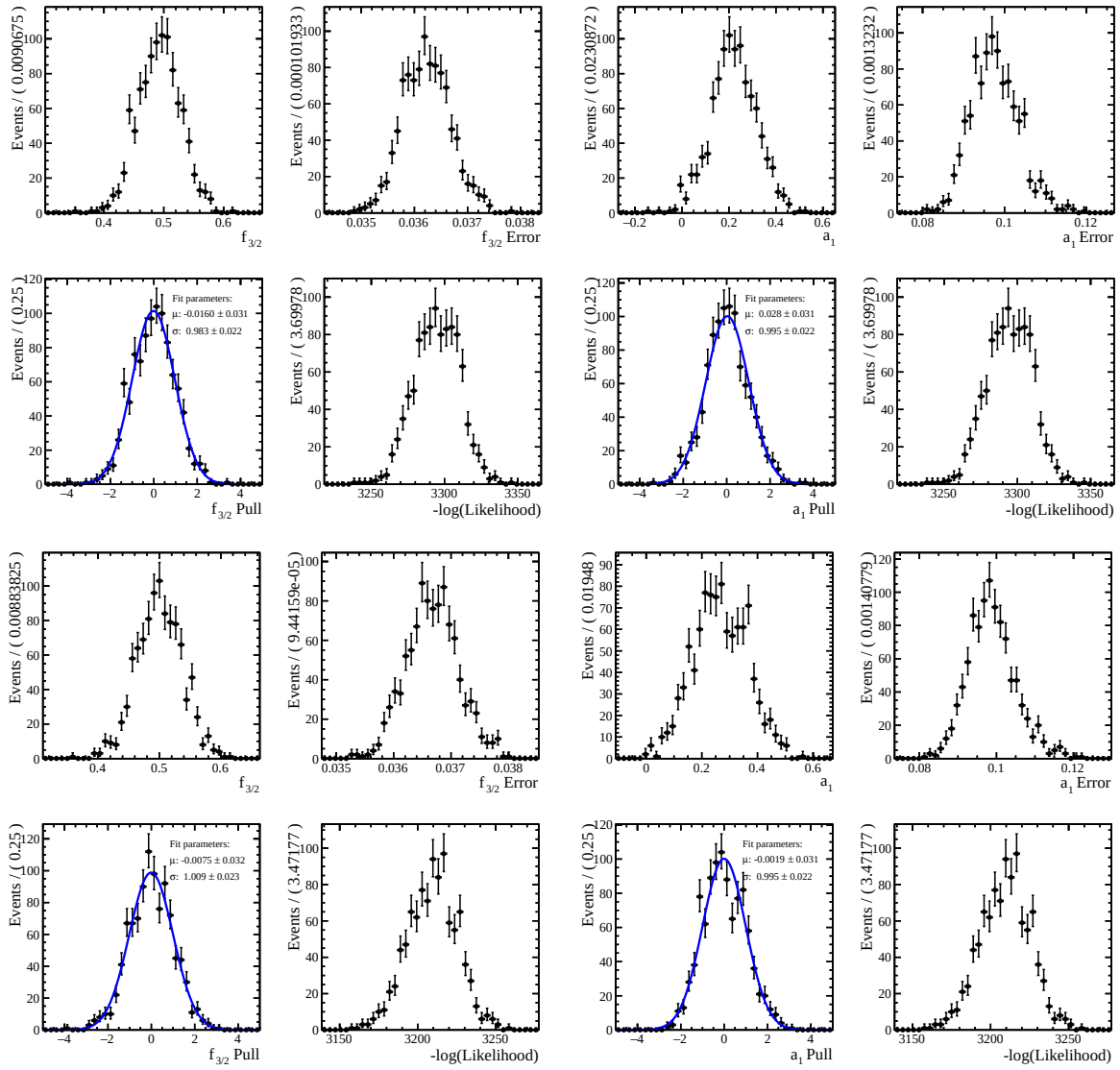

Figure N.5 – The pull distributions of the mass parameters after generating 1000 pseudo-experiments in the J/ψ bin with yields corresponding to those in the $\psi(2S)$ bin, where the ${}_s\mathcal{W}eights$ are obtained from the J/ψ-unconstrained (top) and constrained (bottom) Λ_b^0 mass fit.

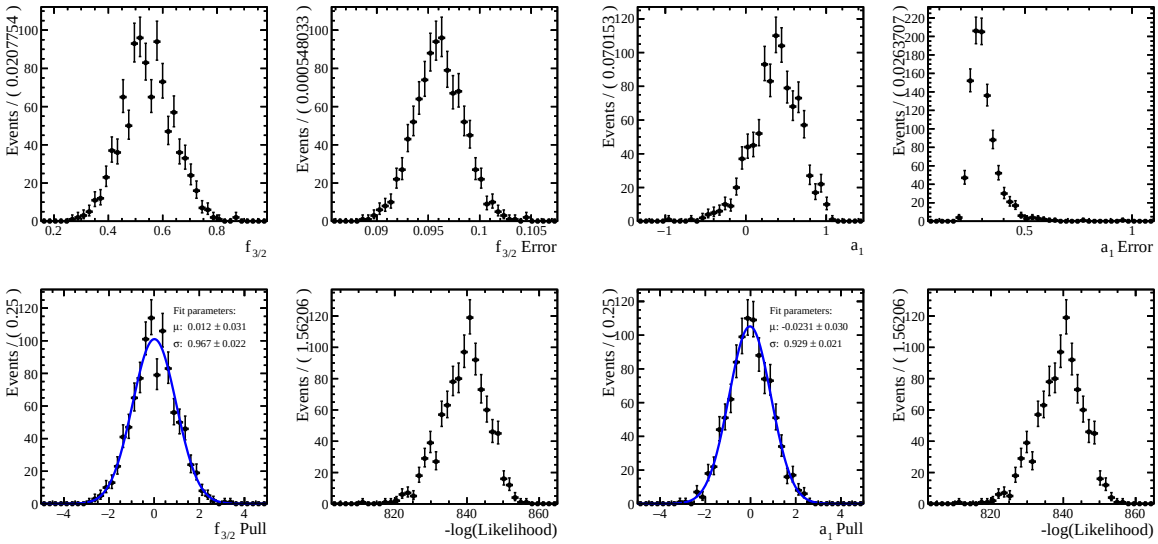

Figure N.6 – The pull distributions of the mass parameters after generating 1000 pseudo-experiments are shown, which are based on the fits in the $q^2 \in [0.1, 3]\,\mathrm{GeV}^2/c^4$ bin.

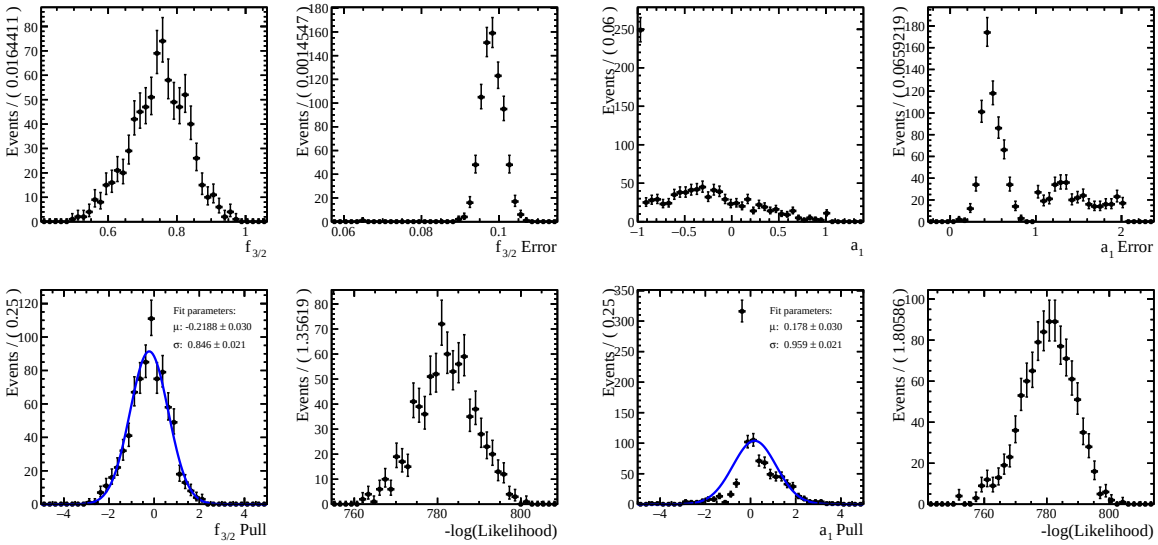

Figure N.7 – The pull distributions of the mass parameters after generating 1000 pseudo-experiments are shown, which are based on the fits in the $q^2 \in [3, 6]\,\mathrm{GeV}^2/c^4$ bin.

The values and errors of the a_1 pull have a more Gaussian shape. However, the value of the $f_{3/2}$ pull is strongly biased, and the pull width is 6σ away from one, as shown in Fig. N.7.

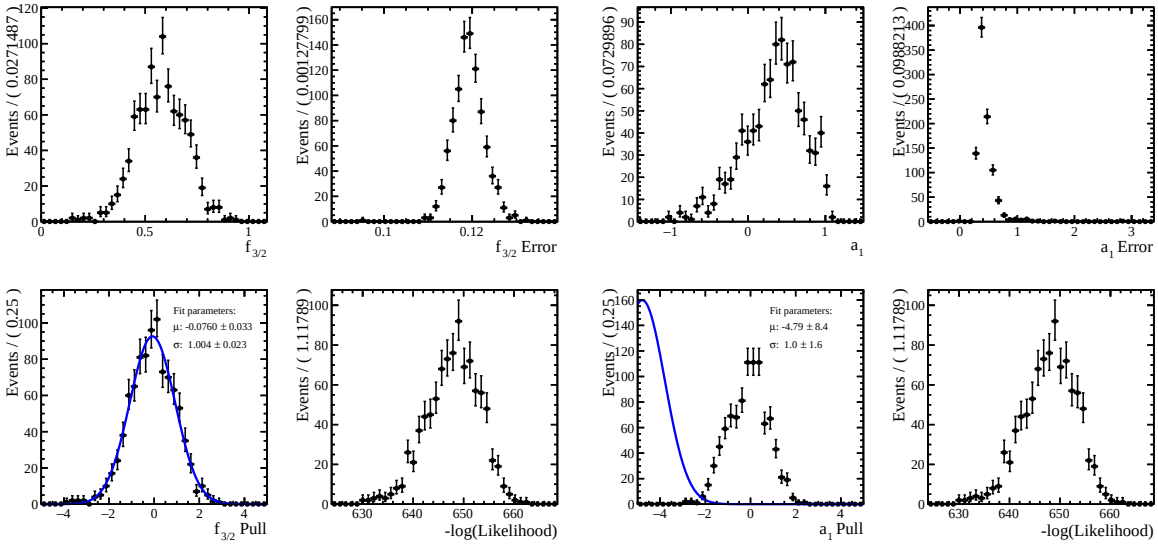

Figure N.8 – The pull distributions of the mass parameters after generating 1000 pseudo-experiments are shown, which are based on the fits in the $q^2 \in [6, 8]\,\mathrm{GeV}^2/c^4$ bin.

The Gaussian fit of the a_1 parameter pull distribution fails in the $q^2 \in [3, 6]\,\mathrm{GeV}^2/c^4$, $q^2 \in [6, 8]\,\mathrm{GeV}^2/c^4$ and $q^2 \in [1.1, 6]\,\mathrm{GeV}^2/c^4$ bin.

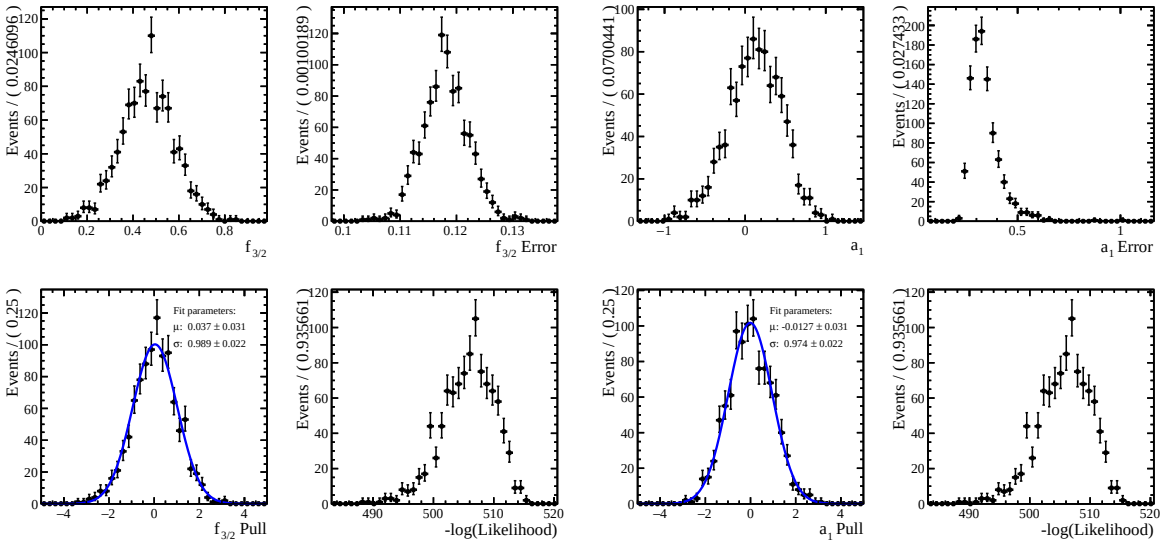

Figure N.9 – The pull distributions of the mass parameters after generating 1000 pseudo-experiments are shown, which are based on the converging angular fits in the $q^2 \in [11, 12.5]\,\mathrm{GeV}^2/c^4$ bin.

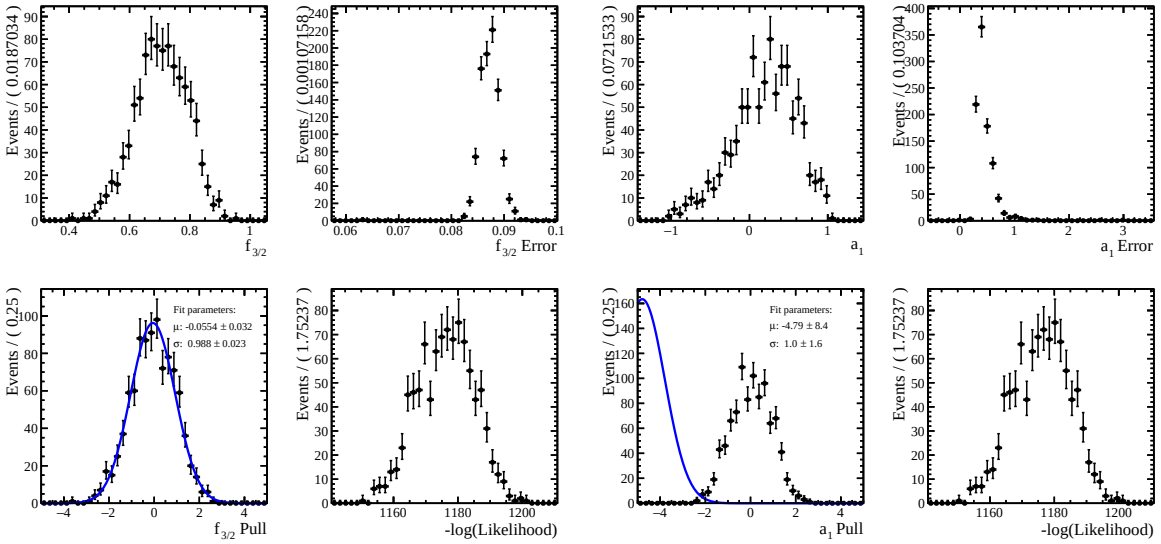

Figure N.10 – The pull distributions of the mass parameters after generating 1000 pseudo-experiments are shown, which are based on the fits in the $q^2 \in [1.1, 6]\,\mathrm{GeV}^2/c^4$ bin.

Appendix O

Correlation tables of the angular fit in the rare mode

	$f_{3/2}$	a_1
$f_{3/2}$	1.000	-0.082
a_1	-0.082	1.000
$f_{3/2}$	1.000	-0.438
a_1	-0.438	1.000
$f_{3/2}$	1.000	-0.018
a_1	-0.018	1.000
$f_{3/2}$	1.000	-0.134
a_1	-0.134	1.000
$f_{3/2}$	1.000	-0.127
a_1	-0.127	1.000

Table O.1 – The linear correlation coefficients, derived by `Minuit` [189], between the different pK^- invariant mass fit parameters are listed for the fit in the $q^2 \in [0.1, 3]$, [3, 6], [6, 8], [11, 12.5] and [1.1, 6] GeV^2/c^4 bins from the top to the bottom.

	$A^{\ell}_{FB,3/2}$	S_{1cc}	$A^{\ell}_{FB,1/2}$	K_{1cc}	i_1	i_2
$A^{\ell}_{FB,3/2}$	1.000	0.104	-0.391	-0.069	0.011	-0.039
S_{1cc}	0.104	1.000	-0.115	-0.883	-0.761	-0.537
$A^{\ell}_{FB,1/2}$	-0.391	-0.115	1.000	0.113	0.091	0.026
K_{1cc}	-0.069	-0.883	0.113	1.000	0.739	0.503
i_1	0.011	-0.761	0.091	0.739	1.000	0.186
i_2	-0.039	-0.537	0.026	0.503	0.186	1.000

Table O.2 – The linear correlation coefficients, derived by `Minuit` [189], between the different angular fit parameters are given for the fit in $q^2 \in [0.1, 3]\,\mathrm{GeV}^2/c^4$ bin.

	$A^{\ell}_{FB,3/2}$	S_{1cc}	$A^{\ell}_{FB,1/2}$	K_{1cc}	i_1	i_2
$A^{\ell}_{FB,3/2}$	1.000	0.104	-0.391	-0.069	0.011	-0.039
S_{1cc}	0.104	1.000	-0.115	-0.883	-0.761	-0.537
$A^{\ell}_{FB,1/2}$	-0.391	-0.115	1.000	0.113	0.091	0.026
K_{1cc}	-0.069	-0.883	0.113	1.000	0.739	0.503
i_1	0.011	-0.761	0.091	0.739	1.000	0.186
i_2	-0.039	-0.537	0.026	0.503	0.186	1.000

Table O.3 – The linear correlation coefficients, derived by `Minuit` [189], between the different angular fit parameters are given for the fit in $q^2 \in [3, 6]\,\mathrm{GeV}^2/c^4$ bin.

Appendix P

Additional material about the Run 3 analysis

P.1 BDT input feature importance

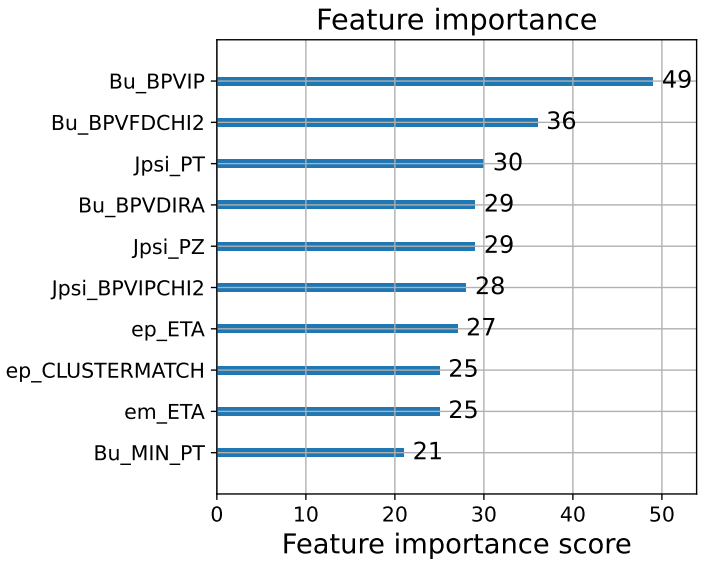

Figure P.1 – The feature importance of the BDT, which is trained on even event numbers.

The impact parameter of the reconstructed B^+ track with respect to the best primary vertex, IP(B^+), is the highest listed input feature. With some distance, the lowest importance is attributed to the Bu_MIN_PT variable, which represents the minimum p_T

value of the daughters of the B^+ meson. All the other features have approximately similar importance.

P.2 Additional 2022 data plots

${}_s\mathcal{W}eight$s are extracted from the fit to the B^+ mass peak originating from the $B^+ \to K^+ J/\psi$ decay in all Brem categories. Applying those to the data sample leads to background subtracted distributions. Some selected comparison plots of the ${}_s\mathcal{W}eight$ted data distribution and one of the simulation samples are already mentioned in Ch. 5.6. All the other comparisons are shown in Fig. P.2 - P.6.

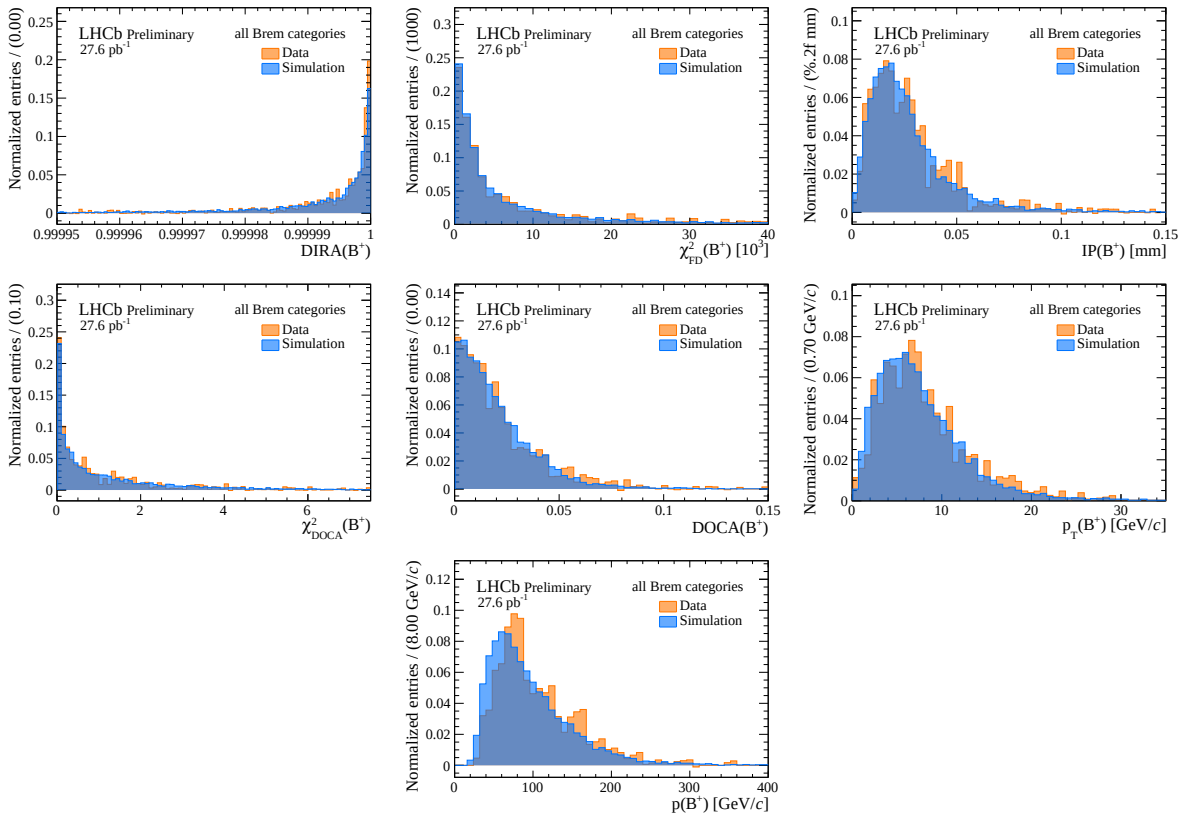

Figure P.2 – Additional comparisons of the variable distributions related to the B^+ in the $B^+ \to K^+ J/\psi(\to e^+e^-)$ simulation sample and the ${}_s\mathcal{W}eight$ted data.

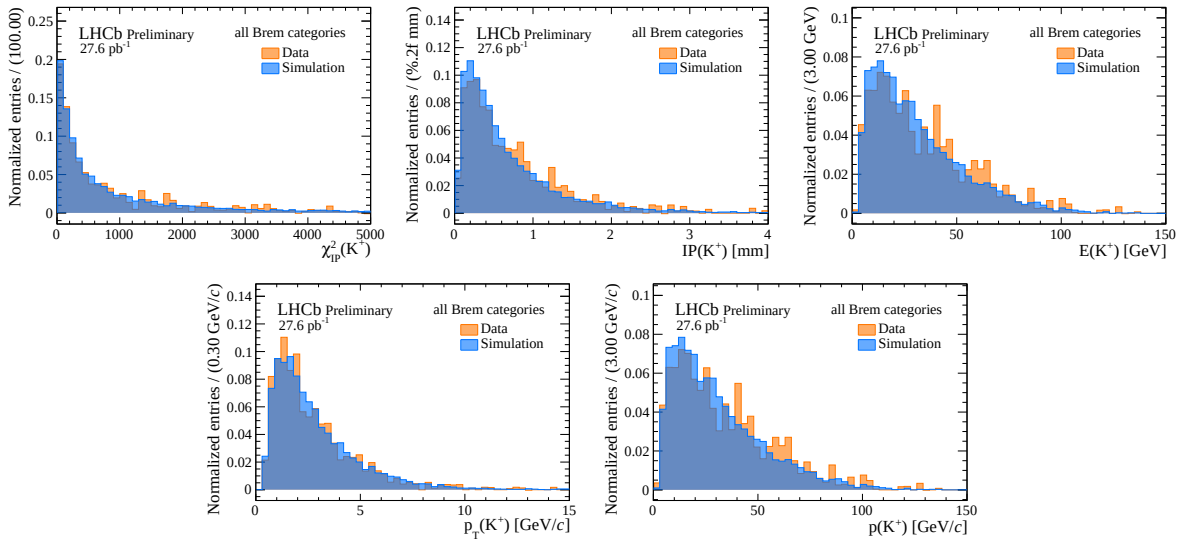

Figure P.3 – Additional comparisons of the variable distributions related to the K^+ in the $B^+ \to K^+ J/\psi(\to e^+e^-)$ simulation sample and the ${}_s\mathcal{W}eight$ted data.

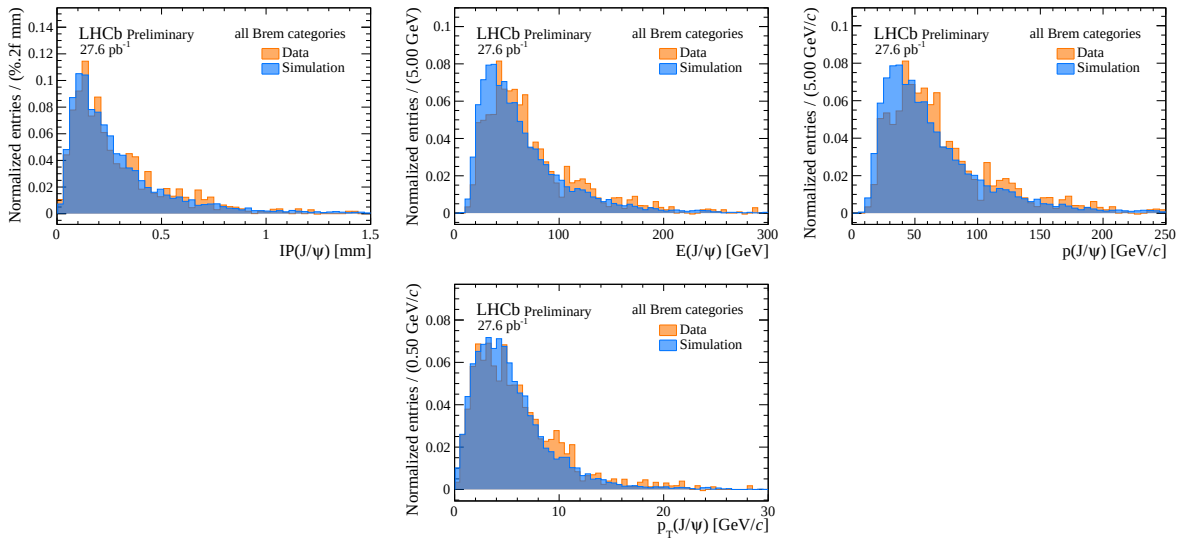

Figure P.4 – Additional comparison of the variable distributions related to the J/ψ in the $B^+ \to K^+ J/\psi(\to e^+e^-)$ simulation sample and the ${}_s\mathcal{W}eight$ted data.

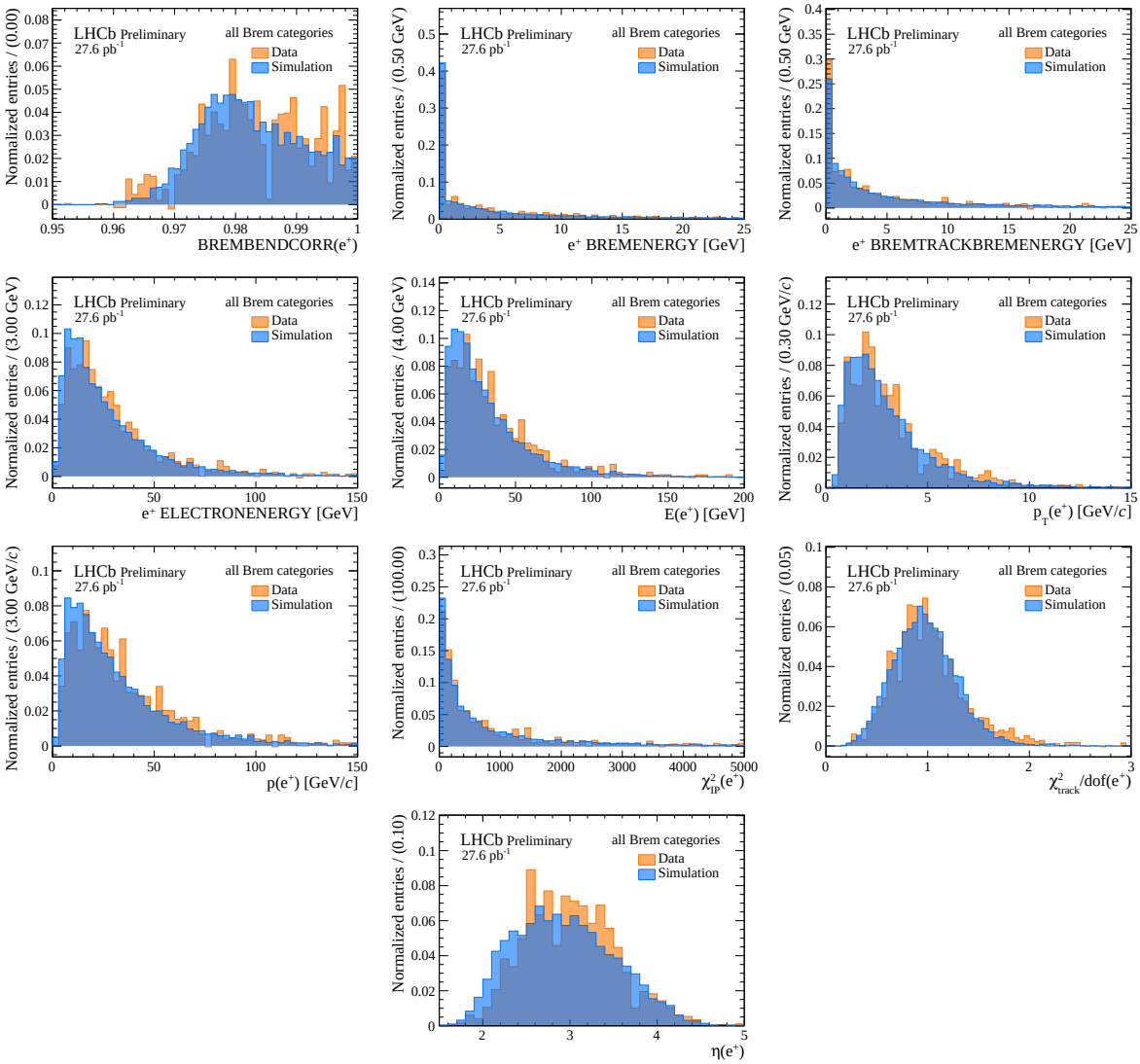

Figure P.5 – Additionnal comparison of the variable distributions related to the e^+ in the $B^+ \to K^+ J/\psi(\to e^+e^-)$ simulation sample and the ${}_s\mathcal{W}eight$ted data.

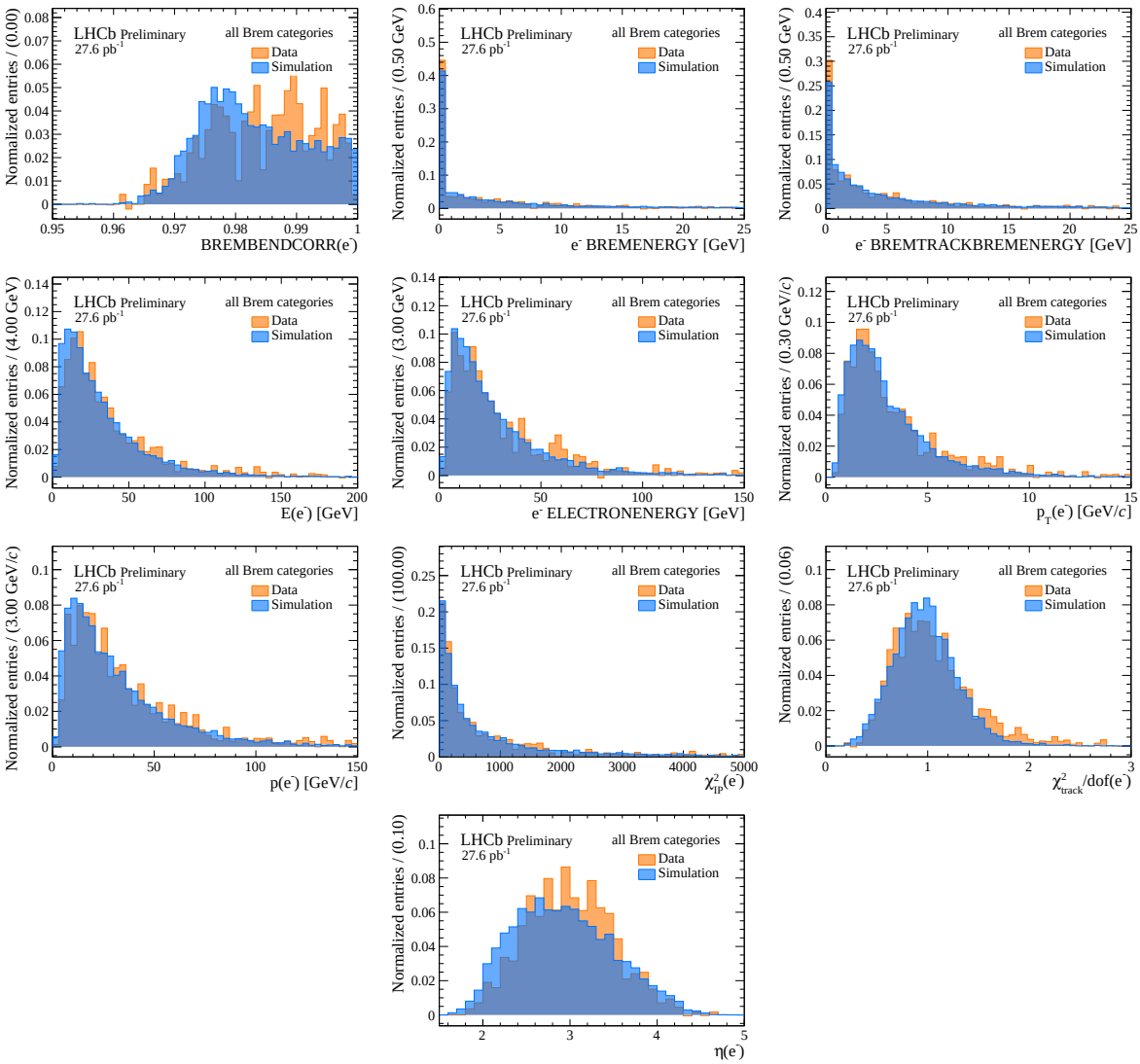

Figure P.6 – Additionnal comparison of the variable distributions related to the e^- in the $B^+ \to K^+ J/\psi(\to e^+e^-)$ simulation sample and the ${}_s\mathcal{W}eight$ted data.

Bibliography

[1] T. Aoyama *et al.*, *The anomalous magnetic moment of the muon in the Standard Model*, Phys. Rept. **887** (2020) 1, arXiv:2006.04822.

[2] S. Borsanyi *et al.*, *Leading hadronic contribution to the muon magnetic moment from lattice QCD*, Nature **593** (2021) 51, arXiv:2002.12347.

[3] LHCb collaboration, *Physics case for an LHCb Upgrade II — Opportunities in flavour physics, and beyond, in the HL-LHC era*, arXiv:1808.08865.

[4] LHCb collaboration, R. Aaij *et al.*, *Observation of $J/\psi p$ resonances consistent with pentaquark states in $\Lambda_b^0 \to J/\psi p K^-$ decays*, Phys. Rev. Lett. **115** (2015) 072001, arXiv:1507.03414.

[5] S. Descotes-Genon and M. Novoa Brunet, *Angular analysis of the rare decay $\Lambda_b^0 \to \Lambda(1520)(\to NK)\ell^+\ell^-$* , JHEP **06** (2019) 136, arXiv:1903.00448.

[6] L. Mott and W. Roberts, *Rare dileptonic decays of Λ_b^0 in a quark model*, Int. J. Mod. Phys. A **27** (2012) 1250016, arXiv:1108.6129.

[7] S. Meinel and G. Rendon, *$\Lambda_c \to \Lambda^*(1520)$ form factors from lattice QCD and improved analysis of the $\Lambda_b^0 \to \Lambda^*(1520)$ and $\Lambda_b^0 \to \Lambda_c^*(2595, 2625)$ form factors*, Phys. Rev. D **105** (2022) 054511, arXiv:2107.13140.

[8] Y. Amhis, M. Bordone, and M. Reboud, *Dispersive analysis of $\Lambda_b^0 \to \Lambda(1520)$ local form factors*, arXiv:2208.08937.

[9] D. Martínez Santos and F. Dupertuis, *Mass distributions marginalized over per-event errors*, Nucl. Instrum. Meth. A **764** (2014) 150, arXiv:1312.5000.

[10] P. Böer, T. Feldmann, and D. van Dyk, *Angular Analysis of the Decay $\Lambda_b^0 \to \Lambda(\to N\pi)\ell^+\ell^-$*, JHEP **01** (2015) 155, arXiv:1410.2115.

[11] S. Berryman, *Democritus*, in *The Stanford Encyclopedia of Philosophy* (E. N. Zalta and U. Nodelman, eds.). Metaphysics Research Lab, Stanford University, Spring 2023 ed., 2023.

[12] D. Griffiths, *Introduction to elementary particles*, WILEY-VCH Verlag GmbH & Co, 2008.

[13] J. Woithe, G. J. Wiener, and F. F. V. der Veken, *Let's have a coffee with the standard model of particle physics!*, Physics Education **52** (2017) 034001.

[14] M. Thomson, *Modern particle physics*, Cambridge University Press, New York, 2013.

[15] M. D. Schwartz, *Quantum Field Theory and the Standard Model*, Cambridge University Press, 2014.

[16] UA1 collaboration, G. Arnison *et al.*, *Experimental Observation of Lepton Pairs of Invariant Mass Around* 95 GeV/c^2 *at the CERN SPS Collider*, Phys. Lett. **B126** (1983) 398.

[17] UA1 collaboration, G. Arnison *et al.*, *Experimental Observation of Isolated Large Transverse Energy Electrons with Associated Missing Energy at* $\sqrt{s} = 540$ *GeV*, Phys. Lett. **B122** (1983) 103.

[18] ATLAS collaboration, G. Aad *et al.*, *Observation of a new particle in the search for the Standard Model Higgs boson with the ATLAS detector at the LHC*, Phys. Lett. **B716** (2012) 1, arXiv:1207.7214.

[19] CMS collaboration, S. Chatrchyan *et al.*, *Observation of a new boson at a mass of 125 GeV with the CMS experiment at the LHC*, Phys. Lett. **B716** (2012) 30, arXiv:1207.7235.

[20] C. Burgard and D. Galbraith, *Example: Standard model of physics*, https://texample.net/tikz/examples/model-physics/, 2016. Accessed: 2023-01-04.

[21] Particle Data Group, R. L. Workman *et al.*, *Review of particle physics*, Prog. Theor. Exp. Phys. **2022** (2022) 083C01.

[22] Y.-R. Liu *et al.*, *Pentaquark and tetraquark states*, Progress in Particle and Nuclear Physics **107** (2019) 237.

[23] L. Marleau, *Introduction à la physique des particules*, Département de physique, de gènie physique et d'optique, Université Laval, Québec, Canada, 1998-2008.

[24] Y. Kawamura, *Yukawa interactions, flavor symmetry, and non-canonical Kähler potential*, PTEP **2019** (2019) 043B05, arXiv:1808.06315.

[25] OPAL collaboration, G. Abbiendi *et al.*, *Precise determination of the Z resonance parameters at LEP: 'Zedometry'*, Eur. Phys. J. C **19** (2001) 587, arXiv:hep-ex/0012018.

[26] ATLAS collaboration, M. Aaboud *et al.*, *Precision measurement and interpretation of inclusive* W^+ *,* W^- *and* Z/γ^* *production cross sections with the ATLAS detector*, Eur. Phys. J. C **77** (2017) 367, arXiv:1612.03016.

[27] ATLAS collaboration, G. Aad *et al.*, *Test of the universality of τ and μ lepton couplings in W-boson decays with the ATLAS detector*, Nature Phys. **17** (2021) 813, arXiv:2007.14040.

[28] L. Wolfenstein, *Parametrization of the kobayashi-maskawa matrix*, Phys. Rev. Lett. **51** (1983) 1945.

[29] A. J. Buras, M. E. Lautenbacher, and G. Ostermaier, *Waiting for the top quark mass, $K^+ \to \pi^+$ neutrino anti-neutrino, B_s^0- anti-B_s^0 mixing and CP asymmetries in B decays*, Phys. Rev. **D50** (1994) 3433, arXiv:hep-ph/9403384.

[30] C. Jarlskog, *Commutator of the Quark Mass Matrices in the Standard Electroweak Model and a Measure of Maximal CP Nonconservation*, Phys. Rev. Lett. **55** (1985) 1039.

[31] M. B. Gavela, P. Hernandez, J. Orloff, and O. Pène, *Standard model CP violation and baryon asymmetry*, Mod. Phys. Lett. **A9** (1994) 795, arXiv:hep-ph/9312215.

[32] T. Aoyama *et al.*, *The anomalous magnetic moment of the muon in the Standard Model*, Phys. Rept. **887** (2020) 1, arXiv:2006.04822.

[33] D. Tong, *Lectures on cosmology*, http://www.damtp.cam.ac.uk/user/tong/cosmo/one.pdf, 2019. Accessed: 2023-01-18.

[34] B. T. Cleveland *et al.*, *Measurement of the solar electron neutrino flux with the Homestake chlorine detector*, Astrophys. J. **496** (1998) 505.

[35] J. G. Learned, *The saga of atmospheric neutrinos*, in *International Conference on History of the Neutrino: 1930-2018*, 2019.

[36] T. A. Kirsten, *Solar neutrinos: the pioneering experiments*, in *International Conference on History of the Neutrino: 1930-2018*, 2019.

[37] Super-Kamiokande collaboration, Y. Fukuda *et al.*, *Evidence for oscillation of atmospheric neutrinos*, Phys. Rev. Lett. **81** (1998) 1562, arXiv:hep-ex/9807003.

[38] LIGO Scientific, Virgo collaboration, B. P. Abbott *et al.*, *Observation of Gravitational Waves from a Binary Black Hole Merger*, Phys. Rev. Lett. **116** (2016) 061102, arXiv:1602.03837.

[39] J. H. Christenson, J. W. Cronin, V. L. Fitch, and R. Turlay, *Evidence for the 2π decay of the k_2^0 meson*, Phys. Rev. Lett. **13** (1964) 138.

[40] UTfit collaboration, M. Bona *et al.*, *Model-independent constraints on $\Delta F = 2$ operators and the scale of new physics*, JHEP **03** (2008) 049, arXiv:0707.0636.

[41] M. Kobayashi and T. Maskawa, *CP-violation in the renormalizable theory of weak interaction*, Prog. Theor. Phys. **49** (1973) 652.

[42] ARGUS collaboration, H. Albrecht *et al.*, *Observation of $B^0 - \overline{B}^0$ Mixing*, Phys. Lett. B **192** (1987) 245.

[43] CDF collaboration, F. Abe *et al.*, *Observation of top quark production in $\overline{p}p$ collisions*, Phys. Rev. Lett. **74** (1995) 2626, arXiv:hep-ex/9503002.

[44] D0 collaboration, S. Abachi *et al.*, *Search for high mass top quark production in $p\overline{p}$ collisions at $\sqrt{s} = 1.8$ TeV*, Phys. Rev. Lett. **74** (1995) 2422, arXiv:hep-ex/9411001.

[45] M. Ciuchini *et al.*, *Charming penguins and lepton universality violation in $b \to s\ell^+\ell^-$ decays*, Eur. Phys. J. C **83** (2023) 64, arXiv:2110.10126.

[46] W. Wang and S. Zhao, *Implications of the R_K and R_{K^*} anomalies*, Chinese Physics C **42** (2018) 013105.

[47] S.-L. Chen *et al.*, *Signatures of a flavor changing Z' boson in $B_q \to \gamma Z'$*, Nucl. Phys. B **962** (2021) 115237, arXiv:2006.03383.

[48] G. C. Branco *et al.*, *Theory and phenomenology of two-Higgs-doublet models*, Phys. Rept. **516** (2012) 1, arXiv:1106.0034.

[49] P. Fayet and S. Ferrara, *Supersymmetry*, Phys. Rept. **32** (1977) 249.

[50] T. Blake, G. Lanfranchi, and D. M. Straub, *Rare B Decays as Tests of the Standard Model*, Prog. Part. Nucl. Phys. **92** (2017) 50, arXiv:1606.00916.

[51] B. Grinstein, R. P. Springer, and M. B. Wise, *Effective Hamiltonian for Weak Radiative B Meson Decay*, Phys. Lett. B **202** (1988) 138.

[52] G. Buchalla, A. J. Buras, and M. E. Lautenbacher, *Weak decays beyond leading logarithms*, Rev. Mod. Phys. **68** (1996) 1125, arXiv:hep-ph/9512380.

[53] U. Egede and J. Serrano, *Rare b-hadron decays*, Comptes Rendus. Physique **21** (2020) 93.

[54] N. Gubernari, M. Reboud, D. van Dyk, and J. Virto, *Improved theory predictions and global analysis of exclusive $b \to s\mu^+\mu^-$ processes*, JHEP **09** (2022) 133, arXiv:2206.03797.

[55] N. Gubernari, D. van Dyk, and J. Virto, *Non-local matrix elements in $B_{(s)} \to \{K^{(*)}, \phi\}\ell^+\ell^-$*, JHEP **02** (2021) 088, arXiv:2011.09813.

[56] G. Tetlalmatzi-Xolocotzi, *Rare Leptonic B decays*, PoS **BEAUTY2018** (2018) 043, arXiv:1809.00637.

[57] S. Jäger, M. Kirk, A. Lenz, and K. Leslie, *Charming new physics in rare B-decays and mixing?*, Phys. Rev. D **97** (2018) 015021, arXiv:1701.09183.

[58] LHCb collaboration, R. Aaij *et al.*, *Test of lepton universality in $b \to s\ell^+\ell^-$ decays*, arXiv:2212.09152, to appear in Phys. Rev. Lett.

[59] L. collaboration, *Material for conferences*, https://twiki.cern.ch/twiki/bin/view/LHCbPhysics/RareDecayConferenceMaterial, 2015. Accessed on 21/07/2023.

[60] LHCb collaboration, R. Aaij *et al.*, *Measurement of the $\Lambda_b^0 \to \Lambda(1520)\mu^+\mu^-$ differential branching fraction*, arXiv:2302.08262, submitted to JHEP.

[61] LHCb collaboration, R. Aaij *et al.*, *Differential branching fractions and isospin asymmetries of $B \to K^{(*)}\mu^+\mu^-$ decays*, JHEP **06** (2014) 133, arXiv:1403.8044.

[62] LHCb collaboration, R. Aaij *et al.*, *Measurements of the S-wave fraction in $B^0 \to K^+\pi^-\mu^+\mu^-$ decays and the $B^0 \to K^*(892)^0\mu^+\mu^-$ differential branching fraction*, JHEP **11** (2016) 047, Erratum ibid. **04** (2017) 142, arXiv:1606.04731.

[63] LHCb collaboration, R. Aaij *et al.*, *Differential branching fraction and angular analysis of the decay $B^0 \to K^+\pi^-\mu^+\mu^-$ in the $K^*_{0,2}(1430)^0$ region*, JHEP **12** (2016) 065, arXiv:1609.04736.

[64] LHCb collaboration, R. Aaij *et al.*, *First measurement of the differential branching fraction and CP asymmetry of the $B^+ \to \pi^+\mu^+\mu^-$ decay*, JHEP **10** (2015) 034, arXiv:1509.00414.

[65] LHCb collaboration, R. Aaij *et al.*, *Differential branching fraction and angular analysis of $\Lambda_b^0 \to \Lambda\mu^+\mu^-$ decays*, JHEP **06** (2015) 115, Erratum ibid. **09** (2018) 145, arXiv:1503.07138.

[66] LHCb collaboration, R. Aaij *et al.*, *Branching fraction measurements of the rare $B_s^0 \to \phi\mu^+\mu^-$ and $B_s^0 \to f_2'(1525)\mu^+\mu^-$ decays*, Phys. Rev. Lett. **127** (2021) 151801, arXiv:2105.14007.

[67] CMS collaboration, V. Khachatryan *et al.*, *Angular analysis of the decay $B^0 \to K^{*0}\mu^+\mu^-$ from pp collisions at $\sqrt{s} = 8$ TeV*, Phys. Lett. B **753** (2016) 424, arXiv:1507.08126.

[68] W. Detmold, C.-J. D. Lin, S. Meinel, and M. Wingate, *$\Lambda_b^0 \to \Lambda\ell^+\ell^-$ form factors and differential branching fraction from lattice QCD*, Phys. Rev. D **87** (2013) 074502, arXiv:1212.4827.

[69] Belle collaboration, J.-T. Wei *et al.*, *Measurement of the Differential Branching Fraction and Forward-Backward Asymmetry for $B \to K^{(*)}\ell^+\ell^-$*, Phys. Rev. Lett. **103** (2009) 171801, arXiv:0904.0770.

[70] BELLE collaboration, S. Choudhury *et al.*, *Test of lepton flavor universality and search for lepton flavor violation in $B \to K\ell^+\ell^-$ decays*, JHEP **03** (2021) 105, arXiv:1908.01848.

[71] BaBar collaboration, J. P. Lees *et al.*, *Measurement of Branching Fractions and Rate Asymmetries in the Rare Decays* $B \to K^{(*)} l^+ l^-$, Phys. Rev. D **86** (2012) 032012, arXiv:1204.3933.

[72] CMS collaboration, S. Chatrchyan *et al.*, *Angular Analysis and Branching Fraction Measurement of the Decay* $B^0 \to K^{*0}\mu^+\mu^-$, Phys. Lett. B **727** (2013) 77, arXiv:1308.3409.

[73] CDF collaboration, T. Aaltonen *et al.*, *Observation of the Baryonic Flavor-Changing Neutral Current Decay* $\Lambda_b^0 \to \Lambda\mu^+\mu^-$, Phys. Rev. Lett. **107** (2011) 201802, arXiv:1107.3753.

[74] Flavour Lattice Averaging Group (FLAG), Y. Aoki *et al.*, *FLAG Review 2021*, Eur. Phys. J. C **82** (2022) 869, arXiv:2111.09849.

[75] C. Bobeth *et al.*, $B_{s,d} \to l^+ l^-$ *in the Standard Model with Reduced Theoretical Uncertainty*, Phys. Rev. Lett. **112** (2014) 101801, arXiv:1311.0903.

[76] M. Beneke, C. Bobeth, and R. Szafron, *Power-enhanced leading-logarithmic QED corrections to* $B_q \to \mu^+\mu^-$, JHEP **10** (2019) 232, arXiv:1908.07011, [Erratum: JHEP 11, 099 (2022)].

[77] W. Altmannshofer, C. Niehoff, and D. M. Straub, $B_s \to \mu^+\mu^-$ *as current and future probe of new physics*, JHEP **05** (2017) 076, arXiv:1702.05498.

[78] LHCb collaboration, R. Aaij *et al.*, *Measurement of CP-averaged observables in the* $B^0 \to K^{*0}\mu^+\mu^-$ *decay*, Phys. Rev. Lett. **125** (2020) 011802, arXiv:2003.04831.

[79] LHCb collaboration, R. Aaij *et al.*, *Angular analysis of the* $B^+ \to K^{*+}\mu^+\mu^-$ *decay*, Phys. Rev. Lett. **126** (2021) 161802, arXiv:2012.13241.

[80] LHCb collaboration, R. Aaij *et al.*, *Angular analysis of the rare decay* $B_s^0 \to \phi\mu^+\mu^-$, JHEP **11** (2021) 043, arXiv:2107.13428.

[81] ATLAS collaboration, M. Aaboud *et al.*, *Angular analysis of* $B_d^0 \to K^*\mu^+\mu^-$ *decays in pp collisions at* $\sqrt{s} = 8$ *TeV with the ATLAS detector*, JHEP **10** (2018) 047, arXiv:1805.04000.

[82] Belle collaboration, S. Wehle *et al.*, *Lepton-Flavor-Dependent Angular Analysis of* $B \to K^*\ell^+\ell^-$, Phys. Rev. Lett. **118** (2017) 111801, arXiv:1612.05014.

[83] CMS collaboration, A. M. Sirunyan *et al.*, *Measurement of angular parameters from the decay* $\mathrm{B}^0 \to \mathrm{K}^{*0}\mu^+\mu^-$ *in proton-proton collisions at* $\sqrt{s} = 8$ *TeV*, Phys. Lett. B **781** (2018) 517, arXiv:1710.02846.

[84] LHCb collaboration, R. Aaij *et al.*, *Strong constraints on the* $b \to s\gamma$ *photon polarisation from* $B^0 \to K^{*0}e^+e^-$ *decays*, JHEP **12** (2020) 081, arXiv:2010.06011.

[85] LHCb collaboration, R. Aaij *et al.*, *First experimental study of photon polarization in radiative B_s^0 decays*, Phys. Rev. Lett. **118** (2017) 021801, arXiv:1609.02032.

[86] LHCb collaboration, R. Aaij *et al.*, *Measurement of the photon polarization in $\Lambda_b^0 \to \Lambda\gamma$ decays*, arXiv:2111.10194, submitted to PRL.

[87] LHCb collaboration, R. Aaij *et al.*, *Observation of photon polarization in the $b \to s\gamma$ transition*, Phys. Rev. Lett. **112** (2014) 161801, arXiv:1402.6852.

[88] BaBar collaboration, B. Aubert *et al.*, *Measurement of Time-Dependent CP Asymmetry in $B^0 \to K_S^0\pi^0\gamma$ Decays*, Phys. Rev. D **78** (2008) 071102, arXiv:0807.3103.

[89] Belle collaboration, Y. Ushiroda *et al.*, *Time-Dependent CP Asymmetries in $B^0 \to K_S^0\pi^0\gamma$ transitions*, Phys. Rev. D **74** (2006) 111104, arXiv:hep-ex/0608017.

[90] LHCb collaboration, R. Aaij *et al.*, *Measurement of CP-violating and mixing-induced observables in $B_s^0 \to \phi\gamma$ decays*, Phys. Rev. Lett. **123** (2019) 081802, arXiv:1905.06284.

[91] G. Hiller and F. Kruger, *More model-independent analysis of $b \to s$ processes*, Phys. Rev. D **69** (2004) 074020, arXiv:hep-ph/0310219.

[92] M. Bordone, G. Isidori, and A. Pattori, *On the Standard Model predictions for R_K and R_{K^*}*, Eur. Phys. J. C **76** (2016) 440, arXiv:1605.07633.

[93] LHCb collaboration, R. Aaij *et al.*, *Tests of lepton universality using $B^0 \to K_S^0\ell^+\ell^-$ and $B^+ \to K^{*+}\ell^+\ell^-$ decays*, Phys. Rev. Lett. **128** (2022) 191802, arXiv:2110.09501.

[94] LHCb collaboration, R. Aaij *et al.*, *Measurement of lepton universality parameters in $B^+ \to K^+\ell^+\ell^-$ and $B^0 \to K^{*0}\ell^+\ell^-$ decays*, arXiv:2212.09153, to appear in Phys. Rev. D.

[95] LHCb collaboration, R. Aaij *et al.*, *Test of lepton universality using $\Lambda_b^0 \to pK^-\ell^+\ell^-$ decays*, JHEP **05** (2020) 040, arXiv:1912.08139.

[96] Belle collaboration, A. Abdesselam *et al.*, *Test of Lepton-Flavor Universality in $B \to K^*\ell^+\ell^-$ Decays at Belle*, Phys. Rev. Lett. **126** (2021) 161801, arXiv:1904.02440.

[97] LHCb collaboration, R. Aaij *et al.*, *Test of lepton universality in beauty-quark decays*, Nature Physics **18** (2022) 277, arXiv:2103.11769.

[98] LHCb collaboration, R. Aaij *et al.*, *Test of lepton universality with $B^0 \to K^{*0}\ell^+\ell^-$ decays*, JHEP **08** (2017) 055, arXiv:1705.05802.

[99] N. Gubernari, M. Reboud, D. van Dyk, and J. Virto, *Improved theory predictions and global analysis of exclusive $b \to s\mu^+\mu^-$ processes*, JHEP **09** (2022) 133, arXiv:2206.03797.

[100] (HPQCD collaboration)§, HPQCD, W. G. Parrott, C. Bouchard, and C. T. H. Davies, *$B \to K$ and $D \to K$ form factors from fully relativistic lattice QCD*, Phys. Rev. D **107** (2023) 014510, arXiv:2207.12468.

[101] B. Capdevila, *Status of the global $b \to s\ell^+\ell^-$ fits*, https://indico.cern.ch/event/1166059/contributions/5305415/attachments/2655326/4598548/FPCP_2023_Talk.pdf, 2023. Accessed on 21/07/2023.

[102] M. Algueró *et al.*, *To (b)e or not to (b)e: No electrons at LHCb*, arXiv:2304.07330.

[103] A. Greljo, J. Salko, A. Smolkovič, and P. Stangl, *Rare b decays meet high-mass Drell-Yan*, JHEP **05** (2023) 087, arXiv:2212.10497.

[104] M. Ciuchini *et al.*, *Constraints on lepton universality violation from rare B decays*, Phys. Rev. D **107** (2023) 055036, arXiv:2212.10516.

[105] T. Hurth, F. Mahmoudi, D. Martinez Santos, and S. Neshatpour, *Neutral current B-decay anomalies*, in *8th Workshop on Theory, Phenomenology and Experiments in Flavour Physics: Neutrinos, Flavor Physics and Beyond*, 2022, arXiv:2210.07221.

[106] V. Lisovskyi, *Study of rare b-baryon decays and test of lepton universality at LHCb*, PhD thesis, Université Paris-Saclay, 2019, Presented 09 Sep 2019.

[107] Y. Amhis *et al.*, *Prospects for New Physics searches with $\Lambda_b^0 \to \Lambda(1520)\ell^+\ell^-$ decays*, Eur. Phys. J. Plus **136** (2021) 614, arXiv:2005.09602.

[108] LHCb collaboration, R. Aaij *et al.*, *Measurement of the $\Lambda_b^0 \to J/\psi\Lambda$ angular distribution and the Λ polarisation in pp collisions*, JHEP **06** (2020) 110, arXiv:2004.10563.

[109] LHCb collaboration, R. Aaij *et al.*, *Angular moments of the decay $\Lambda_b^0 \to \Lambda\mu^+\mu^-$ at low hadronic recoil*, JHEP **09** (2018) 146, arXiv:1808.00264.

[110] Y.-S. Li, S.-P. Jin, J. Gao, and X. Liu, *The transition form factors and angular distributions of the $\Lambda_b^0 \to \Lambda(1520)(\to N\bar{K})\ell^+\ell^-$ decay supported by baryon spectroscopy*, arXiv:2210.04640.

[111] T. Blake and M. Kreps, *Angular distribution of polarised Λ_b^0 baryons decaying to $\Lambda\ell^+\ell^-$*, JHEP **11** (2017) 138, arXiv:1710.00746.

[112] D. Das and J. Das, *The $\Lambda_b^0 \to \Lambda^*(1520)(\to N\bar{K})\ell^+\ell^-$ decay at low-recoil in HQET*, arXiv:2003.08366.

[113] S. Meinel and G. Rendon, *$\Lambda_b^0 \to \Lambda^*(1520)\ell^+\ell^-$ form factors from lattice QCD*, Phys. Rev. **D103** (2021) 074505, arXiv:2009.09313.

[114] M. Bordone, *Heavy Quark Expansion of $\Lambda_b^0 \to \Lambda^*(1520)$ Form Factors beyond Leading Order*, Symmetry **13** (2021) 531, arXiv:2101.12028.

[115] G. Hiller and R. Zwicky, *Endpoint relations for baryons*, JHEP **11** (2021) 073, arXiv:2107.12993.

[116] LHCb collaboration, *LHCb reoptimized detector design and performance: Technical Design Report*, CERN-LHCC-2003-030, 2003.

[117] J. Haffner, *The CERN accelerator complex. Complexe des accélérateurs du CERN*, https://cds.cern.ch/record/1621894, 2013. General Photo.

[118] J.-L. Caron, *LHC layout. Schema general du LHC*, https://cds.cern.ch/record/841573, 1997. AC Collection. Legacy of AC. Pictures from 1992 to 2002.

[119] ALICE collaboration, K. Aamodt *et al.*, *The ALICE experiment at the CERN LHC*, JINST **3** (2008) S08002.

[120] ATLAS collaboration, G. Aad *et al.*, *The ATLAS Experiment at the CERN Large Hadron Collider*, JINST **3** (2008) S08003.

[121] CMS collaboration, S. Chatrchyan *et al.*, *The CMS Experiment at the CERN LHC*, JINST **3** (2008) S08004.

[122] LHCb collaboration, A. A. Alves Jr. *et al.*, *The LHCb detector at the LHC*, JINST **3** (2008) S08005.

[123] LHCb collaboration, S. Amato *et al.*, *LHCb technical proposal: A Large Hadron Collider Beauty Experiment for Precision Measurements of CP Violation and Rare Decays*, 1998.

[124] LHCb collaboration, R. Aaij *et al.*, *LHCb detector performance*, Int. J. Mod. Phys. **A30** (2015) 1530022, arXiv:1412.6352.

[125] LHCb collaboration, C. Elsasser, *$\bar{b}b$ production angle plots*, https://lhcb.web.cern.ch/lhcb/speakersbureau/html/bb_ProductionAngles.html. Accessed on 18/07/2023.

[126] LHCb collaboration, R. Aaij *et al.*, *Measurement of b-hadron fractions in 13 TeV pp collisions*, Phys. Rev. **D100** (2019) 031102(R), arXiv:1902.06794.

[127] LHCb collaboration, R. Aaij *et al.*, *Study of the kinematic dependences of Λ_b^0 production in pp collisions and a measurement of the $\Lambda_b^0 \to \Lambda_c^+ \pi^-$ branching fraction*, JHEP **08** (2014) 143, arXiv:1405.6842.

[128] C. Abellan Beteta *et al.*, *Monitoring radiation damage in the LHCb Tracker Turicensis*, arXiv:1809.05063.

[129] LHCb collaboration, *LHCb magnet: Technical Design Report*, CERN-LHCC-2000-007, 2000.

[130] R. Aaij *et al.*, *Performance of the LHCb Vertex Locator*, JINST **9** (2014) P09007, arXiv:1405.7808.

[131] LHCb collaboration, P. Collins, *Approved velo conference plots*, https://lbtwiki.cern.ch/bin/view/VELO/VELOConferencePlots. Accessed on 19/07/2023.

[132] C. Elsasser *et al.*, *The LHCb Silicon Tracker* , CERN, Geneva, 2013. On behalf of the LHCb Silicon Tracker Group, Accessed on 20/07/2023.

[133] R. Aaij *et al.*, *Performance of the LHCb trigger and full real-time reconstruction in Run 2 of the LHC*, JINST **14** (2019) P04013, arXiv:1812.10790.

[134] P. d'Argent *et al.*, *Improved performance of the LHCb Outer Tracker in LHC Run 2*, JINST **12** (2017) P11016, arXiv:1708.00819.

[135] R. Arink *et al.*, *Performance of the LHCb Outer Tracker*, JINST **9** (2014) P01002, arXiv:1311.3893.

[136] C. Lippmann, *Particle identification*, Nucl. Instrum. Meth. A **666** (2012) 148, arXiv:1101.3276.

[137] LHCb RICH collaboration, A. Papanestis and C. D'Ambrosio, *Performance of the LHCb RICH detectors during the LHC Run II*, Nucl. Instrum. Meth. A **876** (2017) 221, arXiv:1703.08152.

[138] LHCb RICH Group, M. Adinolfi *et al.*, *Performance of the LHCb RICH detector at the LHC*, Eur. Phys. J. C **73** (2013) 2431, arXiv:1211.6759.

[139] LHCb collaboration, E. Picatoste Olloqui, *LHCb preshower(PS) and scintillating pad detector (SPD): Commissioning, calibration, and monitoring*, J. Phys. Conf. Ser. **160** (2009) 012046.

[140] C. Abellan Beteta *et al.*, *Calibration and performance of the LHCb calorimeters in Run 1 and 2 at the LHC*, arXiv:2008.11556, submitted to JINST.

[141] P. Perret and X. Vilasis-Cardona, *Performance of the LHCb calorimeters during the period 2010-2012*, J. Phys. : Conf. Ser. **587** (2015) 012012, see LHCb-TALK-2014-236.

[142] V. V. Gligorov, *Conceptualization, implementation, and commissioning of real-time analysis in the High Level Trigger of the LHCb experiment*, PhD thesis, Paris U., VI-VII, 2018, arXiv:1806.10912.

[143] D. A. Berninghoff, J. Albrecht, and V. Gligorov, *Bremsstrahlung Recovery of Electrons using Multivariate Methods* , CERN, Geneva, 2016.

[144] J.-M. Basels, *Search for the lepton flavour violating decay* $B_s^0 \to \phi e^{\pm}\mu^{\mp}$, Master's thesis, Rheinisch-Westfälische Technische Hochschule Aachen, Germany, 2019. Unpublished.

[145] A. A. Alves, Jr. *et al.*, *Performance of the LHCb muon system*, JINST **8** (2013) P02022, arXiv:1211.1346.

[146] A. A. Alves Jr. *et al.*, *Performance of the LHCb muon system*, JINST **8** (2013) P02022, arXiv:1211.1346.

[147] LHCb collaboration, *LHCb: Second addendum to the muon system technical design report*, 2005.

[148] R. Calabrese *et al.*, *Performance of the LHCb RICH detectors during LHC Run 2*, JINST **17** (2022) P07013, arXiv:2205.13400.

[149] LHCb collaboration, D. Derkach, M. Hushchyn, and N. Kazeev, *Machine Learning based Global Particle Identification Algorithms at the LHCb Experiment*, EPJ Web Conf. **214** (2019) 06011.

[150] LHCb collaboration, F. Dordei, *LHCb detector and trigger performance in Run II*, EPJ Web Conf. **164** (2017) 01016.

[151] R. Aaij *et al.*, *The LHCb Trigger and its Performance in 2011*, JINST **8** (2013) P04022, arXiv:1211.3055.

[152] O. Callot, M. Ferro-Luzzi, and P. Perret, *Using the spd multiplicity in the level-0 trigger* , CERN, Geneva, 2003.

[153] O. Callot, *FastVelo, a fast and efficient pattern recognition package for the Velo* , CERN, Geneva, 2011. LHCb.

[154] LHCb collaboration, *RTA and DPA dataflow diagrams for Run 1, Run 2, and theupgraded LHCb detector* , https://cds.cern.ch/record/2730181, 2020.

[155] *Letter of Intent for the LHCb Upgrade* , CERN, Geneva, 2011.

[156] LHCb collaboration, *Framework TDR for the LHCb Upgrade: Technical Design Report*, CERN-LHCC-2012-007, 2012.

[157] LHCb collaboration, *LHCb VELO Upgrade Technical Design Report*, CERN-LHCC-2013-021, 2013.

[158] LHCb collaboration, *LHCb Tracker Upgrade Technical Design Report*, CERN-LHCC-2014-001, 2014.

[159] LHCb collaboration, *LHCb PID Upgrade Technical Design Report*, CERN-LHCC-2013-022, 2013.

[160] M. Pivk and F. R. Le Diberder, *sPlot: A statistical tool to unfold data distributions*, Nucl. Instrum. Meth. **A555** (2005) 356, arXiv:physics/0402083.

[161] T. Sjöstrand, S. Mrenna, and P. Skands, *A brief introduction to PYTHIA 8.1*, Comput. Phys. Commun. **178** (2008) 852, arXiv:0710.3820.

[162] I. Belyaev *et al.*, *Handling of the generation of primary events in Gauss, the LHCb simulation framework*, J. Phys. Conf. Ser. **331** (2011) 032047.

[163] D. J. Lange, *The EvtGen particle decay simulation package*, Nucl. Instrum. Meth. **A462** (2001) 152.

[164] N. Davidson, T. Przedzinski, and Z. Was, *PHOTOS interface in C++: Technical and physics documentation*, Comp. Phys. Comm. **199** (2016) 86, arXiv:1011.0937.

[165] Geant4 collaboration, S. Agostinelli *et al.*, *Geant4: A simulation toolkit*, Nucl. Instrum. Meth. **A506** (2003) 250.

[166] Geant4 collaboration, J. Allison *et al.*, *Geant4 developments and applications*, IEEE Trans. Nucl. Sci. **53** (2006) 270.

[167] V. V. Gligorov, *Reconstruction of the Channel $B^0 \to D^+\pi^-$ and Background Classification at LHCb (revised)* , CERN, Geneva, 2007. revised version submitted on 2008-01-24 12:46:44.

[168] E. Aslanides *et al.*, *The level-0 muon trigger for the LHCb experiment*, Nuclear Instruments and Methods in Physics Research Section A: Accelerators, Spectrometers, Detectors and Associated Equipment **579** (2007) 989.

[169] V. V. Gligorov and M. Williams, *Efficient, reliable and fast high-level triggering using a bonsai boosted decision tree*, JINST **8** (2013) P02013, arXiv:1210.6861.

[170] T. Likhomanenko *et al.*, *LHCb Topological Trigger Reoptimization*, J. Phys. Conf. Ser. **664** (2015) 082025, arXiv:1510.00572.

[171] K. Do, T. Tran, and S. Venkatesh, *Matrix-centric neural networks*, CoRR **abs/1703.01454** (2017) arXiv:1703.01454.

[172] A. Hocker *et al.*, *TMVA - Toolkit for Multivariate Data Analysis*, arXiv:physics/0703039.

[173] I. Goodfellow, Y. Bengio, and A. Courville, *Deep Learning*, MIT Press, 2016. http://www.deeplearningbook.org.

[174] H. Deng, Y. Zhou, L. Wang, and C. Zhang, *Ensemble learning for the early prediction of neonatal jaundice with genetic features*, BMC Medical Informatics and Decision Making **21** (2021) , Use of original Fig. 2, licensed under a Creative Commons Attribution 4.0 International License.

[175] LHCb collaboration, R. Aaij *et al.*, *Measurement of the mass and production rate of Ξ_b^- baryons*, Phys. Rev. D **99** (2019) 052006, arXiv:1901.07075.

[176] CDF collaboration, T. Aaltonen *et al.*, *Observation of the Ω_b^- and Measurement of the Properties of the Ξ_b^- and Ω_b^-* , Phys. Rev. D **80** (2009) 072003, arXiv:0905.3123.

[177] LHCb collaboration, R. Aaij *et al.*, *Measurement of the mass difference and relative production rate of the Ω_b^- and Ξ_b^- baryons*, arXiv:2305.15329, submitted to Phys. Rev. D.

[178] BESIII collaboration, M. Ablikim *et al.*, *First observation of the semileptonic decay* $\Lambda_c^+ \to pK^-e^+\nu_e$, Phys. Rev. D **106** (2022) 112010, arXiv:2207.11483.

[179] S. Tolk, J. Albrecht, F. Dettori, and A. Pellegrino, *Data driven trigger efficiency determination at LHCb*, LHCb-PUB-2014-039, 2014.

[180] L. Anderlini *et al.*, *The PIDCalib package*, LHCb-PUB-2016-021, 2016.

[181] C. Langenbruch, *Parameter uncertainties in weighted unbinned maximum likelihood fits*, Eur. Phys. J. C **82** (2022) 393, arXiv:1911.01303.

[182] LHCb collaboration, R. Aaij *et al.*, *Observation of* $\Lambda_b^0 \to \psi(2S)pK^-$ *and* $\Lambda_b^0 \to J/\psi\pi^+\pi^-pK^-$ *decays and a measurement of the* Λ_b^0 *baryon mass*, JHEP **05** (2016) 132, arXiv:1603.06961.

[183] F. Beaujean, M. Chrząszcz, N. Serra, and D. van Dyk, *Extracting Angular Observables without a Likelihood and Applications to Rare Decays*, Phys. Rev. D **91** (2015) 114012, arXiv:1503.04100.

[184] R. A. Kycia and S. Jadach, *Relativistic Voigt profile for unstable particles in high energy physics*, J. Math. Anal. Appl. **463** (2018) 1040, arXiv:1711.09304.

[185] P. T. Matthews and A. Salam, *Relativistic field theory of unstable particles*, Phys. Rev. **112** (1958) 283.

[186] F. von Hippel and C. Quigg, *Centrifugal-barrier effects in resonance partial decay widths, shapes, and production amplitudes*, Phys. Rev. **D5** (1972) 624.

[187] A. Beck, T. Blake, and M. Kreps, *Angular distribution of* $\Lambda_b^0 \to pK^-\ell^+\ell^-$ *decays comprising* Λ *resonances with spin up to* $\leq 5/2$, arXiv:2210.09988.

[188] W. Verkerke and D. P. Kirkby, *The RooFit toolkit for data modeling*, eConf **C0303241** (2003) MOLT007, arXiv:physics/0306116.

[189] F. James and M. Roos, *Minuit: A System for Function Minimization and Analysis of the Parameter Errors and Correlations*, Comput. Phys. Commun. **10** (1975) 343.

[190] Y. Xie, *sFit: a method for background subtraction in maximum likelihood fit*, arXiv:0905.0724.

[191] A. V. Sarantsev *et al.*, *Hyperon II: Properties of excited hyperons*, Eur. Phys. J. A **55** (2019) 180, arXiv:1907.13387.

[192] G. J. Feldman and R. D. Cousins, *A Unified approach to the classical statistical analysis of small signals*, Phys. Rev. D **57** (1998) 3873, arXiv:physics/9711021.

[193] Particle Data Group, P. A. Zyla *et al.*, *Review of particle physics*, Prog. Theor. Exp. Phys. **2020** (2020) 083C01.

[194] A. Puig, *The LHCb trigger in 2011 and 2012*, LHCb-PUB-2014-046, 2014, do not cite this note in a paper. Its purpose is to document the trigger for data preservation.

[195] LHCb collaboration, R. Aaij *et al.*, *Design and performance of the LHCb trigger and full real-time reconstruction in Run 2 of the LHC*, JINST **14** (2019) P04013, arXiv:1812.10790.

[196] A. Scarabotto, *Tracking on GPU at LHCb's fully software trigger*, https://cds.cern.ch/record/2823783, 2022.

[197] LHCb collaboration, *Mass plots with early Run 3 data*, https://cds.cern.ch/record/2848498, 2023.

[198] LHCb collaboration, R. Aaij *et al.*, *Measurement of J/ψ production cross-sections in pp collisions at $\sqrt{s} = 5$ TeV*, JHEP **11** (2021) 181, arXiv:2109.00220.

[199] LHCb collaboration, R. Aaij *et al.*, *The LHCb upgrade I*, arXiv:2305.10515.

Acknowledgements

The three years of PhD were an exciting adventure with innumerable nice memories. The journey started with my NPAC internship under the supervision of Carla and Yasmine. You introduced me to the beauty of flavour physics, which changed my mind about b-physics. Both of you are brilliant scientists, and it became clear to me that I wanted to work with you for my PhD thesis. I would like to thank Carla for always having an answer to my questions, whether it was about coding, RTA, rare decays or theory. I appreciated all our nice discussions about physics, women in science and life in general.

A special thank you to Yasmine, who supervised and accompanied me during all three years of my PhD. I learned from you everything about angular analyses, b-baryons, dispersive bounds and $g_\mu - 2$. You trained me to be curious and to enrich my physics culture, whether it is about muon colliders, the understanding of tracking algorithms or new predictions of BSM models. In all the happy and difficult moments, you have been there for me. Thank you for not only being a great PhD supervisor but also being a marvellous human being.

I would like to express my gratitude to the two referees, Lesya Shchutska and Gianluca Inguglia, who studied this thesis manuscript entirely. You improved its quality with your questions and comments. Thank you to Achille Stocchi, Luca Silvestrini and Tim Gershon for agreeing to act as examiners. It is a pleasure for me that all of you attend the thesis defense in person.

This thesis manuscript was read entirely by Vitalii, who discussed with me the physics content and improved the writing. A huge thank you very much for your close look. I am also grateful for the support of Méril, Janina and Sebastian, who reviewed parts of the manuscript.

Thank you to Marie-Hélène for sharing her broad knowledge about $b \to s\ell^+\ell^-$ decays and advising me about the analysis strategy. I would like to thank Patrick for creating a pleasant and harmonious atmosphere in the lab. You recommended writing a manuscript of about 150 pages. (It became a bit longer; I'm sorry for every reader.) I appreciated

the nice discussions with Frédéric about life and politics. Thank you also to Guy, Sergey and Jacques.

Thank you to all the PhD students at IJCLab for the nice time we spent together, for going out and for becoming friends. I liked a lot our tradition of the "tour de monde de la nourriture". I am grateful to Chiara for cheering me up in difficult moments with apéros at the Seine, eating fancy food or watching movies outside. I will miss a lot our runs until "la tour Eiffel"! A big thank you to all the Penguins Gaëlle, Guillaume, Janina, Marie, Piera and Zhenzi. Thank you to Yuya, with whom I shared the office during all three years. There was always a nice atmosphere in our office(s) at the end of the floor. Thank you also to Bo, Vsevolod and Valeriia. I would like to thank the Belle II group of IJCLab, who were as interested in the b-anomalies as us.

I am thankful for the support of the LHCb group at IJCLab, which enabled me to travel to CERN, conferences and workshops. An amazing experience was the Lake Louise conference in Canada and the QCD@LHC conference dinner at the musée d'Orsay. During my thesis, I had the chance to spend two months at CERN. I had a great time in Geneva (and Saint-Genis-Pouilly) with Anja, Aniol, Albert, Nuria, Lukas, Paula and Alessandro. Thank you to Kara, Oscar and all the other LHCb colleagues for creating a friendly environment in our experiment.

I also would like to thank Peter Stangl for helping with the implementation of the $\Lambda_b^0 \to \Lambda(1520)\ell^+\ell^-$ differential decay width and the angular observables in FLAVIO. Thank you to Danny van Dyk for discussing the differential decay width of the $\Lambda_b^0 \to \Lambda_{1/2}^*\ell^+\ell^-$ decays, where the $\Lambda_{1/2}^*$ is decaying weakly. I learned a lot from the discussions with all the other theorists I got to know during my thesis.

A big thank you to all my family and friends, who cheered me up in difficult times. I enormously appreciate your support, and I am really grateful to have you. Sorry to everybody I did not mention, and thank you for reading all of this.